Advanced Materials and Engineering Applications

Edited by
Jiatao Zhang

TRANS TECH PUBLICATIONS

Advanced Materials and Engineering Applications

Edited by
Jiatao Zhang

Advanced Materials and Engineering Applications

Selected, peer reviewed papers from the
2012 SREE Conference on
Advanced Materials and Engineering Applications
(AMEA 2012),
May 5-6, 2012, Hong Kong

Edited by

Jiatao Zhang

Trans Tech Publications Ltd
Kreuzstrasse 10
CH-8635 Durnten-Zurich
Switzerland
http://www.ttp.net

Volume 161 of
Applied Mechanics and Materials
ISSN 1662-7490

Full text available online at *http://www.scientific.net*

***Distributed** worldwide by*

Trans Tech Publications Ltd
Kreuzstrasse 10
CH-8635 Durnten-Zurich
Switzerland

Fax: +41 (44) 922 10 33
e-mail: sales@ttp.net

and in the Americas by

Trans Tech Publications Inc.
PO Box 699, May Street
Enfield, NH 03748
USA

Phone: +1 (603) 632-7377
Fax: +1 (603) 632-5611
e-mail: sales-usa@ttp.net

Preface

SREE Conference on Advanced Materials and Engineering Applications (AMEA) aims to bring together academic scientists, leading engineers, industry researchers and scholar students to exchange and share their experiences and research results about all aspects of advanced materials and their engineering applications, and discuss the practical challenges encountered and the solutions adopted.

In 2012, AMEA will be held in Hong Kong, May 5-6 , 2012. AMEA 2012 aims to provide a forum for theoretical and technical exchanges regarding the advanced theories, methodologies and techniques about all aspects of advanced materials and their engineering applications. It has attracted some scholars, managers and researchers in relevant fields to discuss their ideas and experience together.

AMEA 2012 received about 190 submissions, which are involved in the fields as follows: *a*) Material Science; b) Metal materials; c) Non-metallic materials; d) Composite materials; e) Medical materials; f) Chemical materials; g) Electrician / Electrical Materials; h) Building Materials; i) Biological materials; j) Electronic / magnetic / optical materials.

55 selected papers are published in the AMEA 2012 proceedings, which are divided into seven topics: Material Science; Metal materials; Biological materials and Medical materials; Chemical materials; Electronic / magnetic / optical materials; other Materials; Advanced Materials Applications in Engineering.

I would like to thank Thomas Wohlbier, Anne Wohlbier and other editors from Trans Tech Publications for their excellent work, and hope AMEA 2012 will be successful.

Sponsored by

Society for Resources, Environment and Engineering（SREE）

Table of Contents

Chapter 4: Electronic / Magnetic / Optical Materials

Chapter 5: Chemical Materials

Chapter 6: Other Materials

Chapter 7: Advanced Materials Applications in Engineering

doi:10.4028/www.scientific.net/AMM.161.1

Organic pretreatment of recycled aggregates of rural construction waste

Jun LIU[1,2,a], Yao LI[1,b], Xuming WANG[3,c], Runqing LIU [1,d]

[1] School of Materials Science and Engineering, Shenyang Jianzhu University, Shenyang 110168,China

[2] School of Materials Science and Engineering, Shenyang Ligong University, Shenyang 110168,China

[3] School of Management Science and Engineering, Shenyang Jianzhu University, Shenyang 110168,China

[a] liujun2699@126.com, [b] 13998802511@163.com

[c] wangxumingfan@163.com,[d] liurunqing1980@163.com

Keywords: Recycled coarse aggregates; Discarded clay bricks; Physical and mechanical performance

Abstract: Through using acetic acid resin, asphalt and urea resin organic pretreatment methods to pretreat the surface of rural construction waste, and testing of crush index and water absorption rate of recycled coarse aggregate after pretreatment, the research for the influence of organic pretreatment technology on physical and mechanical performance of recycled coarse aggregate. The results prove that organic infiltrating pretreatment technology can effectively enhance the density of the coarse aggregate and decrease the crush of recycled coarse aggregate index, in a certain extent. The crush index of recycled coarse aggregates after organic pretreatment decreases at almost 17.63%, what's more, organic pretreatment technology can decrease the water absorption rate of coarse aggregate by a large margin. The water absorption rate of coarse aggregate can be reduced to a minimum of 2.03% which closes to the level of natural aggregates. Because of urea resin solidified into film at fast speed, high integrity and high wear resistance, and relatively cheap, urea resin's pretreatment effects on recycled coarse aggregates is better than acetic acid resin and asphalt.

Discarded clay bricks sintered is the main component of rural construction waste. The traditional processing method is making it piled up or buried. Not only consumes much of the farm- land and causes environmental pollution, but also a large number of money and labor for cleaning and transporting these construction are wasted. If these discarded clay bricks sintered are recyced effectively and used to the preparation of recycled concrete products by the crushing process in construction project, not only can solve the abandon problem of discarded clay bricks and make waste profitable, but also can protect the ecological environment, save natural sand resources. And they also play a positive role in reducing the waste of energy and resources.

At present, our country for construction waste recycling researches focuses mainly on the city. There are fewer researches on the villages, what's more, there are more lack of the pretreatment researches for turning rural construction waste into recycled coarse aggregate. As recycled coarse aggregate of discarded clay bricks in rural construction waste have the characteristics of small density, low strength and big water absorption rate than natural aggregate concrete or recycled coarse aggregate. And the difficulty of recycling is greater. In order to improve the performance of the coarse aggregate, we need to consider using some modification enhanced methods of the pretreatment. Organic pretreatment technology is just a very novel modification method for recycled coarse aggregate. It makes organic grout fill the pore and crack of the surface of coarse aggregate. In the surface of the coarse aggregate there is a higher consistency layer of film packaged after curing. It can make up of the surface defects of recycled coarse aggregate in a certain extent. This article chooses three different organisms slurry with acetic acid resin, asphalt, and urea-formaldehyde resin to infiltrate pretreatment of recycled coarse aggregate. Through testing

the index of the recycled coarse aggregate's crushing and water absorption rate index, study on the degree of improving recycled coarse aggregate basic physical mechanics by organic pretreatment technology. To provide the theory basis and practical basis for rural construction waste as recycled coarse aggregate used for wall materials.

1 The raw material and the test methods

1.1 The raw material. The uses in laboratory come from villages and small towns of Shenyang, and the essential component of construction waste of discarded clay bricks which physical index sees at table 1. Cement choosed is 32.5 magnitude ordinary Portland cement by Shenyang Jidong cement plant; The fineness modulus of sand is about 2.65; The pretreatment of organic solvents are commonly using acetic acid resin, petroleum bitumen emulsion and 531 urea formaldehyde resin adhesive. The diluents are spirit of vinegar and xina water.

Table 1 Physical performance indexes of discarded clay bricks

Apparent density (kg • m^{-3})	Bulk density (kg • m^{-3})	Water absorption rate（%）	Crush index（%）
1680	795	10.3	41.4

1.2 The test methods. The apparent density test, bulk density test, crush index test and water absorption rate test of recycled coarse aggregate all refer to The standard of quality and testing method of ordinary concrete with sand, stone(JGJ52-2006).

2 The test results and the analysis

2.1 The influences of acetic acid resin pretreatment technology on physical and mechanical performance of recycled coarse aggregate. The dosages of spirit of vinegar is 2%, 4% and 6%, and the time of blending spirit of vinegar with grout mix is 2h, 4h, 6h. The basic physical and mechanical performance indexes of recycled coarse aggregate which is pretreated by acetic acid resin and spirit of vinegar see in Fig.1

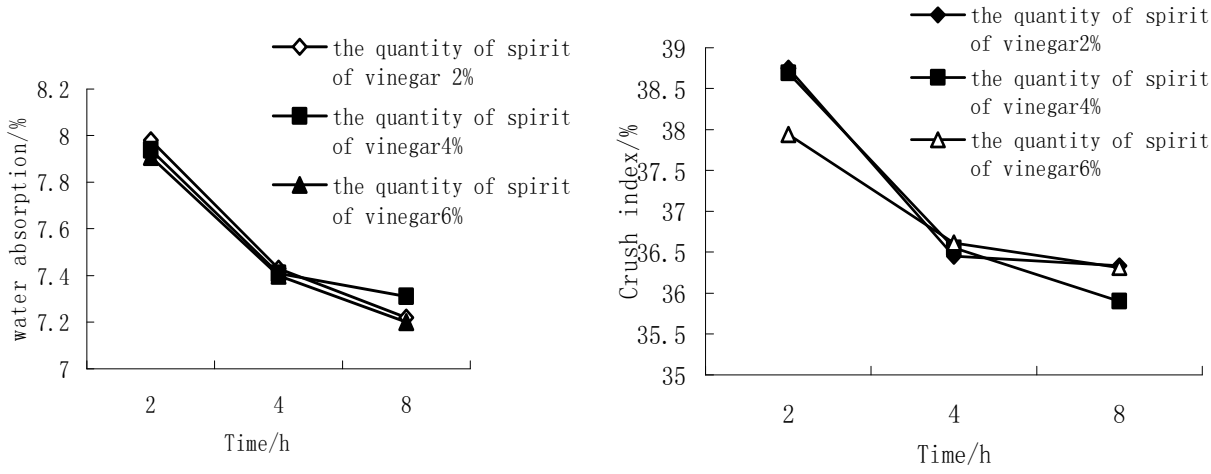

(a) Water absorption rate (b) Crush index

Fig.1 Performance of recycled coarse aggregate after pretreated by acetic acid resin and spirit of vinegar

In Fig.1(a) and (b), the graphs show that water absorption rate and crush index of recycled coarse aggregate with the increasing infiltration time will reduce, but the impact of the mixed quantity of spirit of vinegar is light. This shows that extending infiltration time is beneficial to uniform thickness and integrity of acetic acid resin and slurry of spirit of vinegar. Because of the water absorption rate of aggregate after wrapped film depends on the water absorption rate and complete degree of thin film, therefore, water absorption rate and strength of membrane structure have directly affected on the water absorption rate and crush indicators of recycled coarse aggregate

2.2 The influences of asphalt pretreatment technology on physical and mechanical performance of recycled coarse aggregate. Using asphalt replaces acetic acid resin, and make xina water as diluents, which quantity and infiltration time are the same as 2.1. The basic physical and mechanical performance of recycled coarse aggregate after pretreatment of asphalts and xina water see in Fig.2.

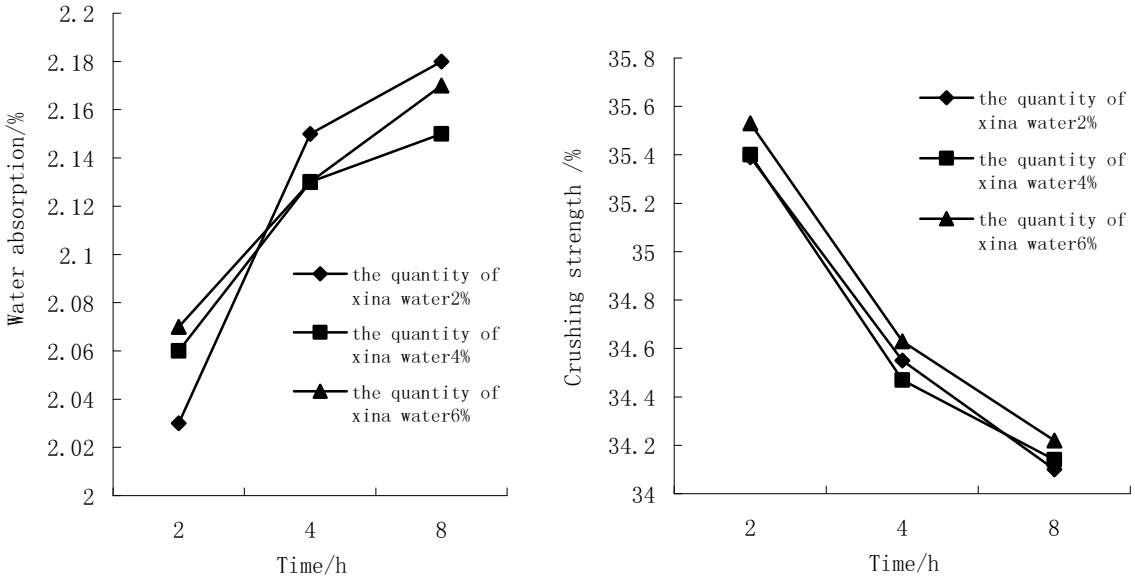

(a) Water absorption rate (b) Crush index

Fig.2 The performance of recycled coarse aggregate after pretreatment of asphalts and xina water

In Fig.2(a), the graph shows that asphalt treatment of recycled coarse aggregate water absorption rate is greatly improved. When recycled coarse aggregate infiltrates the asphalt adding 2% xina water after 2 hours, Water absorption rate of recycled coarse aggregate can drop to 2.03%, and has been closed to water absorption rate of natural aggregate.

In Fig.2(b), as is shown , recycled coarse aggregate infiltrates the asphalt adding 2% xina water after 8 hours. Crush index of the recycled coarse aggregate drops to a minimum of 34.10 only. This shows the membrane method of the pretreatment of the asphalt, won't fundamentally make recycled coarse aggregate close to the strength of the natural aggregate level. It's all because of low intensity of clay brick itself, adding to the broken screening process cause a secondary damage and make surface of recycled coarse aggregate crack defects and further increase. In addition, as the use of clay bricks fixed a number of years is much longer, the effect such as physical weathering the durability is fairly new clay bricks poor. The pretreatment of organic method is similar to the slurry wrapped stone process, But because after pretreatment organic material surface solidified into film, the strength of the coarse aggregate is far lower than the strength of the hardened cement, so the improvement of crush index don't change apparently.

2.3 The influences of urea resin pretreatment technology on physical and mechanical performance of recycled coarse aggregate. Considering strong dangers of the asphalt with volatile components to man`s body and the environment， and the asphalt has a strong temperature susceptibility. The asphalt easy to be brittle in winter，and easy to be soften in summer. These characteristics make the organic pretreatment process , mechanics and durability of recycled concrete in later stage have adverse effects. So consider using more convenient and much smaller pollution of resin products replace asphalt slurry to do infiltrate pretreatment test of recycled coarse aggregate.

When recycled coarse aggregate immerses in urea-formaldehyde resin grout 30 minutes，and at room temperature after 24 hours by air drying，the performance indexes of aggregate can be tested

Table 3 Performance testing table after urea resin modified recycled coarse aggregate

Infiltration time/h	Apparent density/（kg/m^3）	Bulk density /（kg/m^3）	Water absorption rate /%	Crush index /%
0.5	1850	905	2.63	35.22

As is shown from table 3, urea resin curing into the film makes the water absorption rate of recycled coarse aggregate be obviously reduced. This is because that urea-formaldehyde resin can permeate into the surface crack of recycled coarse aggregate and tiny compartments, produce mechanical meshing and inlay which make recycled coarse aggregate combine more firmly，and then make rough surface of coarse aggregate become lubricant. In addition, compared with acetic acid resin after curing the surface of recycled coarse aggregate, urea resin film in itself strength is higher and has excellent bonding, there is no appearance like acetic acid resin membrane into the breakage of phenomenon. The production of urea-formaldehyde resin is the poly condensation process of interaction between urea formaldehyde and urea. The raw materials of the preparation of the resin can be easily gotten, production equipment is simple, the price of raw materials is low, applicability is good, and can be used widely. Bonding strength is high, heat resistance and resistance to damp are good. These are positive aspects of organic pretreatment of recycled coarse aggregate of all rural construction wastes. But urea-formaldehyde resin itself has its disadvantages: when the production control is improper, it will contain traces of free formaldehyde, overflow penetrating odor. It is worth to pay attention to the process of organic pretreatment.

2.4 Organic pretreatment technology in the optimization of slurry. As water absorption rate directly affects the work-ability of mixture of recycled concrete, and has decisive effect on the later dry shrinkage of concrete, so the decrease of water absorption rate is the most essential to the treatment effect evaluation index. In consideration of choice for water absorption rate from acetic acid resin, asphalt factors the pretreatment of the test to select the lowest water absorption rate(That is acetic acid resin mixes with 6% spirit of vinegar and infiltrates eight hours; Asphalt content 2% xina water , infiltrates 2 hours), and compare the unmodified urea-formaldehyde resin before with the pretreatment of recycled coarse aggregate basic performance comparison, The results as shown in figure 3 below (recycled coarse aggregate performance of the various data calibration marked as 1, the infiltration of preprocessing performance indexes of the aggregate respectively with corresponding, taking ratio for the vertical axis).

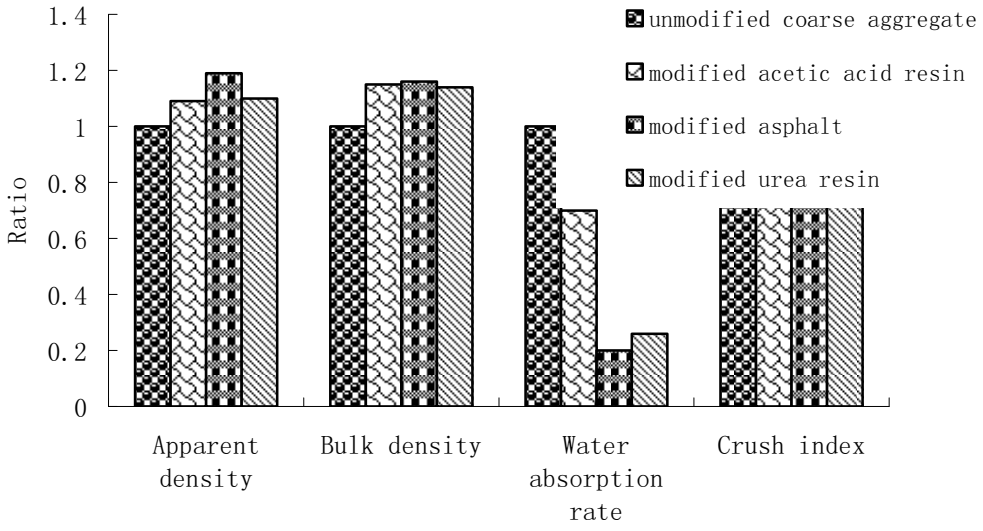

Figure 3 Comparison of modification effect of recycled coarse aggregate after pretreated by three kinds of organic grout

In figure 3, it can be directly seen that all kinds of basic physical and mechanical performances of recycled coarse aggregate after pretreatment of organic infiltration. That is to say, through infiltrating processes, enhancing the basic mechanical properties of recycled coarse aggregate is feasible. In apparent density, bulk density and crush index these indexes, the infiltrating pretreatment of three kinds of organic grout all can improve recycled coarse aggregate in a certain extent, but the gaps between three kinds of organic grout are not big. For water absorption rate of recycled coarse aggregate which is a important index, we can get the effects of pretreatment by the asphalt mixing diluents and infiltration of urea resin is better than acetic acid resin's

Through making a comprehensive comparison of pretreatment effects of recycled coarse aggregate which is pretreated by three kinds of slurry, the results show that infiltrating pretreatment method of urea resin grout has the characteristics of handiness, good integrity of Solidified into membrane, high density and lower water absorption rate and lower crush index of recycled coarse aggregate after pretreated. So this method can be used as a preparation of recycled coarse aggregate when making recycled coarse concrete. Even though infiltrating pretreatment methods of three kinds of Organic improving the strength of recycled coarse aggregate is limited, this is the reason that crush index of recycled coarse aggregate being pretreated by three kinds of organic grout are close to each other

3 Conclusion

(1) It is feasible to improve the performance of recycled coarse aggregate through processing method of organic slurry infiltration, it can not only increase the apparent density and bulk density of recycled coarse aggregate, but also can improve crush index, especially decrease the water absorption rate of recycled coarse aggregate more than 70 percent.

(2) Using acetic acid resin to infiltrate the pretreatment of the recycled coarse aggregate，it can effectively decrease its water absorption rate and crush index; The test of the best improvement effect with using acetic acid resin to infiltrate pretreatment of the recycled coarse aggregate is that adding 6% spirit of vinegar into the acetic acid resin and then infiltrating 8 hours.

(3) The effect of using asphalt to pretreated the recycled coarse aggregate is better than acetic acid resin, and also has a more obvious effect on improving the mechanical properties of recycled coarse aggregate; the test of the best improvement effect with using asphalt to infiltrate and pretreat the recycled coarse aggregate is that: adding 2% xina water into the asphalt and then infiltrating 2 hours.

(4) Urea resin solidified into film have the characteristics of high speed, good integrity, wear resistance, and relatively cheap costs. So the recycled coarse aggregate pretreatment effect can be maken better than acetic acid resin and asphalt

Acknowledgements

This work was financially supported by National Key Technology R&D Program of China for the 11th Five-Year Plan (2006BAJ04A04)

References

[1] DENG Shouchang, ZHANG Xuebing, LUO Yingshe, Abandon the concrete present condition of the reborn exploitation analysis and the research outlook, J. Concrete, 2006 (11): 20-24.
[2] XING Zhenxian, WANG Xiaoying, ZHAO Yuqing, Optimum mix ratio selection of PFA regenaration concrete by orthogonal design, J. Low Temperature Architecture Technology, 2004(4): 1307-1312.
[3] Ilker B, Sdim S, Properties of concretes produced with waste concrete aggregate, J. Cement and Concrete Research, 2004(4):1307-1312.
[4] Tam VW, GaoX F, Tam CM, Micro structural analysis of recycled aggregate concrete produced from two stage mixing approach, J. Cement and Concrete Research, 2005, 35(6):1195-1203.
[5] SHI Jianguang, XU Yuezhou, Experiment research and analysis of aggregate gradation on the strength and workability of recycled concrete, J. Concrete, 2008(1):82-86.

doi:10.4028/www.scientific.net/AMM.161.6

Application of Intensifying Secondary Concentration Technology in reverse flotation of bauxite

Xiaolin Zhang[1, a], Jianjun Fang [2,b] and Dianwen Liu [3,c]

[1] Kunming University of science and technology, Kunming, Yunnan province, China

[2] Kunming University of science and technology, Kunming, Yunnan province, China

[3] Kunming University of science and technology, Kunming, Yunnan province, China

[a]xiaolin6001@sina.com [b] ruiyuanju@126.com [c] ldwkust@126.com(corresponding author)

Keywords: Diasporic-bauxite; Intensifying Secondary Concentration Technology; De-silicate of Flotation

Abstract: In order to resolve the problem of fine particle flotation in the reverse flotation of bauxite. a new method of intensifying secondary concentration technology was firstly advanced, and author applied it to ore, achieved eximious experimentation index. The reverse flotation tests of intensifying secondary concentration aiming at bauxite from Guizhou province were studied. The results show that diaspore concentrate directly used in the Bayer-mineral processing method can be obtained by using the intensifying secondary concentration technology without pre—desliming. The average A/S of the concentrate is 10.28 with a recovery rate of 85.41%.

Introduction

The bauxite resource is very abundant in China, proved reserves comes up to 2300 million tonnes, ranked fifth in the world. In China, around 98.33% of the resource is diasporic-bauxite and more than 70% of the resource has the ratio of Al_2O_3 to SiO_2 lower than 7. The diasporic-bauxite in China is different from the gibbsite-bauxite and boehmite-bauxite in other countries by its high content of $A1_2O_3$ and SiO_2 and low mass ratio of Al_20_3 to SiO_2. In Gui-zhou province, the bauxite reserves accounts for about 17% in China, and its main feature is high-aluminum, high-silica, low-iron, low ratio ofAl_20_3 to SiO_2, fine mineral crystal, complexity disseminated relationship and variety silica-mineral, the bauxite resource which ratio ofAl_20_3 to SiO_2 is more than 10 accounts for about 10%, and most of bauxite resource is less than 8.Due to ore nature, aluminum oxide production uses “sintering” or “combining” technologies in our country, therefore, China’s alumina industry is uncompetitive in the international arena.

Although direct flotation is an efficient method for de-silicate from bauxite using oleic-acid as collector of diaspore in the range of slurry pH 9—10,reverse flotation has more superiority for bauxite de-silicate than direct floatation，such as lower cost, easy filtration．The mechanism of flotation for the diaspore de-silicate have also been studied in China.But the variability of surface properties，similar floatability of these aluminum—silicate minerals and the nature of easily over—crushed make the cationic reverse flotation to de-silicate difficult by conventional flotation methods and flotation reagents．

Phase analysis and test results showed that difference of grindability is very obvious between valuable minerals and gangue, thus, mud phenomenon of crushing and grinding process produces unavoidably. Because micro-fine particles attached to the coarse surface, it is very easy to form mud covers at coarse surface. It reduced significantly selectivity of flotation reagent and flotability of high-silicate coarse particles in reverse-flotation. Author advanced firstly the technology of intensifying secondary concentration and applied successfully it to reverse-flotation de-silicate.

With industry continuous development, high ratio ofAl_20_3 to SiO_2 mineral resources will be exhausted, the potential mining crisis will endanger health development of entire alumina industry. Because Bayer’s processing is currently key industries encouraged by the state, we must exploit low ratio ofAl_20_3 to SiO_2 bauxite resource to meet the needs of Bayer’s processing alumina production,

reduce loss of resources, and solve the de-silicate problem economically. It is very important to promote regional economic development and ensure sustainable development of the national economy. Therefore，the aim of this paper is to advance a new method on de-silicate for reverse flotation of diasporic-bauxite ores.

Experimental

Materials

Test ores were obtained from Guizhou, in China, they were crushed though jaw crusher and roller crusher, then screened to -3mm size for flotation test. The chemical compositions of these samples are listed in Table 1.From Table 2, we could see that diaspore was major mineral, and its content was 68.13%, halloysite was 8.02%, quartz was 6.76%, and kaolinite was 3.98%.

Table 1 Chemical composition of tested /%

Elements	Al_2O_3	SiO_2	Fe	TiO_2	S	Remarks
Contents	62.03	10.97	4.32	2.95	0.65	Dried

Table 2 Main mineral composition analysis result /%

Mineral Name	Despore	Halloysite	Kaolinite	Quartz
Molecular Formula	AlO(OH)	$Al_2Si_2O_5(OH)_4.2H_2O$	$Al_2Si_2O_5(OH)_4$	SiO_2
Contents	68.13	8.02	3.98	6.76
Mineral Name	**Goethite**	**Anatase**	**Pyrite**	**Others**
Contents	FeO(OH)	TiO_2	FeS_2	-
Molecular Formula	6.01	2.94	1.82	3.0

Test methods and reagents

Bauxite materials were placed in XFD-type (3L) laboratory flotation machine, which was then filled with water. After adding the desired amount of reagents, the suspension was agitated for 3 minutes and the pH was measured before flotation. The flotation wan conducted for four minutes. The products were collected, dried and weighed. The recovery was calculated according to dried products obtained.

Flotation reagents (such as SHMP and Sulfuric acid) were industry production, but collector of BS-3(mixed reagent) and regulator of TZ-1(denaturalized reagent) were synthesized reagents in the laboratory.

The basic principle of de-silicate with reverse-flotation

We must ensure the monomer dissociation between valuable minerals and gangue minerals if valuable minerals and gangue minerals can be separated, under this condition, mineral surface has the tendency of adsorbing collector molecules. While mineral surface is absorbed by collectors, mineral surface has hydrophobic feature, which can attach to the bubble surface.We separate valuable minerals from gangue minerals according to potentiodynamic difference among minerals. It must meet the following conditions:

Mineral 1，$pZC_1<pH<pK_a$；Mineral 2，$pZC_2<pH<pK_a$；$pZC_2<pH<pZC_1$

In the formula, pKa is dissociation constant for reagents, pZC_1 and pZC_2 are Zero-point pH of mineral 1 and mineral 2. In conditions above, surface charge of mineral 1 is positive, and surface charge of mineral 2 is negative, therefore, mineral surface with negative charge is absorbed by cationic collectors, makes valuable minerals can separate from gangue minerals.

Flotation tests

Ore samples sieving–hydraulic classifying test

For investigating grade distribution of production ground and mineral ratio of Al_20_3 to SiO_2, we carried out sieving test and hydraulic classifying test. Test results were given in table 3.

Table 3 Grinding product analysis results

Size composition /mm	Yield /%	Grade /%		A/S ratio of concentrate
		Al_2O_3	SiO_2	
+0.150	0.46	55.70	13.71	4.06
-0.150+0.074	6.72	58.30	13.45	4.33
-0.074+0.037	26.18	59.24	11.50	5.15
-0.037+0.019	10.49	53.72	12.23	4.39
-0.019+0.010	9.37	62.89	9.81	6.41
-0.010	46.78	62.19	9.77	6.37
	100.00	60.30	10.75	5.61

Guizhou bauxite has the feature of selective grinding according to variety ratio ofAl_20_3 to SiO_2 in table 3.The concentrated thing of Al_2O_3 increases gradually from coarse size to fine size, and reduces for SiO_2; Ratio ofAl_20_3 to SiO_2 is increasing gradually.But selective grinding feature is reverse with North bauxite. Main reason lies in different types of silicate-minerals, on the other words, hardness of silicate-minerals was higher than aluminum minerals, so aluminum minerals is ground to fine size firstly.

Flotation flowsheet design

We found that Al_2O_3 concentrated to fine size from test results (Table 3), and SiO_2 concentrated to coarse size. Furthermore, we also found that less than -0.037mm mineral particles could attach to bubbles. For separating diaspore from bauxite using cationic collectors, we must assure most of gangue minerals was ground to fine size (-0.037mm) on the premise of minerals monomer dissociation. If grinding flowsheet designed was once, many valuable minerals would be over-crushed, muddy phenomenon was very serious, and flotation efficiency was very low. Thus author designed the flowsheet of stage-grinding and stage-separating according to feature of high-silicate bauxite. Test flowsheet is shown in Fig.1

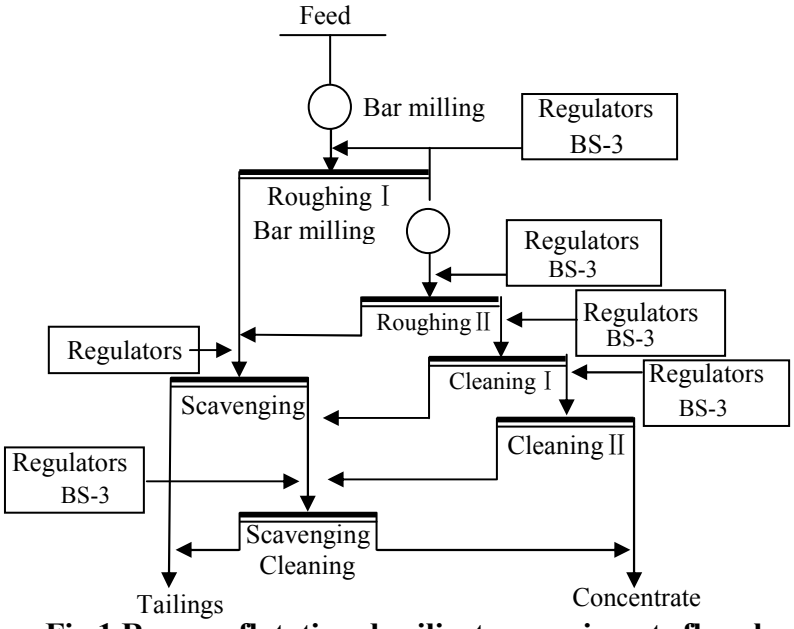

Fig.1 Reverse flotation de-silicate experiments flowsheet

Conventional flotation test

Based on design ideas of reverse-flotation, we carried out open circuit test. Test flowsheet was shown in Fig.1, and test results were shown in table 4. Test results showed that the ratio of Al_20_3 to SiO_2 was 11.00 and Al_20_3 recovery was 71.24% through the flowsheet of two roughings— three cleanings (twice cleanings, once cleaning of middling product), once scavenging. If sub-concentrate was mixed to concentrate, ratio of Al_20_3 to SiO_2 was decreased to 8.00. Therefore we dealt with the high-silicate bauxite with other ways if we want to increase the ratio of the ratio of Al_20_3 to SiO_2.

Table 4 Reverse flotation results of bauxite

Production name	Yield /%	Grade /%		Recovery /%		A/S ratio of concentrate
		Al_2O_3	SiO_2	Al_2O_3	SiO_2	
Concentrate	67.36	64.58	5.87	71.24	36.00	11.00
Middlings	19.64	58.37	14.82	18.78	26.49	3.94
Count	87.00	63.18	7.89	90.02	62.49	8.00
Tailings	13.00	46.90	31.71	9.98	37.51	1.48
Ore Samples	100.00	61.07	10.99	100.00	100.00	5.56

Application of intensifying secondary concentration technology

For conventional flotation, quality of concentrate is relation to collectors and regulators. During reverse flotation, if collecting ability of collectors is strong, recovery of value minerals is low, contrarily, recovery is high; and if selective ability of collectors is good, grade of concentrate is high, otherwise, grade is low. However, if feed size is relatively smaller, froth entrainment phenomenon is very serious in the process of flotation; this will ultimately lead to lower grade of concentrate. For the condition, the author firstly brought intensifying secondary concentration technology to reduce negative factors of entrainment, and to achieve the purpose of separating valuable minerals from gangue minerals.

The main characteristics of intensifying secondary concentration technology are the application of spraying water, which can wash flotation foam, make foam merged and secondly enriched. While spraying, some of washing water will be left in the concentrate, but most of washing water will form dropping flow, valuable minerals can not go in froth flotation zone by this way, thereby increase floating rate of non-purpose mineral.

Authors carried out open circuit test with intensifying secondary concentration technology. Test results were shown in Table 5.

Table 5 Test results of intensive flotation

Production name	Yield /%	Grade/%		Recovery/%		A/S ratio of concentrate
		Al_2O_3	SiO_2	Al_2O_3	SiO_2	
Concentrate	81.04	64.55	6.28	85.41	48.16	10.28
Middlings	4.26	49.68	25.57	3.46	10.31	1.94
Tailings	14.70	46.39	29.86	11.13	41.54	1.55
Ore Samples	100.00	61.25	10.57	100.00	100.00	5.79

The results were shown that effect of dealing with high-silicate bauxite with intensifying secondary concentration technology was very obvious, ratio of Al_20_3 to SiO_2 reached to 10.28, Al_2O_3 recovery was 85.41%, and middlings ratio of Al_20_3 to SiO_2 was 1.94, which could be incorporated into the tailings.

CONCLUSIONS

It can be seen from the results and discussion above that:

(1) Synthetical depressors (TZ-1) have the feature of strong depressing effect on diaspore in acidic conditions. That is to say, TZ-1 is effective depressor on diaspore in reverse flotation of bauxite.

(2) New collectorS(BS-3) have strong selective collecting function to gangue minerals, so, BS-3 is a kind of effective collector to de-silicate with reverse-flotation.

(3) The application of intensifying secondary concentration technology has changed the negative impact on over-crushed in the process of reverse-flotation, achieved excellent indicators of test.

(4) Slime has evident effect on the reverse flotation of cationic collector，so it is necessary to deal with high-silicate bauxite with new technology and method.

(5) A bauxite concentrate(A/S=10.28，Al_20_3 recovery=85.41%)can be obtained by the new flotation technology(Intensifying Secondary Concentration Technology).

It is therefore concluded that intensifying secondary concentration technology is effective for recovering diaspore from high-silicate bauxite and the high separation indicators achieved without pre-desliming.

References

[1] Guo Jian,Ren Aijun,etc.A study on separation diaspore and kaolinite by reverse flotation. Non-ferrous metals,2003(3),1~5;

[2] Hu Yue-hua，Jiang Hao，Qiu Guan-zhou.Solution chem istry of flotation separation on aluminum and silicate in diasporic-bauxite[J].The Chinese Journal of Nonferrous Metals, 2001, 11(1)：125—130.(in Chinese)

[3] Huang Chuanbing,WangYuhua ect. Review of research on desilication of bauxite ores by reverse flotation. Metal Mines,2005(6),21~24;

[4] Jiang Yu-ren，HU Yue-hua，Cao Xue-feng.Synthesis and structure-activity relationships of carboxyl hydroxidoximein bauxite flotation[J].The Chinese Jounral of Nonferrous Metals, 2001, 11(4)l 702—706.(in Chinese)

[5] Li Long-feng.Desilication and iron removal research for diasporic-bauxite by mineral processing[J].Journal of Central South Institute of Mining and Metallurgy，1980(4)：82—84.(in Chinese)

[6] Liang An-zhen，Li Ting-hui.Discussion on reasonable technology flowsheet of bauxite processing[J].Light Metal，1982(11)：1—6．(in Chinese)

[7] Lu Yi-ping，Zhang Guo-fan，etal.A novel collector RL for flotation of bauxite[J].Jounral of Central South University of Technology.2002，9(1)：21—24.

[8] Luo Zao-jun，Hu Yue-hua，Wang Yu—hua，eta1.Mechanism of dispersion and aggregation in reverse flotation for bauxite[J].The Chinese Journal of Nonferrous Metals, 2001, 11(4): 680—683.(in Chinese)

[9] WangYu-hua，Hu Yue-hua，Chen Xiang-qing. Aluminum—silicates flotation with quaternary ammonium salts [J].The Chinese Journal of Nonferrous Metals, 2003, 7:715-719.

[10] Zhang Guo-fan. Theory and Technology of Flotation on Bauxite Desilicate[D].Changsha: Central South University，2001.(in Chinese)

[11] Zhang Qin,Yue Zilong. Exploration on desilication process of local bauxite ore. Non-ferrous metals,2006(5),9~11;

[12] Zhang Yunhai,Wei Dezhou. The separation of kaolinite and diaspore by reverse flotation. Non-ferrous metals,2004(2),45~47;

doi:10.4028/www.scientific.net/AMM.161.11

First principles study of La-doped ZnTe on electrical properties

Zhongqiu Xia[1, a], Rongping Li[2, b]

[1]Key Laboratory of Semiconductor Photovoltaic Technology at University of Inner Mongolia Autonomous Region, School of Physical Science and Technology, Inner Mongolia University, China

[2] Key Laboratory of Semiconductor Photovoltaic Technology at University of Inner Mongolia Autonomous Region, School of Physical Science and Technology, Inner Mongolia University, China

[a]anorc@yahoo.cn, [b]rongpingli@sina.com

Keywords: La-doped ZnTe, first principles, electrical properties, solar cells

Abstract. The band structure and the intensity of states of La-doped ZnTe were obtained using the plane wave ultra soft pseudo potential method based on density functional theory (DFT) and generalized gradient approximation (GGA) according to the generally used design of the low resistance Ohmic contact in CdS/CdTe solar cells. We analyzed the electrical properties in the aspect of conductivity, which was improved by the lager electron effective mass and the high level of carrier concentration. In addition, the lattice constant of La-doped ZnTe increased, and La-doped leads to the ZnTe semiconductor degeneration.

Introduction

The CdS/CdTe solar cell is a type of photovoltaic device that consists of varies of semiconductor films from the basis of the band theory, of which the widely used structure was shown in Fig. 1 [1]. The photovoltaic conversion appears in the (n) CdS - (p) CdTe heterojunction, and the electrons flow from the CdTe absorber layer to front contact when the holes move to the opposite direction at the same time. Many metals used for the back contact can form a Schottky barrier with p-type CdTe against the holes movement, which will results in a high contact resistance, so we can dope the CdTe film heavily to obtain a tunnel barrier for a higher short circuit current—a important parameter of conversion efficiency, however, p-type dopants are not easily incorporated into CdTe in a high density [2]. The ideal Ohmic contact is usually obtained by making a thin heavily doping district on the p-type or n-type semiconductor layer to contact with the metal [3], thus, a possible approach is to insert a heavily doping ZnTe layer between CdTe layer and the metal.

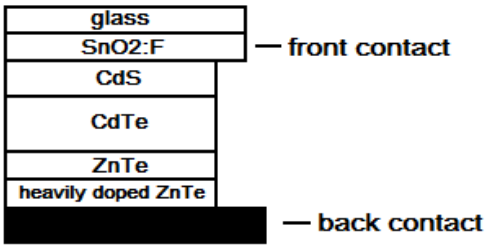

Fig. 1 Solar cell structure

Cu has been used in doping ZnTe by lots of experiment method, which show that it will diffuse via the grain boundaries to the CdS/CdTe active junction [4]. Kevin *et al.* emphasize that the role of Cu as a major factor can limit the stability of solar cell devices particularly [5]. The presence of deep defects in CdS/CdTe thin film solar cells strongly affects the electrical properties and the performance of the cells [6]. In this paper, we take La as a substitutional impurity to take the place of Cu, and obtained the band structure and the density of states of substitutional La-doped ZnTe using the plane wave ultra soft pseudo potential method based on density functional theory and generalized gradient approximation. We analyzed the influence of La-doped on lattice constants, band structure, density of states and electrical properties.

Calculate model and method

ZnTe crystalline structure is cubic sphalerite, which belongs to space group F-43m, as shown in Fig. 2 [1], where 1, 2 and 3 represent Zn atoms, Te atoms and La atoms, respectively. Zn atom is located in the tetrahedral gap formed by four adjacent Te atoms, and Te atoms are arranged similar to Zn atoms. ZnTe supercell is a unit (2×2×2) extended in the direction of the base vectors, and La doping is to replace the position of Zn atom with La atom. The lattice constant is a = b = c = 0.6101nm, and α = β= γ = 90°.

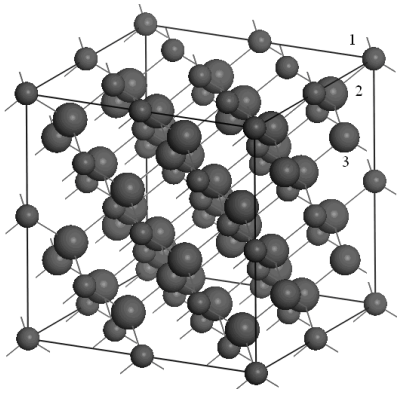

Fig. 2 La-doped ZnTe cell structure

The Castep module of Material Studio 5.5 software is used in our calculation, which based on the plane wave pseudo potential theory of total energy, and replaced the ion potential with the pseudo potential. The electronic wave function was obtained in plane wave expansion method, and the exchange correlation potential caused by the interaction between electrons was calibrated by generalized gradient approximation (GGA). We selected the plane wave energy cutoff and the K grid points firstly for convergence, in order to ensure the reliability of the results. Convergence tolerance of SCF is 2.0×10^{-6}eV/atom in the iteration and the force on each atom is less than 0.05eV/nm. Internal stress of the crystal is less than 0.1Gpa, and the Fast Fourier Transform (FFT) grid is (48×48×48). The calculations were carried out in reciprocal space.

Results and discussions

The La-doped ZnTe structure is still cubic sphalerite according to the substitutional doping, and the lattice constant increases to 0.7717nm compared with the intrinsic ZnTe, of which the lattice constant was set as 0.6101nm in calculate model before. We obtained the lattice mismatch between the intrinsic ZnTe and the La-doped ZnTe by the Eq.1

$$\frac{2(a_2 - a_1)}{a_2 + a_1}, \tag{1}$$

where $a_1 = 0.6101nm$ and $a_2 = 0.7717nm$, to decide if the interfacial state needs to be considered in the solar cells production process, and this value is 23.4% that means more interfacial states will be brought in. In addition, the bulk modulus is 1.53131GPa after the geometry optimization.

The band structure of La-doped ZnTe is shown in Fig. 3, where the vertical coordinate 0 indicates the Fermi energy level and the electrons involved in this calculation contain Zn3d10, Zn4s2, Te5s2, Te5p4, La5s2, La5p6, La5d1, and La6s2. We can see that the Fermi characteristic energy level has gone in the conduction band, which means that the bottom energy levels of the conduction band below the Fermi energy level were occupied completely by electrons and the doping density is a large one [3]. We obtained the effective mass from the Eq. 2

$$\frac{1}{h^2}\left(\frac{d^2E}{dk^2}\right)_{k=0} = \frac{1}{m_n^*}, \tag{2}$$

where h is the Planck constant and the second derivative was made for the bottom of the conduction band. The result is 0.31647592×10^{-68} which is between Y-doped ZnTe and Gd-doped ZnTe in the previous work [7]. The effective mass decreased after doping compared with the intrinsic ZnTe, and this will improve the film conductivity because of the greater electron acceleration in the same external force.

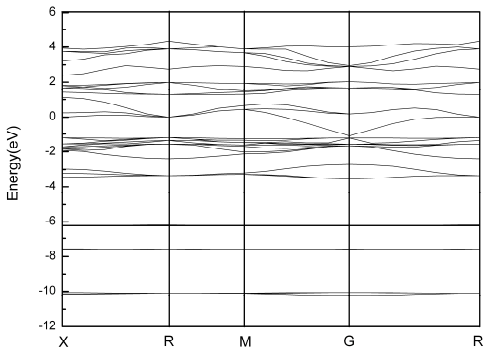

Fig. 3 La-doped ZnTe band structure

The conductivity is related to the carrier concentration as well according to the Eq. 3

$$\sigma = nqu_n + pqu_p, \tag{3}$$

where n is much greater than p in n-type semiconductor, thus, we ignore the second term of Eq. 3 to analyze the conductivity property by the n-type carrier concentration, which can be obtained from the Eq. 4

$$n = \frac{1}{V}\int_{E_c}^{\infty} f(E)g_c(E)dE, \tag{4}$$

where V is the cell volume and $g_c(E)$ is the density of states as show in Fig. 4. We used the Fermi distribution function to analyze the statistical distribution of electronic in the band conduction as the Eq. 5

$$f(E) = \frac{1}{1+\exp\left(\frac{E-E_F}{K_0T}\right)}, \tag{5}$$

where the Pauli Exclusion Principle was considered because of heavy doping and $f(E)=1$ when $T=0K$ and $E<E_F$. The integration of the density of states was made from the conduction band bottom level to the Fermi energy level, and the result is $5.42\times10^{26}m^{-3}$, which shows that the doping was carried out in a high density.

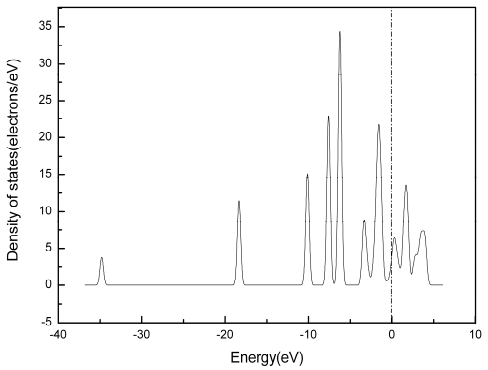

Fig. 4 La-doped ZnTe density of states

Summary

The band structure and the intensity of states of La-doped ZnTe were obtained using the plane wave ultra soft pseudo potential method based on density functional theory (DFT) and generalized gradient approximation (GGA). We calculated the lattice mismatch between the intrinsic ZnTe and the geometry optimization La-doped ZnTe lattice constant, which shows a large one, and the bulk modulus is 1.53131GPa. The doping has a high level by the analysis of the band structure and the density of states. Moreover, conductive band effective mass and the carrier concentration near the Fermi character energy level were calculated, which show that the effective mass decreases and the carrier concentration is very high, and this will improve the film conductivity on electrical properties.

References

[1]Xia Zhong-Qiu and Li Rong-Ping: submitted to Chinese Physics B (2011)
[2]Dennis Rioux, David W.Niles and Hartmut Höchst, ZnTe: A potential interlayer to form low resistance back contacts in CdS/CdTe solar cells, J. Appl. Physics 73 (1993) 8381
[3]Liu E K, Zhu B S and Luo J S, Physics of semiconductor, National Defense Industry Press, Beijing, 2010, pp212-214
[4]Zheng Xu, Li Bing, Wang Zhao, Zhang Dong-Ting, Feng Liang-Huan, Zhang Jing-Quan, Cai Ya-Ping, Zheng Jia-Gui, Wu Li-Li, Li Wei, Lei Zhi and Zeng Guang-Gen, Cu deep level center in CdTe solar cell, Acta Physica Sinica, 59 (2010) 2783
[5]Kevin D. Dobson, Iris Visoly-Fisher, Gary Hodes and David Cahen, Stability of CdTe/CdS thin-film solar cells, Solar Energy Materials & Solar Cell, 62 (2000) 295
[6]J. Versluys, P. Clauws, P. Nollet, S. Degrave and M. Burgelman, DLTS and admittance measurements on CdS/CdTe solar cells, Thin Solid Films 451-452 (2004) 434
[7]Xia Zhong-Qiu and Li Rong-Ping: submitted to Acta Physica Sinica (2011)
[8]Björn Lange, Christoph Freysoldt and Jörg Neugebauer, Native and hydrogen-containing point defects in Mg_3N_2: A density functional theory study, Phys. Rev. B 81 (2010) 224109

doi:10.4028/www.scientific.net/AMM.161.15

Influence of Structure and Property of Plasticizers on Viscosity and Aging Process of PVC Plastisols

XU Guo-min [a] , Ji Yu-bi [b], Yang Zhao [c], Tan Hong*

National Engineering Research Center for Compounding and Modification of Polymer materials, Guiyang 550014, Guizhou, China

([a]Email: xuguomin@nercp.org.cn, [b]Email:Yubi.ji@163.com,[c]YZhao@163.com
*Email:jenny2000820@sina.com(corresponding author))

Keywords: PVC;Plastisol;Plasticizer;viscosity.

Abstract. The molecular structure of DEDB,ATBC,DOTP was simulated by Chemoffice. The viscosity and aging process of PVC plastisols prepared by the three plasticizers were investigated by vibrational viscometer, and the influence of selective interactions between PVC resins and plasticizers on the viscosity and aging process of PVC plastisols were analysed. The results indicate that the viscosity and aging process of PVC plastisols are associated with the number of effective interaction groups of a plasticizer, and the more the number of effective interaction groups a plasticizer has , the higher the viscosity of the plastisols is and the more unstable the plastisols is.

1 Introduction

Poly(vinyl chloride)(PVC) plastisol is a suspension of fine particles of PVC in a plasticizer. One of important properties for a plastisol is the viscosity and aging process, which shows great influence on the final performance of the products. Plasticizer is an important component in plastisol formulations, and shows great effect on the viscosity and aging process for the plastisol. In previous research[1-3], it had been proven that the compatibility between plasticizer and PVC particles perform great effect on the viscosity and aging process, and the compatibility capacity is associated with the structure of plasticizers.

A great number of studies have been devoted to develop several theories about PVC/plasticizer compatibility, based on different parameters that can be responsible of this compatibility, as polarity, internal pressures, dielectric constants, solubility parameters, and modified polarity parameters[2]. Recent publications[4-5], have established compatibility relations as a consequence of the existence of selective interactions between polymer and plasticizer. Therefore, in this work, we used chemoffice to simulate the molecular structure of plasticizers and carried out a comparative study on the interactions between PVC particles and plasticizers, which affect the viscosity and aging process of PVC plastisols.

2 Experimental

2.1 Materials

Three commercial PVC resins from two PVC manufactures were used, one containing friable agglomerates and the others containing nonfriable agglomerates. With the friable-agglomerate resin, about 78.0% of the initially present agglomerates deagglomerated, with the nonfriable-agglomerate resin, about 20.7% and 2.0% of the initially present agglomerates deagglomerated. The characteristics of the resins, Polymerization Degree (D_w), particle size distribution D(υ,0.1), D(υ,0.5) and D(υ,0.9), i.e. particle sizes below which there are 10, 50 and 90% of the PVC particles, respectively, are shown in Table 1, and the morphology of PVC particles is shown in Fig 1. Three commercial plasticizers of different molecular structures were considered. Table 2 shows a summary properties of these plasticizers, as provided by the suppliers.

Table 1 Properties of PVC resins employed

PVC resin	D_w	$D_{(\upsilon,0.1)}$ μm	$D_{(\upsilon,0.5)}$ μm	$D_{(\upsilon,0.9)}$ μm
CPM-31	1300±100	0.85	2.51	8.67
P440	1500±100	56.1	138.94	397.16
R1069	1900±100	45.81	121.55	336.13

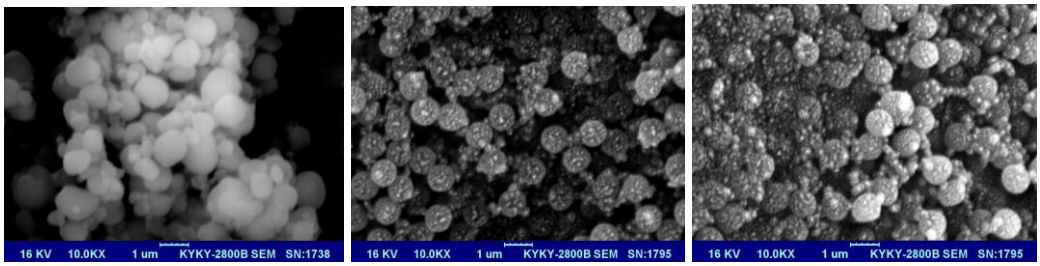

Fig 1 Morphology of PVC particles:(a)CPM-31;(b)P440;(c)R1069

Table 2 Properties of plasticizers employed

property	DEDB	ATBC	DOTP
Viscosity at 25℃， mPa s	150±10	50±10	100±10
Refraction index，25℃/D	1.5320-1.5340	1.4410-1.4425	1.4860-1.4880
Ester content %	≥99.5	≥99.5	≥99.5
Relative molecular mass	314.4	402.48	390.56
Density，g/cm	1.1751	1.050	0.984

2.2 Experimental procedure

The plastisols were prepared by mixing the dry resin in diethylene glycol dibenzoate(DEDB), acetytributyl citrate(ATBC) or Dioctyl terephthalate(DOTP) in the standard proportion of 100 parts resin to 60 parts plasticizer by weight, with a laboratorytype plastisol mixer. A vibrational viscometer was used to monitor the initial viscosity and the viscosity at preassigned times at certain intervals after the plastisols were prepared. The variety of viscosity is calculated by the equation of $\eta_v=\eta_t-\eta_{t-1}$, where η_v is the variational viscosity, η_t and η_{t-1} are the viscosity of plastisol preserved t and t-1 days respectively. The average particle size of different plastisols was investigated by Mastersizer.

3 Results Discussion

3.1 The molecular structure of plasticizers

Fig 2 shows molecular structure of DEDB, DOTP and ATBC simulated by Chemoffice. It can be seen from Fig 2 that the polar part of a plasticizer is ester linkages, but the location of these ester linkages and the spatial structure of the molecular chain show difference in different plasticizers. In the molecular structure of DEDB, there are two ester linkages and two aromatic rings, which symmetrically distribute over the molecular chain. In DOTP, there are two ester linkages and a

aromatic ring, and the two ester linkages locate in the diagonal position of the aromatic ring, which is the center of the molecular chain, the flat structures symmetrically distribute over the aromatic ring. However, in ATBC, there are three ester linkages, which locate in the intersection of three aliphatic long-train structures respectively.

Table 3 shows the dipole moment of DEDB, DOTP and ATBC calculated by semiempirical algorithm of MOPAC program in Chemoffice. It can be seen from the table that DEDB shows the biggest molecular polarity, followed by DOTP and ATBC which shows the smallest.

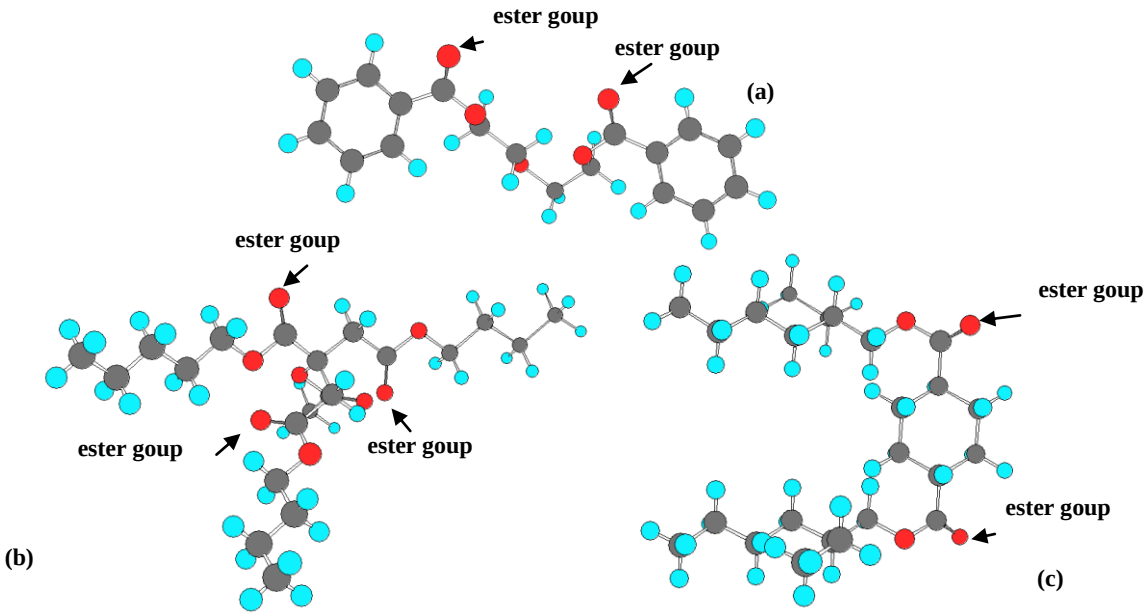

Fig 2 Molecular structure of plasticizers: (a) DEDB;(b) ATBC;(c)DOTP

Table 3 Dipole moments of the DEDB;DOTP;ATBC calculated by Chemoffice

property	DEDB	DOTP	ATBC
Diople moment (Debye)	5.954	5.615	3.72

3.2 Analyzing the Viscosity and Aging Process of PVC Plastisols

Fig 3 shows the initial viscosity of plastisols prepared by different plasticizers. It can be seen that the DEDB-based plastisols shows the highest initial viscosity, followed by DOTP-based plastisols and the ATBC-based plastisols which show the lowest viscosity.

It has been proven that the viscosity and aging process of a PVC plastisol is associated with the compatibility between PVC resin and plasticizer[1-3], and plasticizer with different chemical structure display a different interaction capacity with PVC resin, which lead to different viscosity characteristic. From Fig.2 we can see that in the DEDB-based plastisols, the proper structure of DEDB makes the two ester linkages and aromatic rings interact easily with the polarized carbon-chlorine bonds in PVC polymer chain via dipole-dipole interactions and van der waals force[6], so the effective interaction groups between PVC and plasticizer are the two ester linkages and aromatic rings. Therefor, the compatibility between PVC resin and DEDB is very strong, which lead to high viscosity of the plastisol (Fig.3(a)). However, in the DOTP-based plastisols, because the space resistance effect of the long-train flat structure grafting in the diagonal position of the aromatic ring and the lack of a aromatic ring structure, which means the number of effective interaction groups are less than that of DEDB, the compatibility between PVC resin and DOTP is the worse than PVC/DEDB system, so the viscosity of the plastisol is much lower than that of PVC/DEDB system, which accords with the experimental results very well (Fig.3(a)). But in ATBC molecular structure, the space resistance effect is stronger than that of DOTP as a consequence of the three ester linkages

locate in the intersection of three aliphatic long-train structure respectively, and the number of effective interaction groups are less than that of DOTP, so the compatibility between PVC resin and ATBC is weaker than that of PVC/DOTP system, and the viscosity of the plastisol is lower than that of PVC/DOTP system (Fig.3(a)).

Furthermore, from Fig.3(b) we also can see that in PVC/DEDB plastisol system and PVC/DOTP plastisol system, the viscosity of plastisol prepared by friable-agglomerate resins is lower than that of nonfriable-agglomerate resins, which may be the influence of emulsifier according to N.Nakajima et al[7]. But in PVC/ATBC plastisol system, the viscosity character is opposite, which attributed to the large particle size and the perfectly spherical particles of PVC resins(Fig 1)[8].

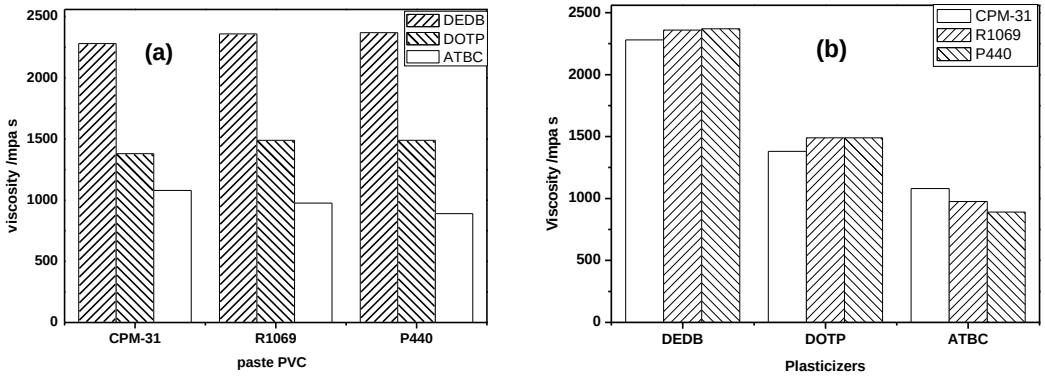

Fig 3 Initial viscosity of the plastisols

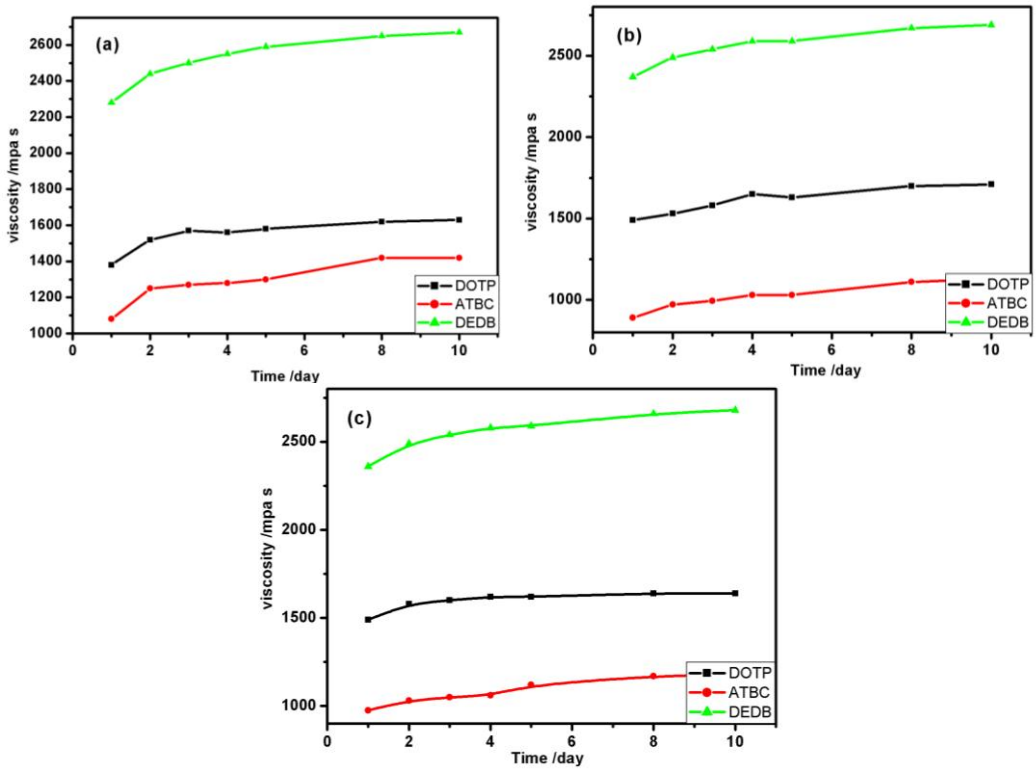

Fig 4 Aging process of the plastisols prepared by different resins: (a)CPM-31; (b)P440; (c)R1069

Fig.4 and Fig 5 respectively show the aging process and the variety of viscosity for different plastisols prepared by different resins. It can be see that the viscosity of the plastisols increases rapidly in the beginning and becomes very small after a certain period of time, which in accordance with other authors[1,7]. Moreover, from Fig 5 we can also conclude that the viscosity of plastisols prepared by DEDB shows more unstable than that of other plastisols, on the whole. The phenomenon may be a result of either the deagglomeration of agglomerated particles or the dissolution of low-molecular-weight PVC into the plasticizer[7], and there is an indication that a major portion of PVC resin is not touched by plasticizer after several months to years of storage[1].

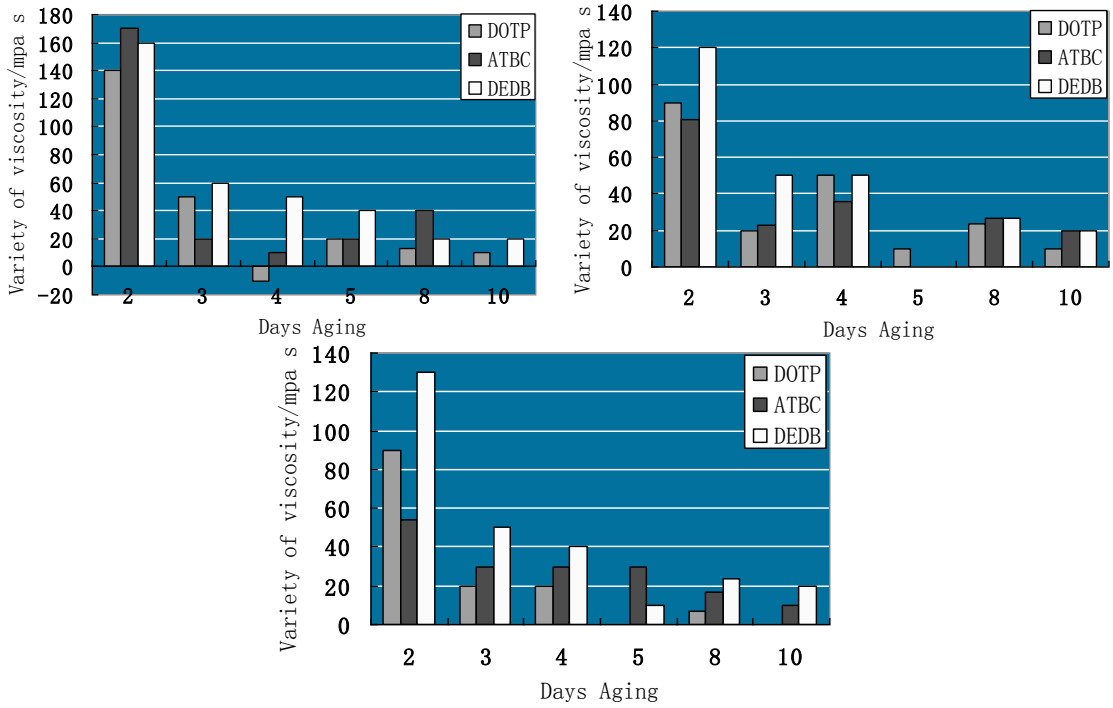

Fig 5 Variety of viscosity for different plastisols prepared by different resins: (a) CPM-31; (b) P440; (c) R1069

There are several models to predict the viscosity behavior of a plastisol; some of them, based on the simple suspension model, do not fit well for low concentration ranges. Better results are obtained with other models that assume more complexity in the plastisol structure. Ram and Schneider proposed the following simplified empirical expression[3]:

$$\eta_r = A \exp\left[\frac{BW}{1-W/W_P}\right] \quad (1)$$

Where ηr is the apparent viscosity of the plastisol, A and B are empirical constants, W is the weight fraction of the polymer, and Wp is the critical weight fraction (defined as the weight fraction to gel when the viscosity rises to high values).

The concept of critical weight [strictly, the critical volume (φ_c)] was also used by Johnston and Brower to develop one of the expressions that better describes the relationship between ηr and its suspension fraction. This expression is validated for different plasticizer resin systems, and it is independent of particle size changes and distribution. This expression is as follows[3]:

$$\log_{10}\eta_r = \left(1.33 - 0.84\frac{\varphi}{\varphi_c}\right)\left(\frac{\varphi}{\varphi_c - \varphi}\right) \quad (2)$$

The application of the two models allowed us to calculate the corresponding value of Wp and φc. Table 4 shows φc values for Different Plasticizers according to the Ram and Schneider and Johnston and Brower Viscosity Models. From the table we can see that the φc values for DEDB is lower than that of other two plasticizers, which indicates a higher plasticizer compatibility[3].

Table 4 φ_c values for Different Plasticizers according to the Ram and Schneider and Johnston and Brower Viscosity Models

Model	DEDB	DOTP	ATBC
Ram and Schneider	68.00	68.41	68.86
Johnston and Brower	74.05	75.03	75.6

Fig 6 shows the average particle size of plastisols prepared by different plasticizers. We can observe that the average particle size in DEDB-based plastisol is much bigger than that of other two platisols. It is because the plasticizer penetrates in PVC solid particles and swells them. According to N.Gonzalez et al[2], this wetting capacity depends on the interaction capacity between PVC and plasticizer. In general, a plasticizer possessed great interaction capacity with PVC displays a stronger wetting capacity, which lead to a large average particle size.

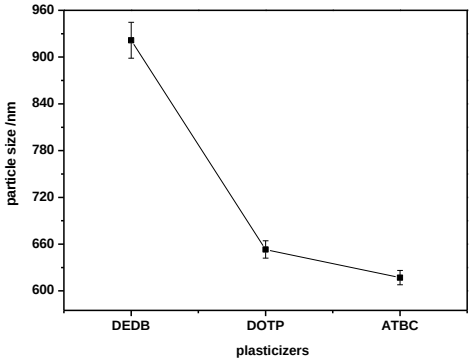

Fig 6 The average particle size of plastisols

4 Conclusions

The viscosity and aging process of a PVC plastisols are associated with the number of effective interaction groups of a plasticizer, and the more the number of effective interaction groups a plasticizer has , the higher the viscosity of the plastisols is and the more unstable the plastisols is.

References

[1] N.Nakajima, E.R.Harrelly, Rheology of PVC Plastisol: Particle Size Distribution and Viscoelastic Properties, Journal of Colloid and Interface Science. 238(2001)105-115.

[2] N. Gonza´lez, M. J. Ferna´ndez-Berridi, Application of Fourier Transform Infrared Spectroscopy in the Study of Interactions Between PVC and Plasticizers: PVC/Plasticizer Compatibility versus Chemical Structure of Plasticizer, Journal of Applied Polymer Science. 101(2006)1731-1737.

[3] J. E. Crespo, R. Balart, L. Sanchez, J. Lopez, Substitution of Di(2-ethylhexyl) Phthalate by Di(isononyl) Cyclohexane-1,2-Dicarboxylate as a Plasticizer for Industrial Vinyl Plastisol Formulations, Journal of Applied Polymer Science.104(2007)1215.

[4] van Oosterhout, J. T.; Gilbert, Interactions between PVC and binary or ternary blends of plasticizers. Part I. PVC/plasticizer compatibility, M. Polymer. 44(2003)8081.

[5] Jan-Chan Huang, Rudolph D. Deanin, Concentration Dependency of Interaction Parameter Between PVC and Plasticizers Using Inverse Gas Chromatography, Journal of Applied Polymer Science. 91(2004) 146.

[6] Paul H. Daniels, A Brief Overview of Theories of PVC Plasticization and Methods Used to Evaluate PVC-Plasticizer Interaction, Journal of vinyl and additive technology.(2008)13.

[7] N. Nakajima, E. R. Harrell, Viscosity Aging of Poly(vinyl chloride) Plastisol: The Effect of the Resin Type and Plasticizer Type. 95(2005)448.

[8] B.Sathre, T.Thorjussen, H.Jacobsen, et al, Improved plastisol flow and reduced level of plasticizer in paste poly(vinyl chloride) formulations, Plastics, Ruber and Composites. 28(1999)170.

doi:10.4028/www.scientific.net/AMM.161.21

Research on the Prediction of Static Contact Anglein Circular Capillary Tubes

J.B. Wang [a], D.Z. Zeng [b] and J.J. Jiang [c]

School of Mechatronics, Northwest Polytechnic University, Xi'an 710072, China

[a]wangjunb@nwpu.edu.cn, [b]zengdongzi@163.com, [c]jianjun@nwpu.edu.cn

Keywords: Contact Angle Prediction, Jurin Formula, Rayleigh Formula, Refinement, Equivalence Height

Abstract. New discovery was found by the capillary experiments with circular glass tubes and partial-wetting liquids that the partial liquid volume under moon surface could be expressed by equivalent height function H(r). Contact angle models suggested in this work, evaluated by Eq. 5, was eventually given by the concept of equivalent height, and so-determined models presented a much higher accuracy on prediction of contact angle compared to Jurin formula.

1 Introduction

Solid/liquid interface contact angle is a fundamental phenomenon in engineering applications including oil exploiting, dye, and composites manufacturing industries [1]. It is determined by material physical characteristics and reflects the liquid wetting performance. In 1805, Young [2] introduced the mathematical concept of mean curvature of a surface, and derived the first correct approximation for the liquid column height h in circular capillary tube of small radius r immersed vertically in a large liquid bath:

$$\frac{2\sigma\cos\theta}{r}=\rho gh, \tag{1}$$

with σ equal to liquid surface tension, g magnitude of the local gravitational accelerate, θ the contact angle inner the wall, ρ the density of liquid. See Fig. 1. Eq. 1 is generally called Jurin formula [3,4,5] which can be derived by the equilibrium between pull force along the inner wall and hydrostatics on the reference level. For the ignorance of the partial liquid volume under moon surface, the contact angles from Jurin's present larger than optical ones. In the work by Rayleigh [6] in 1916, a more theoretical model, called Rayleigh formula, was derived but only aimed at perfect-wetting system where θ is strictly equal to 0:

$$\frac{2\sigma\cos\theta}{r}=\rho gh[1+\frac{1}{3}\frac{r}{h}-0.1288\left(\frac{r}{h}\right)^2+0.1312\left(\frac{r}{h}\right)^3]. \tag{2}$$

However, in general solid/wetting liquid system, contact angle always presents $\theta>0$ [7,8,9]. The purpose in this study is to carry out capillary rise experiments and to make refinement of Jurin formula so as to adapting to this case with reasonable precisions.

2 Materials and equipment

Solid materials: glass capillary tubes with internal radii of 0.15, 0.5 and1.4 [mm].
Partial-wetting liquids: alcohol, distilled water and sesame oil.
Apparatuses: liquid density and surface tension analyzer, ruler.

3 Modeling theories and processes

With numerical analysis and computer technology, the real meniscus surface status inside circular capillary tube can be easily determined by Bashforth-Adams equation [10]:

$$\sigma\left\{\frac{\frac{d^2y}{dx^2}}{\left[1+\left(\frac{dy}{dx}\right)^2\right]^{\frac{3}{2}}}+\frac{\frac{dy}{dx}}{x\left[1+\left(\frac{dy}{dx}\right)^2\right]^{\frac{1}{2}}}\right\}=\rho g(h+y), \tag{3}$$

where x and y both the coordinate values of Cartesian coordinate established at the lowest point of the meniscus interface. See Fig.1.

Firstly, with the measurements of liquid density, surface tension and the column height inner the capillary tube, feature points can be produced by Bashforth-Adams equation with integral approach. Then, to translate the liquid volume under moon surface into equivalence height H which appears a relationship of H(r). Jurin formula will be refined subsequently with the formulation shown in Fig. 1.

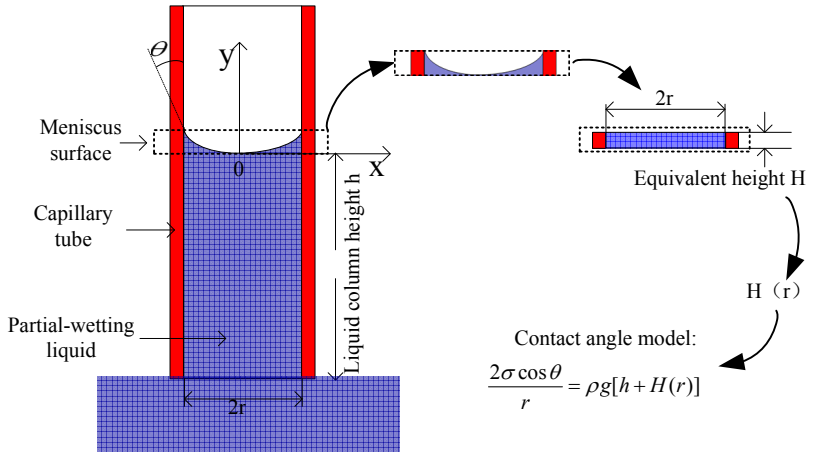

Fig. 1 Experiment and modeling process

3.1 Experiments and measurements

Liquid column heights in the capillary tubes were measured by capillary rise method and capillary decline method which were separately noted by ↑and↓ in the following paper, Table 1.

Table 1 Liquid column heights

r[mm]	Experiment methods	distilled water	sesame oil	alcohol
		h[mm]	h[mm]	h[mm]
0.15	↑	73.9	39.4	28.3
	↓	75.7	44.3	29.0
0.5	↑	10.8	10.2	9.8
	↓	27.1	14.1	10.0
1.4	↑	8.0	3.9	2.7
	↓	8.4	3.9	2.7

3.2 Feature points on the meniscus

Feature points incorporating coordinate values and the real contact angle on the rightmost position, shown in Fig. 2 with discrepant marks, can be obtained by Matlab and Eq. 3.

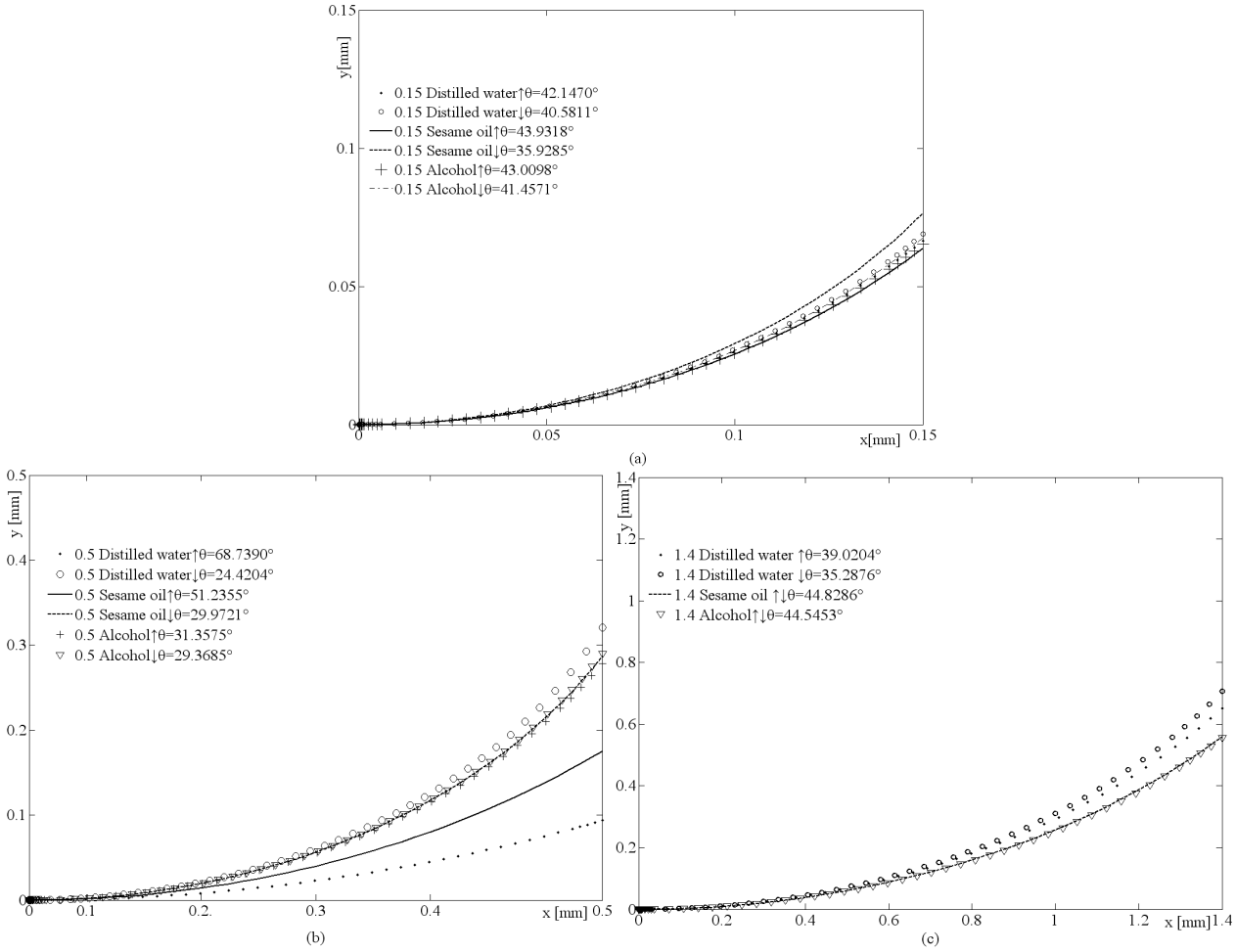

Fig. 2 Feature points on semi-meniscus (a, b and c are respectively corresponding to the experiments with capillary tubes of radii 0.15, 0.5 and 1.4[mm])

3.3 Modeling of equivalent heights

Definition: equivalent height is defined as the liquid column height under the same tube corresponding to the partial liquid volume under moon surface.

Following to the principle of equal volume, equivalent heights, see Table 2, can be determined by definite integral process to meniscus curves fitting from feature points. As it is shown bellow, equivalent heights present some specific order: equivalent heights appear positively correlation with tube radii under the same experiment conditions, which is the hypostasis for further procedure. In this work, equivalence height H was written as an expressing for H(r):

$$H(r)=\frac{1}{3}r+ar^2+br^3, \tag{4}$$

with a and b appear as the materials coefficients. See Table 2 and Fig. 3.

Table 2 Equivalent heights and their functional coefficients (units of [mm])

H	r			Eq. 4	
	0.15	0.5	1.4	a	b
distilled water↑	0.03112	0.04626	0.2995	-0.7054	0.4429
distilled water↓	0.03209	0.1383	0.3200	-0.1462	0.051
sesame oil↑	0.03006	0.08396	0.2613	-0.4645	0.2569
sesame oil↓	0.03510	0.1275	0.2613	-0.1939	0.06363
alcohol↑	0.03062	0.1245	0.2575	-0.2149	0.07729
alcohol↓	0.03161	0.1282	0.2575	-0.1912	0.06038

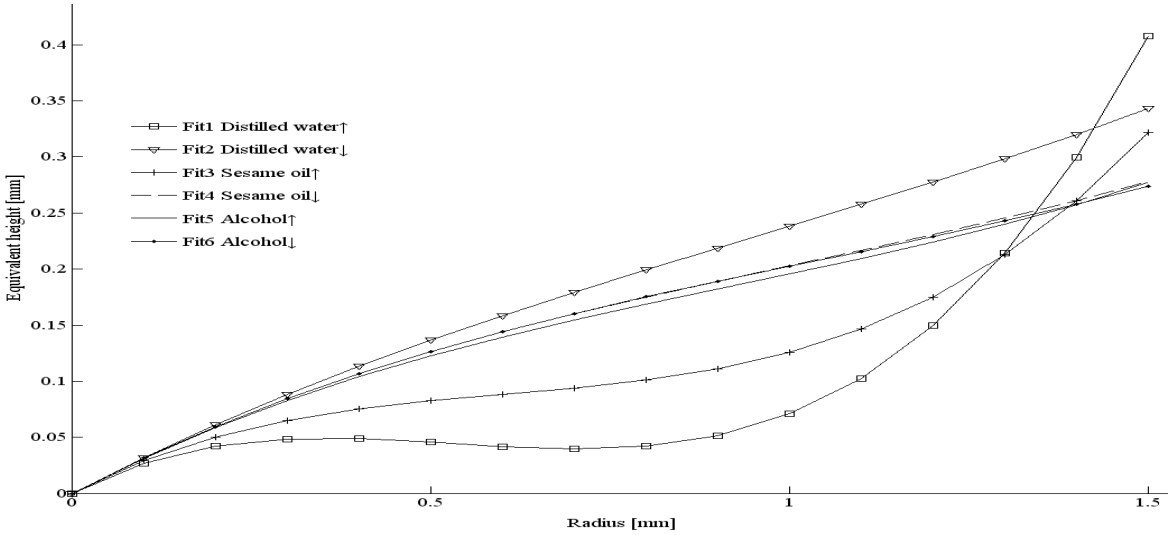

Fig. 3 Fitting cures of equivalent heights corresponding to functions in Table 2.

3.4 Modeling of contact angle

Considering the flaw of Jurin formula, equivalent height function H(r) is introduced into contact angle model:

$$\frac{2\sigma\cos\theta}{r} = \rho g h[h + H(r)], \tag{5}$$

here parameters of H(r) corresponding to given material systems, Table 2.

3.5 Empirical evidences

Capillary rise experiments of radius 0.25[mm] on the methods introduced above produced the measurements of liquid column heights, just as recorded in Table 3.

Table 3 Liquid column heights with tube radius of 0.25mm

r[mm]	Experiment methods	Distilled water	Sesame oil	alcohol
		h[mm]	h[mm]	h[mm]
0.25	↑	55.3	28.2	20.3
	↓	57.9	31.3	20.9

Respective related errors of Jurin angles and ‘angles from Eq. 5’ comparing to real contact angles given by Eq. 3 can be illustrated on Fig. 4.

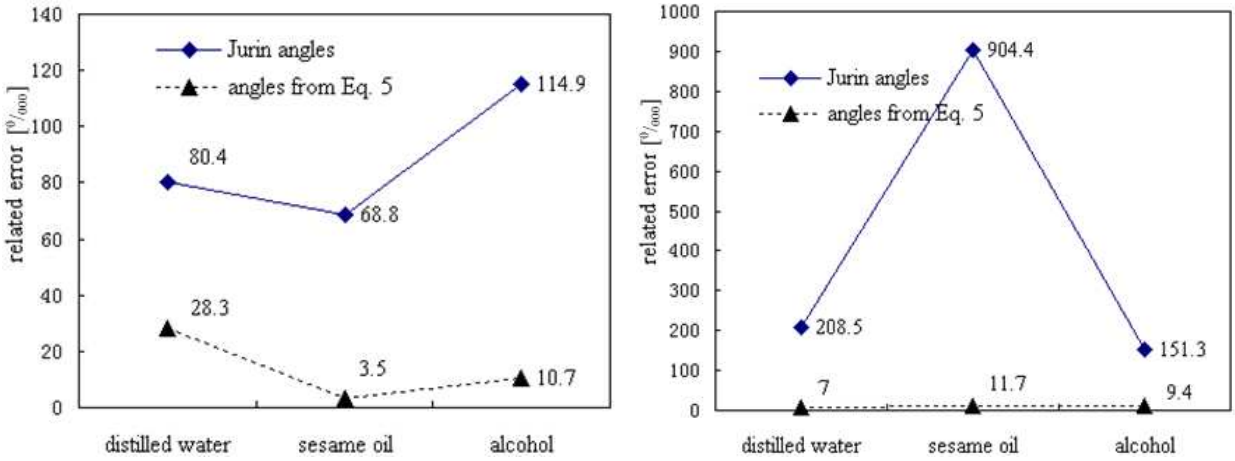

Fig.4 Related errors with capillary rise method (left) and decline method (right)

It is clearly shown that formulas proposed in Table 2 with a much higher quality on accuracy than its of Jurin's.

4 Conclusions

Equivalent heights were found to positively correlate to tube radii by capillary rise experiments in this paper. With this hypostasis, Jurin formula was refined successfully so as to eliminate the flaw widely known.

With great increase of precisions compared to Jurin formula, the models for given materials and the refinement methods for Jurin formula in this investigation are eventually convinced to be available and efficient to engineering application for contact angle prediction.

References

[1] R. Finn, Capillary Surface Interfaces, J. Notices of the AMS. 46 (1999) 770-781.
[2] T. Young, An essay on the cohesion of fluids, J. Philosophical Transactions. 95 (1805) 65-87.
[3] J. Jurin, An account of some experiments shown before the Royal Society; With an enquiry into the cause of the ascent and suspension of water in capillary tubes, J. Philosophical Transactions. 30 (1717-1719) 739-747.
[4] J. Jurin, An account of some new experiments, relating to the action of glass tubes upon water and quicksilver, J. Philosophical Transactions. 30 (1717-1719) 1083-1096.
[5] S.Q. Gao, H.P. Liu, Capillary mechanics, first ed., J.Y. Geng, Beijing, 2010.
[6] L. Rayleigh, On the theory of the capillary tube, J. Proceedings of Royal Society of London Series A. 92 (1916) 184-195.
[7] R.Z. Huang, Why does not the liquid column in capillarity rise to the expected height? J. College Physics. 18 (1999) 12-13.
[8] C.W. Li, Y. Hong, X.Z. Wang, et al, Another method for measuring the height in a capillary tube, J. College Physics. 15 (1996) 20-21.
[9] J. Li, Errors in measuring the surface tension coefficient of pure water with capillary tube, J. Physics Experimentation. 23 (2003) 45-47.
[10] T.R. Gu, B.Y. Zhu, W.L. Li, et al, Surface Chemistry, first ed., S.Q. Lu, Beijing, 1994.

doi:10.4028/www.scientific.net/AMM.161.26

Bending solid elastic waves with arbitrary angles by bricks

Jin Hu[1, a] and XiangYang Lu[1, 2]

[1]1School of Information and Electronics, Beijing Institute of Technology, Beijing 100081, People's Republic of China

[2] School of Electronic and Information Engineering, Zhongyuan University of Technology, Zhengzhou 450007, People's Republic of China

[a] bithj@bit.edu.cn (corresponding author)

Keywords: cloak, transformation optics, transformation acoustics, transformation elastodynamics

Abstract. Transformation method provides an efficient way to control wave propagation by materials. Recently, this method has been extended to control elastic waves in solids in case of high frequency or small material gradient. An important device in practice, elastodynamic beam bender with isotropic materials, can be designed by this method. In this paper, we will explore some characteristics of the isotropic elastodynamic beam bender and show that it can be used as bricks to guide the solid elastic beam to arbitrary angles, providing more flexibility in engineering practices. Examples are conceived and validated by numerical simulations.

Introduction

Recently, the transformation method provides a new tool to design devices which control electromagnetic waves propagation [1,2,3]. Such devices usually have complex material properties with spatial variation, which is difficult to be realized by nature material. However, this difficulty can be overcome with the development of metamaterials [4]. Many interesting devices based on transformation method, such as cloak [4], have been reported. The method is also extended to acoustic wave for liquid materials [5], heat conduction [6] and matter waves [7]. Based on physical interpretation of form-invariance [8], Hu et al. [9] derived the transformed material parameters for solid elastic wave in case of high frequency or small material gradient. Based on that results, Chang et al. [10] obtained the transformed material parameters for elastic wave under local conformal mapping, and such isotropic materials, which can have many advantages in easy fabrication and broadband application, are then applied to design a beam bender, a directional antenna, and an approximately carpet cloak. As one of the interesting devices, the beam bender can change the propagation direction of waves, it surely have many applications in practices. Therefore, to improve the convenience and flexibility for this device, deeper study on the isotropic beam bender for solid elastic wave is necessary; this is the objective of this paper.

Design of the isotropic beam bender

According to the transformation elastodynamics, during the mapping, the stress $\boldsymbol{\sigma}$, displacement $\mathbf{u}$, stiffness $\mathbf{C}$ and density ρ attached on a spatial element at the point $\mathbf{x}$ in the virtual space will experience a rigid rotation $\mathbf{R}$ and then scaling to reach the point $\mathbf{x}'$ in the physical space. Symbolically the transformations can be written as [8,9]

$$\mathbf{V_q R}: \mathbf{q} \mapsto \mathbf{q}', \quad \mathbf{q} = \boldsymbol{\sigma}, \mathbf{u}, \mathbf{C}, \boldsymbol{\rho}, \tag{1}$$

where $\mathbf{V_q}$ is the scaling tensor for the quantity $\mathbf{q}$, and it has a diagonal form in the specially established frame, i.e.,

$$\mathbf{V}_{\boldsymbol{\sigma}} = \mathrm{diag}[a_1, a_2, a_3], \mathbf{V}_{\mathbf{u}} = \mathrm{diag}[b_1, b_2, b_3], \mathbf{V}_{\mathbf{C}} = \mathrm{diag}[c_1, c_2, c_3], \mathbf{V}_{\boldsymbol{\rho}} = \mathrm{diag}[d_1, d_2, d_3], \tag{2}$$

where a_i, b_i, c_i and d_i are scaling factors for stress, displacement, stiffness and density, respectively, and they can be obtained by [9]

$$\frac{a_i a_j}{d_J b_J} = \lambda_i, \quad \frac{a_i a_j}{c_I c_J c_K c_l b_k} = \frac{1}{\lambda_l}, \quad a_i a_j b_I = \frac{\lambda_j}{\lambda_1 \lambda_2 \lambda_3}. \tag{3}$$

The capital letter in index means the same value as its lower case but without summation. Further consider a local conformal mapping at each point, i.e., $\lambda_1 = \lambda_2 = \lambda_3 \equiv \lambda$, then the transformed material parameters are finally derived in the global frame as [10]

$$\mathbf{C}' = a^4 \lambda^N \mathbf{C}, \rho' = a^4 \lambda^{N-2} \rho, \boldsymbol{\sigma}' = a^2 \mathbf{R}\boldsymbol{\sigma}\mathbf{R}^{\mathrm{T}}, \mathbf{u}' = a^{-2} \lambda^{1-N} \mathbf{R}\mathbf{u}. \tag{4}$$

This equation provides the transformed material parameters for a local conformal transformation, and both modulus and density are isotropic in the physical space.

To design a 2D device which can bend the elastic wave, we consider the transformation that maps a square area to a sector area, as shown in Fig. 1. Under a spatial transformation that makes the plate be transformed into the arc shape (see Fig. 1) with a polar angle β, it is easily shown that there is only no-zero stretch in $\hat{\boldsymbol{\theta}}$ direction during the transformation, and this stretch can be easily obtained by comparing the arc length of the bender βr with its original length ka. Therefore, the two principle stretches at each points of the bender have the following forms [11]

$$\lambda_\theta = \beta r / (ka), \tag{5a}$$

$$\lambda_r = 1. \tag{5b}$$

It can be shown that in this spatial transformation the stretches λ_θ and λ_r are independent to each other. Thus, we can set $\lambda_r = \lambda_\theta = \lambda = \beta r / (ka)$ and the bender can be isotropic.

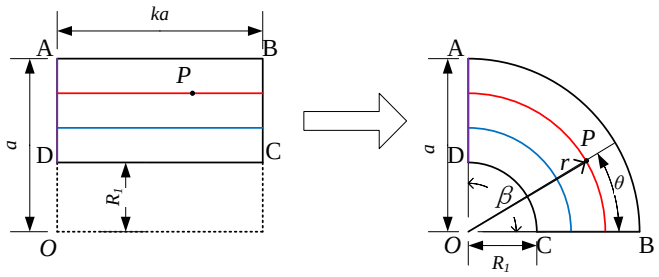

Figure. 1 Transformation for a beam bender.
Left: virtual space; right: physical space.

Characteristics of the isotropic elastodynamic beam bender

Impedance matched on the boundaries. For perpendicularly incident waves, the impedance matched condition for both S and P waves is given as [12]

$$\rho' \mathbf{C}' = \rho \mathbf{C}. \tag{6}$$

From Eq. (4), the impedance-matched transformed material parameters are derived as

$$\mathbf{C}' = \lambda \mathbf{C},\ \rho' = \rho / \lambda, \tag{7a}$$

or

$$E' = \lambda E,\quad \upsilon' = \upsilon,\quad \rho' = \rho / \lambda, \tag{7b}$$

where E and υ denote Young's modulus and Poisson's ratio of the media, respectively.

Material parameters are independent to the angle. From Eq. (5a) and (7), we see that the material parameters are only the functions of r and independent to angle θ in the cylindrical coordinate system, as shown in Fig. 2, which is the bender of k=1, $\beta = \pi/2$, where the Young's modulus and density of the background materials 200 GPa and 7850 kg/m^3, respectively.

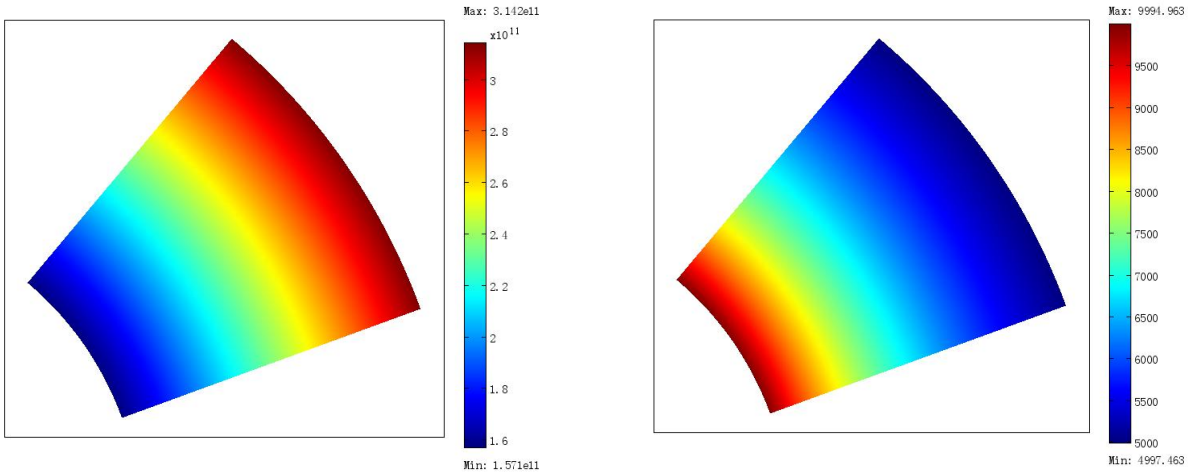

Figure. 2 Material parameters in a beam bender.
Left: Young's modulus; right: density.

Isotropic brick-bender

Generally, a beam bender can only bend the waves to a certain degree, depend on the polar angle β of the bender. Therefore, in order to bend the beam to different angles, we need to design different benders. However, by utilizing the characteristics of the isotropic elastodynamic beam bender in the previous section, one can design only one kind of bender, called bricks-bender, and assemble the bricks-benders to make a whole bender, which can guide the beam to arbitrary angle in a predefine resolution. This is possible because the material parameters are independent to the angle coordinate, thus a bricks-bender can be placed on any angle in the bender; in addition, as the material parameters are continuous between boundaries of the bricks-benders and are impedance matched to the background materials, there are no reflections in any boundary. Since one only need to prepare limited kinds of bricks-bender and can manufacture these bricks before any application, this idea can provide more flexibility in engineering practices.

For example, if the resolution of the bending is 10°, then the bricks-bender is a bender with polar angle $\beta = 10^\circ$. Any bender that tries to bend the elastic beam to degrees of integer multiples of 10° (namely, $n \times 10^\circ$, n is integer and $0 \le n \le 36$) can be simply built by assembling these bricks-benders. Figure 3 shows a bender made of by 18 such bricks-benders, and the whole bender can bend the incident wave to new direction have 180° to the original direction, or, inverse the incident wave.

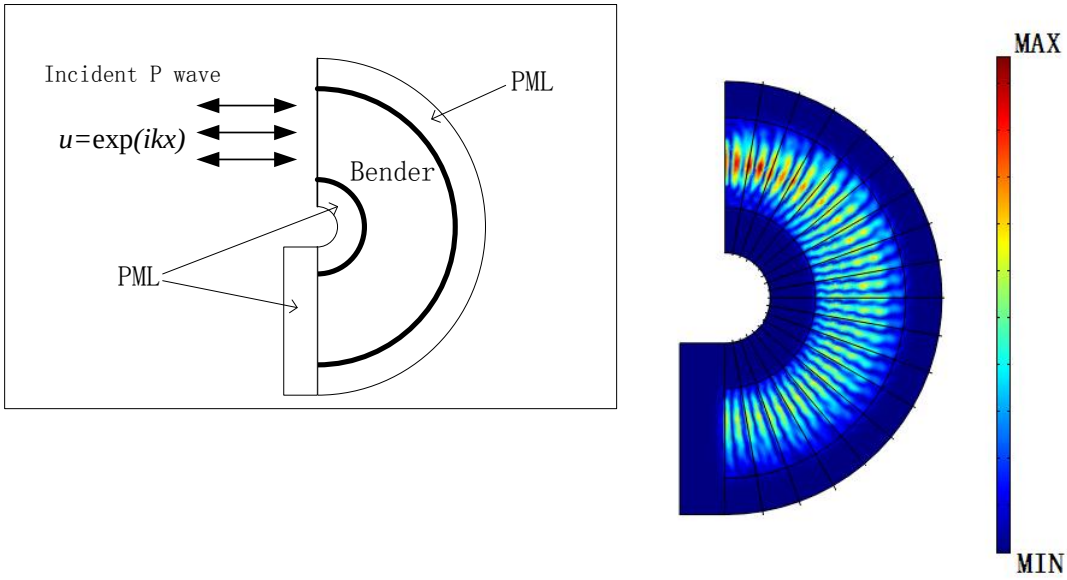

Figure. 2 The whole 180° beam bender make of by 10° bricks-benders.
Left: the computing domain; right: the total displacement in the bender, for incident P wave.

Summary

To conclude, the isotropic beam bender for elastic wave has been introduced, and some important characteristics of this device are disinterred. Subsequently, the idea of assembling bricks-benders to make a whole bender to guide the beam to arbitrary angle is developed, based on these characteristics. Such a strategy can bring more flexibility in engineering practices. Numerical simulations verified such an assembled bender.

Acknowledgements
This work was supported by the National Natural Science Foundation of China (11172037).

References

[1] J. B. Pendry, D. Schurig and D. R. Smith, Science 312, 1780 (2006).
[2] U. Leonhardt, Science 312, 1777 (2006).
[3] A. Greenleaf, M. Lassas and G. Uhlmann, Math. Res. Lett. 10, 685 (2003).
[4] D. Schurig, J. J. Mock, B. J. Justice, S. A. Cummer, J. B. Pendry, A. F. Starr, D. R. Smith, Science 314, 977 (2006).
[5] H. Chen and C. T. Chan, Appl. Phys. Lett., 91, 183518, 2007.
[6] T. Chen, C. N Weng and J. S. Chen, Appl. Phys. Lett., 93, 114103 (2008).
[7] S. Zhang, D. A. Genov, C Sun and X. Zhang, Phys. Rev. Lett., 100, 123002 (2008).
[8] J. Hu, X. N. Liu and G. K. Hu, arXiv:0912.5462.
[9] J. Hu, Z. Chang, and G. Hu, Phys. Rev. B 84, 201101(R) (2011).
[10] Z. Chang, J. Hu, G. Hu, R. Tao and Y. Wang, Appl. Phys. Lett. 98, 121904 (2011).
[11] Q. Deng, J. Hu, Z Chang, X. Zhou and G. Hu, Adv. Mater. Res. 150-151, 1508 (2011).
[12] J. Achenbach, *Wave Propagation in Elastic Solids*. (North-Holland Pub. Co., Amsterdam, 1973).

doi:10.4028/www.scientific.net/AMM.161.30

Tensile Properties of 4D In-plane C/C Composites

GAO Bo[1,2,a], TANG Min[1,2,b], and SHI Hong-bin[2,c]

[1.] Xi'an Hi-tech Institute, Xi'an 710025, P.R.China

[2.] The institute of Xi'an aerospace and propulsion, Xi'an 710025, P.R.China

[a]leegoop@126. com, [b]tm7414@sohu.com,[c]tm41@sohu.com

Key words: 4D in-plane C/C composites; Hoffman criterion; Twin shear strength theory; Interface

Abstract. The tensile properties of 4D in-plane carbon/carbon (C/C) composites were researched by MTS machine and ARAMIS optical strain test system. A damage model for analysis the gradual damage was proposed, which chose hoffman criterion and twin shear strength theory as the failure criterion of fiber bundle and matrix, respectively. Cohesive zone model was used to simulate the interfacial debonding at the fiber bundle/matrix interface. The effect of shear strength of fiber bundle/matrix interface on the tensile strength was researched. It is shown that the major factor caused by the failure of the material at axial tensile is the interface debonding, which make the fiber bundle pull out from the matrix. The failure factor for the radical tensile is the crack through out the fiber bundle and matrix, and that make the material fracture. Simulation result shows the interface shear strength have a significant effect on the tensile strength. With the strength promote, the tensile strength increase, and the best value of interface strength is 11MPa.

1. Introduction

4D In-plane C/C Composite is an advanced material for its property of thermal ablation. It is widely used in aerospace industry, for which the mechanical and thermo physical properties could satisfied the working condition of the engine. Due to its own weave mode, the stretch performance of the material is weak. Therefore, it is important to have focus on the tensile properties.

Until recently, there are many researchers focused on the general properties of C/C Composite [1-5]. However, the study of 4D In-plane C/C Composite is insufficient. C.F.Baker[6] had focused on the mechanics and thermal properties of the material and the work give a guide for characterizing its properties. He had given the tensile and compresses strength in radical and axial direction. Tang[7] had predicted the engineer constants by homogenization theory. Liao[8] had analysis the axial tensile properties of the material by suppose the layer of each fiber bundle direction is isotropy and he give a conclusion that the major factor of axial tensile failure is the interface debonding.

However, there are few literatures on the nonlinear behavior of 4D In-plane C/C composites. Recently, the authors develop a numerical method to predict mechanical properties. The purpose of the present paper is to apply this numerical method to predict the nonlinear response and failure of 4D In-plane C/C composites, and got the effect of interface strength on it.

2. Experimental procedure

2.1. Materials

In the 4D in-plane architecture composites, shown in Figure 1, three fiber bundles are placed in X-Y plane at orientation to each other (i.e. along 0^o ,120^o ,240^o to the X-axis) and the forth fiber bundle is oriented along the Z-axis[9]. Finally, the architecture is hot processed for carbonized, and followed by heat treatment for graphitization.

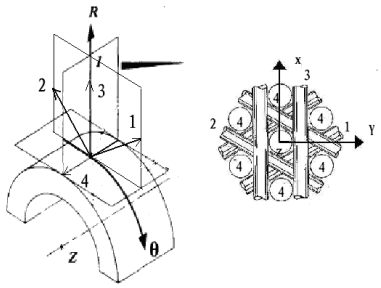

Figure.1 Braid manner of 4D in-plane C/C composites

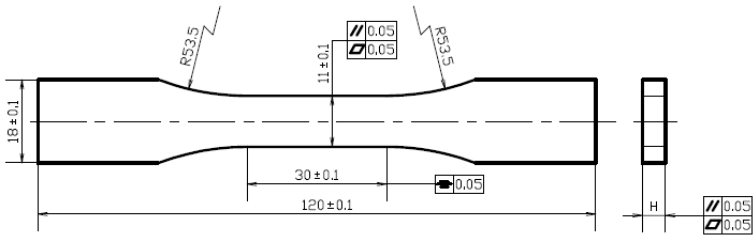

Figure.2 Tensile sample

2.2 Sample

According to the braid manner and the production size, the size of the tensile sample is illustrated in Fig.2. In the sample, the size of H is 5mm, which make the sample have two unite cell. Aluminum tabs were fixed on both ends of the specimen to prevent crushing of the specimen due to gripping in the machine jaws.

2.3 Experiment

Tensile tests were performed on 4-directional in-plane C/C specimens using a MTS testing machine at a cross-head speed of 0.5 mm/min. Longitudinal deformation was measured by using ARAMIS optical test system. Every batch has six samples.

2.4 Experiment result

The radical tensile strain figure is illustrated in fig.3. It shows that the cracks produce in the surface of matrix and propagation along the fiber bundle. Interface has made the crack deflection, which is proved in the microstructure illustrated in fig.4. Along the ply, the cracks expand like stage. Lastly the fiber bundle fractured wholly.

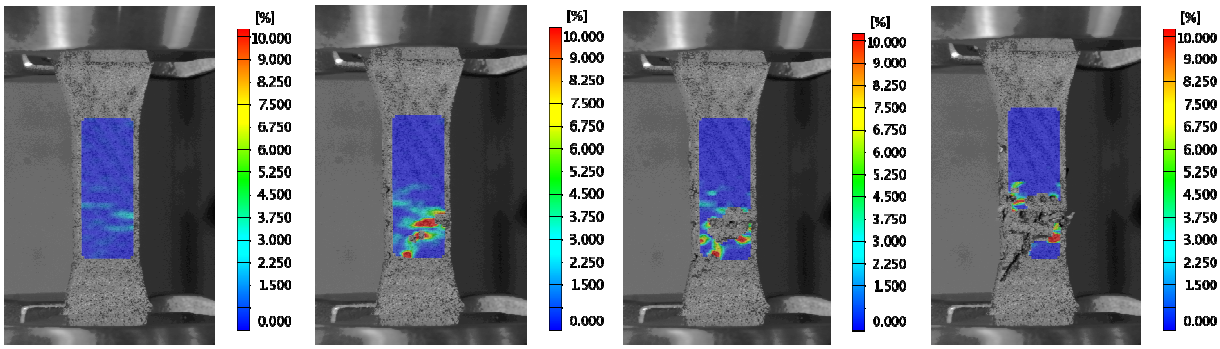

Figure.3 Tensile strain of radical tensile

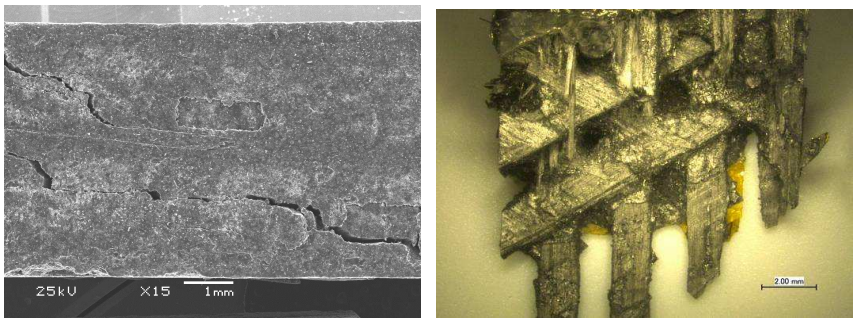

Figure.4 Failure mode of radical tensile

Fig.5 is the strain of axial tensile. Crack propagation along the layers of fiber bundles, and that make the layers separation. The interface between the fiber bundle and matrix is destroyed then. Lastly, the fiber bundles are pulled out from the matrix accompanied by part of fiber bundles fracture. The SEM of axial tensile fracture illustrated in fig.6 shows the failure mode which embodies the interface is weakly.

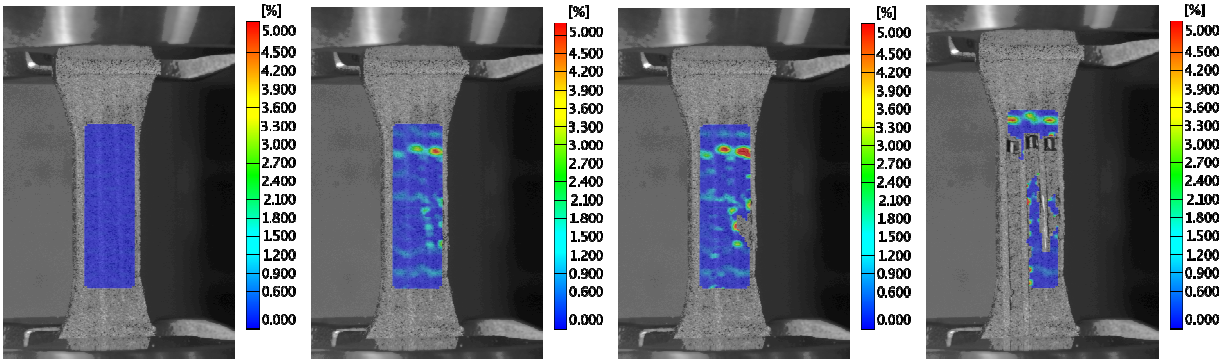

Figure.5 Tensile strain of axial tensile

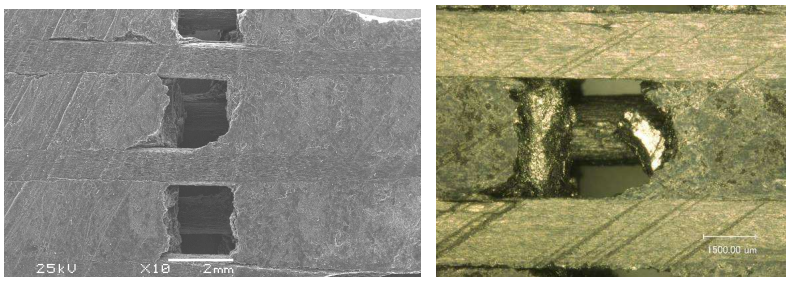

Figure.6 Failure mode of axial tensile

3 Damage Model for 4D In-plane C/C composite

3.1 Unite cell of 4D In-plane C/C composite

According to the braided structures, a model of unit cell is proposed, and the typical size of it is 5.88mm×3.4mm×3.2mm. The unite cell which is meshed with eight-noded isoparametric hexahedral elements is illustrated in Figure 7. The interface thickness is defined as 0.05mm according to the microstructure of interface.

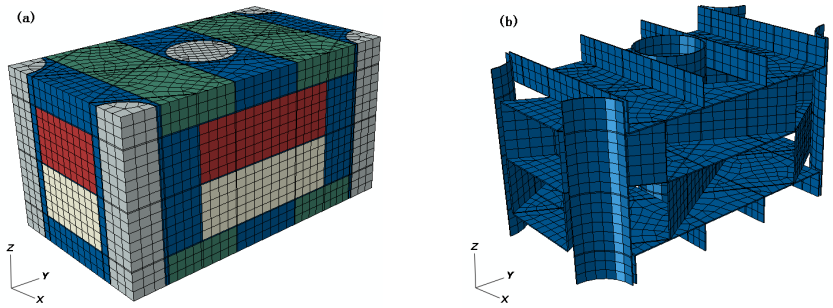

Figure. 7 (a) Finite element model of 4D in-plane unit cell (b) Interface in unit cell.

3.2 Damage model

The stiffness will be degraded when damage occurs. Stiffness degradation is associated with damage mode. Hoffman strength criterion is used to judge the failure of carbon rod and fiber bundle, and the concrete form of Hoffman strength criterion is defined as follow.

$$\begin{aligned} Hf &= C_1(\sigma_2-\sigma_3)^2 + C_2(\sigma_3-\sigma_1)^2 + C_3(\sigma_1-\sigma_2)^2 + C_4\sigma_1 + C_5\sigma_2 \\ &\quad + C_6\sigma_3 + C_7\tau_{23}^2 + C_8\tau_{31}^2 + C_9\tau_{12}^2 \geq 1 \\ C_1 &= 1/YY' - 1/(2XX'),\ C_2 = C_3 = 1/(2XX'),\ C_4 = (X'-X)/XX' \\ C_5 &= C_6 = (Y-Y')/YY',\ C_7 = 1/(S')^2,\ C_8 = C_9 = 1/S^2 \end{aligned} \tag{1}$$

where X and X′ are the tensile and compress strength along fiber direction, Y and Y′ are the tensile and compress strength perpendicular to fiber direction. S^* and S are the shear strength of in-plane and out-plane, respectively.

Once the above criterion is satisfied, the fiber damage variable, d_k^f, evolves according to the equation (2).

$$d_k^f = 1-[1/Hf]\exp[-C_{ij}e_{ij}^f[Hf-1]L/G_n],(k=LL,TT,ZZ,ZT,LT,LZ;i,j=1,2,3) \tag{2}$$

Where, L^c is the characteristic length associated with the material point.

Similarly, damage initiation in the matrix is governed by the following criterion

$$\begin{cases} \phi_m = [\sigma_1 - \alpha(b\sigma_2+\sigma_3)/(1+b)]/\sigma_t > 1, \sigma_2 \le (\sigma_1+\alpha\sigma_3)/(1+\alpha) \\ \phi_m^{'} = (\sigma_1+b\sigma_2)/(1+b) - \alpha\sigma_3/\sigma_t > 1, \sigma_2 \ge (\sigma_1+\alpha\sigma_3)/(1+\alpha) \\ b = [(1+\alpha)\tau_0 - \sigma_t]/(\sigma_t - \tau_0), \alpha = \sigma_t/\sigma_c \end{cases} \tag{3}$$

Where τ_0, σ_t, σ_c are the shear strength, tensile strength and compress strength, respectively. The parameter b show influence of the middle principle stress and the positive stress .The evolution law of the matrix damage variable, d_k^m, is

$$d_k^m = 1-[1/\phi_m]\exp[-C_{ii}e_{ii}^f[\phi_m-1]L/G_n],(k=L,T,Z;i=1,2,3) \tag{4}$$

During progressive damage the effective elasticity matrix is reduced by the damage variables d_k^f and d_k^m, and the damage elasticity matrix C_d is expressed as the equation (5).

$$C_d = \begin{bmatrix} f_l^2C_{11} & f_lf_tC_{12} & f_lf_zC_{13} & 0 & 0 & 0 \\ & f_T^2C_{22} & f_Tf_zC_{22} & 0 & 0 & 0 \\ & & f_Z^2C_{33} & 0 & 0 & 0 \\ & sym & & f_{LT}C_{44} & 0 & 0 \\ & & & & f_{ZL}C_{55} & 0 \\ & & & & & f_{TZ}C_{66} \end{bmatrix} \tag{5}$$

Where , $f_L = 1-D_L, f_T = 1-D_T, f_Z = 1-D_Z$, $f_{LT} = (2(1-D_L)(1-D_T)/(2-D_L-D_T))^2$, $f_{TZ} = (2(1-D_T)(1-D_Z)/(2-D_T-D_Z))^2, f_{ZL} = (2(1-D_Z)(1-D_L)/(2-D_Z-D_L))^2$.

The value of $D_I(I=L,T,Z)$ are determined by the following equation.

$$\mathrm{D}_L = d_{LL}, D_T = \max(d_{TT},d_{LT},d_{TZ}), D_Z = \max(d_{ZZ},d_{ZT},d_{LZ}) \tag{6}$$

The matrix is supposed as isotropy, and the damage tensor are determined by the equation (7).

$$D_L = D_T = D_Z = d_k^m, k = L,T,Z \tag{7}$$

The stresses are updated according to the following equation.

$$\sigma = C_d : \varepsilon \tag{8}$$

The Jacobian matrix can be obtained by differentiating the above equation.

$$\frac{\partial\sigma}{\partial\varepsilon} = C_d + \left(\frac{\partial C_d}{\partial D_L}:\varepsilon\right)\left(\frac{\partial D_L}{\partial\varepsilon}\right) + \left(\frac{\partial C_d}{\partial D_T}:\varepsilon\right)\left(\frac{\partial D_T}{\partial\varepsilon}\right) + \left(\frac{\partial C_d}{\partial D_Z}:\varepsilon\right)\left(\frac{\partial D_Z}{\partial\varepsilon}\right) \tag{9}$$

To improve convergence, a technique based on viscous regularization of the damage variables is implemented. In this technique we do not use the damage variables calculated from the before mentioned damage evolution equations directly; instead, the damage variables are “regularized” via the following equations.

$$\dot{D}_I^V = \left(D_I - D_I^V\right)/\eta_I, I = L,T,Z \tag{10}$$

To update the "regularized" damage variables at time $t_0 + \Delta t$, the above equations are discretized in time as follows.

$$D_L^V\Big|_{t_0+\Delta t} = \frac{\Delta t}{\eta + \Delta t} D_L\Big|_{t_0+\Delta t} + \frac{\eta}{\eta + \Delta t} D_L^V\Big|_{t_0} \tag{11}$$

From the above expressions it can be seen that

$$\frac{\partial D_L^V}{\partial D_L} = \frac{\partial D_T^V}{\partial D_T} = \frac{\partial D_Z^V}{\partial D_Z} = \frac{\Delta t}{\eta + \Delta t} \tag{12}$$

Therefore, the Jacobian matrix can be further formulated as follows.

$$\frac{\partial \Delta\sigma}{\partial \Delta\varepsilon} = C_d + \left[\left(\frac{\partial C_d}{\partial \Omega_T^V} : \varepsilon\right)\left(\frac{\partial D_T}{\partial f_t}\frac{\partial f_t}{\partial \varepsilon}\right) + \left(\frac{\partial C_d}{\partial D_Z^V} : \varepsilon\right)\left(\frac{\partial D_Z}{\partial f_z}\frac{\partial f_z}{\partial \varepsilon}\right) + \left(\frac{\partial C_d}{\partial D_L^V} : \varepsilon\right)\left(\frac{\partial D_L}{\partial f_l}\frac{\partial f_l}{\partial \varepsilon}\right)\right]\frac{\Delta t}{\eta + \Delta t} \tag{13}$$

3.3 Simulation for Interface

Surface-based cohesive behavior is implemented numerically in ABAQUS Version 6.9 to simulate the debonding of interface between fiber bundle and matrix. The interface between the fiber bundle and matrix is defined using traction separation constitutive relation.

The available traction-separation model in ABAUS assumes initially linear elastic behavior followed by the initiation and evolution of damage. Damage initiation refers to the beginning of degradation of the stiffness of a material point. The process of degradation begins when the stresses or strains satisfy certain damage initiation criteria that you specify. The damage evolution law describes the rate at which the material stiffness is degraded once the corresponding initiation criterion is reached. In this paper, maxs criterion and linear softening pattern were used as the damage initiation criteria and evolution pattern.

The HIT-300 machine was used to get the interface strength of the material made from different batch. The average normal and shear fracture energy of the interface are taken as 123 J/m^2 and the average normal and the shear strength of the interface as 8MPa and 3.5MPa, respectively. For study the effect of interface strength on the tensile strength, the shear strength is changed from 5MPa to 17MPa.

3.4 Boundary condition

In order to keep forces continuity and displacements compatibility of the opposite faces of the RVC, the periodic boundary conditions (BCs) should be imposed in the simulation. So the boundary condition for using unite cell to simulation the tensile properties is expressed in the following equation.

$$u_i(L_i) - u_i(0) = U_i, \quad \text{i=2,3} \tag{14}$$

$$\int_0^{L_i}\int_0^{L_1} \vec{t}\, dX_1 dX_i = 0, \quad \text{on } X_j = 0 \text{ or } L_j, \quad (i = 2\text{or}3, j = 3\text{or}2) \tag{15}$$

Where ,the direction 1 is the load direction, u_i is the node displacement in i direction, U_i is the displacement difference in I direction casued by the possion's effect, $\vec{t}$ is the integral vector, which made the external force on no-load surface be zero.

3.5 Simulation process

Eight-node Hex element is implemented to mesh geometry of the RVC. The above anisotropic damage model are carried out in material constitutive equation by User subroutine UMAT of ABAQUS nonlinear finite element codes. The simulation process can be described as follows.

(1) The local strains and stresses of yarns and matrix in the RVC are obtained by Newton–Raphson incremental method after the periodic BCs are applied.

(2) The strains, stresses and damage variables of integral point are introduced to UMAT. The integral point of element is identified whether it has damaged or not based on its damage variable values.

(3) Eqs. (1), (3) is used to judge whether the element integral point has damaged. Damage variables of the element integral point are updated by Eqs. (2), (4)–if it has damaged.

(4) Tangent constitutive tensor is updated. The values of stress and strain are calculated.

(5) The analysis goes to next increment after the convergence criterion is reached by several equilibrium iterations.

4. Results and discussion

Fig.8 is the simulation result of axial tensile. The curve shows the prediction value is higher than the experiment value, which is major caused by the difference between the experiment failure mode and the simulation failure mode. The failure mode in experiment is interface debonding accompanied by a part of fiber bundles failure, but that for the simulation is the whole fiber bundle fracture. With the increase of Z direction strain, the interface damaged firstly, and the matrix followed. When the damage percent of fiber bundles reach to 11% of the whole element of reinforce phase element, the material became destruction. The simulation result of radical tensile illustrated in fig.9 is the same as the axial. When the radical strain reach to 0.11%, the interface became damage, and that make the stiffness degrade firstly. The tensile strength is major controlled by the fiber bundles.

The change of tensile strength caused by the interface strength varied from 5MPa to 17MPa is illustrated in Fig.10. The effect of interface strength on the radical strength is than that of axial strength. When the interface strength reach to 11MPa, the gain of tensile strength decrease. The interface strength is increase with the decrease of voids according to porous media theory, and the interface strength can be estimated by the following equation.

$$S = R \times (1 - 1.209 V_p^{2/3}) \tag{16}$$

Where, R is the strength of interface without void, V_p is the value of voids. The value of R can use the strength of high purity graphite to replace, and that is 12.5MPa.

Because it is difficult to decrease the void when it reaches to 3%, so the best value of interface strength is 11MPa.

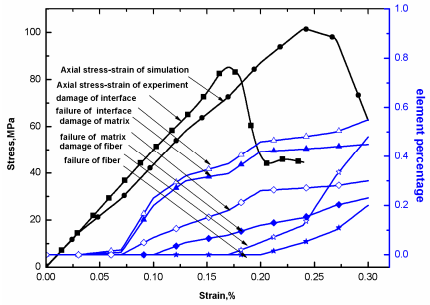

Figure.8 Damage process of axial tensile

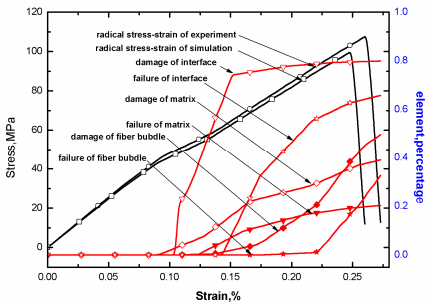

Figure.9 Damage process of radical tensile

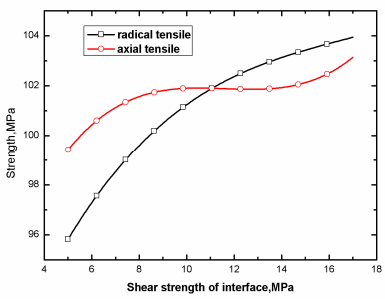

Figure.10 Effect of interface of strength on the tensile strength

5. Conclusion

Tensile properties of 4D in-plane C/C composites are obtained. Experiment results shown the failure of axial tensile is major due to the interface debonding between layers that make the fiber bundles pull out from the matrix, but the failure of radical tensile is the fracture of the fiber bundle.

Simulation results show the interface strength has a great effect on the tensile strength of radical, and that for the axial strength is smaller. When the interface strength has a change from 5Mpa to 11MPa, the tensile strength of radical direction will have a significantly increase. The best value of interface is 11MPa.

Reference

[1] Diss P, Lamon J, Carpentier L, Loubet JL, Kapsa P. Sharp indentation behavior of carbon/carbon composites and varieties of carbon,J. Carbon .2002, 40(14):2567–2579.

[2] Ozcan S, Filip P. Microstructures and wear mechanisms in C/C composites, J. Wear 2005,259 (1):642–650.

[3] Marx DT, Riester L. Mechanical properties of carbon–carbon composites components determined using nanoindentation.Carbon (UK). 1999, 37(11):1679–684.

[4] Ozcan S, Krkoska M, Filip P. Frictional Performance and local properties of C/C composites ,J. Ceram Eng Sci Proc. 2005, 26(8):127–138.

[5] Meng songhe, Kan jin, Xu chenghai,et al. Relations between microstructures and mechanical properties of fiber-matrix interfaces in C/ C composites,J. Acta Materiae Compositae Sinica .2010, 27(1): 129-132.

[6] C.F.Bake. low cost,low erosion,advanced material. AIAA-94-3187.

[7] Tang Min, GAO Bo,et al. Homogenization Based Method for Predicting Mechanics Properties of 4D-inplain Carbon/Carbon Composites.J.2011.(1)109-118.

[8] Liao Y ing qiang, L iu Yong qiong . Progressive Damage of C /C Composite Made by Axial Rod Method Under Axial Tension Load. Aerospace material & technology.J.2011, (2):51-54.

[9] Su Junming,Cui Hong,Su Zhean,et al. Research of 4D C/C composites material throat insert by mix weaved with carbon fiber and axial carbon rod,J.Carbon.2004,117(1):12-16.

doi:10.4028/www.scientific.net/AMM.161.37

Study and Design on Clean Steel Production Platform

ZHANG Fuming

Beijing Shougang International Engineering Technology Co.,LTD,Beijing 100043, China

Email: zhangfuming@bsiet.com

Keywords: steelmaking; continuous casting; clean steel; hot metal pretreatment; secondary refining

Abstract: The technology for clean steel production in modern steel plant is analyzed, a philosophy with production efficiency, manufacturing cost and product performance in its core. A review on functions is also made which of high-efficiency, low-cost and high-quality steel products manufactured by the new generation iron and steel plant, in combination with the study on design of steelmaking – continuous casting process of Shougang Jingtang iron and steel plant. By applying precise and dynamic design system to optimize and allocate systems and working procedures of hot metal pretreatment, converter smelting, secondary refining, continuous casting process, etc, a platform of high-efficiency, low-cost and high-quality clean steel production is built.

Introduction

In the development of iron and steel industry, the production of clean steel has speeded up the optimization of process flow and improvement of product quality, demand by the society for clean steel production are growing up, a construction of a brand new, large scale, high efficient and low cost clean steel production system is urgently needed.

Shougang Jingtang plant is a new generation of cycling iron and steel plant designed and constructed with cycling economy concept. The product is positioned at high level prime steel plate, the designed capacity is 9.275 million ton of steel. Two 5500m^3 BFs with capacity of 8.982 million ton, one steel plant equipped with two 300t dephosphorization converters, three 300t decarburization converters and three slab CCM are built; 2250mm and 1580mm hot tandem rolling lines are built with 2230mm, 1700mm and 1550mm three cold rolling lines, the hot-cold rolling conversion ratio is 57.2% and coating-galvanizing ratio is 65.7%. Leading product of hot rolling is high quality auto plate, featured products are pipe line steel, pressure vessel steel and ship building steel. Tensile strength of high strength steel can reach 1200MPa max., the grade of pipe line steel is X100. Cold rolled products include high strength steel such as solid solution type, precipitation type, bake-hardening type, DP steel and TRIP steel, the highest strength level of which is 780MPa; the highest strength level of hot dip galvanized product is 590MPa and the highest strength level of color coated product is 440MPa [1].

The design and construction of Shougang Jingtang follows the design concept of "modern process, high efficient process flow and optimized benefits", in steelmaking-continuous casting procedure, design mode of hot metal "3-all-removal" pretreatment is adopted, hot metal is pre-treated with full-amount desulphurization, desilicification and dephosphorization, the dynamic precision design system is used to optimize the process flow of each unit from BF hot metal transportation→hot metal pre-treatment→ converter smelting→ secondary refining→ continuous casting, constructing a dynamic precision production system based high efficient, low cost and high quality clean steel production system [2].

Composition of Clean steel Production System

Shougang Jingtang steelmaking plant, through analysis and integration of each procedure of steelmaking-continuous casting and in accordance with the design concept of hot metal "full-3-removal" established a dynamic, orderly, compact, continuous, high efficient and stable clean steel production system. Steelmaking plant is equipped with 4 KR hot metal desulphurization facilities, two 300t converters for hot metal desilicification - dephosphorization pretreatment, three

300 high efficient converters, one multi-function LF, two multi-function RH, two CAS molten steel secondary refining facilities and three high efficient slab CCM, established a optimized production process of hot metal short flow–hot metal pre-treatment→ high efficient converter smelting→ secondary refining→ high efficient continuous casting.

Hot metal Transportation and Pretreatment

Hot metal transportation. Hot metal transportation adopts "one-ladle-through" technology, eliminating torpedo car, BF hot metal is charged directly into hot metal ladle and transported to steelmaking plant. This technology reduced hot metal re-ladling, shortened process flow, avoided fume pollution, increased hot metal temperature and is beneficial for hot metal desulphurization. Practice shows that the hot metal temperature of "one-ladle-through" technology is 25℃ higher than that of torpedo transportation.

Hot metal pretreatment process. Hot metal pre-treatment procedure includes hot metal desulphurization, desilicification, dephosphurization- "full-3-removal treatment", equipped with 4 sets of KR desulphurization devices and two sets of 300t desilicification-dephosphurization converters. Figure 1 shows the KR hot metal desulphurization process flow.

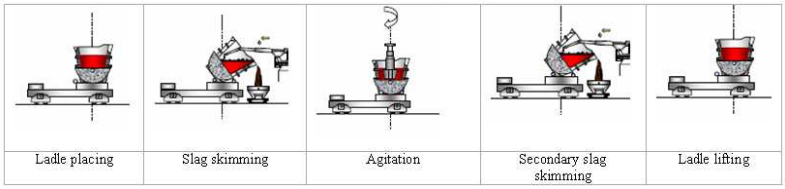

Fig.1 KR hot metal desulphurization process flow diagram

Hot metal desulphurization adopts 4 sets of KR mechanical agitation desulphurization facilities, which can high efficiently and stably satisfy the requirement of clean steel plate on sulphur content. The main technical features of KR desulphurization process as follows: Excellent kinetic condition, high desulphurization efficiency, desulphurization efficiency is 90%~95%; Desulfurizer is lime and a few fluorite, price is moderate and operation cost is low; Lime powder produced by active lime shaft kiln is used, and pneumatic conveying is used, operation cost is low; KR desulphurization process can effectively prevent hot metal from resulphurization, desulphurization result is stable; KR desulphurization process adopts secondary slag skimming, treating cycle is 38~42min, operating time matches dephosphurization converter.

Through the analysis and integration of converter smelting function, in order to further increase production efficiency and molten steel cleanliness, converter staged smelting concept is adopted, traditional converter integration of desilicification, dephosphurization and decarburization is changed to dedicated converters for hot metal desilicification and dephosphurization pretreatment, while top and bottom compound blown converter is used for decarburization and heating up only, thus the metallurgical reaction efficiency and molten steel cleanliness is further increased. Converter staged smelting is realized, traditional converter operation mode is changed, former smelting function by one converter is realized by serial operation of two converters [3]. Operation mode is that two converters are in series operation, i.e.the converter for hot metal pretreatment is mainly for hot metal desilicification and dephosphurization which is called dephosphurization converter; the converter for decarburization takes the "semi-steel hot metal" from dephosphurization converter, mainly for decarburization operation. This optimized "full-3-removal" smelting mode shortens converter smelting cycle and increases converter smelting efficiency and molten steel cleanliness.

Steelmaking plant is equipped with "2+3" 300t converters and can realized hot metal "full-3-removal" treatment, the process flow is optimized; main technical features are: Dephosphurization reaction space inside the converter is large, large gas volume bottom blown and agitation can be realized, dephospurization reaction can be speed up, excellent kinetic condition is created, operation cost is low and low phosphorus hot metal can be economically obtained; Converter charged material is optimized and operation with concentrate material is realized; Dephosphurization

time is short, converter smelting process is simplified, quick rhythm production is realized by high speed blowing and smelting [4]; Staged smelting is beneficial for decarburization converter to use manganese ore and reduce Fe-Mn alloy consumption and operating cost; Refining slag from decarburization converter can be used as dephosphuring agent to save cost; Converter less-slag smelting will reduce slag volume, and is energy saving and environment friendly, thus green production is realized; High phosphorous iron ore can be adequately utilized to reduce raw material procurement cost.

So, dedicated converter for hot metal desilicification and dephosphourization pretreatment is not only beneficial for production of low phosphorous steel but also beneficial to optimize process flow, increase production efficiency, reduce operating cost, presenting the developing direction of modern steelmaking plant cycling economy and reduction production and it is a systematic project for steelmaking plant economic operation and is beneficial to increase competitiveness of the product. Hot metal pretreatment procedure adopts 4 sets of KR desulphurization devices and two desilicification-dephosphurization converters, 2 to 1 operating mode, i.e. two KR match one desilicification-dephosphurization converter, total throughput is about 11Mt/a, satisfying the production requirement of 9.275 Mt/a molten steel by converter. Based on the requirement of different steel grade and after "full-3-removal" treatment, hot metal silicon, phosphorous and sulphur content can reach the set standard in Table 1.

Table 1 Quality target of hot metal after pre-treatment

Hot metal quality	[Si]/ %	[P]/ %	[S]/ %
Common hot metal	0.05-0.23	<0.015	<0.01
Low phosphorous low sulphur hot metal	0.05-0.23	<0.015	<0.005
Ultra low phosphorous hot metal	0.05-0.23	<0.01	<0.01

Converter Smelting Process

Converter smelting procedure is configured with three 300t decarburization converter. Due to application of pretreatment process of hot metal "full-3-removal", main task of converter working procedure is decarburizationg and temperature rising, as well as smelting cycle shortened, which can shortened to below 30min. in comparison of 36~38min of conventional smelting, to realize high efficiency and less slag smelting. To ensure cleanness of molten steel, some techniques of are applied, for instance, top and bottom combined blowing, sub-lance, slag-stopped tapping, ladle slag modification treatment, etc. As per the requirements of different steel grades, final composition of converter molten steel can reach to quality listed in Table 2. Figure 2 shows the two stage converter smelting flow process.

Table 2 Quality of final converter molten steel

Molten steel quality	[C] /%	[Mn] /%	[P] /%	[S] /%
Normal molten steel	0.06	0.6	<0.01	<0.01
Ultra-low sulphur molten steel	0.06	0.8	<0.01	<0.004
Ultra-low phosphorus molten steel	0.03	0.6	<0.005	<0.01

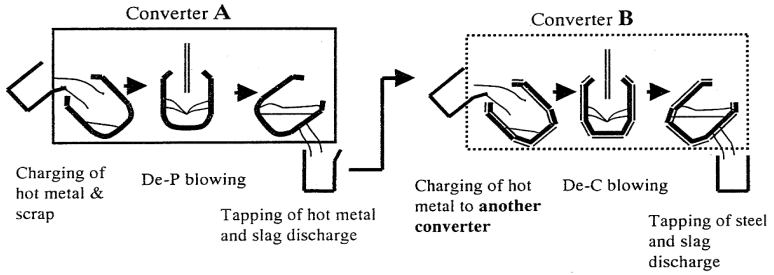

Fig.2 Process flow diagram of two stage converter smelting technology

Refining Process

According to requirement of cold and hot rolled products as well as functions of different refining devices, this refining procedure is configured with the refining station with 2 RH furnaces, 1 LF and 3 CAS devices. As per quality requirement of the product, every refining facility can be run individually or dual refining treatment process can be applied.

Two multi-function RH vacuum treatment devices are applied, and can be run individually or in serial with CAS and LF to realize molten steel secondary refining function. Multi-function RH treatment process is mainly used for decarburization, vacuum oxygen removal (light treatment), hydrogen removal and nitrogen removal to have further precise adjustment of molten steel composition and temperature. Composition of molten steel after treatment by the multi-function RH vacuum treatment device can reach to quality of $[C]<15\times10^{-6}$, $[H]<2\times10^{-6}$, $[N]<30\times10^{-6}$ and $[O]<30\times10^{-6}$. The multi-function RH vacuum refining process is very suitable for modern converter smelting and slab casting production, and for large scale production of low carbon quality steel grades, such as ultra-low carbon IF steel, silicon steel, and so on. For treatment of some steal grades like low carbon steel and ultra-low carbon steel, which requires strict control requirement to gas content, for instance, DQ, DDQ and EDDQ serial steel plates, RH vacuum device is used for natural or forced decarbonization, vacuum oxygen removal and gas removal treatment. RH vacuum treatment device adopts duplex with configuration of multi-function top lance. Oxygen blowing by top lance is used to produce ultra-low carbon steel; Aluminium addition and oxygen blowing is used for chemical temperature rising; Additional heating is realized by fuel gas and oxygen top blowing to the vacuum chamber in order to reduce temperature lowering during RH treatment, eliminate cold steel in the vacuum chamber, and avoid pollution produced between steel grades. Refer to Table 6 for major technical parameters of RH facility.

LF (Ladle Furnace) has the following refining functions: By heating function, production of steel making and casting procedure can be adjusted to ensure smooth running of multi-heat sequence casting; Reduction atmosphere is used to produce basic slag and ultra-low sulphur molten steel; By addition of alloy and slag, oxygen removal, desulfurization and alloying is carried out and composition of molten steel is controlled to improve molten steel quality; Bottom argon-blowing stirring system is used to equalize molten steel temperature and composition. For steel grade which requires low oxygen and low sulphur, for instance, low alloy steel, low grade pipeline steel, etc., LF treatment is applied.

CAS, as the paratactic or alternative process of LF refining, besides function of desulfurization, CAS can complete a large quantity of its functions of LF furnace. CAS refining process can be used individually for normal hot rolled products, for instance, SS400, SM490, etc. Two top lances are equipped, which has heating function for CAS refining facility, with main technical parameters in Table 8 as follows.

As to some steel grades with special quality requirement, for instance, high grade pipeline steel, high strength structural steel, etc., LF and RH dual treatment can be applied. For most LCAK steel ([Si]<0.03%)hot rolled products, LF and RH dual treatment can be applied to exert characteristics of high efficiency and low cost.

Refining procedure facility of Shougang Jingtang steelmaking plant is complete. During actual production, division can be made according to products of converter and CCM in order to have special discipline production line of Converter-Refining-CCM. Product specialization production concept is considered to realize integrated combination of various unit procedure of the steel making plant for benefit of production stability and operation management.

Continuous Casting Process

Continuous casting procedure is configured with 3 high efficiency slab casters with capacity is 9.043 Mt/a. More than 30 advanced technologies are applied in aspects of guarantee of molten steel cleanness, improvement of slab surface and inner quality, improvement of casting productivity and reliability as well as high temperature hot charging of slab, energy saving and environment

protection, comprehensive utilization, etc. Application of advanced technologies on continuous casting procedure embodies today's international continuous casting development level and technical characteristics.

Continuous casting machine with characteristics of compact sectionized roll rows, continuous curving and continuous straightening type is applied to meet requirement of inner cleanness of slab under high casting speed, reduce curving and straightening deformation, and ensure inner quality of slab. EMBR technology is specially suitable for casting at high casting speed with speed more than 2.0m/min. EMBR is used to control speed and direction of molten steel and to make molten steel flow field in the mould at the rational status all the times and to prevent slagging. It can guarantee the surface quality and inner quality of slab under high casting speed condition to improve slab cleanness efficiently. Hydraulic mould oscillation can change frequency and amplitude during casting process to realize sinusoidal and non-sinusoidal oscillation, reduce oscillation mark depth on slab efficiently, and it is very suitable for protection flux supply under high casting speed and improvement of slab surface quality. By establishing secondary cooling control model, liquid core inside the strand can be judged at real time. At the adequate position of strand guide section, control system automatically adjusts opening of the roll gap of the segments so as to have soft reduction to the strand. Technology of strand soft reduction can improve the central segregation and central fluffing inside strand in order to have better inner quality of slab. Obvious result is obtained in aspect of elimination of central segregation of strand.

Conclusions

(1) Shougang Jingtang steelmaking plant, is equipped with the international leading technology and equipment for multi-procedure from hot metal transfer - hot metal pretreatment - converter steel making - molten steel secondary refining - high efficiency casting to ensure high production efficiency and high production quality, and lays a strong foundation of production of high grade and high quality products.

(2) Improvement of steel product cleanness is a key task for future iron and steel industry. Production of clean steel is a complicated and system project, is a technical system based on process flow, technical equipment, production operation and quality management. The new generation iron and steel plant should build a platform for clean steel production. By applying process flow optimization, improvement of technical equipment, production operation and quality level, high efficiency, low cost and large batch production of clean steel demanded by customer is realized.

(3) Shougang Jingtang Iron and Steel Plant adopts hot metal “full-3-removal” design concept. By applying dynamic and precise design philosophy to optimize and allocate process flow and equipment, a system of dynamic, compact, continuous, high efficiency, stable clean steel production is built with characteristics of recyclable, high-efficiency, low-cost, and high-quality. Construction of clean steel production system of Shougang Jingtang iron and steel plant put forward technical development model and direction of high-efficiency, low-cost, recyclable production of clean steel.

References

[1] ZHANG Fuming, Construction of High-Efficiency and Low-Cost Clean Steel Production System in Shougang Jingtang, Journal of Iron and Steel Research International, 2011, 18(Supplement 2), 42-51.

[2] YIN Ruiyu, Metallurgical Process Engineering, Beijing, Metallurgical Industrial Press, 2005, pp.325-328.

[3] LIU Liu, Development of Converter Steelmaking Technology, China Metallurgy. 2004, 14(2) 7-11.

[4] LIU Liu, Technical Progress in Converter Steelmaking in China, Iron and Steel, 2005, 40(2) 1-5.

doi:10.4028/www.scientific.net/AMM.161.42

Analytical Approach for Describing Solid-State Phase Transformation

Yihui Jiang[1], Bao Sun[1], Feng Liu[1a]

[1]State Key Lab. of Solidification processing, NWPU, Xi'an Shaanxi, 710072, China

[a]liufeng@nwpu.edu.cn (corresponding author)

Keyword: Analytical; Isothermal; Non-isothermal; Transformation

Abstract. A general analytical phase transformation model has been proposed and successfully applied to describe the crystallization of amorphous alloys. The "additivity rule" is proved to be compatible with the analytical model; the effects of anisotropic growth based on Monte Carlo (MC) simulations is reinterpreted using the analytical approach; and an improved temperature integral is also proved to be compatible with the analytical model. Kinetic analysis basing on the analytical model declares the transformation mechanism, e.g. nucleation, growth and impingement mode. On this basis, the kinetic behaviors of isothermal and non-isothermal crystallization of amorphous $Zr_{50}Al_{10}Ni_{40}$ are analyzed.

Introduction

In studies of solid-state phase transformations involving nucleation and growth, often the Johnson-Mehl-Avrami (JMA) equation is assumed to be valid [1]. In practice, mixed nucleation mode or Avrami nucleation mode (both site saturation and continuous nucleation occur) [2], parabolic growth [2], non-random dispersed nuclei [3] or anisotropic growth [4], etc, all lead to deviations from the JMA kinetics. Recently, an analytical model [5], taking the above deviations into consideration, leads to the equations for transformation degree that have the structure of JMA equation but with transformed fraction f dependent kinetic parameters. The model has been successfully applied to describe the crystallization of amorphous alloys [5]. Here, the most recent development of the analytical model is reviewed.

The development and application of the analytical model

The analytical model assuming different nucleation (site saturation, continuous nucleation, mixed nucleation and Avrami nucleation), growth (interface-controlled growth and diffusion-controlled growth) and impingement (randomly dispersed nuclei, anisotropic growth and non-random nuclei dispersion) modes has an explicitly expression for extended and real fraction, x_e and f [5],

$$x_e = K_0^n \exp\left(-nQ/(RT)\right)\alpha^n \tag{1}$$

$$f = 1-\exp\left(-x_e\right);\ \text{for impingement due to randomly dispersed nuclei} \tag{2a}$$

$$f = 1-\left[1+(\xi-1)x_e\right]^{-1/(\xi-1)};\ \text{for impingement due to anisotropic growth (with } \xi\geq 1) \tag{2b}$$

$$df/dx_e = 1-f^{\varepsilon};\ \text{for impingement due to non-random nuclei dispersion (with } \varepsilon\geq 1) \tag{2c}$$

where α is identified with either the annealing time t for isothermal transformation or with RT^2/Φ for non-isothermal transformation, n the growth exponent, Q the overall effective activation energy, K_0 pre-exponential factor of rate constant and ξ and ε impingement factors. Explicit expressions for the n, Q and K_0, in terms of general nucleation and growth modes are given in Refs. [5].

Compatibility of the analytical model with the additivity rule. The general condition following the additivity rule is that the transformation rate *df*/*dt* is a state function independent of the thermal path by which it reaches to the state [6]. That is to say, *df*/*dt* depends only on *f* and *T*,

$$df/dt = h(T)/g(f) \tag{3}$$

where $h(T)$ and $g(f)$ are functions only of T and f, respectively. A non-isothermal transformation assuming mixed nucleation, interface-controlled growth and impingement due to randomly nuclei can be given as (substitution of Eq. (1) into Eq. (2a)),

$$f = 1 - \exp\left(-K_0^{\,n} \exp\left(-nQ/(RT)\right)\alpha^n\right) \tag{4}$$

Substitution explicit expressions for $n(T)$, $Q(T)$ and $K_0(T)$ into Eq. (4), after some treatment, the following is obtained [6]:

$$df/dt = \Phi(1-f)(-\ln(1-f))\left(nQ/(RT^2) + 2n/T\right) = h(T)/g(f) \tag{5}$$

It can be concluded that Eq. (5) complies with Eq. (4). That is to say, the additivity rule is compatible with analytical model assuming mixed nucleation.

Compatibility of the analytical model with the anisotropic effect. The analytical description in agreement with MC simulations was achieved for several growth modes (e.g. *np* growth, *no* growth and *rNRo* growth) [4]. However, the growth exponent can not be deduced reasonably from these descriptions. Employing the analytical approach used to derive analytical model [7], the explicit expression for the growth exponent can thus be given.

The analytical description of x_e for *no* growth in a 2-D space can be expressed as [4],

$$x_e = 2Cw\sqrt{I(t-t^*)} + wIG(t^*)^2 \tag{6}$$

where t^* is the time when the transition from JMA behavior to blocking behavior occurs, w the width of the growing grain, G the growth rate and C a constant. From Eq. (6), the extended fraction can be considered to be composed of two parts, one with n=0.5, the other with n=2. Adopting the analytical approach, the explicit analytical expression for growth exponent can be obtained,

$$n = 2 - (3/2)/[1 + r_2/r_1] \tag{7}$$

with r_2/r_1 as the model parameters, for the expression, see Ref. [7]. In combination with MC simulations, the effects of anisotropic growth change the transition from JMA to non-JMA at t^*, thus leading to a change of growth exponent which can be analytically described by Eq. (7) (see Fig. 1).

Compatibility of the analytical model with approximations for "temperature integral". For non-isothermal transformation with constant heating rate, to derive an analytical model, the term called the "temperature integral" has to be approximated.

$$\int_0^T \exp(-Q/RT')dT' = RT^2/Q\exp(-Q/RT) \tag{8}$$

For Q/RT>>1, Eq. (8) holds without introducing large error. This approximation leads to the original analytical model [5].

Recently, many approximations for "temperature integral", which are more accurate than Eq. (8), have been proposed [8]. Incorporating these approximations, the analytical approach leads to similar equations with the analytical model for transformed fraction (i.e. Eq. (4)) but a modified model parameter [9]. This modified analytical model considers not only a choice of nucleation and

impingement mechanisms, but also a choice of approximations to the "temperature integral" according to the value of Q/RT (its value need not be much higher than unit), thus extended the analytical model's application range and more precise than the original one (see Fig. 2).

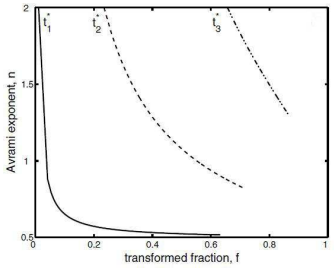

Fig. 1 The Avrami exponent, n, as a function of f for pure continuous nucleation and *no* growth mode with different t^* [7]

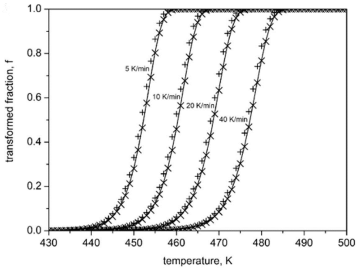

Fig. 2 Evolution of transformed fraction with T predicted by the original analytical model (+) and by the extended analytical model (×) [9]

Determination of nucleation and growth modes from evaluation of transformed fraction. Based on the analytical model, it has been proved that the transformations with varying kinetic parameters can also be assumed as "iso-kinetics". From this new character (i.e. time-dependent kinetic parameters), the nucleation and growth modes can be determined [10].

For isothermal transformation, on the basis of Eqs. (1) and (2), the most popular methods to determine n and Q from f was proved to be practicable for the mixed nucleation modes,

$$d\ln x_e / d\ln t = n(f) \tag{9a}$$

$$d\ln t_f / d(1/T) = Q(f)/R \tag{9b}$$

The evolutions of n and Q with f are determined by the nucleation mode, and the variation range of n is determined by the growth mode. i.e. for mixed nucleation, Q decreases with f, whereas, for Avrami nucleation, Q increases with f (for the case of activation energy for nucleation Q_N smaller than activation energy for growth Q_G); the range of n values is between d/m to $d/m+1$, for volume-controlled growth, m=2 whereas, for interface-controlled growth, m=1. For an example of mixed nucleation, the variation of n and Q is shown in Fig. 3.

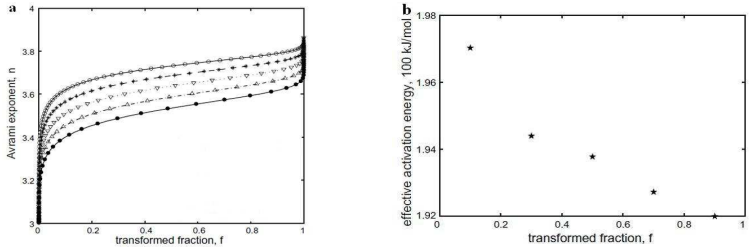

Fig. 3 (a) the growth exponent n and (b) the overall activation energy Q as a function of transformed fraction for isothermal transformation assuming mixed nucleation and interface-controlled growth [10]

A conversion from a continuous cooling transformation (CCT) or continuous heating transformation (CHT) into an isothermal transformation, i.e. a CCT (CHT)-TTT conversion, can be described using the additivity rule [6,10]. For non-isothermal transformation, a relation according to the additivity rule holds [6,10],

$$\Phi(f,T) = \int_{T_i}^{T} d\theta / t(f,\theta) \Leftrightarrow (\partial T/\partial \Phi)_f = t(f,T) \tag{10}$$

where $\Phi(f, T)$ is the heating rate necessary to reach f corresponding to T. On this basis, according to Eq. (4), the transformed fraction can be given by

$$f = 1 - \exp\left(-K(T)^{n(T)}\left(\partial T/\partial \Phi\right)_f^{n(T)}\right) \tag{11}$$

with $K(T)=K_0(T)\exp(-Q(T)/RT)$. Upon the conversion, the prevailing modes of nucleation and growth do not change. On this basis, the determination of modes of nucleation and growth for non-isothermal transformations traces back to the determination for isothermal transformations.

Determination of impingement mode from evaluation of transformation rate maximum. On the basis of analytical model, an evaluation of the maximum in transformation rate leads to a lot of kinetic information [11]. For non-isothermal transformation,

$1 + \ln\left(1 - f_p\right) = 0$; for randomly dispersed nuclei (12a)

$\xi - \left(1 - f_p\right)^{1-\xi} = 0$; for anisotropic growth (12b)

$\varepsilon f_p^{\varepsilon-1} x_e\left(f_p\right) = 1$; for non-random nuclei dispersion (12c)

According to Eq. (12), the impingement mode is directly determined from the position of peak maximum, f_p. The values for n_p (using Eq. (9a) at/around f_p) give the possible prevailing of nucleation and growth mode. In combination with the value for Q_p (using Eq. (9b) at/around f_p), the preliminary determination values for Q_N and Q_G are given. This efficient method leads to a pre-selection of the nucleation, growth and impingement mode and values for Q_N and Q_G. In combination with the full transformation-curve fitting program, the kinetics parameter will be determined quickly and precisely. In the following, an example is shown.

During the non-isothermal transformation of as-quenched amorphous $Zr_{50}Al_{10}Ni_{40}$ [12], the position of $(df/dT)_p$ changes from f_p=0.66 to f_p=0.52 with increasing heating rate (see Fig. 4a). It follows from Eq. (12) that the impingement mode changes from non-random nuclei dispersion to anisotropic growth upon increasing the heating rate (it is consistent with the TEM experimental, see Fig. 4b). By applying Eq. (9a) to the present data at the transformation-rate maximum, the value of n_p can be determined: n_p varies between 5.5 and 7.5 for the heating rates applied. It can be assumed that the non-isothermal transformation is three-dimensional interface-controlled growth and accelerating continuous with nucleation index, a between 4 and 8. Then, the full transformation-curve fitting program leads to precise kinetic parameters, which provide a detailed description of the crystallization kinetics.

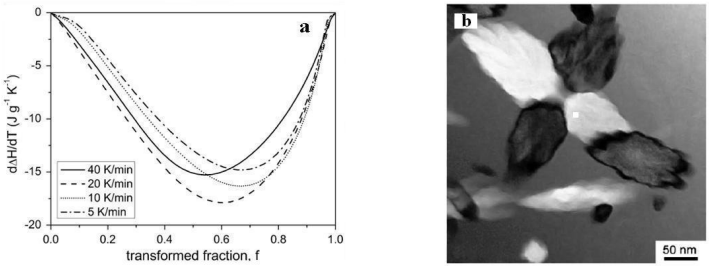

Fig. 4 (a) Evolution of the rate of enthalpy change with f for non-isothermal DSC scans of amorphous $Zr_{50}Al_{10}Ni_{40}$. (b) Bright-field TEM images after non-isothermal annealing with 20 K/min until the beginning [12]

Summary

It has been proved that the analytical model is compatible with additivity rule. Based on additivity rule, CCT (CHT)-TTT conversion can be described. With the help of the conversion, the nucleation and growth mode can be determined for isothermal and non-isothermal transformation. Adopting

the analytical approach, the effects of anisotropic growth have been reinterpreted. Employing more accurate approximation for “temperature integral”, the analytical model was extended to more general case. Incorporating the evaluation of transformation rate maximum, the full transformation fitting program leads to detailed description of the kinetics. The crystallization of amorphous $Zr_{50}Al_{10}Ni_{40}$ has been studied by this method.

Acknowledgements
The authors are grateful to the financial support of the Free Research Fund of State Key Laboratory of Solidification Processing (09-QZ-2008 and 24-TZ-2009), the Natural Science Foundation of China (51071127 and 51134011), the Fundamental Research Fund of Northwestern Polytechnical University (JC200801), the Key Project for Undergraduate Research of Northwestern Polytechnical University, China National Funds for Distinguished Young Scientists (51125002) and National Basic Research Program of China (973 Program, 2011CB610403).

Reference

[1] J.W. Christian, The theory of transformation in metals and alloys, part1: equilibrium and general kinetics theory, 2nd ed., Pergamon Press, Oxford 1975.
[2] A.T.W. Kempen, F. Sommer, E.J. Mittemeijer, Determination and interpretation of isothermal and non-isothermal transformation kinetics; the effective activation energies in terms of nucleation and growth, J. Mater. Sci. 37 (2002) 1321-1332.
[3] A.T.W. Kempen, F. Sommer, E.J. Mittemeijer, The kinetics of the austenite-ferrite phase transformation of Fe-Mn: differential thermal analysis during cooling, Acta Mater. 50 (2002) 3545-3555.
[4] B.J. Kooi, Monte Carlo simulations of phase transformations caused by nucleation and subsequent anisotropic growth: Extension of the Johnson-Mehl-Avrami-Kolmogorov theory, Phys. Rev. B 70 (2004) 224108.
[5] F. Liu, F. Sommer, E.J. Mittemeijer, Analysis of solid state phase transformation kinetics: models and recipes, Inter. Mater. Rev. 52 (2007) 193-212.
[6] F. Liu, C. Yang, G. Yang, Y. Zhou, Additivity rule, isothermal and non-isothermal transformations on the basis of an analytical transformation model, Acta Mater. 55 (2007) 5255-5267.
[7] F. Liu, C. Yang, Effects of anisotropic growth on the deviations from Johnson-Mehl-Avrami kinetics, Acta Mater. 55 (2007) 1629-1639.
[8] J.J.M. Órfão, Review and evaluation of the approximation to the temperature integral, AIChE J. 53 (2007) 2905–2915.
[9] Y.H. Jiang, F. Liu, S.J. Song, Improved analytical description for non-isothermal solid-state transformation, Thermochim.Acta 515 (2011) 51–57.
[10] F. Liu, S.J. Song, J.F. Xu, J. Wang, Determination of nucleation and growth modes from evaluation of transformed fraction in solid-state transformation, Acta Mater. 56 (2008) 6003-6012.
[11] F. Liu, S.J. Song, F. Sommer, E.J. Mittemeijer, Evaluation of the maximum transformation rate for analyzing solid-state phase transformation kinetics, Acta Mater. 57 (2009) 6176-6190.
[12] F. Liu, H. Nitsche, F. Sommer, E.J. Mittemeijer, Nucleation, growth and impingement modes deduced from isothermally and isochronally conducted phase transformations: Calorimetric analysis of the crystallization of amorphous $Zr_{50}Al_{10}Ni_{40}$, Acta Mater. 58 (2010) 6542-6553.

doi:10.4028/www.scientific.net/AMM.161.47

Nano-crystalline Sn-Co-X Alloy Alternative to Decorative Chromium Plating

Wenhua Hui[1, a], Fanjuan Meng[2,b], Yueliang Li[3,c], Zhanping Li[4,d], Xiaofeng Xie[5,e] and Lili Cao[4,f]

[1]Shining Surface Systems, Inc. (SSSI), Ewing, NJ 08628, USA

[2]Department of Thermal Engineering, Tsinghua University, Beijing 100084, China

[3]Beijing National Center for Electron Microscopy, Department of Materials Science and Engineering, Tsinghua University, Beijing 100084, China

[4]Analysis Center, Tsinghua University, Beijing 100084, China

[5]Institute of Nuclear and New Energy Technology, Tsinghua University, Beijing 100084, China

[a]hui@surface-systems.com, [b]rnxmfj@mail.tsinghua.edu.cn, [c]li-yl05@mails.tsinghua.edu.cn, [d]zhanpingli@mail.tsinghua.edu.cn, [e]xiexf@tsinghua.edu.cn, [f]caoll@mail.tsinghua.edu.cn

Keywords: Nano-Crystalline, Sn-Co-X alloy, Alternative decorative Chromium, Chromium Plating.

Abstract.
Decorative chromium demand in the worldwide market is more than three times of hard chromium. But chromium plating processes has long been known to hazardous. The corrosion resistance of a nano-crystalline Sn-Co-X alloy intended as an alternative for decorative chromium has been studied. The corrosion resistances of Sn-Co-X are all better than trivalent chromium, hexavalent chromium, and it is further better than coarser gained Sn-Co alloy. The microstructures of Sn-Co-X alloy were analyzed by SEM, TEM, XPS and AES. The mechanism of its excellent corrosion resistance is described.

Introduction

Chromium plating processes has long been known to be hazardous, but studies in the last decade have known it to be particularly dangerous, especially for workers in chromium plating facilities [1]. In response to growing health concerns, the U.S Environmental Protection Agency (EPA) began to regulate emissions into the air of chromium, citing strong evidence that chromium causes lung cancer and other serious conditions. The compliance deadline for the EPA's new plating and polishing area sources rule was set to go into effect on July 1, 2010 for:

(1) Non-chromium electroplating
(2) Electropolishing
(3) Electroforming
(4) Electroless plating
(5) Thermal metal spraying
(6) Chromate conversion coating
(7) Coloring
(8) Mechanical polishing of metals and formed products

For more than forty years, academic and industrial researchers from all over the world have taken a strong interest in alternative processes for hard chromium and decorative chromium. Among them, nanotechnology is the most promising. The nanograined micro-structure has been found beneficial in imparting resistance against localized corrosion in the acidic environment. For example, superior localized corrosion resistance in HCl was observed for nano-crystalline Ni-Co-X alloy [2]. Similar observation of improved resistance against inter-granular corrosion in the acidic environment has been reported for electrodeposited nano-crystalline Ni and Ni-P alloy [3, 4].

Decorative chromium demand in worldwide market is more than 3 times of hard chromium ($15.91 billion in worldwide market in 2003). There is, however, no report of nano-crystalline Sn-Co alloy for decorative application. This represents a new potential application for nanotechnology. In order to evaluate the corrosion and tarnish resistance of the nano-crystalline Sn-Co-X alloy, comparing tests were performed among the well-known chromium coating and coarser-grained Sn-Co alloy.

Experimental

The corrosion resistances were performed under the conditions of CASS (ASTM B368 or, ISO 17025). A brass flat panels, 2.75 inch x 4.0 inch, were polished with SiC sandpaper (1200 mesh) and MgO powder. They were etched in 10% H_2SO_4 at room temperature for 0.5-1.0 minutes and rinsed with distilled water. Plating processes were followed Table 1. The specimens were then thoroughly rinsed with distilled water and dried by cool air blast after plating. METTEX13 (M13), a nano-crystalline Sn-Co-X alloy, was patented by Shining Surface Systems, Inc. (3S). A JEOL 6301F SEM was used to study the morphology. A FEI TECNAI G^2 20 TEM was used to study the morphology and micro-structure. The XPS measured were made on ULVAC-PHI PHI Quantera Scanning X-ray Microprobe operated at 15kV, 25W; The AES measured were made on ULVAC-PHI PHI 700 Scanning Auger Nanoprobe. Survey and high resolution XPS spectra were generated with the analyzer pass energy setting at 280eV and 55eV respectively. The voltage and current of the electron beam for AES analysis were 5kV and 10uA, respectively. An argon ion gun with a voltage of 2kV, an emission current of 15 mA, and scan area of 2mm x 2mm were used for depth profiling study. The sputter rate is 10nm/min for SiO_2.

Results

Corrosion resistance of the nano-crystalline M13(Sn-Co-X).

Table 1 CASS Test

	Cr+3	Cr+6	Cr+3	Cr+6	Sn-Co	M13
Semi-Bright Nickel	~22 um	~22 um	~22 um	~22 um	~22 um	
High Sulfur Nickel	~1.5um	~1.5 um				
Bright Nickel	~11 um	~11 um	~11 um	~11 um	~11 um	
Microporous Nickel			~1.5 um	~1.5 um	~1.5 um	
Noble Nickel	~1.5um	~1.5 um				
M8(Nano-Ni-Co-B)						7+10um
Sn-Co(Coaser-gained)					~1 um	
Trivalent Chromium	~0.3um		~0.3 um			
Hexavalent Chromium		~0.3		~0.3 um		
M13(Nano-Sn-Co-X)						1.5+1.5um
24 hours CASS Rating	10	10	10	10	10	10
48 hours CASS Rating	8	8	10	10	10	10
96 hour CASS Rating			9	9	9	10
120 hrs CASS Rating			9	8	8	10
144 hrs CASS Rating			7	7	7	10
168 hrs CASS Rating						9

The results of CASS test of METTEX 13(M13), a nano-crystalline Sn-Co-X alloy, comparing to the third generation of trivalent chromium, hexavalent chromium and coaser gained Sn-Co are shown in Table 1.

The corrosion resistances of nano-crystalline M13 are all better than trivalent chromium, hexavalent chromium, and it is further better than coaser gained Sn-Co alloy.

XPS and AES investigation of nano-crystalline M13.

The composite elements were analyzed by XPS and AES before and after sputtering by Ar^+ beam (SPT). For the nano-crystalline Sn-Co-X (M13) plating coatings, survey spectra of XPS show Sn, Co, C, O, etc. exist (Fig. 1). The AES results also suggest the existence of Sn, Co, O and C. After 0.5 minutes of Ar^+ SPT, the C band disappeared. This suggests that C mostly exists in the contamination of the coating surface. Fig. 2 shows the composition of the coat at different sputtering time by AES depth profiling technique. The relative atomic content fractions (AC %) of the elements were calculated by computer. The composition of the coating was stable after 0.5 minutes of SPT. With the reference of SiO_2 and the SPT speed of 10 nm /min, the atomic percentages in the median stable area during the SPT are Sn: 32.58%, Co: 62.68%, O: 4.80%.

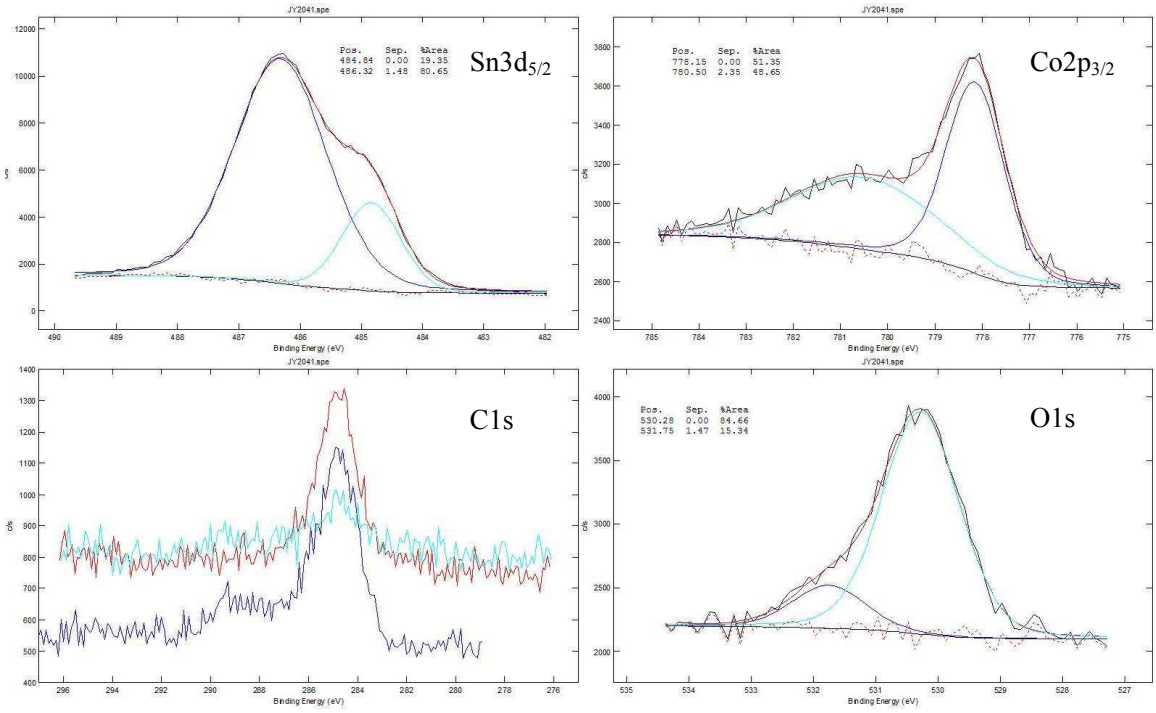

Fig. 1 Binding energy of elements in the nano-crystalline Sn-Co-X (M13) alloy

High resolution XPS of the Nano-crystalline Sn-Co-X alloy coating is shown in Fig. 1. The binding energies of Sn 3d before and after SPT are shown in Fig. 1. The peaks at 484.84 eV and 486.32 eV indicate that tin exists in oxidation states of 2^+ and 0 both in surface and interior. Cobalt exists in oxidation states of 2^+ and 0 both in surface and interior, because two different binding energies of 778.15 eV and 780.50 eV of $Co2p_{3/2}$ before and after SPT appear. No nickel before SPT and Ni 3.0^+ (Ni_2O_3) and Ni^{2+} (NiO) after SPT indicate nano-crystalline Ni-Co-B alloy under top layer nano-crystalline Sn-Co-X (M13) alloy. The binding energies of O 1s before and after SPT are 530.28 eV and 531.75 eV, respectively, which indicate the O exists in the oxidation state of 2 both on the surface and inner coating. The very interested in was the O on the surface was 7-8 nm using the sputter rate of SiO_2 as a reference. It is much thicker than that of coaser grained Sn-Co's 6.7-10.4 Å [5], because the sputter rate of Au can be ~5 times higher than that of SiO_2 [6].

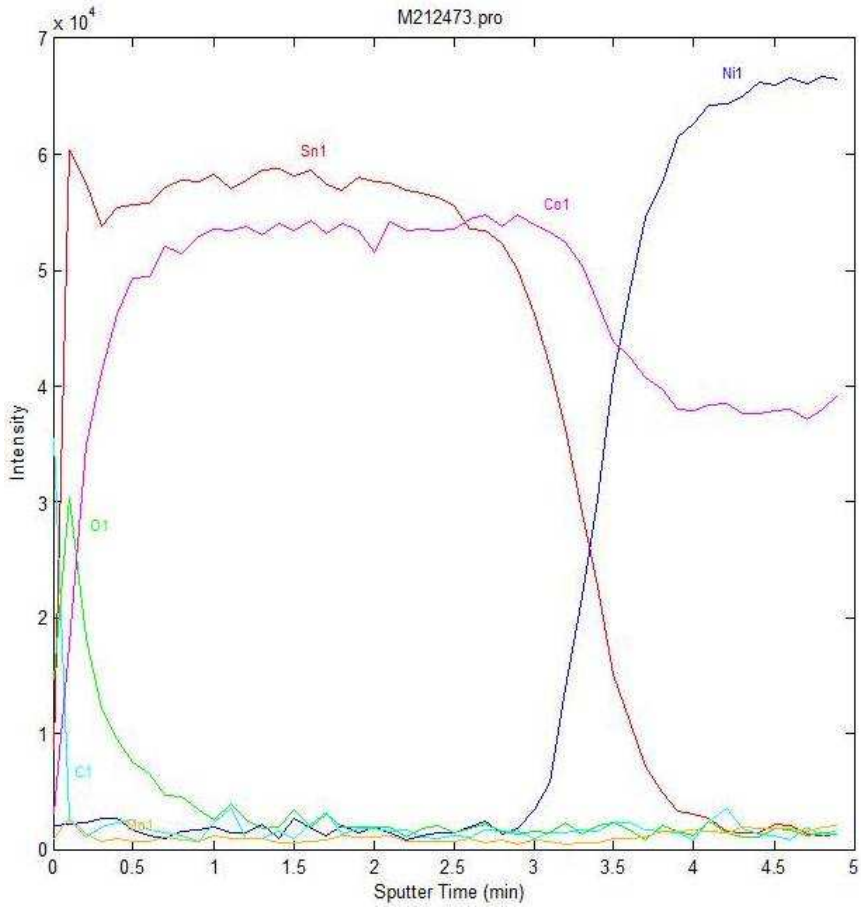

Fig. 2 The composition depth profiling od nano-crystalline Sn-Co-X (M13) alloy composite coating

SEM and TEM investigation of nano-crystalline M13.

In order to explore the reasons why the nano-crystalline Sn-Co-X (M13) alloy shows such excellent corrosion resistance, the following analyses were carried out.

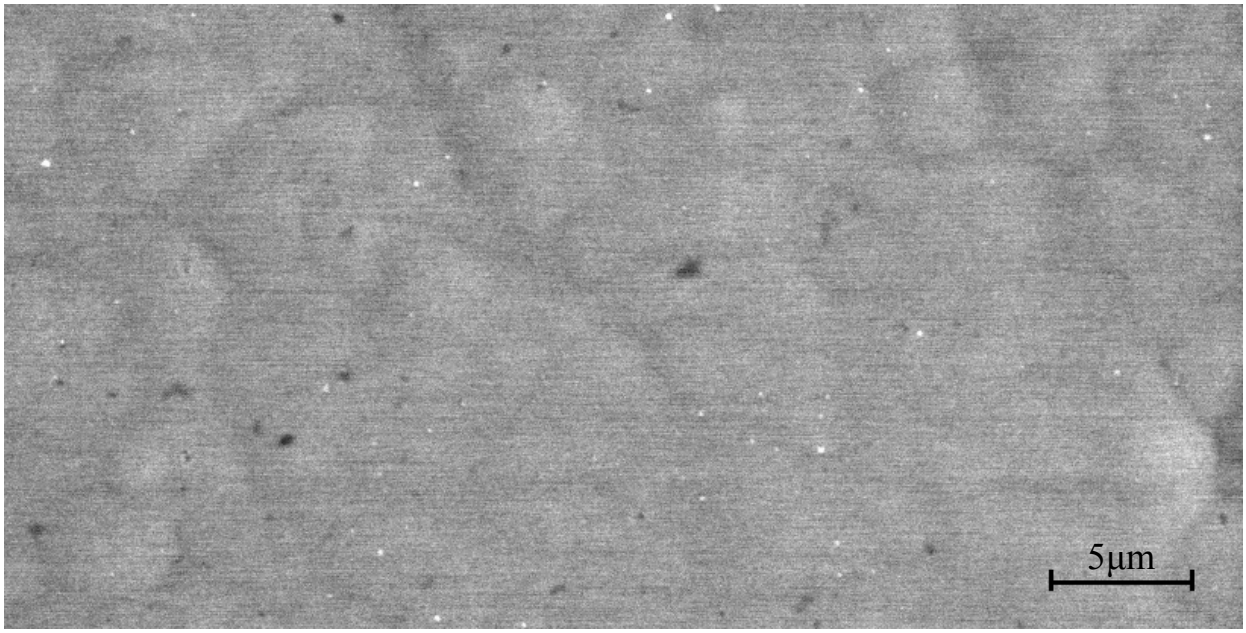

Fig. 3 SEM of nano-crystalline Sn-Co-X (M13) alloy

Fig. 3 shows nano-crystalline M13 surface morphology, its surface was smooth, no porosity and cracks.

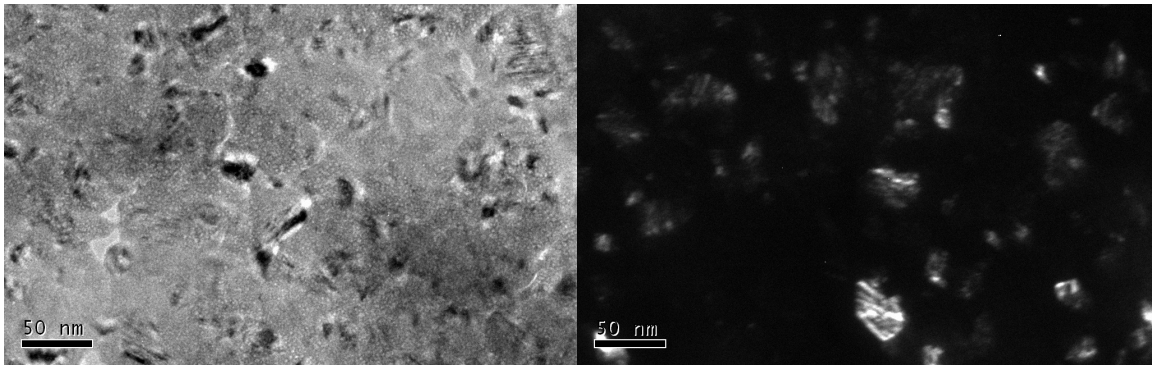

(a) Bright field image (b) Dark field image

Fig. 4 TEM of nano-crystalline Sn-Co-X (M13) alloy

Fig. 4 shows the TEM morphology of the nano-crystalline Sn-Co-X (M13) alloy. It can be seen that there are many finely dispersed precipitates, about 6-8 nm in size present in the matrix. The selected area diffraction pattern (Fig. 5) show diffraction rings characteristic of a multi-crystal structure. The distribution of spots on the rings suggest that the main contribution to this diffraction pattern arises from an ordered hexagonal structure with a lattice constant of a=0.528 nm and c=0.426, it is CoSn alloy. Because the grain size of the matrix is so small, the grain boundaries are invisible and it is, therefore, difficult to determine the grain size by the dark field image method. Using the micro-beam diffraction method instead, at least four sets of diffraction patterns could be observed when the diameter of the electron beam was about 4 nm. In the view of this, the grain size can be estimated as being 2.5 nm.

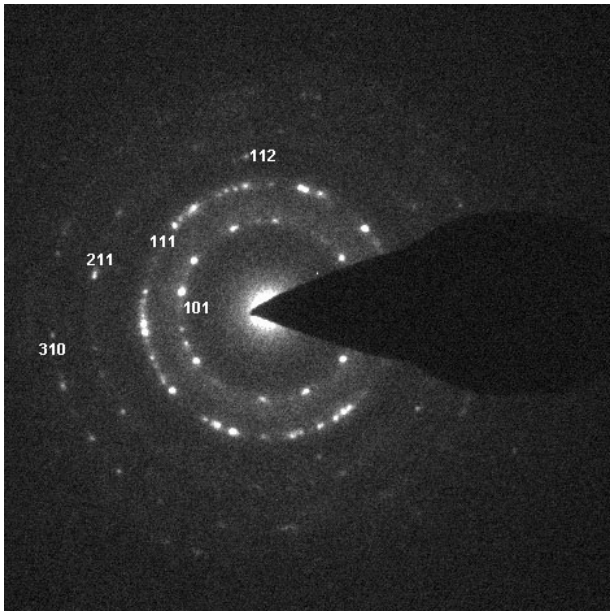

Fig. 5 Selected area diffraction pattern of nano-crystalline Sn-Co-X (M13) alloy

Based on the above studies, it can be concluded that the structure of nano-crystalline Sn-Co-X(M13) plating coatings consists of an amorphous matrix including some nano-crystals containing dispersed CoSn inter-metallic compound. The grain size of nano-structure in the matrix is about 2.5 nm and the inter-metallic compound was 6-8 nm.

Conclusion

The nano-crystalline Sn-Co-X(M13) plating alloy coating intended as a alternative to decorative Chromium, show similar color and excellent corrosion.

The corrosion resistance of nano-crystalline Sn-Co-X(M13) plating alloy coating is related closely to its microstructure:

(1) Nano-crystalline Sn-Co-X(M13) plating coatings consists of an amorphous matrix including some nano-crystals containing dispersed CoSn inter-metallic compound. The grain size of nano-structure in the matrix is 2.5 nm and the inter-metallic compound is 6-8 nm.

(2) Nano-structure and amorphous structure can greatly decrease its sensitivity to localized corrosion.

(3) The absorbed oxygen of nano-crystalline Sn-Co-X(M13) plating alloy coating was more higher than coaser grained Sn-Co. The absorbed oxygen can prevent the dissolution of the metal coating, thus promoting the growth of the passive film and in turn increasing its stability.

References

[1] Scott Moore, Products Finishing. 12 (2003) 1.

[2] Wenhua Hui, Yuanming Zhang, et al, Surface Engineering. 10 (1994) 275.

[3] R. Rofagha, R. Langer, et al, Nanostructured materials. 25 (1991) 2867.

[4] R. Rofagha, U. Erb, et al, Nanostructured materials. 2 (1993) 1.

[5] J.H. Thomas and S.P. Sharma, J.Vac. Sci. Technol. 15 (1978) 1706.

[6] John F, Moulder et.al, Handbook of X-ray Photoelectron Spectroscopy, Edit by Jill Chastain et.al. (1995) 27.

doi:10.4028/www.scientific.net/AMM.161.53

Numerical Simulation of Process Parameters in Flexible Discrete Clamp Stretch Forming

Heli Peng[1,a], Mingzhe Li[1,b] and Pengxiao Feng [1,c]

[1]Dieless Forming Technology Center, Jilin University, Changchun, Jilin, 130025, China

[a]phl12616040811@126.com, [b]limz@jlu.edu.cn, [c]fengpengxiao@163.com

Keywords: Sheet forming, Discrete clamp, Process parameters, Numerical simulation

Abstract. Flexible DCSF technology was put forward, and its forming character was described. The flexible DCSF machine was developed and related stretching experiment were carried out. The experimental photos show the DCSF technology is feasible and the DCSF machine is practicable. The FE model of flexible DCSF was set up, and extensive numerical simulations for spherical parts, saddle parts and S-type parts were carried out by Abaqus. The numerical results show that the longer the transitional length is, the more homogeneous the stretching strain and the thickness become. The smaller the friction coefficient is, the more homogeneous the stretching strain and the thickness become. The larger the clamp number is, the better the fit degree becomes. This work may provide useful guidance on the flexible DCSF process.

Introduction

Stretch forming is an important technology to form sheet metal in the aerospace industry. With the improvement of industrial level, sheet metal with complex shape and good forming quality are needed rapidly in the field of aeronautics and astronautics, naval vessels and modern architecture.

Stretch forming was used extensively in fabrication of aircraft outer skin parts, it has the characters of high forming accuracy and small springback value. However, the clamp of traditional stretch forming machine is integral structure, there isn't relative movement between clamp and sheet metal, which results in the wrinkle and crack happened frequently when forming parts with short free length and large transversal curvature [1]. To solve these defects, extensive studies for stretch forming process were carried out. The process of stretch forming after heat treatment was proposed to decrease the strain of sheet metal [2]. A hybrid forming process of incremental forming combined with stretch forming was put forward to improve the situation of sheet metal adjusting the die [3]. Multi-step stretch forming process was studied, related numerical simulation and experiment were carried to prove the process can reduce deficiencies of deformation [4, 5].

The above researches have improved the problem of stretching mechanic in some extent, but not thoroughly. So, based on the principle of multi-point forming [6,7], flexible discrete clamp stretch forming (DCSF) technology was proposed [8], and flexible DCSF machine was developed by dieless forming technology center of Jilin University to improve the forming quality and increase the material utilization ratio [9].

The flexible DCSF technology and machine

Flexible DCSF technology has the following characters contrasted to traditional stretch forming technology. Firstly, the Pascal principle of multi-cylinder hydraulic system was used to adjust the pressure, which has not only reduced the complexity of controlling, but also saved the cost of manufacture. Secondly, the concept of loading assorts with deforming was applied. The clamps are arranged into a horizontal line state when they hold sheet metal. During the forming process, the clamps can make real-time position in according with the transversal sectional shape of the stretching die. The sectional shape of hydraulic cylinders and clamps for different stretching stages are shown in Fig.1.

Fig.2 is the structural diagram of flexible DCSF machine. It shows that flexible discrete clamps is used to replace traditional integral clamp, and each discrete clamp is connected by universal joint and a set of hydraulic cylinders, which consists of horizontal cylinder, vertical cylinder and leaning cylinder.

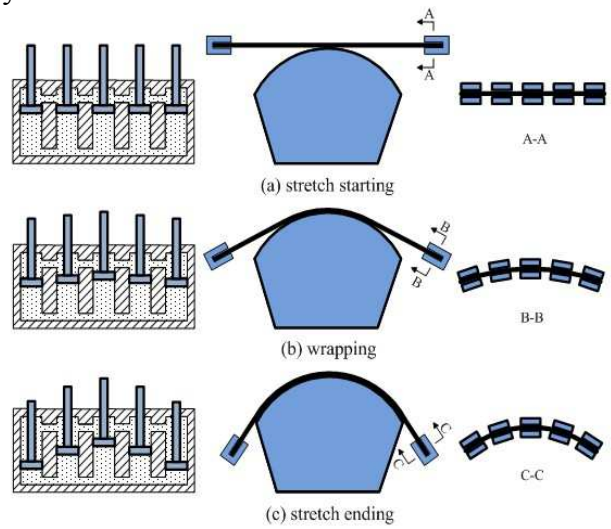

Fig.1 The section of cylinders and clamps

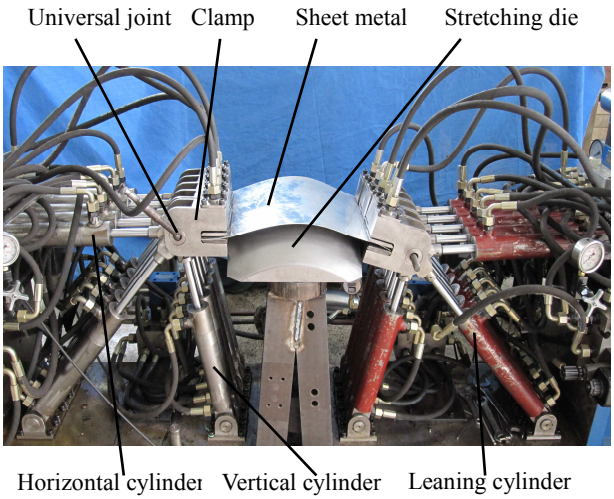

Fig.2 The flexible DCSF machine

Fig.3 presents the photograph of spherical part and saddle part formed by the flexible DCSF machine. The forming parts show that the part edge is curve shape and the forming quality is good, which illustrates flexible DCSF machine is practicable.

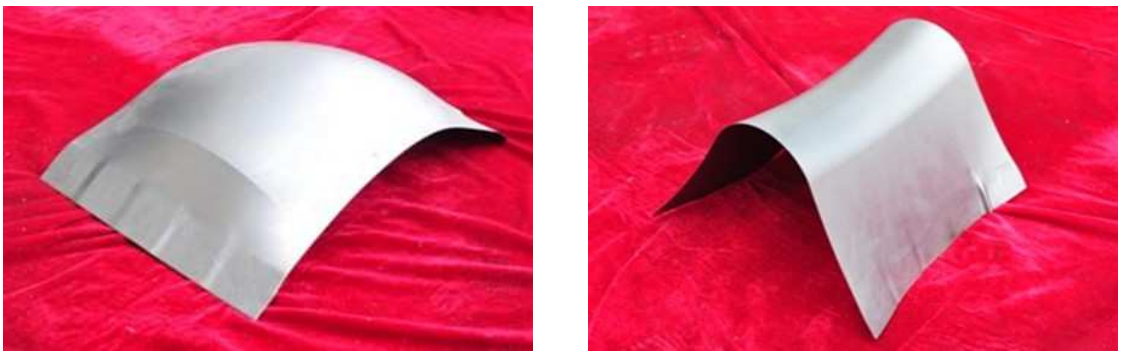

(a) spherical part (b) saddle part

Fig.3 The experimental photos formed by DCSF machine

Numerical simulation of DCSF

Aluminum alloy 2024-O is selected as the simulation analysis material of metal sheet stretch forming process in this paper. It is presumed that the material obeyed the von Mises yield criterion, Prandtl-Ruess flow rule and isotropic hardening model. The mechanical properties of 2024-O are: elastic modulus is 40.54GPa, yield strength is 77.5MPa, Poisson's coefficient is 0.33 and density is 2.78g/cm^3 .Fig.4 (a) is the real stress and strain curve of 2024-O obtained by uniaxial tensile test.

Numerical simulation of flexible DCSF has been performed by Abaqus. Fig.4 (b) presents the finite element model of spherical surface for discrete clamp stretch forming process. Due to the symmetry, only a quarter of FE model is set up. The FE model is composed of three parts: sheet metal, stretching die and clamps. The sheet metal was modeled with shell element S4R. The stretching die and the clamps were modeled with complicated rigid element R3D4. In Fig. 4 (b), OA and OB are the symmetrical axis of sheet metal respectively. The line DF represents the transitional length of sheet metal. The stretching direction agrees with y-. The size of each clamp is 52mm×40mm, and the distance between adjacent clamps is 10mm.

Fig. 4 (c) shows the Numerical result of spherical part formed by discrete clamp with transitional length of 40mm. It can be observed from these results that the edge of sheet metal is curve shape, which realized the object of flexible DCSF technology.

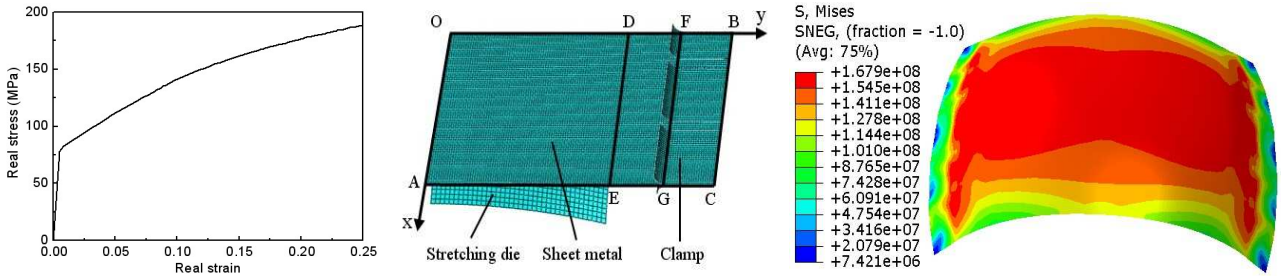

(a) The stress-strain of 2024-O (b) FE model of DCSF (c) Numerical result of spherical part

Fig.4 Numerical simulation of spherical part based on DCSF

Effects of process parameters

In order to study the effects of transitional length to the forming results of DCSF, spherical part with radius of 300mm is selected as object surface, and the forming area is 300mm×300mm. Fig.5 presents the stretching strain distribution of spherical part with different transitional length along symmetry axis OA and OB. The curves show that in the forming area, the longer the transitional length is, the more homogeneous the stretching strain becomes. But in the transitional area, the longer the transitional length is, the larger the stretching strain becomes. Fig.6 presents the thickness distribution of spherical part with different transitional length along symmetry axis OA and OB. Obviously, the thickness distribution of spherical part with transitional length of 30mm is more uniform than that with transitional length of 90mm, and the shorter the transitional length is, the larger the maximum thinning ratio becomes. A shorter transitional length should be used to increase the material utilization rate, but a shorter transitional length may take larger stretching strain and thinning ratio. So the choice of reasonable transitional length should be based on actual situation.

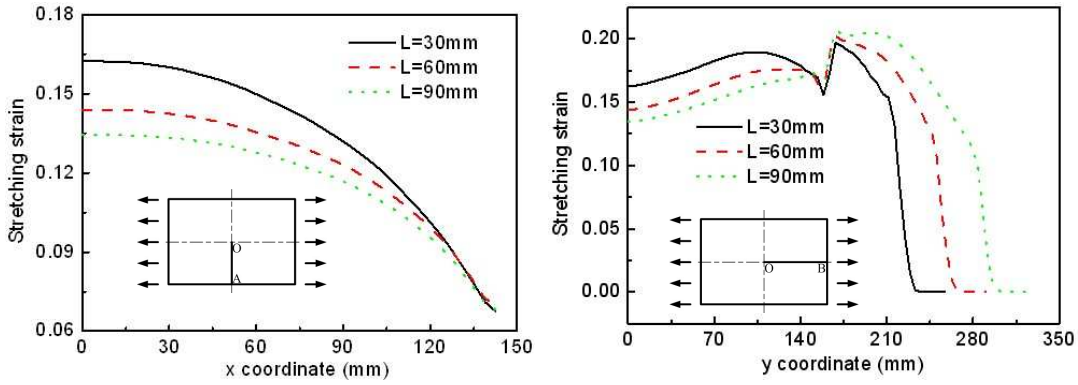

(a) Along the line OA (b) Along the line OB

Fig.5 The stretching strain distribution of spherical part with different transitional length

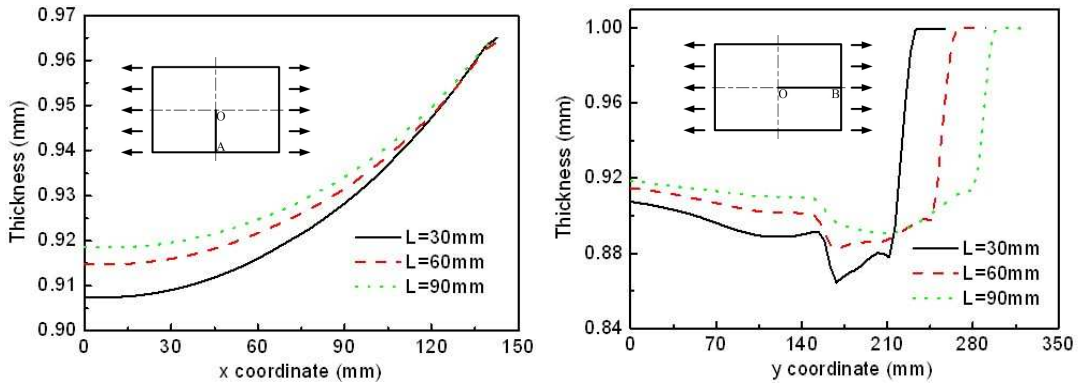

(a) Along the line OA (b) Along the line OB

Fig.6 The thickness distribution of spherical part with different transitional length

Lubrication condition is an important parameter in stretching process, and lubrication condition is set to friction coefficient in numerical simulation. Saddle part is selected as the object surface to study the effects of lubrication condition to forming quality, the bidirectional radius is both 300mm, and the forming area is 300mm×300mm. The size of sheet metal is 440mm×300mm×1mm. The stretching strain distribution of saddle part with different friction coefficient along symmetry axis OA and OB are shown in Fig.7. The curves show that the smaller the friction coefficient is, the more homogeneous the stretching strain becomes. The thickness distribution of saddle part with different friction coefficient along symmetry axis OA and OB are shown in Fig.8. Obviously, the smaller the friction coefficient is, the more homogeneous the thickness becomes. Therefore, good lubrication condition can improve the flowing state and forming quality of sheet.

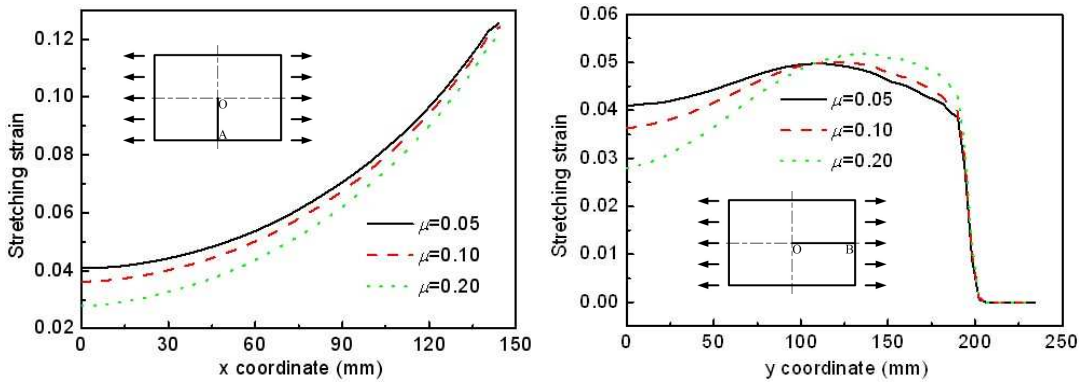

(a) Along the line OA (b) Along the line OB

Fig.7 The stretching strain distribution of saddle part with different friction coefficient

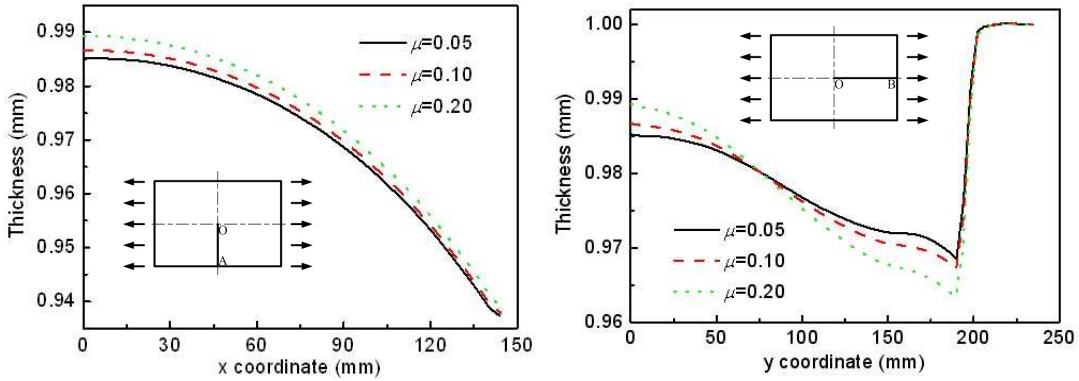

(a) Along the line OA (b) Along the line OB

Fig.8 The thickness distribution of saddle part with different friction coefficient

Complex surface of S-type is selected to study the effects of clamp number. The object S surface is shown in Fig.9 (a), the three radii of S surface are 200mm, 200mm and 1000mm, the forming area of stretching die is 600mm×600mm. The size of sheet metal is 900mm ×600mm ×1mm. Numerical simulation of S-type part was carried out with different clamp number. Fig.9 (b) presents the stress distribution of S-type part with 12 discrete clamps, which shows that formed part has uniform stress distribution and fit the stretching die completely. Fig.9 (c) presents the spatial location of line DE, the curves show that the larger the clamp number is, the better the fit degree becomes. In other words, the higher the discrete degree is, the better the flexibility becomes.

Conclusions

The flexible DCSF machine was developed based on the flexible DCSF technology. The stretching experiment of spherical part and saddle part show the DCSF technology is feasible and the DCSF machine is practicable, and it is suitable to form part with large transversal curvature. The numerical results show that the longer the transitional length is, the more homogeneous the stretching strain and the thickness become. The better the lubrication condition is, the better the forming quality becomes. The higher the discrete degree is, the better the flexibility becomes.

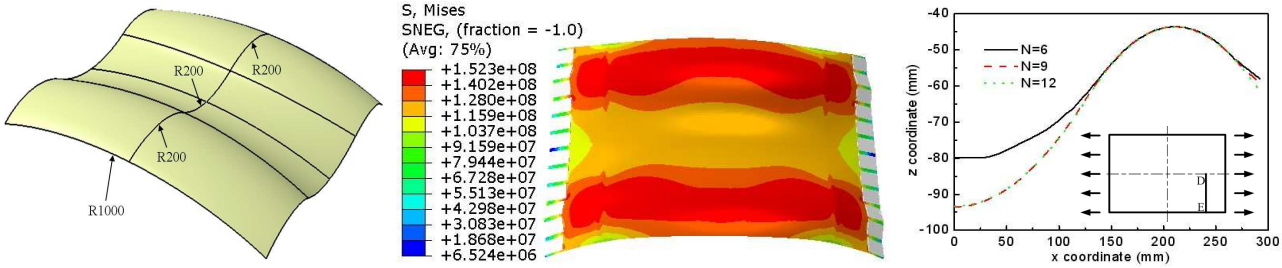

(a) The object S-type surface (b) Numerical result of S-type part (c) Along the line DE

Fig.9 Numerical simulation of S-type part with different clamp number

Acknowledgement

This project supported by the EU Sixth Research Framework (ASTS-CT-2006-030877)

References

[1] Q.G. Han, W.Z. Fu, P.X. Feng, M.Z. Li, X.Z. Liu and R.B. Wang: Aeronautical Manufacturing Technology, Vol. 24 (2010), p. 87

[2] R. Suri, K. Otto and G. Boothroyd: Annals of the CIRP, Vol. 48 (1999), p. 397

[3] B. Table Araghi, G.L. Manco, M. Bambach and G. Hirt: CIRP Annals Manufacturing Technology, Vol. 58 (2009), p. 225

[4] D.H. He, X.Q. Li, D.S. Li and W.J. Yang: Transactions of Nonferrous Metals Society of China, Vol. 20 (2010), p. 1053

[5] D.H. He, D.S. Li, X.Q. Li and C.H. Jin: Transactions of Nonferrous Metals Society of China, Vol. 20 (2010), p. 2350

[6] M.Z. Li, Y.H. Liu, S.Z. Su and G.Q. Li: Multi-point forming: Journal of Materials Processing Technology, Vol. 87 (1999), p. 227

[7] M.Z. Li, Z.Y. Cai, Z. Sui and Q.G. Yan: Journal of Materials Processing Technology, Vol. 129 (2002), p. 333

[8] F.X. Tan, X.D. Xu, G.J. Li, M.Z. Li and G.Z. Zhang: Journal of Xi'an Jiao Tong University, Vol. 42 (2008), p. 1160

[9] X. Chen, M.Z. Li, W.Z. Fu and P.X. Feng: Forging and stamping technology, Vol. 35 (2010), p. 32

doi:10.4028/www.scientific.net/AMM.161.58

EIS study on the deterioration process of organic coatings under immersion and different cyclic wet-dry ratios

Wei ZHANG[1,a], Xue-zheng CHEN[1,b], Peng-fei YIN[1,c],

Zheng-kai XU[1,d], BING Han[1,e], Jia WANG[2, 3,f]

[1] Qingdao NCS Testing and Protection Technology Co., Ltd., Qingdao 266071, China
[2]College of Chemistry and Chemical Engineering, Ocean University of China, Qingdao 266100, China
[3]State Key Laboratory for Corrosion and Protection of Metals, Shenyang 110016, Liaoning，China
[a]email: zghnzw33@yahoo.com.cn (corresponding author);
[b]email: qdchen165@163.com; [c]email: ypf1201@163.com;
[d]email: we125912@yahoo.cn; [e]email: hanbing@qrimc.com;
[f]email: jwang@mail.ouc.edu.cn

Keywords: Organic coatings; Wet-dry cycles; Electrochemical Impedance Spectroscopy.

Abstract：Under immersed and we-dry cyclic conditions, the deterioration processes of the organic coating on carbon steel surface have been comparatively studied using electrochemical techniques. The wet-dry cycles were carried out by exposure to 4 h immersion and 4h dryness (4-4h cycles) and 12h immersion and 12h dryness (12-12h cycles) conditions, respectively. The immersion condition was carry out in a 3.5% NaCl solution and drying at 298K and 50% RH. According to the EIS characteristics, the entire deterioration processes under above three mentioned conditions can be divided into three main stages, consisting of the medium penetration, corrosion initiation and corrosion extension. Comparing with the immersed, the 4-4h wet-dry cycles greatly accelerated the entire deterioration process; especially during the corrosion initiation and the corrosion extension periods, leading the paint system lose its anti-corrosive performance in a short period. However, the 12-12h wet-dry cycles decelerated the entire deterioration process, prolonging the coatings anticorrosive ability. The acceleration mechanism of the coatings and underlying metal corrosion under wet-dry cycles was discussed based on the above results.

1. Introduction

Organic coatings are widely applied to prevent metal corrosion in the marine domain. Under weathering exposure, wet-dry cycles, H_2O and O_2 are three critical factors for coatings degradation. The evolution of the water absorption process in an organic coatings immersed in a solution is a very important phenomenon because it precedes phenomena such as paint/metal interface loss of adhesion, electrochemical reactions and the reduction of the resistance to the passage of ions through the coating itself[1-4]. It has been proven that the loss of adhesion between the organic coating and the iron sample is induced by cathodic delamination which is caused by reaction products, like radicals from the paint/metal interface redox[5-6]. The synergistic effect of oxygen reduction and water penetration was strengthening by wet-dry cycles during the coatings degradation and interface metal corrosion processes [4, 7-11].

Electrochemical impedance spectroscopy is widely used to monitor and quantify the corrosion protection abilities of organic coatings on metal substrates. The impedance data can be collected over a broad frequency range. The coating deterioration behavior can be evaluated by anglicizing

the coating resistance, coating capacitance, charge transfer resistance, as well as the double layer capacitance obtained at different frequency ranges, when properly modeled using an equivalent circuit.

Impedance spectra of painted metals are characterized by different spectra depending on the state of the paint coating. The main response characteristics of the EIS during the deterioration processes of the organic coatings can be divided into four types shown as follows [12-14]: (1)Protective and intact coating display a capacitive arc in the Nyquist plot. (2) When the electrolyte penetrates the coating, the arc becomes a semi-circle. (3) For longer immersion, disbondings between the coating and the metal substrate take place where a corrosion process arises. Then, two semi-circles can be detected in Nyquist plot. (4) Eventually, a Warburg type Impedance W can be incorporated in series with charge transfer resistance due to the diffusion processes through the connecting pores. Such equivalent circuits have been extensively used in literature to model coating degradation and are applied in this work, as a first approach.

In our previous works, the degradation processes of organic coatings both under immersed and wet-dry cyclic conditions have been studied by the techniques of EIS combining with SKP and SOM network, respectively. We divided the above four types EIS characteristic response into three stages named: (Ⅰ) the medium penetration into coatings, (Ⅱ) corrosion initiation underlying coatings and (Ⅲ) the corrosion extension [15, 16,]. However, though the respective study on the deterioration process of the organic coatings under immersed and wet-dry cyclic conditions have been paid much more attention; the research under different cyclic ratios and immersed conditions synchronously were seldom done. In order to get a closer look at the how the cyclic wet-dry effect the coatings deterioration process, the comparing study under cyclic and immersed conditions is seriously need.

The purpose of this paper is, to take a further study on how the wet-dry cycles influenced the whole deterioration process and the sub-processes of the organic coating deterioration.

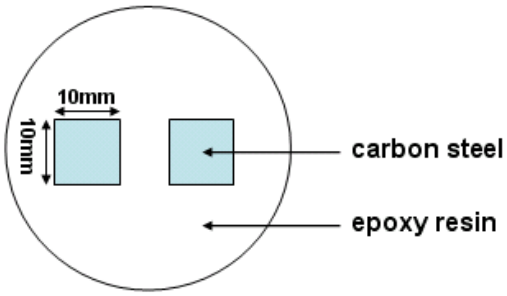

Fig. 1. Schematic diagram of the experimental cell for immersed and wet-dry cyclic tests

2. Experimental procedure

2.1. Electrochemical cell and specimen preparation

To guarantee data reliability, lots of reliable measures were carried out during the samples preparation: (1) For surface treatment consistency, each experimental cell was comprised of two carbon steel electrodes (10×10×10 mm) embedded in epoxy, as shown in Fig. 1. (2)All the cells were pretreated by abrasion with #600 SiC paper, degreasing in acetone and rinsing with methyl alcohol. (3)The pretreated samples were coated with iron oxide red alkyd primer, dried in the desiccators for one week. The thickness results are the mean value of 20 measurements. And the coatings with 45 μm thickness were used in this paper. (4) For all that, for each group four samples were selected to avoid adulterations due to pores or local defects that cannot be observed by the naked eyes.

2.2. Cyclic wet–dry condition

The cells were exposed to alternate conditions of 4 h immersion and 4 h dryness (4-4h cycles) and 12h immersion and 12h dryness (12-12h cycles), respectively, at about 298 K and 50% RH in 3.5% NaCl solution.

2.3. EIS measurement

Three electrodes system was used, including coated Q235 carbon steel, platinum counter and SCE reference. The electrochemical impedance spectroscopy (EIS) measurements were performed under immersed state at intervals of 1 or 2 h in the frequency range of 100 kHz-10 mHz using 2263 potentiostat. The amplitude of the sinusoidal voltage signal was selected in 10-50 mV according to the corresponding coating resistance measured.

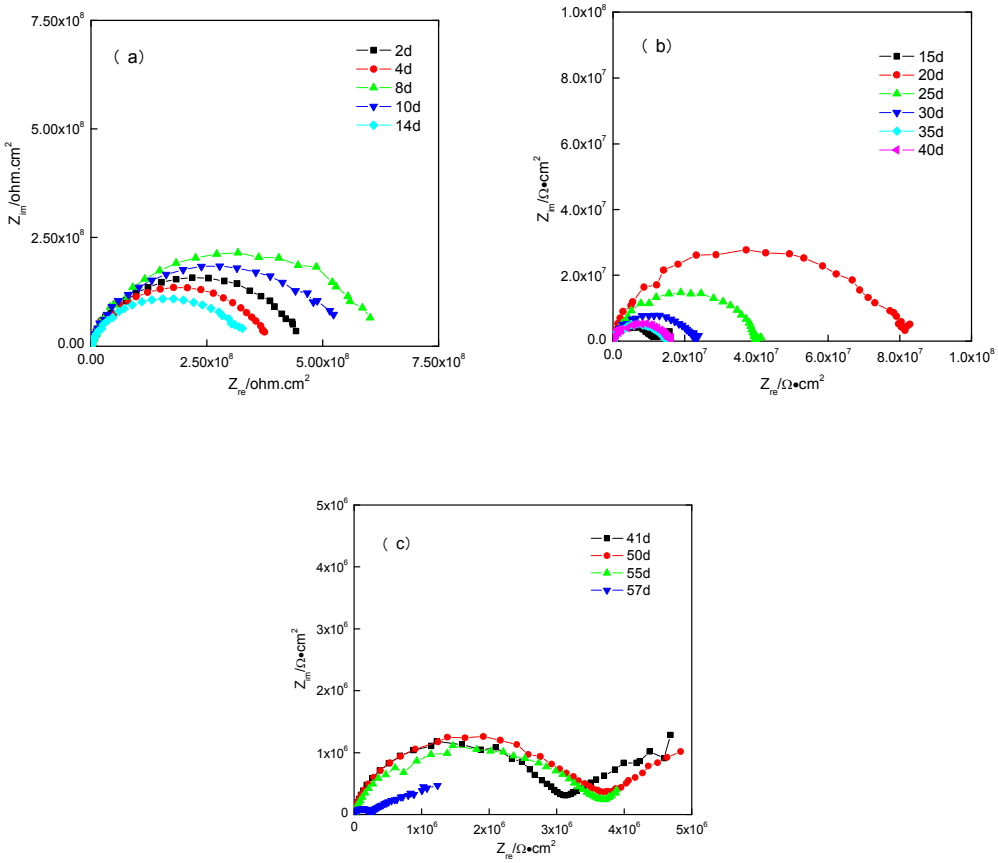

Fig. 2. The EIS changes for coating deterioration under constant immersed condition in 57 days: (a) 2—14 days, (b) 15—40 days and (c) 41—57 days

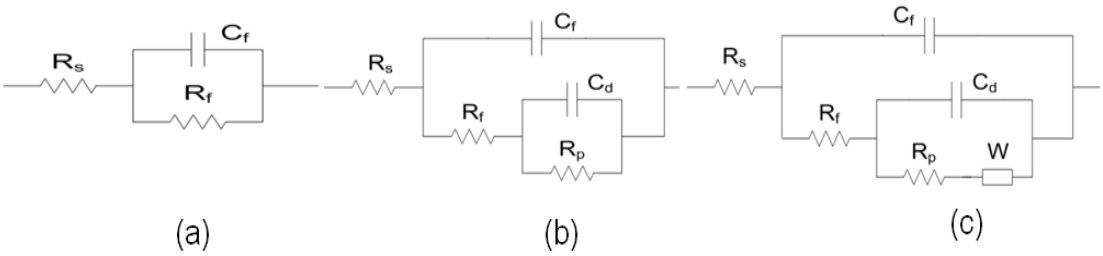

Fig. 3. The equivalent circuit models used for fitting the impedance results of cyclic wet-dry and immersed states: (a) for organic coated metals at the beginning time of immersion; (b) for organic coated metals immersed in testing solution after the interface corrosion initiated; (c) for organic coated metals after presence of two time constant and Warburg diffusion.

3. Results and discussion

3.1. Electrochemical impedance spectroscopy measurements

As shown in Fig. 2, the plots of coating deterioration after constant immersed test can be divided into three patterns, which represent three different stages of the whole deterioration process [13, 15, 16].

Stage Ⅰ (the first 24 days) was characterized by a single semi-circle with high-impedance which may indicate that some water penetrated into the coating, but did not reach the coating/metal interface [13]. It is the typical characteristics of water penetration into coatings. This behavior can be represented by an equivalent circuit including the solution resistance, R_s, in series with a parallel combination of the coating capacitance, C_f, and the film resistance, R_f, related to the ionic conduction through the coating (Fig.3a). This stage was called the medium penetration. It must be noted, however, that all the capacitances shown in the equivalent electrical circuits are mathematically modeled using a constant phase element (CPE) in order to consider also the electrochemical behavior of systems which do not correspond exactly to a pure capacitance [15,17,18].

Stage Ⅱ, including day 27 to day 40, during this period the impedance reduced sharply and the EIS diagrams began to show two time constants although the second time constant not clearly to be seen in the LF. It means that, with the transportation of oxygen, water and ions to the coatings/metal interface, disbondings between the coating and the metal substrate take place where a corrosion process arises. The explanation of the second time constant was related with the commencement of the corrosion process on the metallic substrate. Since at the beginning the active surface was too small, the time constant associated was shifted towards higher frequencies and it can be overlapped to the paint properties time constant [19-21]. So the second time constant, associating to the interface corrosion, could not be clearly shown in the LF. The charge transfer resistance, R_p, and the double layer capacitance, C_d, are added to the previous equivalent circuit (Fig. 3b). The high frequency time constant is representative of the organic coating and the low frequency time constant made reference to an electrochemical corrosion process under coatings. This stage was called the corrosion initiation.

Stage Ⅲ, form day 41 to day 57, the diagram in the low frequency began to show a diffusion tail [12]. The Nyquist plots of electrochemical impedance showed a capacitive loop in the high frequency (HF) range and an oblique line in the low frequency (LF) range, which probably indicated that corrosive medium had diffused into the coating/metal interface and the coating began to delaminate. This part of the electrochemical impedance data interpretation was critical since several equivalent electrical circuits can be used [12-14]. Considering the coating still have the anticorrosion ability, the equivalent electrical circuit containing two time constants used was shown in Fig.3c, where a Warburg type impedance W was incorporated in series with R_p due to the diffusion processes through the connecting pores. Explanations for this diffusion behavior were not known at the present. In agreement with the literature [13], it may attribute to the new formed diffusion layer because of the accelerated substrate corrosion in the interface. This period of the deterioration process is called the corrosion extension，which caused the coating delamination and lose its corrosion protection eventually.

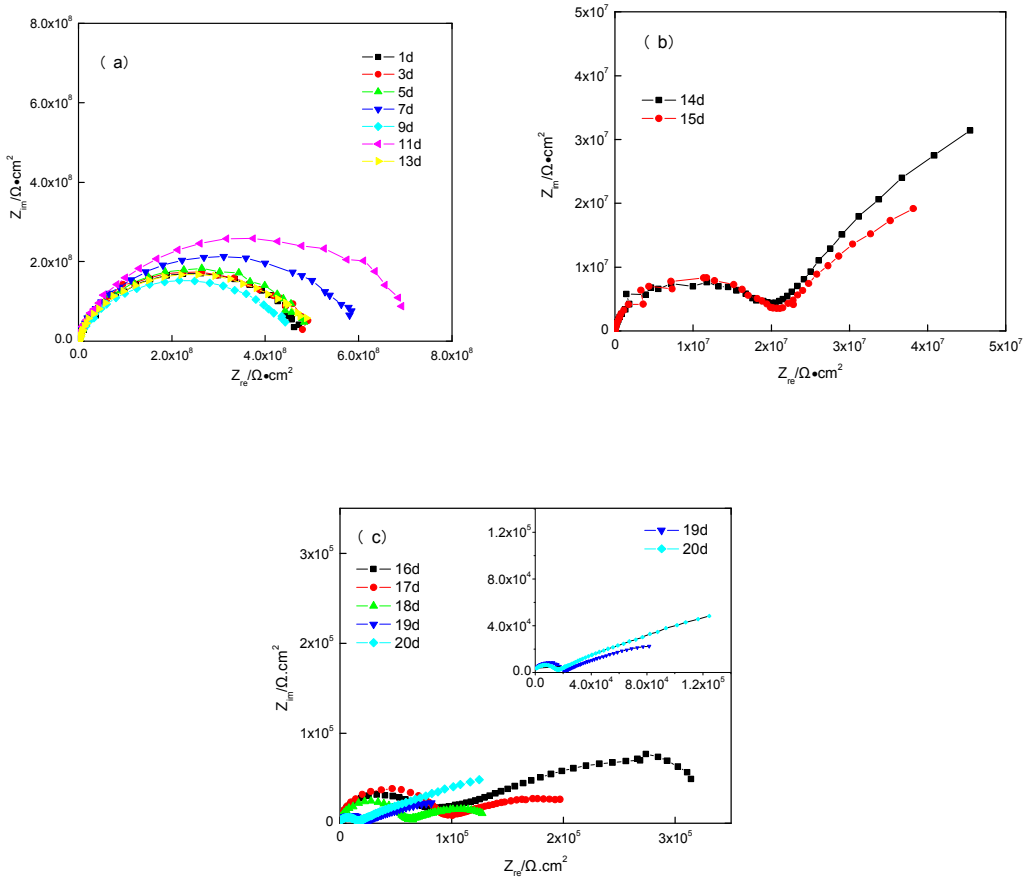

Fig. 4. The EIS changes for coating deterioration of 4-4h cycles in 20 days: (a) 1—13 days, (b) 14—15 days and (c) 16—20 days.

Fig. 4 was the Nyquist plots and the Bode plots determined at the 3th hour of immersed state after the 4-4h cyclic test. As shown in Fig. 4, the plots can also be divided into three patterns.

Stage Ⅰ, the first 13 days, one time constant with the single semi-circle diameter decreased slowly along with the immersion time. Stage Ⅱ, including the period from day 14 to day 15, was a transition period from stage Ⅰ to stage Ⅲ, in which the resistance decreased sharply and the two semi-circles was clearly detected in Nyquist plot. In stage Ⅲ (from day 16 to day 20), the resistance was very low.

In the same way, the three stages of EIS responses were called the medium penetration, corrosion initiation and corrosion extension. The equivalent circuit models in Fig. 3 were used respectively to fit the EIS results of the three deterioration processes and good fitting results were also obtained.

Fig. 5 was the Nyquist plots determined at the 3th hour of immersed state after the 12-12h cyclic test. As shown, the plots can also be divided into three patterns.

Stage Ⅰ, the first 18 days, one time constant with the single semi-circle diameter decreased slowly along with the immersion time. Stage Ⅱ, from day 19 to day 22, was a transition period. In stage Ⅲ, from day 23 to day 68, the resistance was very low.

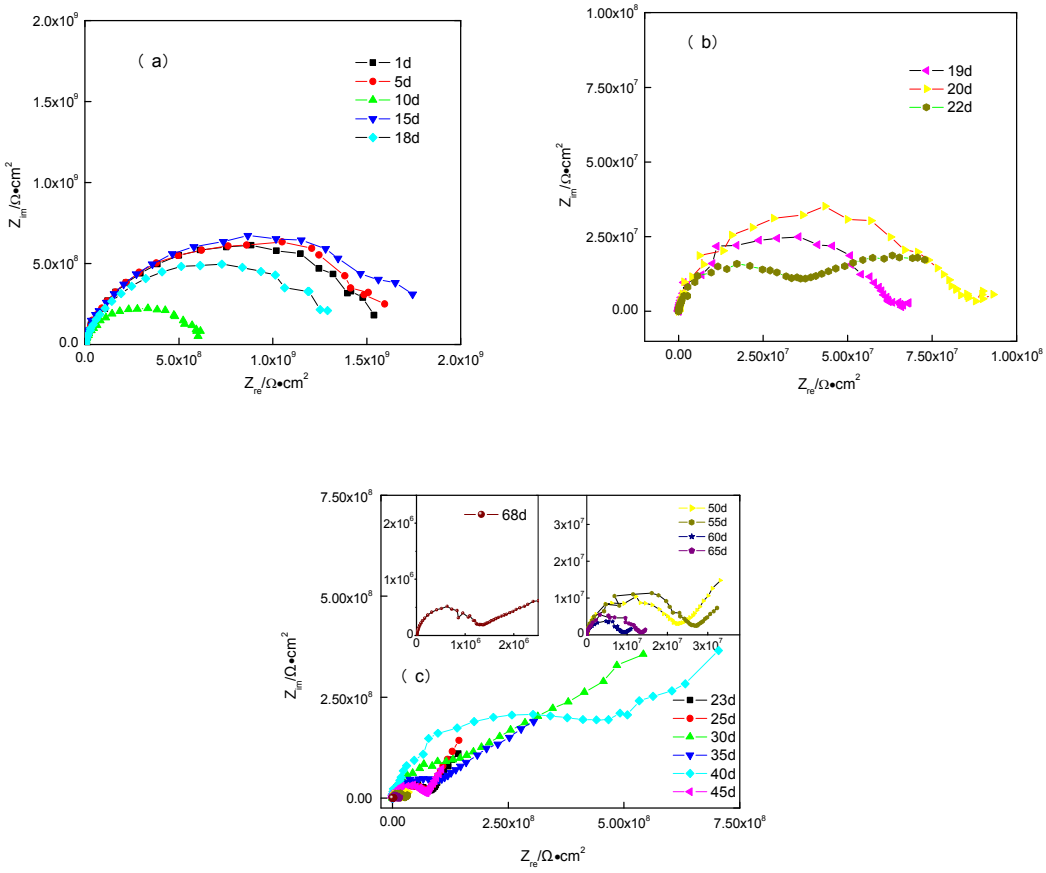

Fig. 5. The EIS changes for coating deterioration of 12-12h cycles: (a) 1—18 days, (b) 19—22 days and (c) 23—68 days.

3.2 Period's comparison of three different coatings deterioration processes

The stage comparison of three different coatings deterioration processes are given in Table 1. Comparing with the immersed, the higher cyclic ratios of 4-4h wet-dry cycles greatly accelerated the entire deterioration process; especially during the corrosion initiation and the corrosion extension periods, leading the paint system lose its anti-corrosive performance in a short period. When it comes to the lower cyclic ratios, the 12-12h wet-dry cycles decelerated the entire deterioration process, prolonging the coatings anticorrosive ability. However, for the 4-4h and 12-12h cycles, the accelerating or decelerating effects are quite different during the three periods.

Table 1. The stage comparison of three different coatings deterioration processes

types/stages	medium penetration	corrosion initiation	corrosion extension	Coatings failure ($<10^6\Omega.cm^2$)
4-4h	1-13d	14-15d	16-20d	16d
12-12h	1-18d	19-22d	23-68d	68d
Immersion	1-14d	15–40d	41-57d	57d

3.3 Monitoring results of the coating capacitance C_f and coating resistance R_f

By comparison, the R_f and C_f parameters extracted from EIS data are presented in Fig. 6 as a function of exposure time. C_f is one of the most frequently studied parameters obtained by EIS measurements for characterising the protective properties of organic coatings, because by analysing this parameter it is possible to measure the water uptake phenomena which are very important in barrier coatings [1,2,22].

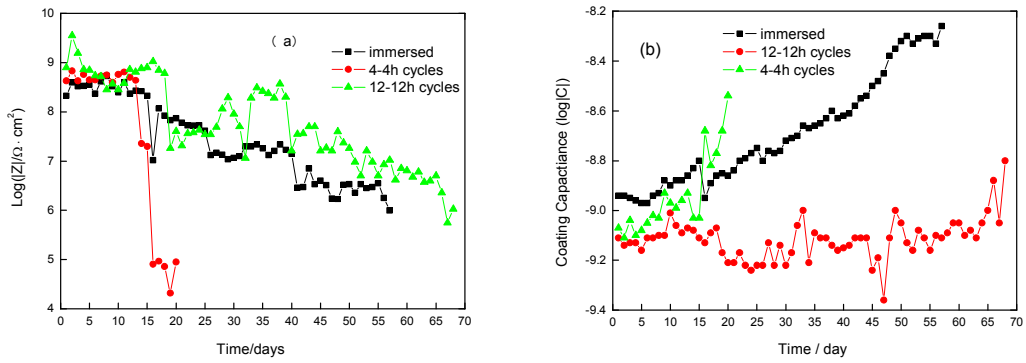

Fig. 6. The changes in (a) coating resistances R_f and (b) coating capacitances C_f as a function of exposure time under wet-dry cyclic and immersed tests

For the 4-4h and 12-12h cycles, one of the notable phenomenon was that, despite the data dispersion, R_f were always higher and C_f were lower than the immersed during period Ⅰ. The explanation of such higher R_f values and lower C_f values during the period Ⅰ is related to the starting of the water absorption and desorption on the interface. For the organic coatings, the process of water uptake starts at the dry film-water interface during wetting. At the beginning of the exposure, however, the swelling of the polymer particles close to the interface will hinder the penetration of the water into the interior of the film [23]. Under cyclic wet-dry condition, the coating experienced repeated starting of the water uptake processes, resulting in the low content of water absorption and good anti-corrosive performance. Thus, during period Ⅰ, lower C_f and higher R_f were observed under wet-dry cyclic condition.

During the stage Ⅰ, the 4-4h wet-dry cycles and the immersed coatings experienced the same degrading period, shorter than the 12-12h wet-dry cycles, as it shown in table 1. For the 4-4h wet-dry cycles, the cyclic ratio is so higher that the absorbed water during the wetting period didn't lost completely when it comes to the drying process, and then the coatings entered the next immersion cycles again. So, the coatings wetting situation is the same like the immersed. But for the 12-12h wet-dry cycles, the penetrated water can be exudates completely for the long drying process.

During the stage Ⅱ, on the onset of the interface corrosion, however, the R_f values under cyclic tests decreased drastically, lower than the immersed. And the C_f values became higher than the immersed; even it experienced a sudden decrease at the beginning of the interface corrosion initiation [24].

However, comparing with the immersed, both the 4-4h and the 12-12h wet-dry cycles accelerate the corrosion initiation period for the faster oxygen transportation and reduction at the polymer/metal interface during drying stages, as it shown in table 1. The oxygen reduction at the coating/metal interface has to be regarded as the main detrimental reaction which gives rise to the destruction of the interface and, therefore, to the extension of the delaminated zone. The oxygen transportation was much faster in air pore of the coatings during drying process than the immersed state, and the high oxygen content in the wetting coating accelerated the cathodic reduction rate resulting in a rapid coating delamination from the metal substrate.

When it comes into stages Ⅲ, for the 4-4h wet-dry cycles, the quickly oxygen reduction at the coating/metal interface during drying stage accelerate coating delaminating process, making the coatings lost its anti-corrosive ability quickly. For the immersed state, without the fast oxygen

transportation process, the delamination speed is lower, and the anodic reactions can only take place in the limited blisters, making heavy local substrate corrosion. However, although the 12-12h wet-dry cycles also experienced the fast oxygen reduction processes during the drying stages, the longer dying period made the water desorbed completely and than the underlying metal corrosion stagnated without the connection of the electrolyte solution between the anodes and cathodes. So, as the results show, comparing with the immersed， the deterioration process are decelerated.

4. Conclusions

1) EIS results indicated that the entire deterioration of the organic coatings under wet-dry cycles and immersed conditions can be divided into three main stages. Comparing with the immersed, the 4-4h cycles greatly accelerated the coatings deterioration, leading the coating rapidly lose its anticorrosive performance in a short period. But the12-12h cycles decelerated the entire deterioration process.

2) For the three coatings deterioration stages, the accelerating and decelerating effects of the two type cycles are quite different. Comparing with the immersion, the 4-4h cycles did not affect the medium penetration process, but it apparently accelerated the corrosion initiation and corrosion extension processes when the underlying corrosion initiated. However, although the 12-12h cycles accelerated the corrosion initiation stage, it decelerated the medium penetration and corrosion extension processes, prolonged the coatings service life.

Acknowledgements

The authors gratefully acknowledge the support by National Natural Science Foundation of China under the contact 50971118.

References

[1] F. Deflorian, L. Fedrizzi, P. L. Bonora, Influence of the photo-oxidative degradation on the water barrier and corrosion protection properties of polyester paints, Corr. Sci. 38 (1996) 1697-1708.

[2] M. D. G. Destreri, J. Vogelsang, L. Fedrizzi, L. Deflorian, Water up-take evaluation of new waterborne and high solid epoxy coatings, Prog. Org. Coat. 37 (1999) 69-81.

[3] X. F. Yang, D. E. Tallman, S. G. Croll, G. P. Bierwagen, Morphological changes in polyurethane coatings on exposure to water, Polymer Degradation and Stability, 77 (2002) 391-396.

[4] J. H. Park, G. D. Lee, H. Ooshige, A. Nishikata, T. Tsuru, Monitoring of water uptake in organic coatings under cyclic wet–dry condition, Corr. Sci. 45 (2003) 1881-1894.

[5] L. H. Jr, W. Wang, L. Igetoft, The mechanism for the cathodic delamination of organic coatings from a metal surface, Prog. Org. Coat. 11 (1983) 19-40.

[6] A. Leng, H. Streckel, M. Stratmann, The delamination of polymeric coatings from steel. Part 1 : Calibration of the Kelvinprobe and basic delamination mechanism, Corr. Sci. 41 (1999)547-578.

[7] N. D. Tomashov, Development of the electrochemical theory of metallic corrosion, Corrosion, 20 (1964) p.7-14t.

[8] M. Stratmann, H. Streckel, K. T. Kim, S. Crockett, On the atmospheric corrosion of metals which are covered with thin electrolyte layers-iii. the measurement of polarisation curves on metal surfaces which are covered by thin electrolyte layers, Corr. Sci. 30 (1990) 715-734.

[9] J. Wang, T. Tsuru T, An investigation on oxygen reduction under thin electrolyter layer using kelvin probe reference electrode, J. Chin. Soc. Corr. Prot. 15 (1995) 180-188.

[10] T. Tsuru, A. Nishikata, J. Wang, Electrochemical studies on corrosion under a water film, Mater. Sci. Eng, A198 (1995)161-168.
[11] A. Nishikata, Y. Ichihara, T. Tsuru, An application of electrochemical impedance spectroscopy to atmospheric corrosion study, Corr. Sci. 37 (1995) 897-911.
[12] A. Amirudin, D. Thierry, Application of electrochemical impedance spectroscopy to study the degradation of polymer-coated metals, Prog. Org. Coat. 26 (1995) 1-28.
[13] J. Q. Zhang, C. N. Cao, Study and evaluation on coatings by electrochemical impedance spectroscopy, Corrosion and Protection 19 (1998) 99-104.
[14] Q. L. Thu, H. Takenouti, S. Touzain, EIS characterization of thick flawed organic coatings aged under cathodic protection in seawater, Electrochim. Acta. 51 (2006) 2491-2502.
[15] X. Zhao, J. Wang, Y. H. Wang, T. Kong, L. Zhong, W. Zhang, Analysis of deterioration process of organic protective coating using EIS assisted by SOM network, Electrochem. Commun. 9 (2007)1394-1399.
[16] W. Zhang, J. Wang, Z. Y. Zhao, J. Jiang, Study on deterioration process of organic coatings by EIS and SKP , Chem. J. Chin. Uni. 30 (2009)762-766.
[17] P. L. Bonora, F. Deflorian, L. Fedrizzi, Electrochemical impedance spectroscopy as a tool for investigating underpaint corrosion, Electrochim. Acta. 41 (1996) 1073-1082.
[18] L. Fedrizzi, F. Deflorian, G. Boni, P. L. Bonora, E. Pasini, EIS study of environmentally friendly coil coating performances, Prog. Org. Coat. 29 (1996) 89-96.
[19] R. L. Howard, S. B. Lyon, J. D. Scantlebury, Accelerated tests for prediction of cut edge corrosion of coil-coated architectural cladding. Part II: cyclic immersion, Prog. Org. Coat. 37 (1999) 99-105.
[20] A. Gamal, El-Mahdy, A. Nishikata, T. Tsuru, Electrochemical corrosion monitoring of galvanized steel under cyclic wet–dry conditions, Corr. Sci. 42 (2000) 183-194.
[21] A. Gamal, EL-Mahdy, Atmospheric corrosion of copper under wet/dry cyclic conditions, Corr. Sci. 47 (2005) 1370-1383.
[22] F. Deflorian, L. Fedrizzi, S. Rossi, P. L. Bonora, Organic coating capacitance measurement by EIS: ideal and actual trends, Electrochim. Acta. 44 (1999) 4243-4294.
[23] G. Lendvay-Gyorik, T. Pajkossy, B. Lengyel, Corrosion-protection properties of water-borne paint coatings as studied by electrochemical impedance spectroscopy and gravimetry, Prog. Org. Coat. 56 (2006) 304-310.
[24] A. P. Yadav, A. Nishikata, T. Tsuru, Electrochemical impedance study on galvanized steel corrosion under cyclic wet–dry conditions—influence of time of wetness, Corr. Sci. 46 (2004) 169-181.

doi:10.4028/www.scientific.net/AMM.161.67

Microstructure and Mechanical Properties Analysis of X70 Pipeline Steel with Polygonal Ferrite plus Granular Bainite Microstructure

Zhanzhan Zhang[1,a], Xiurong Zuo[1,b], Yueyue Hu[1,c], Rutao Li[1,d] and Zhiming Zhang[2,e]

[1]School of Physics and Engineering, Zhengzhou University, Zhengzhou 450052, PR China

[2]Nanjing Julong Steel Pipe Company Ltd, Nanjing 210061, PR China

[a]zhangzhanzhan031@126.com, [b]zuoxiurong@126.com, [c]hucheng85@126.com, [d]lrt851@126.com, [e]876384606@qq.com

Keywords: X70 pipeline steel, ferrite plus bainite, mechanical properties, melded joint

Abstract. Microstructure and mechanical properties of X70 pipeline steel with polygonal ferrite plus granular bainite were characterized using tensile tests, Charpy V-notch impact tests, drop weight tear tests, hardness tests and scanning electron microscopy. The results of experiment indicated that X70 pipeline steel with polygonal ferrite plus granular bainite showed an excellent combination of high strength and toughness. The base metal with polygonal ferrite plus granular bainite microstructure exhibited perfect mechanical properties in terms of the transverse yield ratio of 0.81, elongation of 46%, an impact energy of 335 J at -10 ℃ and a shear area of 90% at 0 ℃ in the drop weight tear test. The heat affected zone contained coarse grain zone and fine grain zone, which exhibited good low temperature toughness of 216 J at -10 ℃. The weld metal primarily consisted of intragranularly nucleated acicular ferrites which led to the high strength and toughness.

Introduction

In the transportation of oil and natural gas, pipeline steels have been widely used. High strength and good low temperature toughness are required in pipeline steels [1,2,3,4], with the increasing demand for oil and natural gas, and the finding of oil and natural gas in the severe environment far from major market. At the same time, in order to improve oil and natural gas transportation efficiency through high pressure operation, large wall thickness and diameter of pipeline steels are adopted.

At present, X70 pipeline steels with thin wall thickness have already been investigated widely, however the properties of X70 pipeline steels with large wall thickness are not very clear, which are used in high pressure transportation in the complex terrain and acidic soil [5]. In addition, due to the weld thermal cycling effect, toughness and strength of the welded joint are easy to decline comparing to the base metal [1], leading to the fracture in pipeline when transporting oil and natural gas under high pressure operation [6]. Hence it is necessary to study the microstructure and properties of the welded joint of X70 pipeline steel with large wall thickness.

In this study, the mechanical properties of the base metal and welded joint were examined by tensile tests, Charpy V-notch impact tests, drop weight tear tests (DWTT) and hardness tests. The microstructures of the welded joint were characterized by scanning electron microscopy (SEM). The mechanical properties and microstructure in welded joint were evaluated, and the relationships between them were established. The results will be beneficial to the practical application of large wall thickness and diameter of pipeline.

Experimental Procedure

Material. Material used in this study was X70 pipeline steel plate of 26.2 mm thickness. Table 1 lists the chemical compositions of the base metal and the weld metal. The investigated steel plate was manufactured by thermomechanical control process (TMCP) to produce the microstructure of polygonal ferrite plus granular bainite. The plate was welded by double submerged arc welding to form into a cylindrical, and then the pipe was subjected to cold expend.

Mechanical Test. The full thickness tensile specimens with a width and gauge length of 38.1 and 50 mm for tensile tests which were conducted at room temperature using a 100-ton-capacity WAW-Y1000C material testing machine, were cut from the base metal which was 180 degrees away from the welded joint in the transverse. To evaluate the Charpy impact energy of the tube, weld and heat affected zone (HAZ), the specimens with a size of 10×10×55 mm were used. The specimens (305×76×26.2 mm) for DWTT were cut from 180 degrees away from the welded joint in the transverse. The Charpy impact was performed at -10 ℃, and the DWTT was performed at 0 ℃. Furthermore, the hardness testing was carried out with a Digital Microhardness Tester HVS-1000, hardness readings at 1.5 mm from the external surface were taken on the interval of 1 mm in the weld and the base of near weld, and the interval of 0.5 mm in the HAZ.

Table 1 Chemical compositions of the experimental steel pipes (wt.%).

Location	C	Mn	Si	P	S	Mo	Ni	Cr	V+Nb+Ti
Base metal	0.04	1.58	0.25	0.010	0.002	0.13	0.15	0.166	0.081
weld metal	0.05	1.70	0.30	0.010	0.002	0.13	0.17	0.165	0.058

Microstructure. The microstructure of the welded joint was observed by JSM-6700F scanning electron microscope. For SEM observation, the specimens were ground, mechanically polished and etched in a 4% nital solution.

Result and Discussion

Mechanical Properties. The results of tensile and impact test for the pipe are shown in table 2. The yield strength and tensile strength of the base metal were 514 and 634 MPa, respectively, and the transverse yield ratio of 0.81 which satisfied the standard that is less than 0.9. In addition, the base metal also exhibited the perfect mechanical properties in terms of elongation of 46%, an impact energy of 335 J at -10 ℃ and a shear area of 90% at 0 ℃ in the DWTT, indicating good ductility and toughness. It also could be seen that the tensile strength of the weld metal was slightly higher than the base metal. The impact absorbed energy of the base metal at -10 ℃ was much higher than that of the HAZ and the weld, and the HAZ which was always the weak link of welding still reached 216 J.

Table 2 Results of tensile and impacts properties of the pipe

Position	Yield strength [MPa]	Tensile strength [MPa]	Elongation [%]	Yield ratio	CVN (-10 ℃) [J]	DWTT (0 ℃) [%]
Base metal	514	634	46	0.81	335	90
Weld metal	-	663	-	-	173	-
HAZ	-	-	-	-	216	-

Note: CVN is the Charpy impact energy

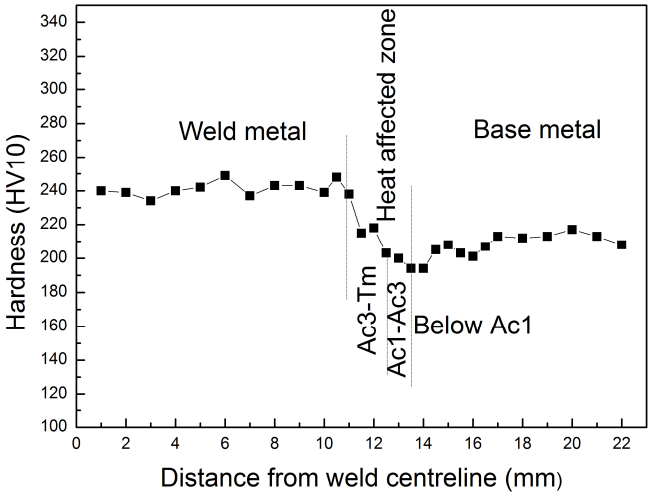

Fig. 1 Variation of hardness from weld center to base metal

A hardness profile of the base metal, HAZ and weld zones was shown in Fig. 1. The hardness in the weld zone was higher than that in the base metal and HAZ, which indicated that the welded joint did not experience significant softening. The HAZ was divided into two parts, coarse grain zone (temperature between Ac3-Tm) and fine grain zone (temperature between Ac1-Ac3). The hardness decreased rapidly from the weld toward the base metal near the weld and increased slowly into the base metal, which could be seen from the hardness-distance profile in Fig.1. It also could be seen that there was a sightly soft zone of the fine grain zone and base metal near the weld, but the minimum hardness still achieved 196 HV10.

Microstructure. Fig. 2 shows the microstructures of different parts of the base metal. The microstructure of the base far away from the weld (Fig. 2a) contained polygonal ferrite, granular bainite and a small amount of pearlite. The microstructure of the base near the weld is shown in Fig. 2b. Compared with the base far away from the weld, the volume fraction of bainite reduced, and the volume fraction of ferrite increased. Fig. 2c and d show the high-magnification SEM micrographs, which are correspond with the base far away from the weld and near the weld, respectively. There were many discrete strip carbides in bainite, and a lot of rectangular, circular and irregular precipitates were observed in ferrite matrix (Fig. 2c). However, strip carbides in bainite were sphered in the base near the weld (Fig.2d). In low-carbon micro-alloyed steel, stronger carbonitrite-forming alloy elements such as Nb and Ti formed carbonitride dispersions, which precipitated easily in the rolling process playing precipitation strengthening [7]. The base metal near the weld was equivalent to tempering zone according to the variation of welding temperature and microstructure. Bainite occurred recovery and recrystallization during welding process in the temperature above 600 ℃ [8], and finally decomposed and formed ferrite. In addition, carbides were sphered in order to decrease the interfacial energy during this processing. Therefore the increase of the ferrite amount and the sphere of carbides in bainite resulted in the reducing of hardness in the base zone near the weld.

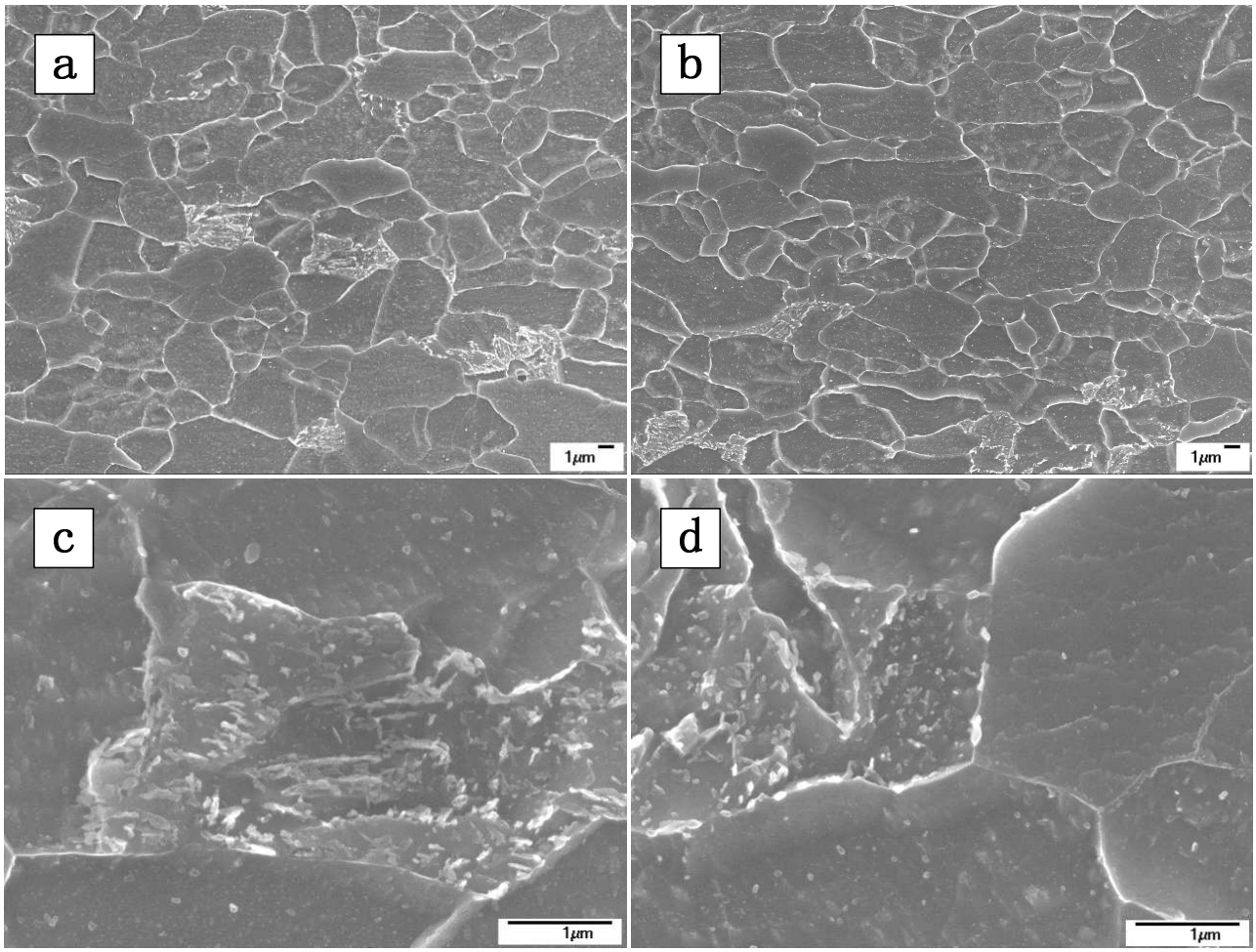

Fig. 2 SEM micrographs showing the microstructures of different parts of the base metal (a)(c) far away from the weld, (b)(d) near the weld.

The microstructures of different parts of the HAZ are shown in Fig. 3a and b. According to the peak temperature and microstructural characteristics, the heat affected zone contained coarse grain zone in Fig. 3a and fine grain zone in Fig. 3b. Coarse grain zone near the weld (Fig. 3a) contained granular bainite with clear prior austenite grain boundaries. Nearing the fine grain zone, the grain size of granular bainite gradually decreased, at the same time some ferrite occurred, resulting in the gradual decrease of hardness in coarse grain zone when nearing the fine grain zone. Fine grain zone (Fig. 3b) contained polygonal ferrite, granular bainite and martensite with island shape. Only partial transformation to austenite could occur in fine grain zone where peak temperature ranged between Ac1-Ac3 during the weld thermal cycle. Consequently, the microstructure would contain untransformed ferrite and a mixture of martensite and bainite transformed from the austenite. The volume fraction of bainite/martensite gradually decreased and ferrite gradually increased, and hence the hardness in fine grain zone gradually reduced when nearing the base.

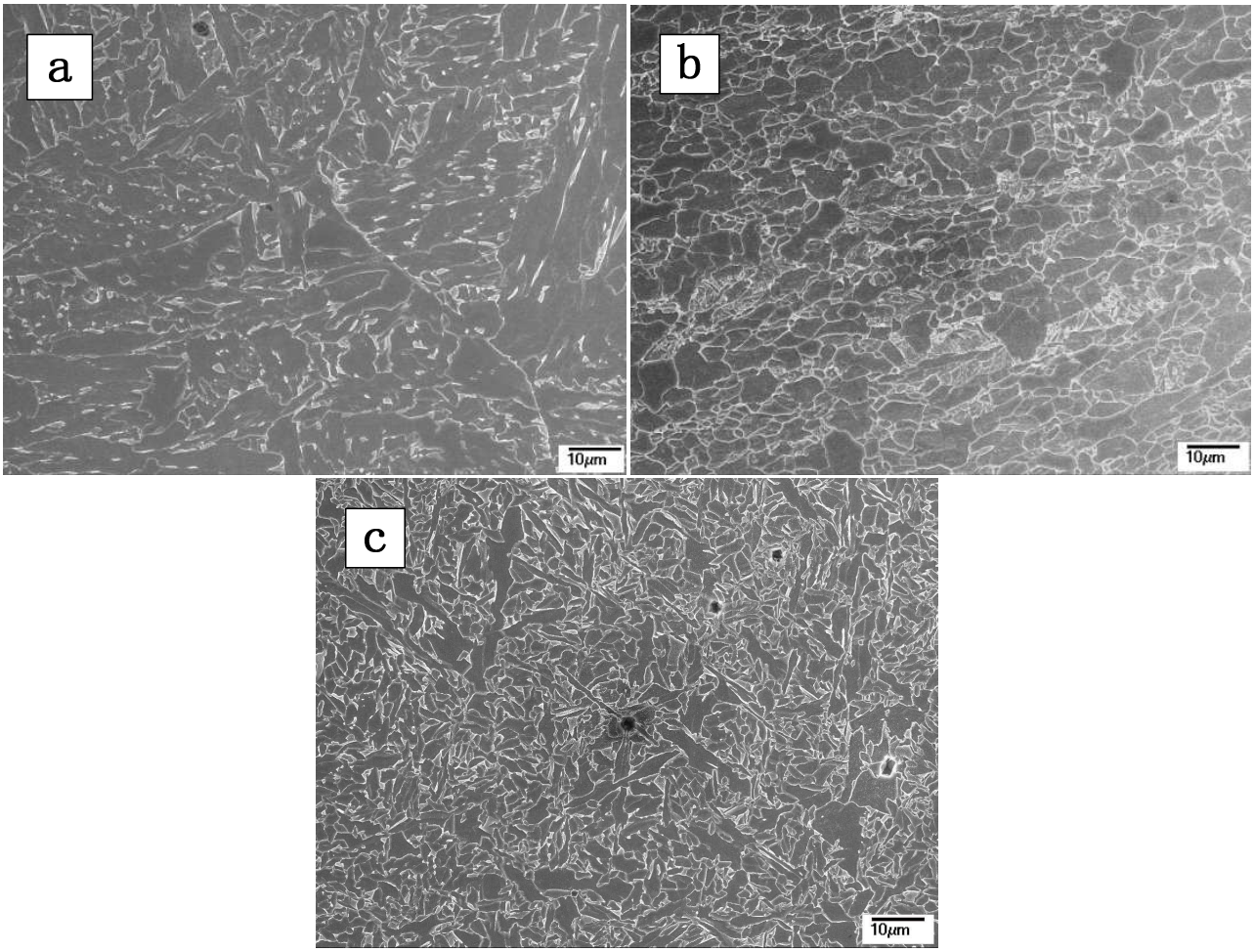

Fig. 3 SEM micrographs showing the microstructures of weld and different parts of the heat affected zone (a) coarse grain zone, (b) fine grain zone, (c) weld.

Fig. 3c shows the microstructure of the weld, which contained intragranular nucleated acicular ferrite, small amount of polygonal ferrite, granular bainite and degenerated pearlite. In the high-temperature welding process, liquid steel dissolved large amount of oxygen in weld, and oxygen reacted with some of deoxidizing elements, such as Ti and Mn, to form complex oxide which could induce the formation of intragranular nucleated ferrite nucleation [9,10,11]. A large austenite grain was divided into smaller regions by interwove microstructure of intragranular nucleated acicular ferrite (Fig. 3c), which was beneficial to the toughness of the weld [12]. In addition, acicular ferrite contained high dislocation densities, which increased the strength of weld [4].

Conclusions

The X70 pipeline steel of 26.2 mm thickness with a ferrite plus granular bainite microstructure showed an excellent combination of high strength and toughness. The welded joint did not suffer significant deterioration through the double submerged arc welding.

(1) X70 pipeline steel with polygonal ferrite plus granular bainite possessed a good combination of mechanical properties such as high strength and excellent low temperature toughness in terms of the transverse yield ratio of 0.81, elongation of 46%, an impact energy of 335 J at -10 ℃ and a shear area of 90% at 0 ℃ in the drop weight tear test.

(2) The heat affected zone was divided into coarse grain zone and fine grain zone. The hardness gradually decreased from coarse grain zone to fine grain zone. The impact energy of heat affected zone was 216 J at -10 ℃, indicating the excellent low temperature toughness. The microstructure of weld metal mainly contained intragranularly nucleated acicular ferrite which divided austenite grain into smaller regions, therefore the weld possessed an excellent combination of strength and toughness.

References:

[1] R.T. Li, X.R. Zuo, Y.Y. Hu, Z.W. Wang, D.X. Hu. Microstructure and properties of pipeline steel with a ferrite/martensite dual-phase microstructure, Mater. Charact. 62 (2011) 801-806.

[2] I.A. Yakubtsov, P. Poruks, J.D. Boyd. Microstructure and mechanical properties of bainitic low carbon high strength plate steels, Mater. Sci. Eng. A. 480 (2008) 109-116.

[3] A.M. Guo, R.D.K. Misra, J.Q. Xu, B. Guo. S.G. Jansto. Ultrahigh strength and low yield ratio of niobium-microalloyed 900 MPa pipeline steel with nano/ultrafine bainitic lath, Mater. Sci. Eng. A. 527 (2010) 3886-3892.

[4] F.R. Xiao, B. Liao, Y.Y. Shan, G.Y. Qiao, Y. Zhong, C. Zhang, K. Yang. Challenge of mechanical properties of an acicular ferrite pipeline steel, Mater. Sci. Eng. A. 431 (2006) 41-52.

[5] Canadian Standards Association Z662-07, oil and gas pipeline systems, Canadian Standards Association, 2007, pp.31-51.

[6] M. Zrilic, V. Grabulov, Z. Burzic, M. Arsic, S. Sedmak. Static and impact crack properties of a high-strength steel welded joint, Int. J. Press. Vessel. Pip. 84 (2007) 139-150.

[7] S.G. Hong, K.B. Kang, C.G. Park. Strain-induced precipitation of NbC and Nb-Ti microalloyed HSLA steels, Scripta. Mater. 46 (2002) 163-168.

[8] S.W. Yang, C.J. Shang, X.L. He, X.M. Wang, Y. Yuan. Stability of ultra-fine microstructures during tempering, J. Univ. Sci. Technol. Beijing. 8 (2001) 119-122.

[9] K.M. Wu, Y. Inagawa, M. Enomoto. Three-dimensional morphology of ferrite formed in association with inclusions in low-carbon steel, Mater. Charact. 52 (2004) 121-127.

[10] J.H. Shim, Y.W. Cho, S.H. Chung, J.D. Shim, D.N. Lee. Nucleation of intragranular ferrite at Ti_2O_3 particle in low carbon steel, Acta. Mater. 47 (1999) 2751-2760.

[11] A.G. Fox, D.G. Brothers. The role of titanium in the non-metallic inclusions which nucleate acicular ferrite in the Submerged ARC Weld (Saw) fusion zones of Navy HY-100 steel, Scripta. Metall. Mater. 32 (1995) 1061-1066.

[12] X.L. Wan, R. Wei, K.M. Wu. Effect of acicular ferrite formation on grain refinement in the coarse-grained region of heat-affected zone, Mater. Charact. 61 (2010) 726-731.

doi:10.4028/www.scientific.net/AMM.161.72

Numerical Investigation on the Process of Multi-point Holder Forming for Titanium Mesh Sheet

Zhiwei Liu [a], Mingzhe Li [b], Qigang Han [c], Zhou Sui [d], Heli Peng [e]

Dieless Forming Technology Center, Jilin University, Changchun 130025, China

[a] lzwlws@163.com, [b] limz@jlu.edu.cn, [c] hanqg@jlu.edu.cn,

[d] zhousui0011@yahoo.com.cn, [e] phl12616040811@126.com

Keywords: sheet metal forming; multi-point forming; wrinkle; titanium mesh; numerical simulation

Abstract: Multi-point holder forming (MPHF) adopts series of coupled holder punches, arranged between forming punches, to clamp the whole sheet in the forming zone. The multi-point holder forming processes of spherical parts of titanium mesh plate were simulated by finite element code, and the results were compared with those of multi-point die forming (MPDF). The influence of holder punch load on the deformation of spherical part in multi-point holder forming was investigated. The shape error analysis of titanium mesh formed by MPHF was performed in finial. The results showed that the spherical part had more excellent performance in multi-point holder forming, and the more deformation the titanium mesh was, the larger force of holder punch would be needed. In addition, there was a small shape error for titanium mesh part formed by MPHF before springback.

0 Introduction

Titanium mesh is characterized by its unique corrosion resistance, light weight, high strength, high performance and so forth [1]. It is widely used in aviation, electronics system and medical engineering. Especially in the field of medical engineering, titanium mesh because of its excellent biocompatibility and excellent mechanical properties, as well as facilitate the in vivo tissue growth and other characteristics, is seen as ideal cranial bone repair material [2-4]. Today cranial titanium prostheses in the medical field are in great demand, and traditionally they are produced by pressing flat titanium plate into mold or by handcraft [5-6]. That leads to long lead time and high cost, and it is also difficult to match the defect area, which objectively discourages clinical application of titanium mesh plate. However, the application of multi-point forming (MPF) technology makes this problem has been resolved [7-8]. Multi-point forming is a flexible means for forming double curve surfaces in sheet metal [9-11]. The substance of MPF is dividing the curved surface of traditional die into many discrete punch members whose heights can be adjusted respectively. Because titanium mesh plate has a certain dimension, and in order to prevent wrinkle during the forming process of titanium mesh, often need to put an auxiliary steel plate between titanium mesh and elastic cushion, simultaneously, a blank holder device was adopted to act on the boundary of the steel plates [12]. However, the upper and lower steel plates cannot be reused, resulting in an additional waste of material. Here, a different strategy multi-point holder forming (MPHF) is introduced. It adopts discrete holder punch to clamp the titanium mesh in forming zone. In this work, the explicit finite element method was utilized to investigate the forming process of titanium mesh in this mode, compared with multi-point die forming (MPDF).

1 Basic principles of forming process

As shown in Fig. 1a, MPDF is a relatively simple and classical forming mode in multi-point forming technology. The central component in MPDF is a pair of multi-point dies constructed by upper and lower matrices of discrete forming punches placed one by one. The matrices of forming punches are adjusted to the desired shape by computer control system before forming. And similar to conventional stamping, the positions of the adjacent forming punches are not varied during the

forming process. However, wrinkle is easy to occur in the forming process, auxiliary blank holder device should be adopted in this mode. While in multi-point holder forming (Fig. 1b), series of holder punches controlled by hydraulic devices are adopted. The holder punches are placed with the forming punches alternately, and fluctuate with the deformation of metal sheet. Therefore the holder punches can functionally replace blank-holder to prevent the blank to wrinkle in forming zone, and the way of work for forming punches is the same with MPDF.

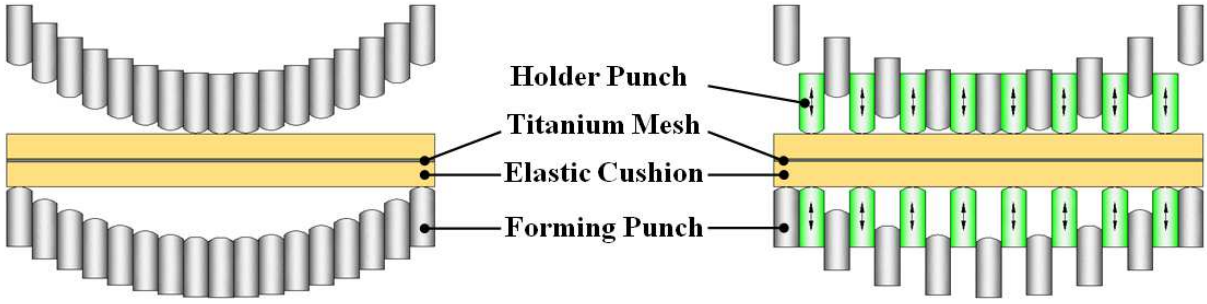

(a) Multi-point die forming (b) Multi-point holder forming

Fig. 1 Forming diagrams of two basic multi-point forming

2. Finite element formulation and models

In this study, the cross section of a punch was a 10×10 mm^2 square and its hemispheric end had a radius of 8 mm, the matrix of multi-point dies was composed of 17×17 punches. For the purpose of comparison, the blank holder was not adopted in MPDF. The initial size of titanium mesh plate was 152×152 mm^2, and it had 30×30 holes with thickness of 0.5mm. The size of the elastic cushion was 170×170 mm^2 with the thickness of 10 mm. Considering the symmetry of the models, only a quarter of the finite element model was modeled separately as shown in Fig. 2. Constant solid 8-node element, with hourglass control, was employed to build the model of elastic cushion which used isotropic material mode. In addition, to improve the computation speed, the punches were modeled with sophisticated, rigid surfaces using shell elements. A 4-node doubly curved thin shell element with reduced integration, hourglass control and finite membrane strain was used to model the titanium mesh sheet. And the typical mechanical properties of titanium mesh are presented in table 1[12-13].

Table 1 Typical mechanical properties of material

Material	Elastic modules [GPa]	Yield strength [MPa]	Tensile Strength [MPa]	Elongation @Break [%]
Ti-6Al-4V	113	830	965	15

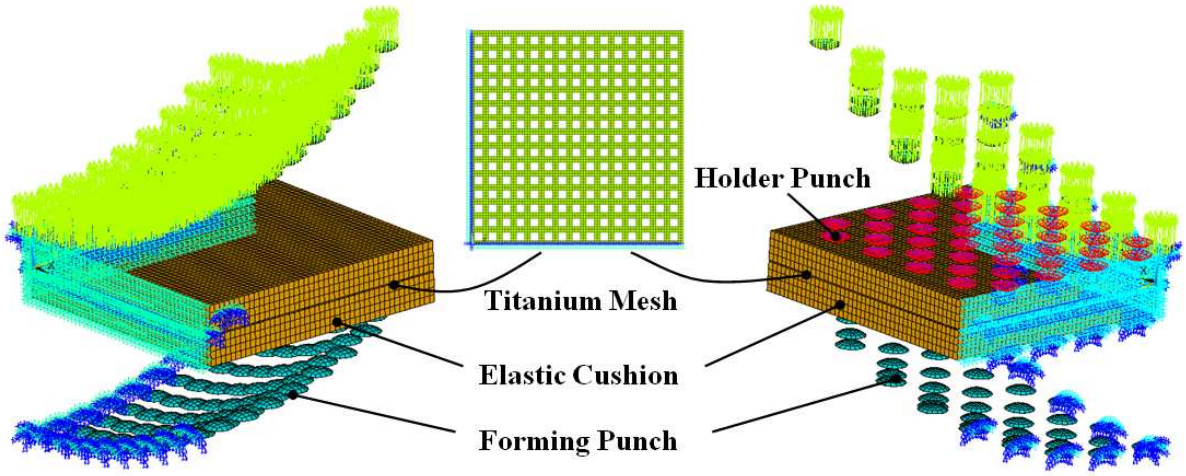

(a) Multi-point die forming (b) Multi-point holder forming

Fig. 2 Finite element modes of two basic multi-point forming

3. The results of simulation

3.1 The shaping effects of multi-point holder forming

The forming results of titanium mesh sheets were investigated by the two forming technologies of MPDF and MPHF. The desired radius of curvature was 150mm for spherical part, and the load of each holder punch was 500N in MPHF. The simulated results of two methods forming process for spherical part are shown in Fig. 3. There are distinct wrinkles in the work-piece formed by MPDF. But at the same condition the work-piece formed by MPHF achieved well result, it can be seen that the surface of work-piece is smooth and has not any wrinkle. Fig. 4 shows the edge contours of forming parts in the two modes. The edge profile of spherical part formed in MPDF is wavy, while that in MPHF is smooth. With the upper matrix of forming punches down going, radial tensile stress was produced in the plate, the metal flowed into the center, and outer diameter reduced continuously. Then the circumference compressive stress increased continuously on the titanium mesh edges. In MPDF, because of lacking of supports in normal direction of panel, the instability was very easy to generate in edges. While for MPHF, the whole sheet mental was holed by the discrete holder punches during the forming process, this increased the carrying zone in normal direction of panel. Therefore the titanium mesh was constrained effectively during the multi-point holder forming process and the ability of anti-buckling of sheet was enhanced.

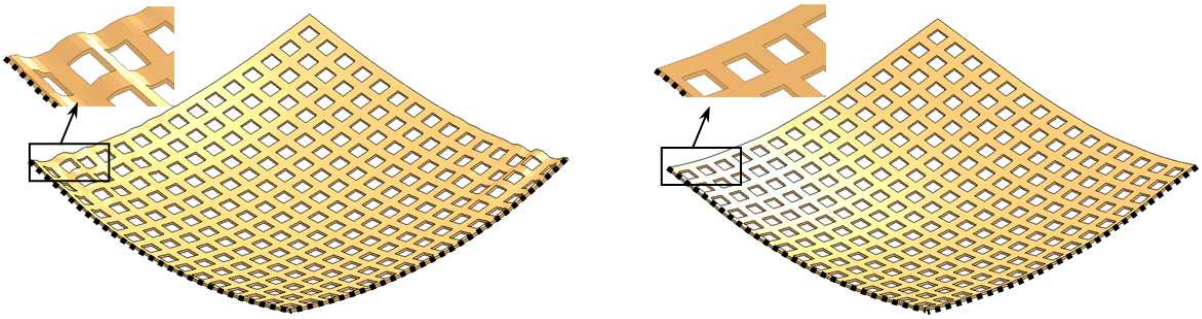

(a) Deformation result obtained by MPDF (b) Deformation result obtained by MPHF

Fig. 3 Finite element analysis results of two modes for spherical part

3.2 Influence of forming technology on strain

Fig. 5 is the circumferential strain distributions along the edges of spherical parts formed by the two modes. It shows that both of curves are zigzag shapes in the middle of the edges, but the strain fluctuating range of spherical part formed in MPDF is significantly larger than that in MPHF, and the former is nearly 3 times that of the latter. In MPDF, due to lacking of support for sheet, the strain increased rapidly, so that wrinkle occurred on sheet. However in MPHF, the titanium mesh sheet was holed by the discrete holder punches, and no wrinkle occurred on it, there was a little strain fluctuating range on the edge of titanium mesh sheet. In addition, there is nothing differences for the two strain distributions near the corners of forming parts, and both of them are small (Fig.5). Because sheet metal in the edges flowed into the center during the forming process, and the size of corner area was small in the circumferential direction tangent, the extrusion force was also small in corner region.

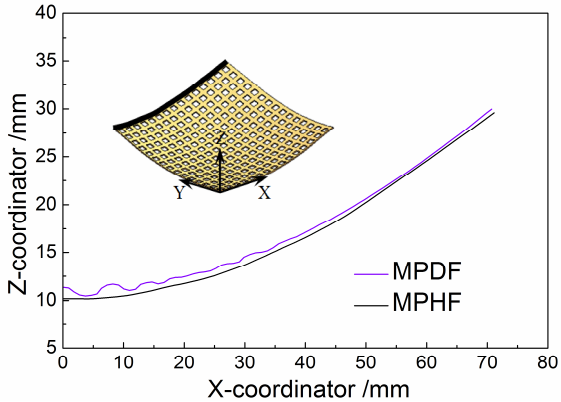

Fig. 4 Edge contours of forming parts

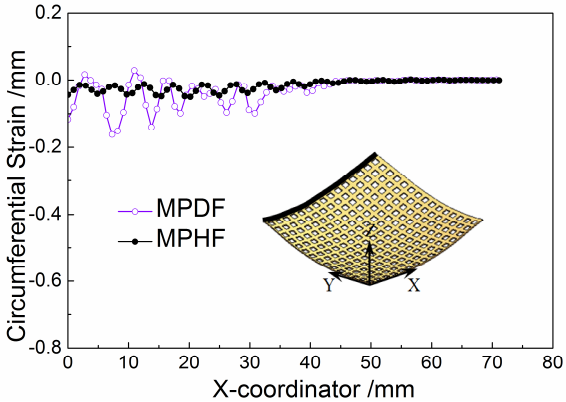

Fig. 5 Strain distribution along the edges of parts

3.3 Influence of holder punch load on deformation

Serials of Spherical parts with different radius were formed in MPHF. For each part with desired radius, the holder punch force was increased with 0N as the initial value in increments of 5N, until the result of spherical part did not appear wrinkle. And the force was the minimum value for the titanium mesh achieved this deformation. The results are shown in Fig.6. It indicates that different deformation of titanium mesh requires different minimum force of holder punch. The smaller the desired radius is, the greater holder punch load will be required. The reason for this is that increasing the amount of deformation can make titanium mesh compress more seriously in circumferential direction, resulting in larger force of holder punch is needed to contain the titanium mesh in normal direction. However, it is worth mentioning that there are different maximum deformation amounts for MPDF and MPHF when the load of holder punch is 0N in MPHF. For MPDF, the minimum forming radius was 200mm, while for MPHF, that was 230mm when the force was 0N. Because in the later of MPDF process, the clamping pressure of forming punch could flat the weak wrinkles, but in MPHF when load was zero, due to holder punch did not work, and the forming punches was poor to flat the wrinkle.

3.4 Influence of holder punch load on shape error

Fig. 7 is the shape error along the diagonal direction of the titanium mesh before springback, and while taking into accounts the effect of thickness on shape error. The radius of desired part is 150mm. As it shows, there are small shape errors for spherical parts formed by MPHF. However, the shape errors are lager in the middle of sheet. The reason for that is the amount of compression for upper elastic cushion in the middle. The amount of compression of elastic cushion was not considered when calculating the heights of forming punches, due to the cushion had non-uniform deformation in the forming process (Fig. 8). In addition, the thicker the titanium mesh is, the larger the error in the middle will be. Because titanium mesh became difficult to deform when increasing the thickness, and the compression of cushion would be decreased more in forming process. Especially the compression in the middle area was decreased most due to where was subject to the greatest force. It is also can be seen that the shape in the corner area is also large from Fig. 7. Because in the late of multi-point holder forming process, the lines of action of the upper and down holder punches to the titanium mesh were not on the same hot spot, so an anti-torque would had been produced and it would hinder the deformation of the edges.

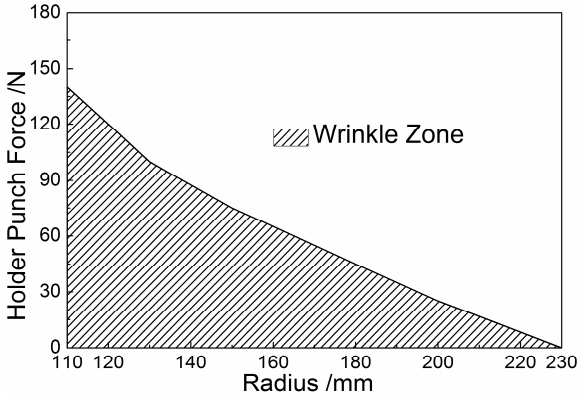

Fig. 6 Wrinkle zone in MPHF

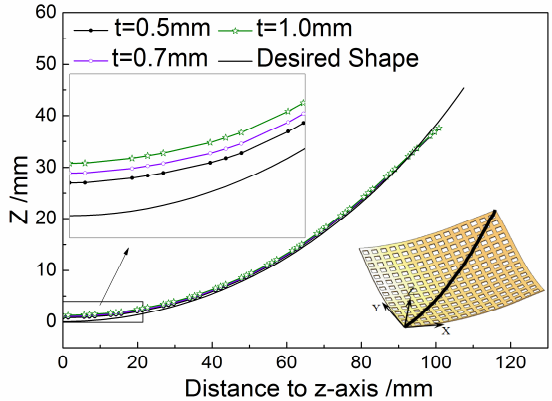

Fig. 7 Shape error along diagonal direction of sheet

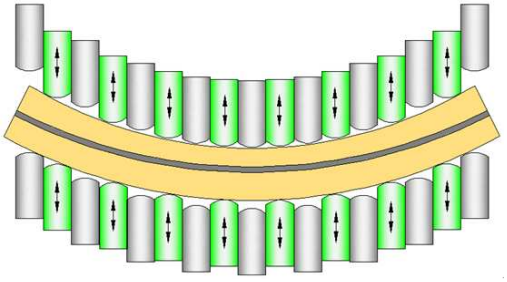

Fig. 8 Wrinkle zone in MPHF

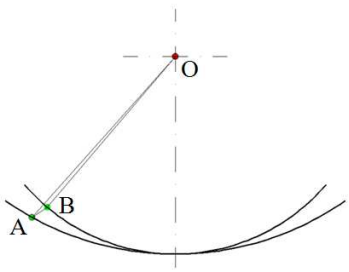

Fig. 9 Movement of one node in titanium mesh after the forming

Fig. 9 displays the movement of one node in titanium mesh after the forming. The node moves form point B to point A in springback. Point O is the center of desired part. The shape error before springback is OB minus R, the shape error after springback is OA minus R, where R is the radius of desired part, and the resilience value is BA. The shape errors of titanium mesh sheets formed by MPDF are illustrated in table 2.Where the mean value refers to root mean square. It can be see that the thicker the titanium mesh sheet, the smaller the rebound.

Table 2 Shape errors of titanium mesh sheets formed by MPDF

Thickness of titanium mesh sheet [mm]	Before springnback		After springback		Maximum resilience value [mm]	Mean resilience value [mm]
	Maximum shape error [mm]	Mean shape error [mm]	Maximum shape error [mm]	Mean shape error [mm]		
0.5	1.150	0.407	7.602	3.850	7.914	4.155
0.7	1.344	0.409	8.144	3.940	7.806	4.118
1	1.613	0.454	8.335	3.906	7.716	3.922

4 Conclusions

1. Multi-point forming adopts discrete holder punches to constrain the titanium mesh in forming zone can improve its capacity of wrinkle resistance.

2. Titanium mesh has excellent performance in multi-point holder forming process, and the wrinkles can be suppressed effectively by holder punches.

3. In multi-point holder forming, the bigger deformation the titanium mesh is, the greater force of holder punch will be needed.

4. The thicker the titanium mesh is, the larger shape error will be before springback. And the shape error in the central area of titanium mesh, as well as in border regions, is relatively large.

References

[1] M. A. Khan, R. L. Williams, D. F. Williams , The corrosion behavior of Ti–6Al–4V, Ti–6Al–7Nb and Ti–13Nb–13Zr in protein solutions, Biomaterials, 17(1999) 631-637.

[2] E. D. Spoerke, S. I. Stupp, Colonization of organoapatite-titanium mesh by preosteoblastic cells, Journal of Biomedical Materials Research Part A, 3(2003) 960-969.

[3] A. Yuda , S. Ban, Y. Lzumi, Biocompatibility of apatite-coated titanium mesh prepared by hydrothermal-electrochemical method, Dental Materials Journal, 4(2005) 588-595.

[4] M. P. Martin, S. Olson, Post-operative complications with titanium mesh, Journal of Clinical Neuroscience, 8(2009) 79-82.

[5] Q. F. Yang, S. K. Qian, X. B. Chen, et al, Comparison of digitized titanium net cranioplasty with manually generated titanium net cranioplasty, Chin J Clin Neurosurg,10(2001) 600,608.

[6] M. Thomasson, H. Hedman, D. Guo, et al, Lrigl and epidermal growth factor receptor in renal cell carcinoma: a quantitative RT-PCR and immunohistochemical analysis, Bu J Cancer,7(2003) 1285-1289.

[7] J. J. Chen, W. Liu, M. Z. LI, et cal, Digital manufacture of titanium prosthesis for cranioplasty, Int J Adv Manuf Technol, 27(2006) 1148-1152.

[8] X. R. Liu, B. Zhang, J. Yu, The clinical applications of titanium mesh multi-point forming in craniocerebral trauma patients, Jouranl of Neurotrauma , 5(2008) A14-A14.

[9] M. Z. Li, Z. Y. Cai, Q. G. Yang , Multi-point forming technology for sheet metal, J. Mater. Process. Technol., 1-3(2002): 333-338.

[10] M. Z. Li, Z. Y. Cai, C. G. Liu, Flexible manufacturing of sheet metal parts based on digitized-die, Robot. CIM- Int. Manuf., 1(2007): 107-105.

[11] M. Z. Li, Z. Y. Cai, C. G. Liu, W. Z. Fu, Recent development in multi-point forming technology, Proceedings of the 8th International Conference on Technology of Plasticity, 2005. p. 707-708.

[12] F.X. Tan, M. Z. Li, Z. Y. Cai, Research on the process of multi-point forming for the customized titanium alloy cranial prosthesis. J. Mater. Process. Technol., 187(2007) 453-457.

[13] F.X. Tan, M. Z. Li, Z. Y. Cai, et cal, Formability analysis on the process of multi-point forming for titanium alloy retiary sheet, Int J Adv Manuf Technol, 41(2009) 1059-1065.

doi:10.4028/www.scientific.net/AMM.161.77

Research of Polycarbonate Sheet Processing Based on Multi-point Forming

Junhui Cao[1, a], Wenzhi FU[1, b], Mingzhe Li[1, c], Chunguo Liu[1, d], Heli Peng[1, e]

[1] Dieless Forming Technology Center, Jilin University, Changchun 130025, PR China

[a] caojunhui911@163.com, [b] fwz@jlu.edu.cn (corresponding author), [c] limz@jlu.edu.cn, [d] liucg@jlu.edu.cn, [e] phl126160408@126.com

Keywords: Multi-point forming; Polycarbonate sheet; Numerical simulation; Accuracy

Abstract: Although multi-point forming (MPF) is an advanced processing technique and has been investigated comprehensively as a metal working operation, there are few papers published to deal with MPF of polymers. The present paper reviews the features of MPF and evaluates the possibility of producing polymer components by means of MPF. The experimental research work makes use of PC sheets with a thickness of 3.82 mm. Numerical simulations were performed with the software ABAQUS, then spherical and saddle-shaped components were manufactured by MPF. The geometrical deviations between shaped components and their original CAD/CAM models were obtained to investigate the forming accuracy. The results confirm that MPF of PC sheet has potential for the manufacture of complex components.

Introduction

Polycarbonate (PC) is a typical thermoplastic polymer exhibiting many properties ideally, such as dynamic ductility, mechanical robustness, light weight, low processing temperature and pressure (compared to metal), and ease of forming into complex shape. Thermoforming is a set of techniques for transforming flat thermoplastic polymer sheets or films into complex shapes in the past decades. In the process, the polymeric sheet is heated above its glass transition temperature (T_g), where the material is softened, then placed on a fixed die (can be made of metal, wood or polymer composites) and forced to assume the desired shape by pressure. After cooling, the component is obtained. The conventional thermoforming is generally utilized for mass production due to the high capital investments and long life cycles for developing and manufacturing the die.

Multi-point forming (MPF) was named by one of the authors in 1992[1]. The critical innovation of MPF is the replacement of fixed die by discrete die consisting of individual punches in a matrix, which can be reconfigured by changing the position of each punch. By this improvement, MPF can configure a surface of desire shape in very short time and nearly cost free. Fig.1 shows a saddle-shape multi-point die, the matrix of punches approximates to a continuous surface through controlling the position of each punch. It is obvious that the smaller the punches are, the smoother the surface is. In the past decade, MPF is successfully used in sheet metal forming applications, a series of investigations and improvements have been made by researchers. Cai proposed a technique to avoid wrinkling and tearing [2]. Li developed a technique to manufacture large size parts of sheet metal in a small MPF press and named it as “sectional MPF”[3]. Cai computed the relative position of each punch to determine the 3D surface of the multi-point die from a given geometry by an 18 d.o.f. high-precision triangular finite element representation technique [4]. Cai investigated the wrinkling, dimpling and spring-back in MPF process by numerical simulation and pointed that the simulation results provide valuable and sufficient guidance on determining MPF parameters [5]. Tan applied multi-point forming equipment with blank-holder device to process titanium alloy retiary sheet into cranial prosthesis [6].

The present need for flexible polymer processing techniques requires an innovative technological solution with the capability of reducing the capital costs and production lead times for small-batch production. The focus of this paper is twofold: (I) feasibility of processing PC sheet by MPF, (II) accuracy of the PC components. Finite element model for the process was established in ABAQUS, numerical simulations of spherical and saddle-shape components were preformed in the software too. Experiments were carried out on a multi-point forming press and the 3D data of the formed components was measured by a 3D sensing system (3DSS).

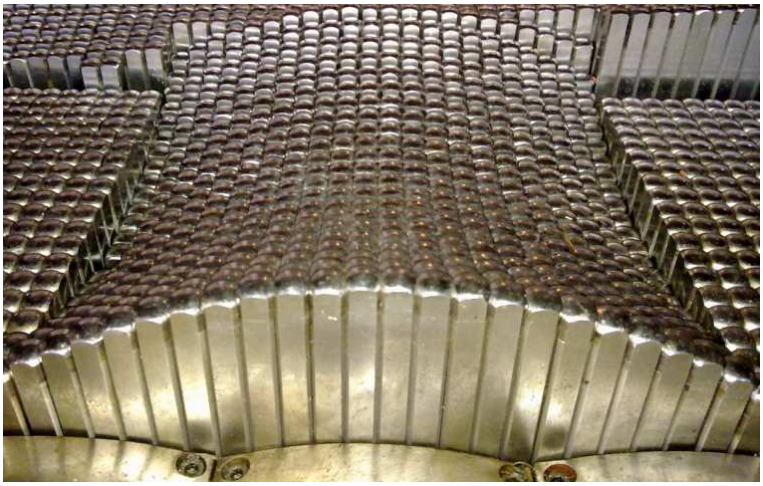

Fig.1. The multi-point die with saddle-shape.

Process of MPF of PC sheet

Conventional thermoforming consists of three distinct phases: heating, forming and cooling down. The process of MPF of PC sheet is divided into four steps: configuring of the multi-point die; heating of a PC sheet, generally above T_g; forming by means of pressure and the multi-point die; cooling down through thermal conduction or fans, as shown in Fig. 2. There is one step more than conventional thermoforming, the configuration of the multi-point die.

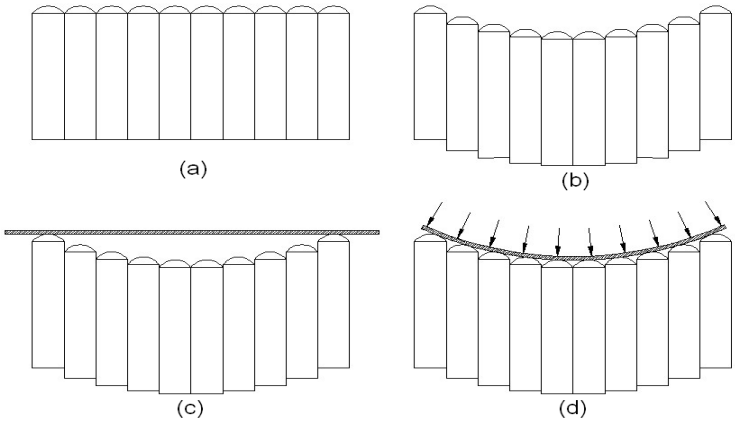

Fig.2. The forming process of MPF for PC sheet. (a) Original shape of the multi-point die (b) configured shape of the multi-point die (c) heating of the sheet (d) forming and cooling down.

Numerical simulations and experiments

Material. The experimental tests were performed on commercial PC sheet blanks having a uniform thickness of 3.82mm. PC is a low cost thermoplastic polymer and nearly amorphous. According to the tensile tests of PC at high temperature, the T_g is about 150 ℃ and the forming temperature range is 155-165℃.

Numerical simulations. Numerical simulations were carried out with ABAQUS, spherical and saddle-shape components were performed in the simulations. For saving the computing time, a rigid shell element was employed for the multi-point die and the punches were simplified to spherical tips. Considering the symmetry, 1/4 models were used and symmetrical restraint was applied on the edges, as shown in Fig.3. A deformable shell element was applied to divide the PC sheet blanks.

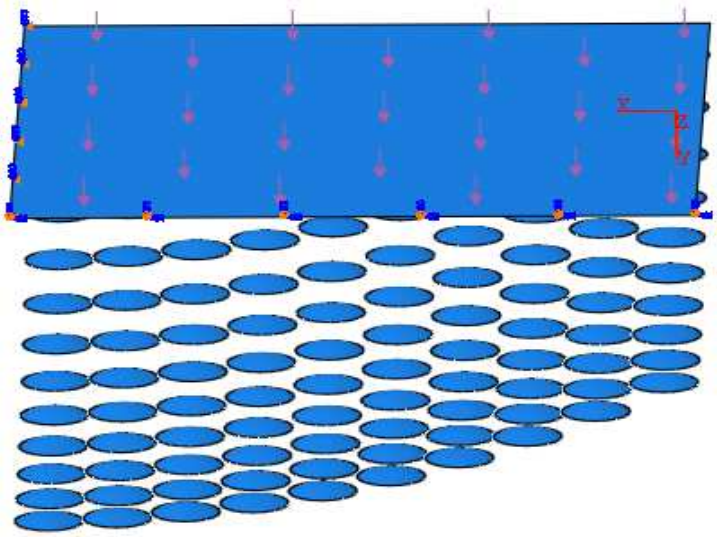

Fig.3. FEM model for MPF of PC sheet

Experiments. The experiments were designed in order to demonstrate the feasibility of processing PC sheet by MPF and were conducted on a multi-point press. The cross section of each punch is 10 ×10 mm and the radius of its spherical tip is 10mm. In this case, the multi-point die was compose of 400 punches (20×20)and the forming area was 200×200 mm, at least three replicates were produced for each shape. The forming temperature was 160 ℃. The desired radius of spherical component was 200 mm and the double direction radiuses of saddle-shape component were both 200 mm. Fig. 4 shows the formed PC sheet components. Owing to the transparency of PC sheet, the imaging agent was sprayed on the components. The thicknesses at 10 points along the center line of the components were measured by an ultrasonic thickness gauge. A 3D sensing system was used to measure and reconfigure the 3D geometry of the formed components.

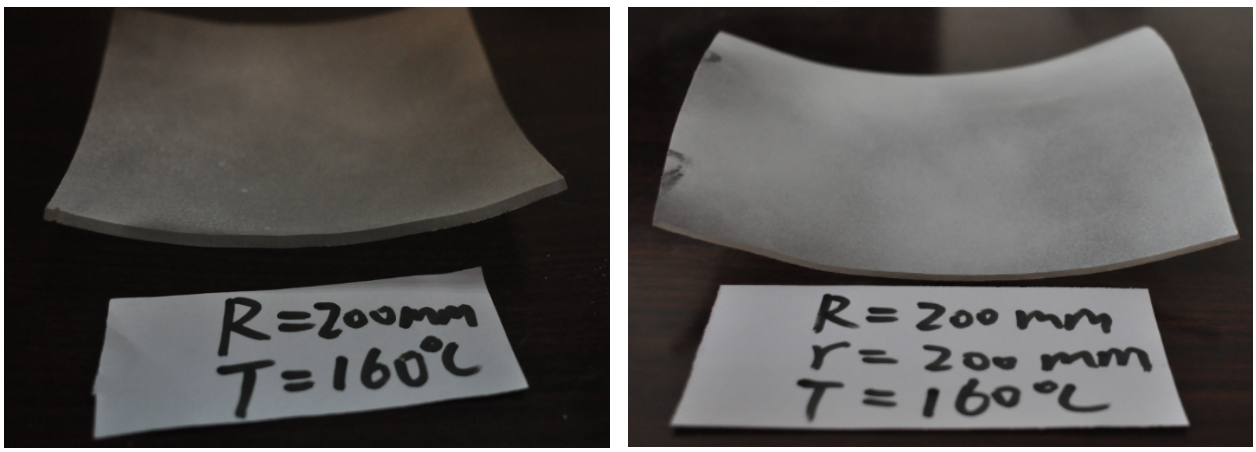

(a) (b)

Fig.4. Photos of the PC sheet components. (a) Spherical component (b) Saddle-shape component.

Results

The thickness distributions of experiments and numerical simulations are depicted in Fig. 5: (a) for spherical component and (b) for saddle-shape component. The thickness distribution trends of experiments and numerical simulations are basically consistent. The minimum measured thickness is located at the center of spherical component and at the side edge of saddle-shape component. Measurements show that the numerical simulation results agree with the experimental ones, as shown in Fig. 5.

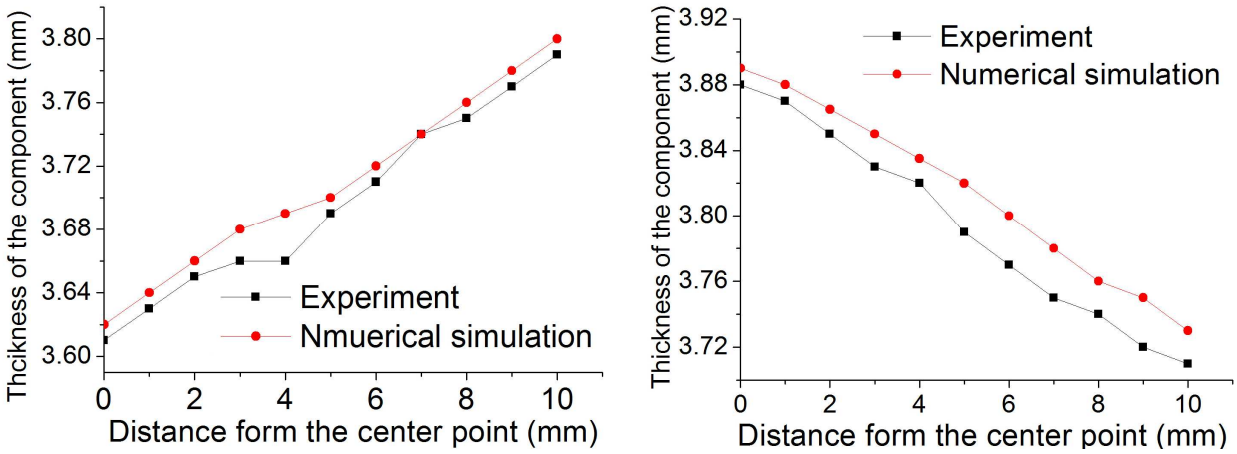

(a) (b)

Fig. 5. Thickness distributions. (a) Spherical component (b) saddle-shape component

Fig. 6 shows the geometrical deviation between PC component and the numerical model. The maximum geometrical difference magnitudes of the spherical component and the saddle-shape component are respectively equal to 1.038 mm and 0.812 mm. These values proved the high accuracy of the PC sheet components processed by MPF.

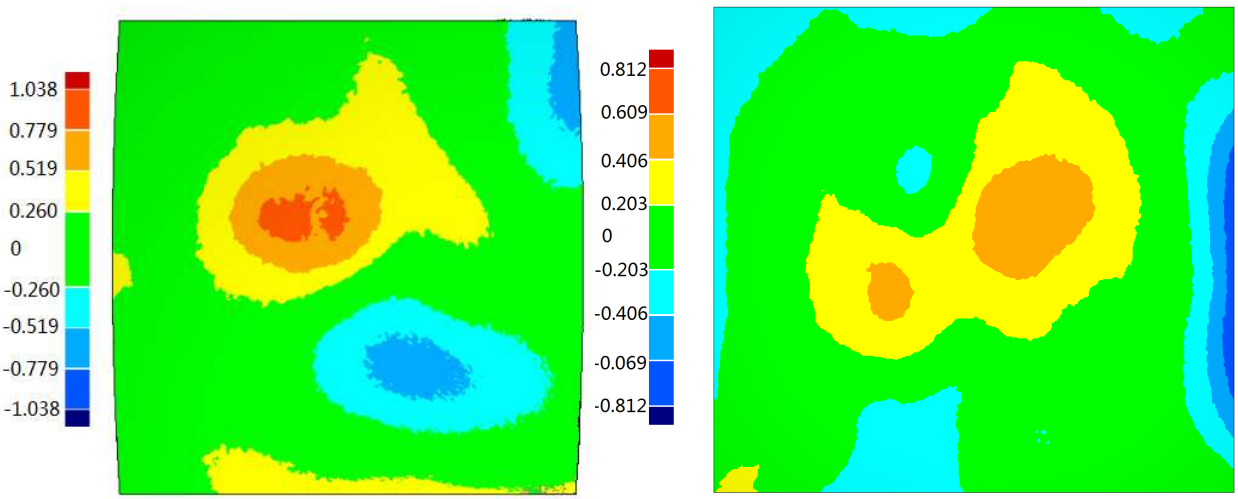

(a) (b)

Fig. 6. Geometrical differences. (a) Spherical component (b) Saddle-shape component

Conclusions

The experimental and the numerical simulation results demonstrate that Multi-point forming is feasible for processing PC sheet at high temperature and may be a potential and promising technique in some application areas.

The thickness measurements of the experimental components show that the formed components have uniform thickness. The thickness distributions of the components are reasonable and the thickness variations are small.

The magnitudes of the geometrical differences are very small. The components formed by MPF have good surface quality and very high accuracy.

Acknowledgements

This work is supported by the EU Seventh Research Framework (FlexiTool-2010-2691925). Authors wish to thank the participating personnel for their support and suggestions.

References

[1] M.Z. Li, Nakamura, S. Watanabe, Study of the basis principles (first report: research on multi-point forming for sheet metal). Proceedings of the Japanese Spring conference for Technology of Plasticity. 519–522 (in Japanese).

[2] Cai Zhongyi, Li Mingzhe, Optimum path forming technique for sheet metal and its realization in multi-point forming. J. Sci. Material Processing Technology. 110 (2001) 136–141.

[3] M.Z. Li, Z.Y. Cai, Z. Sui, Q.G. Yan, Multi-point forming technology for sheet metal. J. Sci. Material Processing Technol. 129 (2002) 333–338.

[4] Zhong-Yi Cai, Ming-Zhe Li, Multi-point forming of three-dimensional sheet metal and the control of the forming process. J. Sci. Pressure Vessels and Piping. 79 (2002) 289-296.

[5] Zhong-Yi Cai, Shao-Hui Wang, Ming-Zhe Li, Numerical investigation of multi-point forming process. J. Sci. Advanced Manufacturing Technology. 37 (2007) 927-936.

[6] F.X. Tan, M.Z. Li, Z.Y. Cai, Research on the process of multi-point forming for the customized titanium alloy cranial prosthesis. J. Sci. Material Processing Technology. 187–188 (2007) 453–457.

doi:10.4028/www.scientific.net/AMM.161.82

Optimization of combined microwave-ultrasonic wave extraction of cochineal dye by response surface methodology

Yuanheng Guo[1, a], Hua Zheng[1,b], Hong Zhang[1,c], Liyi Ma[1], Juan Han[2], Kun Li[1]

[1]Research Institute of Resources Insects, Chinese Academy of Forestry, Kunming, 650224, China

[2]College of Forestry, Southwest Forestry University, Kunming, 650224, China

[a]eastgeneva@163.com, [b]hua-zheng@sohu.com (corresponding author), [c]kmzhhong@163.com

Keywords: cochineal dye; microwave; ultrasonic wave; extract; response surface methodology (RSM)

Abstract. For more efficient and economical extraction of cochineal dye, combined microwave-ultrasonic wave extraction was applied. It was approached 4 factors as microwave power, treated time, materials-to-liquid ratio and ultrasonic wave power. Results showed that the optimal condition individually for cochineal dye extraction was at 400W microwave power, 17min treated time, 1:8 materials-to-liquid ratio and 600W ultrasonic wave power. On the basis of single factor test, RSM optimization of the extraction was achieved at 464W microwave power, 18.48min treated time, 1:8.23 materials-to-liquid ratio and 627W ultrasonic wave power. The verification was very approximate to the predicted value from the modelling regression equation. And the best extraction grade was tesified as 4 times.

Introduction

Cochineal (*Dactylopius coccus* Costa) insect is famous for its natural product named cochineal dye or carminic acid with good quality in the color of red. Originated from South America and host in cacti, the insect was introduced to China and cultivated successfully in the Southwest regions by research teams of the Research Institute of Resources Insects (RIRI), Chinese Academy of Forestry (CAF) at the beginning of this century[1-2]. Carminic acid is good in dyeing and free radical scavenging, with relatively stable and cancer resistant characteristics, thus it is widely applied in food, medical therapy and cosmetics[3-6]. It was also reported that carminic acid was taken as color developing agent for some elements determination[7-9] and as reacting agent with TiO_2 for the preparation of new nano grade photosensitive materials[10]. It was usually extracted from water[10] or alcohol[12-13] solution. Beyond the conventional way, there were other reports in recent years on the preparation of cochineal dye by microwave and ultrasonic wave assisted extraction[14-15]. Microwave, which could permeate the extractives and accelerate the inner molecular vibration, was applied for rapid rising of inner temperature within the raw materials and rising of soluble velocity of target substance in the extractives. Therefore, it improved the mass transfer driving force and the diffusion velocity of target substance from inside to outside of the materials. Ultrasonic wave, with characteristics of cavitation, crushing of cell, mechanical vibration and emulsified diffusion, was perfectly available for transformation, diffusion and extraction of the effective substance of treated materials. But it was no studies on combined extraction for cochineal dye by microwave and ultrasonic wave. This investigation was based on low cost, easily achieved and clean solvent, using response surface methodology (RSM) for the optimization of technique on combined microwave and ultrasonic wave assisted water extraction of cochineal dye.

1. Materials and Method

1.1. Materials and chemical reagents

a) Dried cochineal insect, originated from South America, provided by Mid-Yunnan Highland Experimental Station, RIRI, CAF; b) petroleum ether (60-90℃), carbon tetrachloroform, ethanol, analytical grade, Chongqing Chuandong Chemical Reagents Co. Ltd.,, China; c) purified water, self-made by Key Lab in RIRI, CAF.

1.2. Instruments and apparatus

a) Reaction system of combined microwave and ultrasonic wave, Nanjing Xian'ou Bio-tech Co. Ltd.,, China; b) DU 800 ultraviolet-visible spectrophotometer, Beckmann-Coulter Co., Ltd., USA; c) AB204-S electronic balance, Mettler-Toledo (China) Co. Ltd.,, China; d) HHS-11-2 electron constant temperature water bath, Jiangsu Provincial Medical Apparatus Factory, China; e) DZF-1B vacuum drying chamber, Shanghai Yuejin Medical Apparatus Factory.

1.3. Method

1.3.1 Sample preparation

Dried cochineal insect was treated in turn by petroleum, carbon tetrachloroform and ethanol within the Soxlet. After removal of wax and lipid, it was dried in vacuum drying chamber for the following experiments.

1.3.2 Single factor experiment

After weighing 10g sample, in the condition of 60mL (i.e. materials-to-liquid ratio of 1:6) purified water, 200W ultrasonic wave and (4s:4s) pulse time, treat individually at 100W, 200W, 300W, 400W, 500W, 600W and 700W microwave in the reaction system for 10min. The absorbance value of filtered liquid was determined at the wavelength of 494nm[16]. Then it was achieved suitable microwave power by calculating extraction rate.

For the selection of treated time, the same quantity of sample was individually treated in the same condition mentioned above and 400W microwave in the reaction system for 2min, 5min, 8min, 11min, 14min, 17min and 20min. After determining absorbance value and calculating extracting rate, the suitable treated time was achieved. And for the selection of materials-to-liquid ratio and ultrasonic wave power, the treated time was 17min and other conditions were same as above, with materials-to-liquid ratio of 1:4, 1:5, 1:6, 1:7, 1:8, 1:9 and 1:10, and ultrasonic wave power of 200W, 300W, 400W, 500W, 600W, 700W and 800W individually.

1.3.3 RSM experiment

On the basis of single factor experiment, it was selected 4 influence factors which were microwave power, treated time, materials-to-liquid ratio and ultrasonic wave power. The extraction rate of dye was taken as response value. Box-Behnken Design[17-20] was applied by software Design Expert 7.1 (DE 7.1), containing 4-factor and 3-level test which was showed in Table 1. It was also determined the absorbance value and calculated the extraction rate.

Table 1 Variables and levels of the Box-Behnken experimental design

independent variable	true value code	levels		
		-1	0	1
microwave power (W)	X_1	300	400	500
treated time (min)	X_2	14	17	20
liquid-to-materials ratio	X_3	7	8	9
ultrasonic wave power (W)	X_4	500	600	700

Statistics were obtained by DE 7.1 to establish regression equation and response surface graphs. It was analysed between any two mutual effects for a best estimation and then made it into verification.

All of the above samples were weighed accurately at 0.0001g grade and were taken into experiment with 3 equal tests. The extraction after microwave treated was 75℃ in the water bath.

1.3.4 Selection of extraction grade

Under the optimal condition, cochineal dye was extracted individually for 10 times. It was selected for the best extraction grade according to the yield of dye.

2. Results and Analyses

2.1. Extraction rate influenced by single factors

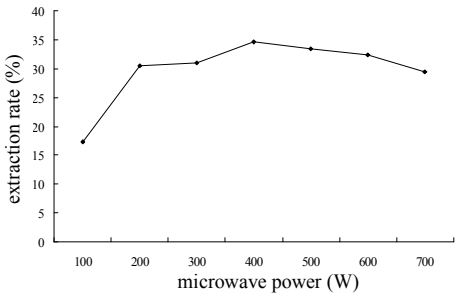

Fig. 1. Influence on extraction rate by microwave power

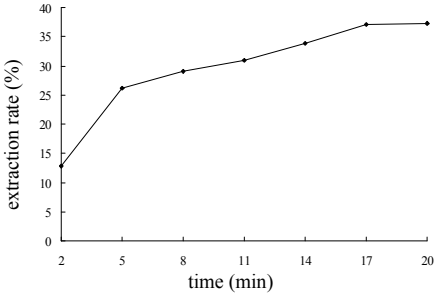

Fig. 2. Influence on extraction rate by treated time

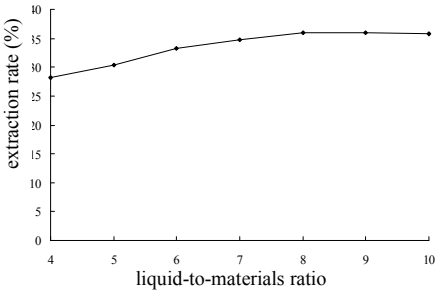

Fig. 3. Influence on the rate by materials-to-liquid ratio

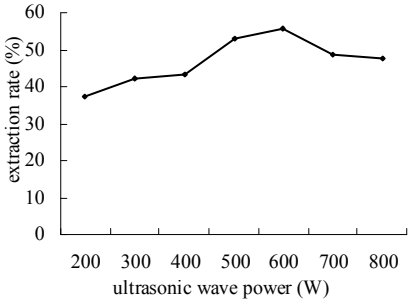

Fig. 4. Influence on the rate by ultrasonic wave power

The effects on extraction rate from microwave power, treated time, materials-to-liquid ratio and ultrasonic wave power were showed in Fig. 1 to Fig. 4.

It was indicated in Fig. 1 that when the microwave power was below 400W, the extraction rate increased accord with the rising of power. When it reached 400W, the rate did not increase but decrease slightly. This was probably due to the double molecular structure of proteins and phospholipids, the main constituents of cochineal insect epidermis. An increasing power caused the inactivation and denaturation of protein, and the flow ability of cell membrane became slow. Thus it was more obstacles for cochineal dye diffusing from the inside to the outside of cell. And 400W microwave power was selected as a best condition.

From Fig. 2, it was showed that the treatment before 17min was helpful to increase extraction rate with the elongation of time, but after 17min it was almost no increase of the rate. Concerned about effectiveness, the treated time of 17min was selected.

When the materials-to-liquid ratio was during 1:4 to 1:8 (in Fig. 3 it was showed in liquid-to-materials ratio), the more the liquid, the higher the extraction rate. But when it reached above 1:8, the rate did not increase again due to more diluted concentration of cochineal dye.

And for ultrasonic wave power, it could be seen in Fig. 4 that the extraction rate increased during the range from 200W to 600W and decreased from 600W to 800W. The estimation for its reason was that the amplitude of vibration increased accord with the rising of ultrasonic wave power. But the insect could not be split uniformly, so the amount of soluble dye in the liquid became lower. Obviously, 600W ultrasonic wave power was selected for an efficient and cost operation.

2.2. RSM optimization and verification

It was showed in Table 2 of factors, levels and results. The range of extraction rate of 27 experimental samples was from 47.82% to 59.35%.

According to Box-Behnken experimental design and test, statistics were imitated for quadratic regression. And it was modeling the equation by DE 7.1 as the follow:

$Y=58.92+3.26X_1+2.36X_2+1.72X_3+1.07X_4-0.26X_1X_2+0.23X_1X_3+0.24X_1X_4-0.82X_2X_3+1.44X_2X_4-1.32X_3X_4-2.98X_1^2-2.81X_2^2-2.71X_3^2-3.17X_4^2$.

Significance test and analysis of variance of the regression equation was showed in Table 3.

According to the P value in Table 3, the modeling regression equation for the extraction rate of cochineal dye was in very significant level ($P<0.01$) with the imitation degree of 92.71%. It was suggested that the model was in good response, so that the experimental tests were credible and

accurate. One degree terms such as microwave power (X_1), treated time (X_2), liquid-to-materials ratio (X_3) and ultrasonic wave power (X_4) were very significant to the extraction rate, so were quadratic terms such as microwave power (X_1^2), treated time (X_2^2), liquid-to-materials ratio (X_3^2) and

Table 2 Arrangement and results of Box-Behnken experimental design

run No.	microwave power (W)	treated time (min)	liquid-to-materials ratio	ultrasonic wave power (W)	extraction rate (%)
1	400	14	8	700	47.82
2	500	20	8	600	57.73
3	400	17	7	700	54.06
4	400	17	7	500	47.96
5	500	14	8	600	54.57
6	400	14	9	600	54.30
7	500	17	7	600	54.88
8	300	17	7	600	47.88
9	500	17	9	600	54.90
10	300	17	8	700	51.31
11	400	20	7	600	55.04
12	300	20	8	600	52.42
13	500	17	8	500	53.62
14	400	14	8	500	50.68
15	400	20	8	700	56.99
16	300	14	8	600	48.21
17	400	17	8	600	59.35
18	400	17	9	700	55.70
19	500	17	8	700	58.03
20	300	17	8	500	48.89
21	400	17	8	600	58.49
22	300	17	9	600	50.02
23	400	14	7	600	49.24
24	400	17	8	600	58.92
25	400	20	8	500	54.08
26	400	20	9	600	56.83
27	400	17	9	500	54.86

Tabel 3 Analysis of significance of the regression model

source	sum of squares	degree of freedom	F value	P value	significant level
term	353.1796	14	16.85664	< 0.0001	**
X_1	127.2054	1	84.99804	< 0.0001	**
X_2	66.5994	1	44.5014	< 0.0001	**
X_3	35.3633	1	23.62961	0.0004	**
X_4	13.6533	1	9.123091	0.0107	*
X_1X_2	0.2756	1	0.184171	0.6754	
X_1X_3	0.2162	1	0.14448	0.7105	
X_1X_4	0.2352	1	0.157176	0.6987	
X_2X_3	2.6732	1	1.786236	0.2062	
X_2X_4	8.3232	1	5.561539	0.0362	*
X_3X_4	6.9169	1	4.621839	0.0527	
X_1^2	47.3886	1	31.66485	0.0001	**
X_2^2	42.0626	1	28.10602	0.0002	**
X_3^2	39.0843	1	26.11592	0.0003	**
X_4^2	53.5801	1	35.80193	< 0.0001	**
residual	17.9589	12			
lack of fit	17.5890	10	9.512723	0.0988	
pure error	0.3698	2			
Total	371.1385	26			

Note: imitation degree R^2=0.9271, *significant ($P<0.05$), **very significant ($P<0.01$).

ultrasonic wave power (X_4^2). Interaction terms were not significant to the rate. In general, it was the most significant to the extraction rate by one degree terms, and followed by quadratic terms. Interaction terms were in less influence to the rate. Kinds of experimental factors mentioned above were not in simple linear relation, therefore, the extraction should be optimized. It was showed in Fig. 5 to Fig. 10 about effects on extraction rate from microwave power (MWP), treated time (TT), liquid-to-materials ratio (LMR) and ultrasonic wave power (USWP).

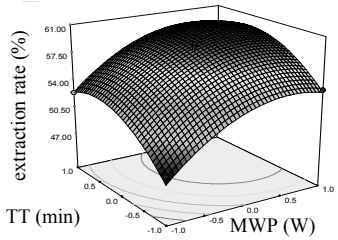

Fig. 5. RSM graph of MWP and TT

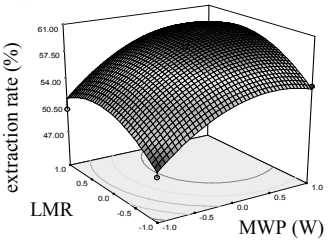

Fig. 6. RSM graph of MWP and LMR

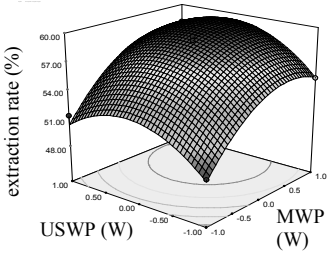

Fig. 7. RSM graph of MWP and USWP

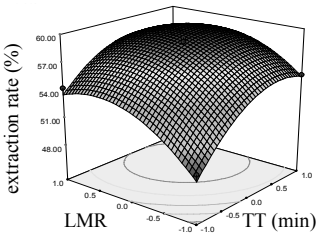

Fig. 8. RSM graph of TT and LMR

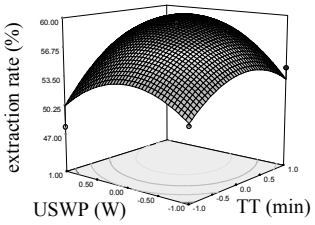

Fig. 9. RSM graph of TT and USWP

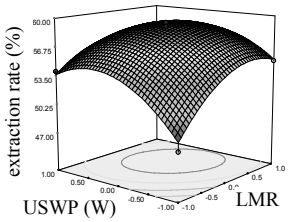

Fig. 10. RSM graph of LMR and USWP

By the DE 7.1 analysis of regression equation and response surface, it was achieved the optimal extraction parameters of 464W microwave power, 18.48min treated time, 1:8.23 materials-to-liquid ratio and 627W ultrasonic wave power. The expectation value of cochineal dye extraction rate was 60.32%. For further verification on optimum condition of the combined extraction, it was tested 3 times of such experiment under the selected condition mentioned above, which lead to an average rate of 59.97%. It was 0.59% of relative error between the predicted value and verified value. Although the latter value was less than the former, their relative error was in permitted range. It meant that the comprehensive influence to cochineal dye extraction rate made by the 4 factors was approximately embodied in the regression equation.

2.3. The appropriate grade of extraction

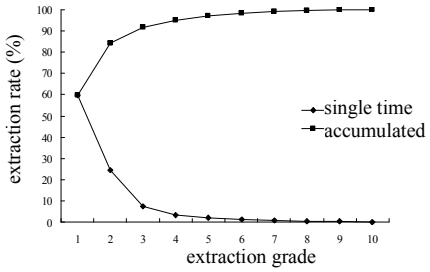

Fig. 11. Relation between extraction rate and extraction grade

Each of the single time extraction rate and the accumulated extraction rate were showed in Fig. 11. Results showed that the 10th rate was less than 0.1% of the 1st rate. So it was considered that all of cochineal dye was extracted fully from the insect after 10 times of extraction. According to the accumulated extraction rate, when the extraction grade reached 4, it could approach 95.04% of the accumulated rate. For the consideration of effectiveness and cost, it was selected for the appropriate grade of extraction at 4 times.

3. Conclusion

3.1. In the single factor experiment, it was selected for cochineal dye extraction at 400W microwave power, 17min treated time, 1:8 materials-to-liquid ratio and 600W ultrasonic wave power in the combined microwave and ultrasonic wave extraction system.

3.2. By RSM optimization, it was achieved the best extraction condition based on the modelling regression equation, which was at 464W microwave power, 18.48min treated time, 1:8.23 materials-to-liquid ratio and 627W ultrasonic wave power. And it was verified well concord with the predicted value.

3.3. For an appropriate extraction grade, 4 times were enough and available to reach the accumulated extraction rate over 95%.

Acknowledgements

This investigation was supported by Fund Program in Conversion of Agricultural Science and Technology Achievement, Ministry of Science and Technology of the People's Republic of China (2010GB24320619) and the Special Fund Project for the Scientific Research of State Forest Public Welfare Industry, SFA, China (201204602). Authors gratefully thank these financial support.

References

[1] Z. H. Zhang, X. Z. Yang, Z. L. Wang, et al, Study on experimental population of cochineal insect (*D. Confusus* (Cockerell)). Fore. Res. 16 (3) (2003) 254–261.

[2] Z. H. Zhang, L. Shi, L. F. Xu, et al, The present research and utilization situation of cochineal insects in the world. Fore. Res. 15 (6) (2002) 719–726.

[3] E. A. González, E. M. García, M. A. Nazareno. Free radical scavenging capacity and antioxidant activity of cochineal (*Dactylopius coccus* C.) extracts, Food Chem. 119 (1) (2010) 358–362.

[4] Y. H. Guo, L. Y. Ma, H. Zheng, et al, Free radical scavenging capacity of carminic acid. Food Sci. 31 (17) (2010) 73–76.

[5] J. Méndez, M. González, M. G. Lobo, et al, Color quality of pigments in cochineals (*Dactylopius coccus* Costa). J. Agr. Food Chem. 52 (5) (2004) 1331–1337.

[6] E. Takahashi, T. H. Marczylo, T. Watanabe, et al, Preventive effects of anthraquinone food pigments on the DNA damage induced by carcinogens in *Drosophila*. Mut. Res./ Fund. Mole. Mech. Mutag. 480-481 (2001) 139–145.

[7] H. K. L. Gupta, D. F. Boltz, Spectrophotometric study of the determination of boron by the carminic acid method. Microchimica Acta 62 (3) (1974) 415–428.

[8] L. López-Martínez, J. L. Guzmán-Mar, P. L. López-de-Alba, Simultaneous determination of uranium(Ⅵ) and thorium(Ⅳ) ions with carminic acid by bivariate calibration. J. Radioanal. Nuc. Chem. 247 (2) (2001) 413–417.

[9] J. L. Manzoori, M. H. Soroiraddin, M. Amjadi, Spectrophotometric determination of osmium based on its catalytic effect on the oxidation of carminic acid by hydrogen peroxide. Talanta 53 (1) (2000) 61–68.

[10] S. Gaweda, G. Stochel, K. Szaciliwski, Photosensitization and photocurrent switching in carminic acid/ titanium dioxide hybrid material. J. Phys. Chem. C 112 (48) (2008) 19131–19141.

[11] H. Zhang, Y. M. Lu, H. Zheng, et al, Optimization of water extraction of cochineal dye. Food Sci. 30 (16) (2009) 115–118.

[12] Y. Cui, W. H. Li, X. Tang, et al, Study on extracting pigment from cochineal insect. Chem. Engin. 35 (6) (2007) 66–69.

[13] M. Gonzaälez, J. Meändez, A. Carnero, Optimizing conditions for the extraction of pigments in cochineals (*Dactylopius coccus* Costa) using response surface methodology. J. Agr. Food Chem. 50 (24) (2002) 6968–6974.

[14] Y. M. Lu, H. Zheng, H. Zhang, et al, Ultrasonic extraction of cochineal dye. Food Sci. 30 (16) (2009) 142–145.

[15] Y. M. Lu, H. Zheng, M. C. Zhou, et al, Study on extraction of cochineal dye by microwave technique. Hubei Agr. Sci. 48 (3) (2009) 707–709.

[16] Y. H. Guo, L. Y. Ma, H. Zheng, et al, Comparison of HPLC and spectrophotometric methods for quantitative analysis of carminic acid. Food Sci. 30 (18) (2009) 303–306.

[17] G. M. Zhao, G. H. Zhou, X. L. Xu, et al, Changes of dipeptidyl peptidase Ⅳ in the processing of Jinhua Ham. Scientia Agricultura Sinica 38 (1) (2005) 151–156.

[18] J. Jia, L. Yang, Y. G. Zu, Homogenated extraction of oligomeric proanthocyanidins from larch bark and its optimization by response surface methodology. Chem. Indus. Fore. Prod. 29 (2009) 78–84.

[19] X. J. Shang, J. Q. Qian, H. Guo, Optimazation of extraction of alkaloids from *Corydalis yanhusuo* W. T. Wang by response surface methodology. Chem. Indus. Fore. Prod. 30 (2010) 32–36.

[20] L. Yang, Z. Y. Wang, Optimization of the processing parameters for extraction of antioxidants from blackberry using response surface methodology. Chem. Indus. Fore. Prod. 30 (2010) 67–72.

doi:10.4028/www.scientific.net/AMM.161.88

Expression, Purification and Characterization of Amantadine Receptor in *Escherichia coli*

Haixin Sun [1, a], Limin Cao [1, b], Hong Lin [1, c], Fang Lv

(Food Safety Laboratory, Ocean University of China, Qingdao, China 266003)

[a]hisense_sun@sina.com, [b]caolimin@ouc.edu.cn, [c]linhong@ouc.edu.cn (corresponding author)

Keywords: Avian influenza A; amantadine; rM2 protein; binding property.

Abstract. In order to obtain large quantities of broadly selective receptor as one diagnose agent to detect amantadine residue, the M2 protein gene with a His-tag was ligated into pET11a and transferred into *E. coli* BL21 (DE3) cell. The recombinant *E. coli* was cultured in liquid LB culture. SDS-PAGE result showed the recombinant M2 protein (rM2) was expressed as insoluble inclusion bodies with about 18KDa in molecular size. rM2 protein was further recognized by Western blot and purified by Ni Sepharose 6 Fast Flow and then refolded. The equilibrium dialysis result showed the rM2 protein had the binding constant of 1.1×10^5, and stoichiometry of 4.2. The above result showed the rM2 has the potential as biological diagnose agent to the detection of amantadine residue.

Introduction

Avian influenza A virus (AIV) causes serious global public health threat not only to human beings but also to many animals [1]. Amantadine and rimantadine were confirmed effective for the treatment and prophylaxis of AIV infection [2]. In the past 30 years, amantadine and rimantadine have been widely used for their availability and cheapness. Unfortunately, a serious resistance of AIV to these drugs has been observed, with is considered to a large extent due to the frequent use in animals [3] [4]. Moreover, the residues of amantadine and rimantadine in animals may be transferred to human bodies through the food chain, and then lead to significant side effects such as nerve toxicity and visual (or auditory) hallucinations [5]. To control the potential hazards of residues in edible animals, many counties and areas have been forbidden the use of amantadine and rimantadine in veterinary. However, because of the cheap price, and also because of the lack of alternative drugs to the virus, there were still used in animal breeding. It is necessary to develop the rapid detection method to control such illegal use of amantadine.

Current analysis for amantadine and rimantadine was mainly performed with mass spectrometry (MS) based-techniques, such as liquid chromatography (LC)-MS/MS [6][7]. These techniques were proved accurate and sensitive enough. However, they were demonstrated both time and labor consuming, and greatly rely on expensive laboratory facilities as well as complex pretreatments of samples, which make them unsuitable for routine monitoring. Therefore there is a growing demand to develop alternative techniques for fast and sensitive screening of amantadine or/and rimantadine residues, especially those that can be easily performed without large equipment.

Now, the mechanism of amantadine and rimantadine had been clearly demonstrated. It was clear the M2 protein of AIV was the target of amantadine. As the ion channel inhibitor, amantadine and rimantadine could specially bind with the M2 protein [8]. As a specific receptor, the M2 ion-channel protein could self-assemble as a homo-teramer to form a protein-selective ion-channel, which is then activated in a low pH environment [9][10]. Based on its specific and binding with amantadine and rimantadine, one can reasonably imagine that, the M2 ion-channel protein might be used for effective separation or/and analysis of these residues in order to avoid many shortage of current detection method, with an analytical system somewhat like immunoassays. However, such a technique has not been attempted till now, which could be mainly attributed to the extremely low concentration of the protein, as well as the difficulty to get sufficient protein samples.

This task may be solved by effective expression of the M2 protein in genetically constructed bacteria. In this paper, part of the M2 protein amino (18~60) residues rather than the full-length protein was expressed in *E. coli*. The obtained protein was further purified, and its binding ability with amantadine was preliminarily characterized. Based on the results, the potential of the prepared protein for bioassay of amantadine residues was also evaluated.

2. Experimental

2.1 Material and reagents

Low molecular protein markers were purchased from Fermentas (Lithuania) or Bio-Rad (Richmond, CA, USA). L-Arginine, guanidine hydrochloride (GuHCl), isopropylthiogalactoside (IPTG) and phenylmethylsulfonylfluoride (PMSF) were purchased from Beijing Solarbio Science & Technology Co., Ltd (Beijing, China). Ni-Sepharose 6 Fast Flow gel was obtained commercially from GE Healthcare Company (Sweden). LB Broth was purchased from Beijing Land Bridge Technology Co., LTD (Beijing, China). Goat anti-mouse antibody conjugated with horseradish peroxidase and mouse anti His-tag monoclonal antibody were purchased from Beyotime Co, LTD (China).

2.2 Methods

2.2.1 construction of recombined bacteria

Escherichia coli (*E. coli*) host BL21 (DE3) and the plasmid pET11a which confers M2 gene were constructed by Taihe Biotechnology Co. LTD, Beijing, China. The M2 (18-60) polypeptide construct was expressed as a C-terminal fusion to bacterial trpLE with an N-terminal His tag. The construction procedure was described as following: The DNA fragment was ligated into pET11a vector which was then transformed into *E. coli* BL21(DE3) cells and the aimed cells were selected on ampicilin plates. The purification recombinant *E. coli* was stored at -80℃ for further experiments.

2.2.2 Localization of the crude rM2 proteins

The recombinant *E. coli* was at first incubated in 30 ml LB (containing 100 μg/mL ampicilin) at 37 ℃ for 12 hrs under continuous shaking (200 rpm) as the seed. Then 0.3 mL of the seed suspension was transferred to 30 ml LB (containing 100 μg/ml Ampicilin) and incubated under the same condition as that of the seed. When absorbance value of the bacteria reached 0.6, IPTG was added into the liquid medium with final concentration of 0.1mM, and the culture was incubated for further 16 hrs. After incubation, the suspension was centrifuged at 3500×g for 15 min at 4℃, and cells were collected and re-suspended in 3 mL of fragmentation buffers (phosphate buffer solution, 20 mM, pH 8.0, containing 100 mM of sodium chloride and 1mM of freshly prepared PMSF). The crude culture without centrifugation and 1mL of the supernatant were taken as samples A and B respectively. The collected pellet were treated with ultrasonic for 15mins (5 seconds for each time, with an interval of 5 seconds, SCIENTZ-ⅡD Ultrasonic instrument, Ningbo Scientz Biotechnology CO.,LTD, Ningbo, P. R. China). Then the liquid was mixed with equal volume of urea solutions (8 M, containing 1mM of freshly prepared PMSF) and stirring for 1 hrs at 4℃, the mixture was centrifuged at 9500×g for 50 min, and the pellet was re-suspended in 3 mL of phosphate buffer (0.02 M, pH 7.4, containing 0.15 M NaCl), and 1 mL of the solution was saved as the sample C. The bacteria culture without addition of IPTG was treated with the same procedure and was took out as a blank control sample.

Sample A, B and C ,including the blank control sample, were analyzed by SDS- polyacrylamide on electrophoresis system (Bio-Rad)) according to the explanatory memorandum: Samples were mixed with 1 × Laemmli buffer at a ratio of 4: 1 (V: V), heated at 100 °C for 7 min and applied on SDS-PAGE gels (15%) employing a vertical electrophoresis system.

2.2.3 The further assurance of the recombinant M2 (rM2) protein with western blotting

The SDS-PAGE gels containing rM2 protein were either stained with Coomassie Brilliant Blue R-250 for direct investigation, or transferred to a PVDF membrane (450 nm, Pall-Gelman, USA) for western blotting in the following procedures (according to the explanatory memorandum): The gels were transferred to PVDF membrane at constant current of 0.8 mA/cm^2 membrane for 3.5 hrs, and a

piece of membrane was stained with Ponceau S to verify protein transfer. Blots were blocked with 5% defatted milk in phosphate buffer (0.02 M, pH 7.4, containing 0.05% Tween 20) for 2 hrs at 37°C, and then incubated with mouse anti-His-tag antibody (1: 1000 dilution with dilution buffer) overnight at 4°C. A polyclonal goat-anti-mouse antibody conjugated with horseradish peroxidase (1: 1000 in phosphate buffer (0.02 M, pH 7.4)) was added as detecting antibody after washing. Immuno-reactive bands were developed by enhanced chemi-luminescence after final washing with PBST, and scanned by an automatic digital gel image analysis system (Tanon-4200, Shanghai Tanon Technology Co, LTD，China).

2.2.4 Separation and initial purification of rM2 proteins

The collected pellet was further re-suspended in 10 mL phosphate buffers (20mM, pH 7.4, containing 500 mM NaCl and 6M GuHCl), stirred for about 2 hrs at room temperature and then centrifuged at 9500×g for 50 min. The supernatant was incubated with the Ni Sepharose 6 Fast Flow slurry at room temperature overnight under slowly shaking (The slurry was pre-treated according to the explanatory memorandum). Then the mixture was packed into a column (1.6×5 cm). The column was washed with 25 mL of phosphate buffer (20mM, pH 8.0, containing 500mM NaCl, 20mM imidazole and 6M GuHCl) and eluted with 50 mL phosphate buffer (20mM, pH 8.0, containing 500mM NaCl, 500mM imidazole and 6M GuHCl). The protein fraction was collected as the purified rM2 protein according to the absorbance at 280 nm.

2.2.5 Refolding treatment of recombinant rM2 protein

6 mL of affinity purified rM2 protein solutions were mixed rapidly with 0.6 L of Tris-HCl (pH 8.0, 100 mM, containing 0.5 M L-arginine and 0.2 mM EDTA, pre-chilled to 10℃) under continuous stirring. Two further additions (6mL for each time) of purified rM2 protein were performed at 1.5 hrs intervals to reach a total amount of 180 mL purified rM2 protein. The mixture was incubated for 48 hrs at 10℃ without stirring. Then the solution was dialyzed against phosphate buffer (pH 8.0, 20 mM, containing 300 mM NaCl, 10mM imidazole and 100mM urea) for 48 hrs, the phosphate buffer was changed every 12 hrs. The dialyzed sample (about 780mL) was centrifuged at 9500×g, and the supernatant was filtered through 0.45 μm membrane, frozen-dried and stored at -80℃ for further use.

2.2.6 Equilibrium dialysis

5 g rM2 protein powder (with protein concentration of 0.3%) was dissolved in 10 ml of PBS and averagely transferred into 5 dialysis tubes (with a molecular weight cutoff of 12000), and then dialyzed against different concentration of amantadine (200 mL, PBS) for 48 hrs with continuous stirring under 4℃, respectively. According to our experience, such a condition is enough to reach a steady-state concentration of dialysate. Control experiments were performed in the same conditions, except that equal volume of PBS was used instead of the rM2 protein solution. After dialysis, the concentration of amantadine remained in dialysate (outer solution) were determined by HPLC-MS/MS (Tandom mass spectrometer, Quantum Access, thermo, HPLC, Accela, Thermo), according to the following conditions: positive ion mode, C18 column of 50 mm × 2.1 mm, (Thermo Hypersil Gold, 1.9 μm), column temperature of 30℃, sample room temperature of 4℃, sample volume of 10 μl. Mobile phase A: 0.005 M ammonium acetate solution with 0.1% formic acid; mobile phase B: methanol; speed: 0.3 mL/min; grad elution procedure: eluted with 90% mobile phase A and 10% mobile phase B for 1 min, then eluted with 20% A and 80% B for 3 min, and finally eluted with 90% A and 10% B.

The results from equilibrium dialysis were cast into the Scatchard plot [11]:

$$R/Cf = Ka(N-R)$$

where Cf is the concentration of free amantadine remaining in the out dialysate after dialysis, R is the ratio of the free rM2 protein concentration and the total rM2 concentration, the free rM2 protein concentration is the difference between total amantadine concentration and free concentration, Ka is the binding constant, and N is the binding stoichiometry.

3 Results

3.1 Construction of the recombinant E.coli system for rM2 protein

The plasmid with the M2 gene was shown in Fig.1. The vector was generated by fusing M2-enconding sequence with the TRPLE gene and the His-tag of pET11a. This construct is predicted to encode a recombinant protein with the molecular weight of ~18KDa. In this recombinant protein, the first residues are His-tag residue followed by the Trple residue and rM2 protein. The vector was transformed into BL21 (DE3) host cells. Small-scale cultures of the positive clones were subjected to IPTG induction to identify clones capable of expressing the predicted recombinant protein. Of the BL21 (DE3) clones identified, the one that exhibited a maximal rM2 protein production was selected for further experiments (data not shown).

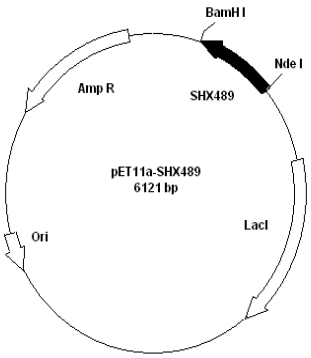

Fig.1 The map of plasmid pET-D11a.

3.2 Production and localization of the rM2 proteins from the recombinant E. coli

To localize the distribution of the recombinant rM2 protein in the culture, different groups after centrifugation was analyzed by SDS-PAGE. As shown in Fig.2, one significant 18KD protein band was clearly demonstrated in the pellet of test group, in comparison to samples from the supernatant of cultures. Such a result allowed us to suggest that, the expected rM2 proteins may mainly produce inside the pellet as inclusion bodies.

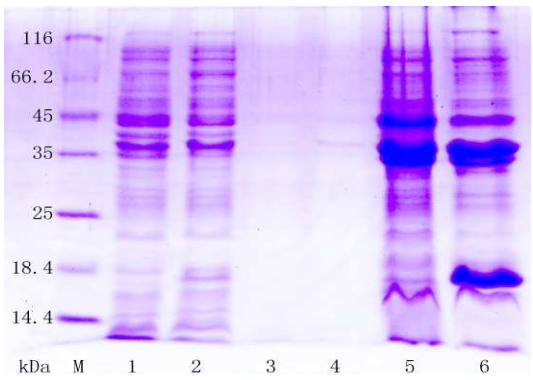

Fig.2 SDS-PAGE results of different products from the recombinant *E. coli*.

M: the protein marker. 1: the total liquid medium of control. 2: the total liquid medium of test group. 3: the supernatant of control. 4: the supernatant of test group. 5: the pellet of control. 6: the pellet of test group.

3.3 The assurance of the aim protein with SDS-PAGE and Western Blotting

For the further assurance of the recombinant rM2 protein, the pellet was analyzed by SDS-PAGE and western blotting (Fig.3 A and B). It was evident that the addition of IPTG resulted in significantly increased expression of the 18KD protein (Fig.3 A). To further confirm the expression of the recombinant rM2 protein, the obtained 18KD protein was analyzed by western blotting, in which an anti-His-tag antibody conjugated with HRP was used. As shown in Fig.3 B, significant positive results were demonstrated, which indicated that the obtained 18KD component was exactly the aimed rM2 protein.

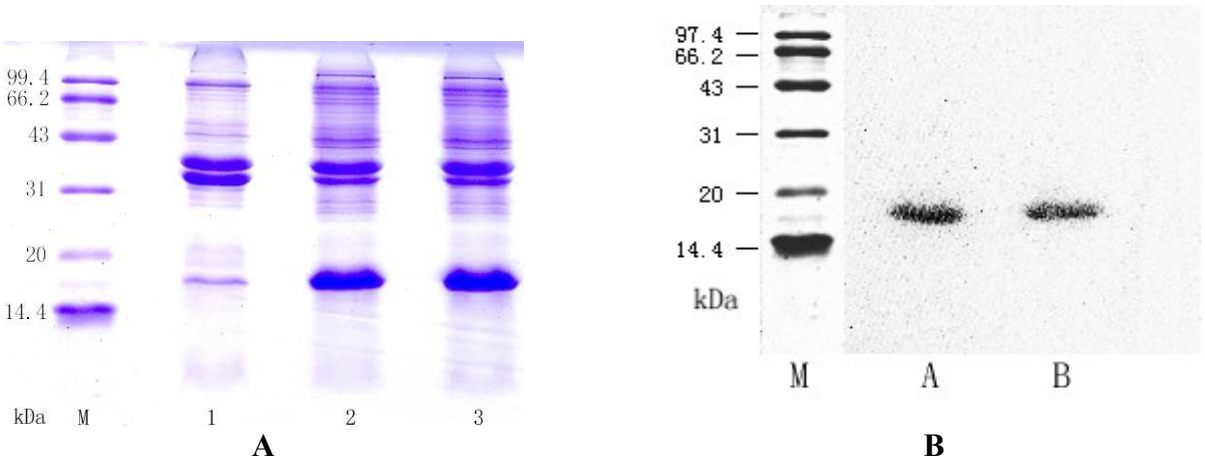

Fig.3 The results of SDS-PAGE (A) and Western Blotting (B). **A:** band M was protein marker. Band1was the pellet of control group without IPTG, and band 2 and band 3 were pellet of test groups in the presence of IPTG. **B:** band M was protein marker, and band A and B were same samples in which M2 protein has been analyzed by SDS-PAGE and transferred to PVDF membrane.

3.4 The binding ability of recombinant rM2 protein to amantadine

The obtained proteins were further purified by an affinity chromatography with Ni sepherose Fast Flow gel and refolded according to the 2.2.5 has mentioned. Then binding properties of refolded rM2 protein to amantadine were investigated by equilibrium dialysis. The data obtained were fitted by a single-site binding model, and linearized by presentation in the Scatchard plot (Fig.4).

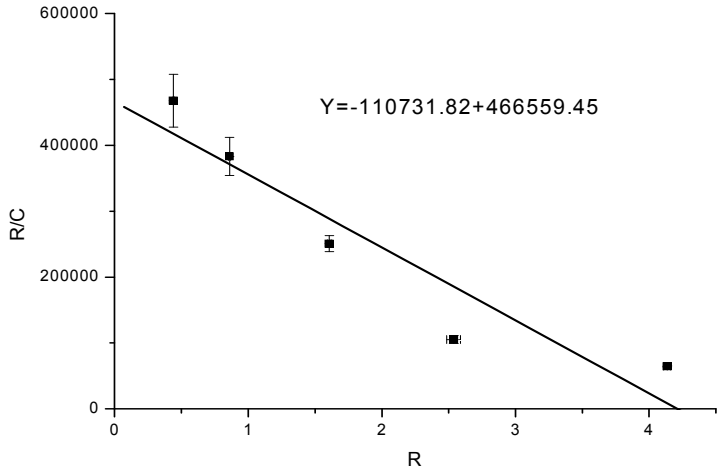

Fig.4 Schatchart plot for amantadien to recombinant rM2 protein.Each point represents the average of three measurements.

The binding constant (Ka) of the rM2 protein for amantadine was calculated as approximately 1.1×10^5, and the binding stoichiometry (referring to the number of amantadine molecules per 100 protein molecules) was 4.2. These results demonstrated a significant efficiency of the obtained rM2 protein to capture amantadine, which indicated its promising potential to be used as a selective potential for analysis of the drug residues. However, the binding constant and binding stoichiometry was not high enough as expected. The refolding procedure may be not suitable enough, which could significantly limit the biological activity of the rM2 protein. The other reason maybe due to the unsuitable pH value and ion strength, because it was reported that some parameters, such as pH or ion strength, could affect the binding activity of rM2 protein to amantadine [12]. Such an optimization of refolding procedures and reaction parameters (such as pH and metal irons) would be performed in our next work.

4 Conclusion

Using *E. coli* BL21 (DE3) as host cells, a bio-expression system for rM2 proteins and its purification procedure were for the first time developed and validated. The binding constants and binding stoichiometry of prepared rM2 proteins to amantadien were measured, and the results suggest that rM2 protein has the potential to be used as a specific receptor for the biological analysis of amantadine residues in food.

Acknowledgements

This work was supported by the Earmarked Fund for China Agriculture Research System (CARS-50-G09) and Program for New Century Excellent Talents in University (NCET-10-0756).

Reference

[1] Frederic G, Hayden M.D, Antiviral Resisitance in influenza Virus-Implications for Management and Pandemic Response, The New England Journal of Medicine. 354(2006)785-788.

[2] Guimei He, JianQiao, Changgui Dong, et al, Amantadine-reisitance among H5N1 avian influenza virus isolated in Northern China, Antiviral Research. 77 (2008)72-76.

[3] Michaela Schmidtke, Roland Zell, Katja Bauer, er al, Amantadine resistance among porcine H1N1, H2N2, and H3N2 influenza A virus isolated in Germany between 1981 and 2001, Intervirology. 49 (2006)286-293.

[4] Gui-Rong Bai, Malinee Chittaganpitch, Yuta Kanai, et al, Amantadine- and oseltamivir-resistant variants of influenza A viruses, Biochemical and Biophysical Research Communication. 390 (2009)897-901.

[5] Earl Justice Smith, Amantadine-induced Psychosis in a Yong Healthy Patient, The American Journal of Psychiatry. 165 (2008)1613.

[6] Yun huan, Zhang Zhaohui, Luo Shengliang et al, Determination of anmantadine residues in food of animal origin by solid-phase extraction/LC-MS/MS, Moderninstrs. 6 (2009)42-45.

[7] Meijuan Xu, Wenzhang Ju, Xiaoyan Xia, et al, Determination of rimantadine in rat plasma by liquidchromatography/electrrospray mass spectrometry and its application in a pharmacrokinetic study, Journal of Chromatography B. 864 (2008)123-128.

[8] Antonios Kolocouris, Raino K. Hansen, William Broadhurst, Interaction between an Amantadine Analogue and the Transmembrane Portion of Influenza A M2 protein in Liposomes Probed by ^{1}H NMR Spectroscopy of the Ligand, J. Med. Chem. 47 (2004)4975-4978.

[9] Jason R. Schnell, James J. Chou, Structure and mechanism of the M2 proton channel of influenza A virus, Nature. 251 (2008)591-596.

[10] Antonios Kolocouris, Christos Zikos, William Brodhurst, ^{19}F NMR detection of the complex between amantadine and the receptor portion of the influenza A M2 ion channel in DPC micelles, Bioorgainc & Medicinal Chemistry Letters. 17 (2007)3947-3952.

[11] Yu Shan-qian, Wang Hong-hai, Zhu Nai-yi, The reaction between antigen and antibody and its application, in: Introduction to Immunology, High education Publication, Beijing, 1999, pp137-151.

[12] Limin Cao, Hong Lin, Vladimir M. Mirsky, Detection of antibiotics in food: Extraction of fluoroquinolones by DNA, Anal Bioanal Chem. 388 (2007)253-258.

doi:10.4028/www.scientific.net/AMM.161.94

Refined technique and characterization of Chinese insect wax

Hong Zhang[1,2,a], Hua Zheng[1,2,b], Jun Chen[1], Xiao-ming Chen[1,2,c], Hong Zhao[1], Wen-wen Zhang[1,2]

[1]Research Institute of Resources Insects, Chinese Academy of Forestry, Kunming, 650224, China

[2]Research Center of Engineering and Technology on Forest Resources with Characteristics, State Forestry Administration, Kunming, 650224, China

[a]kmzhhong@163.com, [b]hua-zheng@sohu.com, [c]eastgeneva@163.com (corresponding author)

Keywords: Chinese insect wax; refine; pilot test

Abstract. For the improvement of processing and the increase of refined products of Chinese insect wax, it was carried out on the raw wax for its refining in the pilot plants. After the treatment, it was raised the melting point and reduced the acid value, iodine value, saponification value and insoluble substances of benzene significantly. The quality of final products was accord to the industrial top-grade requirement. The yield of refined wax was ranging from 72.76% to 74.30% and the whiteness was 51.8% to 56.3%. It was not observed any chemical changes of the wax during the processing.

Introduction

Chinese Insect Wax is a natural white wax secreted by male larvae of the *Ericerus pela* Chavanes parasitized on some Oleaceae plants, such as *Fraxinus chinensis* Roxb. and *Ligustrum lucidum* Ait. during the insect growth period[1,2]. The main chemical components of the wax are esters formed by monoacids such as hexacosanoic acid, octacosanoic acid, tetracosanoic acid, triacosanoic acid, and monohydric alcohols such as hexacosanol, octacosanol, tetracosanol, triacosanol, *etc*., accounting for 93% to 95% of the total esters amount[3,4]. There are also a small amount of pentacosanoic acid, heptacosanic acid, pentacosanol and heptacosanol. With the features of high strength, high melting point, good fluidity, stable physical and chemical properties and moisture-proof, corrosion proof, shining and lubricating, *etc*., they are mainly used as the base materials of high-grade chocolate coating, high floor wax and car wax, food packaging, pharmaceutical coating, cosmetics (lipstick, hair wax, skin care products) and the photosensitive materials of color copying machines, which is recognized as a treasure in the world[5,6]. Recent years, the wax has becomes an important material for the production of policosanols[7-9]. As the whitest natural wax, originated mainly in China, it is also called as Chinese wax, pe-la or insect white wax by the foreigners[1,2].

With changes of customer's ideas, the demands of the white wax are increasing. Since hundreds of years ago, refining ways in China for the wax has been applied mainly by boiling and steaming. The processing was in low efficiency and output, just for crude wax with low requirement on appearance, color, physical and chemical indexes, which cannot be applied in pharmacy, foods, cosmetics and other industries, especially for international trade purposes. Exporting the cheap products and importing the expensive refined wax is offen seen in China, which limits the development of the wax industry. But the prices of natural products rise rapidly, thus it happens to users with problems of mixing animal fats, alum, gypsum and starch into the wax. For a healthy development of the wax industry and an effective improvement of the product value, it is necessary to explore simple and feasible refining techniques.

1. Materials and method

1.1 Main raw materials

Crude white wax: commercially available, purchased from Zhaotong City, Yunnan Province; oxalic acid (industrial grade); activated clay (industrial grade, in compliance with the HG/T2569-94 standard); silicon dioxide (LR); industrial filter cloth -767.

1.2 Instruments and equipments

Devices for pilot test of white wax, installed at Pilot Base of Research and Development on Special Bio-resources, Research Institute of Resources Insects, Chinese Academy of Forestry.

Micro-melting point tester: SGW X-4, Shanghai Precision Scientific Instrument Co., Ltd.; digital whiteness meter: SBDY-1, Shanghai Yuefeng Instruments Co., Ltd.; Fourier transform infrared spectrometer (FTIR): TENSOR 27, Bruker, Germany; X-ray diffractometer: D8-Davance, Bruker, Germany; DSC200F3 differential calorimetry scanner: equipped with proteus data processing system, Netzsch, Germany; precision electronic balance: AB204-S, Mettler-Toledo (China) Co., Ltd..

1.3 Method

Schema of the main process was showed in Fig.1.

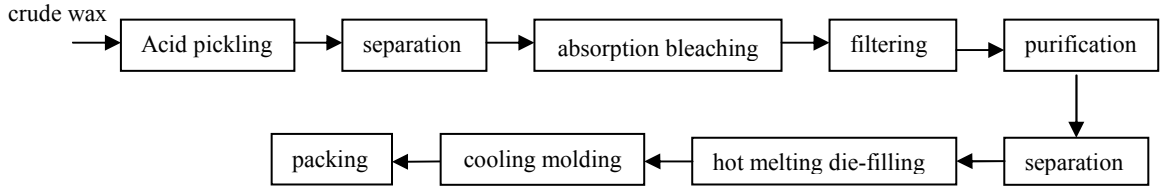

Fig.1 Steps of processes for the white wax refining

The crude wax is weighed and then put into a wax-melting pot with clear water, heated at the solid-to-liquid ratio from 1:2 to 1:10 (W / V). After most of the crude wax melted, it was slowly stirred for completed melt. Oxalic acid was added into the pot and kept its concentration at 1% to 10%. Keep the boiling state for 10-60 min after the acid cleaned. After stop heating and stirring, the wax was eventually solidified.

Remove the pickling solution at the bottom of the pot and wash for several times with cold water. Blow off the residual moisture from surface of the white wax, then add the activated clay and silica, with 5%~10% and 0.5%~3% of the crude white wax respectively. The bleaching temperature was controlled at 85°C to 110°C for 10min to 45min. Completely filter the hot melting liquid and collect it into the storage tank.

After the filtration, the wax was transferred into a purification pot. Add the industrial tap water to wash them, and control the wax and liquid ratio at 1:2 ~ 1:10 (W / V); boil and melt it thoroughly; cut off the heat sources and continue to slowly stir for 10 min, stand still to cool it down; control the cooling rate and when the wax is cooled down and solidified, the liquid and the solid are separated. Wash the white wax for several times until the pH value of the washing waste liquid at 7~8.

Remove the washing liquid at the bottom, dry the liquid on the solid wax surface, heat it and melt the white wax; after the residual moisture of wax is evaporated, place it to the customized wax mold to keep it still for cooling down; when the white wax is formed after condensation, remove the refined white waxes from the mold to package them.

1.4 Characterization of the products

The quality inspection and evaluation of the physical and chemical properties of the white waxes are carried out in accordance with the *Standard of Supply and Marketing Cooperatives of the People's Republic of China - Chinese Insect Wax* [GH 011-80][10]. The whiteness of the crude white wax and the refined white wax is measured with a digital whiteness meter.

Refining yield = (The mass of refined white wax) / (the mass of the crude white wax added) × 100%.

The infrared spectra of the crude white wax and the refined white wax block samples are measured with the Fourier transform infrared spectroscopy. Precisely weigh 1mg of samples. The samples are pressed with the KBr performing method, with the resolution: RES = 4cm^{-1}, the frequency of scanning: SCANS=32, scanning range 4000 ~ 400cm^{-1}.

A 2°/min stepping scanning on the crude white wax and the refined white wax block samples is carried out with the X-ray diffractometer; with the scanning range 10° ~ 100°, room temperature at 25°C.

The temperature scanning of the crude white wax and the refined white wax block samples are carried out under the control of the linear temperature control process with the differential calorimetric scanner. The initial temperature is 0°C, and heated to 100°C at the heating rate of 10°C /min keep the constant temperature 2 min; and then cooled down from 100°C to 0°C at a rate 10°C /min; The heating and cooling process should be under the purge gas and protective gas atmosphere (both high-purity N_2, of which, the purge gas, 20ml/min, protective gas, 50ml/min). The cooling medium is the liquid nitrogen.

2 Results and Analysis

2.1 Quality indexes of the wax

The technical indicators as specified in the *Standard of Supply and Marketing Cooperatives of the People's Republic of China - Chinese Insect Wax* [GH 011-80] see Table 1.

Table 1 Technical index of insect white wax

refined wax	melting point (°C)	acid value (KOH mg/g)	iodine value (g/100g)	saponification value (KOH mg/g)	insolubles in benzene (%)
top-grade	82~85	1.2	3.0	65~85	0.2
middle-grade	81~83.5	1.8	12.0	70~102	0.4
normal-grade	≥80	not specified	15.0	85~110	0.6

The color of the crude white waxes commercially available is yellow or gray ash, uneven cross-section, hollow, with visible mechanical impurities and stains, strong sense of greasy feeling and obvious rancid smell. Through inspection, its saponification value is lower than tri-wax and its melting point and iodine value are lower than the bi-wax. After the pilot processing, the Chinese insect wax is hard and slightly brittle in texture, and fibrous crystals are be seen, milk white with gloss; the surface is smooth, with wrinkles and shrinking feeling, creamy, odorless and tasteless. The quality control indicators are shown in Table 2.

Table 2 Results determined on quality of insect white wax

wax	melting point (°C)	acid value (KOH mg/g)	iodine value (g/100g)	saponification value (KOH mg/g)	insolubles in benzene (%)	whiteness (%)	refining yield (%)
raw materials	80.2	2.5	14.5	116	0.65	39.1	-
refined lot No. 1	82.4	1.06	1.28	81.26	0.19	52.6	73.55
refined lot No. 2	82.2	1.16	1.20	81.34	0.18	51.8	74.30
refined lot No. 3	82.1	1.15	1.00	83.07	0.17	52.1	73.79
refined lot No. 4	82.1	1.08	1.52	79.10	0.14	56.3	72.76

*note: All of the above values are averages of their determined indexes

As shown in Table 2, the refined wax melting point is slightly increased while the acid value, iodine value, saponification value and benzene insoluble substances are significantly reduced. The product quality indicators meet the level of the top level of waxes in the Ministry standard; the whiteness of the refined white waxes is slightly enhanced, with the increase of 12.7 to 17.2 percentage points; the refining yield is 72.76% to 74.30% (calculated by crude white wax), with remarkable refining effect of the white waxes.

2.2 Infrared spectra analysis

The IR spectra of the block samples of crude white waxes and refined white waxes see Fig. 2.

It was seen from Fig. 2 that there was no apparent absorption peak above 3000 cm^{-1}, suggesting that there is no free alcohol in the samples. The comparison spectra, fundamental frequency region and fingerprint region are basically the same, and the absorption peak of the refined wax group is more clear than that of the crude white wax, indicating that the two samples are the same compounds [3,11]; that is, before and after refining of the white waxes, there is no changes to the chemical structures.

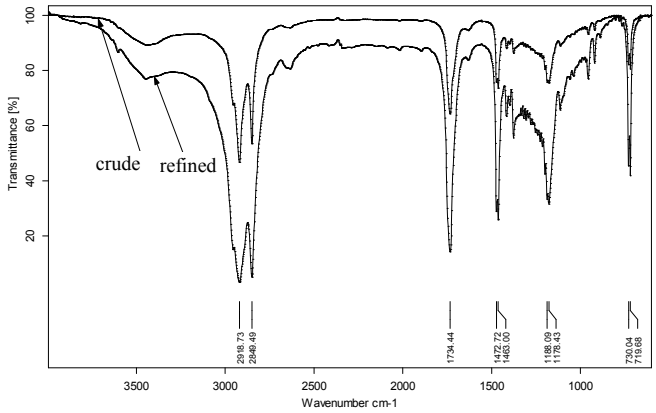

Fig.2 Infrared spectra of crude and refined insect white wax

2.5 X-ray diffraction

The X-ray diffraction curves of the crude white wax and the refined white wax block samples are shown in Fig.3 and Fig.4.

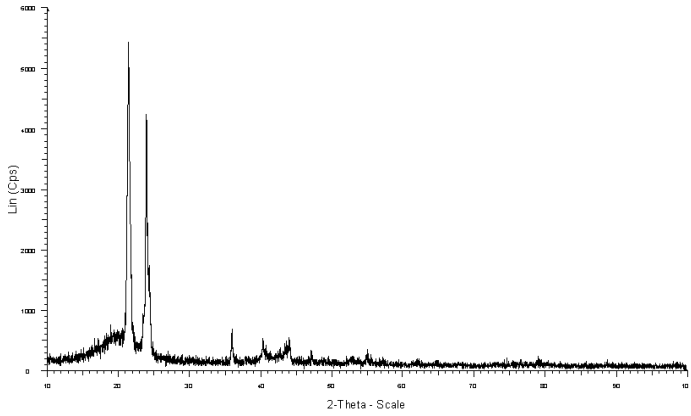

Fig.3 X-ray diffraction pattern of crude insect white wax

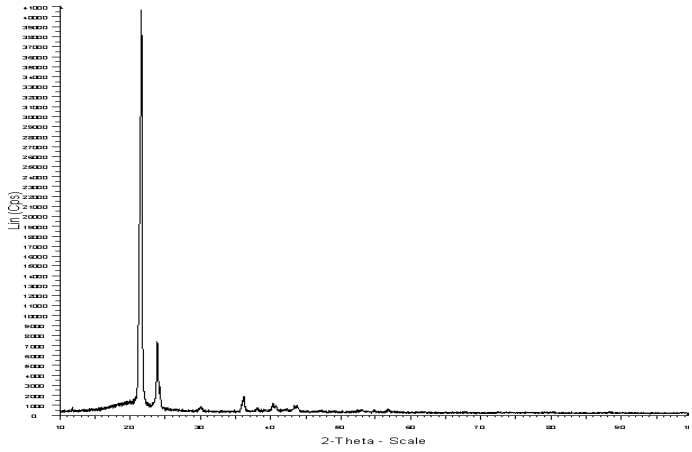

Fig.4 X-ray diffraction pattern of purified insect white wax

As seen from the X-ray diffraction patterns, there are characteristic peak at 21.335° and 23.864° for the crude white wax and the refined white wax test samples, with the diffraction intensity 5400 cps and 4400cps for crude white wax respectively and the diffraction intensity 40500 cps and 7400cps for the refined white wax respectively; the crystallinity is increased from 49% for crude white wax to 92% for the refined white wax[12,13]. The increase in the crystallinity after refining of the white wax contributes to the removal of the impurities in the wax in the refining process and the increase of the homogeneousness, and more stable crystalline state of the white waxes obtained during the melting and cooling formation process [3,14-16].

2.6. DSC spectra

The DSC spectra of the crude and refined white wax bulk samples are shown in Fig. 5 and Fig. 6

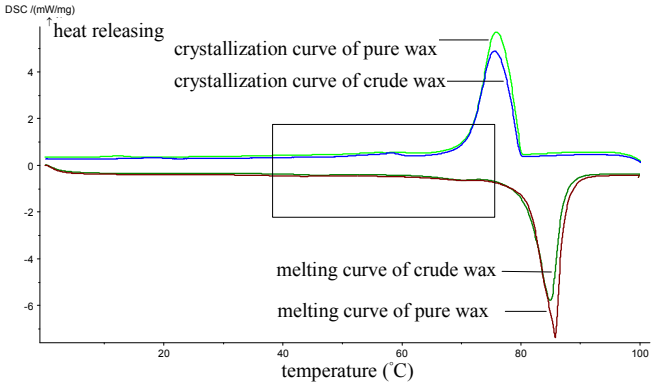

Fig.5 DSC graph of crude and purified insect white wax

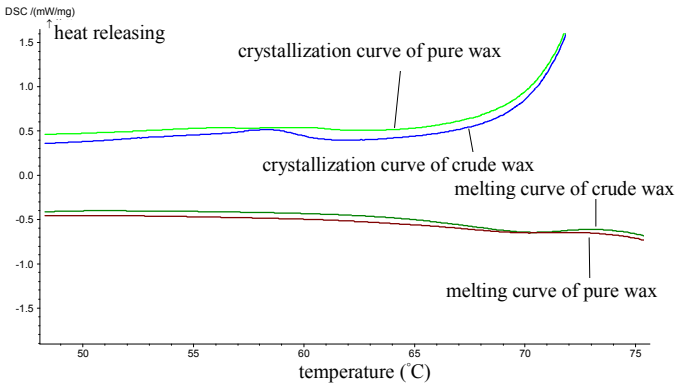

Fig.6 Magnification of low peaks region in DSC curves in Fig. 5

Table 3 Thermodynamic data from DSC curves of insect white wax

sample	mass (mg)	beginning temperature of melting peak (°C)	summit temperature of melting peak (°C)	ending temperature of melting peak (°C)	melting enthalpy (J/g)	beginning temperature of crystallization peak (°C)	summit temperature of crystallization peak (°C)	ending temperature of crystallization peak (°C)	crystallization enthalpy (J/g)
crude wax with slight melting peak	5.1	64.57	70.26	72.05	2.49	60.21	58.13	57.55	3.34
crude wax with significant melting peak	5.1	81.08	84.98	87.25	146.80	79.88	75.63	71.45	156.80
refined wax	4.9	81.01	85.88	87.44	195.10	80.08	75.92	71.68	183.20

As Table 3 showed, there are strong melting peaks at 84.98 ℃ and 85.88 ℃ for crude and refined white wax samples respectively, while for the crude white wax, a weak melting peak occur for the crude white wax at about 70.26℃; in the cooling process, there are strong melting peaks at 75.63℃ and 75.92℃ for crude and refined white wax samples respectively, while for the crude white wax, a weak melting peak occur for the crude white wax at about 58.13℃. Therefore, it can inferred that, the crude white wax, in addition to having the same major components as the refined white wax, contain a small amount of low melting point of components. During the refining process, this component of low melting point is removed and thus the quality of the white waxes is enhanced.

3 Conclusion

3.1 The substandard level of crude white wax was used as the raw materials in the pilot test. After pilot refining process, the melting point of the refined wax slightly increased, while the acid value, iodine value, saponification value and benzene insoluble substances were significantly decreased. The main indexes of the wax quality can meet the level of the top-grade of wax, showing an obvious refining effect.

3.2 After refining, the whiteness of the Chinese insect wax is enhanced. The refined white wax is in milky white color and its whiteness is as high as 51.8% to 56.3%.

3.3 The refining yield of the white wax can reach 72.76% to 74.30%.

3.4 The refining process does not change the chemical structure of the white wax, but its crystallinity is significantly enhanced.

Acknowledgements

This investigation was supported by Fund Program in Conversion of Agricultural Science and Technology Achievement, Ministry of Science and Technology of the People's Republic of China (2010GB24320619) and the Special Fund Project for the Scientific Research of State Forest Public Welfare Industry, SFA, China (201204602). Authors gratefully thank these financial support.

References

[1] X. M. Chen, Y. Feng, Overview of Resources Insects, Science Press, Beijing, 2008.
[2] C. H. Zhang, H. Q. Liu, Insect and Insect White Wax Production Technology in China, China Forestry Press, Beijing, 1997.
[3] Y. L. Bi, Oils and Fats Chemical, Chemical Industry Press, Beijing, 2005.
[4] Q. F. Duan, L. Y. Ma, H. Zheng, et al, A review on research progress of some polycosanol, J. Chem. Indus. Fore. Prod. 39(2) (2005): 42-47.
[5] H. Zheng, L. Y. Tang, R. G. Zhang, et al, Bio-wax and human health, Nat. Prod. Res. Dev. 21 (2009): 313-316.
[6] Y. Q. Wang, Q. F. Duan, H. Zhao, et al, Green products: bio-wax, Quar. Fore. By-prod. Spec. China. (3) (2002): 28-29.
[7] L. Y. Ma, Y. Q. Wang, Z. Q. Zhang, et al, Preparation of policosanol from insect wax by reduction method, Chem. Indus. Fore. Prod. 29(5) (2009): 6-10.
[8] J. Zu, J. Su, Y. S. Yin, Octacosanol production and purification with *Cera chinensis*, J. Southwest Uni. Nationalities (Natural Science Edition), 34(1) (2008): 144-148.
[9] L. Y. Ma, Y. Q. Wang, Z. Q. Zhang, et al, Preparation of policosanol from insect wax, Sci. Tech. Food Indus. 29(2) (2008): 179-181.
[10] H. Zhang, J. Chen, H. Zheng, Purified processing of insect white wax pilot process design, Fore. Constr. (5) (2005): 3-5.
[11] GH 011-80, Standards of Chinese Supply and Marketing Cooperative - Insect White Wax.
[12] M. C. Zhou, Instrumental Analysis, Press of Huazhong University of Science and Technology, Wuhan, 2008.
[13] B. S. Zhang, Y. Q. Zhang, L. S. Yang, et al, A method of determining crystallinity of starch in multi-crystal system, J. South China Uni. Tech. (Natural Science Edition), 29(5) (2001): 55-58.
[14] Y. Li, Comparison of a few commonly used methods in the determination of polymer crystal degree, J. Shenyang Arch. Civ. Eng. Inst. 16(4) (2000): 269-271.
[15] Z. M. Lie, X-ray diffraction technology and its application in foodstuffs and oils, Grain and Oil. (1) (2003): 12-15.
[16] Y. P. Chen, T. T. Guan, Y. F. Cuo, Study on crystal habit of adipates dioctadecyl (OAO), J. Syn. Cryst. 30(4) (2001): 375-378.
[17] J. Lai, B. Wu, Influence of microwave on crystallinity level of chestnut starch, Food Ferm. Indus. 31(5) (2005): 40-42.

doi:10.4028/www.scientific.net/AMM.161.100

Fracture Resistance of Inter-joined Zirconia Abutment of Dental Implant System With Injection Molding Technique

Guangyuan Liu[1, a], Ke Wang[1,b], Dashan Wang[1,c], Jianjun Yang[1,d]

[1]Department of Oral and Maxillofacial Surgery,Affiliated Hospital of Qingdao University Medical College,Qingdao 266003, China

[a]jiushuchangdu@126.com,[b]wkalexadner@163.com,[c]wdsapple@163.com
[d]yjjqd@126.com(corresponding author)

Keywords: zirconia abutment; injection molding technique; fracture resistance; dental implant

Abstract. Objectives: Zirconia powder in nanometers can be fabricated into inter-joined abutment of detal implant system with the injection shaping technique. This study was to detect the resistance of inter-joined zirconia abutment with different angle loading for clinical applications. **Materials and Methods:** The inter-joined abutments were shaped with the technique of injection of zirconia powder in nanometers. Sixty 0sstem GSⅡ5.0mm×10mm implants were used with 30 zirconia abutments and 30 0sstem GSⅡtitanium abutments for fixation using 40N torque force. The loading applications included 90°, 30°, 0° formed by the long axis of abutments and pressure head of universal test machine. The fracture resistances of zirconia and titanium abutments were documented and analyzed. **Results:** The inter-joined zirconia abutments were assembled to the 0sstem GSⅡimplants succssfully. In the 90° loading mode, the fracture resistance of zirconia abutment group and titanium abutment group were 301.46±15.38N, 736.36±120.10N respectively. And those in the 30°groups were 434.66±36.07N, 1073.12±73.96N correspondingly. Significant difference in the two groups was found through T Test. No damage on the abutments of the two groups but S-shaped bending on the implants was found when the 0° loading was 1300~2000N. **Conclusions:** Through the assembly of Zirconia abutments and implants, all the components presented sufficient resistance acquired for the clinical application under loadings with different angle.

Introduction

The successful use of titanium implants, termed as the third generation of teech for mankind, was first confirmed as the treatment for incomplete dentition in the last 60s by the Dr. Brånemark. Subsequent expansion of clinical indication including edentulous or partially edentulous also proved to be a promising technique during last 50 years. Traditionally, titanium abutment supported porcelain fused to metal crown restoration (PFM) was used in the different implant systems. In the recent years, prominent aesthetic effect can be made by the zirconia abutment, then give rise to the research of manufacture and application about zirconia abutments. Depending on the implant system of 0sstem GSⅡ, the zirconia abutment shaped by the injection of zirconia powder was manufactured by the authors and fracture resistance was also documented and analyzed for clinical application.

Materials and Methods

Materials and Instrumentation.zirconia powder(TZ-3YB-E, Tosoh, Japan), Implant system (OsstemGSⅡ5.0mm×10mm,Osstem,Korea),Titaniumabutment(0sstemGSⅡ5.0mm×2.0mm×4.0mm Osstem, Korea)，laser three dimensional gauge (LPX-250, Japan)，Banbury mixer (XSN-15, Taiwan), Injection shaper (XSN-15, German), sintering apparatus (KSX-5-14, Jiangsu, China), Mill (XSM-LC,Beijing, China), universal test machine (AGS-J, Japan).

Zirconia abutment fabrication.1.Threedimensional measurements:According to the measurement made by the laser gauge, liner shrinkage of zirconia materials and the abutment draft was made. (Fig 1) 2.Abutment fabrication protocol: the procedures were mixing, injection molding, degreasing, sintering and refinement.

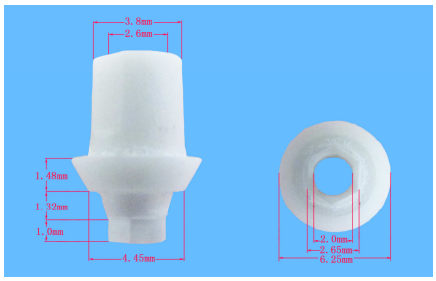

Fig 1. Zirconia abutment with injection shaping technique

Fracture resistance of the zirconia abutment and Osstem GSⅡtitanium abutment.

30 zirconia abutments and 30 Osstem GSⅡ titanium abutments （5.0mm×2.0mm×4.0mm） were fixed to 0sstem GSⅡ5.0mm×10mm implants separately with central retaining screw for 40N torque force. The components of zirconia abutment and implants were group A, divided into subgroup A_1, A_2, A_3. Every subgroup was 10 objects. The components of titanium abutment and implants were group B, divided into subgroup B_1, B_2, B_3. Every subgroup was 10 objects. Different loading was selected for these subgroups. The loading applications were 90°(group A_1 and B_1), 30°(group A_2 and B_2), 0°(group A_3 and B_3), which were formed by the long axis of abutments and pressure head of universal test machine (Fig 2, 3, 4).

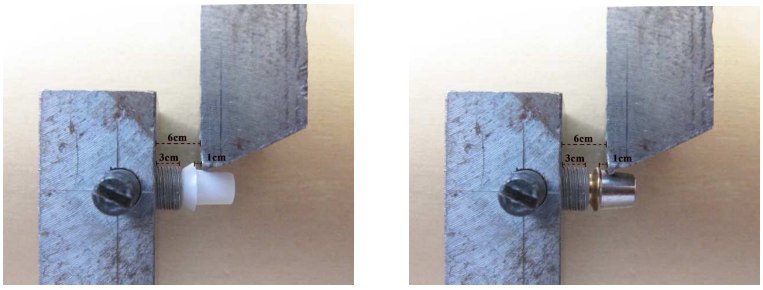

Fig 2. 90° loading (left: group A_1 right: group B_1)

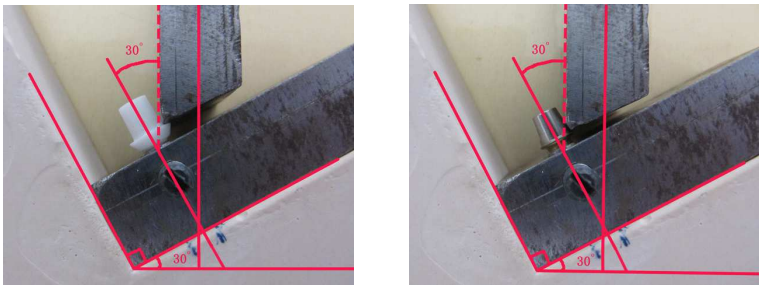

Fig 3. 30° loading (left: group A_2 right: group B_2)

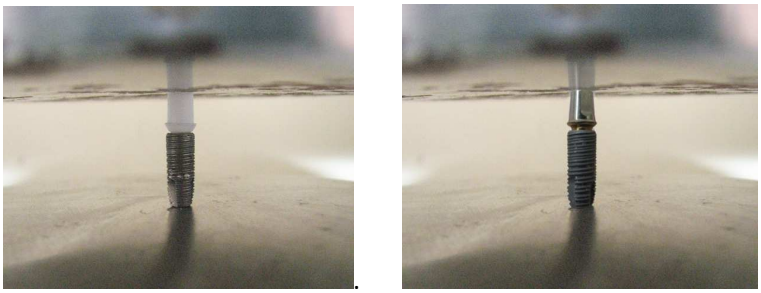

Fig 4. 0° loading (left: group A_3 right: group B_3)

Results

Fig 5. Zirconia abutment and titanium abutment assembled with 0sstem GS Ⅱ implants respectively

Table 1: Fracture resistence of group A_1, B_1 (90°angle); (unit: N)

Experimental groups	maximum	minimum	$\bar{X}\pm S$
Group A_1	319.50	281.60	301.46±15.38
Group B_1	882.60	594.80	736.36±120.10

Table 2: Fracture resistence of group A_2, B_2 (30°angle); (unit: N)

Experimental groups	maximum	minimum	$\bar{X}\pm S$
Group A_2	478.30	394.50	434.66±36.07
Group B_2	1164.80	989.40	1073.12±73.96

For group A_3, B_3, no damage was found on the abutments but S-shaped bending on the implants when the loading was 1300~2000N. (Fig 6)

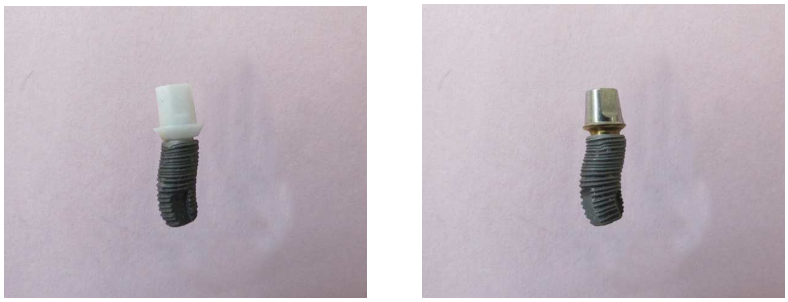

Fig 6. The implants of the components became "S"-shape (left: group A3; right: group B3)

Via the software SPSS 13.0, t test were used to analyse the results of Table 1, Table 2. Significant results were shown in the two groups. ($P<0.05$)

Discussion

Production of zirconia abutments by injection molding.

Injection molding technique is a kind of plasticity shaping technique with binder, plasticizer, lubricant, coupling agent. The products shaped by this technique have high precision and quality for clinical application without or even little modification. In addition, the manufacture of zirconia abutment can be made automatically in quality [1, 2].

The defect of zirconia powder that occurs in the procedure of injection shaping was lower dispersity and stability due to its small size, hydrophilic surface and agglomeration in non polar solvent [3, 4]. In this study, stearic acid [5] was used as modifier to clad the powder of zirconia so that the surface property was transformed into nonpolar powder from polar type. Therefore, more dispersibility and less agglomeration of zirconia powder were obtained [6, 7].

A glycerol-paraffin-polyolefin binder system was selected in this study. Paraffin has the rheological properties, but, during the injection molding and degreasing, paraffin wax was added in the two last phases to reduce the shrinkage commonly. As the major component in the binder system, glycerol was added to decrease transformation and contraction in the phase of injection and cooling. Due to glycerol is easy to be dissolved in the organic solvent [8], the key process of degreasing can be modified. By contrast, the traditional pure solvents can only dissolve most of the binder, and the simple thermal debinding time was long comparatively [9, 10, 11], so that the two components in combination increased the efficiency of degreasing significantly.

The optimal temperature for sintering was 155 0℃. Thus, the products of zirconia abutments have higher density (max: 5.94g/cm^3) and better lustrousness and transparency [12, 13].

The morphosis and fracture resistance of zirconia abutment.

Three parts of zirconia abutments were: the part linked to the dental prosthesis, the part linked to the implant, and the trans-gingival part. The height of the part linked to the dental prosthesis was 7.0 mm，that can be milled to meet the clinical need such as different distance between occlusion plane and gingival margin. The shoulder parameters were: width 1.0mm, axis-cervical line angel 95°, polymerization 5°. The antiglide structure on this part combining the abutment and prosthesis can meet the need of insertion, retention, resistance. In addition, the modification of the shoulder acquired favorable outcomes due to the maximal diameter of shoulder can be aligned with or extended even below the gingival margin. The part linked to the implant concludes Allen and Morse taper connection. Allen played a high resistance to lateral forces meanwhile Morse taper formed a mechanical connection between the abutment and the implant like the self-locking effect, with which good retention and stability were obtained. Although the trans-gingival part was 1.5mm, it may be sufficient for different thickness of the gum needs. After the assembly of the implant and abutment, the grinded shoulder with all-ceramic restorations possessed the aesthetic outcomes due to it may align with or extend below the gingival margin.

In the recent years, some studies reported the fracture resistance of zirconia abutment. The fracture resistance of single-tooth implant supported all-ceramic restorations consisting of alumina all-ceramic crown restorations on different implant abutments, zirconia abutment and titanium abutment. All the abutments received compressive loading in a universal machine with force application at angle of 40 degrees to the long axis of ceramic crowns [14]. Significant difference of the two groups was found according to the fracture resistance, zirconia abutment 443.6N, titanium abutment 1454N. Otherwise, forty 3I certain implant in combination with 20 zirconia abutment (Zireal abutment) and 20 titanium abutment (UCLA abutment) were used to test the fracture resistance with force application 45 degrees. No significant difference was obtained in the study of different abutments although the group of titanium abutment showed higher mean value 792.7N compared to 703.7N [15] of zirconia abutment group.

In this study, three types of loadings were selected to simulate three angles to the teeth axis in the oral environment. According to the long axis of anterior teeth, the force application of 30 degrees simulated the incision. Meanwhile, 0 degree loading was selected like the bite force transmitted by the molars in a mastication status. In addition, the loading of 90 degree simulating outside force to the dental prosthetic restoration was added to the test. Statistical analysis showed the mean value load of the zirconia abutment was lower than that of titanium abutment, however, the fracture resistance was sufficient for strength requirement in the restoration of anterior teeth, because the mean value of bite force in this region was 370N [16, 17]. As for the molar region, no damage was found on the abutments, although the loading of 1300~2000N exceeding the maximum bite force for the molars 847N [18] was selected for the application.

According to the data, the abutment has the physiological property during the application with different loading force like incision and mastication. Especially, when the loading of 90 degree was selected to simulate the most destructive force, the mean value (301.46±15.38N) of fracture resistance was lower than the maximum bite strength 370N of anterior teeth. However, it was still conducive to protect implant out of damage when abnormal loading happens. In this vitro study, the system of zirconia abutment and implant was verified for the treatment of incomplete teeth arch. However, further clinical investigation for single teeth or incomplete dental arch restoration should be carried out.

References:

[1].Wang Xiu, Xie Zhipeng, Li Jianbao, Huang Yong. Progress of Ceramic Injection Molding[J].Rare Metal Materials and Engineering,2004, 33(11)：1121-1126

[2].Xie Zhipeng，Yang Jinlong，Huang Yong. Study on ceramic injection molding [J]. Journal of the Chinese Ceramic Society 1998, 26(3): 324~330

[3].German RM．Powder Injection Molding[M]．Princeton：MPIF，1990：46-89

[4].Fan Jinglian，Huang Boyun，Qu Xuanhui．Effects of milling and active surfactants on rheological behavior of powder injection molding feedstock[J]．Transactions of Nonferrous Mrtals Society of China，2001，11(2)：196-199

[5] Liu Dean-Mo., Lin Jiang-Tsair and Tuan W.H. Interdependence between green compact property and powder agglomeration and their relation to the sintering behaviour of zirconia powder [J].Ceram. Int. 1999, 25: 551~559

[6].Chan Tienyin，Lin Shuntian．Effects of stearic acid on the injection molding of alumina[J]．Journal of the American Ceramic Society，1995，78(10)：2746-2752

[7].Lin S T，German R M．Interaction between binder and powder in injection moulding of alumina[J]．Journal of materials science，1994，(29)：5270-5212

[8] WJ Tseng，DM Liu，CK Hsu，Influence of stearic acid onsuspension structure and green microstructure of injection-molded zirconia ceramics，Ceram Inter，1999，25：191-195；

[9] Zhou Jicheng and Huang Baiyun. Thermal Debinding Behaviours of Hard-metal Feedstock for Powder Extrusion Moulding [J].Rare Metal Materials and Engineering 2002, 31(3):225~228

[10] Tseng Wenjea J. Influence of surfactant on rheological behaviors of injection–molded alumina suspensions [J].Mater Sci Eng A 2000, 289: 116~122

[11] WangWL. Surface modification of zirconia powder and Injection Molding Process [D]. 2008,06:51-53,58-61

[12].Rahaman MN，Gross JR，Dutton RE and Wang Hsin.Phase stability sintering and thermal conductivity of plasma-sprayed Zr02-Gd203 compositions for potential thermal barrier coating applications[J]．Acta Materialia，2006，(54)：1615-1621

[13].Jones RL，Mess D．Improved tetragonal phase stabi1ity at 1400℃ with scandia yttria-stabilized zirconia[J]．Surface and Coating Technology，1996，(87)：94-101

[14].Att W, Kurun S, Gerds T, Strub JR. Fracture resistance of single-tooth implant-supported all-ceramic restorations: an in vitro study [J]. J Prosthet Dent,2006,95(2):111-116.

[15].Aramouni P, Zebouni E, Tashkandi E, Dib S, Salameh Z, Almas K. Fracture resistance and failure location of zirconium and metallic implant abutments[J].J Contemp Dent Pract.2008,9(7):41-48.

[16].Paphangkorakit J, Osborn JW. The effect of pressure on maximum incisal bite force in man[J]. Arch Oral Biol,1997,42:11-17.

[17].Haraldson T, Carlsson GE, Ingervall B. Functional state, bite force and postural muscle activity in patients with osseointegrated oral implant bridges[J]. Acta Odontol Scand, 1979,37:195-206.

[18].Waltimo A, Könönen M. A novel bite force recorder and maximal isometric bite force values for healthy young adults [J]. Scand J Dent Res, 1993,101(3):171-175.

doi:10.4028/www.scientific.net/AMM.161.105

Properties of injectable composite cements and its application in burst fracture of the spine

Kezheng Mao[1.a], Keya Mao[1 .b],Zishen Cheng[1.c], Peng Li[1.d],

Zonggang Chen[2.e], Xumei Wang[3.f],Fuzhai Cui[3.j]

[1]General Hospital of People's Liberation Army, Beijing ,China
[2] National Glyco-engineering Research Center, Shandong University, Jinan, China
[3] Department of Materials Science and Engineering ,Tsinghua University, Beijing ,China

[a]maokezheng@sina.com, [b]maokeya@sina.com, [c]ganlanshu1012@163.com.

[d]lance_slee@yahoo.com.cn,[e]chenzg2008@163.com,[f]wxm@mail.tsinghua.edu.cn

[j]cuifz@mail.tsinghua.edu.cn

Key word: composite bone cements, injectable, α-calcium sulphate hemihydrate, nanohydroxyapatite/collagen, thoracolumbar burst fracture

Abstract: To explore a new type of injectable composite cements similar to the natural bone in both composition and hierarchical structure, the mineralized collagen and calcium sulphate dihydrate （CSD）were incorporated into α-calcium sulphate hemihydrate (α-CSH).The mineralized collagen was synthesized biomimetically by nanohydroxyapatite/collagen. We investigated the injectability, the setting time and the biomechanics properties to find an ideal combination of them to prepare the composite cements. SEM analysis showed biphasic cements consisting of an entanglement of calcium sulfate dihydrate and calcium-deficient hydroxyapatite crystals. We prepared porcine thoracolumbar burst fracture models and made the vertebroplasty for them by the composite cements. Imaging analysis showed the composite cements distributed uniformly and solidified well. Biomechanical test showed the ability of composite cements to repair spinal burst fractures was significant.

1. Introduction

Bone defects caused by infection, tumor, trauma, surgery and fracture nonunion have increased as the population ages[1]. Facing the problems of irregular bony defects and the increasing popularity of minimally invasive techniques, especially in the application of the spine, the search for injectable cements became one of the major hotspots in bone tissue engineering[2,3]. Calcium sulphate hemihydrate cement has good biocompatibility, non- inflammation， chemical stability and machinability, and high mechanical strength and rigidity[4,5]. However, it is absorbed faster than new bone growth,which restrict its wide application in clinical[6,7]. Thus, we modifiedα-CSH by adding the mineralized collagen and calcium sulphate dehydrate (CSD) to produce a new composite bone cement. The mineralized collagen which possessed features of natural bone in both composition and hierarchical structure was synthesized biomimetically by nanohydroxyapatite/collagen[8,9]. Extensive studies on the mineralized collagen had confirmed that it was biodegradable, biocompatible, and bioactive[10,11]. CSD is chemically and crystallographically very similar to DCPD ($CaHPO_4 \cdot 2H_2O$)[12].Therefore, CSD could be used to improve the injectability[13,14]. CSD is a relatively soluble calcium-rich phase. Thus, CSD could be used to accelerate the setting reaction by providing a fast-releasing calcium source[15].

Considering these putatively good properties of the three materials and the absence of studies devoted to this topic, the goal of this article was to assess the effect of a new composite cements composed of CSH, CSD and the mineralized collagen. The particular emphasises were set on the physico-chemical and biomechanical properties. We made the vertebroplasty for porcine thoracolumbar burst fracture models to verify the usefulness of the composite cements.

2. Materials and methods

2.1. Fabrication of injectable composite cements

The powder of mineralized collagen (nano-hydroxyapatite/collagen) was prepared as previously described[8].Medical gradeα-CSH and CSD were purchased from Merk Ltd (Germany). The water used in the experiment was distilled. The α-CSH was mixed with the mineralized collagen and CSD at different ratios (0%,5%,10%,20% respectively) to fabricate 16 different mixtures. The mixtures were added the distilled water with the L/S ratio at different ratios (0.5, 0.6, 0.7, 0.8, 0.9, 1.0 g/mL) and then stirred with a glass rod in a small containers for about 1 min to form homogenous pastes.

2.2 SEM analysis of the composite cements

Scaffold morphology was examined by scanning electron microscopy (SEM). The materials with different composition were fastened by conducting resin on fixed metal station. The samples were sputter coated with a layer of gold for SEM (JSM-6460LV，kabuskiki kaisha).

2.3. Injectability and L/S ratio

A certain amount of paste was extruded through a 5ml syringe (without needle, nozzle diameter of 2.0 mm) by hand to appraise injectability and determine fit L/S ratio[16]. Four grams of prepared paste was added into the syringe and restored at room temperature for pre-set time periods, the paste was gently extruded from the syringe. The standard of the good injectability was that injection process was smooth and stable. Five samples were measured to calculate the average.

2.4. Setting time of the composite cements

The setting time of the composite pastes were measured with a Vicat needle according to ISO9597-1989E. The setting time was defined as the time necessary for the heavy needle (350 g, Ø2.0 mm) to no longer leave a visible print on the surface of the paste. Each sample was repeated five times and the average value was calculated.

2.5 Mechanical test of the composite cements

The prepared paste was added into the steel molds (6 mm diameter × 10 mm high) and stored at 37 °C for 7 days. After storage, the hardened cement samples were removed from the steel molds. The compressive strength of the samples was measured at a loading rate of 0.5 mm min^{-1} using a universal testing machine (Instron-1195, USA) according to ASTM D695-91. Six replicates were carried out for each group and the results measured to calculate the average.

2.6 In Vivo Biomechanical Tests.

By measuring different proportions of t α-CSH, CSD and the mineralized collagen, we found an ideal combination of them to prepare composite cements. Then, we made the vertebroplasty for porcine thoracolumbar burst fracture models, and verified the usefulness of the composite cements to treat the spinal burst fracture. A total of 20 fresh porcine spine specimens (T14–L2) were used in this study. The ages at time of death were 10–11 months, which was approximately equivalent to a human age of 25–30 years of age[17]. Specimens were cleaned of excess soft tissue, leaving the ligaments, joint capsule, and the bony structure intact. Burst fractures were produced with use of the drop-weight method[18].This allowed the impact energy to be varied while the impact velocity was maintained. The superior and inferior vertebrae were mounted in fast dry epoxy resin. And a 2-mm drill bit was used to create a hole in the middle segment of the specimens, extending to a depth of approximately half the width of the vertebral body as determined by a gauge before drilling[17].

After the pre-injury,a 9-kg mass was dropped axially onto the specimen from a height of 0.5 to 1.5 m until the fracture was created in the vertebral body. Radiographic observation showed the vertebral body was fractured.

The fractured specimens were randomly divided into two groups: the control group (10 specimens) and the cemented group (10 specimens). The cements was injected into the spine via a 1.6-mm internal diameter needle through the pedicle of vertebral arch. All injections were performed by a single author. Radiographic observation showed distribution of cements in the fracture cracks. Then, the 20 specimens installed into a biomechanical testing machine (MTS System Inc). The average compressive modulus and the average compressive strength were recorded. All testing procedures were controlled automatically by customized software.

3. Results and Discussion

3.1 SEM analysis of the composite cements

Figure 1 showed the SEM micrographs of the cross section of the composite cements by different composition. From fig.1-A , the structure of the hardened CSD was sheet or plate-like. CSD,α- CSH and the mineralized collagen could be combined in all proportions to lead to biphasic cements consisting of an entanglement of calcium sulfate dihydrate and calcium-deficient hydroxyapatite crystals. The similarities to natural bone in the microstructure of nHAC have been verified via conventional and high-resolution transmission electron microscopy[8]. The nHAC was obviously observed to insert into CSD in fig.1-C.

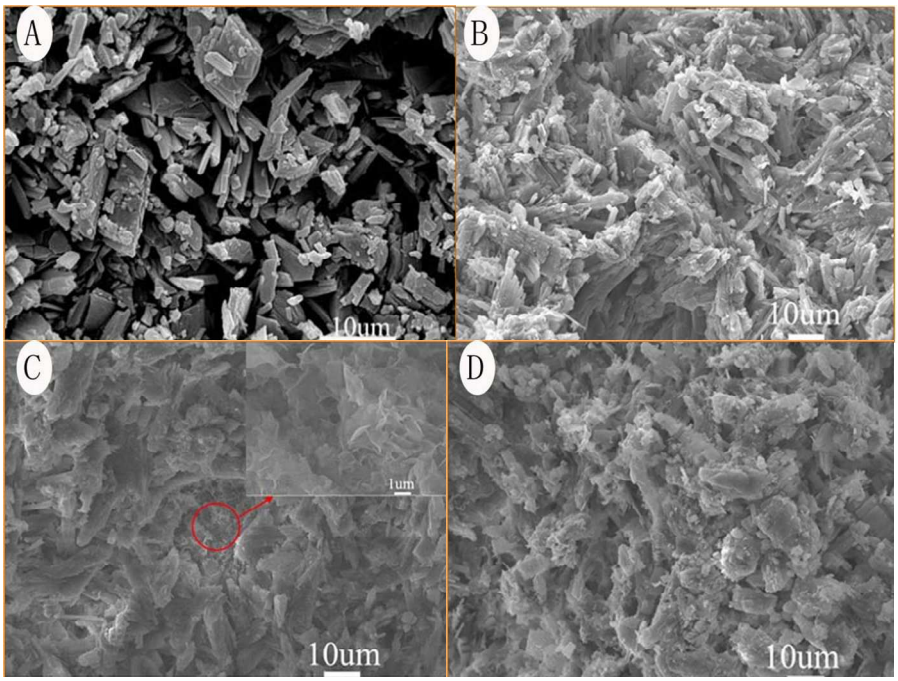

Fig.1. The microstructure of cements with different composition.(the mineralized collagen content after final setting (A) 0%; (B) 5%; (C) 10%; (D) 20%.)

3.2 Injectability and L/S ratio

The rheological properties of the pre-setted composite cements are critical to its applications[19]. As increasing the contents of the mineralized collagen, the outflow volume decreased, and liquid/solid ratio needed to increase to maintain composite cements injectable, as shown in Table 1. The fluidity became weaker for the viscosity increased with the mineralized collagen concentration increasing. Therefore injectability can be improved with the increase of L/S ratio.

Table 1. The Prescription of Injectable Composite Paste

the mineralized collagen(%)	0	5	10	20
Liquid to solid ratio （ml/g）	0.5-0.7	0.5-0.7	0.6-0.8	0.8-1.0

3.3 Setting properties

Taking clinical application into account, an injectable bone material must be applied before it sets and setting time should not be too long after injected, so self-setting property is an important factor for the clinical use of injectable bone materials. Statistical analysis of the data showed the setting time of composite cements compounded by different ratio of the α-CSH, the CSD and the mineralized collagen in Fig. 2. Comparison between the composites with different contents of the mineralized collagen indicated that the setting time increased with increasing weight ratio of the mineralized collagen.However, comparison between the composites with different contents of CSD indicated that the setting time shorten with increasing weight ratio of CSD. Therefore, the mineralized collagen could weaken composite cement solidification properties and CSD had played a role in accelerating solidified[20]. CSD is not only the reactant of preparing CSH but also the final

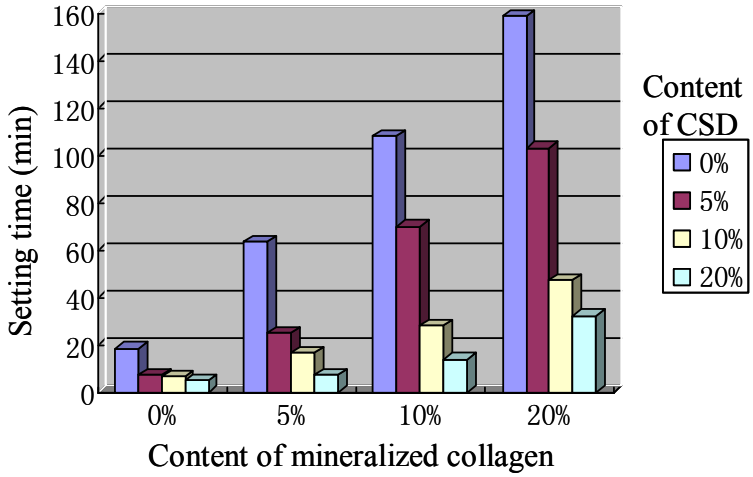

Fig.2.The setting time of the cements with with different composition(the L/S ratio were 0.6,0.6,0.7,0.9 respectively with the mineralized collagen concentration increasing)

Table 2. The setting time of the cements with with different composition (min)

	0%①	5%①	10%①	20%①
0%②	18.3±3.1	63.3±10.4	108.0±18.3	156.7±16.1
5%②	7.0±1.4	24.7±5.7	70.3±8.2	103.0±13.1
10%②	6.3±3.2	16.3±1.5	28.0±3.5	47.0±6.0
20%②	4.7±0.5	7.3±1.1	13.7±0.5	32.3±2.5

Note:①the content of mineralized collagen ,②the content of CSD.

reason can be that phase conversion from CSH to CSD is a hydration and recrystallization course of CSH crystal, and an appropriate amount of CSD crystal could be as initiator and offer recrystallization centre or site for CSH at the beginning of phase conversion. In the following research, further work will be performed to investigate the setting accelerating mechanism of CSD.

3.4 Mechanical test of the composite cements

The mechanical properties of the composite cements are important parameters to maintain the structure in the face of the compression from neighboring tissues[21]. Samples for mechanical properties test were shown in fig.3 and fig.4. In fig.3,the results indicated that the average compressive strength of the samples after setting ranged from about 4 to 12 MPa with the difference content of mineralized collagen, which are more than to the mechanical properties of cancellous bone. In fig.4,the results indicated that the average compressive modulus of the samples after setting ranged from about 300 to 700 MPa with the difference content of mineralized collagen. It

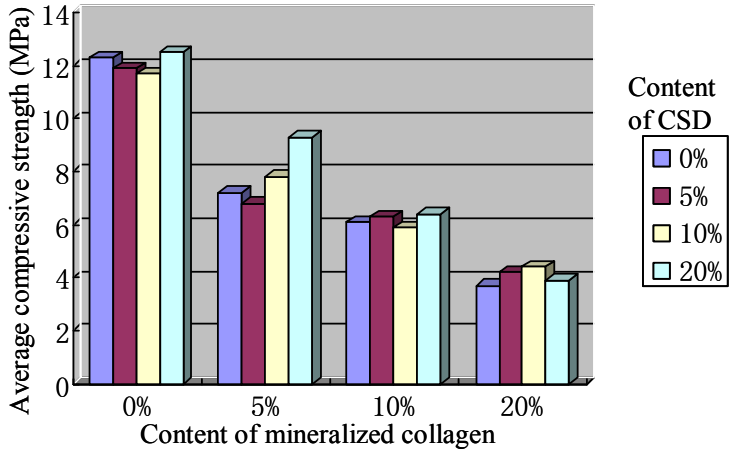

Fig.3 The average compressive strength of the cements with different content of mineralized collagen(the L/S ratio were 0.6,0.6,0.7,0.9 respectively with the mineralized collagen concentration increasing)

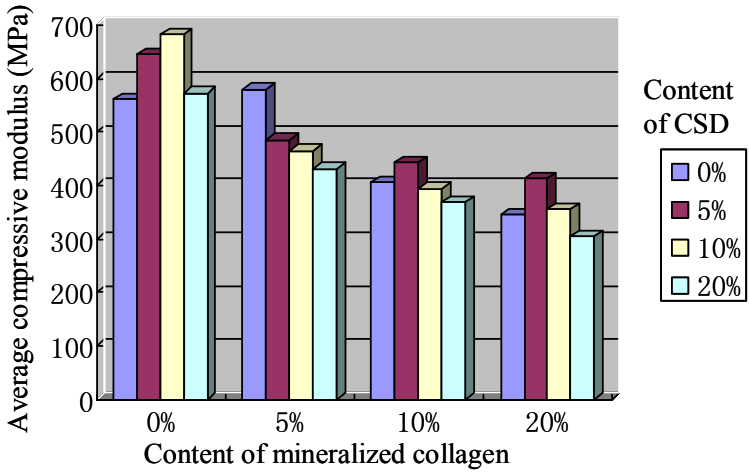

Fig.4 The average compressive modulus of the cements with different content of mineralized collagen(the L/S ratio were 0.6,0.6,0.7,0.9 respectively with the mineralized collagen concentration increasing)

can be seen that as the content of mineralized collagen increasing, the mechanical properties of the composite cements overall showed a decrease trend. Results also indicated that there was no significant difference between samples with various CSD content in the compressive behavior. All these indicated that CSD as setting accelerator has no significant effect on the compressive properties of samples because it is the final solidified product of CSH.

3.5 In Vivo Biomechanical Tests.

All specimens were formed intermediate vertebral burst fracture model, as shown in fig.5. From the X-ray anteroposterior (fig.5-A), the left pedicle was damaged and the height of the vertebral body reduce. From the X-ray lateral (fig.5-B),the intermediate vertebral appeared the bursting fractures. The micro-CT sagittal and axial (fig.5-C,D) could find the vertebral fracture block obviously and confirmed the formation of intermediate vertebral burst fracture. Therefore, through step-by-step drop-weight impact, we successfully prepared a spine burst fracture model. Compared with the previous model[22], our made smaller pre-injury in the vertebral to be closer to clinical reality. Figure 6 showed the imaging observation of intermediate vertebral after vertebroplasty by the composite cements. From the X-ray anteroposterior and lateral (fig.6-A,B) , vertebral body height restored, the fracture line disappeared. The result from the

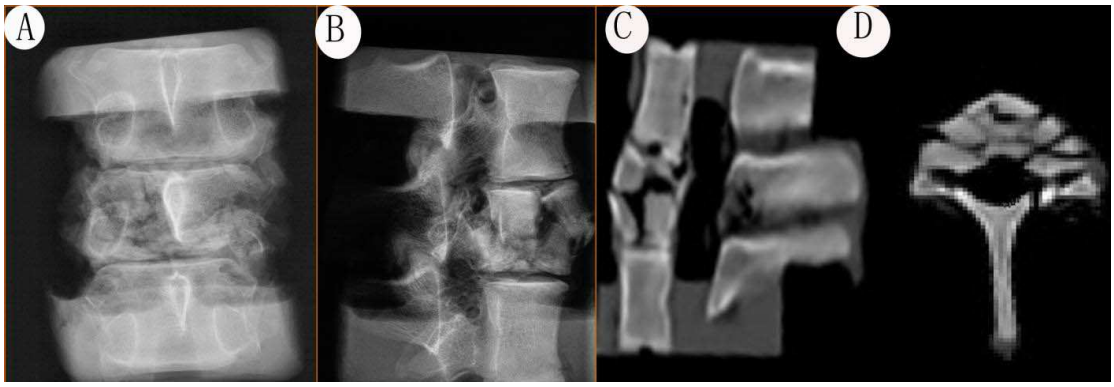

Fig.5. Imaging Observation of intermediate vertebral burst fracture(A:X-ray anteroposterior ,B: X-ray lateral; C: micro-CT sagittal; D: micro-CT axial)

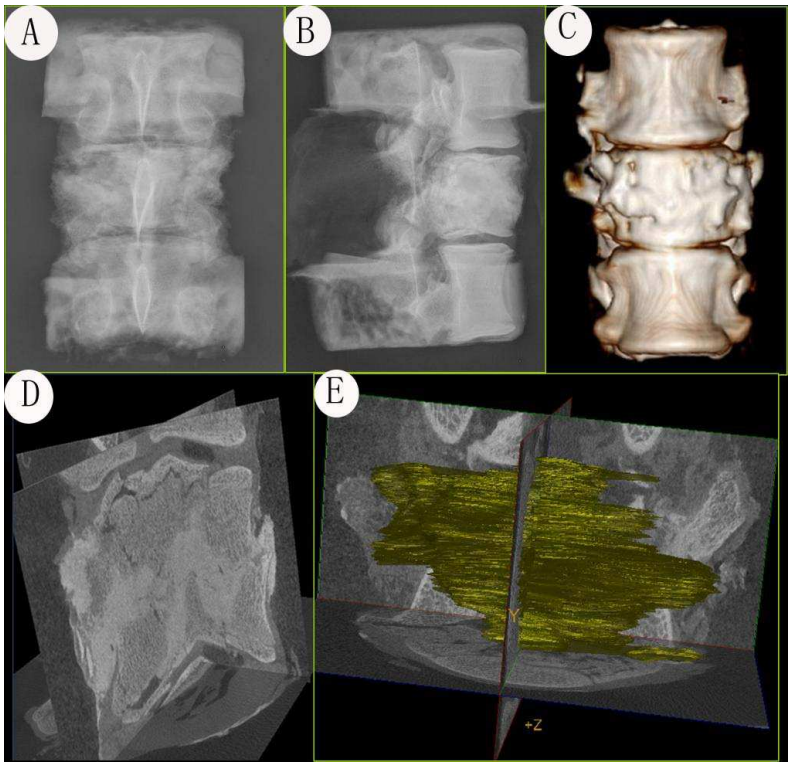

Fig.6. Imaging Observation of intermediate vertebral after vertebroplasty by the composite cements(A:X-ray anteroposterior ,B: X-ray lateral; C,D,E: CT three-dimensional reconstruction)

CT three-dimensional reconstruction (fig.6-C) confirmed the effect of vertebroplasty by the composite cements . The micro-CT sagittal and axial(fig.6-D) showed fracture gaps were fully filled with the composite cements. From the micro-CT three-dimensional reconstruction (fig.6-E), the composite cements were irregular shape in the vertebral body.There were statistically significant differences in the compressive strength ($P<0.01$) and the stiffness ($P=0.03<0.05$),as shown in Table.3. All these indicated that the composite cements were able to effectively repair the spinal burst fracture.

Table 3. Comparison of Compressive strength and Stiffness between two groups.

	Experimental group	Control group
Compressive strength	1200±423N	505±300N
Stiffness	235±134N/mm	36±25N/mm

Conclusion

In summary, we found that the compound of 10% of the mineralized collagen, 20% of the CSD, 70% of the α-CSH was ideal for composite cements. We made the vertebroplasty for porcine thoracolumbar burst fracture models, and verified the usefulness of the composite cements to treat the spinal burst fracture.

Acknowledgement

This research was supported by a grant (code #:50772132, 50830102) from the National Natural Science Foundation of People's Republic of China.

References

[1] Hench, L.L., and Polak, J.M. Third-generation biomedical materials. Science 295, 1014, 2002.
[2] Liu HY, Improvement on the performance of bone regeneration of calcium sulfate hemihydrate by adding mineralized collagen,Tissue Eng Part A, Jun 2010;16(6):2075-84.
[3] Keya Mao, The Preparation and Evaluation of the Combined Artificial Bone, Applied Mechanics and Materials Vol. 140 (2012) pp 1-6© (2012) Trans Tech Publications, Switzerland doi:10.4028/www.scientific.net/AMM.140.1
[4] Zhiguang Huan ,Self-setting properties and in vitro bioactivity of calcium sulfate hemihydrate–tricalcium silicate composite bone cements, Acta Biomaterialia,Volume 3, Issue 6, November 2007, 952-960.
[5] M. Bohner and G. Baroud, Injectability of calcium phosphate pastes. Biomaterials, 13 (2005), pp. 1553–1563
[6] W.S. Pietrzak, Calcium sulfate bone void filler: a review and a look ahead. J Craniofac Surg, 11 4 (2000), pp. 327–333.
[7] M. Nilsson, E. Fernandez, S. Sarda, L. Lidgren and J.A. Planell, Characterization of a novel calcium phosphate/sulphate bone cement. J Biomed Mater Res, 61 (2002), pp. 600–607
[8] Zhang,W., Liao, S.S., and Cui, F.Z. Hierarchical self-assembly of nano-fibrils in mineralized collagen. Chem Mat 15, 3221,2003.
[9] Li XM, Feng QL, Liu XH, Dong W, Cui FH. Collagen-based implants reinforced by chitin fibres in a goat shank bone defect model. Biomaterials 2006;27:1917–1923.
[10] Liao, S.S., Cui, F.Z., Zhang, W., and Feng, Q.L. Hierarchically biomimetic bone scaffold materials: nano-HA/collagen/PLA composite. J Biomed Mater Res , 2004,Part B 69B,158,.
[11] Li XM, Gao H, Uo M, Sato Y, Akasaka T, Feng QL, Cui FZ, Liu XH, Watari F. Effect of carbon nanotubes on cellular functions in vitro.J Biomed Mater Res Part A 2009;91:132–139.

[12] W.M.M. Heijnen and P. Hartman, Structural morphology of gypsum (CaSO4·2H2O), brushite (CaHPO4·2H2O) and pharmacolite (CaHAsO4·2H2O). J Cryst Growth, 108 (1991), pp. 290–300.
[13] I. Khairoun, M.G. Boltong, F.C.M. Driessens and J.A. Planell, Some factors controlling the injectability of calcium phosphate bone cements. J Mater Sci Mater Med, 9 (1998), pp. 425–428.
[14] Song HY, Rahman A, Lee BT. Fabrication of calcium phosphatecalcium sulfate injectable bone substitute using chitosan and citric acid. J Mater Sci Mater Med 2009;20:935–941.
[15] M. Bohner, New hydraulic cements based on α-tricalcium phosphate–calcium sulfate dihydrate mixtures, Biomaterials,Volume 25, Issue 4, February 2004, Pages 741-749
[16] M. Bohner and G. Baroud, Injectability of calcium phosphate pastes. Biomaterials, 13 (2005), pp. 1553–1563
[17] Lu WW, Bioactive bone cement as a principal fixture for spinal burst fracture: an in vitro biomechanical and morphologic study. Spine,2001 Dec 15;26(24):2684-90; discussion 2690-1
[18] Wilcox RK, A dynamic study of thoracolumbar burst fractures, J Bone Joint Surg Am. 2003 Nov;85-A(11):2184-9.
[19] J.S. Temenoff, A.G. Mikos, Biomaterials 21, 2405 (2000). doi:10.1016/S0142-9612(00)00108-3
[20] Lazary A, Balla B, Kosa JP, Bacsi K, Nagy Z, Takacs I, Varga PP,Speer G, Lakatos P. Effect of gypsum on proliferation and differentiation of MC3T3-E1 mouse osteoblastic cells. Biomaterials 2007;28:393–399.
[21] B.S. Kim, D.J. Mooney, Trends Biotechnol 16, 224 (1998). doi:10.1016/S0167-7799(98)01191-3
[22] W. W. Lu, PhD, Bioactive Bone Cement as a Principal Fixture for Spinal Burst Fracture, SPINE ,2001,Volume 26, Number 24, 2684–2691

doi:10.4028/www.scientific.net/AMM.161.113

Characterization and immunological evaluation of chitosan nanoparticles as adjuvants for bovine coronavirus N protein

Qingshen Sun[1,a], Jialing Zhang[1, b], Dequan Han[1,c], Yongbo Yang[1, d], Li Zhu[1,e] and Li Yu[2,f,*]

[1]Laboratory of Microbiology, College of Life Science, Heilongjiang University, Harbin 150080, Heilongjiang Province, China
[2]Division of Livestock Infectious Diseases, State Key Laboratory of Veterinary Biotechnology, Harbin Veterinary Research Institute, Chinese Academy of Agricultural Sciences, Harbin 150001, Heilongjiang Province, China
[a]sun19770928@yahoo.com.cn, [b]zjlwawa1101@126.com, [c]handequan2003@yahoo.com.cn, [d]yybt2001@163.com, [e]al198469327@126.com, [f]yuli1962@gmail.com (*Corresponding author)*

Keywords: chitosan nanoparticles; bovine coronavirus N protein; sustained release

Abstract. Chitosan nanoparticles (CNP) loaded with nucleocapsid protein of bovine coronavirus (BCV N) were prepared by ionic cross-linking method using sodium tripolyphosphate (TPP) as cross-linking agent. CNP loaded with BCV N protein was intramuscularly administered into Balb/c mice. Serum levels of anti-N protein IgG, IgM, and IgA antibodies were dynamically monitored by indirect ELISA method. Results showed that in the BCV N-loaded chitosan group, both IgA and IgG levels were found to increase significantly after the second immunization comparable to those of the Montanide ISA 206 groups. The IgM content in serum increased after the second immunization in the BCV N protein-loaded CNP group. These findings indicate that CNP can be used as adjuvant in veterinary vaccine field.

1 Introduction

Chitosan, α(1→4)-2-amino-2-deoxy-β-D-glucose (N-acetylglucosamine), is a deacetylated form of chitin and is gaining interest because it is biocompatible, biodegradable, non-toxic, and extremely moldable[1-4]. Chitosan also possesses many advantageous features, such as antibacterial, and antiviral activities, as well as the ability to promote tissue repair and stop bleeding [5,6]. Thus, chitosan has wide prospects in the field of biomedicine. For example, Han et al. [7] developed chitosan hydrogel for delivery of doxorubicin on the tumor tissue, which showed good anti-tumor effects.

Chitosan microspheres [8] and chitosan nanoparticle (CNP) [9] loaded with model drugs can attain good sustained release efficacy. In addition, adsorption of model drugs onto nanoparticle surface is also an option. Evidence exists that chitosan, as a novel adjuvant, can enhance antibody levels [10-12]. Therefore, chitosan shows a wide prospect of clinical applications. At present, the drugs enveloped by chitosan carriers include proteins [13,14], hydrophobic drugs [15], anti-cancer drugs [16], vaccines [17-19] and enzymes [20].

Bovine coronavirus (BCV) is one of the pathogens that lead to diarrheic disease of cattle [21]. The key to preventing diarrheic disease caused by BCV is to stimulate the formation of specific antibodies *in vivo*. A newborn calf can be passively immunized *via* colostrums and milk. The level of BCV antibody in the milk is highest during pregnancy and it is rapidly decreased thereafter. In newborn calves, the immunoglobulin adsorbed is secreted into the enteric cavity and adheres to the mucosa of the small intestine, which prolongs the time of passive immunization. Natural infection of BCV in the newborn calves can produce active immunization, but diarrheic disease occurs easily after the decreases of passive immunization and before the formation of active immunization. Therefore, how to prolong the residence time of antibodies *in vivo* is currently a chanllenge for veterinary medical scholars. Coronavirus nucleocapsid protein is the protein-nucleic acid complex of BCV. The nucleocapsid protein of BCV (BCV N protein) appears to be highly conservative in the carboxy-terminus and also exhibits strong immunogenicity, so it can serve as a diagnostic antigen for BCV.

In our previous study, the NO. 487-1287 bases at 3′ side of N protein from bovine coronavirus DB2 strain were synthesized and expressed in *E. Coli* [17]. The present study prepared CNPs by an ionic cross-linking method using sodium tripolyphosphate (TPP) as a cross-linking agent, immunized BALB/c mice after BCV N protein adsorption to the CNP surface, and performed immunological evaluation by indirect ELISA. These results provide experimental foundation for animal vaccine research and clinical application.

2. Materials and methods

2.1. Materials and instruments

Chitosan (deacetylation degree = 94%, Mv = 400 000, purity≥95%) was purchased from Sinopharm Chemical Reagent Co., Ltd., China. TPP, an analytical reagent, was purchased from Tianjin Dongli District Tianda Chemical instruments, Tianjin, China. BCV N protein (MW=39.48ku) was prepared as before with expression yield at 50.5%[17]. The Bradford protein assay kit (P1510) was purchased from Applygen Technologies Inc., China. Horseradish peroxidase (HRP)-conjugated goat anti-mouse IgG, IgA, and IgM antibodies were purchased from Sigma, Louis, MO, USA. The other regents used in this study were of analytical grade.

2.2. Preparation of CNPs

CNPs were prepared by an ionic cross-linking method using TPP as a cross-linking agent. Chitosan was dissolved in 2% (v/v) acetic acid solution to prepare a 2 mg/mL chitosan/acetic acid solution. Following adjustment of pH to 4.8, the mixture was centrifuged at 4 000 r/min for 5 min to discard non-dissolved chitosan. TPP aqueous solution with TPP concentrations at 0.5, 0.75, 1.0 and 1.25mg/mL was prepared, repectively. Under stirring at 600 r/min, 14 mL TPP water solution was slowly dropped into 35 mL chitosan/acetic acid solution and the reaction was continued for 1 hour at room temperature. The resultant CNP suspension was preserved at 4 °C in an airtight container for later use.

2.3. Preparation of BCV N protein-loaded CNPs

4 mL CNP suspension with optimal TPP concentration was placed in a 6-well plate. After the addition of 2 mL BCV N protein solution (diluted with pH 4.8 PBS to 1.0mg/mL), the 6-well plate was decolorized at 4 °C on a shaking table (100 r/m) for 24 hours, and then BCV N protein-loaded CNPs were acquired.

2.4. Characterization of different CNPs

Particle size analysis: CNP suspension prepared by four concentrations of TPP was placed into the sample dish for particle size analysis using a Zeta PALS-90n granulometer (Brookhaven Instruments Corp., New York, USA.).

Fourier transform infrared (FTIR) spectroscopy analysis: KBr pellets of chitosan, CNP and TPP were prepared. Group changes in surface structure of different materials were analyzed by FTIR spectroscopy (spectrum one, PerkinElmer Inc., Waltham, MA, USA).

2.5. Adsorption efficiency of CNPs to BCV N protein

The standard curve was plotted as follows: 2 mg/mL BSA in PBS at pH7.4 was prepared accurately as stock solution, then the solution was serially diluted to 1.000, 0.750, 0.500, 0.250, 0.125, 0.0625 and 0.03125 mg/mL. Bradford protein assay kit (P1510) was used to determine the OD_{595} values versus BSA concentrations according to the manufacturer`s protocol. The linear regression equation was determined as follows:

$A= 0.6913C+0.0205$; $R^2=0.9934$.

Where A and C represent the adsorbance value at OD_{595} and the BSA concentration (mg/mL), respectively.

For BCV N-loaded CNP, 1 mL BCV N-loaded CNP suspension was centrifuged at 20 000 r/min at 4 °C. The BCV N concentration in the supernatant was determined using a Bradford protein assay kit (5×). The adsorption efficiency of BCV N protein to CNPs was calculated according to the regression equation mentioned above.

2.6. In vivo tests

Animal grouping Twenty-four healthy female Balb/c mouse, aged 6-8 weeks, purchased from the Laboratory Animal Center, Harbin Veterinary Research Institute, were acclimatized at 15–20 °C for 1 week before subsequent tests. The mouse were randomly divided into four groups: BCV N-loaded CNP group (group 1), BCV N protein emulsified in Montanide ISA 206 (Seppic, Paris, France) group (group 2), BCV N naked protein group (group 3, positive control), and CNP group in which the mouse were administered CNP suspension only (group 4, negative control).

Antigen preparation For group 1, the antigen was prepared as described in 2.3. For the Montanide ISA 206 group, the BCV N protein was emulsified in Montanide ISA 206 by peptizing using 2.5 mL syringe repeatedly.

Immunization and serum preparation Each mouse was injected at multiple points in lnterfemus. The dose in all groups was calculated based on BCV N amount, i.e., 50 μg BCV N per mouse. The immunizations were boosted once at 2 week interval. The serum was isolated from blood collected from tail bleeds at 0, 10, 20, 28, 36, 43, and 53 days after first immunization, and preserved at –70 °C for use.

Immunoglobulin measurement by ELISA Serum levels of IgG, IgM and IgA were determined by indirect ELISA as described previously [17] to investigate the dynamic changes of immune factors in each group. Briefly, the purified BCV N antigen was diluted to working concentration using pH 9.6 carbonate buffer, and added into 96-well corning plates at 100 μL per well. The plates were coated at 4℃ overnight, and then washed using 1:1000 PBST (PBS+Tween20) 4 times. 200 μL 5% skimmed milk was added to each well as blocking fluid and blocked at 37℃ for 1h; then washed the plate as above. All the serum was diluted at 1:300 using PBST, and then 100 μL diluted sample was added to each well. The plates were incubated at 37℃ for 1h. The HRP-labeled anti-mouse IgG, IgM and IgA were diluted at 1:4000 and added to each well, with 100 μL per well. The incubation and washing process were the same as above. Then 60 μL TMB substrates were added, and incubated at room temperature for 10 min. Finally, 60 μL terminate solution was added to each well and the absorbance at OD_{450} nm were measured on ELISA reader (Versa MAX PLUS 384, Molecular Devices Corporation, Sunnyvale, California, USA).

2.7. Statistical analysis

All the tests were repeated at least in triplicates, and the results were expressed as $\bar{X} \pm$ Std.

3. Results and discussion

3.1. Effects of TPP concentrations on CNPs preparation

Chitosan is a kind of cationic polymer, which can interact with TPP to form polyelectrolytes through electrostatic interactions. Therefore, in this study, the electrostatic interactions-based ionic cross-linking method was used to prepare the chitosan nanoparticles. Fig. 1 showed the effects of TPP concentrations on the size distribution of chitosan nanoparticles. With the increase of TPP concentrations, the transmittance of the chitosan nano-emulsions decreased (data not shown). In the preparation of chitosan nanoparticles through ionic cross-linking process, the electrostatic interactions among the negative charges from the phosphate groups of TPP and the positive charges from the amino groups of chitosan caused the inter- or inner-molecular cross-linking, thus formed the nanoparticles. Under lower TPP concentration, the less negative charges leads to partial cross-linking of chitosan molecules, therefore, the chitosan solution was clear. Under higher TPP concentration, the aggregation process may cause the production of larger particles. In this study, the TPP concentrations ranged from 0.5mg/mL to 1.25mg/mL. At four TPP concentrations, the sizes of the CNP nanoparticles were 14.128±0.026, 29.132±0.032, 39.333±0.104 and 70.284±0.063nm, respectively. When the TPP concentration was 1.0mg/mL, the polydispersity of size distribution was the least as shown in Fig. 1. Therefore, TPP concentration at 1.0mg/mL was selected for the following study.

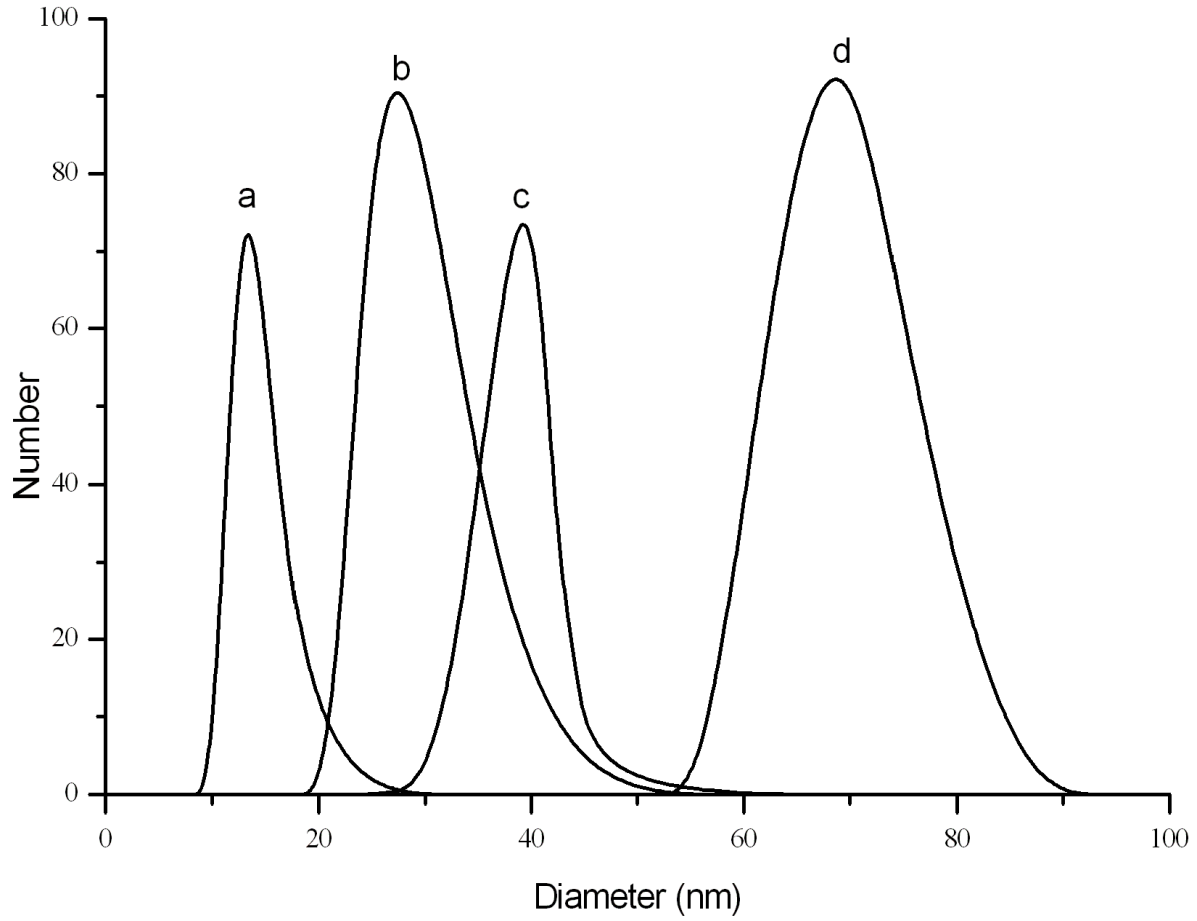

Fig. 1. Particle size distribution of chitosan nanoparticles prepared with TPP concentration at a) 0.5 mg/mL; b) 0.75 mg/mL; c) 1.0 mg/mL and d) 1.25 mg/mL

3.2. FTIR analysis of CNPs

FTIR spectroscopy analysis on chitosan, CNPs and TPP was shown in Fig. 2. All samples showed an adsorption peak in the 3200-3500 cm^{-1} region, which reflected intermolecular stretching vibration of hydrogen bonds (O-H). The adsorption peak of TPP was weakest, and that of CNP was wider when compared with chitosan. Chitosan molecules showed the bending vibration of N-H in the 1638 cm^{-1} and 1590 cm^{-1}.

3.3. In vivo immunological effects

In our previous studies, we have purified and characterized the BCV N protein [17]. In this study, the CNPs loaded with BCV N protein were injected to Balb/c mouse via intramuscular route. According to the standard curve, the concentration of BCV N was 15.31 mg/mL, and CNP had a (73.26±1.32)% adsorption rate to BCV N.

Serum levels of IgG, IgM and IgA in different groups at different periods were determined by indirect ELISA (Fig. 3-5). For IgG detection, the OD_{450} value lower than 0.20 was set as negative. Based on the IgG levels detected, CNPs exhibited strong sustained release effects on BCV N protein, indicating that the N protein was maintained at a certain level for a long time in mice. IgG was not detectable in the CNP group, demonstrating that chitosan cannot stimulate the production of IgG in mice. In the BCV N group, IgG was detected after, but not prior to, the second immunization; but IgG levels stayed at a very low level, peaking after 43 days, followed by a significant decline, and tended to be at a level similar to the CNP group after 53 days. In the BCV N-loaded CNP and Montanide ISA 206 groups, IgG was not detectable after the first immunization, but it was significantly increased after the second immunization, reaching a very high level 1 week after the second immunization (i.e., at 28 days). This level was maintained up to 53 days. In addition, IgG levels were similar between the

BCV N-loaded CNP and Montanide ISA 206 groups, following similar profiles with time. These findings indicated that CNP exhibits sustained release potential and immuno-enhancing effects similar to Montanide ISA 206.

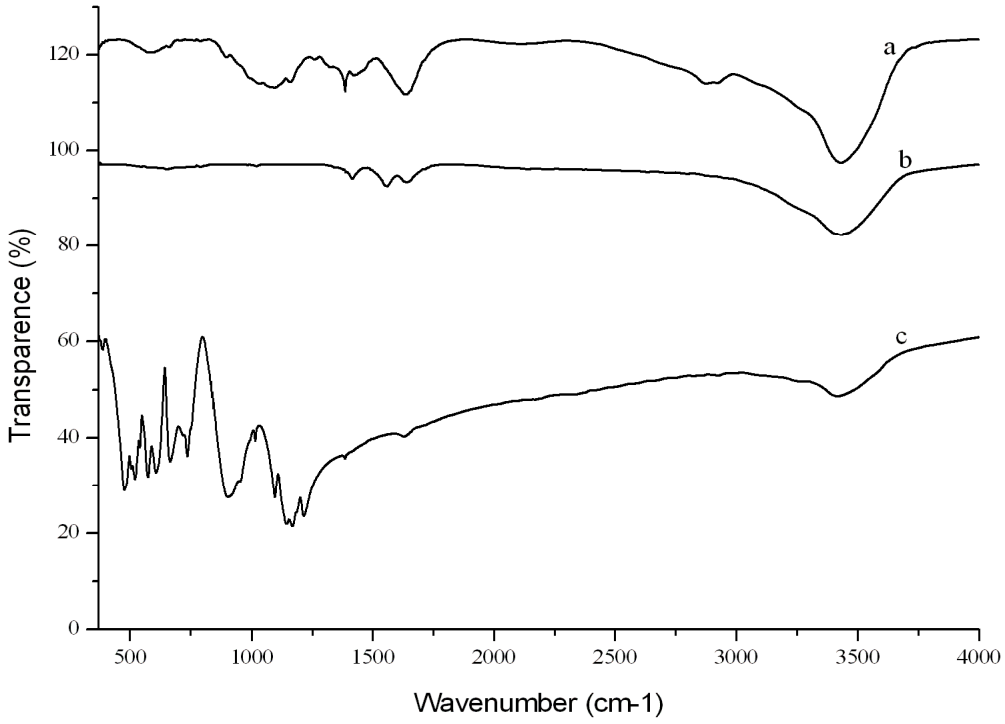

Fig. 2. FTIR spectroscopy analysis. (A) Chitosan; (B) chitosan nanoparticle (CNP); (C) sodium tripolyphosphate

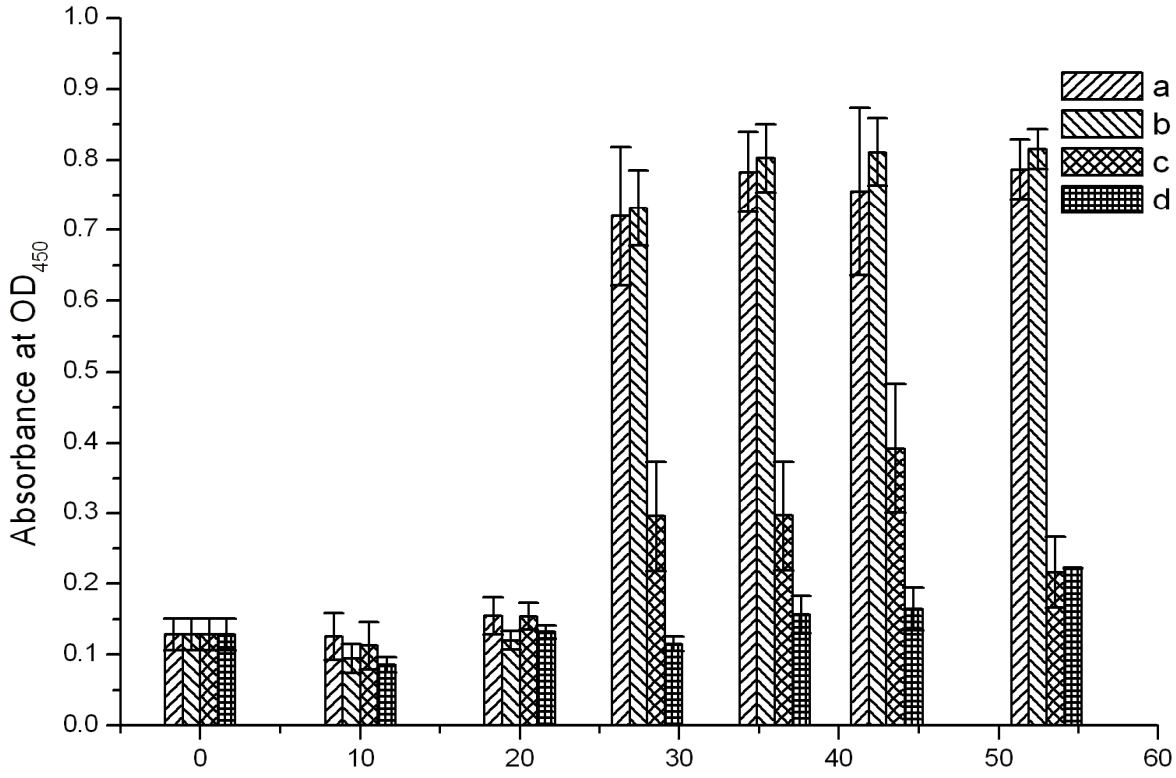

Fig. 3. Serum IgG level in mouse intramuscular injection with different sample: a, b, c, d represent BCV N-loaded CNP, Montanide ISA 206, BCV N, and CNP groups, respectively.

In the IgM detection, the OD value lower than 0.4 was considered as negative. IgM was not detectable in the CNP group. In the BCV N group, IgM was detected after the first immunization, but it returned to the initial level after 20 days, and was only slightly increased after the second immunization, peaking at 43 days. In both the Montanide ISA 206 group and BCV N-loaded CNP group, IgM was not detected after the first immunization, but it was detected after the second immunization and kept higher levels thereafter, compared with that of the other two groups. IgM has been used in diagnosis as it is the earlier emerged antibody after pathogen invasion. In this study, the naked BCV N can cause IgM production at 10d after the first immunization and disappeared quickly, while the IgM tendency in the Montanide ISA 206 group and BCV N-loaded CNP group showed sustained-release profiles of these two kinds of adjuvant to the antigen.

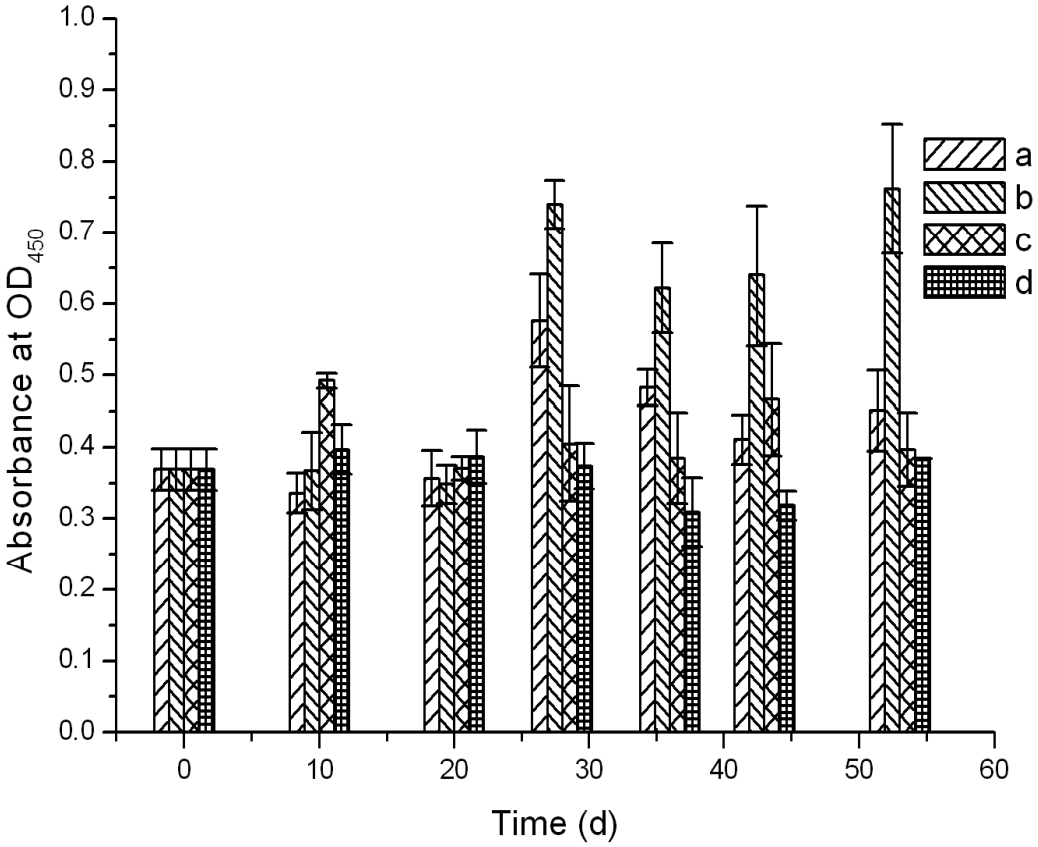

Fig. 4. Serum IgM level in mouse intramuscular injection with different sample: a, b, c, d represent BCV N-loaded CNP, Montanide ISA 206, BCV N, and CNP groups, respectively.

The OD_{450} value lower than 0.25 was set as negative for IgA level. IgA was not detectable in the CNP group. In the BCV N group, the IgA level was detected after the first immunization; this was maintained after the second immunization, peaking at 43 days. In the Montanide ISA 206 group, IgA was not detected after the first immunization, but it was detected after the second immunization and stayed at a very high level thereafter. The BCV N-loaded CNP group showed a similar tendency to the Montanide ISA 206 group, with the exception that the highest IgA level occurred at 36 days.

IgA participates in the immunity of mucous membranes and its level reflects the immune state of the mucosal membrane. In this study, in the CNP and BCV N groups, IgA levels stayed very low level during the whole experimental period. In contrast, in the Montanide ISA 206 and BCV N-loaded CNP groups, serum levels of IgA increased after the second immunization. Evidence exists that suggests chitosan has the potential to break the tight junction of epithelial cells [22, 23]. For this

reason, antigen molecules can be induced to enter into the epithelial inner region to stimulate the immunization of mucous membranes. These results demonstrated that mucous membrane immune pharmaceutics using CNP as an adjuvant are of good clinical feasibility.

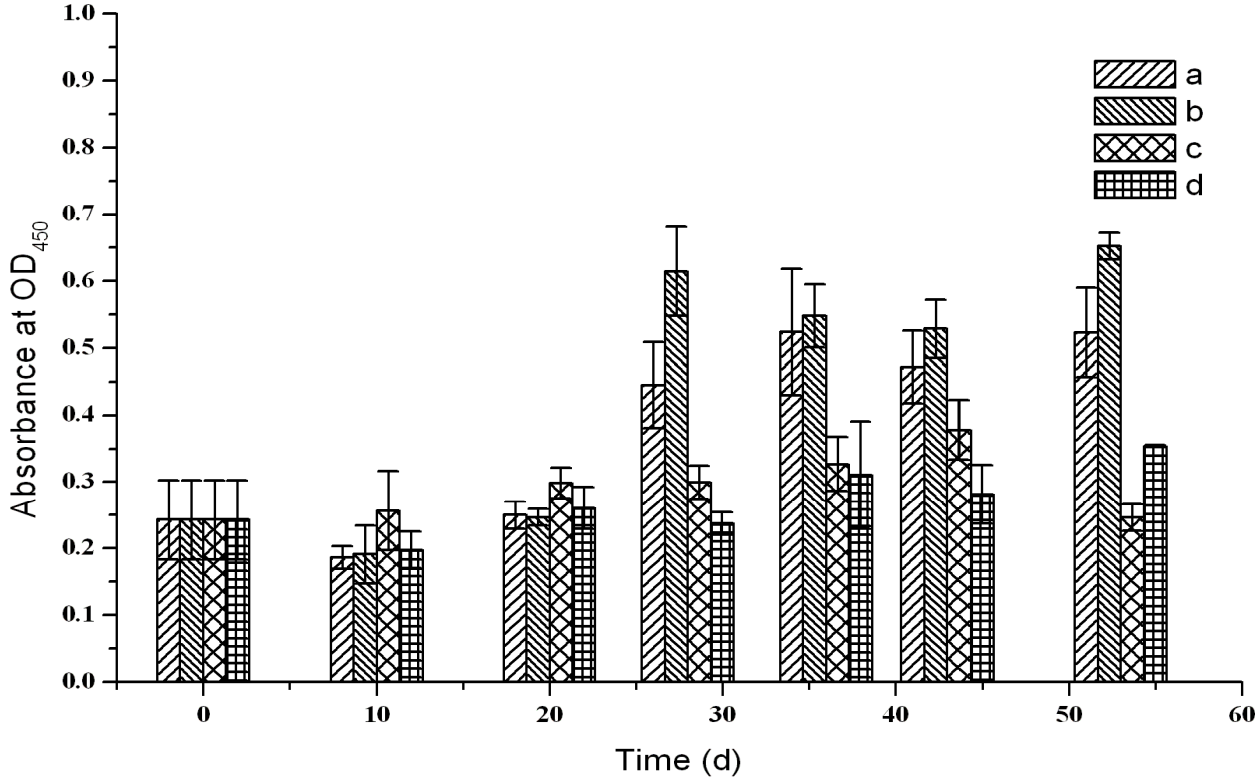

Fig. 5. Serum IgA level in mouse intramuscular injection with different sample: a, b, c, d represent BCV N-loaded CNP, Montanide ISA 206, BCV N, and CNP groups, respectively.: a, b, c, d represent BCV N-loaded CNP, Montanide ISA 206, BCV N, and CNP groups, respectively.

4. Conclusion

Granular CNPs of good disperse, with a particle size of 39.333±0.104 nm, were prepared by an ionic cross-linking method. The adsorption rate of BCV N-loaded CNP was (73.26±1.32)%%. *In vivo* immunological evaluation revealed that CNP can greatly increase serum levels of IgG, IgM and IgA levels in mice after immunization and that CNP has no immunogenicity. Therefore, CNP can be used as a novel adjuvant for clinical study.

Acknowledgements

We are grateful for financial support from the National Natural Science Foundation of China (No. 31000773).

References

[1] A.J. Varma, S.V. Deshpande, J.F. Kennedy, Metal complexation by chitosan and its derivatives, Carbohydr. Polym. 55(2004)77-93.
[2] N.V.Majeti, R. Kumar, A review of chitin and chitosan applications, React. Funct. Polym. 46 (2000)1-27.
[3] M.T. Yen, J.H. Yang, J.L. Mau, Physicochemical characterization of chitin and chitosan from crab shells, Carbohydr. Polym. 75(2009)15-21.
[4] M. Rinaudo, Chitin and chitosan: Properties and applications, Prog Polym Sci. 31 (2006)603-632.
[5] A. Di Martino, M. Sittinger, M.V. Risbud, Chitosan: a versatile biopolymer for orthopaedic tissue-engineering, Biomaterials 26 (2005)5983-5990.
[6] C. Zhang, Y. Cheng, G.W. Qu, Preparation and characterization of galactosylated chitosan coated BSA microspheres containing 5-fluorouracil, Carbohydr. Polym. 72(2008)390-397.

[7] H.D. Han, C.K. Song, Y.S. Park, K.H. Noh, J.H. Kim, T. Hwang, T.W. Kim, B.C.Shin, A chitosan hydrogel-based cancer drug delivery system exhibits synergistic antitumor effects by combining with a vaccinia viral vaccine, Int. J. Pharm. 350(2008)27-34.
[8] Y.B. Ge, D.W. Chen, L.P. Xie, R.Q. Zhang, Optimized preparation of daidzein-loaded chitosan microspheres and in vivo evaluation after intramuscular injection in rats, Int. J. Pharm. 338(2007)142-151.
[9] Y. Aktaş, K. Andrieux, M.J. Alonso, P. Calvo, R.N. Gürsoy, P. Couvreur, Y. Capan, Preparation and in vitro evaluation of chitosan nanoparticles containing a caspase inhibitor, Int. J. Pharm. 298(2005)378-383.
[10] M.L. Kang, S.G. Kang, H.L. Jiang, S.W. Shin, D.Y. Lee, J.M. Ahn, N. Rayamahji, I.K. Park, S.J. Shin, C.S. Cho, H.S. Yoo, In vivo induction of mucosal immune responses by intranasal administration of chitosan microspheres containing Bordetella bronchiseptica DNT, Eur. J. Pharm. Biopharm. 63(2006)215-220.
[11] D.A. Zaharoff, C.J. Rogers, K.W. Hance, J. Schlom, J.W. Greiner, Chitosan solution enhances both humoral and cell-mediated immune responses to subcutaneous vaccination, Vaccine,25 (2007)2085-2094.
[12] Y. Yang, J. Chen, H. Li, Y. Wang, Z. Xie, M. Wu, H. Zhang, Z. Zhao, Q. Chen, M. Fu, K. Wu, C. Chi, H. Wang, R. Gao, Porcine interleukin-2 gene encapsulated in chitosan nanoparticles enhances immune response of mice to piglet paratyphoid vaccine, Comp. Immunol. Microbiol. Infect. Dis. 30(2007)19-32.
[13] G.D. Kang, S.C. Song, Effect of chitosan on the release of protein from thermosensitive poly (organophosphazene) hydrogels, Int. J. Pharm. 349(2008)188-195.
[14] Kofuji, K., Murata, Y., Kawashima, S., 2005. Sustained insulin release with biodegradation of chitosan gel beads prepared by copper ions. Int. J. Pharm. 303(1-2),95-103.
[15] K.M. Park, J.W. Bae, Y.K. Joung, J.W. Shin, K.D. Park, Nanoaggregate of thermosensitive chitosan-Pluronic for sustained release of hydrophobic drug, Colloids Surf. B: Biointerfaces 63(2008)1-6.
[16] P. Lim Soo, J. Cho, J. Grant, E. Ho, M. Piquette-Miller, C. Allen, Drug release mechanism of paclitaxel from a chitosan–lipid implant system: Effect of swelling, degradation and morphology, Eur. J. Pharm. Biopharm. 69(2008)149-157.
[17] Q.S. Sun, X. Li, X.Q. Che, J.T. Chang, Y.B. Yang, L. Yu. Evaluation on the immune efficiency of bovine coronavirus N protein-loaded chitosan microsphere[J]. Chinese J. Prev. Vet. Med. 31(2009)882-886.
[18] H. Zhang, C. Cheng, M. Zheng, J.L. Chen, M.J. Meng, Z.Z. Zhao, Q. Chen, Z. Xie, J.L. Li, Y. Yang, Y. Shen, H.N. Wang, Z.Z. Wang, R. Gao, Enhancement of immunity to an *Escherichia coli* vaccine in mice orally inoculated with a fusion gene encoding porcine interleukin 4 and 6, Vaccine,25(2007)7094-7101.
[19] E. Gavini, A.B. Hegge, G. Rassu, V. Sanna, C. Testa, G. Pirisino, J. Karlsen, P. Giunchedi, Nasal administration of Carbamazepine using chitosan microspheres: In vitro/in vivo studies, Int. J. Pharm. 307(2006)9-15.
[20] D.S. Jiang, S.Y. Long, J. Huang, H.Y. Xiao, J.Y. Zhou, Immobilization of laccase on magnetic chitosan microspheres and study on its enzymic properties, Wei Sheng Wu Xue Bao 45(2005)630-633.
[21] Y. Lin, X. Shen, R.F. Yang, Y.X. Li, Y.Y. Ji, Y.Y. He, M.D. Shi, W. Lu, T.L. Shi, J. Wang, H.X. Wang, H.L. Jiang, J.H. Shen, Y.H. Xie, Y. Wang, G. Pei, B.F. Shen, J.R. Wu, B. Sun, dentification of an epitope of SARS-coronavirus nucleocapsid protein, Cell Res. 13(2003)141-145.
[22] S. Chelladurai, M. Mishra, B. Mishra, Design and evaluation of bioadhesive in-situ nasal gel of ketorolac tromethamine, Chem. Pharm. Bull (Tokyo). 56(2008)1596-1599.
[23] E. Hagesaether, M. Hiorth, S.A. Sande, Mucoadhesion and drug permeability of free mixed films of pectin and chitosan: an in vitro and ex vivo study, Eur. J. Pharm. Biopharm. 71(2009)325-331.

doi:10.4028/www.scientific.net/AMM.161.121

Synthesis of Hole-transporting Materials Containing Triarylamine and Its Properties

Wenzheng Gao [1,a], Xianggao Li [1,b] and Shirong Wang [1,c]

[1]School of Chemical Engineering and Technology, Tianjin University, Tianjin 300072, China

[a]gaowenzheng1026@126.com,[b]lixianggao@hotmail.com(corresponding author),
[c]wangshirong@tju.edu.cn

Key words: Hole-transport materials; Triphenylamine; Synthesis; Performance

Abstract. Two hole-transporting materials containing triphenylamine unit, 4-(4-(di-p-tolylamino)styryl)-N,N-di-p-tolylbenzenamine (TM 1) and 4-(4-(4-(di-p-tolylamino)styryl) styryl)-N,N-di-p-tolylbenzenamine(TM 2), have been designed and synthesized in this paper, which using conjugated bonds as the bridge to connect two molecules of triphenylamine. The optical spectrum, thermo-stabilization and electrochemical properties of two compounds were studied. The results show that these compounds have blue emission, proper HOMO levels and high thermal stability. Furthermore, EL devices with the configuration of ITO/HTL/Alq_3/Al show the activating voltages are 11V for TM 1 and 5.5V for TM 2, respectively. The maximal luminancce efficiencies are 1.135 cd/A for TM 1 and 2.068 cd/A for TM 2, respectively. The difference of EL performance indicates that TM 2 possessing better hole-transporting performance than that of TM 1.

1. Introduction

Organic Electroluminescence was known by professor Pope in 1963[1], they Observed photoluminescence when they put thousands of volt of voltage on the presence of anthracene crystal. However, this phenomenon didn't get enough attention for excessive voltage and badly luminous efficiency. Intense research activity started in the late 1980s after the development of the multilayered cell structure by Tang and Vanslyke[2], it can keep the hole and electron limited in the interface between the Hole-transport Layer and Electron-transport Layer, then carrier recombinated and exciton formated. It can prominently improve the performance of device. It's commercial potential which reflected in low-driving voltage and high luminance grabbed the world's attention. Since then, OLEDs research enter into a rapid development era.

Since found that by triarylamine as hole-transport layer, can dramatically improve the EL efficiency and working stability of device[3], most of the new hole-transporting materials contain part of the group of triarylamine. In this paper, we synthesized two compounds by the combination of triphenylamine units connected by different bridge bonds. It was expected to obtain hole-transporting materials with excellent performance.

2．Experimental

2.1 Measurement technology

All solvents and chemicals were reagent grade and purified before using. Nuclear magnetic resonance (NMR) spectra were recorded on a INOVA 500MHZ spectrometer. All chemical shifts are reported relative to tetramethylsilane (TMS) at 0.0 ppm. Infrared radiation(IR) spectra were

collected by NICOLET380 sensor. Molecular weight of compounds were anlynisd by high resolution mass spectrum(HRMS) through Bruker MicrOTOF-QII mass spectrometer. UV–vis and fluorescence spectra were collected with a Thermo Spectronic HeλIOSγ scanning spectrometer and a Perkin Elmer LS 50B luminescence spectrometer, respectively. T_g of the sythesized compounds was determined by differential scanning calorimetry(DSC) on a TA Q20 thermal analyzer. Cyclic Voltammetry (CV) was carried out on an IM6e electrochemistry workstation with a three-electrode cell. Double-layer OLEDs were fabricated with the structure of ITO/HTL(50 nm)/Alq_3(50 nm)/Al, the L-V and J-V characteristics were measeured with Spectrascan PR 650 photometer and Keithley485 under ambient condition.

2.2 Synthesis of compounds

2.2.1 4-(4-(di-p-tolylamino)styryl)-N,N-di-p-tolylbenzenamine

The target molecular is synthesized by mcmurry reaction. Magnesium metal (0.48g, 0.02mol) was washed with diluted hydrochloric acid to remove oxidate and was added to a stirred slurry of $TiCl_4$ (3.83g, 0.02mol) in 60mL of dry tetrahydrofuran(THF) at room temperature under an N_2 atmosphere, after refluxing for 3h, the black mixture was cooled and 4-(di-p-tolylamino)benzaldehyde (0.6g, 0.02mol) was added. After a further sturred 8h, the reaction was then quenched by adding 40mL of 2M hydrochloric acid, and the reaction mixture was extracted three times with 10mL of CH_2Cl_2, the combined organic layers were dried over $MgSO_4$, and the solvent was evaporated and the residues were chromatographed on a silica gel column (hexamethylene: ethylacetate=30:1 as eluent) to give bright yellow brittle microcrystals (TM 1, 72.2%), mp: 272~274 ℃. IR (ν/cm^{-1}) 3018, 2910, 1610, 1506, 1320, 814; ^{1}HNMR ($CDCl_3$, 500MHz) δ2.324 (s, 12H, CH_3), 6.915 (s, 2H, CH=CH), 6.982-7.019 (m, 12H, PhH), 7.066-7.082 (d, 8H, PhH), 7.315-7.333 (d, 4H, PhH); MS M/z(%) 570.2 (M^+, 100).

2.2.2 4-(4-(4-(di-p-tolylamino)styryl)styryl)-N,N-di-p-tolylbenzenamine

The preparation of the target molecular are sketched in wittig reaction, intermediate compounds were synthesized according to previous literatures[4-6]. 4-[N,N-di(4-tolyl)-amino]benzyl(triphenyl)phosphonium bromide(2g, 3mmol) and terephthalaldehyde (0.19g, 1.5mmol) were dissolved in dry THF, The reaction system was cooled to 0 ℃ and then potassium tert-butoxide (0.72g, 6mmol) in dry THF was added dropwise to the solution as catalyst under stirring, and then the mixture was stirred in room tempreture for 8h until terephthalaldehyde was consumed completely monitored by thin-layer chromatography. THF was removed at reduced pressure and poured into water and neutralized with dilute HCl and then extracted with dichloromethane. TM 2 was obtained as a pure E stereoisomer after treatment of the Z/E mixture resulting from the wittig reaction with a catalytic amount of iodine under refluxing for 6h in THF, then remanent iodine were removed by pouring into sodium hydroxide solution(Wt=10%,100mL) and stirred for 1h. After extracte with dichloromethane, the solvent was removed at reduced pressure and the residues were chromatographed on a silica gel column (hexamethylene: ethyl acetate=20:1 as eluent) to give bright yellow brittle microcrystals (TM 2, 71%). mp: 223~224 ℃. IR(ν/cm^{-1}) 3026, 1600, 1510, 1320, 814; ^{1}HNMR($CDCl_3$, 500MHz) δ2.330 (s, 12H, CH_3), 6.984-7.042 (m, 12H, PhH) 7.075-7.092 (d, 8H, PhH) 7.349-7.367 (d, 4H, CH=CH) 7.464 (s, 4H, PhH); MS M/z(%): 672.9 (M^+, 100).

3. Results and discussion

3.1 Optical properties

Fig. 1 shows the UV-vis absorption and photoluminescence emission spectra of TM 1 and TM 2 in the 10^{-5} mol/L THF, respectively. The compounds show absorption peaks at 302&394 nm for TM 1 and 305&418 nm for TM 2, which are ascribed to the absorption of the n-π^* transition of the triphenylamine moiety and the intramolecular charge transfer of π-π^*, respectively[7]; Relative to TM 1, the maximum absorption peak in solution of TM 2 is red-shift 24 nm, This shift originates from the extension of the conjugated length, and the much better planarity of the whole molecule because the introduction of phenyl.

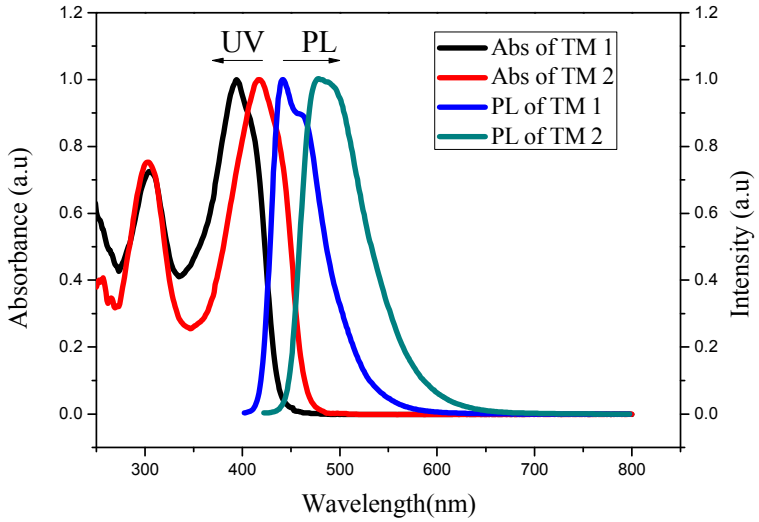

Fig. 1. UV-vis absporption and PL spectra of TM 1 and TM 2

From the spectrum of photoluminescence, we find that the emission wavelength of TM 2 is red-shift 39 nm compared to TM 1, because the expansion of π-π conjugate can make the emission peak of fluorescence move to the range of red light. Actually, we can get the difference contract between the molecular structure. TM 2 have much larger area of conjugate band, better rigidity plane structure, so that the delocalized electron can be excitated much easy, and fluorescent light could be emission with ease. Whereas with TM 1, the structure of molecular accumulate tight excessively, the coplanarity of whole molecule have been destroyed, intensity of fluorescent weakened .

3.2 Thermal properties

When the materials were made after the device, the organic film within the device may type into a part of crystalline state by non-crystalline amorphous in long working-time, make some changes of the physical properties, result in the life-time of the device declined.[8] So the glass transition temperature is one of important index as hole-transporting materials stability. Improve the glass transition temperature of the hole-transport materials is currently an important direction. In this paper, we get the Tg of two compounds through the procedure which heat the materials ramp to 300℃ at a rate of 10℃/min, then sudden cold to 40℃, at last heat up to 300℃ again at a heat-up rate of 20℃/min quickly.

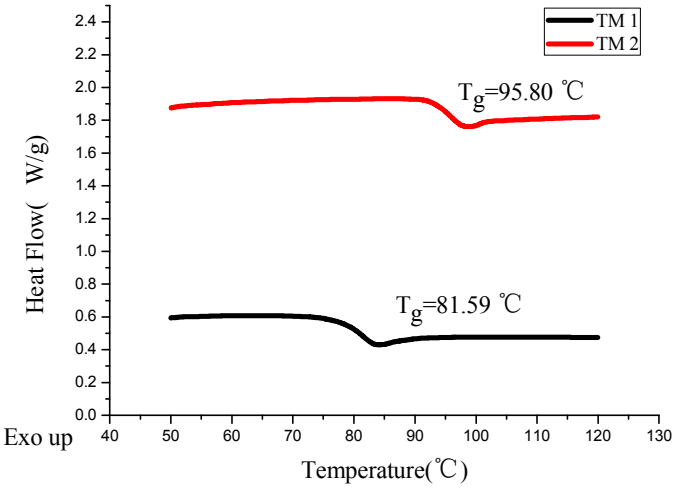

Fig.2 TG curves of TM 1 and TM 2

As shown in Fig. 2, the glass transition temperature of two compounds are 81.59℃ (TM 1) and 95.80℃ (TM 2), respectively. With the enlargement of molecular weight, TM 1(570.2 g/mol)<TM 2(672.9 g/mol), molecular vibrations need bigger energy, that cause the glass transition temperature increasesed, the thermal stability of compounds increase gradually.

3.3 Electrochemal properties

Cyclic voltammetry (CV) was used to assess the ionization potentials (hole-injecting ability) and the electrochemical properties of the compounds. CV was carried out on an IM6e electrochemistry workstation with a three-electrode configuration in 0.10 mol/L etrabutylammonium perchlorate (Bu_4NClO_4) in chloroform as supporting electrolyte with a scanning rate of 100 mV/s at room temperature. Platinum disc and platinum wire were used as working and counter electrode, respectively, and a saturated calomel electrode (SCE) as the reference electrode. The result of CV curve are shown in Fig.3, combined with figure 1, we can get the values of HOMO and LUMO of compounds. The results are shown in Table 1.

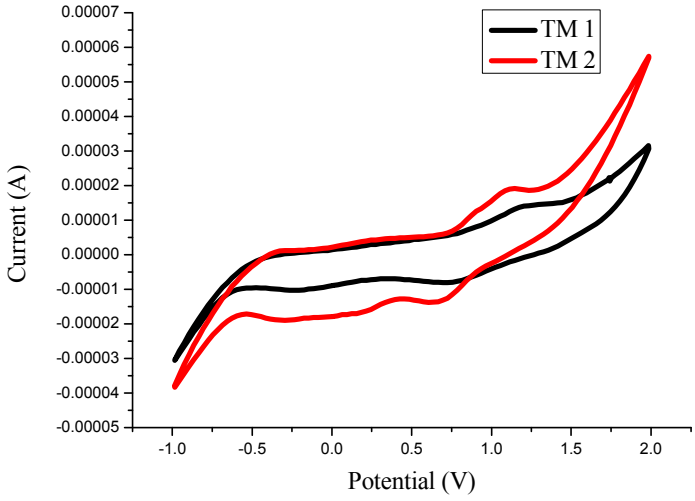

Fig.3 Cyclic Votammogram curves of TM 1 and TM 2

From the table 1, the E0ox of compounds are 1.32eV, 1.15 eV, Eoxonset of compounds are 0.79V, 0.75eV, respectively. The intruction of phenyl make distinct influence to marterials, increase the energy level of HOMO progressively, and the capability of electron-donating incerased gradually. The HOMO values are closed to work function of ITO, the energy gap between materials and ITO are small enough, thus it results the better hole injection from ITO to derivatives.

Table. 1 Electrochemal properties of TM 1 and TM 2.

	λ_{onset}[nm]	E_g[eV][a]	E_{ox}^{onset}[eV]	E_0^{ox} [eV]	HOMO[eV][b]	LUMO[eV][c]
TM 1	438	2.83	0.79	1.32	-5.53	-2.7
TM 2	470	2.64	0.75	1.15	-5.49	-2.85

[a] $E_g^{opt}(eV)=1240/\lambda_{onset}$; [b] HOMO (eV) = −(e$E_{onset}^{Ox}$ + 4.4 ev) [9] ;[c] |LUMO|=|HOMO|−E_g^{opt};

3.4 Hole-transporting properties

In order to study the hole-transporting performance of the two compounds and the influence of the introduction of phenyl, the double-layer EL devices with the structuer of ITO/HTL(50nm)/Alq_3(50nm)/Al were fabricated, using compounds TM 1 and TM 2 as the hole-transporting layer (HTL), respectively, and Alq_3 as the emitting and electron-transporting layer. The current density-voltage(J-V) characteristics of devices are shown in Fig.4. With the larger of driving voltage, the current density show nonlinear growth. In low voltage area, low mobility of ohmic contact and small amounts of heated carrier are the major inject carriers; While in higher voltage area, the improve of the electronic effective mobility, increase the density of the injection, make glowing regional current density and voltage present a exponential relation.The luminance-voltage(L-V) characteristics of devices are shown in Fig.5. the devices exhibit a activating vlotage of 11V for TM 1 and 5.5V for TM 2, respectively. the lower activating voltage of TM 2 suggests that the introduction of phenyl are more helpful to enhance the hole-injection performance.

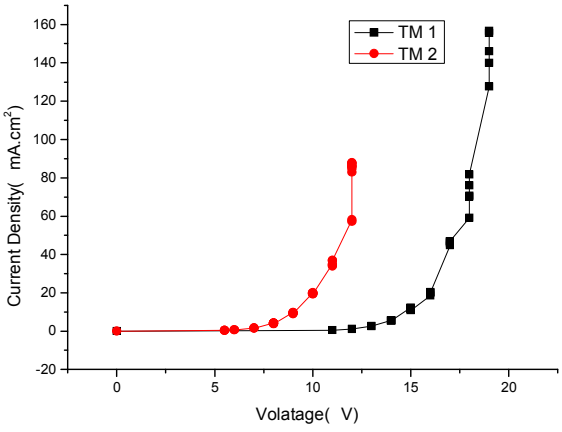

Fig. 4 The current density-voltage curves of TM 1 and TM 2 in two fabricated devices

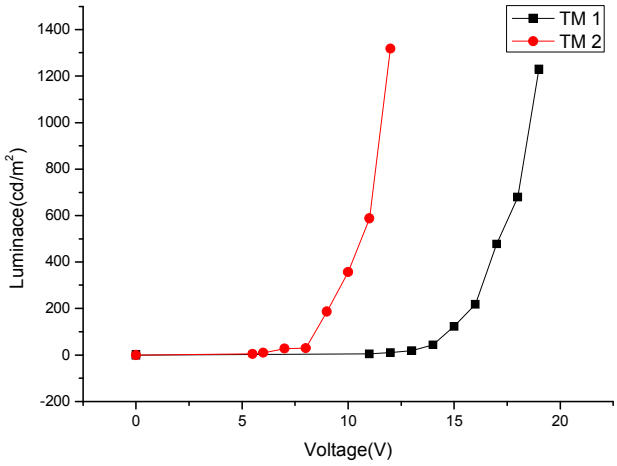

Fig. 5 The luminance-voltage curves of TM 1 and TM 2 in two fabricated devices

The luminous efficiency can be done according to the following equations: $\eta=A*L/I_{OLED}$[10].(Fig.6) The maximum luminous efficiency of device using TM 1 as HTL is 1.135 cd/A, while that device using TM 2 as HTL is 2.068 cd/A. These results indicate that the TM 2 have more better transporting performance. From the above results, it is known that TM 2 possessing better hole-transporting performance than that of TM 1.

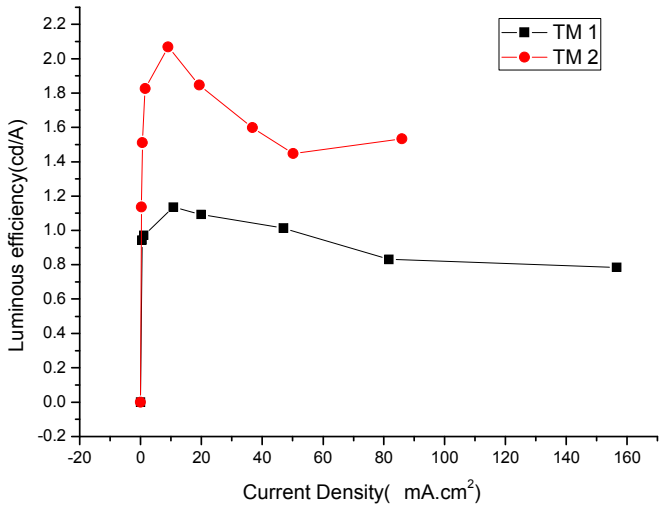

Fig.6 The Luminous efficiency-Current Density curves of TM 1 and TM 2 in two fabricated devices

4. Conclusions

In summary, two hole-transporting materials based on triphenylamine derivatives have been synthesized and characterized. The difference of the optical and electrochemical properties of the two compounds are due to the effect of the different bridge bonds of the target compounds. EL devices results show that the hole-transporting performances of TM 2 are much better than that of the TM 1.

Acknowledgments

The authors gratefully thank the National Natural Science Foundation of China (No. 21176180) for the financial support.

References

[1] M. Pope, H. Kallmann, P Magnate, Light emission from organic material[J], J. Chem. Phys., 38(1963)2042-2043

[2] C. W. Tang, S. A. VanSlyke, Organic Electroluminescent Dioles[J], Appl. Phys.Lett, , 51(1987)913

[3] S. A. Vanslyke, C. W. Tang, US 5061569,(1991)

[4] M.W. Thesen, H. Krueger, S. Janietz, et al. J. Polym. Sci. Pol.Chem. 48 (2010) 389;

[5] H.N. Tian, X.C. Yang , R.K. Chen, et al. J. Phys. Chem. C. 112 (2008) 11023.

[6] Dietmar Seyferth, Samuel O. Grim and Terence O. Read, Studies in Phosphinemethylene Chemistry. III. Triphenylphosphinechloromethylene[J], Journal of the American chemistry society, 83(1961) 1617.

[7] K.P. Li, J.L. Qu, B. Xu, et al. New J. Chem. 33 (2009) 2120.

[8] J. X. Chen, X. W. Huang, Organic Electroluminescent Materials & Devices, Beijing, Tsinghua University Press, (2007)

[9] W. Zhang, Z. Wang, Y.S. Tang, et al. Chin. Chem. Lett. 21 (2010) 245

[10] S. R. Forrest, D. D. C. Bradley, M. E. Thompson, Adv. Mater., 15(2003)1043.

doi:10.4028/www.scientific.net/AMM.161.128

Bi-Functional Magnetical Chiral Ionic Liquids derived from Imidazolium and Pyridinium

Qian Liwei[1, a], Hu Xiaoling[2, b], Guan Ping[3, c] and Guo Xiaoqing[4, d]

[1,2,3,4] School of Natural and Applied Science, Northwestern Polytechnical University, the Key Laboratory of Space Applied Physics and Chemistry, Ministry of Education, Xi'an 710072, China

[a]qianliwei@yahoo.cn, [b]huxl@nwpu.edu.cn, [c]guanping1113@nwpu.edu.cn, [d]413085457@qq.com

Keywords: Chirality, Magnetism, Bi-functional ionic liquids

Abstract. Novel bi-functional magnetical chiral ionic liquids (MCILs) derived from imidazolium and pyridinium were synthesized via simply two step reactions. Optically active ionic liquids have an asymmetric carbon atom linked to the positively charged imidazole ring or pyridine ring, while the magnetical anion contains tetrachloroferrate ($FeCl_4^-$), their properties of chirality and magnetism were characterized. The structure of MCILs would promise a new class of bi-functional ionic liquids.

Introduction

Ionic liquids (ILs) refer to the low-melting organic salts that consist of bulky organic cations and typically inorganic anions [1]. ILs are noted to have a number of unique properties, including negligible vapor pressures, good thermal stabilities, wide liquid temperature range and highly tunable for specific applications [2~3].

Chiral ionic liquids (CILs) that contain an asymmetric center are a versatile and interesting subclass of ILs. They have been successfully used in analytical and synthetic applications such as stationary phase in gas chromatography [4], solvent [5] and organo-catalysts in asymmetric reaction [6~7]. Jodry and Mikami synthesized hydrophobic CILs bearing an imidazolium core derived from the chiral pool, and their structure of 3D network of hydrogen bonding were discussed [8]. The asymmetric aza-Diels-Alder reaction of Danishefsky's diene with imine in chiral imidazolium-based ILs derived from isosorbide was investigated by Olivier and his group [9].

Although ionic liquids with metal complexes in anion are the earliest species for research [10], transition metal-containing ILs (MILs) are promising new materials that allow adding further features to the typical ILs. Owing to their magnetic properties, potential applications have been located in MILs such as separation [11], synthesis [12] and catalysis [13].

Recently, CILs with metal have been designed, and were applied in oxidative kinetic resolution [14~15]. However, there are few literatures reported on ILs with the both properties of chriality and magnetism [16]. Li and co-workers synthesized novel room temperature magnetic chiral ILs (MCILs) derived from ampared to amino acids ILs, ILs based on imdino acids and investigated their magnetic properties as well as chrial discrimination abilities. Comazolium or pyridium draw much more attention for their good thermal stability, relatively favorable viscosity and flexible adjustability [17~18]. Herein, we designed MCILs consisting of imdazolium or pyridium cation with magnetic $FeCl_4^-$ anion moiety, expected their potential application of chiral extraction as well as asymmetric catalysis [7][19].

Experimental details

Materials. Analytical grade pyridine, N-methylimidazole, Iron (III) chloride hexahydrate, Toluene, methanol, ethanol, and ethyl acetate were supplied by Sinopharm Chemical Reagent BeiJing Co., Ltd., China. (S)-(-)-2-chloropropionic ethyl ester (Industrial pure 99%) was obtained from SuZhou J.M.S Chemical Co., Ltd., China. All the liquid reagents were distilled before used.

Syntheses. The synthesis routes of MCIL1 (R)-(+)-β-(1-methylimidazole)-propionate tetrachloro -ferrate and MCIL2 (R)-(+)-β-(pyridinium)-propionate tetrachloroferrate are shown in Scheme 1. Details as follows:

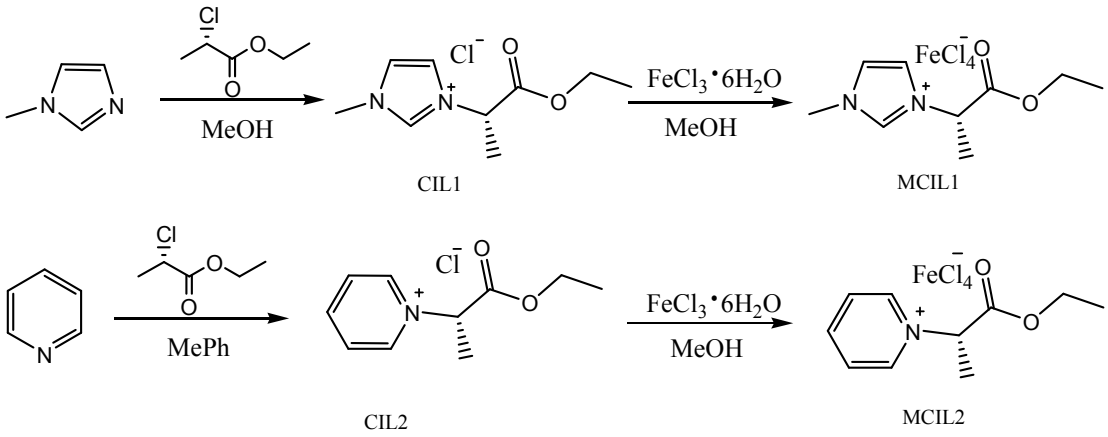

Scheme.1 Synthesis of MCIL 1 and MCIL 2

Synthesis of chloride (R)-(+)-β-(1-methylimidazole)-propionate. Here we named CIL 1. N-methylimidazole 16.42 g (0.20 mol) was mixed with methanol (20 mL) in a 100 mL three neck flask, then (s)-(-)-2-chloropropionic ethyl ester 32.78 g (0.24 mol) was dropped from funnel in 30 mins, the reaction mixture was stirred at 70℃ for 12 h. The compound was washed with ethyl acetate 3 times and evaporated by Rotary Evaporator, the final product CIL1 was dried in a vacuum drying oven at 60℃ over night. The product yields 88%, $[\alpha]^{20}_{D,CIL1}$ =+1.6°,^{1}H NMR (300MHZ, $CDCl_3$): δ (ppm) 1.29(t, 3H) 1.89(d, 3H) 4.13(s, 3H) 4.24(q, 2H) 5.85(q, 1H) 7.70(s, 1H) 7.79(s,1H) 10.43(s,1H), FT-IR(KBr, cm^{-1}): 3416 2948 2099 1740 1636 1578 1561 1464 1301 1218 1179 1085 1017 861 758 621, Elemental analysis calcd(%) for $C_9H_{15}N_2O_2Cl$ (218.50): C 49.43 H 6.86 N 12.81. Found: C 49.68 H 7.01 N 12.64.

Microwave-assisted synthesis of chloride (R)-(+)-β-(pyridinium)-propionate. Here we named CIL 2. Pyridine 11.85 g (0.15 mol) was mixed with (s)-(-)-2-chloropropionic ethyl ester 24.58 g (0.18 mol) in 20 mL toluene container, the mixture was reacting under 189W microwave for 2 mins and cooling to room temperature, the reaction lasted 20 times to afford rufous liquid, and then put the compound in a three neck flask to reflux at 90℃ for 30 h. The immiscible solution of deionized water and ethyl ester was added to the flask, the solution became two layers, got the aqueous phase by a separatory funnel and removed water by Rotary Evaporator, and the final product was obtained after dried in vacuum drying oven. The product yields 64%, $[\alpha]^{20}_{D,CIL2}$ =+1.3°. ^{1}H NMR (300MHZ, D_2O): δ (ppm) 1.17(t, 3H) 1.90(d, 3H) 4.20(q, 2H) 5.68(q, 1H) 8.06(m, 2H) 8.57(m, 1H) 8.85(d, 2H). FT-IR (KBr, cm^{-1}): 3415 2090 1740 1633 1488 1370 1305 1188 1081 1017 860 783 688. Elemental analysis calcd (%) for $C_{10}H_{14}NO_2Cl$: C 55.68 H 6.50 N 6.50. Found: C 55.90 H 6.75 N 6.34.

Synthesis of MCIL1 and MCIL 2. MCILs were prepared as already reported literature [20] by mixing equimolar amount of CIL and $FeCl_3 \cdot 6H_2O$ in methanol under nitrogen. The obtained dark brown viscous material was repeatedly washed using a little amount of deionized water. The product was obtained by drying the material under a vacuum drying oven at 60℃. $[\alpha]^{20}_{D,MCIL1}$ =+1.5°, $[\alpha]^{20}_{D,MCIL2}$=+1.4°.

Characterization techniques. Fourier Transform Infrared (FTIR) spectra were recorded on a WQF-310 Fourier transform infrared spectrometer. Raman tests were carried out using a Renishaw 1000 spectrometer equipped with a 514.5 nm excitation. Thermo-gravimetric analysis (TGA) spectra were recorded using a Q600SDT instrument at a heating rate of 10℃/min under nitrogen. Elemental analyses were measured by Vario EL III elemental analyzer. ^{1}H NMR (300MHZ) spectra were acquired by use of a Avance 300 MHz spectrometer, the ^{1}H chemical shifts are given in parts per million (δ) with TMS as an internal standard. The magnetic susceptibility of MCILs was measured using approximately 100 mg of the sample in a MPMS-XL-7 superconducting quantum interference device magnetometer for fields between -10000 and 10000 Oe. Specific optical rotation of CIL1, CIL2, MCIL1, and MCIL2 was measured by WZZ-1 automatic rotary spectrometer at 20℃ in ethanol.

Results and discussion

Using FT-IR spectrometer to analyze the characteristic absorption peaks of CIL1 and CIL2.The peaks at about 3300 cm^{-1} are the stretching absorption peak of C-H on aromatic ring, overtunes and combination transitions of the aromatic C-H groups may be responsible for bands at 1630 and 2100 cm^{-1} [21], the characteristic absorption peaks between 1600 cm^{-1} and 1400 cm^{-1} confirmed the existence of imidazole ring and pyridine ring. The characteristic absorption peak of C=O and C-O is at wave number 1740 cm^{-1} and 1300 cm^{-1} respectively. In addition, white precipitation appeared when CIL1 and CIL2 dropped in $AgNO_3$ solution, that's proved the existence of Cl^-.

From the results of ^{1}H NMR spectra, we found that the peaks at δ 7.70, 7.79, 10.43 [22] and δ 8.06, 8.57, 8.85 [23] correspond to three type of hydrogen atoms on imidazole ring and pyridine ring. At δ 5.85 and 5.68, they were protons of chiral carbon on imidazole ring and pyridine ring. The peaks at δ 4.24 and 4.20 were accordance with their methylene respectively. The peak at δ 4.13 represented the methyl protons which were linked to nitrogen in imidazole ring [24]. Between δ 1 and 2 in CIL1 or CIL2, there were two peaks which corresponded to two methyls on their branch chain. Both FT-IR and NMR demonstrate the products of CIL1 and CIL2 were in agreement with design objective.

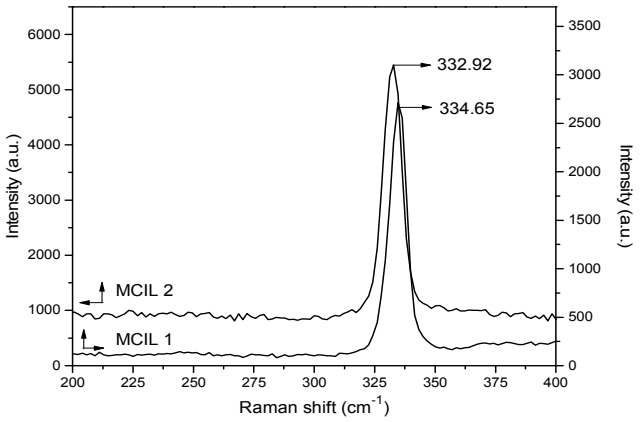

Figure.1 Raman spectrum of MCIL1 and MCIL2

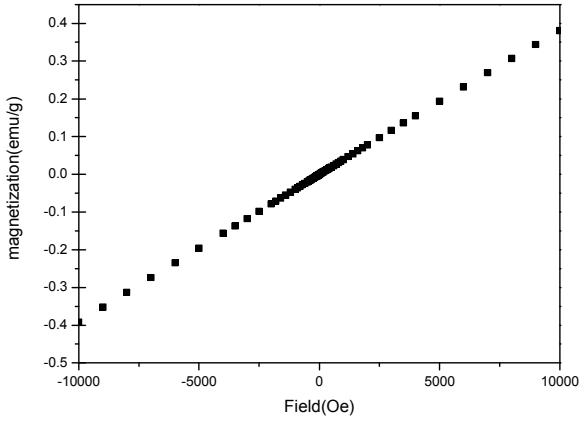

Figure.2 Field dependence of the magnetization of MCIL 1 at 300K

The characteristic of MCILs' structure was carried out by Raman spectroscopy with the 514.5 nm line at room temperature. As shown in Fig.1, the observed Raman spectrum shows a strong peak at about 335 cm^{-1} which was feature of anion $[FeCl_4]^-$, that is correspond well with the literature values [25]. In addition, the fact that there is no more peak observed at 350 to 400 cm^{-1} illustrated inexistence of anion $[Fe_2Cl_7]^-$. Thus, the structure of MCIL1 and MCIL2 can be confirmed and proved the same as design.

Specific optical rotation of CIL and MCIL was measured by automatic rotary spectrometer. The value of +1.6°,+1.5°,+1.3°,+1.4° agreed with the report conducted by Poterala and Plenkiewicz [26], they synthesized a series of CILs based on methylimidazolium, one of their reaction mode was same like ours. However, there was no instruction to this phenomenon. Here, we deduced that the reaction of nucleophilic substitution was mainly performed as SN_2 mechanism, but considering the steric hindrance effect of imidazole ring and pyridine ring, it is possible to possess both SN_1 and SN_2 mechanism in reaction process.

For MCILs' paramagnetic behavior owing to anion of d^5 configuration, herein we set MCIL1 as a sample shown in Fig.2 to analysis their magnetic susceptibilities. Over the applied magnetic field range of -10000 to 10000 Oe, the magnetization of MCIL1 at 300K shows a linear field dependency which means a typical paramagnetic behavior. The molar magnetic susceptibility of MCIL1 was obtained as χ_M =0.01398 emu/mol and magnetic susceptibility was determined to be 3.67×10^{-5} emu/g which is close to the reported value [27].

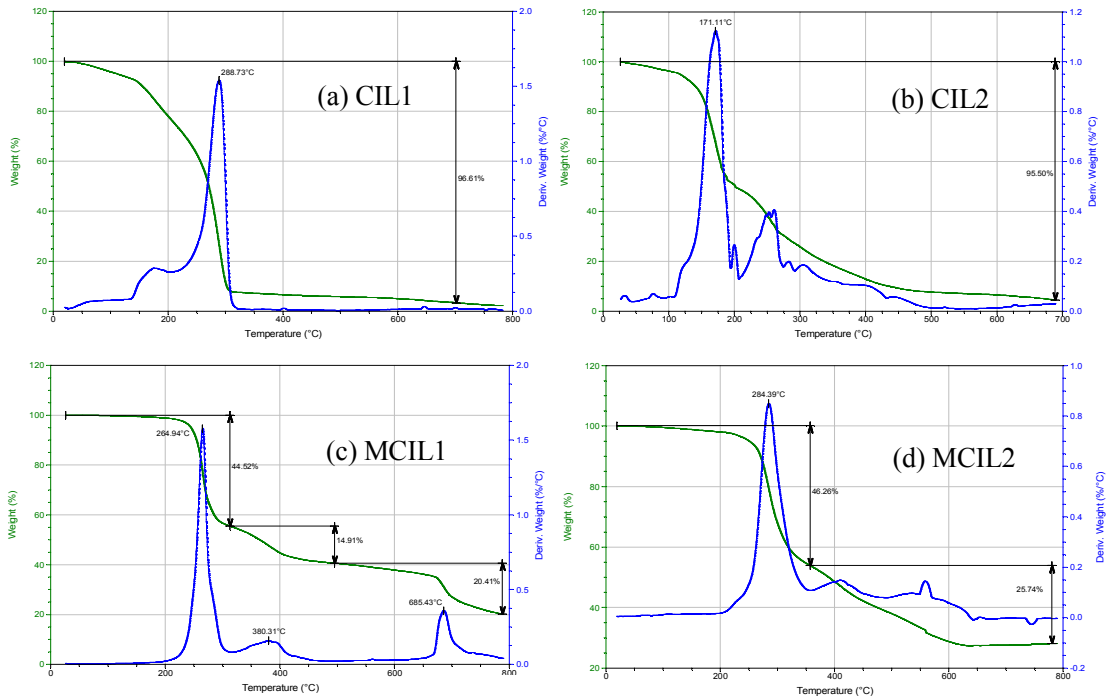

Figure.3 Thermal gravimetric analysis scans of CILs and MCILs

Figure 3 was shown the thermo stability of MCILs and CILs, we observed two steps decomposition process of MCILs. In the first step, a partial decomposition of tetrachloroferrate and the volatile organic solvent took place with CO_2 released, whereas organic part was totally decomposed accompanying with HCl in the second step [28]. In addition, compared the thermo stability of MCILs with CILs, there was a large enhancement in MCILs. This might be attributed to stronger hydrogen bond interaction between cations and anions in MCILs [29].

Conclusions

We synthesized bi-functional MCILs based on imidazolium and pyridinium via simply two step reactions. The MCILs possessed good optical rotation and excellent magnetism as well as thermal stability. They could be potentially applied in chiral extraction and heterocatalysis. And the MCILs' structure of chiral center linked in cation with different magnetic anions such as $[FeCl_4]^-$, $[FeBr_4]^-$ and $[Co(SCN)_4]^{2-}$ would provide a series of novel functional ionic liquids.

Acknowledgement

The project was financial supported by the National Natural Science Foundation of China (Grand Number. 21174111)

References

[1] T. welton, Room-Temperature Ionic Liquids, Solvents for Synthesis and Catalysis, Chem. Rev. 99 (1999) 2071-2083.

[2] A. Mele, C.D. Tran, S.H.P. Lacerda, The Structure of a Room-Temperature Ionic Liquid with and without Trace Amounts of Water: The Role of C-H···O and C-H···F Interactions in 1-n-Butyl-3-Methylimidazolium Tetrafluoroborate, Angew Chem. Int.Ed. 42 (2003) 4364-4366.

[3] C.D. Tran, S.H.P. Lacerda, Determination of Binding Constants of Cyclodextrins in Room-Temperature Ionic Liquids by Near-Infrared Spectrometry, Anal.Chem. 74 (2002) 5337-5341.

[4] J. Ding, T. Welton, D.W.Armstrong, Chiral Ionic Liquids as Stationary Phases in Gas Chromatography, Anal Chem. 76 (2004) 6819-6822.

[5] T. Trucng, G. vo-Thanh, Synthesis of functionalized chiral ammonium, imidazolium, and pyridinium-based ionic liquids derived from (-)-ephedrine using solvent-free microwave activation, Applications for the asymmetric Michael addition, Tetrahedron. 66 (2010) 5277-5282.

[6] S.Z. Luo, L. Zhang, X.L. Mi, Y.P. Qiao, J.P. Cheng, Functionalized Chiral Ionic Liquid Catalyzed Enantioselective Desymmetrizations of Prochiral Ketones via Asymmetric Michael Addition Reaction, J.Org.Chem. 72 (2007) 9350-9350.

[7] D.E. Siyutkin, A.S. Kucherenko, S.G. Zlotin, A new (S)-prolinamide modified by an ionic liquid moiety-a high performance recoverable catalyst for asymmetric aldol reactions in aqueous media, Tetrahedron. 66 (2010) 513-518.

[8] J.J. Jodry, K. Mikami, New chiral imidazolium ionic liquids: 3D-network of hydrogen bonding, Tetrahedron Letters. 45 (2004) 4429-4431.

[9] O. N. V. Buu, A. Aupoix, G. Vo-Thanh, Synthesis of novel chiral imidazoliu-based ionic liquids derived from isosorbide and their applications in asymmetric aza Diels-Alder reaction, Tetrahedron. 65 (2009) 2260-2265.

[10] R.A. Osteryoung, H.L. Chum, V.R. Koch, L.L. Miller, Electrochemical scrutiny of organometallic iron complexes and hexamethylbenzene in a room temperature molten salt, J Am Chem Soc. 97(1975) 3264-3265.

[11] M. Okuno, H. Hamaguchi, Magnetic manipulation of materials in a magnetic ionic liquid, Appl. Phys. Letter. 89 (2006) 132506:1-132506:2.

[12] X.W. Pei, Y.H. Yan, L.Y. Yan, P. Yang, J.L. Wang, R. Xu, C.P. MaryB, A magnetically responsive material of single-walled carbon nanotubes functionalized with magnetic ionic liquid, Carbon. 48 (2010) 2501-2505.

[13] H. Wang, R.Y. Yan, Z.X. Li, X.P. Zhang, S.J. Zhang, Fe-containing magnetic ionic liquid as an effective catalyst for the glycolysis of poly(ethylene terephthalate), Catalysis Communications. 11 (2010) 763-767.
[14] C.Y. Li, J.F. Zhao, R. Tan, Z.G. Peng, R.C. Luo, M. Peng, D.H. Yin, Recyclable ionic liquid-bridged chiral dimeric salen Mn(III) complexes for oxidative kinetic resolution of secondary alcohols, Catalysis Communications. 15 (2011) 27-31.
[15] Y.Y. Song, Q.R. Jin, Su.L. Zhang, H.W. Jing, Q.Q. Zhu, Chiral metal-containing ionic liquid: Synthesis and applications in the enantioselective cycloaddition of carbon dioxide to epoxides, Sci China Chem. 54 (2011) 1044-1050.
[16] M. Li, S.L. De Rooy, D.K. Bwambok, B. El-Zahab, J.F. DiTuse, I.M. Warner, Magnetic chiral ionic liquids derived from amino acids, Chem. Commun. (2009) 6922-6924.
[17] B. Ni, A. D. Headley, Novel imidazolium chiral ionic liquids that contain a urea functionality, Tetrahedron Letters. 47 (2006) 7331-7334.
[18] B. Ni, Q.Y. Zhang, A.D. Headley, Design and Synthesis of pyridinium Chiral Ionic Liquids Tethered to a Urea Functionality, J.Org.Chem. 71 (2006) 9857-9860.
[19] F. Tang, Q.L. Zhang, D.D. Ren, Z. Nie, Q. Liu, S.Z. Yao, Functional amino acid ionic liquids as solvent and selector in chiral extraction, Journal of Chromatography A. 1217 (2010) 4669-4674.
[20] J.Y.Kim, J.T.Kim, E.A.Song, Y.K.Min, H. Hamaguchi, Polypyrrole Nanostructure Self-Assembled in Magnetic Ionic Liquid as a Template, Macromolecules. 41 (2008) 2886-2889.
[21] C.D. Tran, S.H.P. Lacerda, D Oliveira, Absorption of Water by Room-Temperature Ionic Liquids: Effect of Anions on Concentration and State of Water, Applied Spectroscopy. 57 (2003) 152-157.
[22] D.E. Siyutkin, A.S. Kucherenko, M.I. Struchkova, S. G. Zlotin, A novel (S)-proline-modified task-specific chiral ionic liquid-an amphiphilic recoverable catalyst for direct asymmetric aldol reactions in water, Tetrahedron Letters. 49 (2008) 1212-1216
[23] B. Ni, Q.Y. Zhang, A.D. Headley, Pyrrolidine-based chiral pyridinium ionic liquid (ILs) as recyclable and highly efficient organocatalysts for the asymmetric Michael addition reaction, Tetrahedron Letters. 49 (2008) 1249-1252.
[24] S.F. Yu, S. Lindeman, C.D. Tran, Chiral Ionic liquids: Synthesis, Properties, and Enantiomeric Recognition, J.Org.Chem. 73 (2008) 2576-2591.
[25] M.S. Sitze, E.R. Schreiter, E.V. Patterson, R. G. Freeman, Ionic Liquids Based on $FeCl_3$ and $FeCl_2$. Raman Scattering and ab Initio Calculations, Inorg. Chem. 40 (2001) 2298-2304.
[26] M. Poterala, J. Plenkiewicz, Synthesis of new chiral ionic liquids from α-hydroxycarboxylic acids, Tetrahedron:Asymmetry. 22 (2011) 294-299.
[27] S. Hayashi, S. Saha, H. Hamaguchi, A new class of magnetic fluids: bmim[$FeCl_4$] and nbmim[$FeCl_4$] ionic liquids, IEEE Trans Magn. 42 (2006) 12-14.
[28] D. Wyrzykowski, A. Pattek-Janczyk, T. Maniecki, K.Zaremba, Z. Warnke, Thermal analysis of quinolinium tetrachloroferrate(III), Thermochimica Acta. 443 (2006) 72-77.
[29] T. Backer, O. Breunig, M. Valldor, K. Merz, V. Vasylyeva, A.V. Mudring, In-Situ Crystal Growth and Properties of the Magnetic Ionic Liquid [C_2MIM][$FeCl_4$], Cryst.Growth Des. 11 (2011) 2564-257

doi:10.4028/www.scientific.net/AMM.161.134

Application of Bässler's Energy and Position Disorder Model and Hoping Model in Hole Transport Material

Yakun Song[1,a], Jing You[1,b], Shirong Wang[1,c], Xianggao Li[1,d]

[1]School of Chemical Engineering and Technology, Tianjin University, Tianjin, 300072, PR China

[2]Department of Materials Physics and Chemistry, Graduate School of Engineering, Kyushu University, 744, Moto-oka, Nishi-ku, Fukuoka, 819-0395, Japan

[a]syk1984720@gmail.com, [b]rosefly88@hotmail.com, [c]wangshirong@tju.edu.cn, [d]lixianggao@hotmail.com (corresponding author)

Keywords: Hole-transport Material; Hole Mobility; Quantum Chemistry Calculation

Abstract. The Bässler's energy and position disorder model is used to study the relationship between molecular structure of hole-transport materials and performance of the photoreceptor. The result shows that dipolar moments of hole-transport materials (HTM) are inverse proportion to the half decay exposures ($E_{1/2}$) of the Organic photoreceptors (OPC) which closely related with the hole-mobility of hole-transport layer. In this article Marcus hopping theory and DFT method are also used to calculate the hole-mobility of four hole-transport materials (HTM). The compare of the half decay exposures of OPCs used these material as hole-transport layer and hole mobility, dipolar moments of these molecules show that the $E_{1/2}$ increases with decrease of hole mobility and dipolar moment.

Introduction

The hole-transport material (HTM) is mainly used in the core of electrostatic copy machine, the function separate photoreceptor. The hole-mobility of HTM is greatly effect on the half decay exposure [1, 2]. As the definition of copy print is influence by the half decay exposure, therefore the hole-mobility became one of most important parameters for HTM.

The earliest theory[3~5] used to explain charge transport process was band transport model in inorganic semiconductor. In this theory, they believed the charge hop into conduction band from valence band after photo-excitation and transport between different lattices with the electric field effect. But the organic photoconductor doesn't have any crystal so the charge transport process is different with the inorganic semiconductor.

Bässler's energy and position disorder model was used to describe the process of charge transport in solid solution [6]. His group used 1, 1-bis-di-4-tolylaminophenyl)-cyclohexane as the host, and used the low polar material: polystyrene as well as the high polar material: biphenyl-A-polycarbonate respectively as the dope. The time-of-flight (TOF) technique had been used to test hole-mobility. They found that the mobility (μ) was determined by Gaussian width of density-of-states (σ). They predicted that the charge transport process was finish by charge hopping form one molecular to their adjacent molecular, so mobility was determined by the overlap of the adjacent molecules.

Theoretical method

Marcus Hopping model is widely used in charge transfer process [7]. This model described charge transport process as the charge hopping from one site to another, compared with the structural deformed. The hoping rate was described by Marcus theory with Eq. (1):

$$k_{et} = \frac{4\pi^2}{h}\frac{1}{\sqrt{4\pi\lambda k_B}} t^2 \exp\left\{-\frac{\left(\Delta G^0 + \lambda\right)^2}{4\lambda k_B T}\right\}. \quad (1)$$

Here λ is reorganization energy, $\triangle G^0$ is free energy difference between the initial and final site, as all the site is equivalent here $\triangle G^0$ is zero. The *t* here means charge transfer integral.

In the research reported by Zhigang Shuai and his group, they applied the assumption of Fujita and Nakai about the charge transfer coupling in DNA [8, 9]. They believed the charge transfer integral can be described by Eq. (2):

$$t_h = \left\langle \phi_{HOMO}^{0,site1} \middle| F^0 \middle| \phi_{HOMO}^{0,site2} \right\rangle. \quad (2)$$

Here F^0 is Fock operator, $\phi_{HOMO}^{0,site1}$ is wave function of neutral molecular and $\phi_{HOMO}^{0,site2}$ is that of positive molecular. Because the hole-transport molecules dissolve in polycarbonate as solid solution, we assumed that molecules of hole-transport are distributed evenly in the film between proportional. That means there is no crystal in the thin film. All molecules have distance between each other. So the intermolecular interaction is neglected, and the equation (2) is simplified by equation (3).

$$t_h = \left\langle \phi_{HOMO}^{0,site1} \middle| h_{core} \middle| \phi_{HOMO}^{0,site2} \right\rangle. \quad (3)$$

Because butadiene structure is good conjugated structure which is easy to transfer charges from one part to another, the material with this structure is easy to fabric a thin film. So the hole transport material contains butadiene structure has very good performance [10, 11]. In this article, four hole-transport structures (CT1~CT4) which are shown in Fig. 1 are calculated both for hole mobility and molecular dipolar moment. Compared with photo-discharged curves of the OPC derives fabricated by these materials [12, 13].

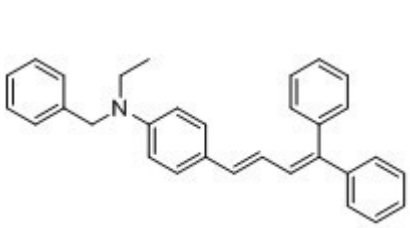

CT1

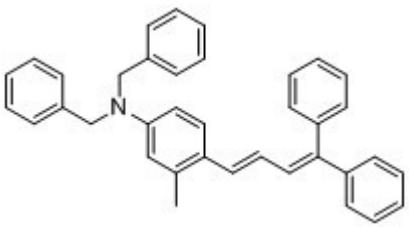

CT2

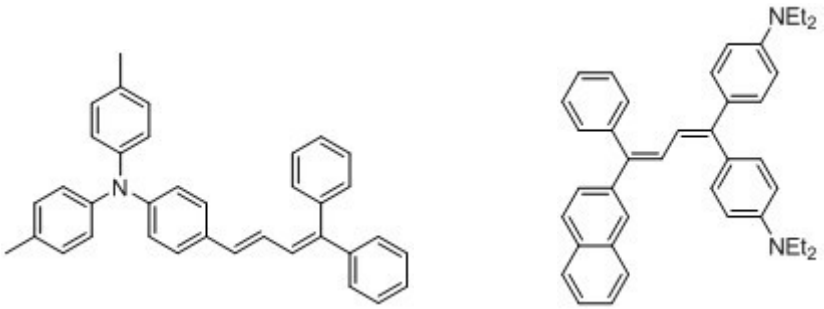

CT3 CT4

Fig. 1 Molecular Structures of CT1, CT2, CT3, CT4

All the calculations are performed with the Gaussian03 package at Hartree-Fock/6-31G level. The optimist geometric structure for both neutral molecule and positive in molecule as well as HOMO energy level, wave function and dipolar moment are calculated. [14]

Results and discussion

Table 1 Optimistic geometric structure of CT1~CT4

	Neutral	Positive-ion
CT1	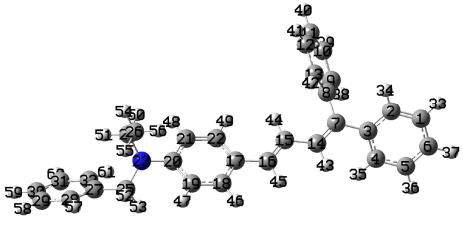	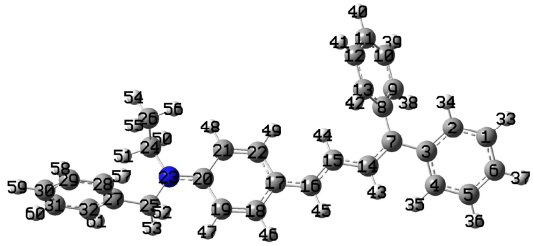
CT2	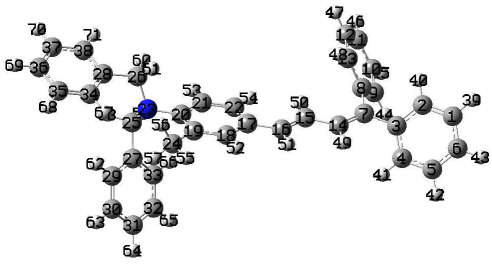	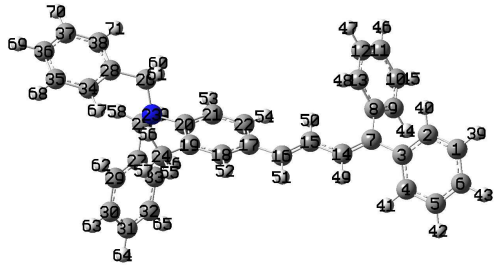
CT3	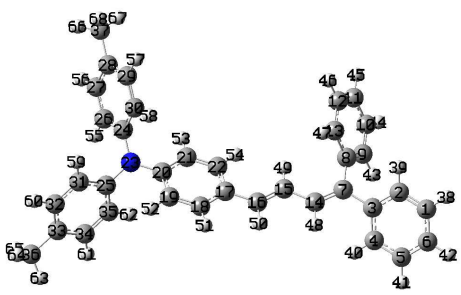	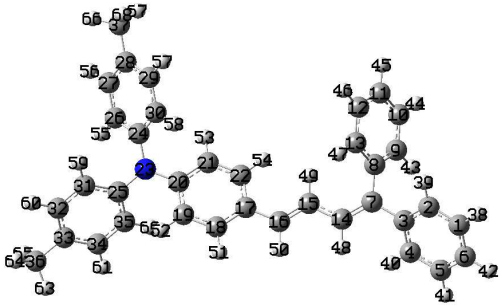

CT4 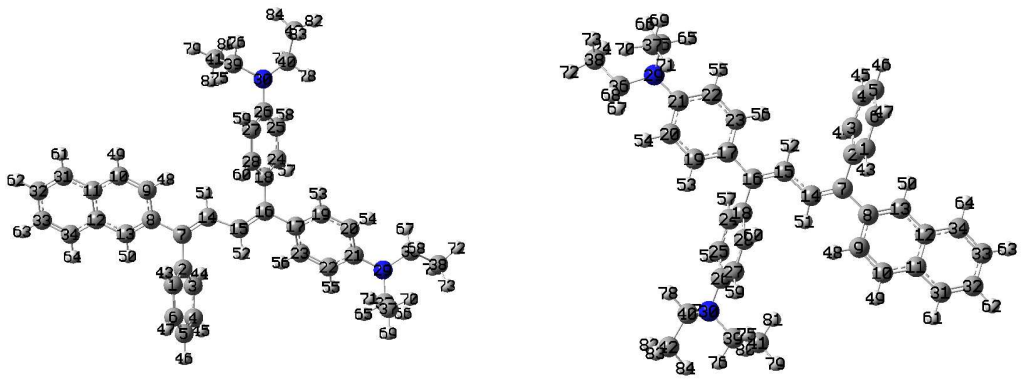

The molecular structure of CT1~CT4 for both neutral and positive-ion which are shown in Table 1 show that, bond lengths of all there positive ion has a tendency of averages on in butadiene. The band length of C=C is longer than the normal C=C, but shorter than the C-C.

Table 2 Bond length of Neutral Structure and Positive-ion Structure

	Bond Length of Neutral[nm]		Bond Length of Positive ion[nm]	
CT1	N23-C20	1.41335	N23-C20	1.35415
	C15-C16	1.33586	C15-C16	1.40467
	C14-C15	1.45753	C14-C15	1.40467
	C7-C14	1.34170	C7-C14	1.39681
CT2	C15-C16	1.33537	C15-C16	1.34575
	C14-C15	1.45770	C14-C15	1.44418
	C7-C14	1.34163	C7-C14	1.35241
CT3	C15-C16	1.33594	C15-C16	1.34611
	C14-C15	1.45744	C14-C15	1.44395
	C7-C14	1.34175	C7-C14	1.35248
CT4	C15-C16	1.34406	C15-C16	1.35336
	C14-C15	1.45786	C14-C15	1.44202
	C7-C14	1.34260	C7-C14	1.35264

From table2 we can see, in CT1 the N-C single bond (1.41335nm) in neutral structure is same as normal N-C single bond (1.4nm). But in positive-ion structure the N-C bond length (1.35415) is short than N-C single bond, but longer than N=C double bond (1.28nm).In CT1~CT4 the positive-ion structure is trend to be delocalization π system rather than butadiene structure.

The photo-discharged curves of OPC devices used CT1~CT4 as hole-transport material are list in Fig. 2:

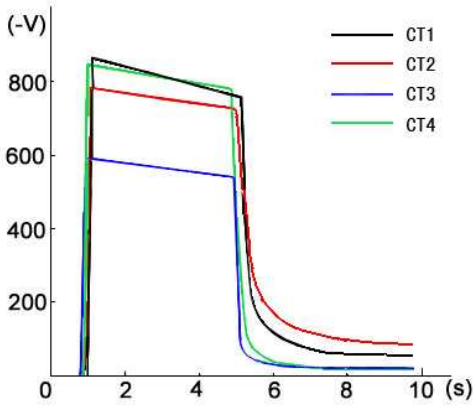

Fig. 2 Photo-discharge curves of OPC devices used CT1~CT4 [12]

The hole-mobility (μ) from calculation, half decay exposure ($E_{1/2}$) and residual potential (Vi) are listed in table 3.

Table 3 Calculation result and OPC data of hole transport material

HTM	CT1	CT2	CT3	CT4
k_{et}	1.105×10^{-7}	3.434×10^{-7}	1.03×10^{-4}	1.757×10^{-6}
μ[cm^2/Vs]	1.859×10^{-6}	6.063×10^{-6}	1.800×10^{-3}	3.221×10^{-5}
-logμ	5.731	5.217	2.745	4.492
$E_{1/2}$[lx·s]	0.98	1.72	0.56	0.93
Dipole moment [Debye]	0.8522	0.8381	0.1718	0.1885
R_d / V·s^{-1}	60	80	20	20

From table3 we can see the half decay exposure of photoconductor decrease with the increase of hole-mobility, except the CT2. The residual potential of OPC fabricated by CT2 is very high. We predicted that there is small crystal in the thin film, and this crystal act as charge trap. These traps change the transport mechanism. That's why the half decay exposure is highest but the hole-mobility calculated is not very low.

The data in table3 show that half-decay exposure ($E_{1/2}$)is proportional with negative logarithm of hole mobility(-logμ), except CT2.

The molecule dipole moment is proportional with half decay exposure. According Bässler's energy and position disorder model, the mobility (μ) is determined by Gaussian width of density-of-states (σ) function of the hopping sites and the standard deviation (Σ) and electrical field (E). And the carrier mobility can be shown by the following equation:

$$\mu(\hat{\sigma},\Sigma,E)=\mu_0\exp\left[-\left(\frac{2\hat{\sigma}}{3}\right)^2\right]\exp\left[C\left(\hat{\sigma}^2-\Sigma^2\right)E^{1/2}\right] \quad (4)$$

The C is determined by dope material as an empirical constant which relative to energetic disorder in Bässler's experiment. Here $\hat{\sigma}$ decrease with increase of the dipolar moment of dope material. So the mobility is inverse proportional with dipole moment of dope material [6].

In his research 1, 1-bis-di-4-tolylaminophenyl)-cyclohexane is used as a host and a polar material polystyrene, and high polar material biphenyl-A-polycarbonate is used as dope, respectively. But here polycarbonate is used as host; CT1, CT2, CT3 and CT4 are used as dope. And the result still agrees with that model.

Conclusions

In this article hole-mobility is calculated by Marcus hopping model and compared with photo-discharge curve of OPC used CT1~CT4 as hole-transport material. The half exposure moment of photoconductor decrease with the increase of hole-mobility, and that is in proportional with molecular dipole moment of CT1~CT4. That is agreeing with the conclusion of Bässler's energy and position disorder model. So this model can use in OPC used polymer as host and small molecular transport material as dope. And the small molecular transport material show designed with small molecular dipole moment.

Acknowledge

The authors gratefully thank the National Natural Science Foundation of China (No. 21176180) for the financial support.

Reference

[1] C.F.Carlson, U.S. Patent 2,297,691.(1942)

[2] R.H.Moser,A.L.Thomas: CRC Press, Vol. 1(1983)

[3] W.D. Gill: J.Appl.Phys., Vol.43(1972), p. 5033

[4] B.G.Bagley: Solid State Commun, Vol.8(1970), p. 345

[5] G.Pfister,H.Scher: Adv.Phys., Vol.27(1978), p. 747

[6] H. Bässler's: Phil.Mag.B., Vol.5(1984), p. 347

[7] R.A.Marcus: Review of Moden Physics, Vol.65-3(1993), p. 599

[8] S.W.Yin,Y.P.Yi,Q.X.Li,Y.Q.Liu,Z.G.Shuai:Phys.Chem.A., Vol.110(2006), p.138

[9] T.Fujita,, H.Nakai,H.Nakatsuji: J.Chem.Phys., Vol.104(1996), p. 2410

[10] Q.Xue,H.Z.Chen,J.Z.Sun,W,Wang: Journal of Functional Marerial, Vol.35-5 (2004), p. 595

[11] E.Toshio,H.Ryo: Appl.Phys., Vol.70-11(1991), p. 6908

[12] X.G.Li,A.S.Wu,L.L.He,S.R.Wang: Fine Chemicals, Vol. 22-08 (2005), p. 572

[13] X.G.Li,A.S.Wu,L.Y.Xing,X.M.Zhao: Journal of Functional Materials, Vol.38-10(2007), p. 1583

[14] M.J. Frisch,et.al.: Caussian03.revision A.1; Gaussian,Inc.;Pittshurgh,PA,2003.

doi:10.4028/www.scientific.net/AMM.161.140

Radiation Effect of Metal-Oxide-Semiconductor Structure Irradiated by Electron

Jian Xin Zhang[1,a], Jun Xing Liu[1,b], You Bao Wan[1,c]

[1] Jiaxing University, Jiaxing 314001, China

[a]zjxox@163.com, [b]ljxoz@yahoo.cn,[c]youbaowan@yahoo.com.cn

Keywords: MOS; electron; radiation; interface density

Abstract. MOS structure has been radiated by electron, dosage is 2×10^{13} cm^{-2} ~ 1×10^{14} cm^{-2}. The interface density distributing in energy band has been tested by quasi-static method. It is found that interface density increase while electron dosage increasing. When dosage arrived to 1×10^{14} cm^{-2}, interface density arrives to 10^{13}($cm^{-2}eV^{-1}$),which is two order of magnitude higher than without irradiation. Further more, the shapes of density increase curve are completely different.

Introduction

Metal-oxide-semiconductor (MOS) structure is highly sensitive to SiO_2-Si interface. It will reflect parameters such as interface density and oxide layer charge expediently. It is an important way to monitor the quality of SiO_2 and the effect of passivation by C-V test of MOS [1,2].

Interface density is an important parameter to characterize the Interface of SiO2-Si.It is a fundamental problem of silicon devices and integrated circuit technology. Also it is an important part for semiconductor research. Interface density will be as a center of generation- recombination, increases the reverse current of PN junction and reduces current gain β of BJT and bring 1/f noise. However, how to test Interface density is a significant work for devices research and monitoring of technology and optimizing performance.

There are very much ways to test Interface density. High frequency C-V test is the simplest one. But you have to use differential coefficient to calculate the distributing in energy band. The temperature method is easy but only applies to narrow ranges. The conductance method has high precision only but complex. The quasi-static method can test distribute of Interface density as a big range. In this paper we test Interface density with the he quasi-static method [3, 4].

Electron radiation will induce interface density at SiO_2-Si interface, and accumulate positive charge into SiO_2 film. We test high and low frequency C-V curves of MOS structure before and after Electron radiation separately in our experiment, for the sake of research of radiation effects [5, 6]. We have tested the interface density and accumulated charge density.

Samples and Conditions

We prepare two kinds of MOS structure with P-silicon and N-silicon. The crystal orientation is <111>, the resistivity is 1~2 Ω·cm. First we oxide samples for growing SiO_2, the order is dry-oxygen/wet-oxygen/dry-oxygen, the thickness of SiO_2 is 100nm. Then we vaporize aluminum as metal contact on SiO_2 with molybdenum mask. There will be found aluminum point array with 10×10, the thickness of aluminum is 1μm, and the diameter of aluminum point is 2mm.

Samples are radiated by electron at Shanghai Institute of Nuclear Research, Chinese Academy of Sciences (CAS), the electron energy is 0.8 MeV, radiation dosage is 2×10^{13} cm^{-2} and 1×10^{14} cm^{-2} separately for sample A and sample B. We did not add voltage at samples during radiation. Samples and Radiation Dosage are shown in Table 1.

Table 1 Samples and Radiation Dosage

Sample	A	B
Type	N	P
Radiation dosage[cm^{-2}]	2×10^{13}	1×10^{14}

Test Method and Conditions

We test the interface density with semi-quiescence method. First, We test high frequency C-V curve C_{HF}(V) and low frequency C-V curve C_{LF}(V) of MOS structure. Then we calculate interface density N_{ss} with computer. The high frequency C-V curve can be obtained immediately by Keithley 590 C-V testing with frequence is 1MHz. The low frequency C-V curve can be obtained by Keithley 4200 I-V with ramp voltage method, the delay factor is 0.1, the voltage step is 1.5mV, the scan speed（$\frac{dV}{dt}$）is 8mV/s.We know that interface capacitor C_{it} is

$$C_{it} = (\frac{1}{C_{LF}} - \frac{1}{C_{OX}})^{-1} - (\frac{1}{C_{HF}} - \frac{1}{C_{OX}})^{-1} \quad . \tag{1}$$

Interface density N_{ss} is

$$N_{SS} = \frac{C_{it}}{q} \quad . \tag{2}$$

The distributing of interface density in energy band $N_{ss}(E)$ can be calculated by low frequency C-V curve through surface potential φ_S and add voltage V. The relationship between φ_S and V is

$$\varphi_S(V) = \int_{V_{FB}}^{V} \left[1 - \frac{C_{LF}}{C_{OX}}\right] dV + \varphi_S(V_{FB}). \tag{3}$$

The interface energy E in energy band is

$$\frac{E_C - E}{q} = \frac{E_g}{2q} + \varphi_S - \phi_B . \tag{4}$$

Hereinto, C_{OX} is capacitor of oxide layer per unit; V_{FB} is voltage of flatband; E_C, E_g is conduction energy and band gap separately; ϕ_B is Fermi potential.

Experiment Results

Fig.1 is the high and low frequency C-V curve and $N_{ss}(E)$ of sample B before radiation. The curve of interface density is close to U, the interface density in the middle of energy gap is $10^{11}(cm^{-2}eV^{-1})$.

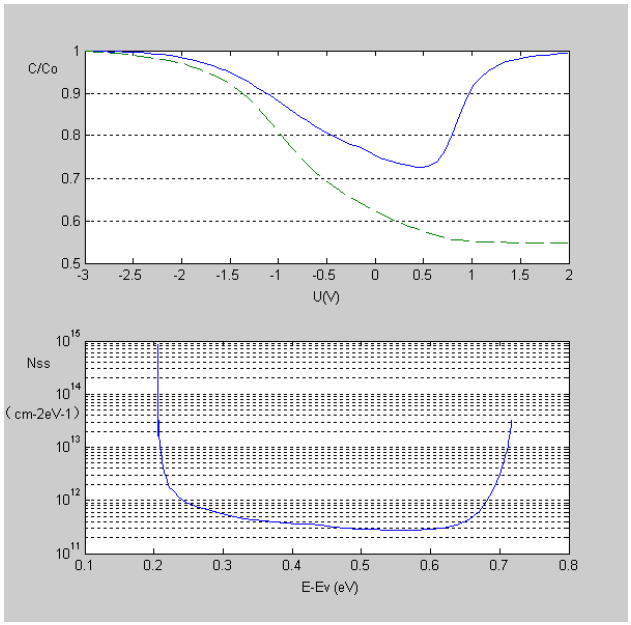

Fig.1 C-V curve and interface density, sample A

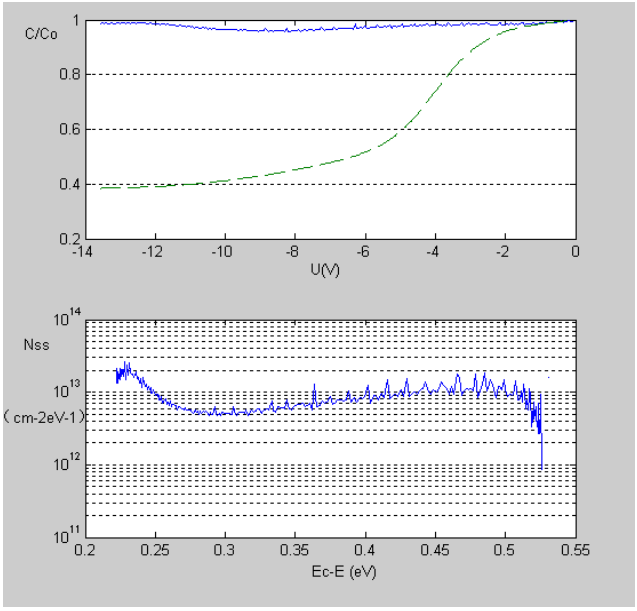

Fig.2 C-V curve and interface density, sample B

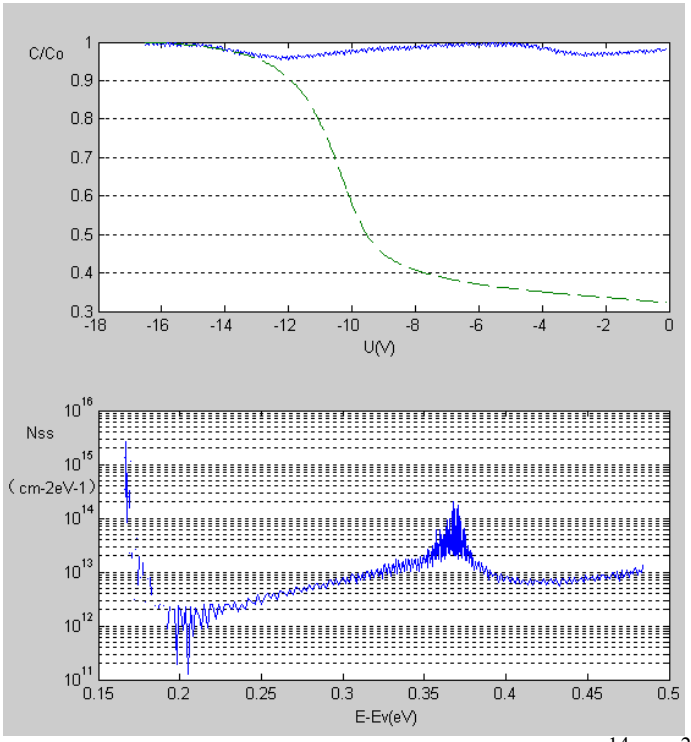

Fig.3 C-V curve and interface density, dosage: 1×10^{14} cm^{-2}， sample B

Fig.2 is the result of sample A after radiated by 0.8 MeV electron with radiation dosage is 2×10^{13} cm^{-2}. Interface density curve looks like a letter "U" shape. Fig.3 is the result of sample B after radiated by 0.8 MeV electrons with radiation dosage is 1×10^{14} cm^{-2}.

Discussion

Compare with sample without radiation, sample radiated by electron have been changed a lot. After radiation by electron, the interface density increases distinctly. From $10^{11}(cm^{-2}eV^{-1})$to $10^{13}(cm^{-2}eV^{-1})$, which is two order of magnitude higher than before. In Fig.2, interface density in the middle of energy gap is $10^{13}(cm^{-2}eV^{-1})$ with radiation dosage is 2×10^{13} cm^{-2} .When we increase the radiation dosage to 1×10^{14} cm^{-2},that is 5 times, now the interface density in the middle of

energy gap is $2\times10^{13}(cm^{-2}eV^{-1})$, that is 2 times. In addition, the shapes of interface density curve are different between samples A and sample B. The former still keep letter "U", while the latter changed distinctly with a peak in the curve at E_T=Ev+0.37.

SiO_2-Si interface is a complex field, which exist a lot of weak-bond and deformation-bond. Such as oxygen-vacancy-center (≡Si—Si≡) and silicon-hydrogen-bond (≡Si—OH,≡Si—H), they will change to dangling-bond (≡Si—) irradiated by electron, that is form of interface. Thus, interface density irradiated by electron decided by both of density of weak-bonds and density of electron-hole pair ionized by incident electron. According to deformation-bond fracture model proposed by Lai[7], deformation-bond existing SiO_2-Si interface will fracture while catches a hole and change to dangling-bond finally. This dangling-bond has been sure that energy level is $E_T=E_V+0.4$, which accord with peak energy level in Fig.3.

Conclusions

Metal-oxide-semiconductor (MOS) structure is highly sensitive to SiO_2-Si interface. It will reflect parameters such as interface density expediently. For the sake of researching of radiation effect of MOS structure irradiated by electron, we adopted 0.8 MeV electron at dosage between 2×10^{13} cm^{-2}~1×10^{14} cm^{-2} as radiation source respectively. We found that electron radiation will induce interface density at SiO_2-Si interface. According to comparison with C-V curve of MOS structure at high frequency and low frequency, we obtain that the experimental data of interface density is up to $10^{14}(cm^{-2}eV^{-1})$. In addition, we also obtain the relationship between the parameter and radiation dosage.

References

[1] E.M.Nicollian. MOS (Metal Oxide Semiconductor) Physics and Technology. New York: J.R.BREWS. Wiley, 1982.

[2] Lai Zuwu, et al. Radiation Hardening Electronics-Radiation Effects and Hardening Techniques. Beijing: Defence Industry Publishing House,1998.

[3] Cao Jianzhong. Radiation Effect of Semiconductor Materials.Beijing :Science Press,1993.

[4] Zhang Jianxin, Chen Yongping, Liang Pingzhi. Radiation Hardness Study of Passivation Film on Si Photodiode,J. Laser Technology.31(1)(2007) 83-85.

[5] Wang Huafu, Wu Ziqin. Experiment Method of Solid Physics. Beijing: Higher Education Publishing Company,1990.

[6] Pavol Pisecny. Determination of Interface Trap Density in Unipolar Structures Quasi-static C-V Method,J. Journal of Electrical Engineering.55(3-4)(2004) 20-24.

[7] N.S. Lai.Interface Trap Generation in Silicon Diode When Electrons Are Captured by Trapped Holed,J. Appl.Phys., 54(5) (1983) 2540-2546

doi:10.4028/www.scientific.net/AMM.161.144

A preliminary study on preparation of lithium ion-sieve flat sheet membrane

Zhiyong JI[1, a], Junsheng YUAN[1, b], Xiaofu Guo[1, c], Jun WANG[1, d], Ling LI[1, e]

[1]Engineering Research Center of Seawater Utilization Technology of Ministry of Education, Hebei University of Technology, Tianjin 300130, China

[a]jizhiyong@gmail.com, [b]jsyuan@hebut.edu.cn

Keywords: flat sheet membrane, lithium manganese oxide, ion-sieve, adsorption

Abstract. Based on preparing high purity powdered lithium ion-sieve precursor $LiMn_2O_4$, using lithium carbonate and manganese carbonate as raw materials, through roasting at high temperature of 800℃, laminar lithium ion-sieve precursor was prepared by commixing poly (vinyl chloride) (PVC) and powdered precursor in DMF (N, N-dimethylformamide) as solvent, and then powder and lithium ion-sieve flat sheet membrane was obtained through washing with HCl solution respectively. Their adsorption capacity and morphology was also characterized. The results show that both powdered lithium ion-sieve and laminar one have high adsorption capacity and selectivity for Li in solutions, and the effect of their retest is good. All these can provide a good foundation for the further study on lithium ion-sieve flat sheet membrane and lithium extraction from seawater.

1 Introduction

Lithium adsorbent was studied since the beginning of 70s last century [1-3]. Lithium ion-sieve developed rapidly because of its high selectivity, high adsorption capacity and high stability [4-7]. Spinel-type manganese oxide is considered the most promising lithium adsorbent, mainly due to the internal pore structure of its ion-sieve effect, and therefore called for the lithium ion-sieve [8-10]. $MnO_2 \cdot xH_2O$(x=0.3, 0.4, etc.) was mostly studied as lithium adsorbent, due to its spinel structure type after extraction of lithium as before [11]. After extraction, the space formed by Li and OH bond was conducive to the formation of lithium re-injection [12, 13]. There is little research on laminar lithium ion-sieve, but it has potential valuable for application relative to powdered one. In this paper, preliminary study on preparation of laminar lithium ion-sieve was carried out.

2 Materials and method

2.1 Reagents and apparatus

Chemical reagents used in the experiment are manganese carbonate, lithium carbonate, N,N-dimethylformamide(DMF) and hydrochloric acid. They are all analytical pure. There are also powdered PVC.

The main instruments used in the experiment are programmed temperature resistance furnace, vacuum oven electric, magnetic stirrer, vacuum pump filters, etc.

2.2 Experimental procedure

In this study, Li_2CO_3 and $MnCO_3$ as raw materials mixed with a certain percentage calcinated at 800℃ for 5 hours as the previous work. Then the pure phase precursor $LiMn_2O_4$ was obtained, which changes to lithium ion-sieve after washing with hydrochloric acid [13, 14].

Using sheet glass as carrier, laminar lithium ion-sieve precursor could be prepared mixed powdered lithium ion-sieve and PVC (about 20wt %) as a template in 80℃ water bath with DMF as solvent, and then it changes into lithium ion-sieve through washing with hydrochloric acid [15].

Put the powder or the laminar lithium ion-sieve into the solution containing lithium (home-made, lithium concentration of 0.17g/L, which is ten times of the concentration in the standard seawater) for 3 days so that the maximum adsorption capacity of the powdered lithium ion-sieve and the laminar one were obtained. After adsorption, hydrochloric acid was used to elute lithium from lithium ion-sieve, and then lithium ion-sieve recovers to its precursor.

The static adsorption experiment was like most of the conditions of the maximum adsorption, but the adsorption time was 16 hours. By the static adsorption experiments, the adsorption properties of the powder and lithium ion-sieve flat sheet membrane were studied and compared, and the corresponding characterization of XRD and SEM tests were carried out.

2.3 Analytical method

Chemical analysis of this study involves the concentration of lithium element analysis by atomic absorption spectrometry, also known as atomic spectrophotometer method. The analysis was carried out with the Shanghai Precision Scientific Instrument AA320 atomic absorption spectrophotometer. Powder X-ray diffraction (XRD) patterns were recorded on a Bruker D8 FOCUS diffractometer with Cu-Kα radiation. Scanning electron microscopy (SEM) was carried out with a Hitachi X-650 microscope operated at 0-40 KV.

3 Result and discussion

The XRD characterizations were shown in Figure 1~4. The results show that the method of high temperature solid was the effective shortcut to obtain the pure phase spinel $LiMn_2O_4$. The main crystal structure of the precursor eluted with hydrochloric acid is the same as the precursor. This is ion-sieve identity. It could be also obtained that laminar lithium ion-sieve has the same crystallographic texture as the powdered one. The characteristic peaks at some 2θ are almost accordant except some tiny skewing, and there is some contrast about the intensity of peaks.

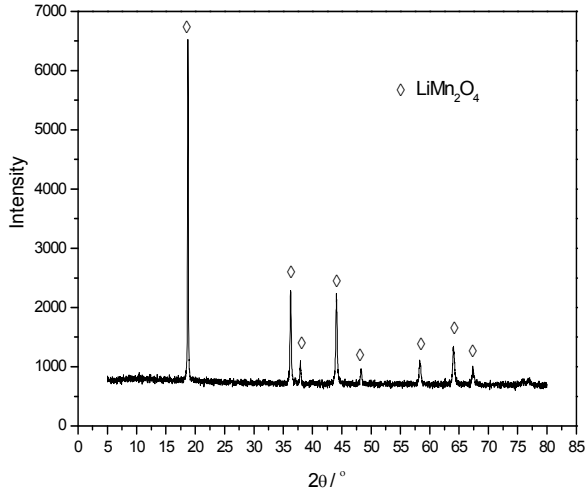

Fig.1 XRD of the powdered lithium ion-sieve precursor

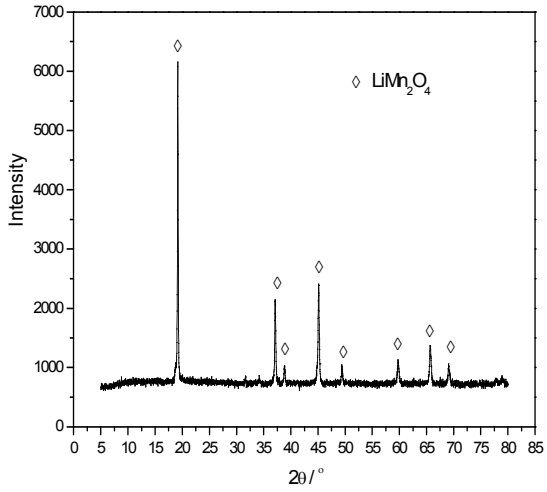

Fig.2 XRD of powdered lithium ion-sieve

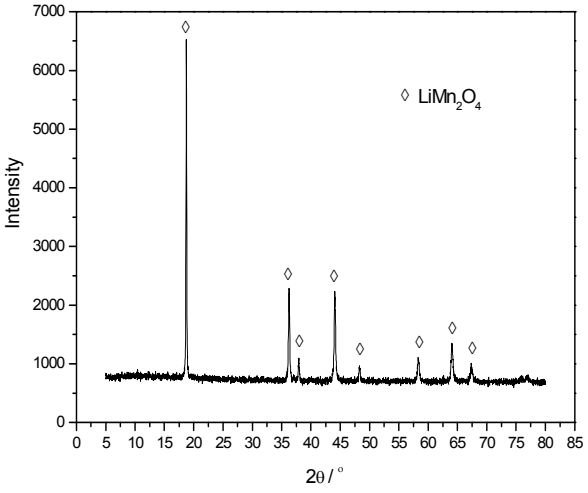

Fig.3 XRD of laminar lithium ion-sieve precursor

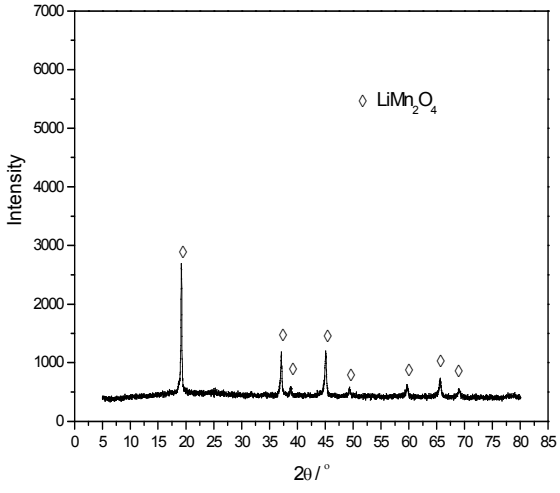

Fig.4 XRD of laminar lithium ion-sieve

Some SEM images are showed in Figure 5 and Figure 6. It could be seen that powdered lithium ion-seive precursor mixed well with PVC in the face side, and the back was in the shade. In the process of eluting with HCl solution, the structure of the laminar one has no obvious change.

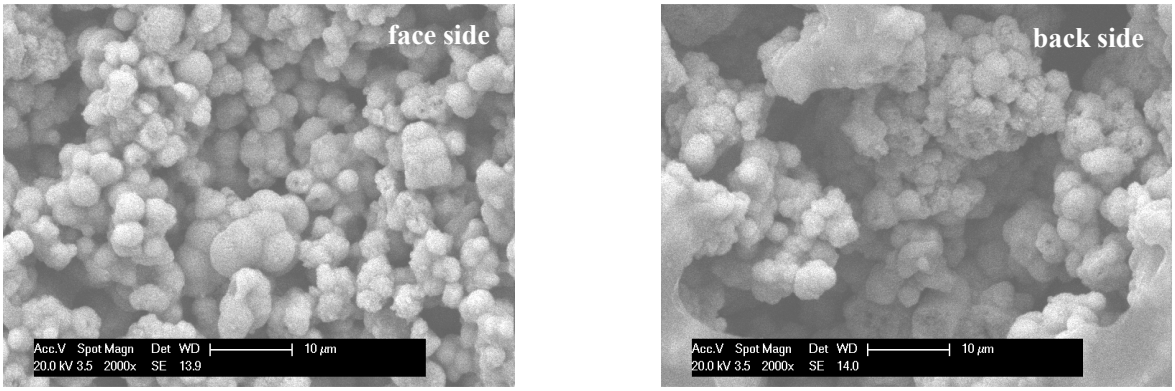

Fig.5 SEM of the precursor of laminar lithium ion-sieve

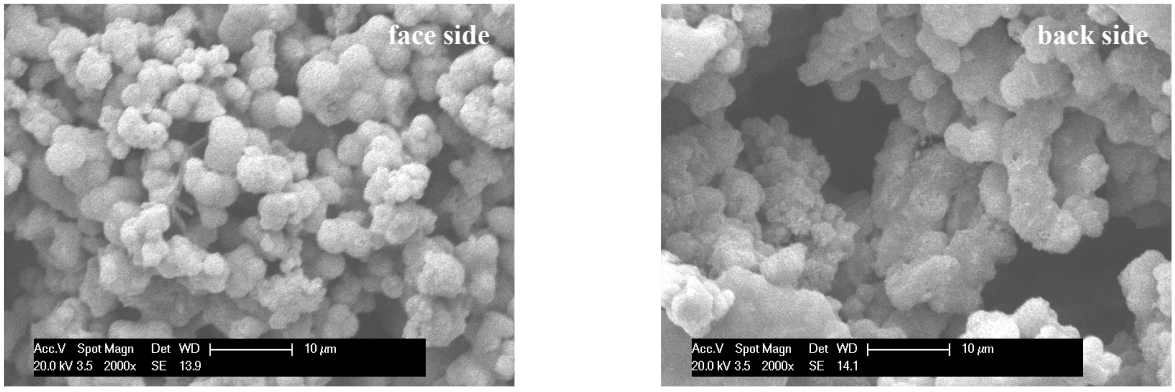

Fig.6 SEM of laminar lithium ion-sieve

The maximum adsorption capacity of the powdered lithium ion sieve and the laminar one were respectively 20.9 mg/g and 10.9 mg/g. The laminar one is lower than the powder. There are two main reasons: PVC content influencing the adsorption capacity; PVC wrapping lithium ion sieve particles. The repeated adsorption experimental data about the adsorption capacity of the powder and the laminar lithium ion-sieve is showed in Table 1. The result shows that either the powder or the flat, its recycling performance is good and its adsorption capacity is unchanged. The upload of the laminar lithium ion sieve is less than the powdered one, but the laminar one is convenient to the powdered one in the applied view. So enhancing the capacity of lithium ion-sieve flat sheet membrane for lithium is valuable in the future.

Table 1 The recycling adsorption capacity for lithium

Type of the lithium ion-sieve	Adsorption capacity [$mg \cdot g^{-1}$]		
	First time	Second time	Third time
Powder	16.6	15.0	16.2
Flat	4.1	4.0	4.1

4 Conclusions

Pure spinel lithium manganese oxide $LiMn_2O_4$ was prepared with the method of high temperature solid calcination. And the laminar lithium ion-sieve was obtained using the $LiMn_2O_4$ and PVC as raw materials at last. They have good adsorption capacity and selectivity for lithium, and the recycling performance is good. The powdered lithium ion sieve has a higher adsorption capacity as 20.9 mg/g, and the lithium ion-sieve flat sheet membrane is 10.9 mg/g because of the influence of PVC. At the point of application, lithium ion-sieve flat sheet membrane is prior to the powdered lithium ion-sieve for further research.

Acknowledgments

The research received financial support from National Natural Science Foundation of China (20806019), Natural Science Foundation of Hebei Province (B2009000024) and Education Department of Hebei Province (2008112). And the work is also supported by Program for Changjiang Scholars and Innovative Research Team in University（PCSIRT，IRT1059）.

References

[1] D. A. Lee, W. L. Taylor, W. J. Mcdowell, et al. Solvent extraction of lithium. J. Inorg. Nucl. Chem. 30(1976)2807-2821.

[2] A. H. Hamzaoui, A. M'nif, H. Hammi, et al. Contribution to the lithium recovery from brine. Desalination, 158(2003)221-224.

[3] Seung-Taek Myung, Hoon-Taek Chung. Preparation and characterization of $LiMn_2O_4$ powders by the emulsion drying method. J. Power Sources, 84(1999)32-38.

[4] Ramesh Chitrakar, Hirofumi Kanoh, Yoshitaka Miyai et al. A new type of manganese oxide derived from $Li_{1.6}Mn_{1.6}O_4$ and its lithium ion-sieve properties. Chem. Mater. 12(2000)3151-3157.

[5] R. Chitrakar, H. Kanoh, Y. Miyai, et al. Recovery of lithium from seawater using manganese oxide adsorbent ($H_{1.6}Mn_{1.6}O_4$) derived from $Li_{1.6}Mn_{1.6}O_4$. Ind. Eng. Chem. Res. 40(2001)2054-2058.

[6] Kenta Ooi, Yoshitaka Miyai, Shunsaku Katoh. Extraction reaction with λ-MnO_2 in the aqueous phase. Chem. Lett. 21(1988)989-992.

[7] K.Sato, D.M.Poojary, A.Clearfield, et al. The surface structure of the proton-exchanged lithium manganese oxide spinels and their lithium-ion sieve properties. J. Solid State Chem. 131 (1997) 391-396.

[8] Y.S.Kim, H.Kanohb, T.Hirotsua, et al. Chemical Bonding of ion-exchange type sites in spinel-type manganese oxides $Li_{1.33}Mn_{1.67}O_4$. Mater. Res. Bull. 37(2002)391-396.

[9] Hideki Koyanaka, Osamu Matsubaya, Yoshio Koyanaka, et al. Quantitative correlation between Li absorption and H content in manganese oxide spinel λ-MnO_2. J. Electroanal. Chem. 559 (2003)77-81.

[10] M. M. Thackeray, Manganese oxides for lithium batteries. Prog. Solid State Chem. 25 (1997) 1-71.

[11] R. Hitrakar, H. Kanoh, Y. Miyai, et al. A new type of manganese oxide ($MnO_2 \cdot 0.5H_2O$) derived from $Li_{1.6}Mn_{1.6}O_4$ and its lithium ion-sieve properties. Chem. Mater. 12(2000)3151-3157.

[12] Qi Feng, Yoshitaka Miyai, Hirofumi Kanoh et al. Li^+ Extraction / insertion with spinel-type lithium manganese oxides. Characterization of redox-type and ion–exchange-sites type. Langmuir, 8(1992): 1861-1867.

[13] Zhiyong Ji, Junsheng Yuan and Yinghui Xie. Synthesis of lithium ion-sieve with fractional steps. Adv. Mater. Res. 96(2010)233-236.

[14] JI Zhiyong, YUAN Junsheng, LI Xingang. Synthesis and property of spinel lithium ion sieve. Ion Exch. Adsorpt. 22(2006)323-329.

[15] JI Zhi-yong, YUAN Jun-sheng, LI Xin-gang. Synthesis of Li-adsorbent and its adsorption property. Chem. Eng.(China) 35(2007)9-13.

doi:10.4028/www.scientific.net/AMM.161.148

Optimum Synthesis of Myrtenal from α-Pinene by Photosensitized Oxidation Using Orthogonal Design

Binbin Zou[1, a], Qianwen Chen* [1,b], Weihua Luo[1,c] and Guiwu Wang[1,d]

[1]School of Material Science and Engineering, Central South University of Forestry and Technology, Changsha, Hunan 410004, China

[a]zbb1308@126.com, [b]cqwcsfu@126.com, [c]lwh6803@163.com , [d]wgwsuper21@yahoo.com.cn

Keywords: Photosensitized Oxidation; Orthogonal Optimization ;Myrtenal; α-Pinene

Abstract. Synthesis of myrtenal from α-pinene by photosensitized oxidation in the self-made photochemical reactor was carried out using the halogen lamp as the light source. The effect of photosensitized oxidation reaction variables on the conversion and selectivity of the reactions was evaluated by the orthogonal experimental design of $L_9(3^4)$.Gas chromatography analysis showed that 94.55% conversion of the materials and 56.16% selectivity of the product were obtained when pyridine-acetic anhydride - copper salt mixture as a catalyst was used for the reaction at 45 ℃ under 0.45 L/min oxygen rate, 0.378 mol/L catalyst concentration and 0.5 mol/L material concentration. Microstructures of myrtenal were characterized using Gas chromatography-mass spectroscopy (GC-MS) and Fourier transform infrared spectroscopy (FTIR).

1 Introduction

Natural bicyclic terpenes like α-pinene, known to be one of the most abundant groups of biogenic volatile organic compounds emitted by forest and woodland, are widely used in fine organic synthesis and the production of perfumes, such as myrtenal[1,2,3]. Myrtenal named 6,6-dimethyl-2-aldehyde-bicyclo [3.1.1]-2-heptheptence has received considerable attention in recent years as oral health supplies, tobacco products, food flavor and important synthetic organic intermediates[4].Many methods have been used to synthesize myrtenal. X G Liu[5] studied synthesis of myrtenal from α-pinene by the technology of microwave irradiation and phase transfer catalytic oxidation. α-pinene conversion was 83.8%. S H Deng[6] used extremely toxic activated SeO_2 as a catalyst and anhydrous ethanol as a solvent to synthesize myrtenal from α-pinene at reflux temperature for 5 hours. 61% yield of the product was obtained and the recovery of Se was 70%. M M Yang[7] synthesized myrtenal from α-pinene by electrochemistry oxidation. The yield of the product was 61%, when C-CrO_3, ethanol and $NaBF_4$ were used as anode material, solvent and sustain electrolyte, respectively.W Liu[8] investigated synthesis of myrtenal from α-pinene by Fe_2O_3-V_2O_5/Al_2O_3 catalytic oxidation.Under the optimal condition that was catalyst amount 5%, reaction temperature 80℃ and reaction time 6h, α-pinene conversion was 84.9%. However, huge power consumption and using expensive and extremely toxic substance as catalyst for the above methods limited their extensive applications in industrial production. Photosensitized catalytic oxidation technology of organic substrates using molecular oxygen as the final oxidant to substitute the traditional hot chemical oxidations had been a tendency from both the increased safety and economic point of view[9,10].

In this study, the effect of photosensitized oxidation reaction variables on the conversion and selectivity of the reactions in the self-made photochemical reactor was evaluated and the validity of the simple and green photosensitized oxidation was demonstrated through studying synthesis of myrtenal from α-pinene.

2 Experimental

2.1 Experimental Materials

Most chemicals used in the experiment were analytic reagents(AR). 95.4% α-pinene was provided by Zhuzhou Forest Chemical Factory; methylene blue was purchased from Shanghai Reagent Factory; 2,6 - dimethyl-pyridine were obtained from Aladdin Reagent Co.Ltd in Shanghai.;

decahydronaphthalene was provided by Enterprise Group Chemical Reagent Co.Ltd.; acetic anhydride ,acetonitriles and sodium bisulfites were purchased from Tianjin DaMao Chemical Reagent Factory; halogen lamps were purchased from Shanghai YaYuan Lighting Co.Ltd..

2.2 Photosensitized Catalytic Oxidation Reaction

The synthesis of myrtenal from α-pinene by photosensitized catalytic oxidation was carried out in a self-made photochemical reactor. First,α-pinene was added to 150 mL acetonitrile solution to form a mixture. Then, 3.4 x 10^{-3}mol/L methylene blue, decahydronaphthalene, a certain amount of 2, 6-two methyl pyridine-acetic anhydride-copper salt composite were added one after the other as photosensitizer, internal standard and catalysts ,respectively. The photochemical reaction was carried out for refluxing 8 h under circulation water when the mixture bubbled through O_2 was heated up to 31℃-45 ℃under the visible light radiation,sampling 3 ml each hour after 4h. Finally, the products reduced by 10% sodium hydrogen sulfite solution were identified by GC, GC-MS and FTIR analysis after being left in the dark for one night.

2.3 Measurements

2.3.1 Gas Chromatography Analysis

The product samples were collected after 6 h and analyzed by a Agilent 6890 gas chromatograph with a aprogrammed oven, a FID detector and a HP5 capillary column using N_2 as carrier gas. The conversion and selectivity values were calculated as the following:

$$\text{Conversion of a-pinene}(C\%)=(1- f_\alpha A_\alpha n_s / A_s n_\alpha) \times 100\%. \quad (1)$$

$$\text{Selectivity for myrtenal } (S\%)= f_P (1-C\%) A_P / C\% A_s \times 100\%. \quad (2)$$

$$f_\alpha = A_s n_\alpha / A_\alpha n_s. \quad (3)$$

$$f_P = A_s n_P / A_P n_s. \quad (4)$$

where A_α,A_s and A_P are GC peak area% of a-pinene,GC peak area% of internal standard and GC peak area% of myrtenal, respectively; n_α(mol), n_s (mol) and n_P (mol)are the number of moles of a-pinene, the number of moles of internal standard and the number of moles of myrtenal ,respectively; f_α and f_P are the mole calibration factor of a-pinene and the mole calibration factor of myrtenal, respectively.

2.3.2 GC-MS Analysis

The reaction products were analyzed by a Thermo science DSQ Ⅱ gas chromatograph-mass spectrometer (America) with aTR-IMS capillary column, a programmed oven, a ion source temperature at 250℃and EI ion source at 70 eV using He as a carrier gas.

2.3.3 FT-IR Analysis

FTIR spectra of myrtenal samples were recorded using a Thermo Fisher AVATAR 330 FT-IR spectrometer (America) in the range of 4000–400 cm^{-1}.The samples were prepared into KBr pellets.

3 Results and Discussions

3.1 GC-MS Analysis

The mass spectrogram of myrtenal is shown in Fig.1.As shown in Fig.1: m/z = 150 is assigned to the molecular ion peak (m^+), m/z = 135 ,m/z = 121 and m/z = 108 are from the fragment ion peak $[m\text{-}CH_3]^+$, $[m\text{-}CHO]^+$and $[m\text{-}C_3H_6]$ +, respectively. And m/z = 91 is considered to the fragment ion peak $[m\text{-}15\text{-}28\text{-}16]^+$ obtained from the molecular which was removed –CHO and the methyl firstly, then rearranged, removed again the methyl.m/z = 53 is assigned to the fragment ion peak of unsaturated olefins cracking.The results almost match the standard mass spectrogram of myrtenal.

3.2 FTIR Analysis

The FT-IR spectrum of myrtenal is shown in Fig.2. The FT-IR spectrum shows a peak at 1680.21cm-1for the –CHO absorption and a absorption peak at 1620.41 cm-1 arising from unsaturated -C=C- stretching vibrations, the absorption at the vicinity of 2976.54 cm-1due to C-H symmetric stretching vibrations of -C=C-H. 2937.96 cm-1,2887.8 cm-1,2814.5 cm-1 and 2714.19 cm-1 can be attributed to C-H stretching vibrations of $–CH_3$ and $–CH_2$, respectively. 1469.94 cm-1and1246.17 cm-1 due to C-H deformation vibration of $-CH_3$ and $-CH_2-$. And 1170.94 cm-1 is C-C stretching vibration, however,779.34 cm-1and 698.32 cm-1 is attributed to C-H deformation vibration of -C = C-H. Consequently, it clearly indicates that the absorption of each peak matchs myrtenal very good.

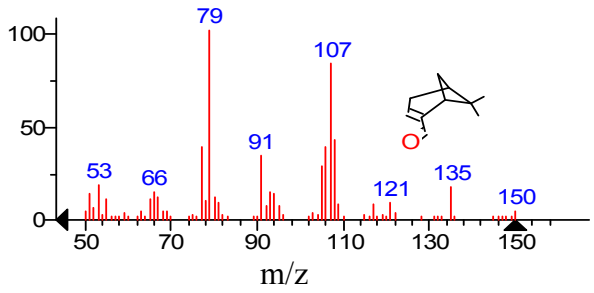

Fig. 1The mass spectrum of the product

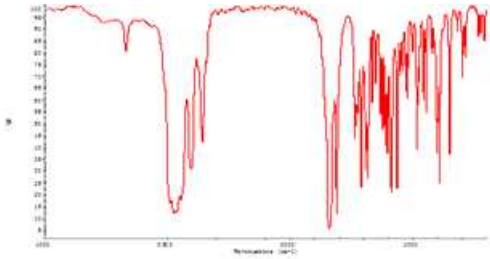

Fig.2 The FT-IR spectrum of myrtenal

3.3 Orthogonal Test

An $L_9(3^4)$ orthogonal experiment was employed for optimizing such technical parameters such as factor A- material concentration, factor B- reaction temperature, factor C- catalystcon centration, factor D- oxygen rate,as shown in table 1. The experimental results are shown in table 2.

Table 1 Factors and their levels of the $L_9(3^4)$orthogonal experiment

Level	Factor A	Factor B	Factor C	Factor D
	material concentration [mol/L]	reaction temperature [℃]	catalyst concentration [℃]	oxygen rate [L/min]
1	0.5	31	0.168	0.06
2	0.75	38	0.253	0.30
3	1.125	45	0.378	0.45

Table 2 Results of the $L_9(3^4)$orthogonal experiment

No.	Factor				Conversion	Selectivity
	A	B	C	D	%	%
1	1	1	1	1	96.01	51.82
2	1	2	2	2	96.63	44.90
3	1	3	3	3	94.55	56.16
4	2	1	2	3	97.16	42.70
5	2	2	3	1	95.48	48.57
6	2	3	1	2	98.52	40.46
7	3	1	3	2	96.04	44.84
8	3	2	1	3	96.93	34.26
9	3	3	2	1	84.64	40.11
kc_1	95.73	96.403	97.153	92.043		
kc_2	97.053	96.347	92.810	97.063		
kc_3	92.537	92.570	95.357	96.213		
Rc	4.516	3.833	4.343	5.020		
ks_1	50.960	46.453	42.180	46.833		
ks_2	43.910	42.577	42.570	43.400		
ks_3	39.737	45.577	49.857	44.373		
Rs	11.223	3.876	7.677	3.433		

(Note: kc is the average of the material conversion, ks is the average of the myrtenal selective,Rc is the range of the material conversion , Rs is the range of the myrtenal selective.)

The results shown in Table 2 indicate that the primary sequence and optimal combination of conversions were D–A–C–B and $A_2B_3C_1D_2$, respectively, by the range analysis. However, for selectivity, the primary sequence and optimal combination of conversions were A–C–B–D and $A_1B_3C_3D_3$.To sum up, according to the $L_9(3^4)$ orthogonal experiment, the best optimization reactions conditions of photosensitized oxidation are that material concentration 0.75 mol/L, reaction temperature 45 ℃,catalyst concentration 0.253 mol/L, oxygen rate 0.45 L/min. 94.55% conversion of the materials and 56.16% selectivity of the product were obtained by this optimization reaction condition.

3.4 Verifying the Optimal Combination

Experiments were repeated for three times under the best optimization reactions conditions based on the orthogonal experiment to verify the optimal combination. The experimental results are shown in table 3. The results show that the optimal combination based on the orthogonal experiment is reliable.

Table 3 Experimental results for verifying the optimal combination

No	material concentration [mol/L]	reaction temperature [℃]	catalyst concentration [℃]	oxygen rate [L/min]	conversion [%]	selectivity [%]
1	0.5	45	0.378	0.44	94.45	56.21
2	0.49	45	0.378	0.45	94.56	56.08
3	0.5	45	0.378	0.45	94.59	56.14

3. Conclusions

(1) The optimized conditions of photosensitized catalytic oxidation reactions are: material concentration 0. 5 mol/L, reaction temperature 45 ℃, catalyst concentration 0.378 mol/L, oxygen rate 0.45 L/min.

(2) GC-MS and FT-IR spectra of the product match very well with those of myrtenal.

(3) Myrtenals have been cost-effectively synthesized by a green photosensitized oxidation technology avoiding use of toxic heavy metals for the traditional hot chemical oxidation. Gas chromatography analysis showed that 94.55% conversion of the materials and 56.16% selectivity of the product were obtained.

4. References

[1] Guenther, A., Hewitt, C.N.and Erickson,D.,A global model of natural volatile organic compound emissions, J. Geophys. Res. (1995) 8873–8892.

[2] Plate A F,Milwtakaya E M Izv and Vcheb Zaved,Synthesis of Perillyl aldehyde Oxime from α-Pinene, J.KhimTeklmol.10(1967)1340.

[3] Acton E M, Yomamo to K and Stone H,Sweeteners based on syn oxirnes of 4-(methoxysubstituted)-cyclohexene- carboxaldehydes, U.S. Patent3,833,654.(1974).

[4] I. V. Il'ina, K. P. Volcho, D. V. Korchagina, V. A. Barkhash and N. F. Salakhutdinov, Transformations of (-)-myrtenal epoxide over askanite-bentonite clay, J. Russian Journal of Organic Chemistry.43(2007) 56-59.

[5] X G Liu and JF Wang,Synthesis of the 1,8-menthadiene-7-oxime from α-pinene, J. Food science.23(2002)76-79.

[6] S H Deng,Q Lin, X F Li, Synthesis of perillaldehyde from α-pinene, J.Guangdong chemical industry.1(1991)16-18.。

[7] M M Yang and N Li, Synthesis of Myrtenal by electrochemistry method, J.Chemical Technology and Development.2(2004) 11-12.

[8] W Liu,N Li and Y H Lv, Study on Oxidation of α-pinene to Myrtenal using Fe_2O_3-V_2O_5/Al_2O_3 Catalyst, J. Chemical Technology and Development.39(2010) 1-3.

[9] Sheldon RA, Dioxygenation activation and homogeneous catalytic oxidation, J. Chemtech. (1991) 566.

[10] Minjoong yoon and Devendra P. S. Negi.,Photoinduced electron transfer in some photosensitive molecules-incorporated semiconductor/zeolites: New photocatalytic systems , J. Journal of Chemical Sciences.114(2002) 593-602.

doi:10.4028/www.scientific.net/AMM.161.153

Fracture toughening of epoxy resins by addition of a novel thermoplastic PPAEs

Xu, Yajuan[1,a], Zhou, Sikai [1,b] and Jian, Xigao [2,c]

[1] School of Materials Science and Engineering, Luoyang Institute of Science and Technology, Luoyang 471023, China

[2] Department of Polymer Science & Materials, Dalian University of Technology, (116012) China

[a] dlxiaoxu@163.com, [b] zhousikai520@163.com，[c] jian4616@dl.cn

Keywords: PPEK, PPENK, epoxy resins, fracture tougheness

Abstract A series of blends have been prepared by adding a novel thermoplastic Poly (aryl ether) s containing phthalazinone moiety (PPAEs) in varying proportions to diglycidyl ether of bisphenol A epoxy resin (DGEBA) cured with *p*-diaminodiphenylsulfone (DDS). The glass transition temperature (T_g) of DGEBA /PPAEs blends were performed using differential scanning calorimetry (DSC) technique. It is proved that the addition of PPAEs resulted in enhancement of thermal properties of the blends, especially PPENK. There was moderate increase in the fracture toughness as estimated by notched impact strength. Compared to that of unmodified epoxy, the maximum toughness of the modified blends had increased 44% by addition of 15 phr PPENK. Fracture mechanisms such as plastic deformation and the ductile nature of the crack of the matrix were responsible for the increase in the fracture toughness of the blends.

Introduction

Thermosetting epoxies possess many desirable properties, such as high tensile strength and modulus, excellent chemical and solvent resistance, high dimensional and thermal stability, good adhesive properties and processability. These characteristics make them ideal candidates for many important applications, especially matrix for high-performance fiber-reinforced composites in aerospace. However, the epoxy resins are generally brittle due to their high cross-link density, which limits their further proliferation into other applications that requires more impact resistant or tougher materials. This drawback has prompted many studies devoted to increasing their fracture toughness without compromising their desirable attributes by thermoplastic [1-8]. Poly (aryl ether) s containing phthalazinone moiety (PPAEs) [9, 10], are a kind of novel high performance polymer. Their special structure endows them with excellent comprehensive properties, including outstanding thermal properties and good solubility. It is expected to toughen epoxy resins without decreaseing their thermal properties. Therefore, the research on the epoxy resins modification by PPAEs, Poly (phthalazinone ether ketone) (PPEK) and Poly (phthalazinone ether nitrile ketone) (PPENK) is proposed on the summarization of early study of thermoplastic modified epoxy resins.

A series of DGEBA / PPAEs blends were prepared by mechanical mixing without any solvent. In order to produce the mixtures with toughness and thermal resistance, we focused on the effects of the kinds and content of PPEAs on the structure and properties of DGEBA / PPAEs mixtures.

Experiment section

Materials

The epoxy resin was two diglycidyl ether of bisphenol A (DGEBA) sold as WSR618, supplied by Lanxing new materials resins Factory of Wuxi, China. The curing agent was *p*-diaminodiphenylsulphone (DDS), (supplied by Shanghai Sanaisi Reagent Co.Ltd, China). The thermoplastic was Poly (phthalazinone ether ketone) (PPEK) and Poly (phthalazinone ether nitrile ketone) (PPENK) (supplied by Dalian polymer novel materials company China).

Blend preparation

Blending systems were prepared using a standard procedure. The samples were prepared with 0, 5, 10, 15 phr of PPAEs in the DGEBA/DDS mixture, where phr represents the weight parts of PPAEs per hundred parts of the DGEBA epoxy resin. The thermoplastic PPAEs (PPEK or PPENK) and DGEBA were mixed together with the electric stirrer at 130 °C, until the thermoplastic was completely dissolved; then the stoichiometric (corresponding to a 1 : 1 epoxy to amine molar ratio) hardener (DDS) was added and mixed continually until the DDS had also completely dissolved to form homogenous solution. Then the samples was poured into an open chrome steel mould and put into a vacuum oven to degass, then to cure in an air circulating oven at 150 ºC for 3h and 180 ºC for 3h and postcured at 200 ºC for 2h.

Characterization Techniques

The thermal analysis work (glass transition temperature (T_g) was carried out by using NETZSCH DSC 204 at a heating rate of 10 °C min^{-1} under nitrogen.

The notched impact strength test was performed using the charpy impact strength measurement set (XCJ-4) according to the ASTM D 5942-96. The specimen dimensions were 60 mm ×6 mm × 4 mm. Five samples were used to measure the average impact strength reported for each condition.

The fracture surfaces of failed specimens from toughness measurement were analyzed with a KYKY2800B scanning electron microscope (SEM).

Results and discussion

The glass transition temperature analysis

To investigate the effect of the PPAEs on the thermal properties of the blends, the glass transition temperatures (T_g's) of the cured samples were measured by differential scanning calorimetry (DSC). The variation of T_g with the different thermoplastic is shown in Fig. 1.

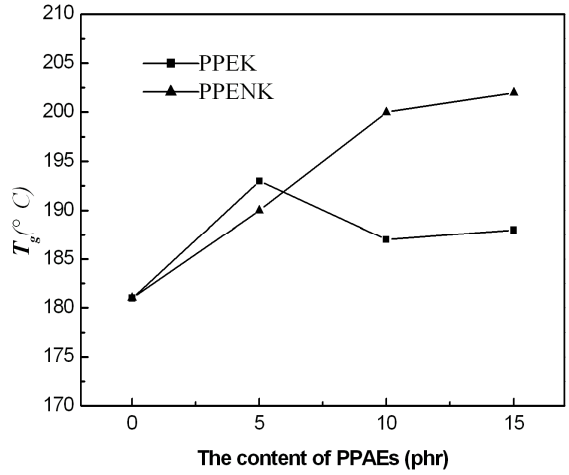

Fig.1 Plot of T_g of the samplaes versus PPAEs content

From Fig.1, we can see that the T_g of the DGEBA / PPEK blends decreased than that of the neat resin except the blends with 5 phr PPEK. The first increase of T_g is due to the high T_g of PPEK (265 °C) and the sequential decrease is caused by the reduced crosslink density of the epoxy

network because the curing reaction is incomplete caused by more content of PPEK[11]. However, the T_g of DGEBA/PPENK blends was higher than that of the pure epoxy. It is possible that strong interaction formed between the hydroxyl of epoxy and polar pendent nitrile group of the PPENK , then the rigid chain of PPENK(T_g =282 °C) are bound to the epoxy network that limited the epoxy phase to move and accordingly increased the T_g of the blends.

Fracture toughness and SEM observation

The fracture toughness of the blends, expressed as notched impact strength, is plotted in Fig. 2.

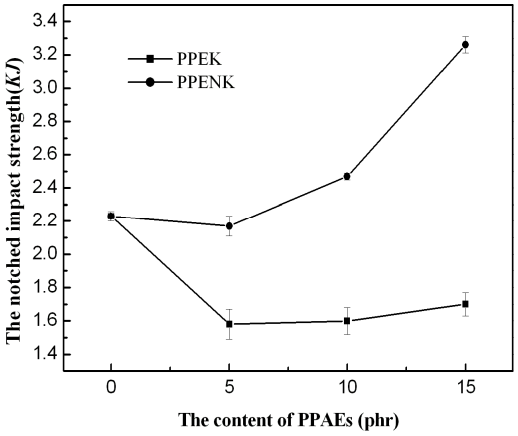

Fig.2 Impact strength of DGEBA/PPAEs blends

The fracture toughness has a tendency to decrease when the PPEK content increases. Fig.3 shows the SEM micrograph of the fracture surface of the blends. We give an example of 15 phr PPAEs. The cracks of DGEBA/15phr PPEK spread freely and regularly and are oriented in the direction of loading, almost remaining the same as the pure epoxy, which suggested typical characteristics of brittle fracture. However, the fracture toughness increased with increase of PPENK content and an increament of 44% was obtained by the addition of 15 phr PPENK. The results of T_g revealed good interfacial adhesion between the matrix and dispersed PPENK domains. Hence the stress is transferred more effectively to the thermoplastic domains, which are more ductile compared to the cross-linked epoxy resin. The scanning electron micrographs of failed specimens from fracture toughness measurements are shown in Fig. 3c. The fracture surfaces of the blends were rough and river marks were also seen on the fracture surfaces, indicating plastic deformation of the matrix and the ductile nature of the crack. One of the important criteria for obtaining increased fracture toughness in rubber or thermoplastic-modified epoxy resin systems was two-phase morphology. Moreover, there should be good interfacial adhesion between the two phases [12]. As a result, functionalized polymers, which are capable of reacting with epoxy, are excellent toughening agents for epoxies.

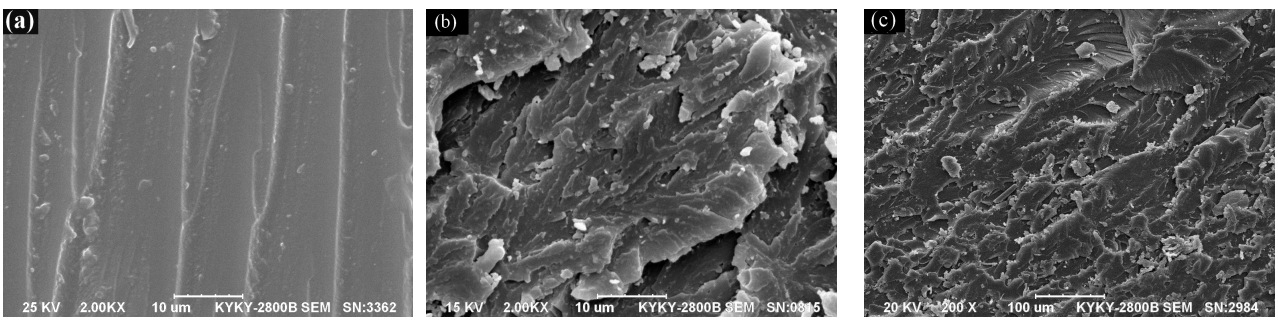

Fig.3 Scanning electron micrographs of failed surfaces of DGEBA/PPAEs blends (a) pure epoxy and (b) 15 phr PPEK and (c) 15phr PPENK

Conclusions

From all the results obtained, it can be concluded that PPENK is more ideal candidate for toughening epoxy resins than PPEK, which attributed mainly to the interaction contribution. The thermal properties were significantly enhanced by the addition of PPENK. The fracture toughness of the blends was higher than that of unmodified resin. The fracture toughness increased with the increase in PPENK content in the blends and the increment of toughness was 44% at 15-phr PPESK. The increase in fracture toughness was attributed to the local plastic deformation of the matrix, ductile tearing of the dispersed thermoplastic, and crack path deflection.

Acknowledgement: This work was financially supported by the Ph D Funding (2009BZ04)

References

[1] R. S. Raghava, Role of matix-particle interface adhesion on fracture toughness of dual phase epoxy-polyethersulfone blend, J. Polym. Sci. Part B: Polym. Phys. 25(1987) 1017-1031.

[2] B. S. Kim, T. Chiba, T. Inoue, Morphology development via reaction-induced phase separation in epoxy / poly(ether sulfone) blends:morphology control using poly(ether sulfone) with functional end-groups, Polymer. 36 (1995) 43-47.

[3] C. Girodet, E. Espuche, H.Sauterau, Influence of the addition of thermoplastic performed particles on the properties of an epoxy/anhydride network, J. Mater. Sci. 31(1996) 2997-3002

[4] R. J. Varley, J. H. Hodgkin, G. P. Simon, Toughening of a trifunctional epoxy system Part IV:Structure property relationships of the thermoplastic toughened system, Polymer. 42(2001) 3847-3858.

[5] S. J. Park, K. Li, F. L. Jin, Thermal stabilities and mechanical interfacial properties of polyethersulfone-modified epoxy resin, J. Industrial. Eng. Chem. 11(2005) 720- 725.

[6] B. Francis, S. Thomas, G. V. Asari, Synthesis of hydroxyl-terminated poly(ether ether ketone) with pendent tert-butyl groups and its use as a toughener for epoxy resins, J. Polym. Sci. Part B: Polym. Phys. 41(2006) 541-556.

[7] A. Saxena, B. Francis, V. Lakshmana, Toughening of an epoxy resin with hydroxyl-terminated poly (arylene ether nitrile) with pendent tertiary butyl groups, J. Appl. Polym. Sci. 106(2007) 1318-1331.

[8] J. X. Song, G. Wu, J. J. Shi, G. X. Chen, Q. F. Li, Properties and morphology of interpenetrating polymer networks based on poly(urethane-imide) and epoxy resin. Macromolecular. Research. 18(2010) 944-950

[9] Y. Z. Meng, A. S. Hay, X.G. Jian, S. C.Tjong, Synthesis of novel poly (phthalazinone ether sulfone ketone) s and improvement of their melt flow properties, J. Appl. Polym. Sci. 66 (1997), 1425-1432.

[10] X.G. Jian, P.Chen, G. X. Liao, X. L. Zhu, S. H. Zhang, J. Y. Wang, Syntheses and properties of novel high performance series Poly(aromatic ethers) polymers containing phthalazinone moieties, Acta Polymerica Sinica. 4 (2003) 469-475.

[11] Y. J. Xu, S. K. Zhou, G. X. Liao, X. G. Jian, Curing kinetics of DGEBA epoxy resin modified by poly (phthalazinone ether ketone) (PPEK), Polymer-Plastic Technology and Engineering, *in press.*

[12] C.B. Bucknall, I.K. Partridge, Phase separation in epoxy resins containing polyethersulphone, Polymer. **24** (1983) 639-644.

doi:10.4028/www.scientific.net/AMM.161.157

The Synthesis of Polystyrene-b-Poly(4-Vinylpyridine) and Its Application

Sikai Zhou[1,a*], Yajuan Xu[1,b], Shaoming Fang[2,c]

[1] School of Materials Science and Engineering, Luoyang Institute of Science and Technology, Luoyang 461703, China

[2] College of Materials and Chemical Engineering, Zhengzhou University of Light Industry, Zhengzhou, 450002, P. R. China

[a] zhousikai520@163.com, [b] dlxiaoxu@163.com, c mingfang@zuli.edu.cn

Keywords: Nitroxide-Medium free radical polymerization, Diblock copolymer, Compatibiliers, Polystyrene, Poly(4-vinylpyridine)

Abstract: a system of polystyrene and polystyrene-block-poly(4-vinylpyridine) (PS-b-P4VP) were synthesized by using living free radical in the presence of 4-hydroxyl-2, 2, 6, 6-tetramethylpiperridine-oxyl-1(HTEMPO•) and (BPO). The polystyrene and diblock copolymers were characterized by gel permeation chromatography (GPC) and atomic force microscope (AFM). The results suggested that the polymerization of styrene in the presence of 4-hydroxyl-2, 2, 6, 6-tetramethylpiperridine-oxyl-1(HTEMPO•) and benzoyl peroxide (BPO) can be prepared with molecular weight distribution in the range of 1.15 to 1.25. The polystyrene with living groups can continuously initiate the living free radical polymerization of 4-Vinylpyridine to form the polystyrene-block-poly (4-vinylpyridine) with molecular weight distribution in the range of 1.08 to 1.35. The AFM of diblock indicated the diblock copolymer（PS-b-P4VP） is a good compatibilizer for PS and P4VP.

Introduction

Recently, the synthesis ot diblock copolymers with well-defined structure by using living polymerization has been paid more attentions in the macromolecule synthetic field [1-3]. Presently, Living polymerization included anionic polymerization [4], cationic polymerization [5], nitroxide-mediated radical polymerization [6], atom transfer radical polymerization [7, 8] and so on. The homopolymers or block copolymers with narrow polydispersities could be prepared by using anionic or cationic polymerization, but they do have some drawback such as rigorous synthetic requirements and only applied little kind of monomers. However, living free radical polymerizations have some advantages, such as, moderate reaction conditions, liable conformity and wide range of applications. So more and more people are interested in the method of living free radical polymerization.

Here, polystyrene was synthesized by using living free radical polymerization in the presence of HTEMPO and BPO, then the PS-HTEMPO was dissolved into 4-vinylpyridine to react continuely. Finally the diblock copolymers PS-b-P4VP with well-definde structure were prapred, which was used the compatibilizer for PS and P4VP to improve the toughness of the blends.

Materials

St (Tianjin 1st Factory of Chemicals, China, 99%), which was distilled under reduced pressure before use; commercially obtained 4-VP (Aldrich, 95%), which was distilled under reduced pressure in the present of calcium hydride before use; BPO (Shanghai Factory of Chemicals, 99%) was purified by recrystallization with absolute ethanol. Calcium hydride (Beijing Factory of Chemicals), 4-hydroxyl-2, 2, 6, 6-tetramethylpiperidine (Beijing Huashan Auxiliary Factory).

Diblock polymer of PS-b-P4VP synthesis

The synthesizing process was described as below: 50-ml of three-necked flask was treated with high pure nitrogen for 30 min. St, BPO, and TEMPO-OH were inject into the three-necked flask and then were treated with five cycles of injecting nitrogen-pump. The three-necked flask was

placed into oil bath, stirred with magneticstirrer, at 95°C for 2 h to allow the decomposition of BPO, and then was heated up to 135°C in the present of nitrogen atmosphere. The polymerization was stopped by cooling the reaction system to 0°C. The polymer was purified through dissolving it in solvent of HNF, and precipitating in methanol. This step was repeated three times.

The former of PS-HTEMPO and 4-VP were added to three-necked flask and then was treated with five crush (nitrogen)—pump cycles. The three-necked flask was placed into an oil bath, stirred with magneticstirrer, at 95 °C for 1h to allow the decomposition of PS-OH, and then was heated up to 135°C in the present of nitrogen atmosphere. The polymerization was stopped by cooling the reaction system to 0 °C. The diblockpolymer was purified through dissolving it in solvent of DMF, and precipitating in ethanol and (1/1,v/v). This step was repeated three times. A schematic description of the synthesizing process is shown in Fig. 1.

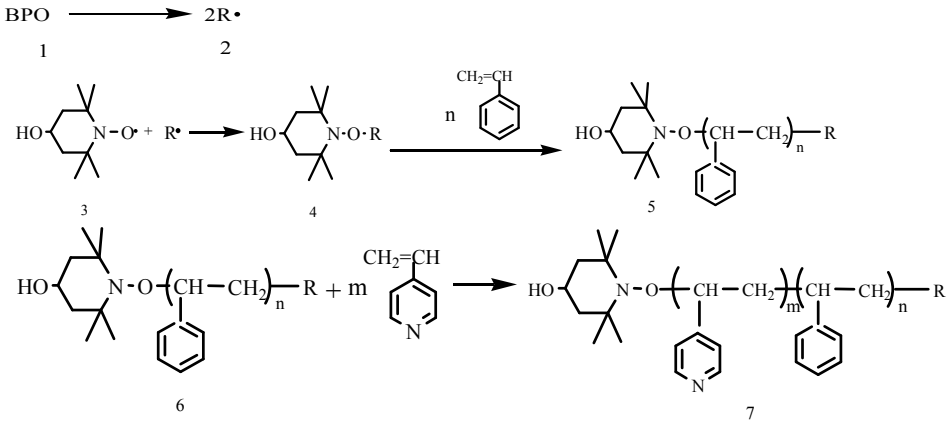

Fig. 1 The Scheme of Polymerization Route of PS-b-P4-VP

The system of compatibiliers synthesis

PS, P4VP, PS-b-P4VP were dissolved in solvent of DMF according to proportion of weight (1/1/0, 1/1/1, 1/1/2). Then their compatibiliers were spin-coated on silicon wafers that were cleared before use. The film was dried for 24 h at 170 °C.

Measurements

Infrared spectra were recorded on Bruker TENSOR27 FTIR spectrometer. The molecular weight (*Mn*,) and distributionindex (M_W/Mn) were determined with a Daojin LC-10AD gel permeation chromatograph (GPC) employed with ultraviolet detector. For the samples for which the molar fraction of PS-b-P4-VP was higher than 0.6, *N*,*N*-dimethylformamide (DMF) was used as elution solvent, and PS tetrahydrofuran (THF) was used as elution solvent. Atomic force microscope measurement (AFM) was performed on Veecoo NanoScope Ⅲa .

Results and discussion

Living free radical polymerization of styrene

Table 1 Data of the polymerization of St

HTEMPO• /BPO	Reaction Time(h)	Mn(10^{-4}) (PS)	Mw/Mn
1.8/1	2	0.96	1.15
	4	1.09	1.15
	6	1.20	1.16
	8	1.30	1.18
	12	2.34	1.19

Reaction at 135±2℃

Table 1 summarizes the data related to molecular weights, and polydispersities of samples obtained using TEMPO-OH–mediated living radical polymerization at 135 °C with different polymerization times. The molar ratio, HTEMPO/BPO was 1.8/1. As expected, the polydispersity

was in the range of 1.153 to 1.189. The molecular weights of PS increased with polymerization time in system. According to Michael theory, we speculate on the reaction mechanism of St as below: BPO decompound at 95 °C, this step gives initial free radicals. The initial free radicals was trapped rapidly by HTEMPO radicals and become steady intermediate because HTEMPO is a good captor for free radicals. As the HTEMPO is surplus, there is few initial free radicals in the reaction system. The polymerization of St in the presence of HTEMPO is a controllable living free-radical polymerization, the polymerization of St in the presence of nitroxide stable free radical has no self-accelerating effect, and the reaction of the inserting of monomers into the bond of C-ON in dormant compound is predominantly propagation.

The preparation of polystyrene-b-poly (4-vinylpyridine)

Table 2 lists the data related to molecular weights and polydispersities of polystyrene-b-poly (4-vinylpyridine) obtained using TEMPO-OH–polystyrene living radical polymerization at 135°C with different polymerization times. The polydispersitie was in the range of 1.2 to 1.35. The molecular weights of PS-b-P4VP increased with polymerization time in the system. The molecular weights of P4VP can be obtained by the molecular weights of PS-b-P4VP subtracting PS's. The molecular weights of P4VP increased with protracting polymerization time. But the polymerization velocity becomes slow with protracting polymerization time, which due to the free radicals was rapped by polymer chains. All results showed that the polymerization of polystyrene-b-poly (4-vinylpyridine) is a controllable living free-radical polymerization, and the reaction of the inserting of 4-VP into the bond of C-ON in dormant compound is predominantly propagation.

Table 2 Data of the polymerization of PS-b-4-VP and 4-VP

Reaction Time PS/P4VP (h)	Mn(10^{-4}) (PS-b-P4-VP)	Mn(10^{-4}) (PS)	Mn(10^{-4}) (P4-VP)	Mw/Mn
2/2	1.39	0.96	0.43	1.21
4/4	1.60	1.09	0.51	1.12
6/6	1.88	1.20	0.68	1.20
8/8	1.99	1.30	0.69	1.31
12/12	3.08	2.34	0.74	1.28

Reaction at 135±2℃

The compatibility of PS/P4VP/PS-b-P4VP

Fig. 2 shows the Atomic Force Microscope of the blend about PS and P4VP with a molar ratio of 1:1. The plane morphology and dimensional morphology of the blend system were expressed in fig. 2a and fig. 2b respectively. From the surface energy of PS and P4VP we know that P4VP is continuous and PS is not continuous on the silicon surface. From Fig. 2 a we see there is clear interface between P4VP and PS, which Prove PS and P4VP relatively poor compatibility. Fig. 2 b exhibit that the mixes system of PS and P4VP presents " island"structure, many PS's particles come out from the base, and the particles is relatively big and smooth.

Fig.3 exhibits the Atomic Force Microscope of the blend about PS, P4VP and PS-b-P4VP with a molar ratio of 1:1:1. From fig. 3 b, we see there are still some particles on the base, but the numbers of particles reduce and the highness of particles becomes low in evidence. Fig.3 a exhibit that interfaces of the mixes system between P4VP and PS become blur, which prove there is strong adhesion between PS and P4VP, the compatibility of the system is improved, which is because of their interfacial activity. Block copolymers as emulsifiers is because of their partitioning to the blend interface, where each block preferentially extends into its respective homopolymer phase, which lead to a finer and more homogeneous dispersion during mixing, and enhances interfacial adhesion.

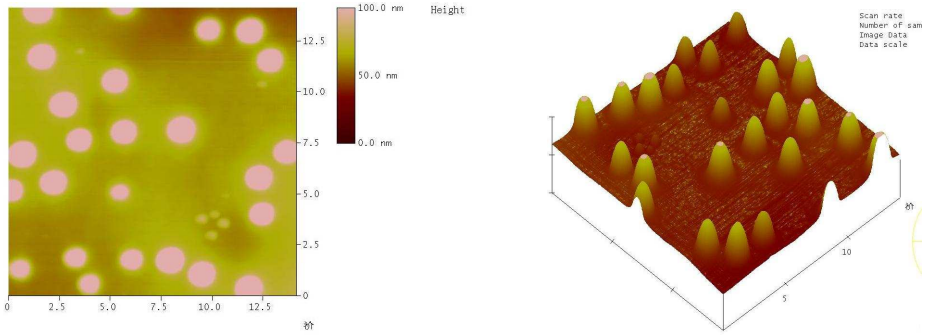

a **b**

Fig. 2 AFM images of mixed system without compatbilier

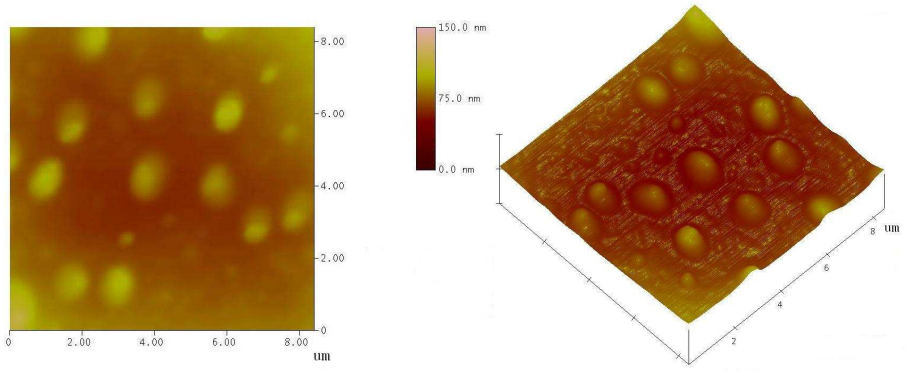

a b

Fig. 3 AFM images of mixed system with compatbilier

Fig. 4 presents AFM images of PS and P4VP blend-system where PS-b-P4VP is a compatibiliers. Here, the ratio of PS and P4VP and PS-b-P4VP is 1:1:2. Fig. 4 a shows that there is rather little PS whose morphology is irregular. What is observed is that the size of dispersed particles of PS is small and the height of it is very low. Furthermore, the smooth surface is obviously seen from phase image of AFM (Fig. 4c) and the color of image is homogeneous, which show the interphase between PS and P4VP is to disappearing. So, union- phase of total system is formed due to strong adhesive force between the phase of PS and P4VP.

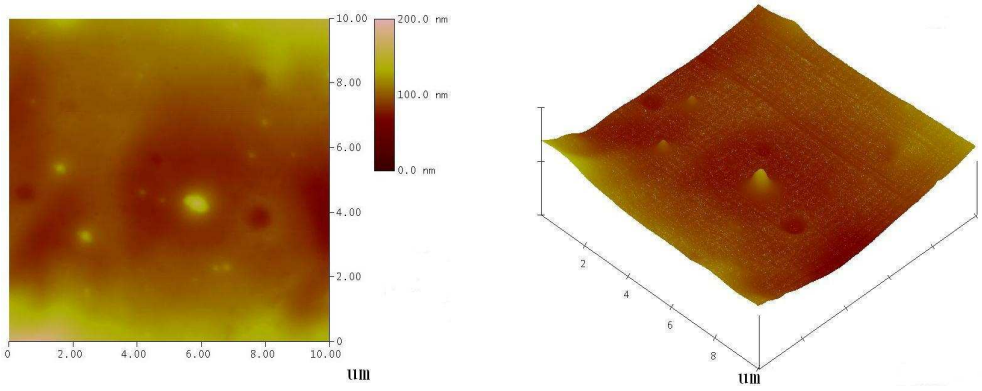

a b

Fig. 4 AFM images of mixed system with compatbilier

As above, addition agent is necessary to the blend system of PS and P4VP. Here, PS-b-P4VP is a good additive and the larger of amount of it, the better of compatibility of them.

Conclusions

1) polystyrene was synthesized by using living free radical in the presence of 4-hydroxyl-2, 2, 6, 6-tetramethylpiperridine-oxyl-1(HTEMPO•) and (BPO), the polydispersity was in the range of 1.1 to 1.2. The molecular weights of PS increased with polymerization time in system.

2) Polystyrene with living radical can continuously initiate 4-vinylpyridine at 135°C to form the polystyrene-block-poly (4-vinylpyridine) with molecular weight distribution in the range of 1.08 to 1.35.

3) The diblock polymerization is good compatibiliers for PS and P4VP, and copatibilier performance increasing with the quantity of PS-b-P4VP increasing.

Reference:

[1] J. Aubrey, G.. J. Richard, M. Graeme. Terminology for reversible-deactivation radical polymerization previously called "controlled" radical or "living" radical polymerization (IUPAC Recommendations)". Pure Appl. Chem. 82 (2010) 483–491.

[2] S.Yamago, E. Kayahara, M. Kotani, B. Ray, Y. Kwak, A. Goto and T. Fukuda. "Highly controlled living radical polymerization through dual activation of organobismuthines". Angew. Chem. Int. Ed. 46 (2007) 1304–1306.

[3] S. Yamago, B. Ray, K. Iida, J.-i. Yoshida, T. Tada, K. Yoshizawa, Y. Kwak, A. Goto and T. Fukuda. "Highly Versatile Organostibine Mediators for Living Radical Polymerization". J. Am. Chem. Soc. 126 (2004) 13908–13909.

[4] N. Hadjichristidis, H. Iatrou, P. Pitsikalis, J. Mays. Macromolecular architectures by living and controlled/living polymerizations. Prog. Polym. Sci. 31 (2006) 1068-1132.

[5] M. Sawamoto. Modern Cationic Vinyl Polymerization. Progress in Polymer Science 16 (1991). 111–172.

[6] Z. Chen, J. Cai. Nitroxide-mediated radical polymerization of 4-vinylpyridine and its application on modification of silicon substrate.Joural of Applied Polymer Science, 86 (2002) 2687～2692.

[7] A. Goto, Y. Kwak, T. Fukuda, S.Yamago, K. Iida, M. Nakajima and J. Yoshida. Mechanism-Based Invention of High-Speed Living Radical Polymerization Using Organotellurium Compounds and Azo-Initiators, J. Am. Chem. Soc. 125 (2003) 8720–8721.

[8] K. Matyjaszewski and J. Xia. Atom Transfer Radical Polymerization. Chem. Rev. 101 (2001) 2921–2990.

[9] G. D. Gunton, M. M. San, P. S. Sahini. Phase Transitions and Critical Phenomena.Domb C, Lebowitz J L, Eds, Academic Press, London,(1983) 18-36.

doi:10.4028/www.scientific.net/AMM.161.162

Adsorption of Mercury Ion on Activated Carbons from Rice Husk

SONG Xiao Lan[1,a], ZHANG Ying[1,b], YAN Cheng Yin[1,c], JIANG Wen Juan[1,d], XIE Hong Jiang[1,e]

[1]School of Mineral Processing and Bioengineering, Central South University, Changsha Hunan 410083, P.R. China

[a]xlsong365@126.com

Keywords: Activated carbon; Rice husk; Mercury ion; Adsorption

Abstract. The adsorption performance of mercury ion onto activated carbon prepared from rice husk with NaOH was carried out at initial concentration of 100 mg/L. The activated carbon obtained at 800 °C possessed the outstanding specific surface area of 2786 m^2/g. And the results showed that the maximum adsorption capacity of Hg^{2+} was recorded as 342.0 mg/g due to abundant micropores of 1.076 nm. In addition, the adsorption data were well explained by the Langmuir model with the monolayer adsorption capacity of 555.6 mg/g.

Introduction

Mercury (Hg), as a typical heavy metal, is the important raw material of chloro-alkali, pharmaceutical and electronic industries. However, the mercury in environment was serious threat to human due to its high toxicity and persistent presence. So the World Health Organization (WHO) recommends a maximum concentration of 1 μg/L in drinking water. Nowadays, the common removing methods include adsorption, membrane filtration, chemical coagulation, ion exchange and electrodialysis [1]. Among them, adsorption is an efficient and inexpensive technology.

Activated carbon (AC) is a well-known porous adsorbent for the removal of heavy metals ions from wastewater, like Hg^{2+} [1], Pb^{2+} [2], Cu^{2+} [3] and Cr^{6+}. But the common raw material of coal shows the high cost. Thus, some wastes, such as the stone [3], wood, tire and sludge, were the potential candidates for preparing AC. As the largest rice producer in the world, China has a large number of rice husk resources (about 20 wt% of rice). But most of rice husk has been disposed or burned. Given this, it is meaningful to use rice husk as the raw material to prepare AC [4,5].

At present, an apparent problem for the utilization of rice husk was its high ash content (mainly silica) obstructed the pore development of AC, leading to the low specific surface area of carbon (< 1500 m^2/g). Nevertheless, traditional activating agents like $ZnCl_2$ [4] and H_3PO_4 cannot react with SiO_2. In view of this problem, NaOH was selected as the activator to reduce ash in this work. Although there were many reports on the adsorption of mercury ion from wastewater, reports on adsorption of Hg^{2+} onto AC originating from rice husk are few. This lack in the existing work is a motivation for our research.

The aim of the present study is to evaluate the adsorption performance of mercury ion onto AC prepared from rice husk. And the batch adsorption experiments for the removal of Hg^{2+} solution had been carried out at room temperature. Meanwhile, the experimental data had been estimated by different adsorption isotherms.

Material and methods

Chemical reagents were all of analytical grade. The rice husk was carbonized at 600 °C in N_2 for 2 h firstly. Then NaOH was mixed with the carbonized rice husk at mass ratio of 3. Subsequently, reactants were heated to 800 °C for 2 h. After the mixture was cooled to room temperature, dilute hydrochloric acid was added to remove excess NaOH. At last, the product was thoroughly washed and dried at 110 °C for 2 h.

Textural characterization of material was measured from N_2 adsorption-desorption isotherms obtained at 77 K with a gas sorption analyzer (Autosorb-1, Quantachrome). The specific surface area (S_a) was calculated by the Brunauer-Emmett-Teller (BET) method. Besides, the total pore volume (V_t) was calculated at a P/P_0 of 0.99. And the micropore specific surface area (S_m) and volume (V_m) were both estimated by using the Dubinin-Radushkevich (DR) model. Furthermore, the pore size distribution was evaluated based on the density functional theory (DFT).

Crystalline structures of samples were examined by an X-ray diffractometer (D/max2550PC, Rigaku). The X-ray diffraction (XRD) pattern was obtained at 40 kV and 250 mA, using Cu Kα radiation (λ=0.154 nm) in the range of 10~70° (2θ) with a step width of 0.02°.

Surface morphology of the AC was investigated by using a scanning electron microscopy (SEM, Quantn-200, FEI) with the accelerated voltage of 20 kV.

In batch adsorption experiments, $Hg(NO_3)_2$ was selected as the adsorbate. The different amounts of ACs (0.05, 0.10, 0.15 and 0.20 g) were added into 200 mL of Hg^{2+} solution (100 mg/L) at 20 °C. And the dithizone ($C_{13}H_{12}N_4S$) was added into supernatant to form the chelateat [6]. Then the concentration of Hg^{2+} was determined by an ultraviolet spectrophotometer (SP-756P, Spectrum) at a wavelength of 490 nm. The adsorption capacity q_e (mg/g) of Hg^{2+} for AC was calculated using the following equations:

$$q_e = \frac{(C_0 - C_e) \cdot V}{M} \tag{1}$$

where C_0 and C_e are initial and equilibrium Hg^{2+} concentrations (mg/L), respectively. V is volume of solution (L) and M is mass of adsorbent (g).

Results and discussion

The adsorption-desorption isotherms of N_2 at 77 K for prepared AC are shown in Fig. 1 (a). It could be seen that isotherms exhibited the sharp part at P/P_0 close to 0 and subsequent smooth part at P/P_0 close to 1. According to the International Union of Pure and Applied Chemistry (IUPAC) classification, the sample presented the isotherm of type I with abundant micropores [7]. Moreover, isotherms contained a hysteresis loop of type H4 corresponded to narrow slit-like pores, indicating the typical microporous characterization [7]. Fig. 1 (b) shows the DFT pore size distribution of material. As shown in Fig. 1 (b), the sample contained a large number of micropores and some mesopores. Besides, it could be found that the most probable pore size (attributed to the peak in model) was 1.076 nm. The pore texture parameters of sample are shown in Table 1. The results exhibited the rice husk-based AC was microporous (S_m/S_a=84.4 %) with high specific surface area and large micropore volume, suggesting the potential adsorption capacity of Hg^{2+}.

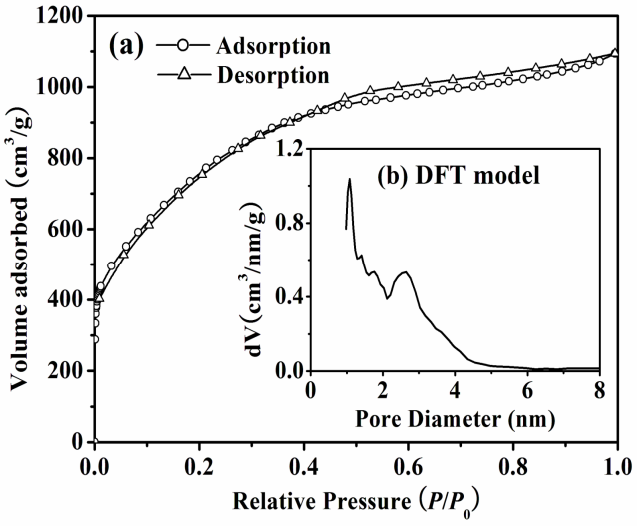

Fig. 1 Adsorption-desorption isotherms of N_2 (a) and DFT model (b) for AC

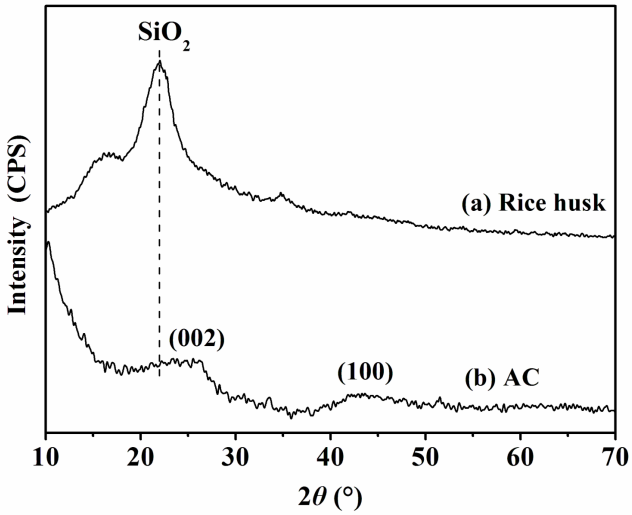

Fig. 2 XRD patterns of rice husk (a) and AC (b)

Table 1 Pore texture parameters of AC

S_a [m^2/g]	V_t [cm^3/g]	S_m [m^2/g]	V_m [cm^3/g]	S_m/S_a [%]
2786	1.688	2350	0.835	84.4

Fig. 2 shows the XRD patterns of rice husk (a) and AC (b). As seen from pattern (a), a significant peak appearing around 2θ=22° was a typical silica characteristic, which corresponded to the presence of cristobalite in ash. But the peak ascribed to SiO_2 almost disappeared in pattern (b), exhibiting the removal of ash by NaOH in activation. Further, two insignificant peaks appeared at approximately 2θ=26° and 44°. The peak at 2θ=26° was due to the reflection from the (002) plane of sample [8], with an inter-layer spacing d_{002} of 0.339 nm. And the peak at 2θ=44° was assigned to the reflection from the (100) plane, with d_{100} of 0.204 nm. Moreover, the irregular diffraction peaks of AC indicated the structure of amorphous carbon in this work.

The morphology of AC is elucidated in the Fig. 3. It could be found that the sample showed irregular shape with fragmentary structure of particles, indicating the pyrolysis of material during preparation [5]. And micrograph showed that the carbon presented a porous structure with some pores randomly distributed on the surface.

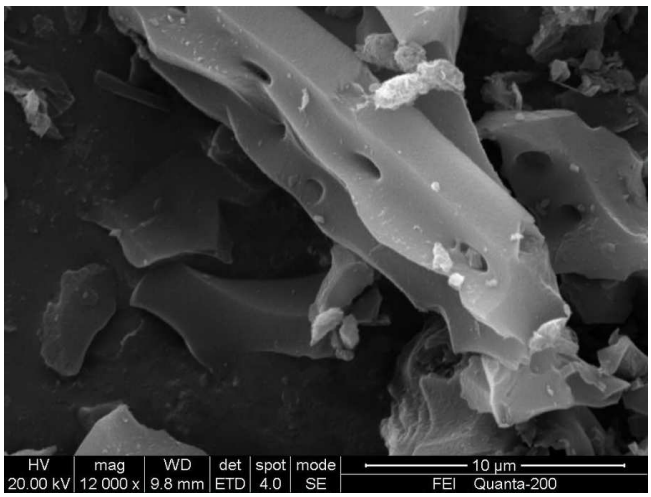

Fig. 3 SEM image of surface for AC

Adsorption of mercury ion

For the adsorption of Hg^{2+} solution (100 mg/L), the adsorption capacities for ACs increased rapidly during the initial stage of 30 min, and became almost constant after 3 h. The equilibrium adsorption capacity of Hg^{2+} was only 98.1 mg/g when 0.20 g of AC was added. While the maximum adsorption amount, up to 342.0 mg/g, was obtained by adding 0.05 g of AC.

Adsorption isotherm reflected the relationship between the amount of an adsorbate at constant temperature and its concentration in the equilibrium solution. Langmuir and Freundlich isotherm models were used to describe the adsorption process. The Langmuir isotherm was developed on the assumption that the adsorption takes place only at homogenous sites within the adsorbent surface with uniform energy level, which concluded that the adsorption was monolayer in nature. Contrarily, Freundlich isotherm was based on the assumption that the adsorption occurred on heterogeneous sites with non-uniform energy level, which was not restricted to the monolayer. The equations of Langmuir (2) and Freundlich (3) were given as follows [9]:

$$q_e = \frac{q_m \cdot K_L \cdot C_e}{1 + K_L \cdot C_e} \tag{2}$$

$$q_e = K_F \cdot C_e^{\frac{1}{n}} \tag{3}$$

where q_e is the equilibrium adsorption capacity (mg/g), C_e is the equilibrium Hg^{2+} concentration (mg/L), q_m (mg/g) and K_L (L/mg) are Langmuir isotherm parameters, and q_m is the maximum saturated adsorption capacity at monolayer. As for Freundlich, K_F is Freundlich constant (mg/g)(mg/L)^n and n is dimensionless heterogeneity factor. In addition, the correlation coefficient (R^2) was evaluated by plotting the graph for models.

Fig. 4 exhibits the plots of two isotherms for Hg^{2+} adsorption. For the Langmuir model, the maximum monolayer adsorption capacity q_m was found to be 555.6 mg/g. On the other hand, the favorable characteristics of the Freundlich model were noted because of the higher value of n (1.64) and K_F (68.5). In summary, the Langmuir isotherm was greatly suitable to explicate the correlation of experimental data due to its maximum R^2, as shown in Fig. 4. As a result, the adsorption of Hg^{2+} onto ACs was hybrid with a mainly component of monolayer adsorption [6,9].

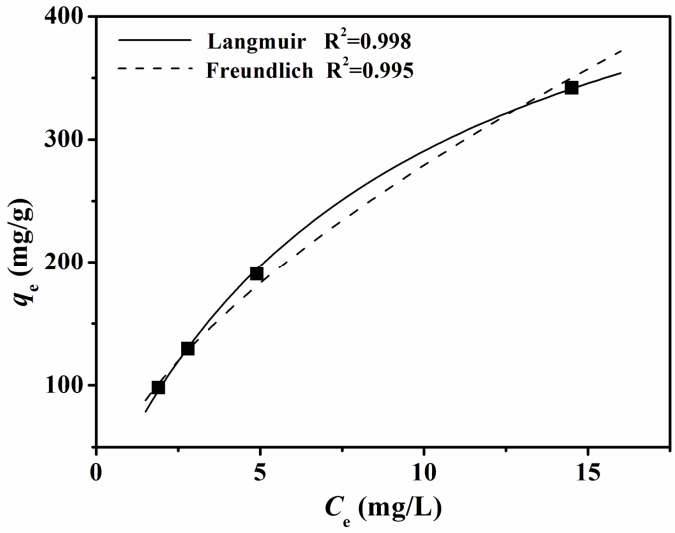

Fig. 4 Langmuir and Freundlich isotherms of Hg^{2+} adsorption

Conclusions

In the present work, ACs prepared from rice husk with NaOH were used for adsorption of Hg^{2+}. The material was microporous with high specific surface area of 2786 m^2/g. Since the most probable pore size was 1.076 nm, Hg^{2+} could be easily diffused into pores of AC. As a result, at added quantity for carbon of 0.05 g, the maximum equilibrium adsorption capacity was recorded at 342.0 mg/g. On the contrary, the minimum adsorption capacity was only 98.1 mg/g at dosage of 0.20 g. Additionally, the experimental data were well explained by the Langmuir model, with a monolayer adsorption capacity of 555.6 mg/g. Therefore, the rapid removment of Hg^{2+} exhibited that the AC from rice husk was suitable for wastewater treatment.

Acknowledgements

This study was supported by the projects of International Cooperation of Science and Technology Ministry of China (No. 2005DFBA028) and Graduate degree thesis Innovation Foundation of Central South University (No. 2010ssxt249).

References

[1] X.W. Wu, H.W. Ma, J.H. Li, J. Zhang, Z.H. Li, The synthesis of mesoporous aluminosilicate using microcline for adsorption of mercury (II), J. Colloid Interface Sci. 315 (2007) 555-561.

[2] X.L. Song, H.Y. Liu, L. Cheng, Y.X. Qu, Surface modification of coconut-based activated carbon by liquid-phase oxidation and its effects on lead ion adsorption, Desalination 255 (2010) 78-83.

[3] J. Jaramillo, V. Gómez-Serrano, P.M. Álvarez, Enhanced adsorption of metal ions onto functionalized granular activated carbons prepared from cherry stones, J. Hazard. Mater. 161 (2009) 670-676.

[4] D. Kalderis, D. Koutoulakis, P. Paraskeva, E. Diamadopoulos, E. Otal, J.O.D. Valle, C. Fernández-Pereira, Adsorption of polluting substances on activated carbons prepared from rice husk and sugarcane bagasse, Chem. Eng. J. 144 (2008) 42-50.

[5] J.H. Zhang, H. Fu, X.S. Lv, J. Tang, X.H. Xu, Removal of Cu(II) from aqueous solution using the rice husk carbons prepared by the physical activation process, Biomass Bioenergy 35 (2011) 464-472.

[6] E.I. El-Shafey, Removal of Zn(II) and Hg(II) from aqueous solution on a carbonaceous sorbent chemically prepared from rice husk, J. Hazard. Mater. 175 (2010) 319-327.

[7] C. Sangwichien, G.L. Aranovich, M.D. Donohue, Density functional theory predictions of adsorption isotherms with hysteresis loops, Colloid Surf. A 206 (2002) 313-320.

[8] P. Barpanda, G. Fanchini, G.G. Amatucci, Structure, surface morphology and electrochemical properties of brominated activated carbons, Carbon 49 (2011) 2538-2548.

[9] Q.S. Liu, T. Zheng, P. Wang, J.P. Jiang, N. Li, Adsorption isotherm, kinetic and mechanism studies of some substituted phenols on activated carbon fibers, Chem. Eng. J. 157 (2010) 348-356.

doi:10.4028/www.scientific.net/AMM.161.167

Surface Modification of Epoxy-Ceramic Coatings by Plasma Treatment

Aijun Yan[1, 2, a], Lajun Feng[2,b], Hongyan Shen[2,c], Jian Wu[1,d]

[1.] Shaanxi Electricity Power Research Institute, Xi'an(710054,P.R.China)

[2.]School of Materials Science and Engineering, Xi'an University of Technology(710048,P.R.China)

[a] yanaijunsdk@163.com, [b] fenlajun@xau.edu.cn,[c.] 402318805@qq.com,
[d.]christinemengmiao@163.com,

Keywords: plasma modification; hydrophilic coating; epoxy resin; electrostatic spraying

Abstract. A coating was made by electrostatic spraying of epoxy resin / TiO_2 particles for the purpose of suppressing audible noise caused by corona discharge on high-voltage transmission lines. Wetting property of the coating was improved by oxygen plasma treatment. It was found that the coating became more wettable as the increase of TiO_2 content during electrostatic spraying process. With respect to the coating for suppression of audible noise from transmission lines, the optimal mass ratio of TiO_2 particles (diameter:5-10μm) to epoxy resin was 30%, and the contact angle was 73°on the epoxy / TiO_2 coating surface which could be reduced to less than 5°after oxygen plasma treatment for 20s.

1. Introduction

With the development of high-voltage transmission, noise pollution caused by hum noise from high-voltage transmission lines has resulted in occasional complaints. Audible noise affected significantly by weather condition is lower in fair weather, however, it increases primarily in rain, fog, and snow environments. The relative levels of random noise and hum noise measured under different weather conditions varied significantly, random noise was higher under rainfall condition while the other was higher under freezing condition [1]. In general, to high-voltage transmission the primary introduction of concerns is referring to random noise, secondly, hum noise with frequency of 100Hz or 200Hz. Audible noise has been a major concern compared with other noises, although the audible sound reduces approximately by half as the decrease of every 10dB of audible noise. The attenuation of audible noise was smaller than that caused by radio interference as the increase in horizontal distance of transmission lines. The degree of noise attenuation was about 3-4dB when horizontal distance was doubled [2]. When it rains, sound waves generated by corona discharges from water drops affixed to the surface of conductors are emitted into the air, and become corona audible noise, apart from this, when water drops or other foreign particles become attached to the surface of a conductor, the electric field at the tip of such objects rises, and a corona discharge is generated there. The more protruding objects there are, and the sharper their tips, the greater the electric field, and the more likely a corona discharge becomes to form noise. It was proposed that noise was softer as the conductor became more hydrophilic, and when extremely hydrophilic, the corona noise was greatly reduced [3,1]. Based on this research result, a hydrophilic coating was fabricated, transmission lines with such coating showed good performance regarding the suppression of audible noise. Hydrophilic coatings used currently with poor weather resistance can not well meet the requirement of transmission lines in service, in contrast, epoxy coating has relatively higher weather resistance but lower hydrophilia. The aim of this investigation is to carry

out surface modification of epoxy coating by plasma, and TiO_2 particles were added into the coating to enhance the hydrophilia of epoxy resin and break down dirt attached to the surface of transmission lines. Since TiO_2 is a material that has excellent super-hydrophilic property, air purification, sterilization, and has effective capacity in degradation of contaminant in water [4].

2. Preparation and Evaluation of Epoxy / TiO_2 Coating

Spraying materials were mechanical mixture of commercial epoxy resin particles and TiO_2 particles (diameter:5-10μm) following the mass ratio (TiO_2 to epoxy) of 20%, 30%, 40% and 50% respectively. Electrostatic spraying of epoxy and TiO_2 mixture was carried on New KCl-CU801 electrostatic spraying equipment. Surface modification was carried out on the plasma generator with plasma torch under oxygen pressure of 0.5MPa[5]. To characterize the wettability, a contact angle measurement apparatus (JC2000A) is used to test contact angles based on the sessile drop method.

Spraying process was as follows, the substrate was firstly treated by sandblasting, epoxy resin was then sprayed onto substrate surface and cured, after this stage was completed, mixed particles were sprayed and cured. The aim of substrate surface sandblasting was to remove rust, on the other hand, a rough surface was obtained to enhance adhesion strength of coating, not until a new surface was exposed the operation stopped, and the pressure was set to 0.5~0.7MPa in this process. Spraying voltage was set to 50~60KV, air pressure was changed from 0.4 to 0.5 MPa, and spraying distance was set to 100~150mm during electrostatic spraying process [6]. The sprayed epoxy coating was limited to a thickness of about 0.1mm and cured in a curing chamber at 140 ℃ for 10 minutes，then spraying of mixing particles was carried out to build a coating with a thickness of about 0.2~ 0.3 mm , and cured at 220℃ for 20~30 minutes for consolidating the mixture coating into the epoxy coating completely to become a whole coating with a perfect leveling surface.

3. Result and Discussion

3.1 Effect of TiO_2 Content on Wetting Property. Table 1 lists the effect of TiO_2 content on wetting property of epoxy resin coating on the surface of test pieces

Table 1 TiO_2 content and measured contact angle for the test pieces

TiO_2 [Wt%]	0	20	30	40	50
contact angle[degree]	88	79	73	70	68

It is shown in Table 1 that wettability correspond to hydrophilia of the epoxy coating was improved notably with the addition of TiO_2 particles. In general, coated surface becomes more hydrophilic as the contact angle is smaller, and contact angle of less than 5° indicates a super hydrophilic surface, also, the surface is completely wetted with a contact angle of 0°. It has been found in Ref [7] that the coated surface became a hydrophilic surface when the contact angle was less than 30°. It can be seen that the coated surface was hydrophobic with TiO_2 particles, although the contact angle began to decrease, the contact angle on the coated surface decreases as the increase of TiO_2 content, and the decrease of contact angle to 68° with 50% TiO_2 particles(5~10μm). The surface smoothness decreases dramatically as TiO_2 particles were added continuously, thereby more protruding objects occurred , and the sharper their tips, the greater the electric field, and the more likely a corona discharge becomes. It is necessary to take surface smoothness into consideration during TiO_2 addition, consequently, the optimal mass ratio of 30%

TiO_2 was determined. Morphology of epoxy coating with different TiO_2 addition are showed in Fig 1, as it can be seen that surface smoothness of epoxy coating decreases as the increase of TiO_2 content, and the roughest epoxy surface occurred in 50% TiO_2 addition.

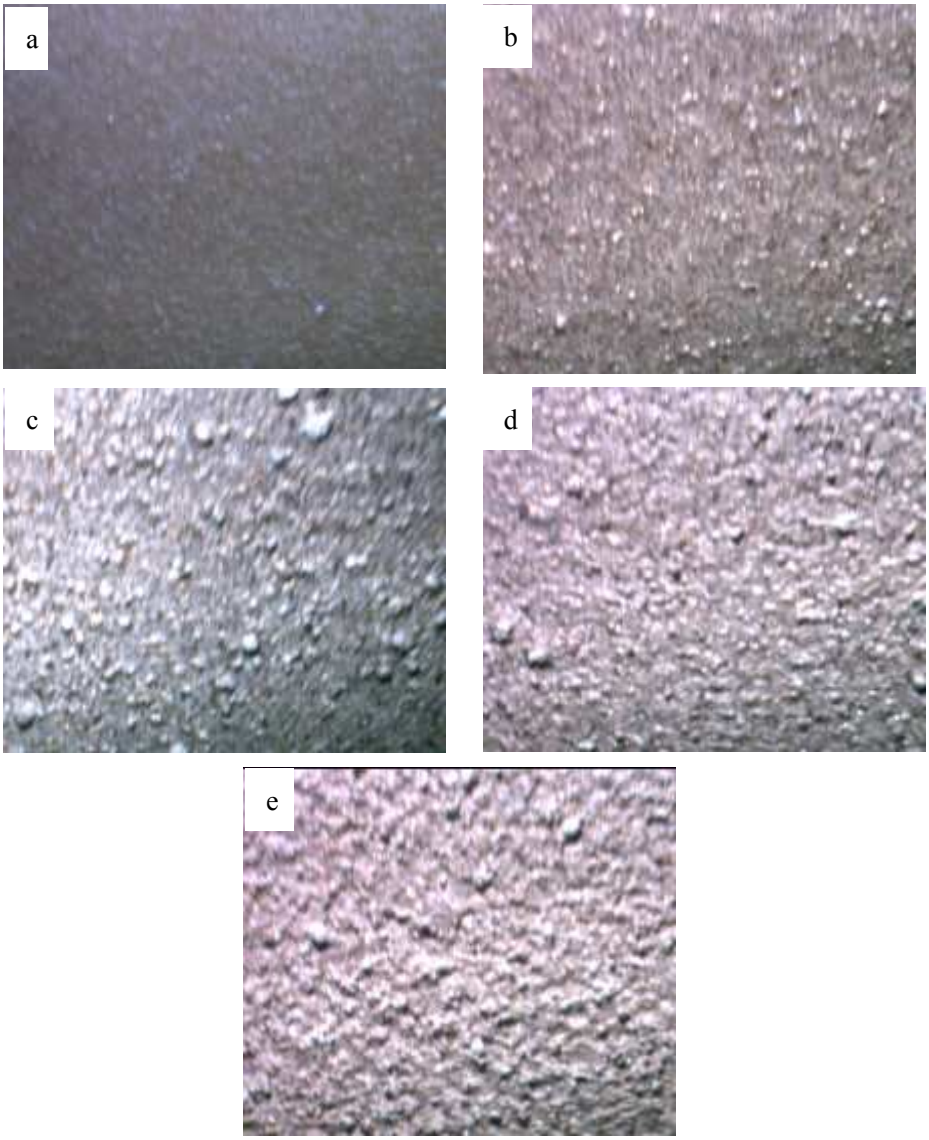

Fig 1 Microphotograph of epoxy coating with different TiO_2 addition
(a pure epoxy coating; b 20%TiO_2 ; c 30% TiO_2 ; d 40% TiO_2; e 50% TiO_2)

3.2 Effect of Plasma Treatment time on Wetting Property of Epoxy Coating. Table 2 represents the effect of plasma treatment time on wetting property of epoxy coating.

Table 2 Relationships between plasma treatment time and wetting property of epoxy coating

Time[second]	5	10	15	20	25	30
Contact angle[degree]	42	22	10	5	3	2

As shown in Table 2, the contact angle on epoxy surface shows remarkable decrease within 15s. In contrast, the contact angle begins to decrease gradually after 15s. With respect to contact angle, during the decrease, it is relatively easer to decrease from 42°to 10°, but it becomes harder to decrease when the contact angle drops to 10°. This result indicates that The wettability of TiO_2 particles were evident since epoxy on the particle surfaces was burnt away by plasma within 5s to

form bare TiO_2 particle tops, as a consequence, the contact angle was decreased. With the increase of treatment time, part of oxygen plasmas O^{2-} bonded with hydrocarbons C-H in the epoxy resin to form hydrophilic groups resulting in a slow decrease in contact angle due to relatively lower reaction rate of O^{2-}/ C-H bonds.

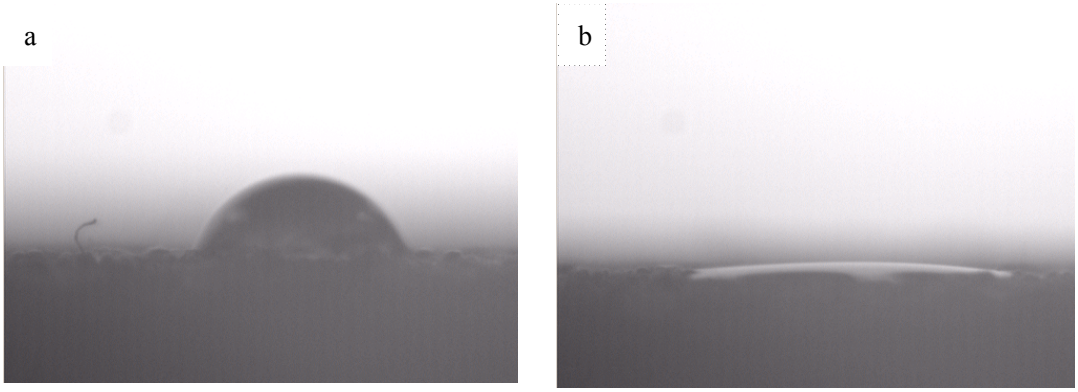

Fig 2 Contact angle measurement of epoxy coating treated by plasma for 5S and 20S respectively ((a) 5s; (b) 20s)

The contact angle measurement of epoxy coating treated by plasma for 5s and 20s respectively are shown in Fig 2, it was found that contact angle as low as 5° corresponding to a super-hydrophilic surface can be realized. Therefore, transmission lines, coated with epoxy resin with 30% TiO_2, showed good performance regarding the suppression of audible noise due to the formation of a super-hydrophilic surface after oxygen plasma treatment for 20s.

3.3 Mechanism of Plasma Treatment. More oxygen containing functional groups (hydroxyl -OH or carboxylic acid COOH) were shown to be present on the plasma treated coating surface than original surface, Therefore, the surface of oxygen plasma treated coating was more wettable, which is consistent with the polarity of the surfaces[8]. After oxygen plasma treatment, there are more oxygen containing chemical groups (as OH or COOH) bonded to the polymer surface. The presence of OH or COOH groups reduced the contact angle on the coating surface from 68°on the original surface to 2°. The OH / COOH bonds are more polar than the original epoxy resin surface and are more susceptible to hydrogen bonding with water molecules to induce a hydrophilic effect on the surface. Overall, with increasing dilution of epoxy resin with O_2, more polar oxygen containing bonds (C-COOH, C-OH) form in the coating, leading to an increasingly hydrophilic coating surface[9].

4. Conclusions

The coating became more wettable as the increase of TiO_2 content during electrostatic spraying of epoxy resin particles and TiO_2 particles. With respect to the coating for suppression of audible noise from transmission lines, the optimal mass ratio of TiO_2 particles (diameter:5-10μm) to epoxy resin was 30%, and contact angle was 73°on the on the epoxy/ TiO_2 coating surface. After plasma treatment for 20s, the contact angle could be reduced to less than 5°. The wettability of TiO_2 particles were evident since epoxy on the particle surfaces was burnt away by plasma within 5s to form bare TiO_2 particle tops, as a consequence, the contact angle was decreased. Part of oxygen plasmas O^{2-} bonded with hydrocarbons C-H in epoxy resin to form hydrophilic groups resulting in smaller contact angle with the increase of treatment time.

References

[1] K. Tanabe , T. Takebe , M. Isozaki , Reduction of Audible Noise Using Asymmetrical Bundles for 1000KVTransmission Lines: Full-scale Test Results of Akagi Test Line , J. Transactions on Power Delivery.11(1996) 1482-1488

[2] K. Miyajima , K. Tanabe. Evaluation of Audible Noise from Surface Processing Conductors for AC Overhead Transmission Line , J. Electrical Engineering in Japan. 159(2007) 415-420

[3] K. Tanabe. Hum Noise Performance of 6 , 8 , 10 Conductor Bundles for 1,000kV Transmission Lines at the Akagi Test Site: A CoMParative Study with Cage Data , J. Transactions on Power Delivery.6(1991)1979-1982

[4] H. Choi, E.Stathatos, D. D. Dionysioua. Photocatalytic TiO2 films and membranes for the development of efficient wastewater treatment and reuse systems,J. Desalination . 202 (2007)199–206

[5] J.D.Louis, I. N . Mermilliod, G. Boiron, S. Staveris. Improvement of Polypropylene Film Adhesion in Multilayers by Various Chemical Surface Modifications [J].International Journal of Adhesion and Adhesives. 15(1995) 205-210.

[6] K.S. Hwang , B.A. Kang , S.D. Kim, S. Hwangbo, J.T. Kim. Amorphous vanadium pentoxide thin films prepared by electrostatic spraying-pyrolysis deposition, J. Ceramics International, 38S (2012) S645–S647.

[7] Q. J. Ning, T.H. Zhang , X. L. Hu. Preparation of hydrophilic TiO2-SiO2 thin films by sol-gel method, J. Transactions of Materials and Heat Treatment. 28（2007）42~45.

[8] S Tang, N .M.Lu, S.W .Yung, H.S. Choi. Enhancement of Adhesion Strength Between Two AISI 316 L Stainless Steel Plates Through Atmospheric Pressure Plasma Treatment , J. Surfaceand Coatings Technology. 200(2006):5220-5228.

[9] G. Grundmeier, M .Stratmann. Plasma Polymerisation - A New and Promising Way for the Corrosion Protection of Stee, J. Materials and Corrosion. 49(1998)150-160.

doi:10.4028/www.scientific.net/AMM.161.172

The study of performance evaluation of alkylphenol polyoxyethylene ether sulfosalt

Hongping Quan[1,2,a], Hongsheng Lu[1,b], Shanshan Dai[1,c], Tailiang Zhang[1,d], Shiyuan Chen[1,e] and Yalu Yu[1,f]

[1]School of Chemistry and Chemical Engineering, Southwest Petroleum University, Chengdu, Sichuan 610500, P. R. China

[2]State Key Laboratory of Oil/Gas Reservoir Geology and Exploitation Engineering, Southwest Petroleum Uinversity, Chengdu, Sichuan 610500, P. R. China

[a]quanhp2005@163.com

Keywords: alkylphenol polyoxyethylene ether sulfosalt; evaluation

Abstract. In this paper, the performance of alkylphenol polyoxyethylene ether sulfosalt that were specially APESO and AESO was evaluated from CMC, interfacial tension, foamability and adsorption. Then these features were analyzed at different conditions, including temperature, time and concentration.

Introduction

At present, domestic chemical flooding is developed towards high-temperature, high-salt petroleum reservoir and combinational flooding technology. Of four key technologies that need to be studied, seeking for or synthesis heat-resistant and salt tolerant surface active agent is extremely important. Alkylphenol polyoxyethylene ether sulfosalt is a kind of nonionic and anionic mixed surfactant, which has the advantages of higher surface activity, less absorption loss, stronger foaming expansion, high temperature resisting and high salinity resisting.

The papers about synthetic way of alkylphenol polyoxyethylene ether sulfonate can be read in many articles, but these methods are not suitable for industrial production owing to the features. Therefore, a problem of developing a process which has low cost, easy and safe operation should be solved quickly. Nowadays, alkylphenol polyoxyethylene ether sulfosalt is synthesized by addition reaction of alkenes, through the two-step reaction: allylation and sulfonation, raw materials of which are low-cost and easy to get. Synthetic steps are simple to operate and the progresses are convenient to control, while also with low yield. In the process of addition reaction of alkenes, a new phase transfer catalyst is used in the allylation process and the composite catalysts are used in sulfonation reaction, which solves the problem of low yield that caused in the traditional methods.

Experimental

Materials. The evaluated alkylphenol polyoxyethylene ether sulfosalt(AESO and APESO) in this paper was synthesized in the following methods:

$$\text{R-O-}(C_2H_4O)\text{nH} + \text{ClCH}_2\text{CH=CH}_2 + \text{NaOH} \xrightarrow{\text{Cat}} \text{R-O-}(C_2H_4O)\text{nCH}_2\text{CH=CH}_2 + \text{NaCl} + H_2O \quad (1)$$

$$R\text{-}O\text{-}(C_2H_4O)nCH_2CH{=}CH_2 + NaHSO_3 \xrightarrow{NaNO_3} R\text{-}O\text{-}(C_2H_4O)nCH_2CH_2CH_2SO_3Na \quad (2)$$

Where R dedicates C_8~C_{20} of alkyl group and alkyl phenate; n=1~20

The equipments used in the experiments were rotating drop interfacial tension meter-TEXAS500 from America and ultraviolet spectrophotometer-UV1800 from Daojing Corporation of Japan.

Preparation. Manufacture a series of fatty alcohols (alkyl) ethoxylates sulfonate solution with different mass concentrations. And immerse quartz sand and kaoline before using, then clean them by deionized distilled water and dry up.

Characteristic. The alkylphenol polyoxyethylene ether sulfosalt(AESO and APESO) in this paper were evaluated from the following aspects:

CMC. When the concentration of surfactant reached CMC (critical micelle concentration -the concentration of surfactant above which micelles are spontaneously formed.), the adsorption of surfactant had to be saturated and the surface tension decreased to the lowest on the surface of water.

Interfacial Tension. The interfacial tension of oil-water was measured by the method of rotating drop with TEXAS500, according to the standard SY/T5370-1999.

Weighted the surfactant to be tested accurately, manufactured it to be water solution and laid it in 24~28h at a constant temperature, then turned on TEXAS500 to set to needed temperature. After filling the measuring tube with the water solution of surfactant and 0.2μL crude oil, we measured the change rules for shape of oil droplet with time and calculated the interfacial tension at different times by the following formula[1]:

$$\sigma=1.2337\times(\rho_W-\rho_O)\times10^6\times(d^3/m^3)\times(1/n^3)\times(1/R^2)\times f\,(L/d) \quad (3)$$

where σ is the interfacial tension, d is the diameter of drop, R is the rotate speed, ρ_W and ρ_O are the density of water and oil, respectively, M is the magnification of equipment, N is the refraction coefficient of external phase, and f (L/d) is the correction factor [L -length of drop, d-diameter of drop, when $L/d \geq 4$, f (L/d) =1]

Foamability. According to GB/T7462—1994, the foamability of APESO, AESO with different concentration was measured by the improved Ross-Miles.

To characteristic the salt-resisting and bivalent ion-resisting, concentration of 0.3% for salt resisting experiment was chosen by the two production that APESO and AESO, (50±1℃) was set as the testing temperature[2].

And to characteristic temperature-resisting, concentration of 0.3% for foamability experiment was chosen by the two productions that APESO and AESO, 50℃~90℃ was set as the testing temperature.

Absorption. Characteristic of adsorption in formation sand is one of the indexes to evaluate the surfactant as oil displacement agent.

The adsorbance should be firstly calculated. The tested ultraviolet adsorption wavelength of APESO and AESO were 216 nm, 275nm, respectively. Manufactured normal solution sample with serial concentrations and measured their adsorbance, a Lambert-Beer law standard curve was

automatically created by the system, and then the unknown solution was measured. The adsorbance was calculated according to the following formula with the concentration that was achieved directly by the system[3] :

$$\Gamma = (C_0\text{-}C) \times V/m \quad (4)$$

Where Γ is adsorbance, C_0 and C are concentration of surfactant before and after adsorbing separately, V is the liquid volume, m is the quality of adsorbent.

To comfirm of the time for adsorption equilibrium, quartz sand and kaoline were chosen as the adsorbent, mass ratio of adsorbent and surfactant was kept as 1:50, filled the 100ml ground flask with 2.0g quartz sand or kaoline, then added the surfactant solution with different mass fraction, and oscillated at room temperature. 10.0g solution with a little suspended solid was brought out at different times, then centrifugated which for 20 min at rate of 4000r/min, supernatant layer upper was brought out.

Solid-liquid ratio could be confirmed in the case of that adsorbed time was 15h, initial concentration of APESO and AESO was set to be 500 mg/L. The influence of solid-liquid ratio on adsorbance was investigated by the adsorbent that were quartz sand and kaoline.

At room temperature, manufactured APESO and AESO solution with series of mass fraction, 1:50 was set as solid-liquid ratio and time was 15h, so that the adsorption isotherm of quartz sand could be obtained.

Results and Discussion

The Measurement of CMC. γ_{cmc} and CMC were measured according to the standard SY/T5370-1999[4].

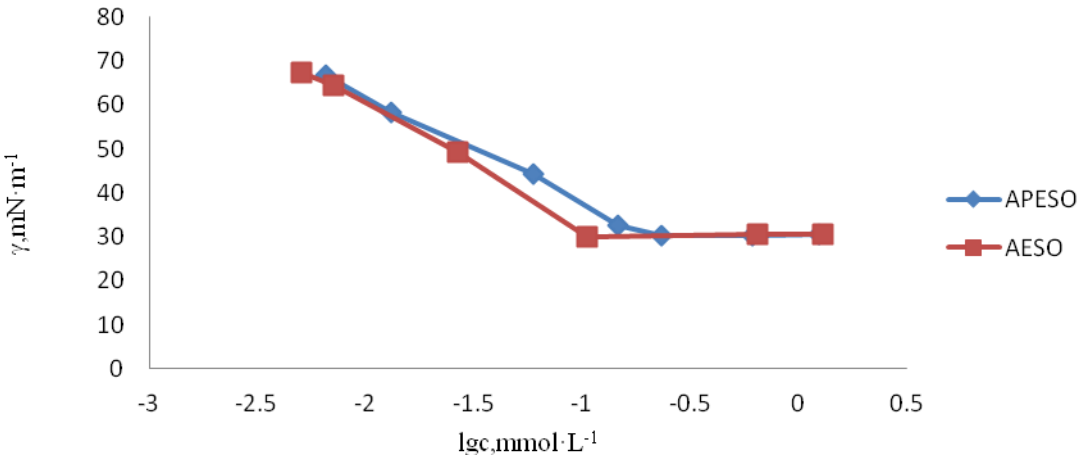

Fig2-1 Surface tension of AESO and APESO

And Fig 2-1 showed:

CMC of APESO=0.232mmol·L^{-1}, γ_{cmc}=30.3mN·m^{-1}

CMC of AESO=0.105mmol·L^{-1}, γ_{cmc}=30.1mN·m^{-1}

Referred to the documents, CMC of sodium tetradecyl sulfate ($C_{14}H_{29}SO_4Na$) and sodium dodecyl benzene sulfonate($C_{18}H_{29}SO_3Na$) were 2.44mmol·L^{-1} and 1.2mmol·L^{-1} respectively. CMC of APESO is an order of magnitude less than that of AESO. The smaller CMC, the lower

concentration of surfactant to form micelle and adsorption to be surface saturated will be, therefore, if we change the interfacial properties such as wetting, penetration, emulsification, solubilization and foaming, the concentration will be smaller.

The Measurement of Interfacial Tension. The capability of decreasing the interfacial tension and the cost were affected by the concentration of surfactant. Set the dehydrate crude oil from Xing five western part of the fourth oil extraction plant as oil phase,0.1% of APESO and AESO solutions were set as the water phase. Interfacial tension of oil-water which changed with time at 50℃, pH =12 was illustrated in Fig.2-2.

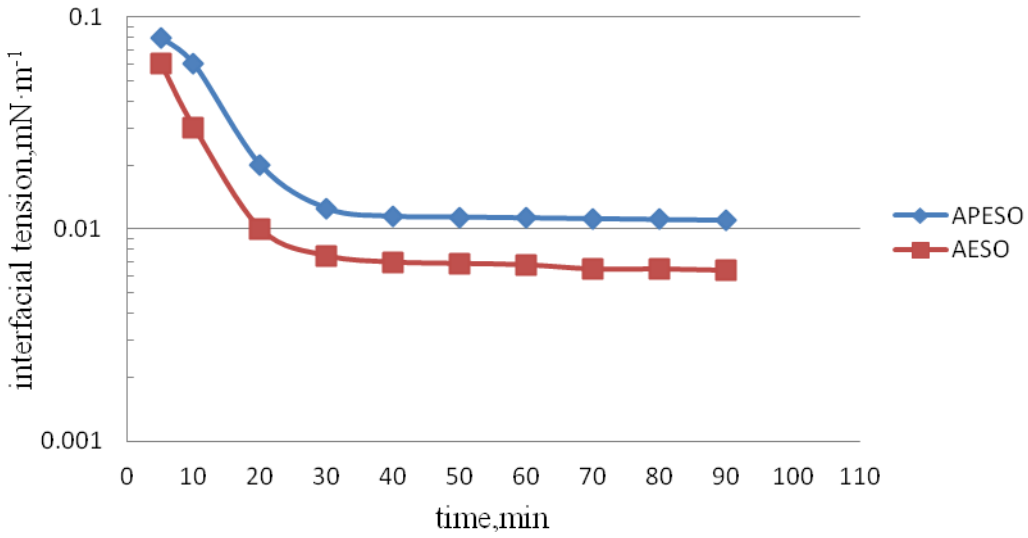

Fig.2-2 Dynamic interfacial tension among APESO, AESO and crude oil

Interfacial tension of oil-water is the evaluation target which is relatively to performance of oil displacement. From the figure, interface activity of AESO was higher than that of APESO. Lipophilic group of AESO is an aliphatic chain, which has a benzene substituent at one side. When APESO surfactant came to saturated adsorption at oil-water boundary, as a reasult of the benzene substituent, the coverage of surfactant hydrophobic group decreased, density becomed low, which was difficult to form the tight interfacial membrane and was hard to decline the interfacial tension; lipophilic group was composed by the tight array of surfactant molecular that from aliphatic chain at oil-water interfacial where had a big coverage of surfactant hydrophobic group,which decreased the interfacial tension seriously.

Inorganic salt(sodium chloride) was added in surfactant,which dereased the interfacial tension further. 0.1% AESO surfactant solution was set as water phase, Fig2-3 illustreated how interfacial tension of oil-water changed with time in the case of different concentration of sodium chloride at 50℃, pH=12. When the content of sodium chloride was 0.04mol/L, interfacial tension became the lowest. Addition of electrolyte compressed the double electrode layer,diminished the repulsion between ions at water wet side,which increased the adsorption of surfactant at contact bed and led to the further decline of interfacial tension.

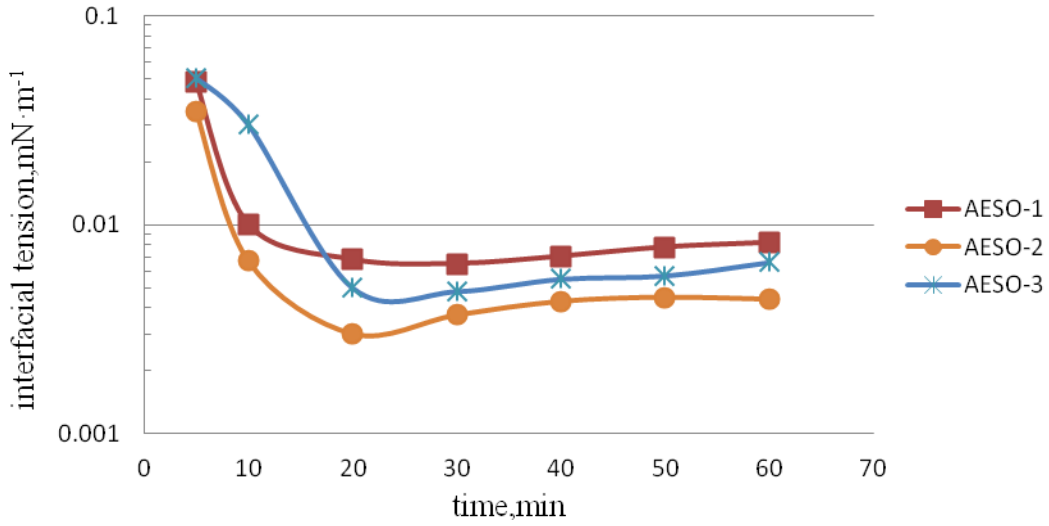

Fig2-3 Time to different concentration of sodium chloride
AESO-1—0.02mol/L；AESO-2—0.04mol/L；AESO-3—0.06mol/L

0.1%APESO and AESO were manufactured by mineralized water with different degrees of mineralization. Fig2-4 showed the comparison of interfacial tension oil-water tested at 70℃ and the stable value after 2h.

When the degree of mineralization was increased from 20000mg/L to 140000mg/L, interfacial tension between surfactant and crude oil appeared the same variation rule, namely which decreased gradually at the first time ,until the interfacial reached the lowest then increased gradually. Different surfactant had the lowest interfacial tension at the regions with different degrees of mineralization that was named optimum degree of mineralization. Because surface active ion had thick hydrated layer at low degree of mineralization and with good water solubility, molecules were almost distributed in water phase, as the degree of mineralization increased, double electrode layer which around the molecules was compassed by electrolyte, hydrated membrane weaken, and water solubility decreased. As the degree of mineralization exceeded a certain value, a great quantity of surfactant entered oil phase and interfacial tension gradually increased.

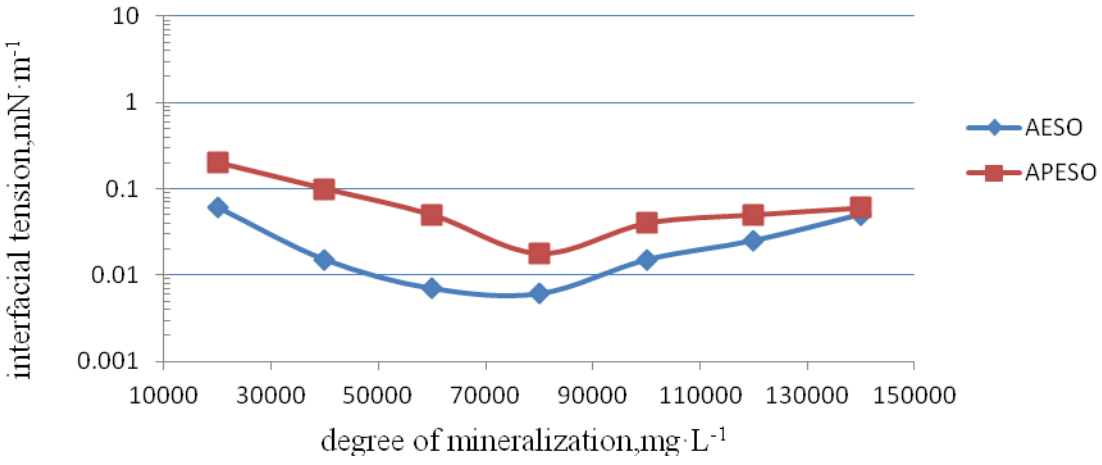

Fig 2-4 Capability of decreasing interfacial tension of APESO and AESO at high temperature and salt

The Measurement of Foamability. The foamability was shown in Table 2-1.

Table2-1 Foamability of APESO and AESO

concentration (%)	foam height (mm)					
	AESO			APESO		
	30s	3min	5min	30s	3min	5min
0.05	220	150	130	210	160	140
0.1	220	150	130	210	160	120
0.2	240	160	130	220	160	120
0.3	250	170	140	240	160	130
0.5	250	180	140	240	180	140

Seen from Table 2-1, APESO and AESO had high foamability even when they were with low concentration, and higher concentration became, more obviously foamability increased. When mass concentration of surfactant in solution ≥0.3%, the foam height of two surfactant solution reached 240mm both, and reached high level. Foamability of AESO was better than that of APESO, while steady ability of it was worse.

Characteristic of Salt-resisting and Bivalent ion-resisting. The table below showed that as the concentration of NaCl increased , foamabilities and steady abilities of the two kind of surfactant strengthened, which also appeared to decline when the concentration exceeded the value (>4%).

Table 2-2 Influence of the content of NaCl

C_{NaCl} (%)	foam height (mm)					
	AESO			APESO		
	30s	3min	5min	30s	3min	5min
0	250	170	140	240	160	130
1.0	265	190	150	250	190	160
2.0	270	200	160	270	200	160
3.0	295	210	160	290	210	170
4.0	280	195	155	270	190	160
5.0	260	185	145	260	180	160

As a result of an ion-atmosphere double electrode layer around APESO and AESO ion, the influence of diffuse electric double layer enhanced and the thickness of ion atmosphere, which belonged to the ion-head of surfactant compressed with increasing concentration of inorganic salt, the repulsion among them was decreased so that it was easy to absorb on the surface then formed micelles, which led to the decrease of interfacial tension and CMC, the foam performance of surfactant solution was strengthened at the same time. But when the concentration of NaCl was too high, diffuse electric double layer in fluid film was compressed, the repulsion between membranes was weaken and the process of liquid film clean-up was accelerated, which led to the trip out of the performance of the two surfactants. From the analysis above, we can add in a little NaCl(＜ 4%)which was helpful for improving the foam performance of APESO and AESO.

Concentration of 0.3% was chosen by the two productions for bivalent ion-resisting experiments, testing temperature was (50±1℃).

Table 2-3 Influence of the content of Ca^{2+} and Mg^{2}

C_{Ca2+}, C_{Mg2+} (mg/L)	foam height(mm)					
	AESO			APESO		
	30s	3min	5min	30s	3min	5min
0	250	170	140	240	160	130
100	235	160	140	220	150	130
400	210	160	130	200	145	120
600	190	145	120	170	130	110

From the table, we can see that when the concentration of $Ca^{2+}$and Mg^{2+} increased, the foamability of the two surfactant solution were both declined, but the steady ability was prone to increase. As a result that hydrophilic group head could form chelate with $Ca^{2+}$and Mg^{2+}, which strengthened interreaction of active agent molecules at gas-oil adsorbed layer, decreased the electric repulsion and increased the absorption, therefore foam membrane became thick and solid, which was unfavorable for the clean-up and broken of membrane.

Characteristic of Temperature-resisting. Table 2-4 showed that there was an obvious influence on the foamability of the surfactant.

Table 2-4 Influence of temperature

temperature (℃)	foam height (mm)					
	AESO			APESO		
	30s	3min	5min	30s	3min	5min
50	250	170	130	240	160	130
70	220	110	50	210	80	30
90	160	40	—	160	50	—

At 70℃, foam height could reach 210mm above. While at 90℃, foam height declined dramatically, it was because that above a certain temperature, the strength of fluid film declined , and foamability decreased but the high temperature foamabilities of AESO and APESO were still stronger than that of other foaming agent like ABS. Due to the limits of equipments, it was not convenient to raise the temperature above 90℃. The steady ability decreased dramatically when the temperature increased, it was because that higher temperature could improve the water evaporation, which led to thin down the fluid film and accelerate clean-up. Surface viscosity decreased and rate of gas diffusion in the foam increased, therefore foam declined. Increase of liquid viscosity and surface viscosity could improve the stability at higher temperature.

Characteristic of Absorption. The adsoption was characterized from the following aspects:

Confirm of the Time for Adsorption Equilibrium. Set supernatant layer of blank after centrifugation as reference, ultraviolet adsorption of supernatant layer of sulfonate after centrifugation was measured, the concentration was achieved by UV-1800 system, adsorption was calculated by the previous formula, then obtained the curve of absorption-time, shown in Fig.2-5:

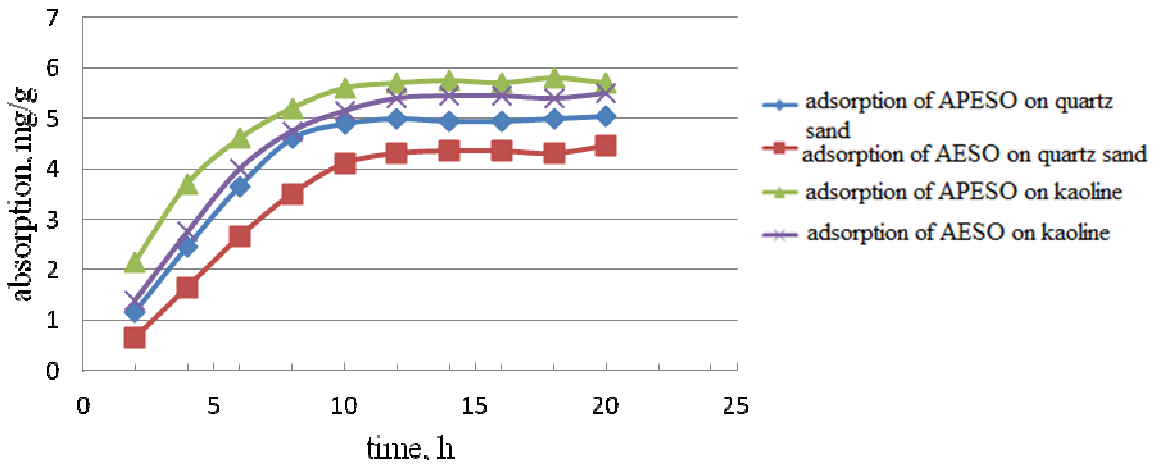

Fig.2-5 Variation curve of adsorbance-time

After the analysis, the adsorption changed slightly with time when APESO and AESO adsorbed on quartz sand for 10h and on kaoline for 12h. In order to adsorb completely, 15h was set as the adsorbed balanced time.

Confirm of Solid-liquid Ratio. The result was shown in Fig2-6. Adsorbent was nearly constant when the solid-liquid ratio was above 40 in the case of quartz sand; while in the case of kaoline, the adsorption got to the balance. And we took 50:1 in the next.

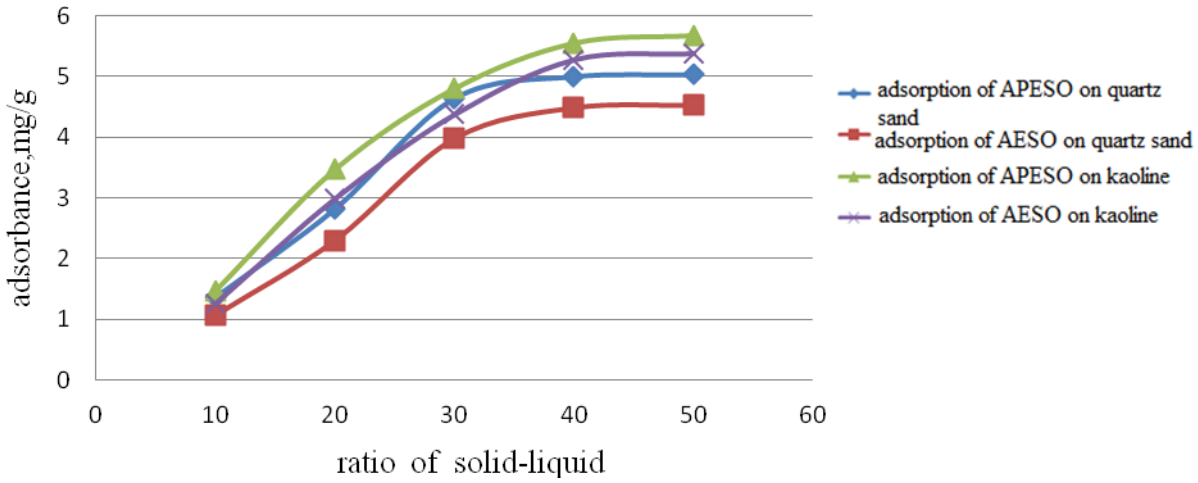

Fig2-6 Variation curve of adsorbance-solid-liquid ratio

Adsorption Isotherm of Quartz Sand. The balanced adsorbance was calculated, and the adsorption isotherm was obtained as following:

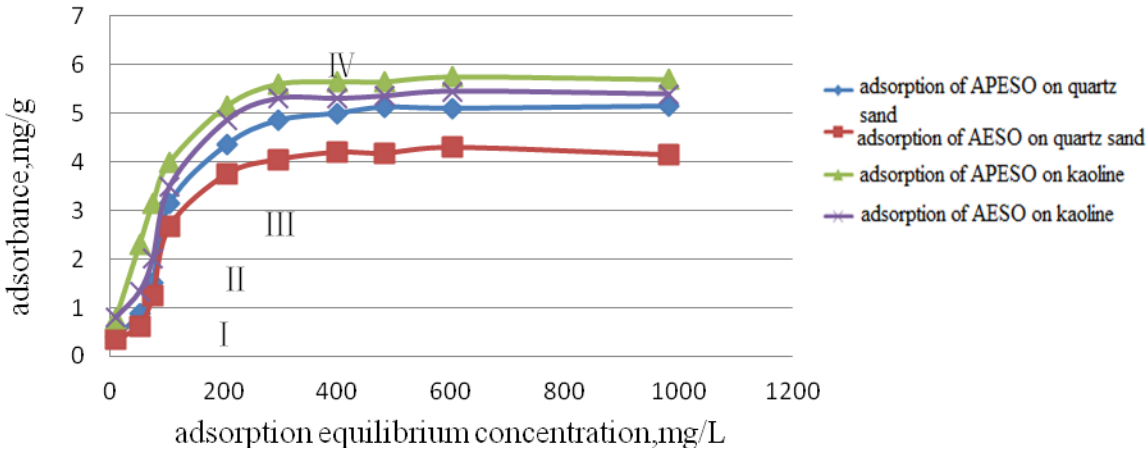

Fig.2-7 Adsorption isotherm

From the curve, adsorption isotherms of APESO and AESO were both "S"-shaped, adsorption isotherms on the surface of kaoline was always above that of clean sand, namely the adsorbance of APESO and AESO were more than that on the clean sand.

"S"-shaped isothermal line was divided into four regions: Ⅰ, Ⅱ, Ⅲ, Ⅳ. Region Ⅰ indicated the lower concentration and adsorbance of surfactant, it was monomolecular adsorption on the solid surface, which generally accorded with Henry's law. Slope of region Ⅱ increased faster, as a result of "semi-micelle" that was formed by surfactant on some parts of solid. Region Ⅲ appeared at later stage of "semi-micelle", the slope decreased, the concentration was close to CMC at the same

time, micelles appeared at the same time. As the concentration of surfactant increased, more micelles were produced, adsorbance was led to decrease by electrostatic repulsion to adsorbed layer after maximum appeared, then adsorption isotherm went to region Ⅳ. Breakpoints of region Ⅲ and region Ⅳ appeared at CMC (CMC of APESO and AESO were 180mg/L and 80 mg/L) around. A platform appeared after region Ⅳ, which meant surface adsorbance was nearly steady with increasing concentration of surfactant.

Conclusion

Excellent performance of polyoxyethylene ether sulfonate surfactant was shown:

Lower CMC. CMC of APESO was 0.232mmol·L^{-1}， γ_{cmc} was 30.3mN·m^{-1}, CMC of AESO was 0.105mmol·L^{-1},γ_{cmc} was 30.1mN·m^{-1}.

Higher Interfacial Activity. The dehydrate crude oil from Xing five western part of the fourth oil extraction plant and 0.1% concentration of AESO surfactant solution were set as oil phase and water phase separately. At pH=12 and 50℃, interfacial tension of oil-water reached a low point that was10^{-3} mN/m(6.4×10^{-3} mN/m), which meant to be the ideal oil displacement capability. 0.1% AESO surfactant solution was manufactured at the case of 80000mg/L (degree of mineralization), interfacial tension could reach reached a low point that was 10^{-3} mN/m (6.1×10^{-3}mN/m), which meant a strong resistance to degree of mineralization.

Stronger Foamability. 0.3%AESO and APESO solution manufactured was measured the foam height that was above 240mm at 30S, which was more obvious than others, performance of salt-resisting and bivalent ion-resisting were excellent. At 90℃,foam height could reach 160mm above, ability of temperature-resisting was excellent. Foamability of AESO was better than APSO, while steady ability was worse.

Less Adsorption Loss. Static adsorption rules of AESO and APESO on clean sand and accorded with Langmuir adsorption isotherm. Adsorption of AESO on quartz sand ≤4.3mg/g, adsorbance on the surface of kaoline was always more than that on the clean sand; adsorption loss of AESO was less than APESO.

References

[1] P.Peng, Surfactant for Oil Recovery, Chemical Industry Press, Beijing, 2003, pp.135-144.

[2] Y.B.Liu, W.F.Pu, Y.Yang, Study on the new foaming agent PAS-12 and foam liquid system, J. Drill Fluid and Completion Fluid. 22(2005)53-56.

[3] G.X.Zhao, Theory of Surfactant, China Light Industry Press, Beijing, 2003, pp.152-220.

[4] P.K.Mao, Industrial Analysis of Surfactant, Chemical Industry Press, Beijing, 2003, pp.407-409.

doi:10.4028/www.scientific.net/AMM.161.181

Extraction of m-β-Hydroxyethylsulfonyl aniline from reactive dye wastewater

Junfeng Hua[1, a], Zaiqing Sun[2,b], Yanfei Wei[3,c] and Mei Huang[1,d*]

[1]Department of Chemical & Biochemical Engineering, Zhejiang University, Hangzhou，310027, China

[2]Wujin Environmental Monitoring Station, Changzhou, 213159, China

[3]Environmental Science Research & Design Institute of Zhejiang Province, Hangzhou, 310007, China

[a]huajf1988@163.com, [b]sunzaiqing2008@sohu.com, [c]weiyf365@tom.com, [d]huangm@zju.edu.cn(corresponding author)

Keywords: m-β-Hydroxyethylsulfonyl aniline; extraction; tributyl phosphate/petroleum ether; reactive dye wastewater

Abstract. m-β-hydroxyethylsulfonyl aniline is one of the important reactants in synthesizing reactive black KNB. In order to recovery m-β-hydroxyehylsulfonyl aniline from reactive dye wastewater, two separation units including tributyl phosphate/petroleum ether extraction and sodium hydroxide solution stripping were studied. It is found that the single stage extraction rate was 85% when extraction phase ratio of organic to aqueous phase (O/A) was 2:1, while the single stripping rate was higher than 50% when 0.5M sodium hydroxide solution was selected and the stripping phase ratio of aqueous to organic phase (A/O) was 2:1.

Introduction

Reactive dyes are widely used in textile industries, characterized for its high stability, excellent colorfastness, bright color and ease application in industry. At the same time, active textile wastewater containing residual dyes has caused serious environment pollution, because it usually looks highly visible and affects their transparency and aesthetics even if the concentration of the dyes is low[1]. The conventional physical and bio-chemical ways to treat it make little sense, such as adsorption, coagulation, photo catalytic degradation and hypochlorite treatment [2-4]. On the other hand, textile industries are known as one of the major consumers as it uses large volumes of water and chemicals for wet processing of textile every year. The release of dyes wastewater containing dye intermediates or reactants without treatment is also a huge waste of resources. Then it is urgent to find an effective and available method to reuse the components existed in dyes wastewater.

In this study, tributyl phosphate diluted with petroleum ether was used to extract m-β-hydroxyethylsulfonyl aniline from reactive dye wastewater. Then loaded organic was stripped by sodium hydroxide solution. Not only the extractant was regenerated and could be reused for times, but also the stripped solution could be sent back for manufacture of reactive black KNB.

Experimental section

Materials. The dye wastewater was obtained from Zhejiang Shunlong Chemical Co. Ltd., China. Tributyl phosphate (TBP), petroleum ether (60~90℃), sodium hydroxide, methanol were supplied by Sinopharm Chemical Reagent Co. Ltd. All chemicals in this work were of chemical reagent grade and used without further purification.

Experimental method. For the extraction process, 50ml dye wastewater and 100ml extractant with various ratio of TBP to petroleum ether, were mixed together in a 250ml beaker for 30min under stirring. After that the sample was poured into a separating funnel and stood for 30min for phase

separation. Then the aqueous phase was taken out and the dyes loaded organic phase was mixed with stripping agents. Being stirred for 30 min, the aqueous phases were separated for reusing. Concentrations of m-β-hydroxyehylsulfonyl aniline in extracted and stripped phases were determined by high-performance liquid chromatography (HPLC).

Results and Discussion

Effect of extraction phase ratio

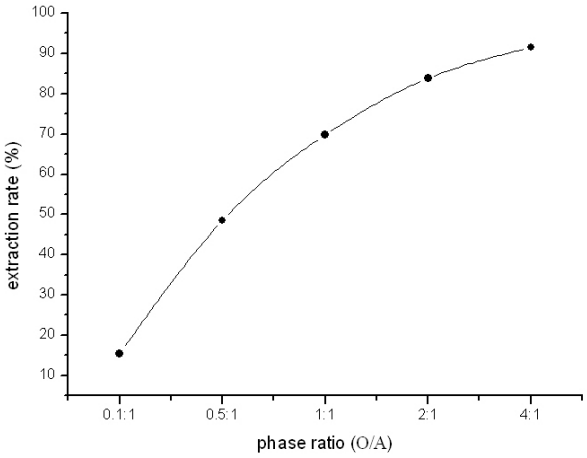

Fig.1. Effect of phase ratio of organic to aqueous phase (O/A) on extraction rate in reactive dyes wastewater (50mL dyes wastewater, pH= 9±0.2, mixing time=30min, equilibration time=30min.)

In the extraction process, tributyl phosphate diluted with petroleum ether was used to extract m-β-hydroxyethylsulfonyl aniline from reactive dye wastewater. Fig.1 shows the relationship between extraction rate and phase ratio in the tributyl phosphate/petroleum ether extraction process. It can be seen that with the increase of phase ratio of organic to aqueous phase (O/A), more m-β-hydroxyehylsulfonyl aniline is extracted from reactive dye wastewater. When extraction phase ratio of organic to aqueous phase (O/A) was 2:1, the single stage extraction rate was 85%.

Effect of stripping phase ratio

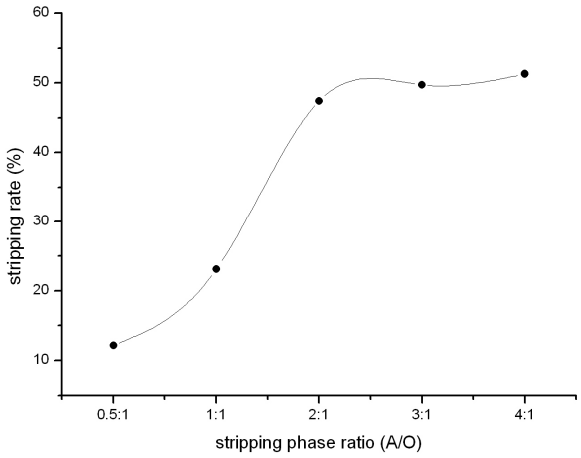

Fig.2. Effect of phase ratio of aqueous phase to organic (A/O) in reactive dye wastewater (stripping reagent volume=200mL, mixing time=30min, equilibration time=30min.)

Since the reaction to synthesize reactive black KNB is carried out under alkaline conditions, it is helpful for sodium hydroxide being selected as the stripping agent. Therefore, the stripped solution containing m-β-hydroxyehylsulfonyl aniline could be reused directly for manufacture of reactive black KNB. Effect of phase ratio A/O on stripping rate is given in Fig.2. It can be seen that the stripping ability of m-β-hydroxyethylsulfonyl aniline closely depends on the increased A/O ratio when the stripping phase ratio of aqueous to organic phase (A/O) is smaller than 2:1. As the stripping phase ratio changes from 0.5:1 to 2:1, it is found that the stripping rate almost four times larger. However, as the stripping phase ratio of aqueous to organic phase (A/O) is higher than 2:1, the stripping efficiency tends to keep unchanged. Hence, the optimal phase ratio A/O of 2:1 was chosen for stripping agent, while the single stripping rate was higher than 50%. Furthermore, our work also demonstrates that regenerated tributyl phosphate/petroleum ether could be reused for times.

Effect of stripping temperature

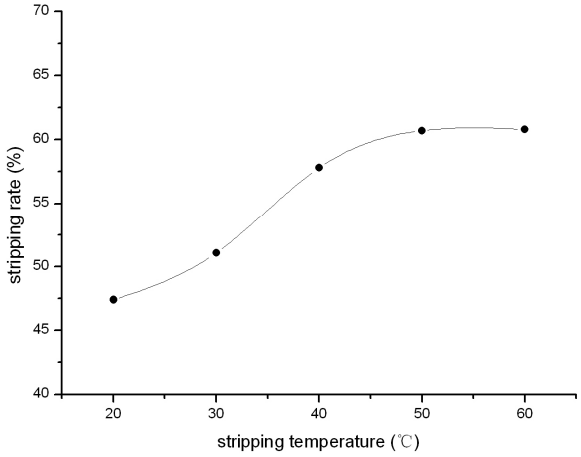

Fig.3. Effect of stripping temperature (extraction ratio O/A=2:1, pH=9, volume of organic phase=100mL, volume of stripping reagent=200mL, stripping reagent concentration=0.5mol/L, mixing time=30min, equilibration time=30min.)

The effect of temperature on stripping rate is given in Fig.3. It can be seen that the stripping rate increased with increasing temperature when 0.5M sodium hydroxide solution was selected as stripping solvent. Since the stripping rate reaches the maximum data of 60.7% at 50℃, the stripping process in our experiment is carried out under this temperature.

Summary

M-β-hydroxyethylsulfonyl aniline was extracted from reactive dye wastewater according to tributyl phosphate/petroleum ether extraction process and sodium hydroxide solution stripping process. Under the optimal conditions, 85% m-β-Hydroxyethylsulfonyl aniline could be extracted at single stage and the stripping rate was more than 50% at 50℃. It is reasonable to conclude that much higher extraction and stripping rates could be obtained after multi-stage treatment. Therefore, not only the reactive dye wastewater with less organics could be disposed more easily, but also the reusable components existed in dyes wastewater could be recycled.

References

[1] H.S.g Hu, M.D. Yang, J. Dang, Treatment of strong acid dye wastewater by solvent extraction, Separation and Purification Technology. 42(2005) 129-136.

[2] O. Gungor, A. Yilmaz, S. Memon, M.Yilmaz, Evaluation of the performance of calyxarene derivatives as liquid phase extraction material for the removal of azo dyes, Journal of Hazardous Materials. 158(2008) 202-207.

[3] G. Muthuraman, K. Palanivelu, Selective extraction and separation of textile anionic dyes from aqueous solution by tetrabutyl ammonium bromide, Dyes and Pigments.64 (2005) 251-257.

[4] G. Muthuraman, T. T. Teng, Solvent extraction of methyl with salicylic acid from aqueous acidic solutions, Desalination. 263 (2010) 113-117.

doi:10.4028/www.scientific.net/AMM.161.185

Study on catalytic oxidatio benzaldehyde to benzoic acid with Keggin polyoxometalate $[(CH_2)_5NH_2]_4SiW_{12}O_{40}$

Yuansheng -Ding[1a], Fei-Lu [2b] Xinbao- Han[3c]

[1] Dept. of Chemical and Pharmaceutical Engineering, Jilin Institute of Chemical Technology, Jilin 132022, China

[2] Dept. of Chemical and Pharmaceutical Engineering, Jilin Institute of Chemical Technology, Jilin 132022, China

[3] Key Lab of Polyoxometalate Science, Department of Chemistry, Northeast Normal University, Changchun 130024,People's Republic of China

[a]email: chxu1970@sina.com; [b]email:l781216@yahoo.com.cn ;[c]email:791271109@qq.com

Key words: $[(CH_2)_5NH_2]_4SiW_{12}O_{40}$；Keggin structure；Catalysis；Benzoic acid

Abstract: The organic–inorganic hybrid catalyst $[(CH_2)_5NH_2]_4SiW_{12}O_{40}$ was prepared by matrix acid and piperidine. The matrix acid was synthesized by sodium molybdate and sodium silicate, and the piperidine was organic ligand. The proposed composition and structure of the catalyst were evidenced by XPS, FT-IR, XRD, TG-DTA and elemental analysis. The results indicated that the heteropoly anions still reserved their Keggin structure in the compound. Its catalytic performance was evaluated in the oxidation of benzaldehyde to benzoic acid. Various reaction parameters were changed to attain the optimal conditions. The optimal reaction conditions were found to be: n(catalyst): n(benzaldehyde)=3.1×10^{-3}:1; n(H_2O_2) ： n(benzaldehyde)=4.5 ： 1; reaction temperature was 80℃; reaction time was 4h. The yield of benzoic acid achieved above 85%.

Introduction

Heteropoly acid（HPA）and related polyoxometalate compounds （POMs）are a class of poly- oxygen metal complexes. The complexes contain central atom (such as P, Si, etc.) and ligands (such as Mo, W, etc.). They combined multi-space oxygen by bridging oxygen atoms. HPA and POMs have clear sizes, shapes and discrete fragments similar to the structure of metal oxides [1]. They play great roles in catalysis, photochemistry, medicine, materials science and magnetic fields [2-6]. As green catalysts, they contain both acid sites and redox active sites that make them to be potential redox molecular sieves and bifunctional catalysts. Furthermore, they display high catalytic activity, selectivity, rapid response, mild reaction conditions, oxidation and optical, magnetic, stability, micro-light corrosion of equipment. Based on these properties, they can be used for homogeneous and heterogeneous reactions, and even can be used for phase transfer catalyst [7-10]. Therefore, synthesis of new efficient POMs catalysts has become a hot spot.

Keggin type coordination $[(CH_2)_5NH_2]_4SiW_{12}O_{40}$ POMs catalyst was synthesized and structurally characterized by means of single crystal X-ray diffraction, IR, and TG. The composite catalyst was applied to the oxidation of benzoic acid with benzaldehyde. The influence factors of the reaction were also investigated in the present article.

Experimental

Materials and Detection Method:

$Na_2WO_4\cdot2H_2O$, hexahydropyridine and benzaldehyde were obtained from Shanghai Chemical Reagent Co. Ltd. H_2O_2 (30%) and H_3PO_4（85%）were purchased from Beijing Chemical Reagent Co. Ltd. The crystal structure was identified using a Dmax 2200PC wide angle X-ray diffraction. Samples were measured at a rate of 2°/min through a range of 5°-40°. The phase transformations of the sample were measured using a Mettler TA 4000 differential scanning calorimeter (DSC). The IR spectrum was measured on a Magna 560 FTIR. Application of Perkin-Elmer 240C Elemental Analyzer for the determination of Carbon, Hydrogen, Nitrogen in the products. Determination of tungsten by Plasma-Spec(I)ICP Analyzer.

Materials Synthesis.

The 20 g $Na_2WO_4 \cdot 2H_2O$ were dissolved in 40 ml deionized water, and kept in boiling water bath for 70°C.After 10 mins, adopting $HClO_4$ regulate the pH value, when pH = 2, the 0.7g Na_2SiO_3 were added in the solutions in the conditions of 70°C, 120r/min. The total reaction time was 2 hours. Firstly, the yellow deposit emerged. After filtered, the liquid was cooled to ambient temperature. After moved to the separatory funnel, the liquid was extracted with ethyl ether and $6mol \cdot L^{-1}$ HCl. The below solutions were one more extracted with ethyl ether and HCl. The extracted oil phase were evaporated under the 60°C water bath until the films appeared with added a small amount of distilled water (10 ~ 20 drops) and a few drops of concentrated HNO_3. Then the transparent phosphatotungstic acid was attained after cooled. The purity of crystal was obtained with nearly 100% after re-crystallized.

The precipitate was prepared by mixing the $H_4SiW_{12}O_{40} \cdot nH_2O$ and hexahydropyridine with mole ratio 1:3 and reaction at 70°C for 2h. After filtered, the precipitate was cleaned by ethanol, ethyl ether and H_2O in order, and dissolved in the mixture of the acetonitrile and water. After filtered, the filtrates were transferred to the beaker and kept at room temperature. For one week, the $[(CH_2)_5NH_2]_4SiW_{12}O_{40}$ crystal would crystallize at the bottom of the beaker.

Result and discussion

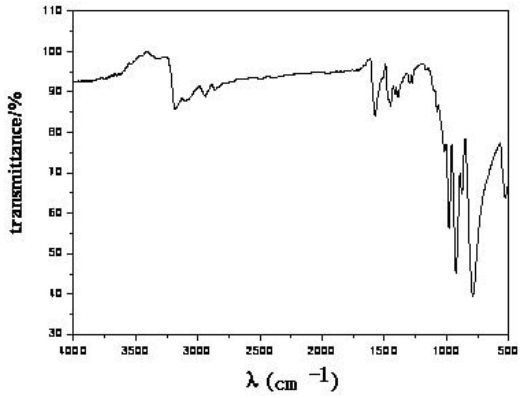

Fig.1 FTIR spectrum of charge transfer POMS$[(CH_2)_5NH_2]_4SiW_{12}O_{40}$

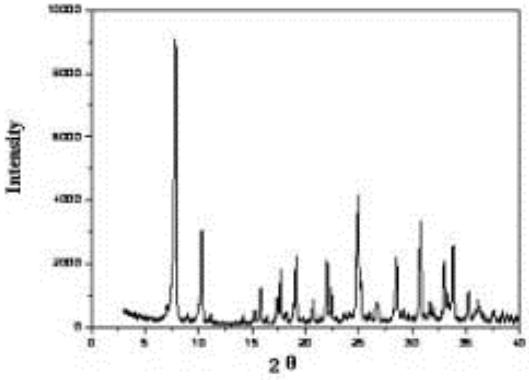

Fig.2 X-Ray powder diffraction patterns of charge transfer POMS $[(CH_2)_5NH_2]_4SiW_{12}O_{40}$

The FTIR spectrum of charge transfer POMs $[(CH_2)_5NH_2]_4SiW_{12}O_4$ (Fig.1) exhibited four bands located at 979.14, 923.51, 876.50 and 793.2cm^{-1}corresponding to Si-Oa, W-Od, W-Ob-W, W-Oc-W vibrations, respectively. These absorption peaks closed to those reported [11] for heteropolyanions $SiW_{12}O_{40}^{4-}$ that peaks at 983.5, 855.3, 796.8 and 792.9cm^{-1}. The result showed the synthesed transfer POMs exhibit Keggin structure. However, relative to the starting heteropoly acids, the absorption peak of Si-Oa and W-Od showed an obvious blue shift, while that of W-Ob-W and W-Oc-W showed a red shift. This may be caused by the charge transfer from protoned piperdine to the heteropolyanions. The absorption bands at 1581 and 1439 cm^{-1} were assigned to the stretching vibrations for piperdine ring. FTIR 2863 cm^{-1} peak and 2939 cm^{-1} peak were assigned to the CH_2 symmetric stretch and asymmetric stretch of the γ-methylene and β-methylene groups. The bands corresponding to the axial amine N-H stretching vibrations appear in the 3174 cm^{-1} region. The FTIR spectrum showed that the stronger charge transfer exist in the polyanions and its counterions that resulted in forming the charge transfer POMs.

XRD result of the prepared catalyst was presented in Fig. 2. Four peaks at around 7.88°, 19.1°, 24.92°and 30.72° were observed for catalyst. These four peaks were similar to the Keggin-type $H_4SiW_{12}O_{40}$ phase[12].

ICP and EA gave the results the contents of C, H, N and W were 7.48%，1.49 %, 1.74 % and 68.5 %, respectively. The data were found to be the same with the calculated results. Therefore, the molecular formula of the product was $[(CH_2)_5NH_2]_4SiW_{12}O_4$.

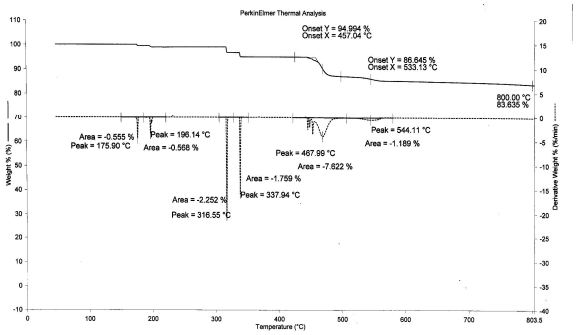

Fig. 3 TG-DTA curve of charge transfer POMS$[(CH_2)_5NH_2]_4SiW_{12}O_{40}$

The TG curve indicated the thermal decomposition processes of $[(CH_2)_5NH_2]_4SiW_{12}O_{40}$ can be divided into four mass loss steps. The first mass loss step was in the temperature range of 175.90°C～196.41°C with similar mass losses of ca. 5.006%. In the process, six crystallization waters that connected with acidic proton via H-bond were lost. The second decomposition step in the temperature range of 316.55°C～457.04°C. The polyanions began to decompose in this process. The third decomposition step started at 457.04℃, and continued up to 533.13℃. The third step can be assigned to the oxidative decomposition of protoned piperdine with a strong exothermic peak marking the collapse of Keggin structure. The mass losses in the third step were 13.355%. The four decomposition step in the temperature range of 533.13°C～800°C. In the four step, the polyanions were totally decomposed into WO_3 and SiO_2. According to DTA, the decomposition temperature of $[(CH_2)_5NH_2]_4SiW_{12}O_{40}$ was at 467.99°C that lower than decomposition temperature (445℃) of the starting heteropoly acid.[15] It can be seen the charge transfer POMs have more thermodynamically stable structures compare to starting heteropoly acid.

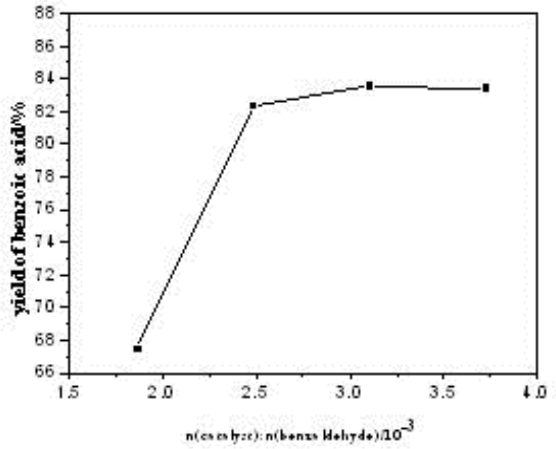

Fig.4Catalytic effect of $[(CH_2)_5NH_2]_4SiW_{12}O_{40}$ dosage on the conversion of benzoic acid (Reaction conditions: n H_2O_2 : benzaldehyde ＝4.0：1, temperature 80°C, time 4hours)

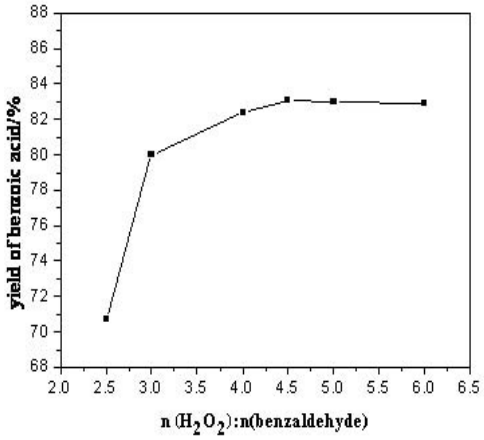

Fig.5 Effect of H_2O_2 dosage on the conversion of benzoic acid (Reaction conditions: n$[(CH_2)_5NH_2]_4SiW_{12}O_{40}$: n benzaldehyde ＝ 3.1×10^{-3} , temperature 80°C, time 4hours)

The effect of catalyst dosage on the yields of products was shown in Fig.4. The molar ratio of $[(CH_2)_5NH_2]_4SiW_{12}O_{40}$ /benzaldehyde was varied from 1.9×10^{-3} to 3.7×10^{-3}. As can be seen, catalyst dosage significantly affected the reaction. The yield of the benzoic acid was promoted with the increase of molar ratio. The most beneficial molar ratio of $[(CH_2)_5NH_2]_4SiW_{12}O_{40}$ /benzaldehyde was chosen to be 3.1×10^{-3}.

The effect of H_2O_2 on reaction was also studied, as shown in Fig.5. The conversion of benzoic acid was promoted with the molar ratio of H_2O_2 /benzaldehyde when the molar ratio was less than 4.5:1. While above the molar ratio 4.5:1, the yield of benzoic acid was decreased with the molar ratio of H_2O_2 /benzaldehyde.

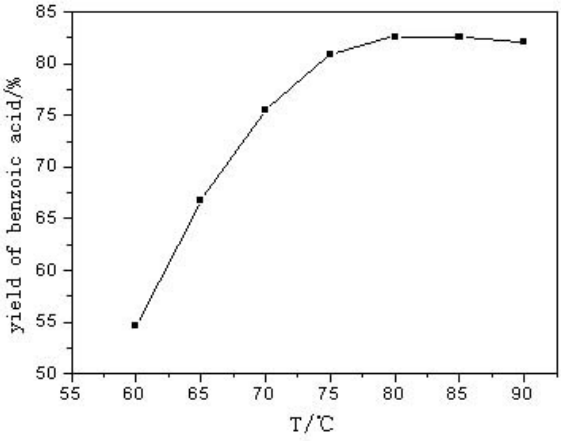

Fig.6 Effect of temperature on the catalytic activity (Reaction conditions: $n[(CH_2)_5NH_2]_4SiW_{12}O_{40}$: n benzaldehyde $=3.1\times10^{-3}$, n H_2O_2 : benzaldehyde= 4.0：1, time 4hours)

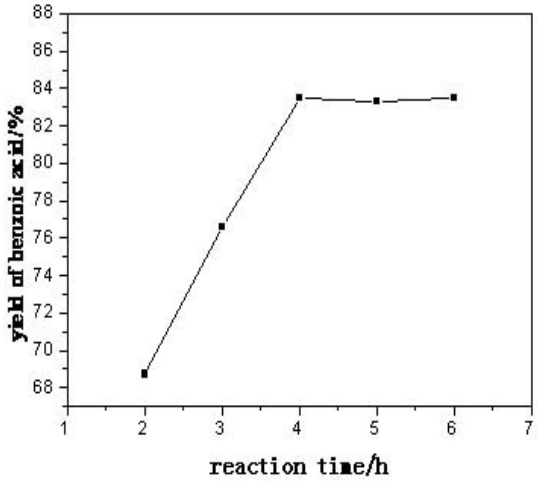

Fig.7 Effect of reaction time on the catalytic activity (Reaction conditions: $n[(CH_2)_5NH_2]_4SiW_{12}O_{40}$: n benzaldehyde= 3.1×10^{-3} , n H_2O_2 : benzaldehyde=4.0：1, temperature 80°C)

The effect of reaction temperature on the reaction was investigated, and the experiments were conducted at 60, 65，70, 75, 80, 85 and 90 °C, respectively. Fig.6 showed the effect of the temperature on the yields of product. It can be observed that temperature have a significant effect on the reactions. When the reaction temperature was increased from 60 to 80 °C, there was a significant increase in the yield of benzoic acid. When the reaction temperature rose above 80 °C, the yield of benzoic acid began to fall, and higher temperatures thus could accelerate the rate of chemical reactions, but unwanted side reactions also appeared at the high temperature. For example, H_2O_2 could decompose, thus the reaction temperature was set to 80 °C in this experiment.

Time course of oxidation was as shown in Fig. 7. The amount of benzoic acid grew very fast for the first two hours. Then it was observed slightly to decrease after 4 hours. It was found that 4 hours were sufficient for completion of the oxidation reaction.

To estimate the potential $[(CH_2)_5NH_2]_4SiW_{12}O_{40}$ contribution in the reaction, benzaldehyde oxidation was also carried out at mole ratio（H_2O_2 /benzaldehyde）of 4.5 : 1 at 80 °C without $[(CH_2)_5NH_2]_4SiW_{12}O_{40}$, the product yield was only 30. 5% that lower than the product conversion of reaction with $[(CH_2)_5NH_2]_4SiW_{12}O_{40}$. While H_2O_2 was not added into the system, no product was formed. It can conclude that the $[(CH_2)_5NH_2]_4SiW_{12}O_{40}$ was not an oxidizing agent, however it only played great role in promoting the benzaldehyde oxidation reaction as catalyst.

Table 1 Reaction conditions (Verification)

Number	n H_2O_2 : n benzaldehyde	Reaction temperature/℃	$n[(CH_2)_5NH_2]_4SiW_{12}O_{40}$: n benzaldehyde /$\times10^{-3}$	Time /h	yeild/%
1	4.5:1	80	3.1	4	85.3
2	4.5:1	80	3.1	4	85.7
3	4.5:1	80	3.1	4	85.6

Above the about analysis, the optimal reaction conditions were drawn. For verification three parallel experiments were carried out, the results were shown in the table one.

Conclusions

The proton-transfer reactions between hexahydropyridine and Keggin-type heteropolyacid produced solid charge transfer hybrid materials $[(CH_2)_5NH_2]_4SiW_{12}O_{40}$. The charge transfer interactions are strong enough to cause evident changes in FTIR spectrum between heteropolyacids and hybrid materials. The optimal reaction conditions were as follows: n$[(CH_2)_5NH_2]_4SiW_{12}O_{40}$: n benzaldehyde＝$3.1\times10^{-3}$, n H_2O_2 : benzaldehyde＝4.5：1, 80°C, 4hours. Under the optimum conditions, the yield of the product is 85%.

Acknowledgements

The authors are grateful for the financial support provided by the Jilin Education Department Science Foundation of China (NO. 2008174 and NO.2009152)

References

[1] S.E. Collins, S.R. Matkovic, A.L. Bonivardi, and L.E. Briand, Acylating capacity of the phosphotungstic wells−dawson heteropoly acid: intermediate reactive species J. Phys. Chem. C, 115 (2011) 700–709

[2] I.V. Kozhevnikov, Catalysis by heteropoly acids and multicomponent polyoxometalates in liquid-phase reactions, Chem. Rev. 98（1998） 171-198.

[3] A.Dolbecq, E.Dumas, C.R.Mayer, P.Mialane, Hybrid organic-inorganic polyoxometalate compounds: From structural diversity to applications, Chem. Rev. 110（2010）6009-6048

[4] S.Q.Liu, Z.Y.Tang, Polyoxometalate-based functional nanostructured films: Current progress and future prospects Nano. today 5 (2010) 267-281 .

[5] W. Qi, L.X.Wu, Polyoxometalate/polymer hybrid materials: fabrication and properties, Polym. Int. 58 (2009) 1217-1225.

[6] Y.X.Qiao, Z.S. Hou, Polyoxometalate-Based Solid and Liquid Salts for Catalysis, Curr. Org. Chem. 13（2009）1347-1365.

[7] P.Liu, Y.Liang, X.Z.Lin, C.X. Wang andG.W. Yang, A general strategy to fabricate simple polyoxometalate nanostructures: Electrochemistry-assisted laser ablation in liquid, Acs. Nano. 5 (2011）4748-4755.

[8] C.Ritchie, C.Streb, J.Thiel, S.G.Mitchell, H.N. Miras, D.L. Long,T. Boyd, R.D.Peacock, T. McGlone , L.Cronin , Reversible redox reactions in an extended polyoxometalate framework solid, Angew. Chem. Int .Ed. 47（2008）6881-6684

[9] S.T. Zheng, J.Zhang,G.F.Yang, Designed synthesis of POM–Organic frameworks from $\{Ni_6PW_9\}$ building blocks under hydrothermal conditions, Angew. Chem. Int. Ed. 47（2008）3909-3913.

[10] X.L.Wang, C.Qin, E.B.Wang, Z.M.Su, Y.G.Li, L.Xu,Self-Assembly of nanometer-Scale $[Cu_{24}I_{10}L_{12}]^{14+}$ cages and ball-Shaped Keggin clusters into a (4,12)-connected 3D framework with photoluminescent and electrochemical properties, Angew. Chem. Int.Ed. 45（2006）7411-7414.

[11] U.L.Štangar, N.Grošelj, B.Orel, P.H. Colomban, Structure of and interactions between P/SiWA Keggin nanocrystals dispersed in an organically modified electrolyte membrane, Chem. Mater. 12 (2000) 3745–3753

[12] I.V. Kozhevnikov, K.R. Kloetstra, A. Sinnema, Study of catalysts comprising heteropoly acid $H_3PW_{12}O_{40}$ supported on MCM-41 molecular sieve and amorphous silica, J. Mol. Catal. A: Chem. 114 (1996) 287-298

doi:10.4028/www.scientific.net/AMM.161.190

Research on the Affective Factors on Passive Film of Atmospheric Tower 304 Stainless Steel

Bing Chen[a] Changjiang Wu[b] Yuguang Fan[c] and Bin Feng[d]

School of Mechanical Engineering, Xi'an Shiyou University, Xi'an, Shannxi, 710065, China

[a]bchen@xsyu.edu.cn, [b]changjiang323297@163.com, [c]ygfan@xsyu.edu.cn , [d]274795609@qq.com.

Keywords: Passive film, 304 stainless steel, Air- cooler, Electrochemical.

Abstract. On condition that the surface of 304 stainless steel has formed passive film, we have done research on the impact that the change of concentration of Cl^- and Na^+, the temperature, pH of Na^+, on 304 stainless steel properties. This experiment is preceded studied with electrochemical method. The results show that along with the increase of temperature, pH improves the repairing capacity of passive film on the surface of 304 stainless steel. However, its stability decreases. Meantime, the pitting corrosion will happen become easier, when the repairing capacity of passive film and stability have been weakened because of the concentration of Na^+, Cl^- increases.

Introduction

The air-cooler in a company confronts very serious leakage problems for the reason of blockage and corrosion caused by demineralized water [1]. According to this situation, the company analyzes demineralized water, finding out the reason is that the condensation water contains a certain amount of chloride ions, and the temperature and pH also have impact on pitting formation [2]. The scaling of the pipe is because the water contains a lot of Na^+. After the analysis, we get four factors: the range of Cl^- concentration is 131~450mg.L^{-1}, the range of pH is 7.5~10.2, the range of the temperature is 37~65℃, the range of concentration of Na^+ is 45~150mg.L^{-1}.

Air-cooled tube, 304 stainless steel can form protective passive film while used [3,4]. In order to evaluate the capability of resisting the corrosion, we need to gain breakdown potential and the number of protection potential. So the Retrace curve always needs to be measured. Through the passivation experiment, we have done research on the impact that the change of concentration of Cl^- and Na^+, the temperature, pH of Na^+, has on 304 stainless steel properties. According to orthogonal method, we do experimental design on the four main corrosion factors of experimental design to resist corrosion.

Experiment

Preparations of 304 Stainless Steel Sample. 304 stainless steel specimens was made into a circular sheet with the surface area of 1 cm^2. The circular sheet was polished with water sandpaper of 400#, 600# and 800# meantime, the wire was led on the other side, and then the rest of this surface and the edges are sealed with epoxy resin. Degreasing should be wiped with acetone before the experiment, and the anhydrous ethanol put in a dry container for later use.

Orthogonal experiment Arrangements of Corrosive Factors. The experimental design of four major corrosive factors was preceded. Temperature, Cl^-, pH values, and Na^+ were marked as *A*, *B*, *C* and *D* respectively in Orthogonal experiment.

Three levels of all factors are shown in Table 1. Orthogonal experiment arrangements among the various factors are shown in Table 2.

Table 1 Test factors level

level	temperature [℃] (*A*)	concentration of Cl^- [$mg.L^{-1}$] (*B*)	pH value (*C*)	concentration of Na^+ [$mg.L^{-1}$] (*D*)
1	40	200	8	50
2	50	250	9	75
3	60	300	10	100

Table 2 Corrosion factor test program

Test Plan	Level of portfolios	Temperature [℃]	Concentration of Cl^-[$mg.L^{-1}$]	pH value	Content of Na^+ [$mg.L^{-1}$]
Plan1	*A1B1C1D1*	40	200	8	50
Plan2	*A1B2C2D2*	40	250	9	75
Plan3	*A1B3C3D3*	40	300	10	100
Plan4	*A2B1C2D3*	50	200	9	100
Plan5	*A2B2C3D1*	50	250	10	50
Plan6	*A2B3C1D2*	50	300	8	75
Plan7	*A3B1C3D2*	60	200	10	75
Plan8	*A3B2C1D3*	60	250	8	100
Plan9	*A3B3C2D1*	60	300	9	50

Passivation Regression Test. Electrochemical measurement is measured by three-electrode system. The electrode is saturated calomel electrode (SCE), and platinum electrode is the auxiliary electrode. The surface area of working electrode is $1cm^2$, and we used 304 stainless steel as the material. Test solution is based on orthogonal design in Table 3. The passivation regression was done on 304 in each analog medium. The scan rate of CS300 electrochemical test system is $0.5mV.s^{-1}$, the frequency 2Hz, and the range of passivation potential -0.1~0.85mV(relatively open circuit potential). The anode current is set to $0.3Acm^{-2}$.

Results and Discussion

We did potentiodynamic scanning on 304 stainless steel for the study of the electrode according to Table 3. We got the regression curve of nine sets test programs. This is shown in Figure 1:

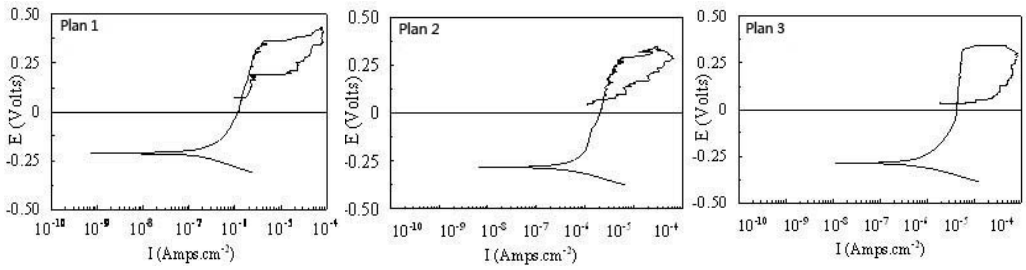

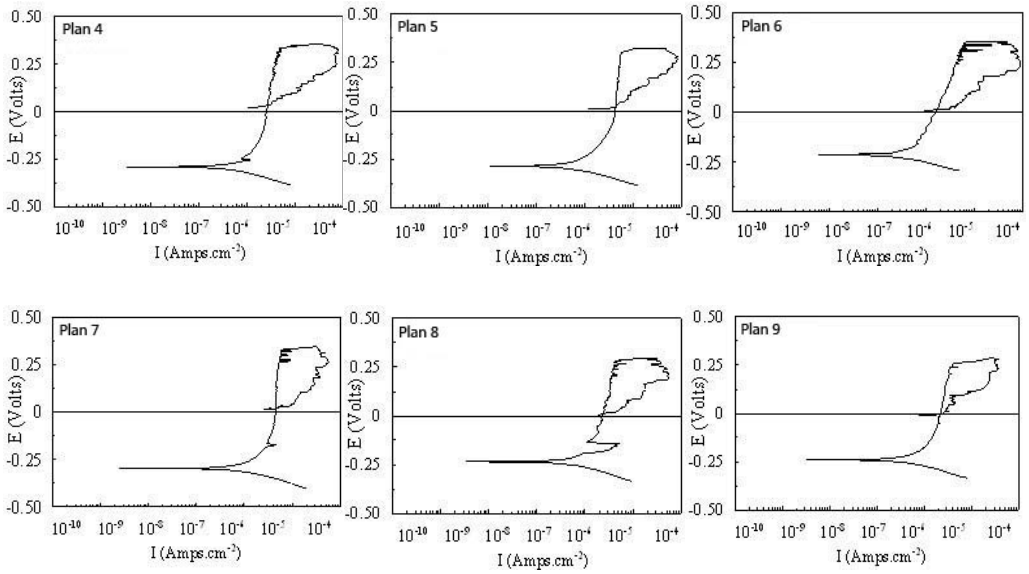

Figure 1 Return curves of 304 stainless steel Passivation in 9 sets of experiments

The passive film-related parameters can be drawn by analyzing Figure 1 on stainless steel passivation: breakdown potential *Eb*, protection potential *Ep*, protection current density *Ip*, and the area size of the hysteresis loop ΔS. The difference between *Eb* and *Ep* is shown in Table 3.

Table 3 Passivation regression analysis table

Test medium	Breakdown potential *Eb*[mV]	Protection potential *Ep*[mV]	ΔE[mV]	ΔS[VuA.cm^{-2}]	*Ip*[uA.cm^{-2}]
Plan 1	367.5	72.1	295.4	8.1	6.3
Plan 2	322.1	25.2	296.9	6.1	4.3
Plan 3	315.6	17.1	298.5	9.2	2.3
Plan 4	312.8	15.7	297.1	8.3	3.8
Plan 5	342.4	43.3	299.1	8.1	5.5
Plan 6	292.3	-4.1	296.3	7.9	2.3
Plan 7	337.9	39.4	298.5	7.8	4.1
Plan 8	272.2	-29.6	301.8	7.7	1.1
Plan 9	306.2	6.4	299.8	7.1	1.2

Pearson correlation coefficient was used to evaluate the relationship between *Eb, Ep,* ΔE, ΔS and temperature, the concentration of Na^+, Cl^-, pH value. Then we found pearson correlation coefficient. The information obtained through the analysis is as follows:

(1) Breakdown potential *Eb* indicates the stability of the passive film of stainless steel. The higher *Eb* is the more stable the passive films. The correlation coefficients of *Eb* and the concentration of Na^+, Cl^-, the temperature of the Pearson are -0.590, -0.532, -0.454 respeetively. *Eb* is moderatly-related to the concentration of Na^+, Cl^-, and the temperature. The higher he concentration of Na^+, Cl^-, and temperature are, the lower *Eb* is.

(2)Protection potential *Ep* indicates that stainless steel passive film has not reached breakdown potential value. The correlation coefficients of *Ep* and the concentration of Na^+, Cl^-,and the temperature of the Pearson are -0.582, -0.529, -0.482 respectively. The relationship is moderately-related. When the concentration of Na^+, Cl^- and temperature increase, *Ep* decreases.

(3) The difference between *Eb* and *Ep* indicates the self-repairing capacity of stainless steel. The capacity increases after pitting: the smaller ΔE is, the greater the ability to repair itself is. The Pearson correlation coefficients between ΔE and the four factors are as follows: temperature being -0.684, concentration of Cl^- being 0.265, concentration Na^+ being 0.228, and pH value being 0.191. The correlation coefficients are highly related with temperature, and hardly have with the concentration of Na^+, Cl^-, a very weak relation with the pH value. When the temperature increases, ΔE decreases and the concentration of Na^+, Cl^-, pH value increases.

(4) The size of ΔS is usually related to the ability to restore and blunt. Generally speaking, the greater ΔS is, the greater difficulty it will have to recover. The Pearson correlation coefficients of ΔS and the four factors are as follows: the concentration of Na^+ being 0.322, pH value being 0.238, temperature being -0.136. The correlation coefficient has weak relation with the concentration of Na^+ and the *pH* value. It has a very weak relation with the temperature and the concentration of Cl^-. When the temperature decreases and the concentration of Na^+ and the pH value increase, ΔS increases, too. The chloride ion concentration does not affect ΔS.

Conclusions

(1) The increase of pH value makes the passive film more stable, while the ability to repair itself decreases. In general, the increase of pH value has both advantages and disadvantages, but they are not so obvious.

(2)The increase of temperate significantly enhances the ability to repair itself. Meantime, the stability of the passive film weakens. In general, the increase of the temperature is good for forming dense passive film.

(3)The increase of the concentration of Na^+, Cl^- weakens the stability of the passive film. Its ability to repair itself decreases, too. However, the former is the main part. It's most likely to be pitting.

(4) The possibility of metal's pitting is related to the nature of the material, if there exists passive film. Meantime, it has some relation with the concentration of ion contained in it.

Acknowledgements

This work was financially supported by the scientific research item of Shaanxi Province Education Commission (2010JK776) and the graduate scientific research item of Xi'an Shiyou University.

References

[1] Gu Guo, Research on the Yanchang Refinery relational model of regular top system of corrosion factors [D]. Xi'an: Xi'an Shiyou University, 2008. In Chinese.

[2] Zhou Bensheng, Corrosion and protection in industry water cooling system. (Chemical Industry Press, China 1993), In Chinese.

[3] Zhan Bolin, Zhu Youlan, Yang Zhuo, etc.Materials Review Vol.20(2006), p.79, In Chinese.

[4] Zhou Lixin, Cheng Jiang, Yang Zhuoru, Corrosion Science and Protect Technology Vol.16(2004), p.375, In Chinese.

doi:10.4028/www.scientific.net/AMM.161.194

The effect of potassium carbonate on the catalytic properties for methane conversion with ceria

Duan Yuejuan[1, 3, a], Wang Hua[2, 3, b], Wei Yonggang[2,3], Li Kongzhai[2,3], Zhu Xing[2,3], Du Yunpeng[1,3]

[1] Faculty of Chemical Engineering, Kunming University of Science and Technology, Kunming 650024, China;

[2] Faculty of Metallurgy and Energy Engineering, Kunming University of Science and Technology, Kunming 650093, China;

[3] Engineering Research Center of Metallurgical Energy Conservation and Emission Reduction, Ministry of Education, Kunming 650093, China

[a] duanyue17@126.com

[b] E-mail: wanghuaheat@hotmail.com (corresponding author)

Keywords: methane conversion; potassium carbonate; ceria; oxygen storage capacity; carbon elimination;

Abstract. Pure CeO_2 and a series of (x %) K-CeO_2 (x=1, 2, 3, 4) catalysts were respectively prepared by the precipitation and incipient wetness impregnation methods, and characterized by means of XRD, BET and H_2-TPR techniques. The catalytic activity was investigated by the gas-solid reaction with methane in the absence of gaseous oxidant in a fixed bed reactor at 800 ºC. The XRD measurement showed that doping of K_2CO_3 did not change the structure of CeO_2 with the addition of K_2CO_3 without formation of Ce-K-O solid solution in these materials. Surface area of catalysts was decreased with the impregnation amount of K_2CO_3. Reducibility of catalysts was obviously enhanced by the addition of K_2CO_3 as shown in H_2-TPR tests. The catalysts activity tests indicated that adding K_2CO_3 to CeO_2 could promote the oxygen storage capacity of catalysts. K species in CeO_2 could affect the CO formation in methane oxidation.

Introduction

Natural gas with the major component of methane is one of the potential alternative energies, as oil resources become depleted [1]. Methane is usually converted to syngas for further utilization in gas to liquid (GTL) technology such as Fischer-Tropsch (F-T) syntheses and methanol production. Steam methane reforming (SMR), carbon dioxide reforming (CDR) and partial oxidation of methane (POM) are three typical routes for methane to syngas [2-3]. Both SMR and CDR demand highly endothermic, but POM is mildly exothermic. Therefore, many investigations were focused on the POM process with gaseous oxygen as oxygen source [4–6]. In this process, since involving direct contact between fuels and gaseous molecular oxygen, there is the risk of explosion, and catalyst hot-spot that causes the sintering problems of catalyst will occur easily. In recent years, the reactions between methane and solid catalysts have been reported. Otsuka et al. [7] and Van Looij et al. [8] reported a novel method for methane conversion to syngas between CH_4 and metal oxides by gas-solid reaction in the absence of gas-phase oxygen. This technology avoids the risk of explosion due to the separate feeding of the methane and gaseous molecular oxygen. Otsuka et al. [7, 9–10] first reported that the directly partial oxidation of methane to syngas with CeO_2 as oxygen source. Subsequently, Ce-based mixed oxides were used to study the directly partial oxidation of methane to syngas [11-14] by gas-solid reactions and showed high activity and selectivity. For the reaction mechanism between methane and CeO_2, some literatures [10-11, 13] implied that methane was activated on the reduced Ce^{3+} sites to form carbon intermediates and hydrogen. Then the carbon deposition was selectively oxidized to CO by lattice oxygen of solid oxide, and the recombination of H atoms or the desorption of H_2 was the process that the formation of syngas. Therefore, the oxidation of carbon deposition is very important for the oxidation of methane to syngas.

Doping alkali metal salts has been shown to bring substantial benefit to soot oxidation [15-18], their results showed that alkali metal increased surface mobility of catalysts and favored the oxidation of soot by consuming the carbon to form carbonate species during soot combustion. Liu et al. [17] suggested that the loading of potassium could improve the oxygen exchange rate of CeO_2-based catalysts via a so-called synergistic effect. In addition, Aneggi et al. [19] reported that doping of potassium to CeO_2 could strongly enhance formation of surface carbonates intermediates species (C–O–K), which helped in the elimination of carbon deposition that was detrimental for the activity of the catalyst as well. Alkali metal carbonates is an important additive for the catalysts of diesel soot combustion [15, 19] due to its high chemical and thermal stability, good mobility, high heat transfer ability because of their high melting points and acting as a good electron donor. On the other hand, it was also reported that the molten carbonates could be used as catalyst and thermal carrier for coal-CO_2 gasification [20-21] and the nonflame combustion technology (NFCT) [22]. As well as, our previous researches showed that the alkali metal molten carbonates could improve the reaction between methane and catalysts to produce syngas [23]. They suggested the CH_4 cracking reaction occurred when high temperature methane passed through the molten salt bath. Then the cracking carbon could further react with alkali metal molten salts, and produce a series of intermediate reactions. These results suggest that the alkali metal molten carbonates played important roles for oxidation of the cracking carbon of methane. In addition, under alkali metal molten carbonate salt conditions, the reaction was in the liquid medium, which could form a uniform temperature field to avoid the hot spot problem. Therefore, alkali metal carbonates also could play the role of eliminating carbon in the process of methane conversion, which prevented the catalyst inactivation caused by coking and sintering.

In this paper, we use K_2CO_3 as an additive to doping the ceria and create the possibility of improving the reactivity of ceria for methane conversion. Pure CeO_2 and (x %) K-CeO_2(x = 1, 2, 3, 4) were prepared by precipitation and incipient wetness impregnation method, respectively. Their catalytic activities were investigated in a fixed-bed reactor by the gas-solid reaction in the absence of gas-phase oxygen. Using XRD, BET and H2-TPR, the effect of potassium carbonate additive on the CeO_2 catalyst for reaction of methane conversion were investigated.

1 Experimental

1.1 Catalysts preparation

CeO_2 carrier was prepared by a precipitation method with ammonia water as precipitant. The $Ce(NO_3)_3$•$6H_2O$ was dissolved into distilled water, ammonia water was gradually added into the solution under strong stirring conditions and the temperature was kept at 70ºC. when the pH value was increased to 10-11 and at this time, stop dropping ammonia water, the resulting solution was maintained at 70 ºC with continuing stirring for 1h. Subsequently, the precipitate was filtered and washed with distilled water and ethanol after a two-hour settlement. The resulting material was dried at 110 ºC for 24 h after natural drying overnight and a primrose massive object was obtained. The massive object was subjected to calcine under ambient air at 800 °C for 6 h, and then the CeO_2 catalyst sample was obtained.

K_2CO_3 was loaded on CeO_2 via incipient wetness impregnation in varying proportions (1%, 2%, 3%, 4%) of K with an aqueous solution of K_2CO_3 for 24 h in air, then these impregnated materials were dried at 110 °C for 12 h, the powders were calcined at 600 °C for 2 h in air atmosphere. Varying K contents of cerium-based catalysts were obtained and named (x %) K-CeO_2 (x=0, 1, 2, 3, 4). Finally, the samples were pressed under 14 MPa for 10 min, then crushed and sieved to 20–40 mesh size.

1.2 Catalysts characterization

The powder X-ray Diffraction (XRD) experiments were performed on a Japan Science D/max-R diffractometer using Cu Kα radiation (λ=0. 15406 nm). The X-ray tube was operated at 40 kV and 20 mA. The X-ray diffraction was recorded at 0. 01° intervals in the range of $10^o \leqslant 2\theta \leqslant 90^o$ with 3s count accumulation per step. The identification of the phase was made with the help of JCPDS cards (Joint Committee on Powder Diffraction Standards).

The BET surface area was determined by N_2 physisorption using a 3H-2000Ⅲ automatic nitrogen adsorption specific surface area analyzer.

Temperature programmed reduction (TPR) experiments were performed on TPR Win v 1.50 (produced by Quanta Chrome Instruments Co.) under a flow of 10% H_2/He mixture (75 ml/min) over 100 mg catalyst using a heating rate 10 ºC/min.

1.3 Catalysts activity tests

Catalysts activity was tested by the isothermal reaction of catalysts and CH_4 and nitrogen mixed gas (10% CH_4) were carried out in a continuous flow fixed-bed reactor system under the atmospheric pressure, the reaction was performed at 800 ºC with the heating rate of 10 ºC/min. 1.5 g catalyst was twice diluted by quartz sand and placed in a quartz tube with 15 mm inside diameter. Prior to the catalytic reactions, the catalysts were heated in air at 300 ºC for 1 h, and then pure N_2 was allowed to flow into the reactor at 300 ºC for 45 min, when the temperature was up to 800 ºC, shifting the N_2 to CH_4 and nitrogen mixed gas (10% CH_4) and capturing the syngas at the same time. The flow rate of the methane mixed gas was controlled by a mass flow controller at 20 ml/min and the flow rate of the N_2 was 50 ml/min. The reactant and product components were analyzed on line by a gas chromatograph (Agilent Technologies 7890A) equipped with a thermal conductivity detector (TCD) and P-Plot 5 A and HP-Plot-Q columns. Argon was employed as a carrier gas.

2 Results and discussion

2.1 Catalysts characterization

The XRD patterns of the prepared (x %) K-CeO_2 (x=0, 1, 2, 3, 4) catalysts are shown in Fig. 1, and all the five samples revealed typical fluorite-type oxide structure of CeO_2. Excepting the 4%K-CeO_2 sample, no characteristic diffraction peaks for K_2CO_3 can be detected on the others, this indicates that the content of the K_2CO_3 is too lower or K_2CO_3 is highly dispersed on CeO_2 surface. In addition, there is no significant change for characteristic diffraction peaks (peak intensity and position) of CeO_2 in all the four K_2CO_3-contained samples, and this indicates no structure evolution of the materials with the addition of K_2CO_3. It also should be noted that the lattice constants of CeO_2 for all the four K_2CO_3-contained samples are closed to the pure CeO_2, such as Table 1, which suggests no formation of Ce-K-O solid solution in these materials. And we can find that the crystallite sizes of all K_2CO_3-contained samples are increased with the content of K_2CO_3, which may be caused by K_2CO_3 covering the CeO_2 surface.

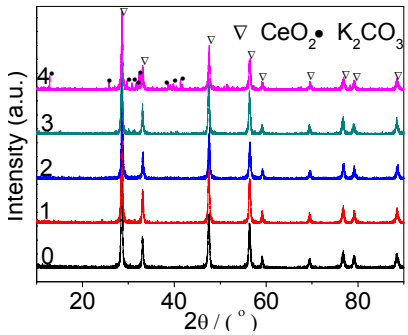

Fig. 1 XRD patterns of the (x %) K-CeO_2 (x=0, 1, 2, 3, 4) catalysts

The BET surface areas are shown in Table 1. It is seen that the specific surface area of CeO_2 decreases after the impregnation with K_2CO_3 and subsequent calcinations. Micropores of the CeO_2 can be plugged by the potassium carbonate to a large extent, which is an important reason for the reduced surface area of CeO_2 impregnated with K_2CO_3. And this conclusion has been demonstrated by Duan et al. [16] and Aneggi et al. [19] as well.

Table 1 Structural characteristics of (x %) K-CeO_2 (x=0, 1, 2, 3, 4) catalysts and BET surface area (m^2/g) of the catalysts

Catalysts	Crystallite size (nm)	Lattice constant (nm) a	BET surface area (m^2/g)
Pure CeO_2	25.1	0.541	20.1
1%K-CeO_2	26.4	0.540	14.08
2%K-CeO_2	27.3	0.540	5.60
3%K-CeO_2	27.8	0.541	4.62
4%K-CeO_2	27.9	0.541	2.24

The reduction properties of different catalysts were examined by the H_2-TPR technique and the results are shown in Fig. 2. It is observed that there are essentially two main peaks in the TPR profiles of the five samples, indicating two main oxygen species in these materials. The first peak in the range of 450-650 ºC is attributed to the consumption of adsorption oxygen or surface lattice oxygen on the catalysts surface, and the second peak at >750 ºC is related to the reduction of the bulk lattice oxygen in catalysts [11, 14]. It is clear that addition of 1% K-CeO_2 slightly reduced the temperature of the first reduction peak, and the reduction temperature increased with increasing the content of K_2CO_3 until it increased to 4%. On the other hand, all the K_2CO_3-contained samples showed higher intensity for the second reduction peak than that of the pure CeO_2. These phenomena suggest that adding K_2CO_3 to ceria could improve the bulk reducibility of CeO_2, and only a moderate content of K_2CO_3 (e.g., 1% K-CeO_2) is beneficial to the surface reduction of CeO_2.

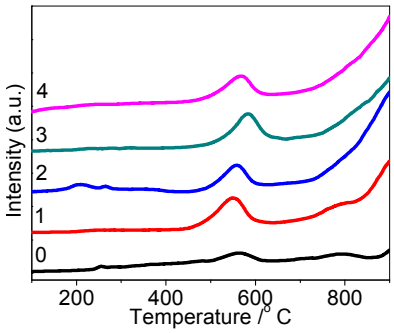

Fig. 2 H_2-TPR profiles of the (x %) K-CeO_2 (x=0, 1, 2, 3, 4) catalysts

2.2 Catalysts activity tests

The activity tests of catalysts were evaluated by methane isothermal reaction in a gas-solid reaction between methane mixed gas and catalysts at 800 ºC in Figure 3. It can find that the CH_4 conversions of 3%K-CeO_2 and 4%K-CeO_2 increase with the K content in Fig.3 (a), the order is 4>3>2≈0>1. The CH_4 conversion for all samples decrease with increasing the reaction time. We can observe the CH_4 conversion of all samples decrease quickly at the initial stage of reaction, it is due to the consumption of surface oxygen species on catalysts. While the CH_4 conversion of the 4%K-CeO_2 and 3%K-CeO_2 decrease slowly than pure CeO_2 after 15min. It indicates that the suitable K_2CO_3 content could affect the lattice oxygen release rate and contents in CeO_2, which is consistent with the H_2-TPR results.

The CO percentage molar concentration of 3%K-CeO_2 and 4%K-CeO_2 increase significantly than pure CeO_2, and the CO percentage molar concentration of all K_2CO_3-contained samples decrease with the increasing of reaction time. We can observe the CO percentage molar concentration of all samples increase quickly at the beginning of reaction, it is due to the consumption of surface oxygen species and the fast release of the bulk lattice oxygen. While the CO percentage molar concentration of K_2CO_3-contained samples decrease after 15min except pure 1%K-CeO_2 and CeO_2 decrease after 5min. It indicates that the more contents of K_2CO_3, the more surface oxygen species on the catalysts. Furthermore, the H_2 percentage molar concentration of K_2CO_3-contained samples decrease with increasing the contents of K_2CO_3 in Fig. 3(c). It is shown that adding K_2CO_3 to CeO_2 could influence the generation concentration of H_2, obviously.

These results indicate that adding K_2CO_3 to CeO_2 can promote the reducibility of catalysts, which is consistent with the result of H_2-TPR. And the suitable K content is conducive to improve the CH_4 conversion and the formation of CO. But it would result in the deep oxidation of H_2, the possibly reason of this phenomenon is that the supply electronic nature of K which inhibits the hydrogen atoms produced by cracked methane to spillover on the surface of catalysts [24], therefore, the hydrogen atoms were oxidized deeply and lead to the H_2 percentage molar concentration decrease for all K_2CO_3-contained samples.

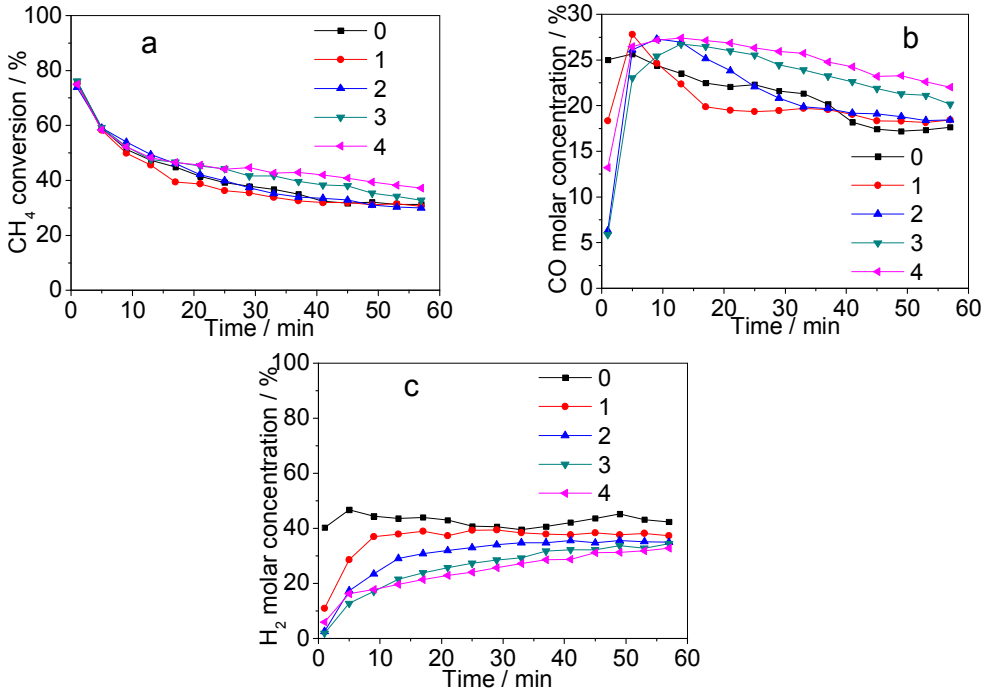

Fig. 3 The CH_4 conversion(a), CO percentage molar concentrations(b) and H_2 percentage molar concentrations(c) as a function of reaction time at 800 ºC over (x %) K-CeO_2 (x=0, 1, 2, 3, 4) catalysts

3 Conclusions

The pure CeO_2 and (x %) K-CeO_2 (x=1, 2, 3, 4) catalysts were prepared by the precipitation and incipient wetness impregnation methods, respectively. The K_2CO_3 was loaded on the surface of CeO_2. The XRD result showed that doping of K_2CO_3 could not significantly change the structure of CeO_2 with the addition of K_2CO_3, and no formation of Ce-K-O solid solution in these materials. The BET result displayed micropores of the CeO_2 might be plugged by potassium carbonate to a large extent and the surface areas of all K_2CO_3-contained samples were reduced. The isothermal reaction between methane and (x %) K-CeO_2 (x=0, 1, 2, 3, 4) catalysts were performed in a fixed-bed reactor. The results indicated that the suitable K content was conducive to increasing the CH_4 conversion and CO percentage molar concentration. This revealed that adding K_2CO_3 to CeO_2 could promote the reducibility of catalysts, which was consistent with the result of H_2-TPR.

Acknowledgements

Supported by the National Natural Science Foundation of China (51004060, 51104074, 51174105), and the Research Foundation for the Doctoral Program of Higher Education of China (20095314120005), Analysis and Test Foundation of Kunming University of Science and Technology (KUST).

References

[1] R. Boswell, Resource potential of methane hydrate coming into focus, J Pet Sci Eng. 56 (2007) 9–13.

[2] B.C. Enger, R. Lødeng, A. Holmen, A review of catalytic partial oxidation of methane to synthesis gas with emphasis on reaction mechanisms over transition metal catalysts, Applied Catalysis A: General. 346 (2008) 1-27.

[3] M. P. Kohn, M.J. Castaldi, R.J. Farrauto, Auto-thermal and dry reforming of landfill gas over a $Rh/\gamma Al_2O_3$ monolith catalyst, Applied Catalysis B: Environmental. 94 (2010) 125–133.
[4] A.T. Ashcroft, A.K. Cheetham, J.S. Foord, M.L.H. Green, C.P. Grey, A.J. Murrell, P.D.F. Vernon, Selective oxidation of methane to synthesis gas using transition metal catalysts, Nature. 344 (1990) 319-321.
[5] D.A. Hickman, L.D. Schmidt, Production of syngas by direct catalytic oxidation of methane. Science. 259 (1993) 343-346.
[6] Q. Miao, G.X. Xiong, S.S. Sheng, L.Cui, X.X. G, Partial oxidation of methane to syngas over nickel-based catalysts modified by alkali metal oxide and rare earth metal oxide, Applied Catalysis A. 154 (1997) 17-27.
[7] K. Otsuka, T. Ushiyama, L. Yamanaka, Partial oxidation of methane using the redox of cerium oxide, Chemistry Letter. 22 (1993) 1517-1520.
[8] F. Van Looij, J.C. Van Giezen, E.R. Stobbe, J.W.Geus, Mechanism of the partial oxidation of methane to synthesis gas on a silica-supported nickel catalyst, Catalysis Today. 21 (1994) 495-503.
[9] K. Otsuka, E. Sunada, T. Ushiyama, L. Yamanaka, The production of syngas by the redox of cerium oxide, Studies in Surface Science and Catalysis. 107 (1997) 531-536.
[10] K, Otsuka, Y. Wang, E. Sunada, I. Yamanaka, Direct partial oxidation of methane to syngas by cerium oxide, Journal of Catalysis. 175 (1998) 152-160.
[11] K.Z. Li, H. Wang, Y.G. Wei, D.X. Yan, Syngas production from methane and air via a redox process using Ce–Fe mixed oxides as oxygen carriers, Applied Catalysis B: Environmental. 97 (2010) 361–372.
[12] Y.G. Wei, H. Wang, K.Z.Li, Ce-Fe-O mixed oxide as oxygen carrier for the direct partial oxidation of methane to syngas, Journal of rare earths. 28 (2010) 560-565.
[13] M. Fathi, E. Bjorgum, T. Viig, O.A. Rokstad, Partial oxidation of methane to synthesis gas: Elimination of gas phase oxygen, Catalysis Today. 63 (2000) 489–497.
[14] K.Z. Li, H. Wang, Y.G. Wei, D.X. Yan, Direct conversion of methane to synthesis gas using lattice oxygen of CeO_2-Fe_2O_3 complex oxides, Chemical Engineering Journal. 156 (2010) 512–518.
[15] Y.H. Zhang, X.T. Zou, The catalytic activities and thermal stabilities of Li/Na/K carbonates for diesel soot oxidation, Catalysis Communications. 8 (2007) 760–764.
[16] W. Duan, J. Li, X.D. Wu, Z.C. Si, Modification of CeO_2-ZrO_2 catalyst by potassium for NO_x-assisted soot oxidation, Journal of Environmental Sciences. 23 (2011) 145–150.
[17] J. Liu, Z. Zhao, C.M. Xu, A.J. Duan, L. Zhu, X.Z. Wang, Diesel soot oxidation over supported vanadium oxide and K-promoted vanadium oxide catalysts, Applied Catalysis B: Environmental. 61 (2005) 36–46.
[18] M.S. Gross, M.A. Ulla, C.A. Querini, Catalytic oxidation of diesel soot: New characterization and kinetic evidence related to the reaction mechanism on K/CeO_2 catalyst, Applied Catalysis A: General. 360 (2009) 81–88.
[19] E. Aneggi, C. Leitenburg, G. Dolcetti, A. Trovarelli, Diesel soot combustion activity of ceria promoted with alkali metals, Catalysis Today. 136 (2008) 3–10.
[20] J. Matsunami, S. Yoshida, Y. Oku, Coal gasification with CO_2 in molten salt for solar thermal/chemical energy conversion, Energy. 25 (2000) 71– 79.
[21] J. Matsunami, S. Yoshida, Y. Oku, Coal gasification by CO_2 gas bubbling in molten salt for solar/fossil energy hybridization, Solar Energy. 68 (2000) 257– 261.
[22] F. He, H. Wang, Y.N. Dai, Thermodynamic analysis and experimental investigation into nonflame combustion technology (NFCT) with thermal cyclic carrier, Chemical Research in Chinese University. 20 (2004) 612– 616.
[23] X.Q. Ao, H. Wang, Y.G. Wei, K.Z. Li, M. Liu, Reduction behavior of methane in alkali molten carbonates, Journal of Fuel Chemistry and Technology. 36 (2008) 455-461.
[24] L.X. Shang, W.G. Xie, S.J. Lü, F.L. Qiu, Effect of alkali metal promoter on the properties of Ni/CaO-Al_2O_3 catalyst for reaction of methane with air, Journal of Natural Gas Chemistry. 10 (2001) 168-175.

doi:10.4028/www.scientific.net/AMM.161.200

Treatment of copper-containing acid mine drainage by neutralization-adsorption process using calcite as neutralizer and polyhydroxamic acid resin as adsorbent

Shuai Wang[a], Gang Zhao, Zhongnan Wang, Qian Zhang, Hong Zhong[b]

[1]College of Chemistry and Chemical Engineering, Central South University, Changsha 410083, China

[2]Key Laboratory of Resources Chemistry of Nonferrous Metals, Ministry of Education, Changsha 410083, China

[a]wangshuai_csu@163.com, [b]zhongh@mail.csu.edu.cn(corresponding author)

Keywords: acid mine drainage, neutralization, poly(hydroxamic acid) resin, adsorption

Abstract. Acid solution and copper-containing acid mine drainage (AMD) was treated by neutralization-adsorption process. The results showed that pH can be adjusted to 4.0 by adding $10g \cdot L^{-1}$ calcite in acid solution with pH=1.0. Adsorption and desorption performance of poly(hydroxamic acid) (PHA) resin for Cu^{2+} and Fe^{3+} ions were investigated by column tests. The results showed that adsorption capacities of PHA for Cu^{2+} and Fe^{3+} ions were satisfying, and the metals adsorbed on PHA can be eluted by sulfuric acid solution effectively. AMD of Dexing copper mine of Jiangxi was treated as a sample. The results showed that $1.5g \cdot L^{-1}$ calcite can remove almost all of the Fe^{3+} ion, and Cu^{2+} ion can be removed by PHA and then be eluted by sulfuric acid solution with adsorption ratio of 98.95% and elution ratio of 98.50%, separately.

Introduction

China is the biggest copper production and consumption country around the world. A large amount of copper containing acid mine drainage (AMD) emerges in the mining areas. If the drainage is discharged without being disposed, it will pollute the environment, threat human health and run off many valuable metals. The amount of copper containing AMD is very large, but the concentration of copper ion is low and concentrations of other ions are very high. Thus, common methods such as chemical sediment and extraction are not suitable for the treatment of AMD due to technology and economic reasons[1]. Ion exchange and adsorption method based on chelating resin is of advantages such as high adsorption capacity, high selectivity and easy operation, especially in the fields of separation and enrichment of metal ions of low concentration. There are hydroxyl and oximido groups in poly(hydroxamic acid) resin (PHA), and the double coordination groups can form chelating structures with transition metal ions, including Cu^{2+}, Fe^{3+}, Ni^{2+} and Co^{2+} ions[2-4]. In this paper, acid water was treated by calcite neutralization, copper was recovered using PHA, and AMD form Jiangxi Dexing Copper Mine was also treated by neutralization-adsorption process.

Experimental

Reagents and instruments. PHA was synthesized by the reaction of poly(methyl methacrylate-divinylbenzene) and hydroxylamine, and other reagents were of AR grade. Acid Cu^{2+} and Fe^{3+} solutions were prepared by $CuSO_4 \cdot 5H_2O$ and $Fe_2(SO_4)_3$ respectivelly. AMD was from Jiangxi Dexing Copper Mine.

Dymanic adsorption experiments were performed in ion exchange column(ϕ1cm, 50 ml). Concentrations of Cu^{2+} and Fe^{3+} were measured by 722S ultraviolet-visible spectrophotometer, and other metal ions were measured by WYX-9003 atomic adsorbtion spectrophotometer.

Neutralization experiments. Calcite was added into acid solution or AMD with agitation. The concentrations of Cu^{2+} and Fe^{3+} in solution were measured when pH kept constant.

Adsorption experiments. PHA was put into ion exchange column, and the height of resin was 3cm. PHA was converted to sodium form by adding 0.01mol·L^{-1} sodium hydroxide solution. Then PHA was washed by distilled water until pH of the effluent was about 7. Acid solution or AMD was added to the column at a certain flow rate, and the concentration of metal ions in the effluent was measured. The adsorption capacity and the adsorption rate of PHA for metal ions were calculated by Equation 1~4[5, 6].

$$q_{\mathrm{B}} = \int_0^{V_B} (c_0 - c)dV \tag{1}$$

$$q_{\mathrm{E}} = \int_0^{V_E} (c_0 - c)dV \tag{2}$$

$$E_{\mathrm{B}} = \frac{q_B}{c_0 V} \times 100\ \% \tag{3}$$

$$E_{\mathrm{E}} = \frac{q_E}{c_0 V} \times 100\ \% \tag{4}$$

Where q is the adsorption capacity, E is the adsorption rate, c is the concentration of Cu^{2+} in solution, and V is volume of the solution. The subscripts means: 0, the initial time; B, the breakthrough point; E, the equilibrium point. The concentrations of Cu^{2+} at breakthrough point and equilibrium point were defined as c_B=0.1c_0 and c_E=0.95c_0 in this paper.

The movement speed and width of adsorption band were calculated by Equation 5 and 6[5, 7].

$$V_{\mathrm{a}} = \frac{u_0 c_0}{\rho_{\mathrm{b}} M q_0} \tag{5}$$

$$Z_{\mathrm{a}} = V_{\mathrm{a}}(t_{\mathrm{E}} - t_{\mathrm{B}}) \tag{6}$$

Where V_{a} is the movement speed of adsorption band, Z_{a} is the width of adsorption band, u_0 is the solution superficial velocity, ρ_{b} is the density of dry resin, M is the molar mass of metal ions, t_{B} is the breakthrough time and t_{E} is the equilibrium time, and q_0 is the static adsorption capacity of resin when equilibrium concentration is c_0, and calculated by Langmuir adsorption isotherm[5].

After adsorption, PHA was eluted by sulfuric acid solution. The desorption rate R_{w} was calculated by Equation 7.

$$R_{\mathrm{w}} = \frac{\text{quantity of metal ion in elutriant}}{\text{quantity of metal ion adsorpted on PHA}} \times 100\ \% \tag{7}$$

Neutralization experiments

The concentrations of metal ions, pH, valence of metals(n) and K_{sp} of metal hydroxides are accord with the following equation.

$$\lg c = \lg K_{\mathrm{sp}} + n(14 - \mathrm{pH}) \tag{8}$$

At 30°C, K_{sp} of $Cu(OH)_2$ and $Fe(OH)_3$ were 1.0×10^{-20} and 4.0×10^{-38}, respectively. Being calculated by Equation 8, complete deposition pH of Fe^{3+} is 3.3 and that of Cu^{2+} was 5.67.

Calcites with particle radius -100 meshes were put into 200ml sulfuric acid water with pH 1.0. The results were shown in Fig. 1. pH raised to 4.0 in 100 minutes when the dosage of calcite was 2.0g. That is to say, 10g·L^{-1} calcite is needed to neutralize the acid water with pH=1.0.

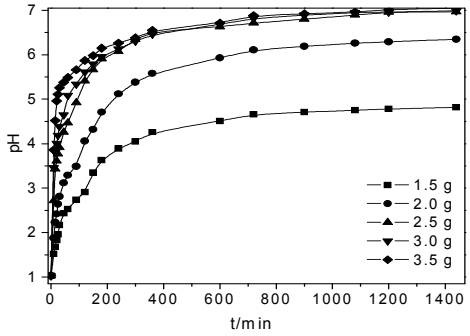

Fig. 1 The results of neutralization of acid water

Adsorption and desorption experiments

Effect of flow rate on breakthrough curve. Column tests were performed under the following conditions: temperature 30°C, initial concentration of Cu^{2+} 200mg·L^{-1}. Breakthrough curves were shown in Fig. 2, parameters calculated according to Fig. 2 were listed in Table 1. It can be seen that the breakthrough and equilibrium points came earlier at higher flow rates, the adsorption bands moved faster and the widths of adsorption bands became narrower when the flow rates increased.

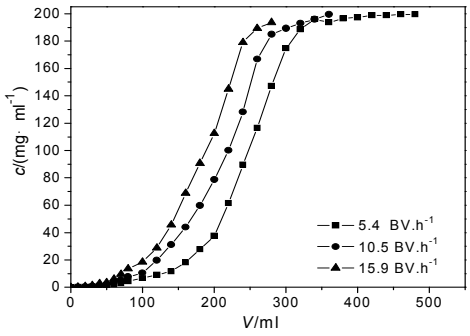

Fig. 2 Effect of flow rate on breakthrough curve of acid water

Table 1 Parameters of breakthrough curves at various flow rates

Flow Rate /(BV·h^{-1})	Static Equilibrium	Breakthrough			Dynamic Equilibrium			Mass Transfer Zone	
	q_0/ (mmol·g^{-1})	t_B/ min	q_B/ (mmol·g^{-1})	E_B /%	t_E /min	q_E/ (mmol·g^{-1})	E_E/ %	$V_a\times10^4$/ (cm·min^{-1})	Z_a/ cm
5.4	1.858	49.33	0.305	99.9	383.7	1.746	74.34	4.589	0.154
10.5	1.858	21.09	0.253	99.9	184.6	1.506	69.08	8.907	0.146
15.9	1.858	9.260	0.168	99.9	106.1	1.310	67.69	13.496	0.131

Effect of initial concentration on breakthrough curve. Effect of initial concentration of Cu^{2+} ions on breakthrough curve was investigated under the following conditions: temperature 30°C, flow rate 5.4BV·h^{-1}. Breakthrough curves were shown in Fig. 3, and parameters calculated according to Fig. 3 were listed in Table 2. It can be seen that the breakthrough points and the equilibrium points came earlier at higher concentrations, and the adsorption bands moved faster, but the width of adsorption bands became wider when the flow concentrations increased.

Desorption experiments. Column adsorption were first performed under the following conditions: initial concentration of Cu^{2+} ion 200mg·L^{-1}, temperature 30°C, flow rate 5.4BV·h^{-1}. Then the resin was eluted by 20 ml H_2SO_4 at 30°C. The results were shown in Fig. 4. It can be seen that when the flow rates were 5.4 BV·h^{-1}, the desorption efficiencies were above 98.0%.

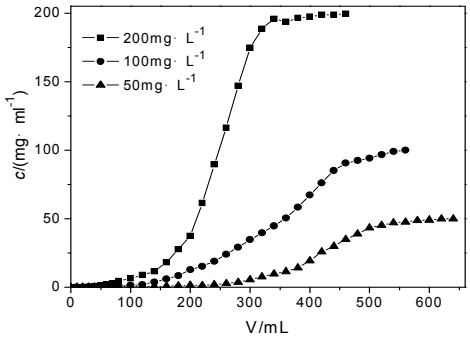

Fig. 3 Effect of initial concentration on breakthrough curve

Table 2 Parameters of breakthrough curves at various initial concentrations

Initial concentration /(mg·L^{-1})	Static Equilibrium	Breakthrough			Dynamic Equilibrium			Mass Transfer Zone	
	q_0/ (mmol·g^{-1})	t_B/ min	q_B/ (mmol·g^{-1})	E_B/%	t_E/ min	q_E/ (mmol·g^{-1})	E_E/ %	$V_a\times10^4$/ (cm·min^{-1})	Z_a/ cm
50	0.843	198.34	0.284	99.9	659.2	0.743	70.35	2.529	0.118
100	1.42	94.86	0.293	99.9	577.7	1.229	72.85	3.003	0.141
200	1.858	49.33	0.305	99.9	383.8	1.746	74.34	4.589	0.154

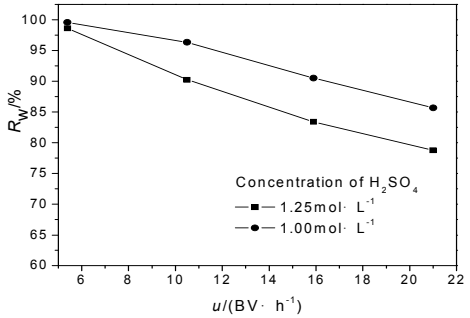

Fig. 4 Effect of eluent flow rate on desorption rate

Treatment of AMD

Neutralization of AMD

AMD from Jiangxi Dexing Copper Mine was used in neutralization-adsorption experiments. Its pH was equal to 2.21, concentrations of Cu^{2+} and Fe^{3+} ions were 58.76 and 336mg·L^{-1}, separately.

pH and concentration of Cu^{2+} ion was measured after 0.3g or 0.4g calcite was put into 200ml AMD, respectively. The results were shown in Fig. 5. pH increased to 4.0 in 40min, the concentrations of Fe^{3+} were about 0 and the concentrations of Cu^{2+} were about 56mg·L^{-1}.

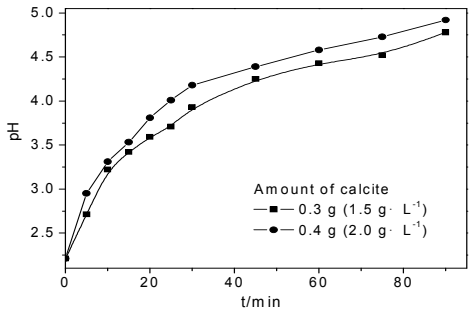

Fig. 5 Neutralization results of AMD

Adsorption experiments of AMD. Three copies of 200ml AMD was neutralized by 0.3g calcites individually until their pH reached 4.5. Then the solutions were added to column with height of 3cm at three different flow rates. The result was listed in Table 3. When the flow rate was 5.4 $BV \cdot h^{-1}$, the adsorption rate of Cu^{2+} can reach 98.95%.

Table 3 The results of adsorption experiments of AMD

Flow Rate/ ($BV \cdot h^{-1}$)	Concentration of Effluent	pH of Effluent	Adsorption rate/%	Adsorption Capacity	Utilization ratio of PHA/%
5.4	0.59	6.33	98.95	0.456	54.10
10.5	1.96	6.25	96.48	0.445	52.79
15.9	4.76	6.07	91.51	0.421	50.01

Desorption experiments of AMD. 1$mol \cdot L^{-1}$ H_2SO_4 solution was used to wash the PHA resin after adsorption at the flow rate 5.4$BV \cdot h^{-1}$. The results were listed in Table 4. When the dosage of sulfuric acid was 20 ml, recovery efficiency was 92.85%, and enrichment ratio reached 9.85.

Table 4 The results of desorption experiments of AMD

Volume/ml	Desorption Quantity/mg	Desorption rate/%	Recovery rate/%	Enrichment ratio
10	9.830	88.20	83.13	17.64
20	10.98	98.50	92.85	9.85

Conclusion

Acid water and AMD were treated by neutralization-adsorption process, and the result shown that calcite was an effective neutralizer and PHA was an effective adsorbent. Fe^{3+} ions in AMD can be removed completely by 1.5$g \cdot L^{-1}$ calcites. The adsorption and desorption rate of Cu^{2+} reached 98.95% and 98.50%, and enrichment ratio reached 9.85.

Acknowledgements

This work was financially supported by the Science and Technology Major Project of Hunan Province(No. 2010FJ1011), the Doctoral Fund of Ministry of Education of China (No. 20100162120028), the Natural Science Foundation of Hunan Province (No. 11JJ6014), and the Freedom Explore Program of Central South University (No. 201012200145).

References

[1] R. K. Sharma and Parul Pant, Journal of Hazardous Materials, 163(2009)295-301.
[2] M. R. Lutfor, S. Sidik, W. M. Z. Wan Yunus, M. Z. A. Rahman, A. Mansor and M. J. Haron, Journal of Applied Polymer Science, 79(2001)1256-1264.
[3] F. A. Alakhras, K. A. Dari and M. S. Mubarak, Journal of Applied Polymer Science, 97(2005)691-696.
[4] G. A. Skarja, A. L. Brown, R. K. Ho, M. H. May and M. V. Sefton, Biomaterials, 30(2009)1890-1897.
[5] Shuai Wang, Synthesis of polymeric ester thiourea resin and its adsorption and separation properties for noble metal ions, Dissertation, Central South University, 2008.(in Chinese)
[6] A. S. Michaels, Industrial and Engineering Chemistry, 44(1952)1922-1930.
[7] Jingjun Chen, Research on Adsorption of Arsenic(Ⅴ) by Fe(Ⅲ)-loaded Chelating Resin, Dissertation, Nanchang University, 2005. (in Chinese)

doi:10.4028/www.scientific.net/AMM.161.205

Numerical Simulation of the Curing and Cooling in Reaction Injection Molding Process of Nylon 6

DENG Xin[1, a], LI Du-xin[2, b], CHEN Jian-shan[1, c] and YANG Su-wen[1, d]

[1]School of Materials Science and Engineering, Central South University of Forestry and Technology, Changsha 410004, PR China

[2]State Key Laboratory of Powder Metallurgy, Central South University, Changsha 410083, PR China;

[a]dengxin81@yahoo.cn, [b]liduxinp@yahoo.com(corresponding author), [c]cjs20044219@126.com, [d]yangsuwen05@163.com

Keywords: Reaction injection molding; Curing; Cooling; MATLAB software; Numerical simulation.

Abstract. A computer simulation model was established to analyze the curing and cooling of reaction injection molding process of nylon 6 based on theory of balance equation of energy, reaction kinetics and crystallization kinetics. The reasonable assumptions and simplifications were introduced in the model, and an explicit finite difference method with MATLAB software was applied to calculate and predict the conversion and temperature distribution within a plate type mold. The results show that the center position reaches the peak temperature about 45s. The effects of the feed temperature, wall temperature, and reaction rate constant on the temperature and conversion were discussed for searching the optimum processing conditions. The results suggests that the effect of reactive rate on crystallization, molecular weight and phase structure is decided by the value of reaction constant; the influence of the mold wall temperature on reactive rate and temperature near the boundary was great; and the control of feed temperature is important in condition of low mold temperature.

Introduction

Reaction injection molding (RIM) [1-2] is polymerization and processing in a single cyclic operation. Two accurately metered streams of prepolymers or monomers fluid are mixed by impingement and the reactive mixture flowed into a heated mold cavity. A series of chemical reactions occurs during the mold curing stage. The rigid part is then attained. RIM process has many characteristics, including high mixing efficiency, good fluidity, flexible formulation of raw materials, high production efficiency, low energy consumption excellent performance, wide adaptation and so on. The process was firstly used in polyurethane processing. Optimization of process parameters and compute simulation of RIM were studied on many materials including polyurethane [3-5], epoxy [6] and unsaturated polyester [7] by many researchers. RIM-nylon 6 material was developed in the 1980s, which has several unique properties, such as good heat resistance, oil resistance, chemical resistance, excellent mechanical properties, wear resistance, non-toxic, pollution-free [8]. However, the development of research on RIM-nylon 6 is slow because of the complexity of numerical simulation of the crystallization process occurred in nylon 6 polymerization process. The impact of crystallization on the curing process in the RIM-nylon 6 system was discussed in this paper. And the mathematical models of time on conversion and temperature in the system were modelled with finite difference method in MATLAB. The effect of process conditions on the system temperature and conversion was analyzed. The qualitative and quantitative information about the technological aspects provided in this paper has instructive significance on the optimization of process parameters.

Computer Simulation

Modeling Hypotheses.

Nylon 6 was synthesized in a tablet-like cavity (length=60mm, width=60mm, height<<60mm) by RIM process. The change of temperature and conversion in the direction of height was ignored in this system. So the reactive process in the cavity is two-dimensional, non-steady-state, heat transfer process with internal heat source.

β_0 is conversion in the initial time, T_0 is initial temperature, T_w is mold temperature.

The following hypotheses are assumed for this model:

(1) Density, thermal conductivity and heat capacity are constant;

(2) Compared with the concentration changes of the functional groups caused by the chemical reaction, the concentration changes of the polymer molecules functional groups caused by the diffusion can be neglected;

(3) The cavity filling time is very short, material in the system does not flow, that means the flow velocity is zero, after the cavity filling is sufficient and complete, curing reaction begins;

(4) At the initial time of reaction, reaction system mixed well;

(5) The non-isothermal crystallization kinetics equation of RIM-nylon 6 system was proposed by Malkin et.al [8].

$$\frac{d\alpha}{dt} = A\exp\left[-\frac{E_D}{RT}\right]\cdot\exp\left[-\frac{\psi T_m^0}{T(T_m^0 - T)}\right]\alpha^{2/3}(\alpha_{eq} - \alpha) \tag{1}$$

Where,E_D=3.18/(1.64-β)+3.25β+3.28(*Kcal/mole*), $\Psi=E_D(T_m{}^0-T_k)^2/[RT_m{}^0(2T_k-T_m{}^0)]$, A=8.33×10^6(*s*), $T_m{}^0$ is the equilibrium melting point of nylon 6 (232°C), T_k is the temperature of maximum crystallization rate (T_k= 87.8β +51.2).

The coefficients are very complex in equation (1) and the values of E_D and Ψ depend on the type and concentration of activator. Therefore, the coefficient of the equation can not be used for modelling. The Avrami equation is usually used to express the non-isothermal crystallization process of RIM-nylon 6 system. Therefore, the temperature change expression caused by crystallization is:

$$(\Delta T)_c = \frac{\Delta H_c}{C_p}\cdot\beta\cdot X_e\cdot\left\{1-\exp\left[-K\left(t-\theta\right)^{n_c}\right]\right\} \tag{2}$$

Where ΔHc is the crystallization heat, Xe is the maximum crystallization, β is the conversion, K is the crystallization rate constant, θ is the crystallization induction time .

The effect of different activators in reaction on the value of (ΔT)c was studied by KAP JIN KIM et al [9]. The result shows that polymerization-induced crystallization process occurs when the polymerization is complete because polymerization rate is fast. And when the polymerization temperature is greater than or equal to 150°C, temperature changes in the system caused by the crystallization heat can be ignored.

Therefore, reaction temperature or mold temperature is set to greater than or equal to 150 °C to simplify the calculation in the numerical simulation during the curing reaction. So the effect of crystallization in the curing process on the temperature in the system is ignored.

(6) the curing reaction begins from the end moment of filling.

Modeling.

(1) The reactive kinetics expression in RIM-nylon 6 system is given by K. H. Lee and S. C. Kim [10]:

$$\frac{d\beta}{dt} = k_0\exp(-\frac{E}{RT})(1-\beta)^n(1+B_0\beta) \tag{3}$$

Where $E = 1.58 \times 104 cal/mole$, $n = 1$, $B_0 = 6.2$, β is the conversion, k_0 is the reaction rate constant, E is the activation energy, R is the gas constant, T is temperature, n is the reaction order in equation (3).

(2) Under above hypotheses, RIM process is a two-dimensional, non-steady-state, heat transfer process with internal heat source. So the heat conduction equation is deduced according to the law of conservation of energy.

$$\frac{\partial T}{\partial t} = \frac{k}{\rho \cdot C_p}\left(\frac{\partial^2 T}{\partial x^2} + \frac{\partial^2 T}{\partial y^2}\right) + \frac{Hr}{\rho \cdot C_p} \cdot \frac{\partial \beta}{\partial t} \tag{4}$$

Where k is the thermal conductivity($cal/(cm{\cdot}s{\cdot}K)$), ρ is the density(g/cm^3), C_p is the specific heat($cal/(g{\cdot}K)$), Hr is the heat of reaction(cal/g), x is the space variable(cm) in equation (4).

Equation (3) and (4) can be discretized using the finite difference method, and set Δx=0.0241cm, Δt=0.2s to fulfill $\alpha \cdot \Delta t/(\Delta x)2=1/4$, where $\alpha = k/(\rho \cdot C\rho)$. So the node equation is simplified:

$$T_{i,j}^{\ p+1} = \frac{1}{4}(T_{i+1,j}^{\ p} + T_{i-1,j}^{\ p} + T_{i,j+1}^{\ p} + T_{i,j-1}^{\ p}) + \frac{Hr}{\rho \cdot C_p}(\beta_{i,j}^{\ p+1} - \beta_{i,j}^{\ p}) \tag{5}$$

(3) Initial and boundary conditions

Initial conditions: $t = 0$, $T = T_0$, $\beta = 0$. The node equation in the boundary is derived by heat balance method of infinitesimal volume. Equation (6) and (7) are node equation of left boundary and right boundary respectively.

$$T_{i,j}^{\ p+1} = \left[2T_{i+1,j}^{\ p} + T_{i,j+1}^{\ p} + T_{i,j-1}^{\ p} + \frac{2a \cdot \Delta x \cdot Tw}{\lambda} + \frac{2Hr}{\rho \cdot C_p \cdot \lambda}(\beta_{i,j}^{\ p+1} - \beta_{i,j}^{\ p})\right] / 2(2 + \frac{a \cdot \Delta x}{\lambda}) \tag{6}$$

$$T_{i,j}^{\ p+1} = \left[2T_{i-1,j}^{\ p} + T_{i,j+1}^{\ p} + T_{i,j-1}^{\ p} + \frac{2a \cdot \Delta x \cdot Tw}{\lambda} + \frac{2Hr}{\rho \cdot C_p \cdot \lambda}(\beta_{i,j}^{\ p+1} - \beta_{i,j}^{\ p})\right] / 2(2 + \frac{a \cdot \Delta x}{\lambda}) \tag{7}$$

The node equations in other boundary are exported using the same heat balance method of infinitesimal volume.

Where, a is the heat transfer coefficient between solid interior and surface; λ is the thermal conductivity; T_w is the mold temperature.

(4)The basic parameters for the numerical simulation in RIM-nylon 6 system are shown in Table 1.

Table.1 Base conditions for the RIM-nylon 6 simulation [11]-[14]

Parameters	Values
Reaction rate constant [k_0]	$1.0\times10^6/0.5\times10^6/2.0\times10^6$
Heat of reaction [Hr, cal/g]	33.0
Thermal conductivity [k, $cal/(cm{\cdot}s{\cdot}K)$]	0.00055
Density [ρ, g/cm^3]	1.13
Specific heat [C_p, $cal/(g{\cdot}K)$]	0.67
Filling temperature [T_0, °C]	120/130/140
Molding temperature [T_w, °C]	150/160/170

Results and Discussion of Simulation

The curing and cooling process of RIM system were simulated using the finite difference method in MATLAB simulation software according to the mold cavity and the boundary node equations. And the changes of temperature and conversion at different locations of the cavity were obtained.

Fig.1(a) shows temperature with time(calculation cycles) in the mold at five positions on Y direction. The cavity temperature continues to rise, and exceed the mold temperature, with occurrence of the curing reaction. The rising of temperature at the center of the cavity is fast. And the temperature at the center is higher than at the boundary, reaches the peak temperature about 45 seconds, which is because of poor thermal conductivity of nylon 6 material and slow heat transfer to the outside. Fig.1(b) shows conversion with time(calculation cycles) in the mold at five positions on Y direction. The reaction rate near mold boundary is fast at initial reaction moment because of the high temperature of the mold wall. The temperature at the center position rises about 40 seconds with acceleration of reaction rate.

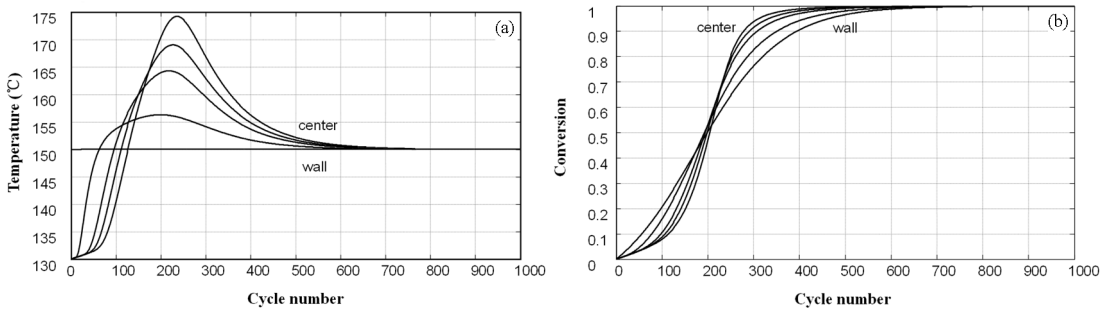

Center-wall: (30, 30), (35, 30), (40, 30), (50, 30), (60, 30)

Fig.1 Temperature (a) and conversion (b) with time(calculation cycles) in the mold at six positions on Y direction

Fig.2 and Fig.3 show the systemic temperature profile and the conversion profile with the mold temperature 150°C, feed temperature 130°C, at different time (20s, 40s, 60s, 80s, 100s, 120s). It can be seen from Fig.2 that the heat transfer to the outside of the system slowly because of the low thermal conductivity, which causes the temperature near the center is higher than the boundary; as time goes on, the system temperature decreases, and finally, keep the system temperature same with with the mold. It can be seen from Fig.3 that at initial reaction moment, the reaction rate near the mold wall is higher than that of the center; as time goes on, the conversion near the center is higher than near the boundary, and finally, the degree of the reaction of the whole system reaches 100 %.

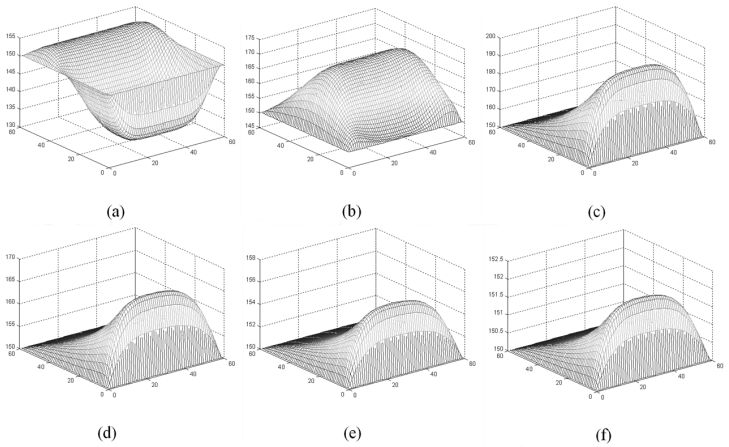

(a)—20s (b)—40s (c)—60s (d)—80s (e)—100s (f)—120s

Fig.2 Temperature distribution at different time

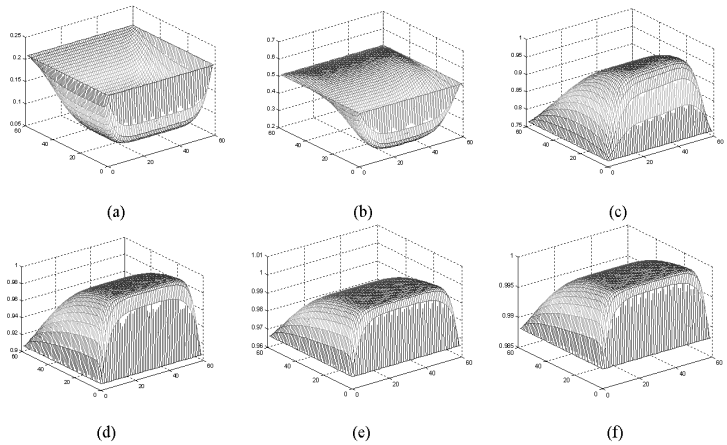

(a)—20s (b)—40s (c)—60s (d)—80s (e)—100s (f)—120s

Fig.3 Conversion distribution at different time

Optimization of process parameters.

Mold Temperature.

Fig.4 shows the effect of the mold temperature on the temperature and conversion at center position respectively. It can be seen from Fig.4, the higher the mold temperature, the faster the reaction rate, but lower product's molecular weight , and make the system temperature increase, even close to the melting temperature and thus affect the product quality. While the lower mold temperature will lead to slow reaction rate, extend the processing period. Therefore, it is necessary to choose the right mold temperature to get a fast reaction rate and high quality product .

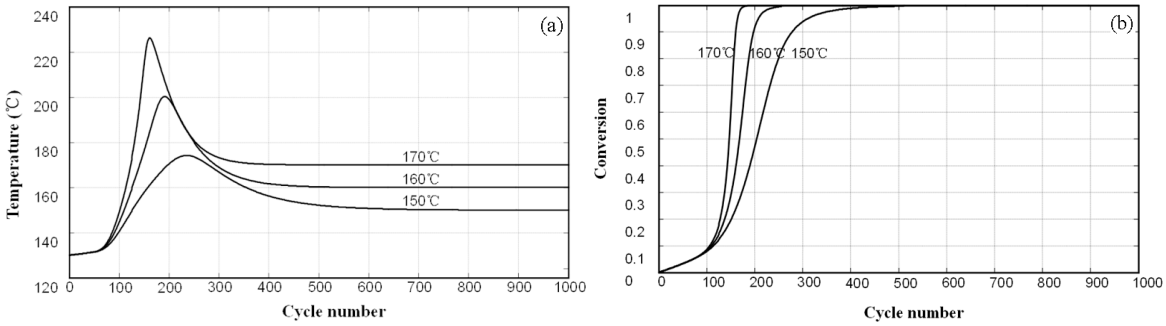

Fig.4 Effect of the wall temperature on temperature(a) and conversion(b) at center position

Reaction Rate Constant.

Fig.5 shows the effect of the reaction rate constant on temperature and conversion at center position respectively. The higher the reaction rate constant, the faster the polymerization reaction, the faster the temperature rises, leading to earlier crystallization of the polymer, and thus affect the quality.

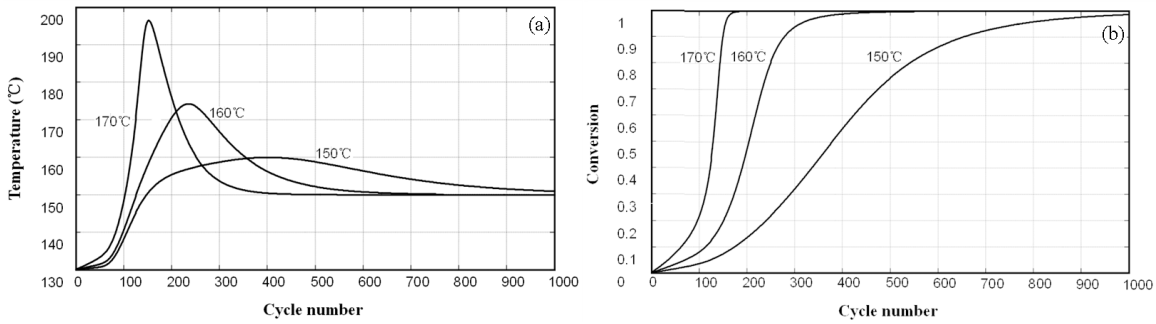

Fig.5 Effect of the reaction constant on temperature(a) and conversion(b) at center position

Feed Temperature.

Fig.6 shows the effect of the feed temperature on temperature and conversion at the center position respectively. Feeding at different temperatures leads to different reaction kinetics, which will cause a big difference in conversion and temperature. High feed temperature lead to rapid reaction and exothermic, the temperature rises fast, high-temperature region increases, and the maximum temperature rises. With high mold temperature, the heat conduction of mold wall increases the reaction rate, so the impact of feed temperature on the maximum temperature is relatively low. With low mold temperature, the minimum conversion will appear near the mold wall, so the impact of the reaction material temperature on the curing time is little.

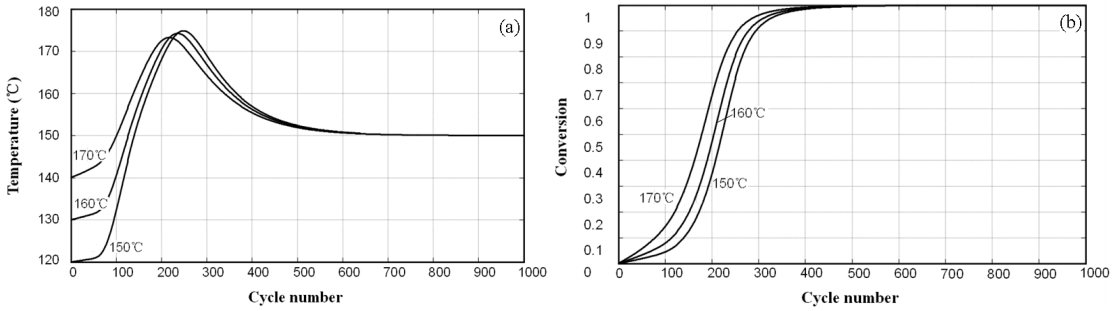

Fig.6 Effect of the feed temperature on temperature(a) and conversion(b) at center position.

Summary

RIM-nylon 6 system curing and cooling process was simulated, the results show that when the curing time passes about 45s, the temperature reaches the peak, the reaction rate accelerates, then the reaction tends to complete, the system temperature began to decline. Furthermore, investigation shows that 100% conversion will cost 100s, which is similar to the time of practical experience. Investigation of the impact of the reaction rate constant, the mold temperature and the feed temperature on the system temperature and the conversion shows that the the reaction rate constant impact is the greatest, it determines the reaction rate, affects the system crystallization, molecular weight, phase structure and so on, thus affects the product quality. Mold temperature has larger impact on the reaction rate and conversion near the cavity boundary, high mold temperature accelerates the reaction rate near the boundary, increases the temperature, but has little effect on the center. The feed temperature has impact on the system highest temperature and conversion, especially at low mold temperature, the control of feed temperature is very important.

Acknowledgements

This work was financially supported by Open Foundation of State Key laboratory of Powder Metallurgy, Central South University and Science Research Project of Central South University of Forestry and Technology (104-0165).

References

[1] L. T. Manztone, J. S. Osinski, Moldability studies in reactive polymer processing, Polym. Eng. Sci., 23 (1983) 576-585.
[2] M. M. Reboredo, A. J. Rojas, Molding by reactive injection of reinforced plastics. Polym. Eng. Sci., 28 (1988) 485-490.
[3] Dongjin Seo, Jae Ryoun Youn, Numerical analysis on reaction injection molding of polyurethane foam by using a finite volume method, Polym., 46 (2005) 6482-6493.
[4] Haberstroh E., Kleba I., Bladder reaction injection molding: Manufacturing of hollow polyurethane foam parts using flexible mold cores, J. Polym. Eng., 21 (2011) 147-165.
[5] Kim Dae Su, Macosko Christopher W., Reaction injection molding process of glass fiber reinforced polyurethane composites, Polym. Eng. Sci., 40 (2000) 2205-2216.
[6] J. M. Castro, C. W. Macosko. Studies of mold filling and curing in the reaction injection molding process, AIChE. J., 28 (1982) 250-260.
[7] J. Mohammad, M. Mohammad, E. Mohammad Reza, H. Naseh, Numerical investigation of curing process in reaction injection molding of rubber for quality improvements, Key Eng. Mater., 462-463 (2011) 1206-1211.
[8] KohanMI, Nylon plastics handbook, Hanser Publishers, Munich, 1995.
[9] A. Y. Malkin, V. P. Beghishev, I. A. Keapin, S. A. Bolgov, General treatment of polymer crystallization kinetics-part 1. A new macrokinetic equation and its experimental verfication, Polym. Eng. Sci., 24 (1984) 1396-1401.
[10] K. J. Kim, Y. Y. Kim, B. S. Yoon, Mechanism and kinetics of adiabatic anionic polymerization of ε-caprolactam in the presence of various activators, J. Appl. Polym. Sci., 57 (1995) 1347-1358.
[11] K. H. Lee, S. C. Kim, Reaction-induced crystallization kinetics during the anionic polymerization of ε-caprolactam, Polym. Eng. Sci., 28 (1988) 13-19.
[12] K. H. Lee, S. C. Kim, Engineering Analysis of reaction injection molding process of nylon 6, Polym. Eng. Sci.,28 (1988) 477-484.
[13] J. K. Kocsis, L. Kiss. Attempts of separation of the polymerization and crystallization processes by means of DSC thermograms of activated anionic polymerization of ε-caprolactam, Makromol. Chem.,180 (1979) 1593-1597.
[14] H. K. Reimschuessel, Nylon 6, chemistry and mechanisms, J. Polym. Sci.: Macromol. Rev., 12 (1977) 65-139.

doi:10.4028/www.scientific.net/AMM.161.212

Application Mechanism and Performance of Cationic Native starch and Cationic Hydrolyzed Starch in Salt-free Dyeing of Reactive Dyes

Wei Ma, Mei Meng, Shufen Zhang*, Benzhi Ju, Min Zhang

State Key Laboratory of Fine Chemicals, Dalian University of Technology, Dalian, 116023, P.R.China.

Email: weima@dlut.edu.en

Keywords: Cationic hydrolyzed starch; cationic native starch; salt-free dyeing; reactive dyes

Abstract. Cationic native starch (CNS) and cationic hydrolyzed starch (CHS) were investigated in physical modification of cotton to realize salt-free dyeing of reactive dyes and their application properties were compared. Adsorption isotherm studies of C.I. Reactive Red 2 on the modified cotton presented the dyeing followed Langmuir-type model. The dyeing properties of the fibers modified with CNS and CHS were investigated and compared. The results showed the dye fixation and fastness properties of both C.I. Reactive Red 2 and C.I. Reactive Blue 19 on CNS modified cotton were inferior to that on the untreated and CHS modified ones.

1.Introduction

Dyeing cotton with reactive dyes employs a large amount of salt (30-100g/L) to promote dyeing, which leads to serious environmental pollution when dyeing effluents containing tremendous salt is released. To avoid addition of salt, many cationic compounds were synthesized and used for modification of cotton to increase the affinity between cotton and reactive dyes. However, most compounds themselves are not eco-friendly [1-4]. In the paper, much biocompatible modification agent—cationic starch (CS) was applied for cotton. CS, as derivative of eco-friendly biomass—starch, has been intensively studied in recent years for taking the place of some synthetic cationic agents [5-7]. Compared with cationic native starch (CNS), cationic hydrolyzed starch (CHS) has much lower molecular weight and viscosity in aqueous solution. In our previous papers, cotton modified with CNS was reported to be used in continuous dyeing of reactive dyes [8]. In this paper, the cotton fibers modified with CNS and CHS were applied in exhaust dyeing process, since in the process, environmental pollution due to salt addition was especially serious.

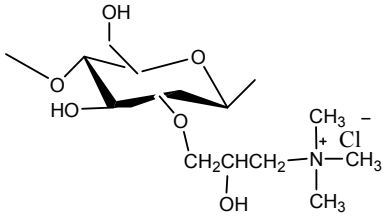

Fig. 1. Sketch figure of cationic starch

The purpose of this paper is to report the dyeing mechanism of the CS modified cotton and to compare the dyeing properties among the untreated, CNS and CHS modified cotton fibers.

2.Experimental

2.1 Materials

In the study, CNS and CHS were synthesized according to the literatures[8,9].100% cotton (150 g/m^2), bleached, desized and mercerized, was purchased from Testfabrics, Inc., Shanghai. C.I. Reactive Red 2 and C.I. Reactive Blue 19 (their structures were listed in Fig.1) were obtained from Shanghai Dyestuff Co. and were used as received. The other reagents and solvents were analytical pure.

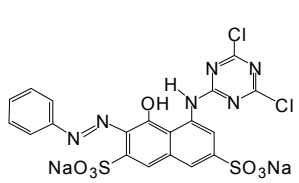

C.I. Reactive Red 2 (MW = 615 Da)

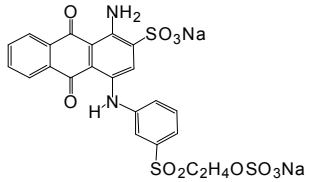

C.I. Reactive Blue 19 (MW = 626 Da)

Fig.2. Structures of the dyes applied

2.2 Pretreatment

Dip-pad-bake procedure was applied in pretreatment. Cotton fabrics were dipped in certain concentration (0.1%-2.5%) of CNS or CHS for 3min under neutral conditions at room temperature, and then it was taken out and padded on mangle. The pressure on the mangle was adjusted to give 80% wet pickup. The samples were pre-dried at room temperature, and then baked at 100℃ for 10min in a Rapid baker. The treated fabrics were ready for dyeing.

2.3 Dyeing procedure

All dyeings were carried out using a liquor ratio of 20:1. Dyeing of cationic hydrolyzed starch treated cotton commenced at 20℃, and kept at this temperature for 30 min. Fixation temperature was chosen according to the recommended fixation temperature in the conventional dyeing. Fixation proceeded for 40 min and 10 g/L sodium carbonate was used for dye fixation. Conventional dyeing on the untreated cotton followed the procedure recommended by the dye manufacturer in the presence of anhydrous sodium sulphate (60 g/L), and 10 g/L of sodium carbonate was added for dye fixation.

After dyeing, the cotton fabric was removed from the bath and rinsed thoroughly in cold, hot then cold water. Then the dyed fabric was subjected to boiling in a solution containing 2 g/L anionic detergent LS (Shanghai) for 15 min and then rinsed and allowed to air dry.

2.4 Measurements

The dye fixation F was determined using HP 8453 UV-vis spectrophotometer as in Equation 1.

$$F= (A_0-A_1-A_2)/A_0\times 100\% \quad (1)$$

A_0-absorbance of the initial dyebath
A_1-absorbance of the dyebath after the dyeing process
A_2-absorbance of the soap bath after the soaping process

It should be specialized that all the absorbance was got under the same volume of the liquor.

2.5 Fastness properties

Wash fastness of the dyed cotton was tested according to ISO 105-B01:1994 using S-1002 two bath dyeing and testing apparatus (Roaches Co., UK). Rub fastness was tested according to ISO 105-X12:1993 using Y(B)571-II crockmeter.

2.6 Microscopic analysis and zeta potential measurements

Cross-sections of dyed cotton with the thickness of 1μm were made by LKB-V ultramicrotome (Sweden). 800 times magnified images of the cross-sections were obtained on BX51 light-microscopy (Olympus, Japan).

The cotton fibers were treated with 2.0% CHS (degree of substitution is 0.7) as described in Pretreatment section, the untreated and the treated cotton fibres were cut to approximately 1 mm length. 0.05% solids were prepared in 0.0010 M KCl at various pH and stirred for 20 min. Then the zeta potentials were measured using ZETAPLUSZETA Zeta Potential Analyzer (Brookhaven Instruments Corporation, USA).

3. Results and Discussion

3.1 Investigation on dyeing mechanism of the modified cotton fibers

3.1.1 Zeta potential measurement of the modified cotton fibers

Zeta potential of the unmodified and modified cotton fibers was measured. Fig.3 showed the zeta potential values (ζ) of the unmodified cotton exhibited a negative charge on the surface over wide pH range of 4-11. However, for the cotton modified with CHS, zeta potential value presented a positive charge of about 20mV at neutral condition which was usually used for dyeing of cotton. So the dyes could be adsorbed on the modified fibers much easier through electrostatic attraction force between the dyes and the fibers.

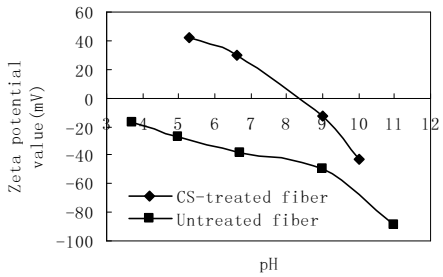

Fig.3. Zeta potential values of the untreated, CS-treated cotton fibers

3.1.2 Investigation on adsorption isotherm

Adsorption isotherms, which are used to examine dye adsorption type on fabrics, were obtained as shown in Fig. 4 when the percentage of neutral exhaustion at various dye concentrations was calculated in terms of concentrations of dye absorbed on cotton (D_f mg/g fiber) and dye remaining in the dyebath (D_s mg/ml solution).

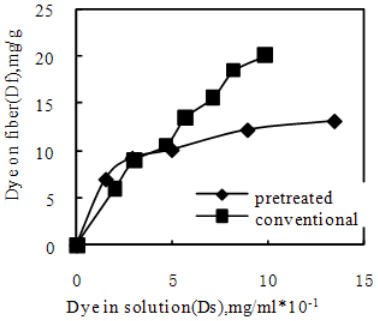

Fig.4. Adsorption isotherms for C.I. Reactive Red 2 on cotton in salt-free and conventional dyeing

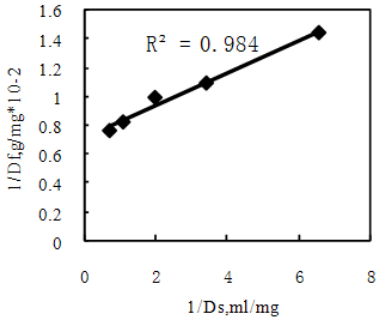

Fig.5. Reciprocal adsorption isotherms for C.I. Reactive Red 2 on the pretreated cotton in salt-free dyeing

The conventional dyeing of cotton with reactive dyes was demonstrated to be a Freundlich-type partition mechanism. However, on the modified cotton, the curve indicating Langmuir-type adsorption on specific sites was got, which could be testified by plotting the reciprocal values of D_f and D_s (see Fig. 5). Therefore it can be deduced that dyeing on modified cotton was mainly promoted by electrostatic attraction between cationic sites of quarternary ammonium salt in CS and disulphonated anions of the dyes.

3.2. Effect of the concentration of CNS and CHS on dye fixation

It could be seen from Fig.6 and 7 that with the increase of concentration of CNS and CHS (DS=0.7), the dye fixation increased first and decreased then for both dyes. In Fig.6, as the concentration of CNS increased to 0.5%, the optimal fixations of 46.3% and 66.2% respectively for C.I. Reactive Red 2 and

C.I. Reactive Blue 19 were obtained. When the concentration of CNS further enhanced, both dye fixation slowly decreased. In Fig.7, dye fixation increased obviously, especially for C.I. Reactive Red 2. At 2.0% and 2.25%, the optimal fixation of 69.4% and 73.8% respectively for C.I. Reactive Red 2 and C.I. Reactive Blue 19 was achieved. Due to that the concentration of dye applied for C.I. Reactive Red 2 was lower than that of C.I. Reactive Blue 19, less cationic groups were needed for adsorption of C.I. Reactive Red 2, therefore, the CHS concentration for obtaining optimal dye fixation of C.I. Reactive Red 2 (2.0%) was lower than that for C.I. Reactive Blue 19 (2.25%).

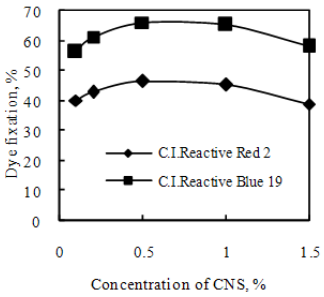

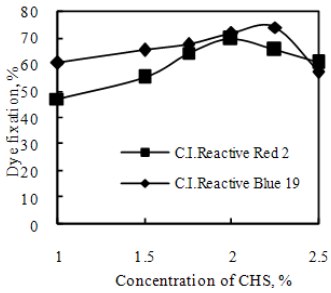

Fig.6. Effect of CNS concentration on dye fixationFig. 7. Effect of CNS concentration on dye fixation

3.3 Investigation of dye penetration

From Fig. 8, penetration properties of C.I. Reactive Red 2 and C.I. Reactive Blue 19 were displayed by the cross-sections under microscope. It exhibited that the dyes were well penetrated to the inner part of the fibers in conventional dyeing. However, as for CNS modified fibers, the dye just colored the outer part of the fibers, which was mainly resulted from prevention of dye penetration by CNS with large molecular weight. As for CHS modified fibers, the dye penetrability was much better compared with that for CNS pretreated fibers. So the dye was easier to be fixed on CHS modified fibers and the dye fixation was much higher on the fibers.

Untreated dyed fiber

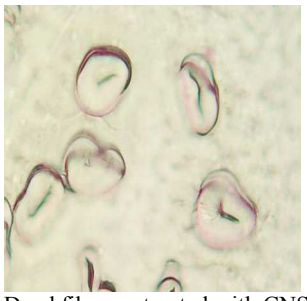

Dyed fiber pretreated with CNS

Dyed fiber pretreated with CHS

Fig. 8. Cross-sections of the untreated and pretreated fibers dyed with C.I. Reactive Red 2

3.4 Fastness property analysis

The fastness properties of the dyeings were determined as in Table 1.

Table 1. Comparison of the fastness properties of the reactive dyes on the pretreated cotton and the untreated one

Dye	No.	F (%)	Wash fastness			Rub fastness	
			Change	Staining		Dry	Wet
				C	W		
C.I. Reactive Red 2	1*	49.1	4	4	4	4	4
	2*	46.3	4	3-4	3-4	3	2-3
	3*	69.4	4-5	4	4	3-4	3
C.I.Reactive Blue 19	1	72.9	4-5	4	4	4	3-4
	2	66.2	4	3-4	3-4	3	2-3
	3	73.8	4-5	4-5	4-5	3-4	3

1*conventional dyeing; 2* salt-free dyeing (CNS), 3*salt-free dyeing (CHS)

The fastness property testing displayed that the perspiration fastness of the dyes on the modified cotton was all good. The wash fastness of both dyes on CHS modified cotton reached 4 or 4-5 grade. However, the color staining of wash fastness on CNS modified cotton was 0.5 grade lower compared with that of the conventional dyeing. The rub fastness of the dyes on CHS modified fibers decreased 0.5-1 grade compared with that of the conventional dyeing and that for CNS modified fibers was 1-2 grade lower. Partial unfixed dye was difficult to be rinsed off from the modified fibers owing to larger electrostatic attraction force between CNS and the dyes, and thus lower fastness properties were resulted.

4. Conclusions

In this paper, the overall application properties of CNS and CHS in salt-free dyeing of reactive dyes were studied. *zeta* potential（ζ）measurement results and the Langmuir-type adsorption of C.I. Reactive Red 2 on the modified cotton were in good agreement, and revealed that the uptake of the reactive dye on the modified cotton occurred by means of electrostatic attraction between the cations of the cotton fibers and the anions of the dyes. By taking the dye fixation and fastness properties obtained in conventional reactive dyeing as standard, salt-free dyeing could realize with application of CHS modified cotton. Under optimal conditions, the fixation of C.I. Reactive Red 2 and C.I. Reactive Blue 19 reached 69.4% and 78.3%, respectively, and the color fastnesses were satisfactory. However, as for CNS, due to its higher molecular weight and viscosity, dye penetration was prevented and thus dye fixation and fastness properties were both affected.

Acknowledgements

The authors gratefully thank the financial support of the National Nature Science Funds of China (Nos. 20806013, 20923006), the National Key Technology R&D Program (No. 2011BAE07B08) and Doctoral Fund of Ministry of Education of China (No. 200801411011).

References

[1] S M Burkinshaw, M Mignanelli, P E Froehling and M J Bide. The use of dendrimers to modify the dyeing behaviour of reactive dyes on cotton. Dyes. Pigm. 47 (2000) 259-267.

[2] P J Hauser and A H Tabba. Dyeing cationic cotton with fiber reactive dyes: Effect of reactive chemistries. AATCC Review 5 (2002) 36-39.

[3] Mehmet Kanik and P J Hauser. Printing of cationised cotton with reactive dyes. Color.Technol. 118 (2002) 300-306.

[4] S H Lim and S M Hudson, Application of a fibre-reactive chitosan derivative to cotton fabric as a zero-salt dyeing auxiliary. Color.Technol. 120 (2004) 108-113.

[5] Murcott, Susan E.; Harleman, Donald R. F. Method for drinking water treatment with natural cationic polymers. USP 5543056 1996.

[6] Aida, Masahiro. Method for hair dyeing or tone-up and method for hair-strengthening cold hair-wave setting. JP 2003231619 2003.

[7] Nechwatal Axel, Nicolai Monika and Mieck Klaus-Peter. Use of absorbers based on starch for the effluent treatment of dyeing liquors. Starch/ Staerke 51 (1999) 286-293.

[8] Zhang, Shu-Fen, Ma, Wei, & Ju, Ben-Zhi. Continuous dyeing of cationised cotton with reactive dyes. Color. Technol. 121 (2005) 183-186.

[9] Min Zhang, Ben-Zhi Ju, Shu-Fen Zhang, Wei Ma and Jin-Zong Yang. Synthesis of cationic hydrolyzed starch with high DS by dry process and use in salt-free dyeing. Carbohydr. Polym. 69 (2007) 123-129.

doi:10.4028/www.scientific.net/AMM.161.217

Development of a phenolic resin-bonded CBN wheel for precision grinding of ferrous materials

JianLin Chen [1,a], Long Wan[2]

[1]Key Laboratory of Regenerative Energy Electric-Technology of Hunan Province, Changsha University of Science & Technology, Changsha 410004, China;

[2]College of Materials Science & Engineering, Hunan University, Changsha 410082, China

[a]cjlinhunu@tom.com

Key words: Cubic boron nitride; Grinding wheel; Ferrous material; Phenolic resin

Abstract. A phenolic resin-bonded cubic boron nitride (CBN) wheel was designed and manufactured for precision grinding ferrous materials. The resin was determined to be a linear phenolic resin pre-polymer added with hexamethylenetetramine by infrared spectrum and the curing reaction, which characterized by an exothermic peak at about 180℃ with release of NH_3, was analyzed by differential scanning calorimeter and thermogravimetry. Based on thermal analysis, a hot press forming process and a post thermal treatment were employed for fabricating the resin-bonded CBN wheel. Grinding experiment results showed that normal grinding forces vary from 7 to 11 N and fluctuate slightly with 1~2 N. The grinding ratio of 585 and the surface roughness of 0.18 μm were obtained under an appropriate grinding condition.

1 Introduction

Precision machining of ferrous materials is important for modern manufacturing fields including aircrafts, automobiles, machines, bearings, and mould fabrication, etc [1]. At the same time, grinding technology is developing into high speed and high efficiency [2-3]. Cubic boron nitride (CBN) exhibits high hardness and good thermal stability used as superabrasive grains of grinding wheels with high efficiency and accuracy [4-6]. More importantly, it is chemically inactive with ferrous materials. On the other hand, resin-bonded abrasive wheels are well known as their great tensile strength, low grinding forces and temperatures, some elastic behaviors, and self-sharpening [7-11]. In this paper, a phenolic resin-bonded CBN wheel for precision grinding ferrous materials was investigated and developed.

2 Experimental procedure

Nickel-coated (60%) CBN with grain size of 140/170 US mesh and phenolic resin (size 70~80μm, density 1.26g/cm^3) were used as abrasives and bonding agent, respectively. White alumina (WA) of #320 was used as aided abrasives. Fillers added into resin bond were mainly copper, zinc oxide, chromic oxide, graphite, molybdenum disulphite, and cryolite, and the specifications are given in Table 1.

The thermal analysis of phenolic resin during curing process was examined by differential scanning calorimeter and thermogravimetry (DSC-TG） from 20 to 800℃ at N_2 atmosphere with 10℃/min temperature ramp rate (NETZSCH STA449C, Germany). The molecular structure of phenolic resin before and after thermosetting was analyzed by Fourier transform infrared spectrum (FTIR, Spectrum one, PERKIN ELMER). Grinding experiments were conducted on KGS-250AH grinding machine.

Table 1. The specifications of fillers or abrasives added into resin bond

Filler	Formula	Purity grade	Density (g/cm^3)	Size
White alumina (WA)	Al_2O_3	Commercially pure	3.96	#320
Copper	Cu	99%	8.92	#200
Zinc oxide	ZnO	Chemically pure	5.6	#200
Chromic oxide	Cr_2O_3	Chemically pure	5.2	#200
Graphite	C	95%	2.25	#200
Molybdenum disulphite	MoS_2	95%	4.8	#200
Cryolite	Na_3AlF_6	Commercially pure	3.0	#200

3 Results and analysis

3.1 Structure analysis and thermosetting mechanism of phenolic resin

The differential scanning calorimetry and thermogravimetric (DSC-TG) curves of phenolic resin during thermal treatment are shown in Fig. 1. It can be observed that there is a sharp exothermic peak at about 180℃ in the DSC curve with the starting, peak, and ending temperature are 140℃, 165℃, 185℃, respectively. Correspondingly, there is a rapid mass loss of 3% at 165℃~185℃ in the TG curve. The exothermic peak should be attributed to the curing reaction of phenolic resin at about 180℃ with release of some volatile small molecules such as NH_3 or H_2O. The large endothermic peak starting from 380℃ with another fast mass loss stage can be associated with the chemical decomposition of phenolic resin thermosetting product. In addition, the melting temperature range of the phenolic resin was determined to be 98~110℃ by melting point analysis.

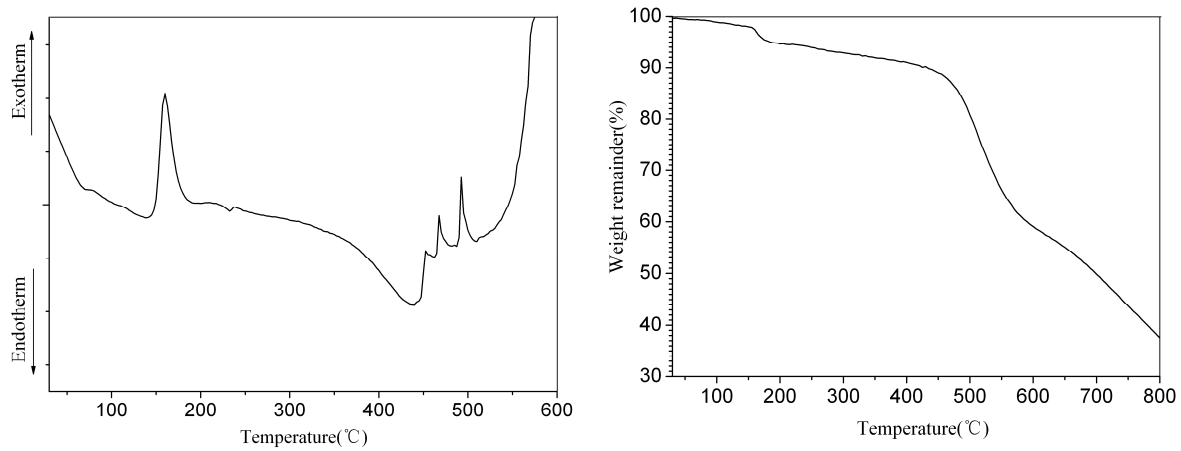

Fig.1. Thermogravimetry-differential scanning calorimetry (TG-DSC) curves of phenolic resin

Thermal analysis results indicate that the phenolic resin should be a linear phenolic resin pre-polymer added with hexamethylenetetramine. The curing chemical reactive formula can be expressed as equation (1).

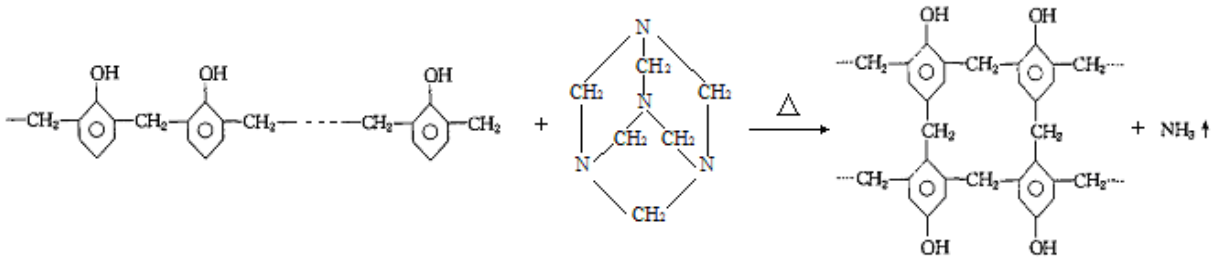

(1)

Fig. 2 shows the comparison of FTIR spectra of phenolic resin before and after thermosetting at 180℃ for 2 hours. The main characteristic absorption peaks of phenolic resin before thermosetting are listed in Table 2. The wavenumber at 690 cm^{-1} disappearing indicates that the free phenol existing in phenolic resin has been completely reactive with hexamethylenetetramine. On the other hand, the disappearing of 910 cm^{-1} peak, the weakening of 1010 cm^{-1} peak, the enhance of 1100 cm^{-1} and 1230 cm^{-1} peaks, the overlap and enhance of 1480 cm^{-1}, 1540 cm^{-1}, and 1620 cm^{-1} peaks all indicate that the linear phenolic resin pre-polymer changes into network polymer.

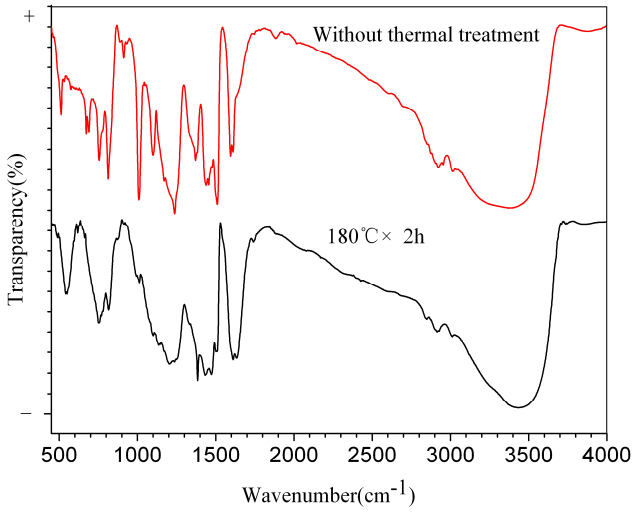

Fig.2. The infrared spectrum (FTIR) of phenolic resin before and after curing

Table 2. The FTIR characteristic absorption peaks of phenolic resin before curing

Absorption peak (cm^{-1})	Attribution
690	5 adjacent H in benzene ring（free phenol）
780	3 adjacent H in benzene ring（1, 2-substitution）
820	2 adjacent H in benzene ring（1, 2, 4-, 1, 4- substitution）
910	Nonplanar rocking vibration of CH_2
1010, 1230	Stretching vibration of C-OH
1100	Planar bending vibration of C-H in benzene ring
1360	Shearing vibration of CH_2
1480, 1540, 1620	Stretching vibration of C=C in benzene ring
1880	Benzene ring
2900, 2980	Stretching vibration of -CH_2-

3.2 Design and manufacturing of the resin-bonded CBN grinding wheel

The prototype and dimensions of resin-boned CBN grinding wheel is shown in Fig. 2 with type of 1A1/T2 200×15×32×5 (mm) and grain size of CBN 140/170. The abrasive layer thickness was 5 mm. Liquid phenolic resin was used as binder between the abrasive layer and aluminum base.

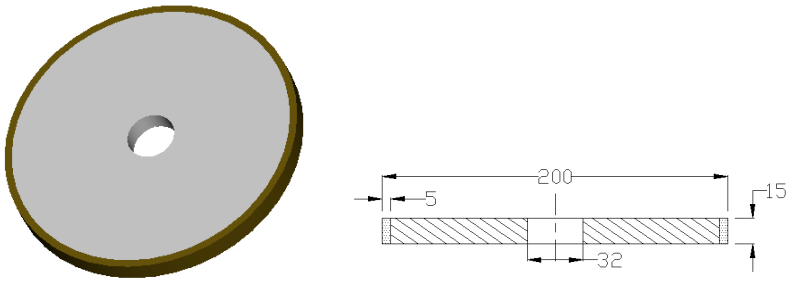

Fig.3. Schematic of the resin-bonded CBN wheel prototype and dimensions (1A1/T2, mm)

The weighs of all constituents in the phenolic resin-bonded CBN wheel were designed and calculated with reference to 100 cm^3. The CBN abrasive, WA aided abrasive, and phenolic resin bond volume percentages were about 24.5 vol.%, 12.5 vol.%, and 46 vol.%, respectively. All the constituents were shown in Table 3.

Table 3. Constituent design of the phenolic resin-bonded CBN wheel

Material name	Density $\rho(g/cm^3)$	Volume (*vol%*)/Weigh fraction $m_0(g)$	Weigh (*g*)
CBN-Ni	4.50	24.5/1.100	55.0
Phenolic resin	1.26	46.0/0.580	24.8
WA（#320）	3.96	12.5/0.495	29.0
Cu	8.92	10.0/0.892	44.6
ZnO	5.60	1.5/0.084	4.2
Cr_2O_3	5.20	1.5/0.078	3.9
Graphite	2.52	1.0/0.025	1.3
MoS_2	4.80	1.0/0.048	2.4
Na_3AlF_6	3.00	2.0/0.060	3.0

A hot press forming process was adopted for fabricating the phenolic resin-bonded CBN wheel. At the pre-press stage, the temperature was 100℃ and the pressure was 3MPa. Thereafter, the phenolic resin-bonded CBN wheel was pressed at 180℃ with the pressure of 8 MPa for 60 min. After hot press forming, based on the thermal analysis results above, a post thermal treatment process was employed as shown in Fig.4.

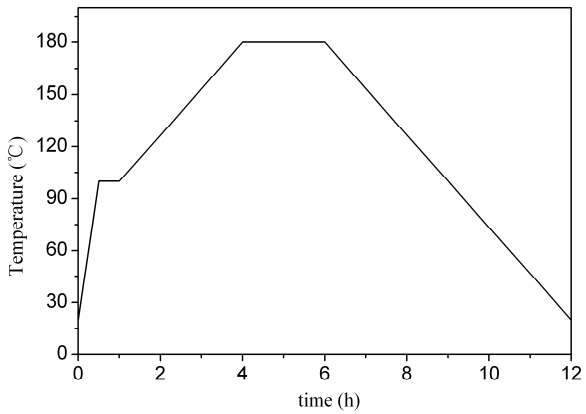

Fig.4. Post thermal treatment curve for the resin-bonded CBN wheel

3.3 Grinding performance of the resin-bonded CBN grinding wheel

Before grinding, the wheel was balanced using a dynamic balancing instrument. After balancing, the CBN wheel was trued and dressed using an electroplated diamond wheel and a vitrified silicon carbide wheel (1A1 75mm×25mm×12.8mm) with coolant, respectively, as shown in Fig.5. The speeds of grinding and truing wheels were 30m/s and 1.8m/s, respectively. The radial feed rate of the CBN wheel was 0.005mm/d.str and the axial feed rate of the truing wheel was 0.5mm/s.

Fig.5. Photograph of truing and dressing the resin-bonded CBN wheel

Surface grinding was employed in a down grinding mode. The workpiece material was steel 45# and the specimen had dimensions of 50mm×10mm×8mm. Various workpiece feed rate and wheel depth of cut were used to study their influences on the grinding performance. The grinding conditions used are listed in Table 5.

Under each set of conditions the grinding process was repeated three times to obtained an average value of grinding force. Grinding forces were measured using a piezoelectric dynamometer (Kistler 9257B) and were recorded into a computer via a data acquisition system, which are shown in Fig. 6. The roughness of ground samples was measured using a profilometer (Taylor Hobson) perpendicular to the grinding direction. For both grinding forces and roughness, the mean values were calculated as also shown in Table 5.

Table 5. Average grinding forces and surface roughness at different grinding conditions

No.	Wheel speed v_s (m/s)	Workpiece feed rate v_w (mm/s)	Depth of cut a_e (μm)	Normal grinding force F_n (N)	Surface roughness R_a (μm)
1#	30	50	0.004	7.7	0.18
2#			0.008	9.2	0.21
3#		60		9.7	0.24
4#		70		10.3	0.27

Fig. 6 shows that the normal grinding forces vs. time recorded at different grinding conditions. The normal grinding forces vary from 7 N to 11 N and fluctuate slightly with 1 N~2 N. It can be seen from Table 5 that an increase in the depth of cut and the workpiece feed rate led to a larger grinding force, but the former influence it more significantly. A reduction in the workpiece feed rate and the depth of cut resulted in an improvement on the surface roughness. However, the grinding efficiency will be improved with the workpiece feed rate and the depth of cut increasing. Therefore, it should choose high workpiece feed rate and depth of cut to improve the grinding efficiency at the premise of the surface roughness meeting the requirements.

In addition, the grinding ratio was calculated to be 585 (material removal: 200 g, wheel consumption: 342 mg) and the surface roughness is 0.18 μm (precision grinding: R_a<0.2 μm), under the grinding condition of v_s =30 m/s, v_w=50 mm/s, and a_e=0.004 mm. Thus it can be concluded that the designed resin-bonded CBN wheel can meet the purpose of precision grinding ferrous materials with high efficiency under an appropriate grinding condition.

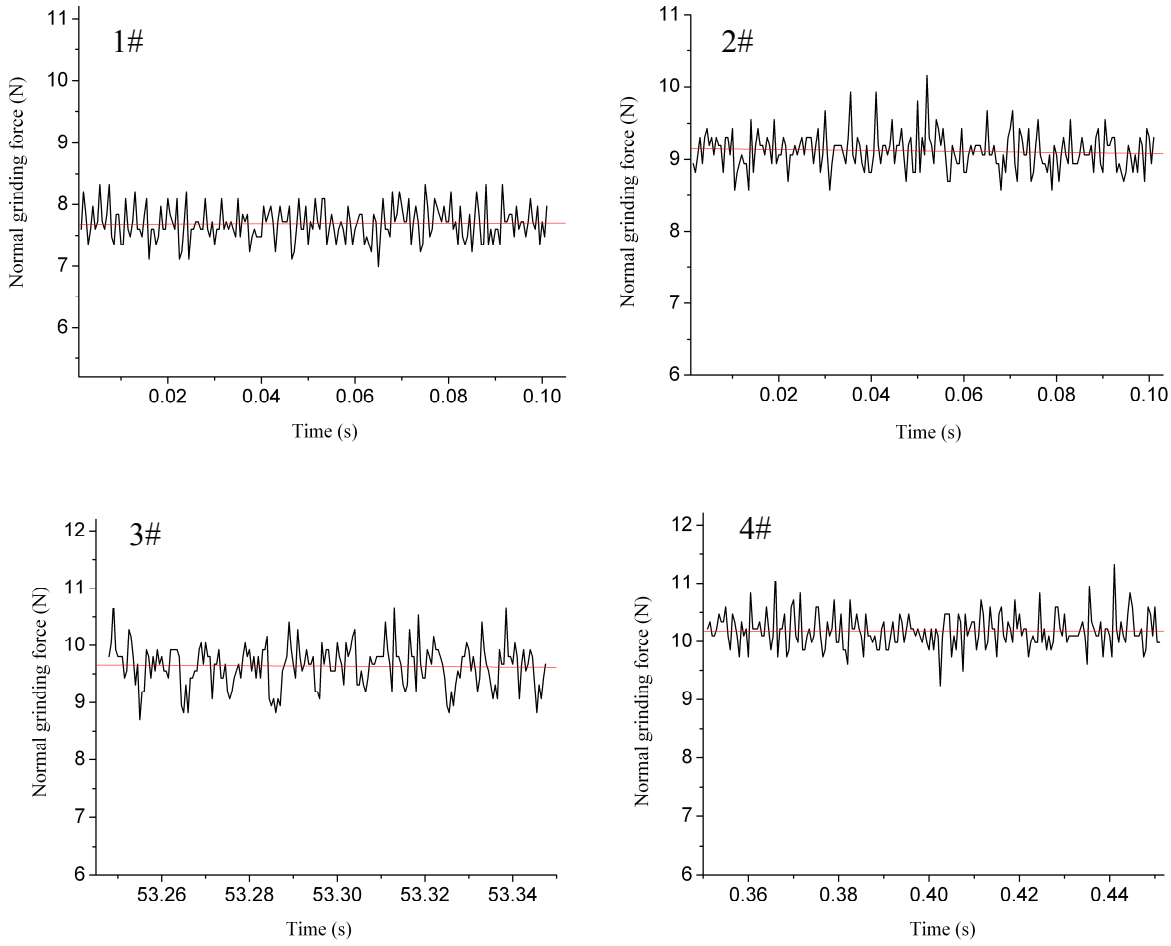

Fig.6. Transient normal grinding forces under different grinding conditions

4 Conclusions

A phenolic resin-bonded CBN wheel of 1A1/T2 200mm×15mm×32mm×5mm with CBN 140/170 abrasive grains has been fabricated. The molecular structure and curing process of phenolic resin bond have been determined by thermal analysis and FTIR spectrum. Based on thermal analysis, a hot press forming process and a post thermal treatment were employed for fabricating the resin-bonded CBN wheel. The grinding experiment results show that the designed CBN wheel can meet precision grinding ferrous materials with high efficiency with normal grinding forces varying from 7 to 11 N and fluctuating slightly with 1~2 N. The grinding ratio of 585 and the surface roughness of 0.18 μm were obtained under an appropriate grinding condition.

Acknowledgements

The authors thank the supports from National Engineering Research Center for High Efficiency Grinding of Hunan University for grinding experiments.

References

[1] K. Fujisaki, H. Yokota, N. Furushiro, et al, Development of ultra-fine-grain binderless cBN tool for precision cutting of ferrous materials, Journal of Materials Processing Technology, 209 (2009) 5646-5652.

[2] M.J. Jackson, C.J. Davis, M.P. Hitchiner, B. Mills, High-speed grinding with CBN grinding wheel – applications and future technology, Journal of Materials Processing Technology 110 (2001) 78-88.

[3] Xiaoping Li, A free-abrasive machining approach to dressing of resin-bonded CBN grinding wheels, Journal of Materials Processing Technology 48 (1995) 223-230.

[4] R.Cai, W.B.Rowe, Assessment of vitrified CBN wheels for precision grinding, International Journal of Machine Tools & Manufacture, 44 (2004) 1391-1402.

[5] Sunarto, Yoshio Ichida, Creep feed profile grinding of Ni-based superalloys with ultrafine-polycrystalline CBN abrasive grits, Journal of the International Societies for Precision Engineering and Nanotechnology 25 (2001) 274-283.

[6] Hua-Yun You, Pei-Qing Ye, Jin-Song Wang, Xing-Yi Deng, Design and application of CBN shape grinding wheel for gear, International Journal of Machine Tools & Manufacture 43 (2003) 1269-1277.

[7] Han Huang, Ling Yin, Libo Zhou, High speed grinding of silicon nitride with resin bond diamond wheels, Journal of Materials Processing Technology 141 (2003) 329-336.

[8] S.Y.Luo, Y.S.Liao, C.C.Chou, J.P.Chen, Analysis of the wear of a resin-bonded diamond wheel in the grinding tungsten carbide, Journal of Materials Processing Technology 69 (1997) 289-296.

[9] S.Y.Luo, Y.C.Liu, C.C.Chou, T.C.chen, Performance of powder filled resin-bonded diamond wheels in the vertical dry grinding of tungsten carbide, Journal of Materials Processing Technology 118 (2001) 329-336.

[10] Jianlin Chen, Long Wan, Xiaopan Liu, Yang Wang, The thermosetting process of diamine-modified bismaleimide resin, Thermosetting Resin 20 (2005) 1-4.

[11] T.Tanaka, Y. Isono, New development of a grinding wheel with resin cured by ultraviolet light, Journal of Materials Processing Technology 113 (2001) 385-391.

doi:10.4028/www.scientific.net/AMM.161.224

Excess Heat Production in a D-Pd Gas-solid System

Xin Lu [1,2 a], Jian Tian [1,b *], Lihong Jin [1,c], Bingjun Shen[1] and Hongyu Wang[1]

[1] Clean Energy Technology Laboratory, Changchun University of Science and Technology, Changchun 130022, China

[2] School of Sciences, Changchun University, Changchun 130022, China

[a] luxin1981@163.com, [b] tianjian@cust.edu.cn(Corresponding author), [c]jinlh@cust.edu.cn

Keywords: D-Pd gas/solid system; excess heat; electric current; pressure variation

Abstract. Evidence of some excess heat triggered by electric current and pressure change in a D-Pd system and details of the calorimetric measurements were reported in this paper. The system produced an excess energy of about 80MJ in 83 hours, which was corresponding to 1.8×10^4eV for each palladium atom. The results of SEM and EDS implied that there might be a nuclear reaction in the exothermic process.

Introduction

S. Focardi et al [1] reported on the existence of a large excess heat production observed in a H-Ni gas loading system. A. Rossi [2] developed the method and enlarged the phenomenon into 1MW in recent days. Few of people knew Rossi's secret catalyzer and had many curiosities and questions on it. With the skeptics a D-Pd gas-loading system was chosen and made a series of experiments in order to prove if the evidence was true[3].

Experimental

Experimental apparatus. Figures 1 and 2 gave a schematic of the experimental system. Figure 1 was a reaction chamber that made up of stainless steel with a double-Jacket structure, where the circulation water could flow through. It has internal dimension of diameter =100mm and hight = 240mm with useful capacity about 1.9 dm^3. Palladium wires(99.98% purity made by National Non-ferrous Metal Research Acadamy, Beijing), with dimension of diameter = 0.5mm and lengh = 210cm (V= $4.123\times10^{-1}cm^3$) for experimental and Φ =0.5mm and L = 400cm ($7.854\times10^{-1}cm^3$) for heating the system. In order to continuous monitoring of its energy balance by measuring the equilibrium temperature at different positions, the reaction chamber has seven Pt100 resistor thermometers (see figure 1 for temperature sensors position). The presence of an excess heat was detected by the increase of all the monitored temperatures. Where 1 inlet of circulation water; 2,4 ceramic tube; 3 Pd wire for heating; 5 Pd wire for experimental; 6 outlet of circulation water; 7 circulation water; T1～7 Pt100 resistor thermometers for taking the temperatures at different purposes: T1 the middle of the chamber inside the ceramic tube; T2 wounded around heating Pd wire; T3 wounded around experimental Pd wire; T4 inside the chamber between inside wall and outside ceramic tube; T5 in the place near the aero-plug; T6 adhesive on the outside wall of the chamber; T7 ambient temperature.

The experimental apparatus for the chember was shown in figure 2, where 1 was the reaction chamber; 2 the inlet and ourlet for circulation water arround the chamber; 3 transition chamber; 4 D_2 needle valve; 5 D_2 generator; 6 air needle valve; 7 gate valve; 8 molecular pump; 9 the inlet and ourlet mouth for water circulation on the top; 10 DC power supply; 11 vaccum gauge; 12 Keithley 2700 multifunction date-inquiration meter; 13 a computer for data recording and controling; 14 a mechanical pump.

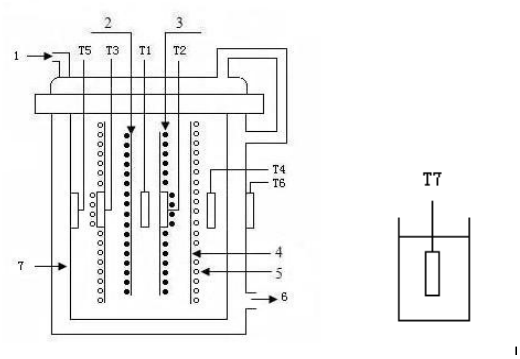

Fig. 1 Schematic of reaction chamber

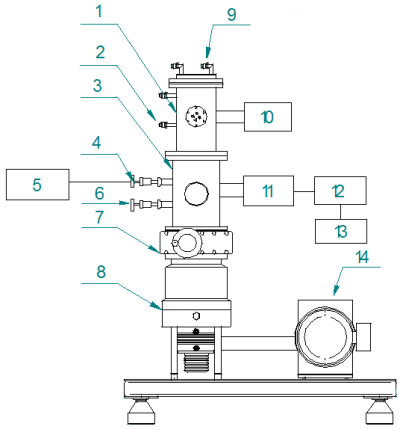

Fig. 2 Experimental apparatus

Calibration. The excess heat power can be calculation by eq.(1), where Po was overheating output power, Pi was input power, because all the physico-chemial processes last for a limited time period, and the heating coefficient (k) can be considered as a constant in the explored temperature range[1].

$$Po = Pi - \frac{T6 - T7}{k} \tag{1}$$

So, before the triggering experiments, a series of calibration were carried out for determine the normal status behavior of the system. The heating Pd wire was passed through some different electrical currents at 9×10^4 Pa under N_2 environment. When the temperature of the system because equilibrium a pair of data (temperature, pressure, voltage and current) were recorded by a 12-bit National Instrument interface Keithley 2700. The results are shown in figure 3.

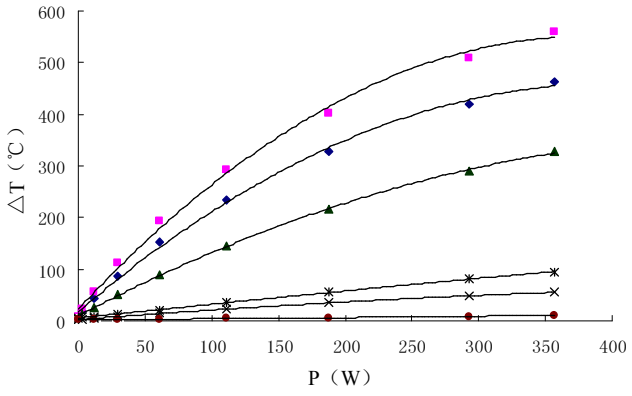

Fig. 3 Calibration curves; temperature (relative to the T7) vs. power under N_2 environment at 9×10^4 Pa (T1(◆), T2(■), T3(▲), T4(×),T5(*) and T6(●))

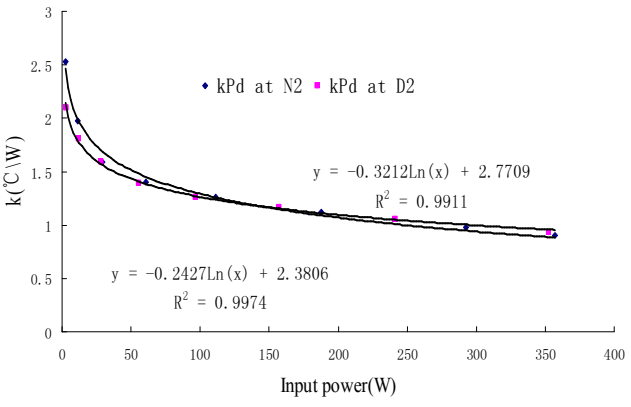

Fig. 4 The fitting curve of input power and k under N_2(◆),D_2(■) environment at 9×10^4 Pa

This work compared the heating coefficient (k) for a D/Pd gas-solid system with N/Pd gas-loading system triggered by same current within different pressures[4,5].

$$k = \Delta T / \Delta P \, (°C/W) \tag{2}$$

ΔT was the temperature of difference equilibrium before and after some certain electric power put into the system. ΔP was the actual input power change on palladium wire. The k in N_2 and D_2 environment at 9×10^4 Pa can be obtained from a calibration procedure during which a known power was supplied to the chamber and the equilibrium temperatures T6 and T7 are measured, as shown in table 1.

Table.1 The k (℃/W) of different input power in N_2 and D_2 environment at 9×10^4 Pa

Input power (W)	357.06	292.81	187.39	111.28	60.74	29.14	11.37	2.62
k (℃/W) N_2	0.905	0.976	1.123	1.261	1.401	1.593	1.977	2.530
k (℃/W) D_2	0.969	1.017	1.124	1.249	1.394	1.571	1.797	2.149

For the case of calculation, the relation between input power and k of experimental palladium wire at N_2 , D_2 were fitted. The fitting curves were as shown in figure 4. From it we can see that the value of k at N_2 environment was greater than thatt at the D_2 environment when input power was less than 150W, but when the input power was greater than 150W, the value of k at D_2 environment was greater than that in the N_2 environment at high temperature. And with the input power increases, the greater the difference between k in D_2 environment and k in N_2 environment. However, taking into account the specific circumstances of laboratory equipment and the palladium wire, we set the input current of 8.0A in the experiment finally.

Experimental process and results

Excess heat estimation. Our previous experimental work indicated that the maximum excess heat power occured at the current 8A through heating palladium wire, pressure 9×10^4 Pa, so we consider whether can repeat the experiment, and can realize the self-sustained heating. Based on this reason, the current decreased gradually from the 8A, in order to find the suitable input power which was the maximum of excess heat power (Po) and input power (Pi) ratio, and at which condition the self-sustained heating experiment could be obtained

Input current decreased from 8A by 1.0A，0.5A，0.25A, to determine the excess heat output power and input power than the maximum input power, the experimental data were shown in table 2. Experimental results showed that, the excess heat power decreased as input power decreased, no matter what the current decline manner, however, its decline rate of different, the manner of 0.25A reduces the current to the 7.0A, excess heat power 35.20W, the manner of 0.5A reduces the current to the 7.0A, excess heat power 32.11W, the manner of 1.0A reduces the current to the 7.0A, excess heat power 11.73W. In addition, the ratio of excess heat output power (Po) and input power (Pi) was also different, with the 0.25A manner to reduce the current to the 7.0A, ratio of 0.143, with the 0.5A manner to reduce the current to the 7.0A, ratio of 0.131, with the 1.0A manner to reduce the current to the 7.0A, ratio of 0.049. So the best of the excess heat power and ratio are appeared at the manner of 0.25A reduces the input current. And when the input current decreased to the 7.25A at the manner of 0.25A, the ratio was maximum about 0.143. So, we decreased the input current from 8.0A to 7.25A witch was the maximum ratio by the manner of 0.25A.

So, we took the maximum ratio at current 7.25A by decreased manner 0.25A under D_2 environment at 9×10^4 Pa, let the current pass heating Pa wire to heat the reaction chamber for about 83 hours 17 minutes. When the system got a thermal equilibrium the excess heat production could be calculated by the difference temperature of T1 ~ T7 as shown in figure 5. The average excess heat power was 265.37W, the total excess heat energy about 79.58MJ, which was corresponding to 1.8×10^4eV/atom Pd. Apparently it was greatly more than the energy the hydrogen atom release in a chemical process.

Table.2 Po and Po/Pi about heating current decreased from 8.0A by 1.0A，0.5A，0.25A

heating current(A)	0.25A		0.5A		1.0A	
	Po(W)	Po/Pi	Po(W)	Po/Pi	Po(W)	Po/Pi
8.00	47.476	0.094	33.711	0.094	18.640	0.053
7.75	45.057	0.136				
7.50	42.285	0.141	32.190	0.108		
7.25	38.969	0.142568				
7.00	35.202	0.142557	32.115	0.131	11.728	0.049
6.75	31.477	0.141				
6.50	27.86364	0.138747	24.238	0.112		
6.25	24.61942	0.13658				
6.00			16.473	0.103	2.702	0.017
5.75						
5.50			11.285	0.089		

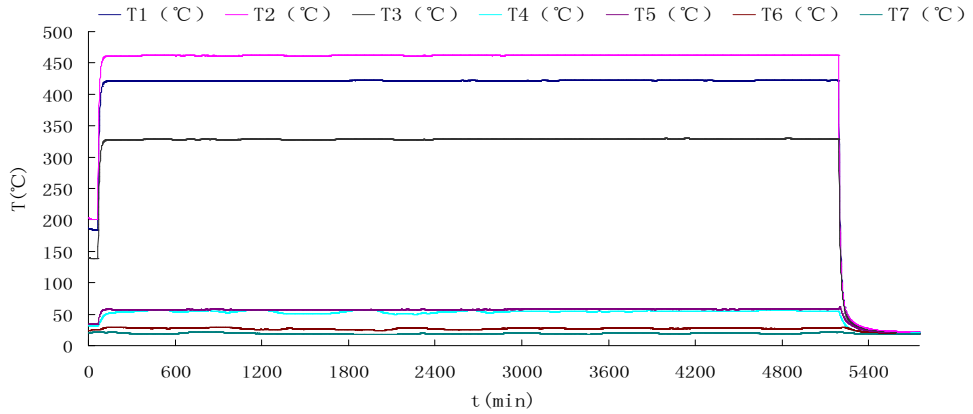

Fig. 5 The difference temperature of T1 ~ 7 under D_2 environment at 9×10^4 Pa

SEM and EDS analysis. Analysised on experimental palladium wire for SEM, a magnification of 2418 times, as shown in figure 6. Observed local with granular particles whiches exceptionally bright produced in the field of view, this region was further amplified by 19345 times, shown in figure 7, and carries on the EDS analysis, the results shown in figure 9 and table 3.

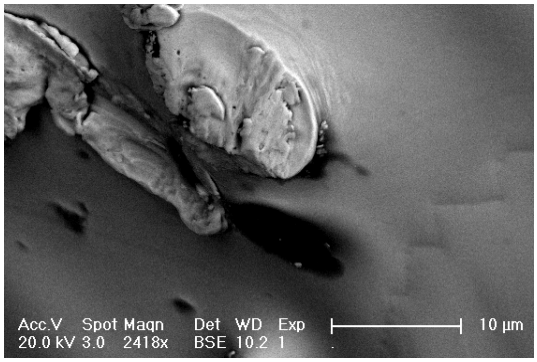

Fig. 6 SEM of experimental palladium wire (2418×)

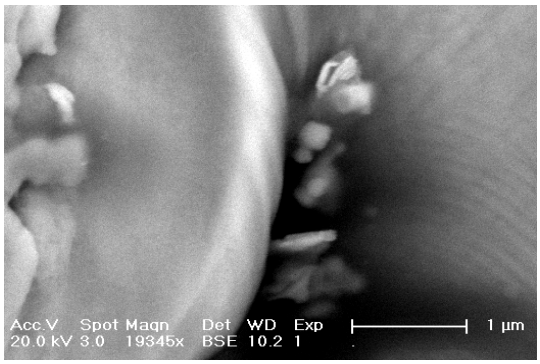

Fig. 7 SEM of partial enlargement experimental palladium wire (19345×)

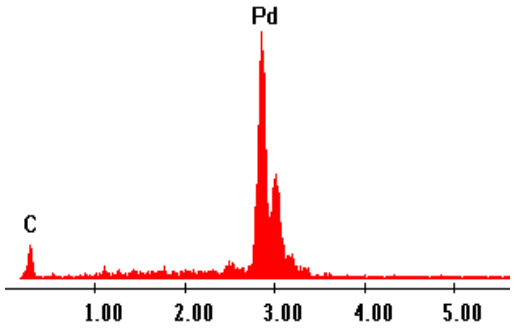

Fig. 8 EDS of palladium origin

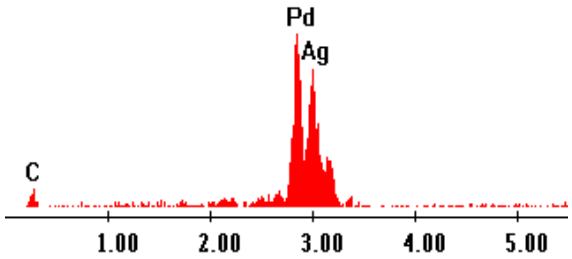

Fig. 9 EDS of Fig7 palladium sample

The original palladium wire was analysised with an EDS (Fig. 8). The result indicated that the sample was of nearly 100% palladium. The experimental palladium wire (show in figure 9) in EDS analysis shown in figure 9, the results of composition and proportion of the elements in table 3. From figures 8 and 9 we chould see that after excess heat, there was Ag which Wt% about 31.26 on experimental palladium surface. Ag might be produced during the excess heat process.

Table.3 Composition and proportion of elements in figure 9

Element	Wt%	At%
C	5.96	36.04
Pd	62.79	42.9
Ag	31.26	21.06
Total	100	100

Conclusions

In the process of achieving self-sustained manner, we got a great amount of excess heat by using the maximum ratio at current 7.25A by decreased manner 0.25A from 8A under D_2 environment at 9×10^4 Pa. The excess heat lasted for about 83 hours 17 minutes, the average excess heat power was 265.37W, the total excess heat energy was about 79.58MJ, which was corresponding to 1.8×10^4eV/atom Pd. Apperently that was much more than the energy in a chemical process. And on the fused section of experimental palladium smoe Ag element was found and its origin might come from a nuclear transmutation process.

References

[1] S. Focardi, V. Gabbani, V. Montalbano, Large excess heat production in Ni-H systems, J. IL Nuovo Cimento. 11 (1998) 1233-1242.

[2] Information on http://ecatnews.com/?p=1160 /2011/10/30

[3] J.Tian et al : "Excess Heat" and "Heat after Death" in a Gas-loading Hydrogen/Palladium System, in The 9th International Conference on Cold Fusion, Condensed Matter Nuclear Science. 2002. Tsinghua Univ., Beijing, China: Tsinghua Univ. Press, p360

[4] Jian Tian et al. An Excess Heat Phenomenon Triggered by Pressure in a H-Pd Gas-loading System, J .Advanced Materials Research Vols. 399-401 (2012) 1433-1438.

[5] Tang Tao et al.Thermodynamic Investigation of Interaction between Palladium withHydrogen (H_2, D_2) , J .Chinese Journal Of Rare Metals.2,28 (2004)308-312.

doi:10.4028/www.scientific.net/AMM.161.229

The study of synthesis of double head viscoelastic surfactant of type C12

Shanshan Dai[1,2,a], Hongsheng Lu[1,2], Tailiang Zhang[1,2],
Shanshan Qu[1], and Yalu Yu[1]

[1]School of Chemistry and Chemical Engineering, Southwest Petroleum University, Chengdu, Sichuan 610500, China

[2]State Key Laboratory of Oil/Gas Reservoir Geology and Exploitation Engineering, Southwest Petroleum Uinversity, Chengdu, Sichuan 610500, China

[a]ashanscu@163.com (corresponding author)

Keywords: amidation; quaterisation; viscoelastic surfactant

Abstract By the methods of amidation and quaterisation, a surfactant, double head viscoelastic surfactant (VES) of type C_{12}, was synthesized for the purpose of reducing the cost of preparation while improving the productivity of surfactant as much as possible. The corresponding conditions, including the choice of solvent, reaction temperature, reaction time, ratio of materials and its charging time were studied in detail. Besides, the chemical structure of the intermediate and the final product were certified by fourier transform infrared spectroscopy.

1. Introduction

Dilute solutions of ionic or nonionic surfactants usually behave as Newtonia liquids with viscosities only slightly greater than that of water. In contrast to these simple fluids, there are viscoelastic surfactant (VES) systems that are known to have a more complicated rheological behavior [1-4]. By shearing, the reversible formation of a continuous three-dimensional structure will be found even at a low concentration of VES. At higher concentrations, the gellike supermolecular structure is already formed in the quiescent state. At present, synthesis methods of amide type of VES, its physicochemical properties and applications are widely studied [5-10] based on the advantages mentioned above.

Usually, the surfactants used in the system of matrix acidizing and acid fracturing of carbonate reservoir mostly focus on sinapic amido propyl betaine [11-13]. However, the huge cost limits its application greatly especially in low output oilfield [13]. Besides, the long fatty chain [14] is difficult to form flexible rod-shape micelle at a comparatively higher temperature. The maximum apparent viscosity appears when the pH value of spent acid varies from 1 to 2 [13], but the range of real value is always between 3 to 4 [15]. Namely, the viscosity of these acid systems will be affected not only by temperature but also by pH. To solve the problems mentioned above, the new betaine surfactant with two-head group is designed in this study for the purpose of reducing the cost of preparation while improving the productivity of surfactant as much as possible. The synthesis was carried out by the methods of amidation and quaterisation. The corresponding conditions, including the choice of solvent, reaction temperature, reaction time, ratio of material and its charging time were studied in detail. Besides, the chemical structure of the intermediate and the final product were certified by fourier transform infrared spectroscopy. The resulting surfactant was directly applied in matrix acidizing and acid fracturing of carbonate reservoir. More importantly, good results have already obtained. However, parts of application research are not introduced in this paper due to the length consideration.

2. Experimental

Lauric acid, chloroacetic acid, sodium bicarbonate, sodium hydrate, acetone, isopropanol, ethanol, hydrochloric acid, and anhydrous calcium chloride were purchased from Chengdu Kelong Company. Hydroxyethyl ethylenediamine was bought from Chengdu Xiya Company. Sodium chloroacetate was purchased from Tianjin Guangfu Institute of Fine Chemicals.

N-lauramid-N′-hydroxyethyl ethylenediamine as intermediate was prepared by the reaction of Lauric acid and β-Hydroxyethyl ethylenediamine with the mole rates varying between 1:1.00 and 1:1.15 at 130-150°C for 8 hours. Water should be removed in time by vacuum distillation in order to improve the production rate of this reversible process. The corresponding equation is listed as follows:

$$C_{11}H_{23}COOH + NH_2CH_2CH_2NHCH_2CH_2OH \xrightarrow[\triangle]{-H_2O} C_{11}H_{23}CONHCH_2CH_2NHCH_2CH_2OH$$

The corresponding product was dissolved in acetone, recrystallized at 0°C, filtered by Buchner funnel, and then dried in a vacuum oven.

N-lauroyl-N'-diethyl hydroxyethyl ethylenediamine salt was prepared as follows:

$$C_{11}H_{23}CONHCH_2CH_2NHCH_2CH_2OH \xrightarrow{2ClCH_2COONa} C_{11}H_{23}CONHCH_2CH_2N^{+}(CH_2CH_2OH)(CH_2COONa)(CH_2COONa)\,Cl^{-}$$

Reaction between sodium chloroacetate and the intermediates obtained from the methods mentioned above at 90-95°C for 16 hours. The mole rate of N-lauramid-N′-hydroxyethyl ethylenediamine/sodium chloroacetate was varying between 1:2.0 and 1:2.5. The corresponding equation is listed as follows:

The corresponding product, double head viscoelastic surfactant (VES) of type C12, was obtained after regulating its pH value to 7~8 by 30% solution of sodium hydroxide.

The chemical structure of purified intermediate and the final product were certified by Fourier Transform Infrared Spectrometer WQF-520, produced by Beijing Reili Analytical Instruments Co. The pellets were prepared by pressing the mixture of the sample and KBr powder. The scanning rate is 20min-1， and the differentiate rate is 4cm^{-1}.

3. Results and discussion

3.1 Synthesis of intermediates

3.1.1 the study of methods of amidation

There are two methods of amidation: vacuum and water-carrying agent. The former one refers to non-solvent, and the reaction temperature is comparatively high. On the one hand, β-Hydroxyethyl ethylenediamine is prone to be oxidated with the increase of temperature, and the color of products is also deepened at the same time. On the other hand, side reaction is strengthened. To avoid the problems mentioned above, sectional heating is often used. Drop β-Hydroxyethyl ethylenediamine at low temperature, and then react with Lauric acid at 150°C. With the method of water-carrying agent, reactions can be carried out at comparatively lower temperature, and the color of the corresponding products was lighter. But β-Hydroxyethyl ethylenediamine was easy to be brought out with water by carrying agent. It must be added continuously to make sure the preparation of single amide in the acidylation. Besides, methylbenzene and dimethyl benzene, which is toxic and harmful, are the solvent usually used in the method of water-carrying agent. Therefore, vacuum method was selected in this study.

3.1.2 the effects of temperature in amidation

The effects of temperature on production rate and production color are shown in Table 1. All the reactions are carried out at a molar ratio of Lauric acid to β-Hydroxyethyl ethylenediamine equals to 1.0:1.1. It can learn from the table, the production rate of intermediate at 135°C was higher than that at 140°C, because some of β-Hydroxyethyl ethylenediamine was brought out of the reaction system by water or probably oxidized at high temperature. Besides, with the increase of temperature, the

color of intermediate deepened gradually and the crystal became bigger and adhesive, which may be caused by the oxidation of amine at high temperature. Therefore, the best temperature of preparation of intermediates is about 135°C. Over loading of β-Hydroxyethyl ethylenediamine, and nitrogen gas protection are both necessary to improve the production rate.

Table 1 The effects of temperature on production rate of intermediate

Temperature [°C]	Production Rate [%]	Color
130	85.25	opal
135	88.68	opal
140	80.47	opal
145	77.93	light yellow
150	74.76	light yellow
155	70.59	yellow
160	66.73	yellow

3.1.3 the effects of molar ratio of materials on amidation

β-Hydroxyethyl ethylenediamine is much less stable than Lauric acid at high temperature. The former one must be a bit excessive for reducing the amount loss caused by oxidation or evaporation. The effects of molar ratio of Lauric acid to β-Hydroxyethyl ethylenediamine on production rate of intermediate at 135°C were listed in Table 2.

Table 2 The effects of material ratio on the production rate of intermediate

Acid Amide Ratio [mol]	Production Rate [%]
1:1.000	65.35
1:1.025	71.29
1:1.050	76.25
1:1.075	80.54
1:1.100	88.76
1:1.125	83.59
1:1.150	78.61

It can be concluded from the table, the optimal molar ratio was 1:1.100 due to the highest value of production rate of intermediate. Before this transition point, the production rate was improved with the increasing amount of amide, because these excessive loading just reduced the loss of β-Hydroxyethyl ethylenediamine caused by oxidation or evaporation. When the acid amide ratio was bigger than 1:1.100, the production rate began to decrease with the increasing amount of amide, indicating more proportion of β-Hydroxyethyl ethylenediamine lossed before anticipating in the reaction. Besides, β-Hydroxyethyl ethylenediamine is very expensive, and it's difficult to apply in the industry when the acid amide ratio is smaller than 1:1.100.

3.1.4 the effects of loading time of β-Hydroxyethyl ethylenediamine on Amidation

The effects of loading time of β-Hydroxyethyl ethylenediamine on production rate of intermediate were shown in Table 3. The acid amide ratio was 1:1.100 and the reaction temperature was 135°C. It can be concluded from the table, loading in a comparatively short time, the concentration of amide was so high and it is easy to evaporate before reaction, leading to low production rate. While the loading time was too long, water vapor generated by reaction would bring amide out of system. Therefore, production rate of intermediate was the highest when the dropping time was about 40min.

Based on all the results mentioned above, the optimum conditions of synthesis of amide intermediates were as follows: drop hydroxyethyl ethylenediamine in 40 min, with molar ratio of Lauric acid to β-Hydroxyethyl ethylenediamine 1:1.100, at 135°C, The reaction termination of 8h was judged by the generation of water evaporated.

Table 3 The effects of loading time of β-Hydroxyethyl ethylenediamine on production rate of intermediate

Loading time of amide	**production rate [%]**
10min	73.43
20min	75.76
30min	80.89
40min	88.56
50min	70.72
disposable added	66.58
two times added	69.15

3.2 Synthetic technology of VES

3.2.1 the effects of solvent on quaterisation

Traditional quaterisation was carried out in aqueous solution, but the water solubility of the amide intermediate in this study is not very good. Besides, the viscosity of solution will become higher and higher with the processing of reaction. Some literatures pointed out, alcohol, propanol, and glycol were also good choice as the solvent for quaterisation. Quaterisation of this study didn't carry out even after 8h in the solvent of alcohol. While with propanol or isopropyl alcohol, the reaction was slow. Consider the situation mentioned above, the mixture of alcohol and water (less than 20%) was chosen as the solvent, which improved quaterisation effectively.

3.2.2 the effects of temperature on quaterisation

At the beginning of the experiment, the temperature was kept at 70~80°C, because the hydrolyzation of sodium chloroacetate seriously was serious at higher temperature. It will lead to the decrease of pH, and then affect the reaction. The sodium chloroacetate with high concentration was then added, and the reaction time of the system with a little water was about 6h. After several attempts, it was proved that the condition was not suitable for the preparation of this surfactant because of phase seperation. The upper was intermediate and the sublayer was water, which indicated the reaction between intermediate and sodium chloroacetate was difficult due to the different solubility. Catalyst and applicable solvent were needed for speeding up the reaction.

To avoid the shortcoming mentioned above, the temperature was improved to 90~95°C after loading. A little water was added to ensure the complete contact among molecules. And the temperature of reaction was kept less than 100°C to decrease the hydrolyzation of sodium chloroacetate. Besides, sodium hydrate is added, which balanced out hydrogen chloride and also took the role of catalyst of carboxylation.

3.2.3 the effects of reaction time on quaterisation

Generally, the increase of reaction time at terminal stage can improve the production rate, but it's almost meaningless, because reaction rate is much faster at the beginning of reaction. The production rate of VES was improved with the increase of reaction time in this study. At the case of a small amount of excess, reaction time was about 20h. Then make sodium chloroacetate more overdose and the reaction time could be shorten to 16h with the same production rate of VES. The corresponding product still for a whole night experienced without phase separation.

3.2.4 the effects of molar ratio of materials on quaterisation

Some literatures proved the conjugation effect between atom C and N on amido link. When -CH2COONa was introduced in, the electronegativity of N in production had obviously decreased, and it was relatively less impossible for quaterisation. The loading of sodium chloroacetate needed to be improved to solve this problem.

The poor water solubility of intermediate leaded to the phase seperation in the reaction. Through catalysis of phase transfer or emulsification, product rate will greatly improved due to the probable homogeneous reaction. The water solubility of product was poor in mole ratio of intermediate to sodium chloroacetate of 1:2.2 at 90°C for 24h, the solution was heterogeneous and some white floater appeared after still for a period, due to the incompletely transformed intermediates, which proved the conversion rate was comparatively low.

Increasing the mole ratio of intermediate to sodium chloroacetate to be 1:2.5, the water solubility of product was good after reaction for 16h. The corresponding solution appeared amber and homogeneous after still in a period, indicating the conversion rate of intermediate increased by the improvement of loading of sodium chloroacetate.

Based on the conclusions mentioned above, the optimum condition of synthesizing VES was obtained as follows: mixture of alcohol and water was chosen as the solvent, water content of which was less than 20%, loading at60~65°C, and then reacted at 90~95°C. The reaction time was about 16h or longer and the mole ratio of intermediate to sodium chloroacetate was1:2.5.

3.3 Characterization of intermediate and double head VES of type C12

Characteristic absorbance peaks of the main groups in intermediates and VES are listed in Table 4 and Table 5 respectively, which indicated the success of preparation.

Table 4 Results of IR Spectrum of intermediate

group	wave number [cm-1]	Vibration mode	Intensity
O-H	3293	νas(O-H)	strong
	1369	δas(O-H)	weak
CH_3-	2919	νas(CH_3-)	strong
	1459	δas(CH_3-)	moderate
-CH_2-	2919	νas(-CH_2-)	strong
	2850	νs(-CH_2-)	strong
	1459	δas(-CH_2-)	moderate
-（CH_2）$_n$-	723	δas(-*(CH_2)$_n$*-)	moderate
N-H（para-amide）	3369	νas(N-H)	weak
	3097	δs(N-H)	weak
	1562	δs(N-H)	moderate
C-N	1272	νas(C-N)	weak
C=O	1625	νas(C=O)	strong
C-O（primaryalcohol）	1068	δs(C-O)	weak

4. Conclusion

By the methods of amidation and quaterisation, a novel surfactant, double head viscoelastic surfactant (VES) of type C12, was synthesized for the purpose of reducing the cost of preparation while improving the productivity of surfactant as much as possible. There are two steps:

(1) Preparation of N-lauramid-N′-hydroxyethyl ethylenediamine intermediate. The optimal condition was as follows: the acid amide ratio was 1:1.100, reaction temperature was 135°C, reaction time was 8h, and the time of loading of hydroxyethyl ethylenediamine was 40min.

(2) Preparation of N-lauroyl-N’-hydroxyethyl ethylenediamine diacetic acid sodium salt. VES was synthesized by N-lauramid-N′-hydroxyethyl ethylenediamine intermediate synthesized in step 1 and sodium chloroacetate. The optimal condition was: the molar ratio of intermediate to sodium chloroacetate was 1:2.5, reaction temperature was 90~95°C, reaction time was 16h, solvent was mixture of alcohol and water, the content of water was less than 20%, the loading temperature was 60~65°C, and pH of reaction was about 7~8.

The N-lauramid-N′-hydroxyethyl ethylenediamine intermediate that was synthesized in the first step recrystallized with acetone as the solvent for purification. Synthesis N-lauroyl-N’-hydroxyethyl ethylenediamine diacetic acid sodium salt VES was considered to recrystallize with mix solvent of ether -alcohol and purification was done through regulating pH by solution of sodium hydroxide. The chemical structure of the purified intermediate and the final product were certified by fourier transform infrared spectroscopy.

References

[1] M. Frank, G. Bellis , U.S. Patent 3,225,074. (1965)
[2] V. Bade, E. Fed, U.S. Patent 4,832,871. (1989)
[3] V. Bade, E. Fed, U.S. Patent 4,861,517. (1989)
[4] D. Alleman, Q. Qi, R. Keck, The development and successful field use of viscoelastic surfactant-based diverting agents for acid stimulation, SPE 80222 (2002).
[5] S. Iglauer, Y. Wu, P. J. Shuler, Y. Tang, W. A. Goddard, Tenside Surfactants Detergents 48(2011) 121-126.
[6] Y. Wu, S. Iglauer, P. J. Shuler, Y. Tang, W. A. Goddard, Tenside Surfactants Detergents 47 (2010) 280-287.
[7] Y. Wu, S. Iglauer, P. J. Shuler, Y. Tang, W. A. Goddard, Tenside Surfactants Detergents 47(2010) 152-161.
[8] S. Iglauer, Y. Wu, P. J. Shuler, Y. Tang, W. A. Goddard, Journal of Petroleum Science and Engineering, 71(2010) 23-29.
[9] S. Iglauer, Y. Wu, P. J. Shuler, Y. Tang, W. A. Goddard, Tenside Surfactants Detergents 47 (2010) 87-97.
[10] S. Iglauer, Y. Wu, P. J. Shuler, Y. Tang, W. A. Goddard, Colloids and Surfaces A: Physcochemical and Engineering Aspects 339(2009) 48-59.
[11] Z. Zhao, X. Yang, S. Lian, X. Zhang, Oilfield Chemistry 22(2005) 307-310.
[12] Y. Zheng, PhD Thesis, Southwest Petroleum Institute, 2005, Chengdu, China.
[13] Y. Zheng, L. Zhao, P. Liu, Oilfield Chemistry, 22(2006) 302-306.
[14] K. Ai, Q. Li, Z. Yuan, L. Zhao, C. Pan, Oil Drilling and Production Technology 30(2008) 71-74.
[15] Z. Zeng, J. Guo, Henan Petroleum (China) 19(2005) 47-50.

doi:10.4028/www.scientific.net/AMM.161.236

Analysis of Structure and Thermal Performance of Roof with reinforced Concrete Prefabricated Corrugated Board

LI Li，BAI Xian-chen，GUO Ji-ping

Faculty of Civil Engineering and Architecture, Henan University, Henan Kaifeng 475004, China,

lylylee@ henu.edu.cn, baixc@ henu.edu.cn, guomarksman@qq.com

Key words: traditional roof; prefabricated corrugated board; structure; thermal performance

Abstract:

This article aims at solving the problems of waterproof layer aging, hollowing, deformation and cracks and other major issues in the process of use of the traditional flat roof. On the basis of using traditional materials on the flat roof, basic-level structure of the roof is designed into reinforced concrete prefabricated corrugated board. Through the analysis of its structure and the thermal performance, this article attempts to explore the adaptability, and the promotion of reinforced concrete pre-cast groove board flat roof structure technology in the new countryside construction.

1 Introduction

The flat roof in the countryside residence construction is the commonly used one kind of roof form, and the traditional flat roof often presents the phenomena of the roofing waterproof layer aging, spatial drum and crack in the process of use, which brings about the following results: the roof seeps and the heat insulation performance reduces or even expires. While reducing the house durability and service life, it also seriously influences house normal use. Because the countryside residence construction quantity is big, environment climate condition, economic development level and housing and life style in different parts are different, moreover, people cannot imitate municipal housing construction pattern [1-3] blindly. Therefore, according to the new countryside residence construction request, unifying the Henan Province sentiment and the present countryside residence construction situation, people make some improvements and transformation to the traditional flat roof, expecting to form technical and economical reasonable feasible roof structure technology in the new countryside residence construction.

2 The flat roof problems and analysis of the reasons

For asphalt parent metal waterproofing material used on flat roof roofing waterproof layer, because of such outdoor synthesis factors such as the sunlight radiation, the cold hot alternation and so on, the asphalt oil and the resin featherweight component will change into the great molecular weight asphalt nature component, asphalt nature component gradually increases, reducing the plasticity of the bituminous material, increasing brittleness, thus causing the roofing waterproof layer aging embrittlement and the roof leakage. There is the spatial drum phenomenon in the roofing waterproof layer, and it is mainly because in the process of housing construction, the basic unit is polluted owing to carelessness or there is moisture content in the roof basic unit, causing the asphalt cementing material and the basic unit imperfect adhesion. When it receives the sun shine or the artificial heat, moisture content vaporizes, volume expands, thus creating the waterproof layer spatial drum. For those houses which are heated during the winter, because the differences between the indoor and outdoor temperatures and humidity are big and the steam partial pressure is bad, the roof building enclosure is also carrying on the steam seepage conduction during heat transfer, the roof building enclosure's steam seepage will also cause the roof waterproof layer spatial drum phenomenon under the controlled condition. When the roof building enclosure interior has the condensation or the roofing waterproof layer aging bursts, and when roofing water leakage permeates heat insulating layer, which will increase the roof insulation material moisture content, the roof heat preservation heat insulation ability and the energy conservation effect will be reduced.

3 Prefabricates the trough board flat roof mechanical design

"USD" roofing developed by overseas researchers, although, may, theoretically, slow down the traditional roofing waterproof layer material component from the progressively changing aging, in practice and in the process of application, this structure procedure proposed both the waterproofing to the thermal insulation material and the durable dual request. Because in the present projects the universally used thermal insulation material is basically the non-water resistant material, therefore "USD" the roofing application also treats further researches and promotions [4-5], it is especially difficult to use and promote in the general countryside area. We, on the basis of the traditional roof structure procedure, mainly carry on the shape transformation design to the roof structure level, changing the design from the reinforced concrete prefabrication structure strip board to corrugated board, other structure level of the roof is intact, and commonly used thermal insulation material such as the inflated pearlite, the foam concrete and so on are still selected as the thermal insulation material, thus enabling the roof building enclosure to achieve the impervious anti drip and the heat preservation heat insulation effect.

Reinforced concrete prefabrication trough board flat roof fundamental construction as is shown in Figure 1, the material selection and the performance are as shown in table 1. The trough board's length and thickness may be the same as the ordinary reinforced concrete prefabrication structure strip board, may also be adjusted according to the mold notational system request. Based on the height request of ventilation of the roof to be built on stilts, the board trough's free height design is 150mm, including buckles, the board thickness (50mm) and thermal insulation material thickness, the intercalated bed between the duplicate lap and the waterproof layer reaches the height of over 200mm, satisfying the height request of the air intercalated bed of the ventilation of the roof, particularly omitting the tradition of using the trough board's side bar to ventilate the roof by putting aside the duplicate lap's brick to pile up, thus organically unifying it with the structure board. From the point of view of draining water from the roofing and preventing the roof leakage, this structure also displayed the remarkable relative superiority, the draining water trench which the trough board formed naturally has provided the condition for draining water from the roofing in precipitation season, the duplicate lap's establishment has avoided the solar radiation to the waterproof layer direct radiation, and has protected the roofing organic material waterproof layer from aged embrittlement effectively. Because the roof leakage is generally realized by permeating through the structure board between board seams and affects indoor, this structure causes a certain height between the structure board (150mm), even if the layer of draining water presents crack, the roof leakage will not pour into the seam, thus achieving the effect of the roof preventing leakage itself.

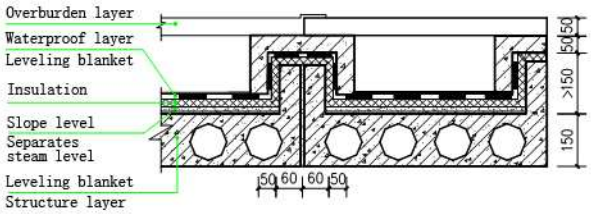

Figure 1. The reinforced concrete prefabricated groove plate flat roof structure

Table 1 Reinforced concrete prefabricated groove plate roof structure and material properties

Tectonic level	Material name	Laminate Thickness (mm)	Coefficient of thermal conductivity (W/m·K)	Coefficient of thermal storage W/m^2·K)	Thermal resistance (m^2·K/ W)
Structure layer	Reinforced concrete groove plate	150	1.74	12.4	0.086
leveling blanket	compo	20	0.93	11.37	0.022
insulation	Different choices	d_3	λ_3	S_3	R_3
leveling blanket	compo	20	0.93	11.37	0.022
waterproof layer	SBS modified asphalt coil	3	0.17	3.33	0.059

4 Flat roof precast groove plate thermal performance analysis

4.1 Roof computation model of palisade structure

The Henan Province occupies five geographic latitudes from north to south, and outdoor average air temperature of the hottest and coldest months of typical areas through years is shown in table 2[6]. By comparing with our country construction hot working design district standard, the south and the north of Henan Province are in the construction hot working design district separately, namely in the area where it is hot in summer and cold in winter and in the cold area, namely "a province two areas". In view of the different areas' climatic conditions, the key of this structure lies in the selection and thickness calculation of the heat preservation thermal insulation layer material.

Table 2 Main representative areas of Henan province in typical outdoor air temperature

The main representative area	Zhengzhou	Kaifeng	Luoyang	Xingxiang	Anyang	Puyang	Shangqiu	Xinyang	Nanyang
Coldest month outdoor average temperature(℃)	-0.3	-0.5	-0.3	-0.7	-1.8	-2.2	-0.9	1.6	0.9
Hottest month outdoor average temperature(℃)	27.2	27.0	27.4	27.0	26.9	26.9	27.0	27.6	27.3

On the basis of using the commonly used heat preservation thermal insulation material, in agreement with the construction hot working design requirements of the different hot working area, people can determine the thermal resistance of the roof and the thickness of heat preservation thermal insulation material through computation. When people choose different heat preservation thermal insulation material, the thickness of the heat preservation thermal insulation material level satisfying different local hot working request is different too. This article takes winter heat preservation of Henan Zhengzhou area as example, determining this roof insulation material level thickness through computation. For several other representative areas in Henan, people can make similar computation. The actual total thermal resistance R_0 of the roof and the smallest thermal resistance will be determined by formulas (1) and (2) respectively:

$$R_0 = R_i + \Sigma R + R_e \tag{1}$$

in the formula: R_0 is the roof building enclosure actual total thermal resistance (m^2·K/ W), and R_i, R_e are the roof building enclosure surface thermal resistance inside and outside respectively (m^2·K/ W), and ΣR is the total amount of various materials level thermal resistance of the roof (m^2·K/ W).

$$R_{0.\min} = \frac{(t_i - t_e)}{[\Delta t]} nR_i \tag{2}$$

in the formula: $R_{0.\min}$ is the smallest thermal resistance of the roof building enclosure (m^2·K/ W); t_i, t_e are winter indoor air calculated temperature and outside air calculated temperature respectively (℃), according to Table 3 value [3]; R_i is the thermal resistance of the roof building enclosure internal surface (m^2·K/ W), the figure being 0.11; For the temperature difference correction coefficient n, the figure being 1.0; For the permission temperature difference between indoor air and the roof building enclosure internal surface $[\Delta t]$ (℃), the figure being 4.0[7].

Table 3 Representative local winter outdoor calculated temperature (℃)

Represent regions	Ⅰ	Ⅱ	Ⅲ	Ⅳ
Zhengzhou	-5	-7	-9	-11
Xinyang	-4	-7	-10	-12
Anyang	-7	-11	-13	-15
Shangqiu	-6	-9	-12	-14
Luoyang	-5	-8	-10	-12

4.2 Roof building enclosure heat insulating layer proper most memoirs thermal resistance R computation

According to the construction building enclosure heat preservation design requirements, the roof building enclosure's actual thermal resistance R_0 should not be lower than the smallest thermal resistance $R_{0.\min}$, according to the above requests, it is possible to calculate the smallest thermal resistance R which the roof building enclosure heat insulating layer should have:

$$R \geq \frac{(t_i - t_e)}{[\Delta t]} nR_i - (R_i + R_e) - (R_1 + R_2 + \cdots\cdots + R_n) \tag{3}$$

Because the reinforced concrete prefabrication trough spatial core board belongs to the built-up section, therefore when people calculate the reinforced concrete prefabrication trough spatial core board thermal resistance, its average thermal resistance $\overline{R}$ and the average regeneration coefficient $\overline{S}$ should be determined by the weighing computation of the built-up section material level thermal resistance formula:

$$\overline{R} = \left[\frac{F_0}{\frac{F_1}{R_{0.1}} + \frac{F_2}{R_{0.2}} + \cdots\cdots + \frac{F_n}{F_{0.n}}} (R_i + R_e) \right] \varphi \tag{4}$$

in the formula: $\overline{R}$ is average thermal resistance of the reinforced concrete prefabrication trough spatial core board (m^2K/W), F_0 is total transfer heat area perpendicular to the heat flow direction (m^2), F_1, F_2, … F_n refer to all heat transfer area divisions parallel to the heat flow direction (m^2), thus successively thermal resistance of all heat transfer spots are $R_{0.1}$, $R_{0.2}$, … $R_{0.n}$ (m^2·K/ W), φ is the correction coefficient in turn, according to Table 4.

Table 4 Correction coefficient φ value

λ_2 / λ_1	0.09～0.10	0.20～0.39	0.40～0.69	0.70～0.99
φ	0.86	0.93	0.96	0.98

$$\overline{S} = \frac{S_1F_1 + S_2F_2 + \cdots\cdots S_nF_n}{F_1 + F_2 + \cdots\cdots F_n} \tag{5}$$

in the formula: F_1, F_2, $\ldots F_n$ are heat transfer area divisions parallel separately to the heat flow direction (m^2), and S_1, S_2, $\ldots S_n$ are the material regeneration coefficient in each heat transfer area ($W/m^2 \cdot K$).

4.3 Roof building enclosure heat insulating layer proper smallest thickness d computation

After calculating the smallest thermal resistance of the roof, according to the thermal insulation material type, in accordance with the project (6) people can calculate and determine the proper smallest thickness of the roof building enclosure heat insulating layer. Calculated heat insulating layer thickness is valued according to the modulus, its thermal inertia target must be calculated to test whether it is appropriate. Otherwise, it must be chosen according to the appropriate thermal inertia target, then make the calculation. In this article in calculating hot working parameter of the steel bar tong prefabricated trough board flat roof, several kinds of common thermal insulation materials such as the inflated pearlite, the foam concrete, the polystyrene froth plastic film and so on are chosen. For the computation results, see Table 5 and Table 6.

$$d = R \times \lambda \tag{6}$$

Table 5 Thermal insulation material selection and hot working target

Material name	Key property request				Thermal conductivity predicted value (W/m·K)	Regeneration coefficient predicted value($W/m^2 \cdot K$)
	Coefficient of thermal conductivity (W/m·K)	Coefficient of thermal storage (W/m2·K)	Compressive strength (MPa)	Dry weight density (kg/m^3)		
Cement inflated pearlite board	0.16	2.49	≥0.3	400	0.240	3.735
Air entrainment concrete slab	0.19	2.81	≥0.4	500	0.285	4.215
Polystyrene froth plastic film	0.042	0.36	≥0.1	20～30	0.055	0.468

Table 6 Zhengzhou area heat insulating layer should have smallest thickness

Cement inflated pearlite board		Air entrainment concrete slab		Polystyrene froth plastic film	
Smallest thickness(mm)	Thermal resistance (m^2.k/w)	Smallest thickness(mm)	Thermal resistance(m^2.k/w)	Smallest thickness(mm)	Thermal resistance (m^2.k/w)
90	0.362	130	0.362	20	0.362

5 Conclusion

(1) The steel bar tong prefabricated trough board flat roof structure can satisfy multiple specifications of the roof impervious anti drip and the heat preservation heat insulation and so on, and it has the widespread project serviceability. Through designing and adjusting roof structure board structure's shape and size, the purpose of postponing roofing waterproof layer aging, crack and preventing the roof leakage may be achieved。

(2) The air intercalated bed built on stilts of the roof whose air intercalated bed thickness is not smaller than 200mm can be formed by using the trough structure board's side bar is. It has the heatproof function of ventilating the roof if used in the summer heatproof area.

(3) In the winter heat preservation area, according to the different areas' climatic conditions and the hot working design requirements, commonly used cement thermal insulation materials such as inflated pearlite, aeroconcrete and polystyrene foam plastics may be chosen, and people can determine the thermal insulation material placing thickness through computation, thus this method can enable people to freely choose different materials and it also has the local compatibility.

Reference:

[1] Ye Linchang. Several suggestions on roofing waterproofing [J]. new building material, 2004 (3):30-33..

[2] Xiong Ying. On the residential building energy conservation designs [J]. engineering construction and design, 2005(2):46-47.

[3] Jia Ruiying, Jide Yun. the energy conservation economic efficiency analysis of the change from the slope roof to even roof. Industrial architecture, 2006(5):40-41.

[4] Liu Fulin, Pan yuqin, Du Yongheng. Brief analysis of heat preservation and heat insulation performance in villages and small towns housing roofing in Henan province [J] energy conservation technology, 2010. (2):158-164.

[5] Zhu Yingbao. The application of thermal insulation material in construction energy conservation [M]. Beijing: The Chinese Building materials Industry Publishing house, 2004.

[6] The residence construction energy conservation design standard of Henan Province (DBJ41/071-2006) [S]. Beijing: China radio and television university Publishing house, 2006.

[7] People's Republic of China Ministry of construction. Civil construction hot working design standard (GB50176-93)[S]. Beijing: China Plan Publishing house, 1993.

doi:10.4028/www.scientific.net/AMM.161.242

Performance Research of Positive Pressure Bio-Protection Suit Polyurethane Antibacterial Composite Fabric

Jin-hui Wu[1,a], Tao Tian[1,b], Li-mei Hao[1], Jing-quan Yang[1], Zheng Wang[1,c]

[1:] (Institute of Military Medical Equipment Tianjin, National Biological Protection Engineering Center, Tianjin 300161, China)

[a:] wujh@npec.org.cn, [b:] tiant@npec.org.cn, [c:] wangzh@npec.org.cn (corresponding author)

Keywords: anti-bacterial composite fabric; polyurethane, positive pressure bio-protection suit, performance challenge.

Abstract: **Objective** To study performance of positive pressure bio-protection suit fabric composited with polyurethane antibacterial film on double-sided, and to evaluate the feasibility of developing the positive pressure bio-protection suit with the composite fabric. **Methods:** Testing such performance as physical, protective, decontamination and antibacterial properties of polyurethane antibacterial composite fabric by standard methods. **Results:** Physical performance and micro-organisms liquid penetration resistance of the composite fabric have reached related standards requirements, while performances have no significant changes after decontamination testing. And its inhibition rates to gram-positive and gram-negative bacteria were so good that could reach 99%. **Conclusions:** According to testing results, this kind of fabric is suitable for developing positive pressure bio-protection suits by its ideal performance indicators and its upstanding decontamination consumption, antibacterial, flexible and lightweight properties.

1 Introduction

In recent years, infection rate of AIDS, tuberculosis, viral hepatitis and other highly pathogenic infectious diseases is higher. Natural disasters, biological safety accidents, bioterrorisms and other public health emergencies are also occurred occasionally. These conditions caused highly pathogenic, infectious and unknown pathogenic microorganisms, which serious threatened and effected people's life and health. Considering personnel safety and environmental suitability, the positive pressure bio-protection suit was selected as a dedication PPE(personal protective equipment) in the" laboratory bio-safety manual", released by WHO(World Health Organization)[1].

Positive pressure bio-protection suit also known as Air-fed pressured suit, is a kind of reusable special protective clothing which can protect people's head, facial, body, hands, feet and respiratory from exposuring to biological hazard environment. To be precise, the pressure gradient of the protective suit could protect people from harmful substances in a higher protection level P[2]P because its inner gas pressure is higher than the environment, and it was a physical barrier to block people exposed to radioactive dusts, aerosol, bioaerosol, splashes and so on in the polluted area. Therefore, people is strict with its fabric due to working environment of the positive pressure bio-protection suit was in higher hazard.

People who dresses positive pressure bio-protection suit always need to do some more elaborate operation, this requires fabrics of positive pressure bio-protection suit not only have excellent air tightness, resistance to liquid penetration resistance and mechanical properties, but also

sufficient flexibility and portability[3]. Fabrics of positive pressure bio-protection suit must have excellent tolerance performance of chemical decontamination agent because it must be decontaminated after it was used.

In order to achieve special requirements of positive pressure bio-protection suit fabrics, some research institutions have developed a variety of composite fabrics in succession. It is great that some of the fabrics have practical application in the suits' production. For example, DELTA© of French produced positive pressure bio-protection suit used a kind of PVC (polyvinyl chloride) composite material fabric, in spite of its weight is up to 330 g / m^2 [4], which has good mechanical strength, flexibility, and tolerance performance of chemical decontamination agent. HVO ISSI © of Germany developed a kind of special PVC fabric with an excellent resistance to acid and alkali, except its correspondingly massive and unideal flexibility. Rolamit® fabric of Switzerland is a multi-purpose laminating film material, which with thickness of 100 μm and weight of 150 g / m^2, could obstruct mustard gas for 24 h. People thought this fabric as a representative of higher level protective fabrics for its good mechanical properties, resistance to breakage and puncture resistance performance[5].

PU(polyurethane) material was widespread concerned in developing composite fabrics, but mainly in the latest years, by its excellent physical properties, stability, environmental adaptability, and shape memory characteristics[6]. So fabrics compounded of Polyurethane have potential advantages to develop positive pressure bio-protection suits for its flexible and lightweight performance. In the paper, we discuss a kind of polyurethane anti-bacterial composite fabric which was developed by compounding polyurethane film on the two surfaces of a knitted basal fabric, evaluate its mechanical properties, protective properties, anti-bacterial and tolerance performance of chemical decontamination agent, and analyse its practicability and advantages in developing positive pressure bio-protection suits.

2 Materials and methods

2.1 design of the polyurethane anti-bacterial composite fabric

Shown in Figure 1, antimicrobial quaternary ammonium salt (Dow Corning© 5700® of U.S.) was added in polyether polyurethane mother liquor by 1% (w / w). Then you can see Tthe liquor was made into two kinds of polyurethane antimicrobial films after fully stirred, with thickness of T0.1

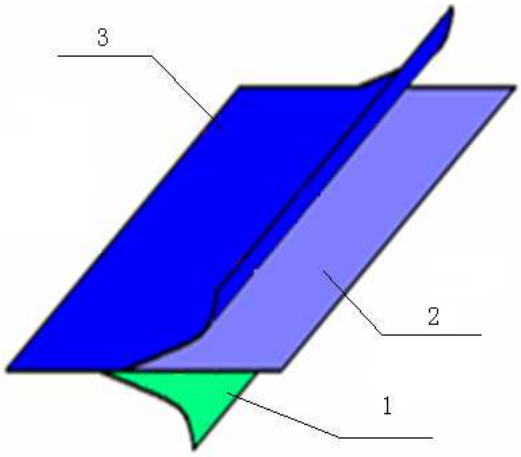

Fig 1 Structure of polyurethane antibacterial composite fabric
1, 0.1 mm thick polyurethane membrane; 2, 240T PONGEE stockinet; 3, 0.2 mm thick polyurethane membrane

mm and 0.2 mm respectively. The polyurethane anti-bacterial composite fabric was developed by the way of heating and rolling two kinds of polyurethane antimicrobial films on the two surfaces of 240T PONGEE stockinet. The thickness of the polyurethane anti-bacterial composite fabric is about 0.4mm, and the weight of per square meter is 180 g/m^2. In addition, the composite fabric, like some PVC fabric, also has a high-frequency thermal processing performance. The side of 0.2 mm polyurethane film of the composite fabric could be used as the fabric surface for its high strength and smoothness while the other side with 0.1mm polyurethane film, could afford better feel and sense of the body for its flexibility

2.2 Physical properties experiment of polyurethane anti-bacterial composite fabric

Physical properties of polyurethane anti-bacterial composite fabric were challenged by methods provided by international or Chinese standards. Standard ISO 16602:2002[7] and EN 943-1:2002[8] were referenced to estimate whether the fabric could meet the necessary of positive pressure bio-protection suit or not. We carry out the experiment follow ISO 16602:2002 standard: samples were placed in a vessel with temperature of 70 ℃ and -40 ℃ respectively for 8 h, then completed the test in 5 min after they were taken out of the vessels. (Major experiment items, reference standard and the instruments were shown in Table 1.)

Tab 1 Methods and apparatus of physical properties examination of polyurethane antibacterial composite fabric

Challenge items	Reference standards	instruments
Tensile strength	GB/T3923.1-1997	5800 universal materials testing equipment , Instron, U.K.
Puncture resistance	GB/T20655	
Tensile strength of seam	GB/T13773.1-2008	
Tear strength	GB/T3917.3	
Abrasion resistance	GB/T21196.2-2007	TSE-A30 wear tester, TST, Germany
Resistance to permeation by liquids	GB/T4744-1997	YG825 Fabric hydrostatic pressure tester, Ningbo, China
Tensile strength after heat treatment	GB24539-2009	5800 universal materials testing equipment , Instron, U.K.
Tensile strength after refrigeration treatment	GB24539-2009	5800 universal materials testing equipment , Instron, U.K.

2.3 Defending performance experiment of polyurethane anti-bacterial composite fabric

Penetration resistance to blood-borne pathogens and liquid containing microorganism of the polyurethane anti-bacterial composite fabric were challenged by the method of standard ISO 16604-2004, while the instrument was set up in accordance with standard ISO16604-2004. And *Phage Phi-X174*, *poliovirus*, *bacillus subtilis*, *white candidiasis* and synthetic blood were selected as testing liquids respectively.

2.4 Tolerance performance to chemical decontamination agents challenge of polyurethane anti-bacterial composite fabric

Tolerance performance to chemical decontamination agents of polyurethane anti-bacterial composite fabric was challenged according to "disinfection technical specifications (2002 edition)" of China. We tested physical properties changes of the composite fabric after it was repeatedly decontaminated by disinfectants and disinfection method of biological protective clothing. Methods are summarized as following:

polyurethane anti-bacterial composite fabric samples were soaked in 1000 mg/L bromine Hain® (HTC©) and 2000 mg/L Sodium trichloro isocyanuric (Jian Zhi Su®) respectively and disinfected for 30min. Then took out samples and dried, tested their tensile strength and penetration resistance after they were treated by the Above-mentioned method for 5 times.

2.5 Anti-bacterial performance experiment of polyurethane anti-bacterial composite fabric

According to standard GB/T 19344-2008 part III: oscillation method, anti-bacterial rates of polyurethane anti-bacterial composite fabric to *Staphylococcus aureus* (ATCC 6538) and *E. coli* (8099) were tested. (Inoculated *Staphylococcus aureus* (ATCC 6538) and *E. coli* (8099) on nutrient agar 1 day at 37 ℃ before the experiment, and made suitable concentration of bacterial suspension solutions (1×10^8 CFU/mL) with sterile saline in 4 ℃ before they were used.)

Polyurethane anti-bacterial composite fabric samples were placed into flasks filled with sterile saline. Then flasks were oscillated for 1 hour under certain conditions after bacterial suspension solutions were added. Caculate the bacterial rate by comparing 1 milliliter solution with blank sample. Please see below equation [9].

$$E = \frac{C_0 - C_1}{C_0} \times 100\% \quad (1)$$

Where: E: anti-bacterial rate, C_0: colonies on control samples; C_1: colonies on testing samples.

3 Results and discussion

3.1 Physical properties of polyurethane anti-bacterial composite fabric

Physical properties testing results of polyurethane composite fabric antibacterial were shown in Table 2. From Table 2, we can see physical properties of polyurethane fabric antibacterial could reach level 4 or above, in addition to wear resistance(level 3). The tensile strength of the fabric did not die down after the temperature treatment.

Tab 2 Physical properties examination results of polyurethane antibacterial composite fabric

Challenge items	Challenge results		Reach the level according to referenced standards
	longitude	latitude	
Tensile strength	652	306	4（>250）
Puncture resistance	100	78	4（>60）
Tensile strength of seam	620	230	4（>150）
Tear strength	132		4（>100）
Abrasion resistance	>500		3（>500）
Resistance to permeation by liquids	>120		*6（>50kPa）*
Tensile strength after heat treatment	690	285	4（>250）
Tensile strength after refrigeration treatment	699	292	4（>250）

3.2 Protecting performance of polyurethane anti-bacterial composite fabric

Penetration resistance testing results of polyurethane anti-bacterial composite fabric to blood-borne pathogens and liquid containing microorganism were shown in Table 3. Results showed that penetration resistance of the composite fabric to *Phage Phi-X174*, *poliovirus*, *bacillus subtilis*, *white candidiasis* and synthetic blood was very well, even under the condition of 20 KPa. It means protective performance of the composite fabric could achieve the highest level requirement of referenced standards.

Tab 3 Micro-organisms liquid penetration resistance examination results of polyurethane anti-bacterial composite fabric

Micro-organism	Challenge pressure（KPa）					
	0	1.75	3.5	7	14	20
Phage Phi-X174	-	-	-	-	-	-
poliovirus	-	-	-	-	-	-
bacillus subtilis	-	-	-	-	-	-
white candidiasis	-	-	-	-	-	-
synthetic blood	-	-	-	-	-	-

"+" Representing micro-organisms be detected. "-" Representing micro-organisms be not detected.

3.3 Tolerance performance of polyurethane anti-bacterial composite fabric to chemical decontamination agents

Tolerance performance testing result of polyurethane anti-bacterial composite fabric to chemical decontamination agents was showed in Table 4. The microbial liquid penetration resistance of the composite fabric still can achieve 20Kpa while its tensile strength is slightly decreased after 5 times decontaminated with bromine and chlorine disinfectants, but it also could achieve level 4 requirement of referenced standards.

Tab 4 Decontamination consumption performance examination results of polyurethane antibacterial composite fabric

Group	microbial liquid penetration resistance（KPa）	Tensile strength（N）	
		longitude	latitude
The control group	20	652	306
Treated by bromine Hain® (HTC©)	20	600	255
Treated by Sodium trichloro isocyanuric (Jian Zhi Su®)	20	620	281

3.4 Antibiosis performance of polyurethane anti-bacterial composite fabric

Antibiosis performance testing results of polyurethane anti-bacterial composite fabric were showed in Table 5. It indicated that anti-bacterial rates of the composite fabric to *Escherichia coli* and *Staphylococcus aureus* has good antibacterial properties, which could achieve more than 99%.

Tab 5 Anti-bacterial performance testing results of polyurethane antibacterial composite fabric

Group		C_0 （CFU/ml）	C_1 （CFU/ml）	anti-bacterial rate（%）	Average anti-bacterial rate（%）
Escherichia coli（8099）	1	1.76×10^6	5250	99.702	99.704±0.0021
	2		5178	99.706	
	3		5235	99.703	
Staphylococcus aureus（ATCC 6538）	1	1.31×10^6	4312	99.671	99.669±0.0029
	2		4407	99.671	
	3		4379	99.666	

3.5 Discussion

According to ISO 16602:2002 and EN 943-1:2002 standards, performance classify of gas-tight protective clothing fabric would not lower than level 3. Just similar to gas tight chemical protective clothing, fabric of positive pressure bio-protection suit also need to achieve this standard. This thesis proceeded the mechanical properties, protective properties, anti-bacterial and tolerance performance of chemical decontamination agent test on the positive pressure composite fabric， which with compounding polyurethane film on the two surfaces of a knitted basal fabric. Results showed this fabric completely meet the need of production of positive pressure bio-protection suit, because the performance of polyurethane anti-bacterial composite fabric could reach the reference standard. And it still could reach the level 3 after it was disinfected by bromine and chlorine decontamination agents, in despite of a slightly decreasing of the tensile strength.

Moreover, the flexibility of the fabric was very good by its elongation at break could achieve 110% or more. Comparing with France DELTA© PVC fabric, polyurethane anti-bacterial composite fabric was lighter, its weight was only 180g per m^2. So people may feel more lighter and comfortable when they wear the positive pressure bio-protection suit which made of the polyurethane anti-bacterial composite fabric. Wearing this kind of positive pressure bio-protection suit, you will feel more comfort and softer, because its weight is only about 5 Kg, including powerful air fed system, boots and other accessories.(see fig 2)

Fig 2 A kind of positive pressure bio-protection suit made of the polyurethane anti-bacterial composite fabric

As a fully enclosed reusable system, unlike general bio-protection suit, positive pressure bio-protection suit must be cleared by spray, wipe and other decontamination methods after it was used. Closed structure of positive pressure bio-protection suit makes its internal difficult or unable to clean. This may effect people's physical and mental health when they wear the suit which with microbial growth and odor after been repeated worn. The high anti-bacterial performance of the polyurethane anti-bacterial composite fabric described in the paper could enhance people's security with non-micro-organisms while keep its interior clean and lessen its maintenance cost.

4 Conclusions

In the paper, it comes to the conclusions as follows.

(1) A kind of polyurethane anti-bacterial composite fabric was developed by compounding polyurethane film on the two surfaces of a knitted basal fabric. And its mechanical properties, protective properties, anti-bacterial and tolerance performance of chemical decontamination agent were roundly tested.

(2) All the performances of polyurethane anti-bacterial composite fabric could achieve requirements of the air tight protection suit. The fabric could be used for developing of positive pressure bio-protection suit with its favourable anti-bacterial performance.

(3) In addition, the polyurethane anti-bacterial composite also has some excellences for developing new typical positive pressure bio-protection suit in the future, such as light weight, strong flexibility, soft and so on, which may overcome the ponderosity and discomfort of nowaday positive pressure bio-protection suits [10].

Acknowledgments

We gratefully acknowledge the financial support of National Major Science & Technology Projects of China (No.2009ZX10004-703).

References

[1] Henry N. W. Four decades of protective clothing development and standardization[J]. J. Chem. Health Safety ,2007,5(3):135-136.

[2] SHEN Feng, Li Tai-hua, Li Yu-fen. One-piece positive-pressure protective suite and its independent source of air supply system in BSL-4 laboratory[J]. Chinese Medical Equipment Journal,2005,26(11):15-17.

[3] Li He-guo, Liu Bin, Li Lei, et al.. Technology of Protective Clothing against Biological and Chemical Material[J]. CHINA PERSONAL PROTECTIVE EQUIPMENT, 2003(3):25-28.

[4] Tian Tao, Duan Hui-li, Wu Jin-hui, et al..Current Situation of Worldwide Biochemical Protective Clothing and Chinese Countermeasures[J]. Chinese Medical Equipment Journal, 2008,29(7):29-31.

[5] Li He-guo, Liu Bin, Li Lei, et al.. Chemical protective clothing materials technology development analysis[A]. Chinese Chemical Society Twenty-fifth Annual Meeting Abstract Corpus (the next volume)[C], 2006.

[6] Yang Jing-quan, Tian Tao, Duan Hui-li, et al.. PROTECTIVE CAPABILITY OF HYDROPHILIC POLYURETHANE MEMBRANE COMPOSITE MATERIAL AGAINST BACTERIA[J]. CHINESE JOURNAL OF DISINFECTION, 2008,25(2)123-125.

[7] Protective clothing for protection against chemicals – Classification, labeling and performance requirements, NEQ[S]. ISO 16602:2002.

[8]Protective clothing against liquid and gaseous chemicals, including liquid aerosols and solid particles – part 1: performance requirements for ventilated and non-ventilated ”gas-tight”(type 1) and “non-gas-tight”(type 2) chemical protective suits[S]. EN 943-1:2002.

[9] Wang Jun-qi, Wang You-bin, Xue Jin-rong, et al.. Study on the detection methods of anti-bacterial function of textile products[J]. CHINESE JOURNAL OF PUBLIC HEALTH ENGINEERING, 2003, 2(3):129- 132.

[10] Wu jin-hui, Tian tao, Lin song, Hao li-mei, Wang zheng, Yang jing-quan. Development of Air-fed Pressurized Biological Protective Suit[J]. CHINA PERSONAL PROTECTIVE EQUIPMENT, 2009,26(11):15-17.

doi:10.4028/www.scientific.net/AMM.161.250

Processing and Properties of Plate 3D Braided Material Based on Space Group $P\bar{3}$ Symmetry

Wensuo Ma[a], Chuang Xu[b], Kai Li[c] and Lingling Zhang[d]

School of Mechatronics Engineering, Henan University of Science and Technology, Luoyang 471003, Henan, China

[a]mawensuo@126.com, [b]xunmeng053@163.com, [c]likai@163.com,[d]zhanglingling@126.com

Keywords: Point Group *S*6, Space Group $P\bar{3}$, Plate 3D Braided Material, Processing and Properties

Abstract. A novel geometry structure of unit cell was deduced by using the point group *S*6 corresponding to symmetry operations. Based on the symmetry of space group $P\bar{3}$, a new 3D braided material was obtained by transforming the new unit cell symmetrically. The plate processing corresponding to this geometry structure was studied. The fiber volume percentage and its variation tendency of the 3D braided material were predicted through establishing mathematical model.

Introduction

Much attention has been given to the 3D braided composite because of its outstanding combination performance in the aerospace, defense and medical industry. Restricted by the braiding process and other factors, 3D braided composites are of very a few of varieties, low processing efficiency and high processing cost. In order to obtain the braided composite materials with better combination performance, it is urgent to research and develop more 3D braided processes. At present, most researches still focused on four-step and two-step method of braided process, the research work in the prediction of new 3D braided process is still in the start-up period [1-4].

The crystals with different lattice structure have different performances. The geometric structure of crystals can be classified using crystal symmetry group theoretical methods. Referring to the research methods on symmetry group, inductive research on unit geometry structures of 3D braided material has been carried out, and many of new 3D yarn-cross structures have been deduced by using the space group and space group symmetry operations [4]. However, the feasibility of new 3D braided process and the potential material properties have not been researched. Under the condition of satisfying all space point group symmetry operations, a new unit-cell with yarn-cross structures is deduced. A kind of cross geometry structure with continuous yarn can be obtained by putting the unit-cell into space lattice content with its symmetry. A new 3D braided technology can be created through researching its processing intensively.

3D Braided Material Based on Space Group $P\bar{3}$ Symmetry

3D braided geometry structure unit cell content with point group *S*6 symmetry. The group elements of space point group $S_6(\bar{3})$ are S_6^n (values of '*n*' is 1-6), their generating element is S_6. Applying symmetry operations of point group $S_6(\bar{3})$ to the yarn segment shown in Fig.1(a), a kind of combination of yarn segment, as shown in Fig.1(b), can be obtained, which is the representative volume unit used for deriving new 3D braided geometry structure.

(a) A yarn segment (b) Combination of yarn segment corresponding to point group $\bar{3}$

Fig.1 Deducing 3D braided geometrical structure unit-cell With space point group $\bar{3}$

Space simple hexagonal lattice corresponding to space group $P\bar{3}$. A simple hexagonal lattice shown in Fig.2 described by crystal symmetry group coordinated with the space group *S*6. The deduced unit-cell as a lattice point is put into the hexagonal lattice, and a new cross geometry structure with continuous yarn, as shown in Fig.3, can be obtained considering the continuity of the yarn.

Translation symmetry operations corresponding to space group $P\bar{3}$. In the *xyz* coordinate system, translation symmetry operation is

$$T_i = ux_i + vy_i + wz_i$$

Where u, v and w are base vectors.

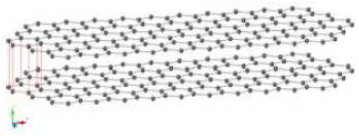

Fig.2 Space simple hexagonal lattice (hP)

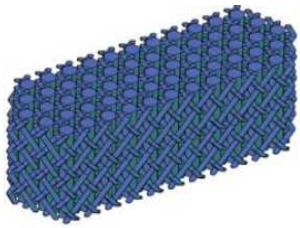

Fig.3 A new continuous yarn geometrical structure

Suppose the thickness of the combination of single layer yarn segment in *z* direction is *t*. In the *xoy* coordinate plane and the plane clusters parallel to it, the translation distance of unit cell is the integer times of diagonal length in the hexagonal section in the *x* or *y* direction, and integer times of 2*t* in the *z* direction.

Considering the feasibility of technology, the axial yarns have been added to new geometry structure shown in Fig.3 without considering the impact on the overall symmetry of the geometric structure in the process of mathematical derivation.Considering the requirements for boundary yarn continuity in real braiding process, if the yarn motion law in the fabric border is studied seriously, an novel 3D braided material can be obtained.

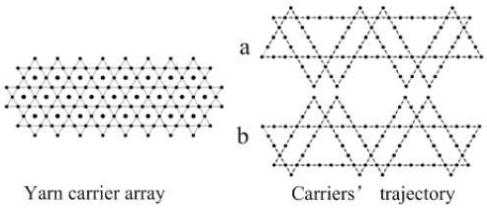

Fig.4 Yarn carrier array and the movement trajectory of the same group yarn

Braided yarn carriers are arranged in the array point, as shown in Fig.4. The enhanced yarns in z direction which are not involved braiding movement are fixed in the hexagonal position.

Braided yarn carriers in the same orbit are in a group. There are two groups in total, named as 'a', and 'b' respectively. In the braiding process, the trajectory of yarn carrier in the same orbit does not change. All yarn carriers in a group move once along the arrow direction, a braiding cycle finished.

Processing of 3D Braided Material on Space Group $P\bar{3}$ Symmetry

A series of novel 3D braided process of fabric based on space group $P\bar{3}$ symmetry can be used to manufacture tabulate and tubular and T-type braided fabric except for hexagonal columnar one. Braided fabrics of different geometrical shapes are shown in Fig.6.

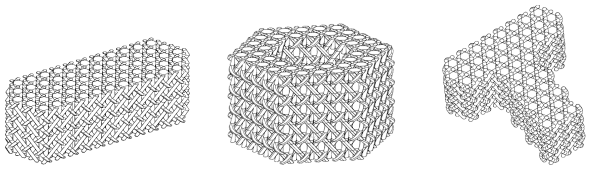

(a) Tabulate fabric (b) Tubular fabric (c) T- type fabric

Fig.5 Braided fabrics of different geometrical shapes

Processing of tabulate braided fabric based on space group $P\bar{3}$ symmetry is shown in Fig.6(a), Carriers and its walking routes of tubular and T-type braided fabric processing are shown in Fig.6 (b) and (c).

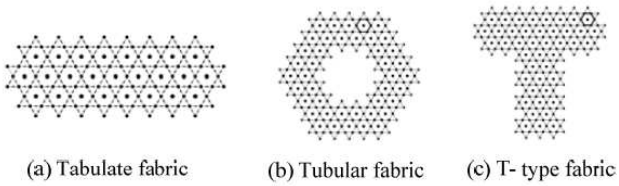

Fig.6 Processing of Braided fabrics

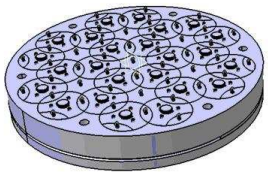

Fig.7 viable processing equipment

The whole carriers are driven continuously according to certain rules, these braided yarns are bring and cross mixed in space.

The viable processing equipment has developed for one of novel 3D braided materials by our group, as shown in Fig.7.

Geometry model of new 3D braided materials

Novel 3D braided geometry structure is expected for the production of new 3D braided composites preform.

Basic hypotheses. Braided yarn is assumed to be elliptical section, the lengths of its two axes are *a* and *b*. The cross-section of yarn in *z* direction is assumed to be regular hexagonal, its size depends on the specific braiding state of fabric.

All braided yarns have the same performance without considering the performance difference caused by the physical damage of braided yarns and other factors.

The whole fabric structure whether the interior, or surface, or corner region has a stable and consistent geometry structure.

3D braided fabrics are divided into interior, surface and corner region, as shown in Fig.9. Respectively, three kinds of unit-cell are interior unit, face unit and corner unit, as shown in Fig.8.

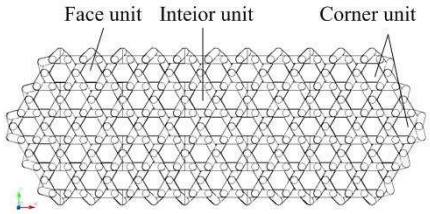

Fig.8 Region and unit-cell of 3D braided fabric

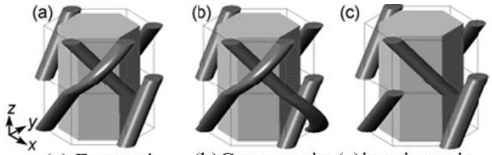

(a) Face unit (b)Corner unit (c)interior unit

Fig.9 Fabric units

Geometric parameters used for describing 3D braided fabric.

(1) Number of braided fabric unit-cells

The number of interior and corner unit and face unit-cell can be expressed separately as N_i , N_c and N_f . Number of braided fabric unit-cells are

$$N = N_i + N_f + N_c \tag{1}$$

(2) Geometry relationship between braided yarn and axial yarn

Geometry relationship between braided yarn and axial yarn can be expressed from Fig.10 as

$$R = \sqrt{b^2 + 3a^2} - \frac{\sqrt{3}}{3}a \tag{2}$$

(3) Braiding angle β of braided yarn

The yarn braiding angle β used for describing braided geometry structure can be expressed from Fig.11 as

$$tg\beta = t / (R + \frac{a}{\sqrt{3}}) \tag{3}$$

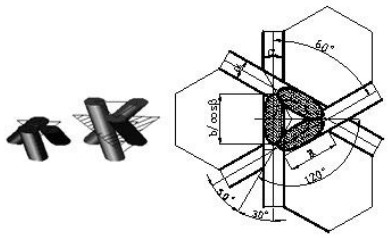

Fig.10 The braided yarns interwoven state between adjacent three unit-cells

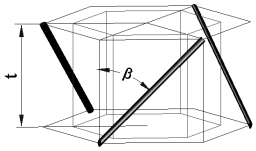

Fig.11 Braided angle β of braided yarn

Substituting Eq. (2) into Eq. (3), there is

$$t = tg\beta\sqrt{b^2 + 3a^2} \tag{4}$$

(4) Fiber volume percentage of the 3D braided fabric

Supposing fiber overall volume of 3D braided fabric is U_y, Fiber volume percentage of the 3D braided fabric

$$V = \frac{U_y}{U} \times 100\% \tag{5}$$

Let $\lambda = a / b$, Fiber volume percentage of the 3D braided fabric can be derived further, there is

$$V = f(\lambda, \beta) \tag{6}$$

Factors of influence on the braided fabric fiber volume percentage

Braided yarns in the same cross section would correspond to different elliptical section with the difference in tightness degree of yarns. The fiber volume percentage of braided fabric is related with yarn braiding angle and its section deformation.

When $ab = 1$ and $a / b \in [1/4, 4]$, the variation law of 3D braided fabric fiber volume percentage V with λ and β is shown in Fig.13.

It can be seen from Fig.10 that the variation of fabric fiber content percentage is in the range of 34 ~ 68%. When λ a constant, 3D is braided fabric fiber volume percentage increases with the increase of angle β. The variation of λ ($\lambda = a / b$) has very a large influence on the fabric fiber volume percentage.

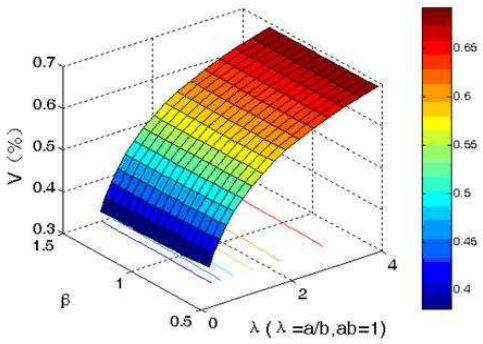

Fig.13 Tendency of 3D braided fabric fiber volume percentage

Conclusion

A novel geometry structure of unit cell is deduced from the point group S6 corresponding to symmetry operations. By transformation the unit cell with symmetry of space group $P\bar{3}$, a new plate 3D braided geometry structure is obtained. The braided technology corresponding to this geometry structure is studied. 3D braided material fiber volume percentage and its variation tendencies are predicted by means of the established geometric model. Some new 3D braided preforms with a high performance could be obtained by optimization the geometric parameters. As the braided array is limited to regular geometrical shape, the motion law of yarn carriers has particularity. The braided technology of arbitrary carrier array needs to be studied further.

Acknowledgements

The subject of research was supported by doctoral fund of Henan University of Science and Technology and Natural Science of Henan, China. No. 082102280009.

References

[1] Feng Wei, Ma Wensuo: Chinese Science Bulletin Vol. 50 (2005), p. 2529-2533.

[2] Ma Wensuo, Feng Wei: Journal of University of Science and Technology Beijing, Vol. 29(2) (2007), p. 226-231+246.

[3] Ma Wensuo, Zhu Jian-xun, Jiang Yun: Journal of Materials Science and Engineering, Vol. 28(5) (2010), p.

[4] Ma Wensuo: Group Theory Analysis of 3D Braided Structural Composites (Shanghai University Press, Shanghai 2010).

[5] Wang Renhui. Guo Kexin: Symmetry Group of Crystallography (Science Press, Beijing 1990).

doi:10.4028/www.scientific.net/AMM.161.255

Self-assembled Graphene for Determination of Catechol in Wastewater at Modified Glassy Carbon Electrode

Meifeng Chen [a], Xinying Ma [b] and Xia Li [c]

Department of Chemistry and Chemical Engineering, Heze University, Daxue Road, Heze, Shandong 274015, China

[a]chenmeifeng456@yahoo.com.cn (corresponding author), [b]lzhaojie2@sina.com, [c] xlr-lx@163.com

Keywords: Catechol, Wastewater, Modified electrode, Graphene.

Abstract. Graphene-modified glassy carbon electrode was made by dropping. In phosphate-citric acid buffered saline, the modified electrode was shown to possess an excellent selective electrocatalytical effect on the redox of catechol, and further used to determine catechol in the presence of resorcin and hydroquinone by cyclic voltammetry. The oxidation peak currents *I*pa showed a linear relationship with the concentrations (*c*) of catechol in the range of 2.97×10^{-7} mol·L^{-1}~9.31×10^{-6} mol·L^{-1} and 9.31×10^{-6} mol·L^{-1}~1.03×10^{-4} mol·L^{-1} with a correlation coefficient as follows: $I\text{pa}_1$(A)= -4.10×10^{-6}-2.31*c*, *R*=0.9971; $I\text{pa}_2$ (A) =-1.50×10^{-5}-0.60*c*, *R*=0.9953, respectively, and the detection limit is 2.50×10^{-8} mol·L^{-1}. The modified electrode is high sensitivity, selectivity, stability, and has been successfully applied to analyzing catechol in wastewater.

Introduction

Catechol (1, 2-benzenediol) is an important material, which is widely used in tanning, cosmetic, chemical materials and pharmaceutical industries. However, it is also a kind of environmental pollutant because it is toxic to human and difficult to degrade. There was maximum allowable concentration of 0.1mg·L^{-1} (9.08×10^{-7}mol·L^{-1}**)** in surface water in Union of Socialist Soviet Republics. Therefore, it is important to establish a sensitive, rapid and convenient method for the determination of catechol. Catechol contains phenolic hydroxy group and possesses excellent electrochemical activity, so various electrochemical methods using different modified electrodes have been reported for the determination of catechol. For example, a mesoporous platinum electrode [1], a penicillamine modified electrode [2], a nano Au/alkanedithiol self-assembled gold electrode[3], and mesoporous Al-doped silica modified electrode [4] were employed. However, electrochemical determination of catechol using graphene has not been reported. Graphene, as one of nanomaterials, has attracted tremendous attention from both the theoretical and experimental scientific communities in recent years because of its unique nanostructure and extraordinary properties [5,6]. It has become a novel and very promising material for nanoelectronics [7,8]. Catechol, hydroquinone and resorcin are phenol isomers with similar molecular structure. Thus, their usually interfere to determine catechol. Herein, the electrochemical response of catechol, hydroquinone and resorcin were studied using cyclic voltammetry (CV), the modified electrode is high selectivity, and has been successfully applied to analyzing catechol in wastewater in the presence of hydroquinone and resorcin.

Experimental

Reagents and Apparatus CHI 660C Electrochemical Workstation was used for electrochemical measurements (Shanghai Chenhua Instrument Corporation, China). A three-electrode system was employed with a bare or graphene-modified glassy carbon electrode as the working electrode, a platinum wire electrode as the counter electrode, and an Ag/AgCl electrode as reference electrode. Infrared spectroscopy (IR) study of the chemical functional groups on the exfoliated graphite and graphene was conducted on Varian660-IR (Agilent Technologies, America).

Graphite powder (<20 μm) were purchased form Qingdao graphite CO., LTD (China), sodium borohydride were purchased form Tianjin Daofu Chemical New Technique Development Co., LTD (China). Graphene was made as described below. Catechol, hydroquinone and resorcinol were

obtained from sigma-aldrich (Shanghai, China). Phosphate buffer solutions (PBS) were prepared by mixing disodium hydrogen phosphate and citric acid. All other chemicals not mentioned here were analytical reagent grade.

Preparation of the Nano-graphene Graphene oxide (GO) was made by Hummers method[9-11] using expandable graphite flake(4g).It was stirred in sulphuric acid (98%)(90 mL) for 10.5 h and then potassium permanganate (12g) was gradually added while keeping the temperature 37 ºC for 35 min. The mixture was then stirred at 80 ºC for 45 min. Water (180 mL) was added and the mixture heated at 100-105 ºC for 35 min. The reaction was terminated by addition of30% hydrogen peroxide solution and distilled water (200 mL). The mixture was washed by repeated centrifugation and filtration, first with 5% hydrochloric acid aqueous solution, and then distilled water until no SO_4^{2-} and filtrated at last. To prepare an aqueous 1mg·mL^{-1} of GO suspension (pH10), sodium borohydride was added. The temperature was strictly controlled by a constant temperature at 80 ºC for2 h. The powder of graphene was obtained by filtration and drying in vacuum.

Characterization of Graphene by IR Figure1 shows IR spectrogram of graphite and graphene. The wave numbers of functional groups of C=C and phenyl are1300 cm^{-1}-1600 cm^{-1}.These results showed that the graphene was successfully synthesized. Graphene sheets also contain C–O–C (1110-1200 cm^{-1}) and C–OH (3400-3500 cm^{-1}) groups. The functionalized and defective graphene sheets are more hydrophilic and can be easily dispersed.

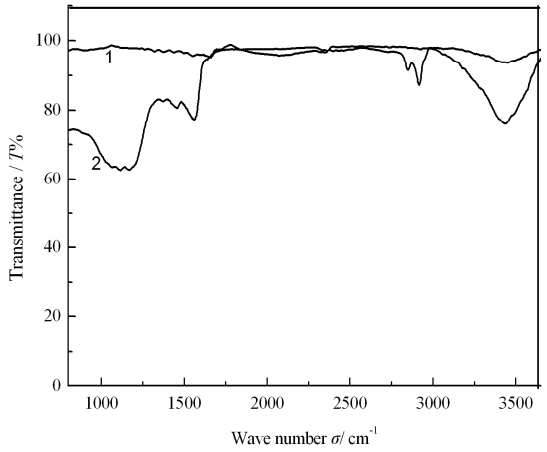

Fig. 1 IR spectrogram of the graphite (1) and graphene (2)

Preparation of Graphene Modified Electrode (GME) Graphene was dispersed in doubly distilled water at a concentration of 0.5g·L^{-1}. Glassy carbon electrode (GCE) was polished with gold sand paper and alumina powder respectively, rinsed thoroughly with doubly distilled water between each polishing step, then washed successively with 1:1 nitric acid, ethanol and doubly distilled water in ultrasonic bath and dried in air. GME was prepared by casting 10 μL of 0.5 g·L^{-1} graphene suspension on the GCE and dried under an infrared lamp.

Analytical procedure Under optimal conditions, a series of different concentrations of catechol were investigated by CV. A three-electrode system was used, including a GME as working electrode, a platinum electrode as counter electrode and Ag/AgCl (1mol·L^{-1}KCl) as reference electrode. Cyclic Voltammogram (CVs) of catechol were recorded .The glassy carbon electrode was treated in PBS (pH 5.0) by repetitive scanning in the potential range between -0.4V and 0.9V at a scan rate of 100 mV·s^{-1}so as to no record and used again.

Result and Discussion

Electrochemical Behaviors of IP on GME Figure2 shows the CVs of 2.0×10^{-5} mol·L^{-1} catechol in 0.1 mol·L^{-1} PBS (pH5.0) at GCE and GME. The peak current intensity at GME was sharply increased and the peak current is near zero at GCE. The higher electrocatalytic behavior to catechol of graphene

was confirmed. This electrochemical sensor shows an excellent performance for detecting catechol. The sensor shows great promise for simple, sensitive, and quantitative. The redox peak currents at the GME with E_{pa}= 0.334V, E_{pc}=0.280V, ΔE =54mV; I_{pa} =-23.42μA, I_{pc}=24.74μA, I_{pa}/I_{pc}~1. The redox performs a reversible reaction.

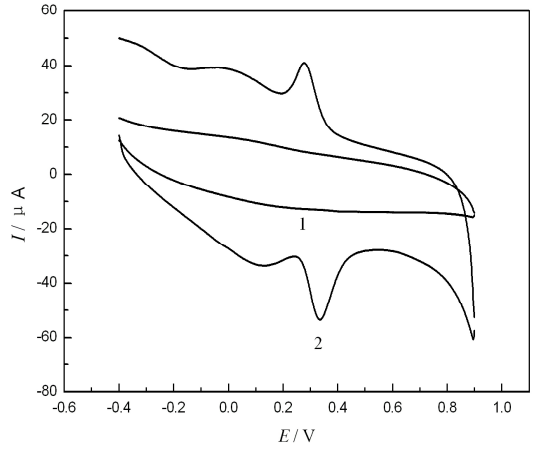

Fig.2 CVs of catechol at a bare electrode (1) and graphene-modified electrode (2)

Optimization of the Experimental Conditions The effect of the medium's pH on the electrochemical signal was analyzed (Fig. 3) .As can be seen with pH value of the solution increasing, the redox peak shifted negatively. The oxidation potential (E_{pa}) and pH showed a linear relationship, the equation was E_p = 0.652 –0.062pH, R=0.9970. The pH of the catechol solutions were changed from pH 2.2~9.0.The redox peak currents increased as the pH changing from 2.2~5.0, then the redox peak currents decreased and catechol is susceptible to oxidation after pH>6.0. In this work, the buffer solution of pH 5.0 was chosen as the supporting electrolyte.

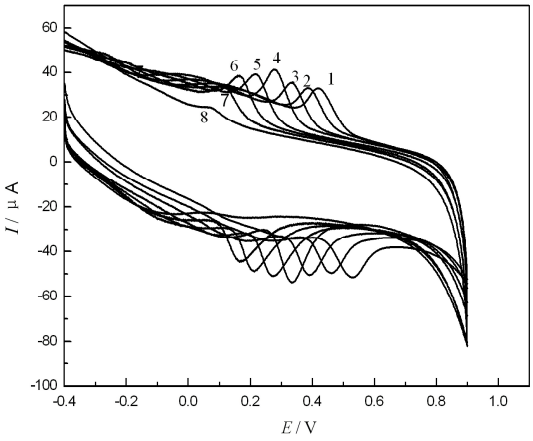

Fig.3. CVs of catechol at modified GCE at scan rate 100 mV·s^{-1} in PBS at different pH from2.2 to 9.0: (1~8).

Figure4 shows the redox peak currents increased with the scan rates ranging from 20 mV·s^{-1}to 260 mV.s^{-1}.The liner regression equations of the *I*pa and *I*pc of the scan rates are expressed as I_{pa}(A) = -1.11×10^{-5}-1.71×10^{-7}v (mV), R=0.9932; I_{pc}(A) = 3.52×10^{-6}+2.56×10^{-7}v (mV), R = 0.9983 respectively. It shows an adsorption process of electrochemical behaviors of catechol on GME .But the symmetry of potential becomes worse with the scan rates ranging from 20 mV·s^{-1} to 260 mV·s^{-1}. Therefore, 100 mV·s^{-1} was used as the scan rate.

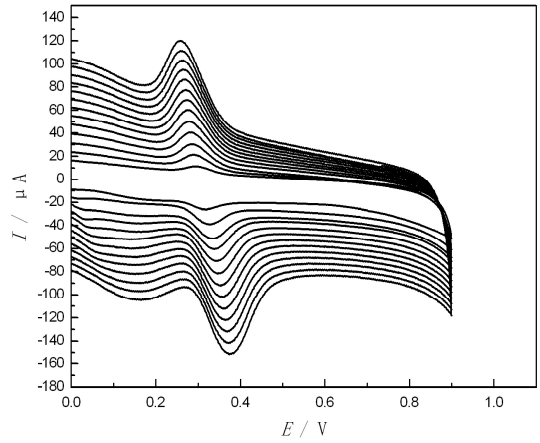

Fig.4 CVs of catechol at GME in PBS (pH 5.0) at different scan rates (20~260 mV·s^{-1}).

The study of the variation of accumulation time was studied. To accomplish this, we recorded CVs every 20 min from 20s to 120s, an equilibration between substance concentration on the surface of the electrode and catechol was reached with shaking. The *I*p increased greatly with time and reached a maximum at 60 s, suggesting that graphene can effectively accumulate catechol .Therefore, 60 s was used as the accumulation time

Effect of Catechol Concentration and Detection Limit Under the selected conditions, the present method allows the determination of catechol over the range 2.97×10^{-7} to 1.03×10^{-4} mol·L^{-1}. The dependence of *I*pa of catechol on its concentration was investigated. The *I*pa was linearly related to the catechol concentration (c) in the range of 2.97×10^{-7} mol·L^{-1}~9.31×10^{-6} mol·L^{-1}and 9.31×10^{-6} mol·L^{-1}~1.03×10^{-4} mol·L^{-1}.The linear regression equation was I_{pa1} (A) =-4.10×10^{-6}-2.31*c*, *R*=0.9971; I_{pa2}(A)= -1.50×10^{-5}-0.60*c*, *R*=0.9953; A detection limit is estimated to be 2.50×10^{-8} mol·L^{-1}.

Interference Studies In this study; it provides a possible method for the selective determination of catechol in the mixture solution containing. In order to confirm the availability of GME to the separated determination of catechol in the presence of resorcin and hydroquinone, we scanned the solution of catechol, resorcin and a mixture containing catechol, resorcin and hydroquinone in PBS (pH 5.0) by CV under the selected conditions.

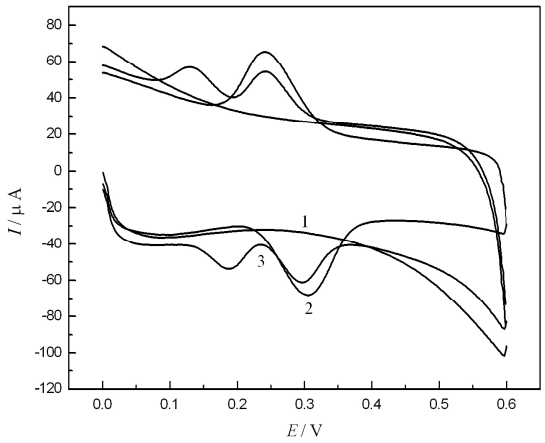

Fig. 5 CVs of resorcin (1), catechol (2) and the mixture of catechol, resorcin and hydroquinone (3) at modified GCE in PBS (pH5.0)

The results (Fig.5) showed that there was no peak of resorcin .The oxidation potentialof catechol was 295mV and the oxidation potential of hydroquinone was 187 mV. The effects of the other substances that often accompany catechol in various pharmaceutical preparations were studied by

analyzing a standard solution of catechol. If a foreign species caused a relative error of less than ±5% during the determination of catechol, no interference has been found when including up to 1000 μmol·L^{-1} of K^+, Na^+, Cu^{2+}, NO_3^-, $C1^-$, SO_4^{2-}, Ac^-, Ca^{2+} and Mg^{2+}.

Analytical application and Recovery The proposed system was applied to the analysis of catechol in wastewater. The results obtained by the proposed method. Recoveries were calculated according to I_{pa}. The results are listed in Tab.1. The recoveries varying from 98.0% to 102.5% of catechol .These results indicate that the method provides a potential tool for the separated determina -tion for catechol.

Table 1 Determination results of catechol in wastwater (n=6)

sample	Amount in wastewater/[mol·L^{-1}]	Amount of standard/ [mol·L^{-1}]	Total amount /[mol·L^{-1}]	Recovery / [%]
1	1.13×10^{-5}	2.00×10^{-5}	3.09×10^{-5}	98.0
2	1.08×10^{-5}	2.00×10^{-5}	3.13×10^{-5}	102.5
3	1.05×10^{-5}	2.00×10^{-5}	3.07×10^{-5}	101.0

Acknowledgements This project is supported by the Shandong City High School Science and Technology Fund Planning Project of (J10LB64) and the Scientific Research Foundation of Heze University (XYJJKJ-4).

References

[1] M.A. Ghanem, Electrocatalytic activity and simultaneous determination of catechol and hydroquinone at mesoporous platinum electroden, Electrochemistry Communications. 9 (2007) 2501-2506.

[2] L. Wang, P.F. Huang, J.Y. Bai, H.J. Wang, LY Zhang, Y.Q. Zhao, Covalent modification of a glassy carbon electrode with penicillamine for simultaneous determination of hydroquinone and catechol , Microchimica Acta.158 (2007) 151-157.

[3] L. Su, L.Q. Mao, Gold nanoparticle/alkanedithiol conductive films selfassembled onto gold electrode: electrochemistry and electroanalytical application for voltammetric determination of trace amount of catechol, Talanta.70 (2006) 68-74.

[4] H.G. Lin, T. Gan, K.B. Wu, Sensitive and rapid determination of catechol in tea samples using mesoporous Al-doped silica modified electrode, Food Chemistry. 113 (2009) 701-704.

[5] K.S. Novoselov, A.K. Geim, S.V. Morozov, D. Jiang, Y. Zhang, S.V. Dubonos, I.V. Grigorie -va, A.A. Firsov, Electric field effect in atomically thin carbon films, Science. 306 (2004) 666-669.

[6] Y.B. Zhang, Y.W. Tan, H.L. Stormer, P. Kim, Experimental observation of the quantum Hall effect and Berry's phase in graphene, Nature. 438 (2005) 201-204.

[7] X.H. Kang, J. Wang, H. Wu, J. Liu, I.A. Aksay, Y.H. Lin, A graphene-based electrochemical sensor for sensitive detection of paracetamol,Talanta. 51 (2010) 754-759.

[8] F.H. Li, J. Chai, H.F. Yang, D.X. Han, L. Niu, Synthesis of Pt/ionic liquid/graphene nanocomposite and its simultaneous determination of ascorbic acid and dopamine, Talanta. 81 (2010) 1063-1068.

[9] W.S. Hummers, J_R, R.E. Offeman, Preparation of Graphitic Oxide, J. Am. Chem. Soc. 80 (1958) 1339-1341.

[10] Y.C. Si, E.T.Samulski, Synthesis of Water Soluble Graphene, Nano. Lett. 8 (2008) 1679-1682.

[11] A.B. Bourlinos, D. Goumis, D. Petridis, T. Szabo, A .Szeri, I .Dekany, Graphite oxide: Chemical reduction to graphite and surface modifcation with primary aliphatic amines and amino acids, Langmuir.19 (2003) 6050-6055.

doi:10.4028/www.scientific.net/AMM.161.260

Growth Mechanism, Structural and Optical properties of ZnO nanoparticles

Xiu juan Liang [1,a] , Xiaofang Hu[2,b], Dawei Hu[2,c]

[1] College of Engineering，Guangdong Ocean University， Zhanjiang 524088，China
[2] College of Mechanical and Automobile Engineering, South China University of Technology, Guangzhou 510640 , China
[a]lxjjhx@163.com,[b]xiaofh@scut.edu.cn, [c]123hudawei@163.com

Kyewords: Electric field; Direct precipitation method; Zinc Oxide; nanoparticles

Abstract. This paper using an electric field-assisted direct precipitation method synthesize the ZnO nanosheets with zinc nitrate hexahydrate and sodium carbonate. The synthesis processes with and without an electric field were compared. The morphology of the ZnO nanosheets was investigated by scanning electron microscopy (SEM) measurements. The SEM results show that the application of an electric field caused the morphology transformation from flake-like to flower-like. It was found that an electric field had an effect on the crystal structure，the particle size and morphology. The photoluminescence spectrum of the synthesized ZnO nanosheets shows a strong ultraviolet emission at 249 nm. In addition，the formation mechanism of the ZnO nanosheets is discussed.

Introduction

ZnO is an important n-type semiconductor with a wide direct band gap of 3.37 [eV] and a large excition binding energy of 60 [meV] at room temperature [1,2]. Due to its unique electrical and optical properties[3]，ZnO could have many potential applications, such as ultraviolet lasers, photodetectors，photodiodes，solar cells [4-8]etc. The novel properties of semiconductors depend on their size, shape, and crystalline structure, it is important to control the shape and size of semiconductors in a controllable way[9,10]. Over the past decade，many methods have been developed for the preparation of ZnO, like metal organic chemical vapour deposition(MOCVD)[11,12],metal-organic vapor-phase epitaxy (MOVPE)[13], vapor–liquid–solid (VLS) process[14],direct precipitation method [15], sol–gel techniques[16], and hydrothermal processing method [17,18]and so on. Each of the reported techniques have some specific deficiencies, such as the use of high temperature, the need for a catalyst and so on. Up to now，there still is a great interest in finding a simple，reliable and rapid method to synthesize ZnO with specific morphologies and properties.

In this paper，we report the successful fabrication of the ZnO nanosheets by an electric field-assisted direct precipitation method.The room temperature photoluminescence spectrum of the synthesized ZnO shows a strong UV emission，therefore it is expected to have a new application in UV emission fields.

Experiment

All the reagents we used are analytically pure. 100mL of 0.1M Na_2CO_3 solution was added to the reactor with stirring and heated to 90 ˚C by the hot water bath, 100mL of $Zn(NO_3)_2$ solution of certain concentration was added to the reactor with constant stirring. During the reaction, a pulse alternative field with a frequency of 50HZ was provided between two faces of the reactor. The duration of the reaction was 2h. The precursor precipitate was separated by centrifugation and

washed for several times with absolute ethanol and distilled water and then dried in vacuum at 80°C for 12h. White ZnO powders were obtained by calcining the precursor in a muffle furnace at 400℃ for 2h.

The phase composition of the samples were examined by X-ray powder diffraction with Cu Ka radiation(λ= 1.54178 Å) by Bruker D8 Advance X-ray diffractometer operated at 40kV voltage and 50mA current, the data were recorded in the 2θ range of 10-90°with a step width of 0.02°.The morphologies and particle sizes of ZnO samples were observed by a model JSM-6490LA scanning electron microscope (JEOL Inc., Germany). Photoluminescence (PL) measurement was performed using a He- Cd laser line of 325 nm as the excitation source.

Results and discussion

The XRD pattern of the samples is shown in Fig. 1 All of the peaks in Fig. 1 can be well indexed to the hexagonal wurtzite ZnO (JCPDS card No. 36-1451, a = 3.249 Å and c = 5.206 Å) with high crystallinity and no other impurities can be found. In addition, all peaks are obviously wider than those obtained by general methods. By the Scherrer equation, D=0.94λ/Bcos θ, where D is the average diameters of obtained wurtzite ZnO nanowires, B is the full width at half-maximum of the XRD peaks, θ is the angle of diffraction, and λ is the wavelength of the X-rays, the sizes of diameters of nanowires can be calculated, in agreement with those observed by SEM .

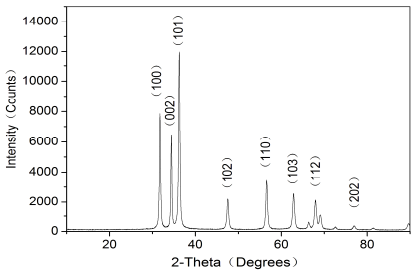

Fig. 1 XRD patterns of the ZnO nanocrystals

Fig. 2 shows the SEM images of ZnO nanocrystals synthesized at various electric field （0-50KV）. Fig. 2a shows the typical morphology of ZnO nanocrystals obtained in the absence of electric field. Clearly, the morphology of the particles synthesized without electric field appears irregular. However, the particles synthesized under electric field appears more uniform in morphology. Fig. 2b shows the ZnO nanocrystals obtained at 20KV seem to flower-like single crystals. the thickness is about 10 nm. Fig. 3c contains flower-like structures growing out of a common nucleus，very different from those synthesized at 0KV. The growth pattern of the particles seems to have a preferential direction, resembling leaves sticking out of a nucleus . However, the structure is formed by uniform flacks with common nuclei, rather than flower-like structures. These observations indicated that the general morphology of the ZnO structures was strongly influenced by the electric field.

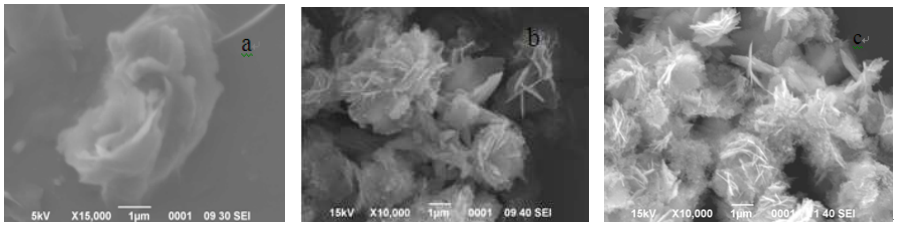

Fig. 2 SEM images of ZnO nanocrystals samples prepared under various conditions.(a)and (b)samples prepared at an electric field of 50 KV,20KV (c) without electric field

ZnO is a polar crystal(Fig. 3), whose polar axis is the c-axis. Weizhuo Zhong[19]suggested that the growth mechanism of the single ZnO nanorod may be explained according to the growth unit model of anion coordination polyhedra. According to this model, the growth rate of the ZnO crystal planes is R(0001)>R(1010)>R(1000). As we known that ZnO is an important n-type semiconductor materials, an electric field could affect the high-energy facets of the nano-particles. The ratio between the growth rates in different directions can vary with respect to the effect of electric field, thus inhibiting the growth in a particular crystallographic direction. The overall specific surface energy was more or less reduced, and the surface reaction rate could be affected.

Fig.4 shows the photoluminescence spectrum of the as-grown ZnO sample at room temperature. A strong ultraviolet emission peak is found at 249 nm. This peak belongs to the near bandedge emission of the wide band gap of ZnO due to the recombination of exciton[20]. Generally speaking，the ZnO with better crystallization and higher purity will have astronger UV emission. the nanowires with large surface-to-volume ratios have a lot of dangling defects on the surface, which can absorb the $O^{2-}$and O^{-} to form the O^{2-}/O^{-} surface system[21]. Schoenmakers[22]have demonstrated that this O^{2-}/O^{-} surface system is the predominant trapper of the holes in the valence band, which play a key role in the formation of the visible emission centers.

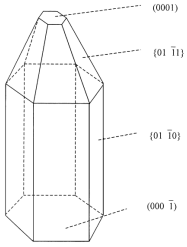

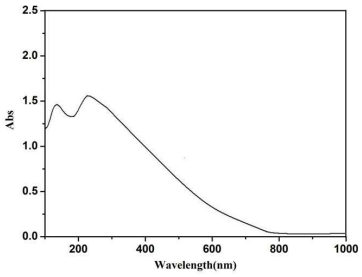

Fig. 3 Idealized growth habit of the ZnO crystal. Fig. 4 PL spectra of the ZnO samples

Conclusions

In summary，we fabricate flower-like particles via the electric field- assisted homogeneous precipitation method, the morphology transformation from flack-like to flower-like in the synthesis occurred due to the effect of an electric field between 0-50 KV. ZnO nano-particles with the larger sizes and the uniform morphology could be obtained with an electric field . We suggest that the formation of the flower-like structure is ascribed to the different growth rates on the different crystal faces. Moreover，a higher deep-level emission is observed from the PL spectrum，which indicates that the ZnO samples have many surface defects.

Acknowledgements

This work was supported by the Key Project of Science and Technology Department of Zhanjiang ,P.R. China(Grant No.2010C3110004).

References

[1] Chen Y, Bagnall D M, Koh H J, et al. Plasma assisted molecular beam epitaxy of ZnO on c-plane sapphire:growth and characterization, J. Appl. Phys. 84(1998) 3912-3918.

[2] Fan Z, Lu J G. Zinc oxide nanostructures: Synthesis and properties, J. Nanosci. Nanotechnol. 5(2005)1561-1573.

[3] Rao C N R, Gundiah G，Deepak F L, et al. Carbon-assisted synthesis of inorganic nanowires, J. Mater. Chem.14(2004)440-450.

[4] Huang M H，Mao S，Feick H，et al. Room-temperature ultraviolet nanowire nanolasers, Science. 292(2001)1897-1899.
[5] Liu C Y，Zhang B P，Lu Z W，et al. Fabrication and characterization of ZnO film based UV photodetector, J. Mater.Sci. : Mater. Electron. 20(2009)197- 201.
[6] Qin Y, Wang X D,Wang Z L. Microfibre-nanowire hybrid structure for energy scavenging, Nature. 451(2008)809-813.
[7] Song J H, Wang X D, Liu J,et al. Piezoelectric Potential Output from ZnO Nanowire Functionalized with p-Type Oligomer, Nano Lett. 8(2008)203-207.
[8] Zhao Su Ling, Kan Peng Zhi, Xu Zheng,et al. Electroluminescence of ZnO nanorods/MEH-PPV heterostructure devices, Organic Electronics .11(2010)789-793.
[9] Michael Breedon, Mohammad Bagher Rahmani, Sayyed-Hossein Keshmiri, et al. Aqueous synthesis of interconnected ZnO nanowires using spray pyrolysis deposited seed layers, Materials Letters . 64(2010)291-294
[10] S. Sepulveda-Guzman,B. Reeja-Jayan,E. De la Rosa,et al. Room-temperature deposition of crystalline patterned ZnO films by confined dewetting lithography, Applied Surface Science. 256(2010)3386-3389.
[11] H.-G. Chen, Sheng-Rui Jiana, Zheng-Wei Li,et al. Epitaxial growth of self-arranged periodic ZnO nanostructures on sapphire substrates grown by MOCVD, J. Alloys Compd. 10(2010)1016.
[12] Y.J. Chen, Y.Y. Shih, C.H. Ho,et al. Effect of temperature on lateral growth of ZnO grains grown by MOCVD, Ceramics International. 36(2010)69–73.
[13] Y.W. Heo, D.P. Norton, L.C. Tien, et al. ZnO nanowire growth and devices, Mater. Sci. Eng. 47(2004)1-47.
[14] M. Huang, Y. Wu, H. Feick, et al. Catalytic Growth of Zinc Oxide Nanowires by Vapor Transport, Advanced Materials. 13(2001)113-116.
[15] A. Kolodziejczak-Radzimska, T. Jesionowski, A. Krysztafkiewicz. Obtaining zinc oxide from aqueous solutions of KOH and $Zn(CH_3COO)_2$, Physicochemical Problems of Mineral Processing. 44(2010)93-102.
[16] Zhang Can-yun. High-quality oriented ZnO films grown by sol–gel process assisted with ZnO seed layer, Journal of Physics and Chemistry of Solids. 71(2010)364-369.
[17] Zhaoyi Zhou, Yaping Zhao, Zaisheng Cai. Low-temperature growth of ZnO nanorods on PET fabrics with two-step hydrothermal method, Applied Surface Science.256(2010)4724-4728.
[18] A. Aimable, M.T. Buscaglia, V. Buscaglia, et al. Polymer-assisted precipitation of ZnO nanoparticles with narrow particle size distribution, Journal of the European Ceramic Society. 30(2010)591–598.
[19] Li W J, Shi E W, Zhong W Z, et al. Growth mechanism and growth habits of oxide crystal, Journal of Crystal Growth. 203(1999)186.
[20] Zhang J，Sun L D，Yin J L，et al. Control of ZnO morphology via a simple solution route, Chem. Mater.14(2002) 4172- 4177.
[21] Genban Sun, Minhua Cao, Yonghui Wang, Changwen Hu, Yichun Liu, Ling Ren , Zhifa Pu. Anionic surfactant-assisted hydrothermal synthesis of high-aspect-ratio ZnO nanowires and their photoluminescence property, Materials Letters. 60 (2006) 2777–2782
[22] G.H. Schoenmakers, D. Vanmaekelbergh, J.J. Kelly, Study of Charge Carrier Dynamics at Illuminated ZnO Photoanodes, J. Phys. Chem. 100(1996) 3215.

doi:10.4028/www.scientific.net/AMM.161.264

Effect of Modified Phosphogypsum on the Mechanical Properties of Super Sulphate Cement

Yu-Xin Gao[1.a], Bao-Ying Yu[1.b], Fen-Lian Xu[1.c]

[1]China Construction Ready Mixed Concrete Chengdu Co.,Ltd, Chengdu Sichuan 610052, China

[a]gao_h313@sina.com.cn, [b]yby2872@163.com, [c]fenlian23@163.com

Keywords: Super sulphate cement (SSC), Phosphogypsum (PG), Specific surface area (SSA), Mechanical properties

Abstract: The effect of phosphogypsum (PG) modified on mechanical properties of super sulphate cement (SSC) was systematically studied in this paper. Then attentions and researches were focused on the relationship between specific surface (SSA) and the mechanical properties of SSC containing PG modified by calcining, floating, neutralizing with alkali. Strengthening mechanisms of SSC were further investigated and analyzed by laser particle size analyzer and chemical composition analyzer at last. Results showed that the high strength SSC with the compressive strength 35MPa at 7 days, over 60MPa at 28 days, and some even more than 70MPa at 56 days, could be successfully developed. This research can provide a key reference for the utilization of PG and development of high performance eco-SSC.

1 Introduction

Phosphogypsum(PG) is one of main industrial by-product gypsum, the annual production of which accounts for 50% or more. Storage of PG not only occupies land, but also wastes resources[1–3]. Super sulphate cement(SSC) is a kind of hydraulic cementitious material which is produced by the activation of alkali and sulfate in combination on slag latent activity. Gypsum-based sulfate activation plays a critical role in SSC system[4]. So it is an important way for the resource utilization, environmental protection, and sustainable development of cement industry by increasing the utilization ratio of PG and taking advantage of sulphate activator in preparing high-performance SSC.

A great deal of tests for determining the optimal alkaline environment and the mixing proportion of PG and natural gypsum were carried in preliminary studies of SSC. In this paper, the influences of modification (calcining, washing, floating, neutralizing with alkali etc.) of PG on mechanical properties of SSC are systematically studied. By the comparison of technical, economical and environmental benefits of the modification methods, and an investigation on the relationships between SSA and mechanical properties of SSC, high strength SSC is successfully developed.

2 Materials and Methods

2.1 Materials

Ordinary Portland cement clinker, slag, PG and natural gypsum were used in this investigation. Their chemical compositions are shown in Table 1.

Table 1 Chemical composition of raw materials [%]

NO.	SiO_2	Fe_2O_3	Al_2O_3	CaO	MgO	SO_3	TiO_2	MnO
clinker	21.95	3.32	5.31	64.94	1.93	0.55	-	-
slag	32.46	0.50	12.92	35.40	8.81	2.03	2.68	0.86
PG	10.06	1.18	1.73	32.26	0.09	44.29	-	-
natural gypsum	2.88	0.37	0.40	31.04	1.49	40.28	-	-

*PG- phosphogypsum.

PG-based high strength SSC: Based on pre-experimental results of the right clinker dosage and suitable ratio between PG and natural gypsum, this research was conducted with the optimum weight ratio of slag, clinker, modified PG and natural gypsum.

2.2 Methods of Specimens molding

Mortars were cast in 40mm×40mm×160mm moulds, and cured in standard conditions (20±1℃, RH 95%) according to GB/T 17671-1999. The modifications of PG in different SSC specimens were listed in Table 2. The water to binder ratio (w/b) for all samples was 0.25.

Table 2 Modifications of PG for B1~B7 samples

No.	B1	B2	B3	B4	B5	B6	B7
modification	raw PG	calcining 1h at 150℃	calcining 1h at 500℃	washing(PG / water = 1 / 3)	floating (PG / water = 1 / 2)	neutralizing with alkali	B6+ B3

* PG from B1 to B7 was grinded to the appropriate fineness.

3 Mechanical properties of SSC system

3.1 The influences of modified PG

In the case of fixed-weight ratio for all admixtures, MTS was used to test the compressive and flexural strength of mortar samples. Figure 1 depicts the strength development tendency of PG-based SSC samples with ages.

The strength growth degree varies widely at different ages compared to the control sample （B1）(Figure 1). Compared to B1, the compressive strength of B2 at each age increases by 10% to 25%. The tests for B4 and B5 show that although low strength is developed in the early stage, the strength grew rapidly in the period of 7d to 28d. The strengths of PG-based SSC modified by neutralizing with alkali, calcining and the combination of two are obviously higher than others at 3 days, the average increasing ratio of compressive strengths on B3, B6 and B7 is over 55% at this age. The 28-day compressive strengths from B3 to B6 are all about 55MPa. The highest compressive strength value of 61.2MPa is obtained in the case of B7.

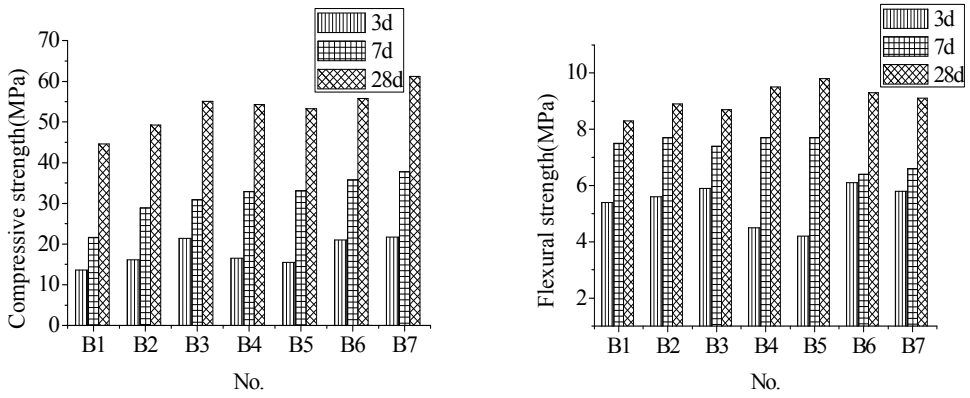

Figure 1 Strength development of SSC samples with PG modified differently

3.2 Effects of specific surface area (SSA)

Energy consumption is minimized and cost savings maximized in the premise of ensuring mechanical properties of SSC. Calcining for 1h at 500℃, floating and neutralizing with alkali are better modified processes for PG than others in SSC system, which refer to B3, B5 and B6. Based on the three optimized modified processes, the relation between SSA and mechanical properties, and long term strength development about SSC are studied in this part.

Samples of B3, B5 and B6 were all grinded to three types of SSA with 420m^2/kg, 490m^2/kg and 560m^2/kg. The strengths of different types of PG-based SSC are compared with each other at 7 days, 28 days and 56 days respectively. Figure 2 shows the strength test results of A1~A3, B1~B3 and C1~C3. A1, A2 and A3 are named Calcining SSC, which means PG calcined for 1h at 500℃. Similarly, B1~B3 and C1~C3 are called Floating SSC and Neutralizing SSC respectively.

With the increase of SSA, the strength increase in varying degrees with ages (Figure 2). Increasing of SSA is beneficial to the development of early strength for Neutralizing SSC. Strengths at 7 days for C2 and C3 are 43.1MPa and 45.9MPa, which are obviously higher than the strength of C1 at the same ages. The later strength of calcining SSC increases steady by 15% from 28 days to 56 days. So strengths of A2 and A3 are 67.5MPa and 72.0MPa separately at 56 days. According to the enhancing effect of B1, B2 and B3 (Figure 2), flotation is also a good modified way. In terms of the flexural strength at later ages, all values are between 10MPa to 11MPa, which are much higher than ordinary Portland cement.

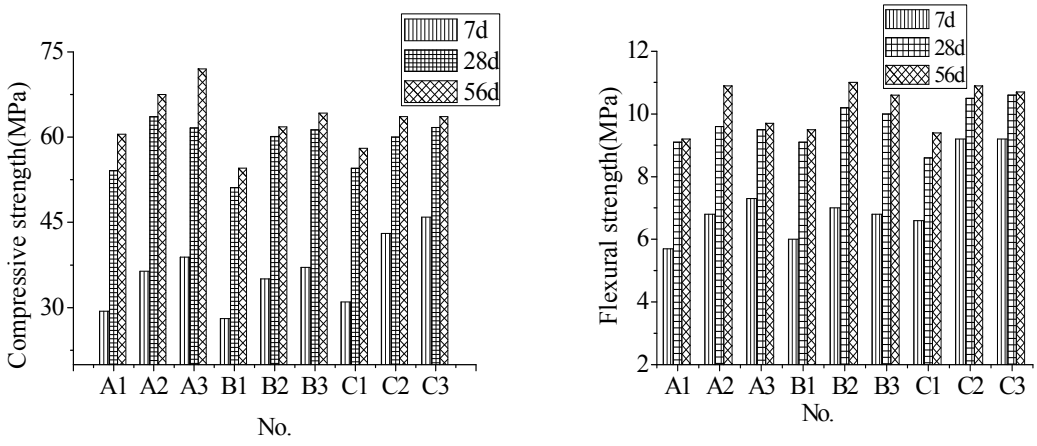

Figure 2 Strength development of SSC with PG modified differently and adding SSA

4 Results analysis and discussion

It can be seen from the above results the successful development of high strength SSC is closely related to the modification methods of PG, which not only lies on particle morphology and particle size distribution of PG, but also depends on SSC's hydrating and hardening caused by impurities [5, 6].

The particle size distribution of raw PG and ground modified PG were analyzed by the means of laser scattering particle analyzer as shown in Figure 3. PG1 is raw PG, samples from PG2 to PG4 are ground fine PG modified by floating, calcining 1h at 500℃ and neutralizing with alkali, respectively. It can be seen that fine particles of PG2, PG3 and PG4 are significantly increased, particle contents of less than 10μm increase from 25% to more than 70%. Particle size distribution has been considerably improved due to grinding. Significant increase and wider particle distribution in small particles for ground modified PG can effectively fill the porosity of hardened paste，improve paste compaction, and thus conducive to the strength development of SSC.

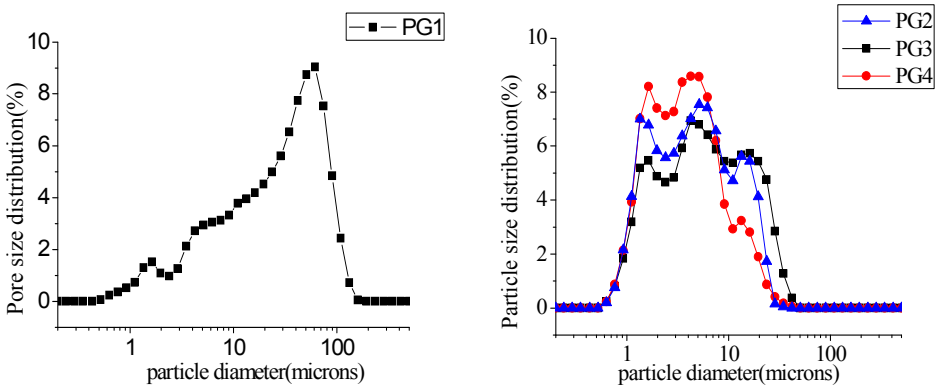

Figure 3 Particle size distribution of raw PG and modified PG

In SSC system containing raw PG, soluble phosphorus turns into insoluble phosphate, then covers the surface of clinker and forms a thin film which is difficult to penetrate. Weak acid delays the emergence time of the required alkalinity scope for slag hydration, extends the setting time, and leads to lower strength, especially the early strength. When PG was modified by floating, calcining 1h at 500℃ or neutralizing with alkali, the adverse effects of impurities from PG can be effectively eliminated, as shown in Table 3. Soluble phosphorus and fluorine dissolve easily in water. Removal rate of them could reach to 83% by floating (PG2). Harmful impurities for PG3 basically breaks down into gas or inert, stable and insoluble compounds under calcining 1h at 500℃[7]. Alkaline neutralization (PG4) can effectively neutralize the acidity materials especially soluble phosphorus and fluoride, and significantly decrease the harm of acidic impurities. So the three modified methods are beneficial to the hydrating and hardening process of SSC and results in positive rapid strength development.

Table 3 Impurities content in modified PG [%]

No.	modification manners	soluble phosphorus	eutectic phosphorus	soluble fluorine
PG1	grinding	1.23	0.46	0.35
PG2	floating	0.25	0.46	0.02
PG3	calcining 1h at 500℃	0.47	0.21	0.03
PG4	neutralizing with alkali	0.12	0.46	0.04

5 Conclusions

Under alkali and sulfate in combination, mechanical properties of different types of PG-based SSC were tested in this paper. Then the optimal modification ways for PG and the best SSA of SSC are determined. The main conclusions are shown below:

(1) Three modified methods of floating, calcining, and neutralizing with alkali for PG can be used to prepare high strength, even super-high strength SSC. Especially, compressive strength at 56 days for A3 (Calcining SSC) reached over 70MPa while 7 days strength of Neutralized SSC which is grinded to 500m^2/kg approximately remains stable above 40MPa.

(2) Results tested by laser size distribution analyzer and chemical composition analyzer show that ground modified PG have much more fine particles, wider particle distribution, and much lower harmful impurities, which could be beneficial to the strength development with ages.

References

[1] E.M. El Afifi, M.A. Hilal, M.F. Attallah, S.A. EL-Reefy, Characterization of phosphogypsum wastes associated with phosphoric acid and fertilizers production, Journal of Environmental Radioactivity 100 (2009) 407–412.

[2] C. Papastefanou, S. Stoulos, A. Ioannidou, and M. Manolopoulou, The application of phosphogypsum in agriculture and the radiological impact, Journal of Environmental Radioactivity. 89 (2006) 188–198.

[3] M. Azouazi, Y. Ouahidi, S. Fakhi, Y. Andres, J.Ch. Abbe, and M. Benmansour, Natural radioactivity in phosphates, phosphogypsum and natural waters in Morocco, Environmental Radioactivity 54 (2001) 231–242.

[4] A.Gruskovnjak, B.Lothenbach, F.Winnefeld, R.Figi, S.-C.Ko, M.Adler, and U.Mäder, Hydration mechanisms of super sulphated slag cement[J].Cement and Concrete Research, 38(2008) 983–992.

[5] M.A. Taher, Influence of thermally treated phosphogypsum on the properties of Portland slag cement[J]. Resources, Conservation and Recycling. 52 (2007) 28–38.

[6] Manjit Singh, Treating waste phosphogypsum for cement and plaster manufacture[J], Cement and Concrete Research 32 (2002) 1033–1038.

[7] Nurhayat Degirmenci, Utilization of phosphogypsum as raw and calcined material in manufacturing of building products, Construction and Building Materials 22(2008) 1857–1862.

doi:10.4028/www.scientific.net/AMM.161.269

Optimization of Process Parameters for Plasma Sprayed HA / ZrO_2 Bioceramic Coating

Yumei Bao[1, a], Lei Wu[1, b], Lijie Weng[2, c]

[1]Key Laboratory of E&M (Zhejiang University of Technology), Ministry of Education & Zhejiang Province, Hangzhou, P.R. China

[2]Taizhou Vocational College of Science & Technology, Taizhou, P.R.China

[a] baoym@zjut.edu.cn (corresponding author), [b] wu_mail@126.com, [c] wenglijie1983@163.com

Keywords: bioceramic coating; preparation; mechanical behavior; numerical simulation

Abstract. Preparation and mechanical property measurement methods of bioceramic coating are introduced. HA/ZrO_2 composite coating was prepared in the titanium alloy substrate with Plasma spraying equipment, and its bonding strength was measured. The influence of process parameters on bonding strength of plasma-sprayed HA/ZrO_2 composite coating is simulated with computing software Mathematica and optimized.

Introduction

Bioceramic, a kind of inorganic biomedical materials, has advantages of innocuity, corrosion resistance, excellent bioactivity and biocompatibility. However, owing to poor mechanical properties, low flexural strength, high brittleness and difficulty to manufacture, its application in the high loading parts of human body is severely restricted. Biomedical metal materials, applied extensively in the early prosthesis replacement, have high strength and toughness while easy corrosion and bad biocompatibility in body fluid resulting in toxic substances. The bioceramic coating, that is coating bioceramic on metal substrate, has the biocompatibility of implants assured by bioceramic and the mechanical properties provided by the metal substrate, and therefore are widely used in clinical applications [1-3].

Various techniques, such as plasma spraying, laser cladding, sol-gel, and biomimetic synthesis, are available for the preparation of bioceramic coatings. In addition to the prerequisite of bioactivity, the complexity of application fields requires bioceramic coatings with excellent performance, such as high bonding strength, low porosity and outstanding resistance to wear, corrosion and heat. Therefore, it is significant to investigate and improve the properties of bioceramic coating.

In what follows, the preparation methods of bioceramic coating are reviewed. And the measurement of mechanical properties typically the bonding strength is discussed. The process parameters for plasma sprayed HA / ZrO_2 bioceramic coating are optimized aiming to improve the mechanical properties.

Preparation methods

Plasma spraying. Plasma spraying is one of the most important parts of modern surface modification technologies as shown in Fig. 1 [1, 3]. Metal or nonmetal powers are heated to melt or partial melt state with the heat produced by gas ionization, and ejected to the surface of workpiece along with high speed gas flow. After cooling solidification, plasma-sprayed coating is formed on the substrate. This method has features of a rapid deposition rate, a sufficiently low cost and simple process and the coating has high density and resistance to wear, corrosion and heat.

Although plasma-sprayed coating is applied widely industry because of its excellent properties, there exist two inherent defeats, i.e. low bonding strength and high porosity, which are determined by the process. In the process of droplet's collision with substrate and its deformation and accumulation on the surface, it is possible to cause pores among the particles where couldn't be filled with melt or partial melt powers. Thus, pores and microcrack are inevitable in the formation of coating. Those are the main reasons why the bonding strength of plasma-sprayed bioceramic coating is lower and the porosity is high. What's more, residual stress caused mainly by rapidly cooling solidification also contributes to the low bonding strength.

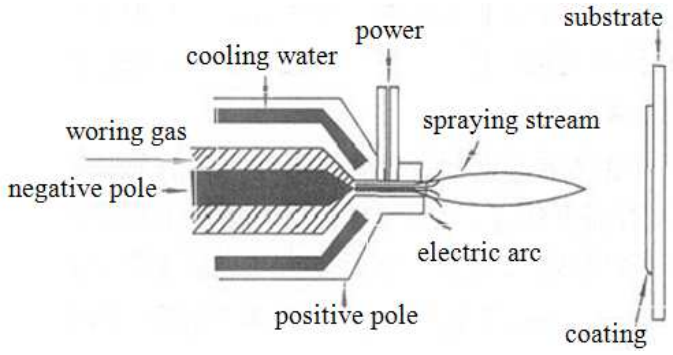

Fig. 1 Plasma spraying[1]

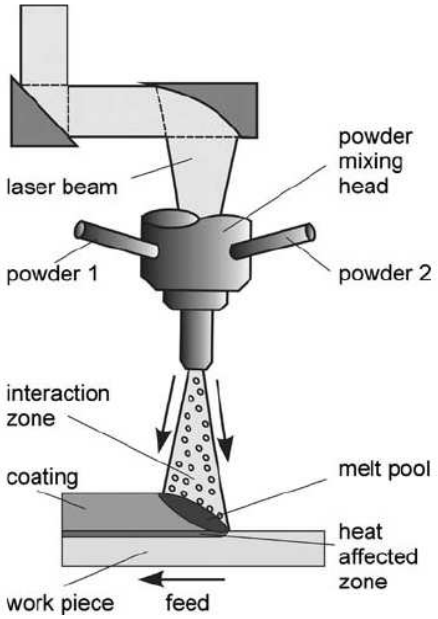

Fig. 2 Laser cladding[4]

Laser cladding. Laser cladding method is one of the most effective ways to produce functionally graded coatings as shown in Fig.2. It is able to yield a strong interfacial bond between the substrate and the coating without significant dilution of one material into the other, by means of rapidly melting and solidifying coating materials and surface layers of the substrate [4].

In addition to above methods, there are many other technologies, such as sol-gel, biomimetic synthesis, self-propagating, magnetron sputtering, micro arc oxidation, etc. with its own advantages and disadvantages.

Numerical simulation and optimization

The influences of technique parameters, such as spraying distance, spraying current, primary gas flow and auxiliary gas flow, on bonding strength of plasma sprayed HA/ZrO_2 coating were studied.

Preparation. In this research, plasma spraying technology was chosen as the preparation method of HA/ZrO_2 composite coating. This study used titanium ally TC4 as substrate, ZrO_2 as interlayer material and HA as working layer. ZrO_2 interlayer was firstly sprayed on TC4 substrate with the same process parameters as shown in Table 1 using DH2080 plasma spraying equipment, and then HA working layer was sprayed with different parameters shown in Table 2.

Table 1 Process parameters of Plasma sprayed ZrO2 as interlayer

Spraying current [A]	Spraying voltage [v]	Spraying distance [mm]	Primary gas flow[slpm]	Auxiliary gas flow[slpm]	Feed rate [g · min^{-1}]
600	80	100	41	12	19

Before spraying, the substrate (Φ25.4mm×30mm) should be dipped into acetone and clear with ultrasonic washer and Al_2O_3 was used to rough the titanium alloy surface. At last the sprayed coating was crystallized at 800℃ for 6 hours to reduce residual stress. Based on uniform design theory, spraying distance, spraying current, primary gas flow and auxiliary gas flow were chosen as design factors. Level values of each factor took nine values and nine experiments would be carried out. Column 1, 2, 3 and 5 of U9(96) uniform experiment table were applied, the experimental design was shown in Table 2.

Table 2 Process parameters of Plasma sprayed HA as working layer and Experimental results

No.	Factors				Results
	Spraying distance [mm]	Spraying current [A]	Primary gas flow [slpm]	Auxiliary gas flow [slpm]	Bonding strength [MPa]
1	75	525	40	14	28.5
2	80	575	48	12	23.4
3	85	625	38	10	33.2
4	90	675	46	8	36.0
5	95	500	36	15	33.8
6	100	550	44	13	25.2
7	105	600	34	11	31.5
8	110	650	42	9	35.6
9	115	700	50	16	30.5

Measurement. Mechanical properties such as Young's modulus, bonding strength, and fracture toughness, have determining influence on the application of bioceramic coating. Among the mechanical properties, bonding strength of a bioactive coating to a substrate affects successful implantation and long-term stability of the implant coated with the bioactive material significantly. As the development and application of bioceramic coatings gain more attention, how to obtain higher bonding strength and avoid coating shedding is becoming the focus of study. There are many ways to measure bonding strength such as bond tensile method, scratch test and indentation method.

Referring to ASTM-C-633-79 and GB8642-88, bonding strength of HA/ZrO_2 composite coating was measured with bond tensile method, as shown in Fig. 1. In order to obtain the values of bonding strength successfully, the tensile strength of the binder should be higher than bonding strength of the coating sample.

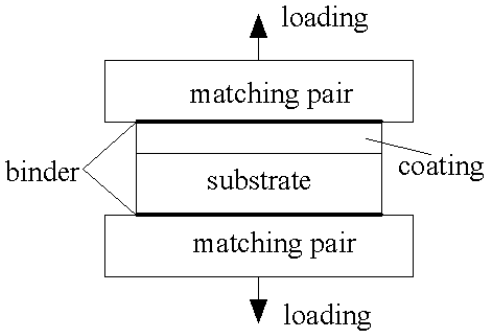

Fig. 3 Schematic of bond tensile method

Results and analysis. As shown in Table 2, the process parameters had a significant influence on bonding strength. In order to show the influence rules clearly, the quadratic polynomial stepwise regression analysis was conducted by using DPS data processing system. A regression model was obtained with significance level of 0.0085 and correlation coefficient of 0.9906:

$$Y=66.9-0.797X_1+0.27X_4^2+0.00041X_1X_2+0.0139X_1X_3-0.159X_3X_4 \quad (1)$$

Where Y is bonding strength, X_1 is spraying distance, X_2 is spraying current, X_3 is primary gas flow, X_4 is auxiliary gas flow. From Eq.1, the bonding strength was related to spraying distance and the square of auxiliary gas flow, but the effects of spraying distance were more obvious than that of auxiliary gas flow. What's more, the cross terms of spraying distance/spraying current, spraying distance/primary gas flow, and primary gas flow/auxiliary gas flow had important influences, too. Based on Eq.1, the optimized process parameters are: X_1 is 114.9 mm, X_2 is 680 A, X_3 is 49 L/min and X_4 is 8 L/min, and the predicted bonding strength is 41.3 MPa.

According to the regression model, Fig. 4-6 directly shows the effect of technical parameters on bonding strength analyzed by Mathematica. As shown in Fig.4, when spraying distance was 115mm and spraying current was 680A, bonding strength of composite coating was related to the value of primary gas flow and auxiliary gas flow. As primary gas flow was about 35 to 40slpm, the bigger auxiliary gas flow was, the larger rising amplitude of bonding strength was. While at primary gas flow was 40-50slpm, bonding strength descended initially and then rose, as auxiliary gas flow increasing. When auxiliary gas flow was 8-10slpm, bonding strength rose as primary gas flow becoming bigger. And at 10-16slpm, the bonding strength first increased and then decreased.

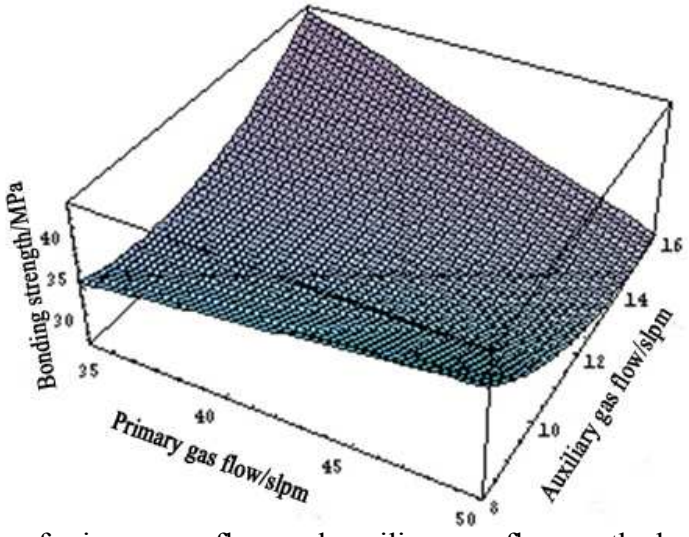

Fig. 4 Influence of primary gas flow and auxiliary gas flow on the bonding strength

Fig. 5 shows the influences of spraying current and primary gas flow on bonding strength at spraying distance =115mm and auxiliary gas flow =8slpm. When spraying current was 80-90A, the coating bonding strength increased first and then decreased along with the increasing of primary gas flow. Within this range, the bigger spraying current was, the larger rising amplitude and the smaller decrease amplitude were, as the primary gas flow increased. When primary gas flow was between 35 and 37slpm, with spraying current increasing, the bonding strength was rising. Bonding strength increased firstly and then decreased with the spraying current for 37-42slpm. At primary gas flow 42-50slpm, bonding strength was gradually declining with spraying current rising.

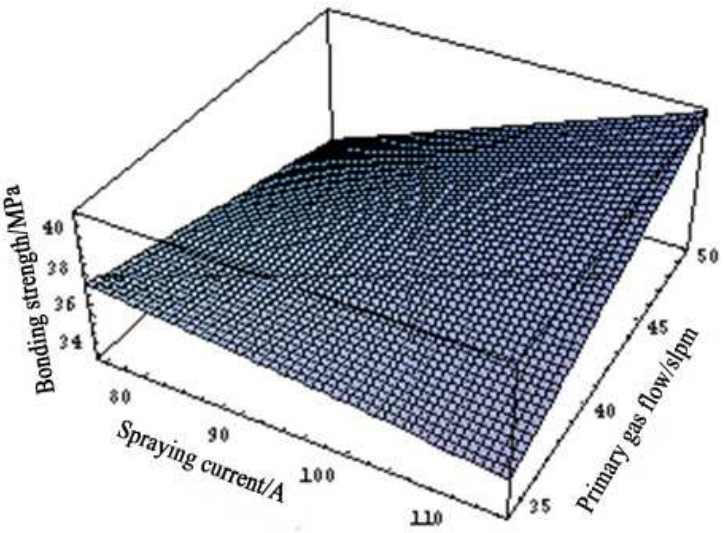

Fig. 5 Influence of spraying current and primary gas flow on the bonding strength

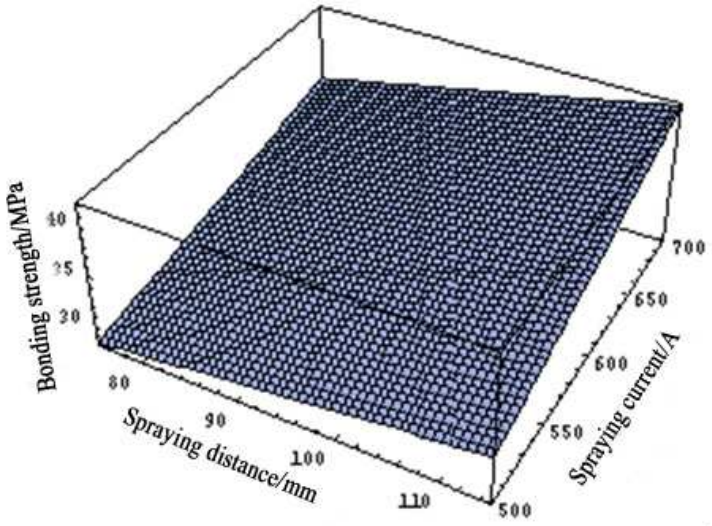

Fig. 6 Influence of spraying distance and spraying current on the bonding strength

Fig. 6 shows linear growth variation of bonding strength with the increasing of spraying distance in different spraying current, when primary gas flow was 50slpm and auxiliary gas flow was 8slpm. The same is the change regularity of bonding strength and spraying current.

Conclusions

The bonding strength of plasma sprayed HA/ZrO_2 composite coating is relevant to the spraying distance, spraying current, primary gas flow and auxiliary air flow.

Experiment data has been analyzed by quadratic polynomial regression with DPS, the bonding strength of HA coating under the optimized parameters of spraying distance 114.9mm, spraying current 680A, primary gas flow 49 L/min, auxiliary gas flow 8 L/min is 41.3MPa.

The bonding strength increases with the spraying current and spraying distance. The interaction of spraying distance and spraying current, spraying current and auxiliary gas flow, primary gas flow and auxiliary gas flow plays an important role on the bonding strength of composite coating.

Acknowledgments

The authors would like to acknowledge the Project 50975259 and 51105339 supported by Natural Science Foundation of China.

References

[1] Weng Lijie, Process parameters optimization and residual stress analysis for plasma sprayed HA composite coating, Zhejiang University of Technology, 2010(in Chinese)

[2] Zhu Qingxia, Feng Qing, Wang Heping, Review on preparation and research progress of hydrpxyapatite ceramics coating, China Ceramics. 44(2008)34-38 (in Chinese)

[3] R. Gadow, A. Killinger, N. Stiegler, Hydroxyapatite coatings for biomedical applications deposited by different thermal spray techniques, Surface & Coatings Technology. 205 (2010) 1157–1164

[4] F. Bru¨ckner, D. Lepski, E. Beyer, Modeling the Influence of Process Parameters and Additional Heat Sources on Residual Stresses in Laser Cladding, Journal of Thermal Spray Technology. 16(2007) 355-373

doi:10.4028/www.scientific.net/AMM.161.274

Simplified Calculation Model of Analyzing Concrete-filled Gypsum Wall Panels

Qing-zhen Ma[1,a] Xin-liang Jiang[2,b] Bao-kui Zhang[3,c]

[1]School of Commerce, Tianjin University of Commerce, Tianjin, 300134, China
[2]School of Civil Engineering, Tianjin University, Tianjin, 300072, China
[3]College of Civil Engineering, Hebei University of Technology, Tianjin, 300401, China
[a]mqz0122@126.com, [b]jiangxinliang@126.com(corresponding author), [c]zbk0101@126.com

Keywords: Composite material；Gypsum Wall Panels；Nonlinear analysis；Calculating model

Abstract. The simplified calculating model for concrete-filled gypsum wall panels was established. The method for calculating the moment-curvature relationship of concrete core and the force-displacement skeleton curves of shear element was then proposed. The test data of concrete-filled gypsum wall panels were analyzed based on this model. The calculated curves agreed well with the experimental ones, which proves that this model has the advantages of clear mechanical conception，simple calculation and relatively good accuracy，and is convenient for calculating integral structure.

Introduction

Gypsum wall panels consists of slaked gypsum，appending gypsum to industry，glass fiber without alkali and chemical additive are an Australian developed and manufactured building walls, which are entitled Rapid Wall because of installed space in construction site. Gypsum wall panels are manufactured in standard sizes of 12m long×3.05m（or 2.85m）high×0.12m thick. A typical cross-section of a standard panel is shown in Fig.1. The cavities inside the panel can be filled with various materials，such as concrete or insulation materials to serve different purposes，such as to increase the strength or the thermal and sound insulation of the walls[1,2,3,4]. Gypsum wall panels can replace tile or block buildings and economize both land and energy sources by reason of fast construction，simple construction techniques and high quality.

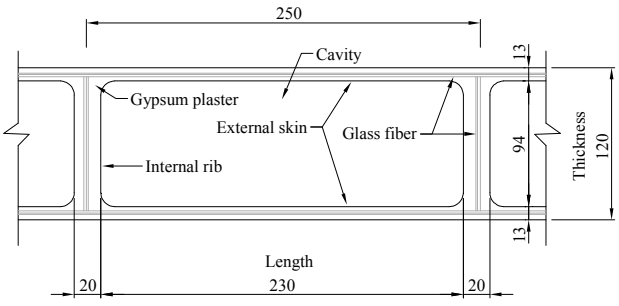

Fig.1 Cross-section of a gypsum wall panel

Concrete-filled gypsum wall panels（Composite panels）consist of reinforced concrete and fiber-reinforced plasterboard are composite bearing members，the reinforced concrete filled in the cavities form concrete cores, and one or two reinforcing bars are filled in a concrete core. The

composite panels can be used in higher buildings, resist both vertical and lateral loads. Not only the process status of the concrete core is different from the fiber-reinforced plasterboard in the course of loading，but also the relative action between the concrete cores and the fiber-reinforced plasterboard is different. In addition， The number of the model is so large that the calculation and constringency are difficult if a model is established by entity elements, so a large building consists of the composite panels is not analyzed based on the entity model. This paper established a simplified calculating model for calculating the composite panels in order to analyze an actual building.

Simplified Calculation Model

In an actual building consists of the composite panels，the closely spaced concrete cores filled in the cavities and the slab floor connected with anchor beam compose the whole frame construction. At the same time， the gypsum panel acts as a “link” between the concrete cores that restricts free relative movements between the concrete cores. Under the action of vertical load and cyclic lateral load， the concrete in the closely-spaced concrete frames and the fiber-reinforced plasterboard work together to resist load effects in which bending moments are mostly resisted by the concrete core， while shear forces are mostly resisted by the fiber-reinforced plasterboard. Therefore, the concrete cores fail in bending， while the plasterboard fail in shear and extrusion[5]. And so a new simplified calculation model named “frame + shear element” is proposed，in which the concrete core representing flexure behavior and the fiber-reinforced plasterboard representing shear behavior(Fig.2). Where H = the height of the wall panel; B = the horizontal length of the wall panel; n = the number of the concrete cores; K_h = stiffness of the shear element. It thinks that anchor beam is rigid on the basis of work performance of the composite panel under the action of vertical load and cyclic lateral load.

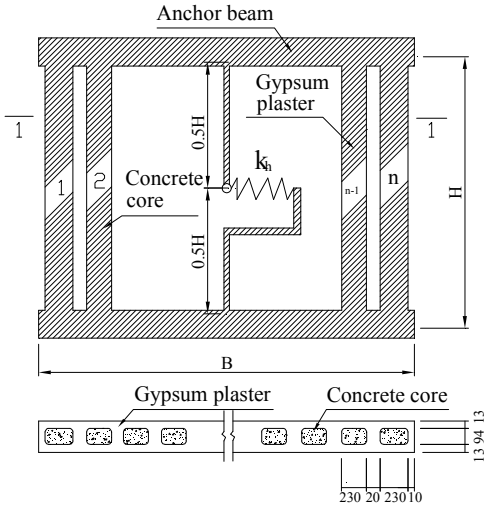

Fig.2 Simplified Calculation Model

Moment-curvature Relationship of a Concrete Core

Reinforcing bars inside the concrete core have little effect on the composite panel to resist cyclic lateral load depending on the test conclusion at the University of Adelaide in Australia [6]. Therefore, this paper ignores the function of the reinforcing bars in the concrete core when calculating a concrete core, regarded it as a plain concrete core. Because the concrete core would be valid as soon as it cracks, it only needs to calculate the cracking moment strength M_{cr} and the corresponding curvature φ_{cr} [7]as follows, respectively.

$$M_{cr} = \frac{rf_t I_0}{y} + \frac{N_0 I_0}{A_0 y} \quad \text{(Eq.1)}$$

$$\varphi_{cr} = \frac{M_{cr}}{0.85 E_c I_0} \quad \text{(Eq.2)}$$

in which r = elastic-plastic coefficient of the tension zone of the cross-section = 1.75 for rectangle cross-section; f_t = the tensile strength of the concrete. Owing to the lack of the test data it is determined from Code For Design of Concrete Structures (GB50010-2002); A_0 = cross-section area of a concrete core; I_0 = cross-section inertia of a concrete core; N_0 = initial axial load plus on a concrete core top; y = tension zone depth = 115mm = half of the cross-section of a concrete core; E_c = Young's modulus of the concrete, which is obtained by the test value.

Force-displacement Skeleton Curve of the Shear Element

The Force-displacement skeleton curve of the shear element is simplified as three lines (Fig.3).

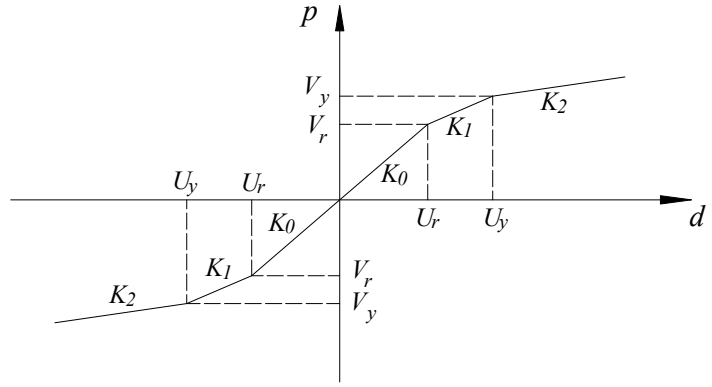

Fig.3 Force-displacement skeleton curves of the shear element

Initial Stiffness K0，Stiffness K1 after Cracking，Stiffness K2 after Yielding

Initial stiffness K_0 of the force-displacement skeleton curves is given by

$$K_0 = \frac{\alpha(1+3\lambda)G_{eq}A}{kH} \quad \text{(Eq.3)}$$

Where *Geq* = equivalent shear modulus of a composite panel; α = the felt coefficient between the concrete and gypsum panel =0.8，which is derived from tentative calculation on the basis of test conclusion; λ = ratio of initial axial load plus on a concrete core top to resisting strength of the corresponding concrete core $= N_0/(f_c A_0)$, f_c is the compression strength of the concrete, which is obtained by test conclusion. The test results [2,8] and the conclusion [9] show that the shear stiffness of a composite panel increases with an increase in λ; A = the total cross–section area of a composite panel; k = revised coefficient to balance distributed unequally shear stress =1.2 for rectangle section.

Both the stiffness K_1 after cracking and stiffness K_2 after yielding are

$$K_1 = 0.3K_0 \quad \text{（Eq.4）}$$

$$K_2 = 0.2K_0 \quad \text{（Eq.5）}$$

Where 0.3 is a stiffness relief coefficient after the composite panel cracks; 0.2 is a stiffness relief coefficient after the composite panel yields. The shear stiffness of the composite panel gradually decreases when the slip occurs between the concrete and the gypsum panel.

Since the material constituting the composite panel is composite, we educe G_{eq} on the basis of reference [10], and premise the shear strain of the concrete is equal to the fiber-reinforced plasterboard. The Geq is given by

$$G_{eq} = \frac{0.22G_p^2 + 0.78G_cG_p}{0.9376G_p + 0.0624G_c} \quad \text{（Eq.6）}$$

in which $G_c = 0.4E_c$;$G_p = 0.2E_p$;E_p = Young's modulus of the fiber-reinforced plasterboard, which is obtained by the test value.

Lateral cracking load V_r, lateral yielding load V_y

The fiber-reinforced plasterboard encircling the concrete cores has a great impact on the shear strength of the composite panel, and acts as a "link" between the concrete cores that restricts free relative movements between the concrete cores. The shear strength is largely determined by the shear strength of the plaster panel and apparently is not affected by the concrete strength and the reinforcement inside the concrete cores [2,8,11]. Shear test results have shown that the shear resistance increases with an increase in axial load [1,2], the shear strength with axial load can be calculated as

$$V_u = \left(q_u + 0.15N\right)B \quad \text{（Eq.7）}$$

Where q_u is the unit horizontal shear strength of the wall without axial load, which is found around about 67.66 kN/m from the Table1; N is the unit axial load.

The skeleton curve of the composite panel shows the cracking load and the yielding load, but it doesn't display clearly yielding point. Based on the shear test curves of the composite panel [2,8, 11,12], the yielding load and the cracking load are defined as 75% and 60% of the shear strength, respectively.

Table1 Test results of the composite wall panels specimen

Specimen	Reinforcing bar	Concrete	Length [mm]	Axial load [kN·m^{-1}]	Cracking load [kN·m^{-1}]	Yielding load [kN·m^{-1}]	Shear strength [kN·m^{-1}]	Load manner
A1	1ϕ12	C25	1520	——	52.63	51.97	65.79	monotonic
A2	1ϕ12	C25	1520	——	34.87	39.47	46.97	monotonic
B1	1ϕ12	C25	2020	——	61.88	59.41	83.71	monotonic
B2	1ϕ12	C25	2020	——	37.62	62.71	71.29	monotonic
B3	1ϕ12	C25	2020	——	53.47	59.41	72.77	monotonic
C1	1ϕ16	C20	1520	——	43.16	52.63	65.79	monotonic
D1	1ϕ16	C20	1520	60	51.45	57.89	74.34	monotonic
E1	1ϕ16	C20	1520	180	72.04	76.97	101.97	monotonic
F1	2ϕ12	C20	1520	184	61.84	67.11	105.92	cyclic
G1	2ϕ12	C30	1520	312	61.18	73.68	98.03	cyclic
H1	1ϕ12	C25	1520	62.5	48.03	57.89	73.03	monotonic

Analysis of the Concrete-filled Gypsum Wall Panels

The composite panel tests which are completed at Tianjin University [8,11,12] and the University of Adelaide in Australia[1] are selected to evaluate the reliability of the simplified model. Modeling parameters for the backbone curves is examined by conducting static pushover analyses. The comparison of measured (experimental) versus calculated (model) composite panel deformations is given in Fig.4. The conclusions are presented as follows.

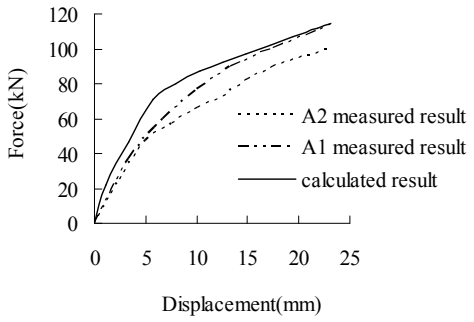

(a) specimen A1 and A2

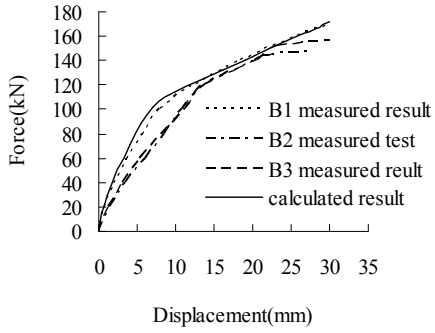

(b) specimen B1, B2 and B3

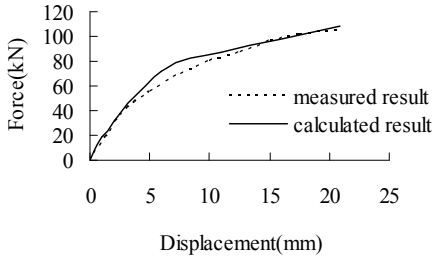

(c) specimen C1

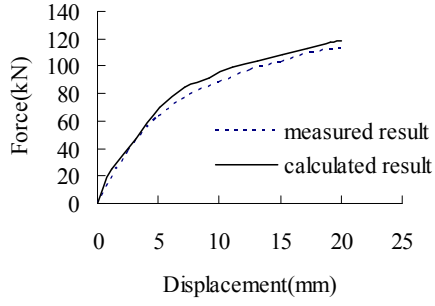

(d) specimen D1

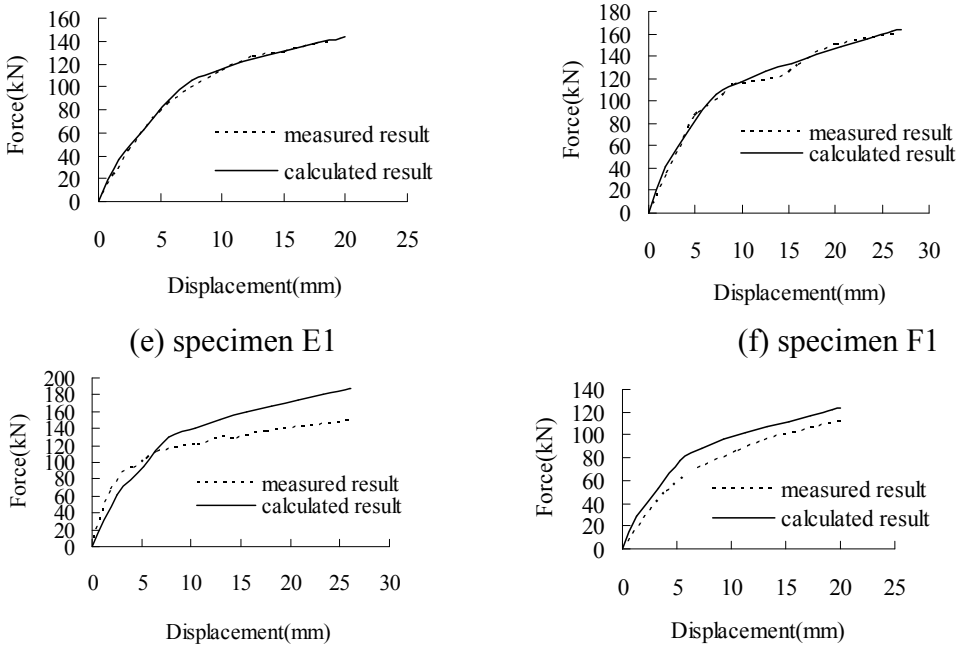

(e) specimen E1 (f) specimen F1

(g) specimen G1 (h) specimen H1

Fig.4 Lateral force-displacement curves of the composite wall panels

(i) The calculated displacement is smaller than the measured displacement under monotonic tests, the measured and calculated displacement show good agreement with each other under cyclic tests. The reason is that their load manners are different, the accumulative damage under cyclic tests is bigger than under monotonic tests, and which could explain that why the measured displacement under monotonic tests is higher than under cyclic tests. The calculated displacement does not represent the measured one in Fig.4(g), the reason is possibly the quality of the specimen. (ii) The calculated and measured base shear versus top displacement curves show good agreement with each other whether with axial load or without axial load, which indicate that the proposed simple model has good applicability.

Conclusions

(i) The proposed simple model as a tool for calculating the concrete-filled gypsum wall panels is simple but effective in nonlinear static analysis, its mechanical conception is clear，foundation of the model is simple, and accuracy is relatively good. Therefore, this model is convenient for calculating actual structure.

(ii) A felt coefficient between concrete and gypsum panel was proposed when calculating the shear stiffness of the model. At the same time, the ratio of initial axial load plus on the concrete core top to resisting strength of the corresponding concrete core was also involved in the shear stiffness of the model. The disposal of the shear stiffness made the calculated model more accord with the actual structure.

(iii) The concrete-filled gypsum wall panel is a sort of composite panel. This paper based on microcosmic mechanics rectangle model educed equivalent shear stiffness on the premise of equal strain, which is beneficial to one structure consists of more than two materials differed greatly in stiffness.

References

[1] Wu YF, A 2002 report into the physical testing and the development of design guidelines for the structural application of Rapid wall in building construction. Adelaide (Australia): Dare Sutton Clarke Engineers, 2002.

[2] Yu-Fei Wu, Mike P. Dare, Axial and Shear Behavior of Glass Fiber Reinforced Gypsum Wall Panels: Tests, Journal of Composites for Construction, ASCE. 8(6) (2004)569-578.

[3] Wu YF,The structural behavior and design methodology for a new building system consisting of glass fiber reinforced gypsum panels, Construction and Building Materials. 23(2009)2905-2913.

[4] YUE Jian-wei, JIANG Xin-liang, GU Yan, Mechanical behavior of glass fiber reinforced gypsum panels, J. Xi'an Univ. of Arch. & Tech.(Natural Science Edition).38(5)(2006)639-645.

[5] Jiang Xinliang，Liu Kang，Gu Yan，et al, Experimental frames-fiber research on behavior of closely spaced concrete reinforced plasterboard under low cyclic loading, Journal of Building Structures.25(4)(2004)50-54(in Chinese).

[6] Wu Yu-Fei, The effect of longitudinal reinforcement on the cyclic shear behavior of glass fiber reinforced gypsum wall panels: tests, Engineering Structures. 26(2004)1633-1646.

[7] He Zheng, Ou Jinping, Nonlinear analysis of reinforced concrete structures, first ed., Harbin Institute of Technology, Harbin, China, 2006(in Chinese).

[8] Liu Kang. Experimental Research and Finite-element Analysis on the Seismic Performance of Fiber-reinforced Plasterboard Filled with Concrete, Tianjin University, Tianjin ,China,2003 (in Chinese).

[9] Li Hongnan, Li Bing, Experimental study on seismic restoring performance of reinforced concrete shear walls, Journal of Building Structures. 25(5)(2004)35-41(in Chinese).

[10] Liu Xili, Wang Bingquan, Basis of Composite Mechanics, China Architecture＆Building Press, Beijing,China,1984 (in Chinese).

[11] Yue Jianwei, Jiang Xinliang, Tests of shear performance of rapid walls, J. of HUST. 23(1)(2006)27-30 (in Chinese).

[12] Liu K, Wu YF, Jiang X, Shear strength of concrete filled glass fiber reinforced gypsum walls, Mater Struct. 41(4) (2008)649-662.

doi:10.4028/www.scientific.net/AMM.161.281

The effect of initial void on the elasto-plastic properties of particle-reinforced composite coating

Shengting Gu [a], Yumei Bao[b], Guozhong Chai [c],

[1]Key Laboratory of E&M (Zhejiang University of Technology), Ministry of Education & Zhejiang Province, Hangzhou, P.R. China

[2]Taizhou Vocational College of Science & Technology, Taizhou, P.R.China

[a]gust1984@126.com, [b] baoym@zjut.edu.cn, [c] chaigz@zjut.edu.cn (corresponding author)

Keywords: particle reinforced composite coating; micro-voids; microscopic theory; elasto-plastic properties

Abstract. Many defects such as micro-voids, micro-cracks are introduced during the preparation of particle reinforced composite coating, which significantly change the mechanical properties of the coating. Based on Mori-Tanaka's concept of average stress in the matrix and Eshelby's equivalent inclusions microscopic theory, an incremental theory coupled with ABAQUS subroutine UMAT, is developed to study the influence of initial void and void growth on elasto-plastic properties of composite coating. In the composite containing hard spherical particles, debonding of particle-matrix interface is a significant damage process, and the effect of initial void on particle damage is also considered.

Introduction

Particle-reinforced composites coatings, due to their good strength, wear, and high temperature anti-oxidation performance, are widely used as engineering materials to improve the surface properties [1-2]. However, during the preparation of particle reinforced composite coating, many defects such as micro-voids, micro-cracks will be introduced, decreasing the elastic modulus, yield stress and fracture strength significantly [3-4]. Bohm[3] points out that using self-consistent method to predict the modulus of composite shows a little overestimation of results, because actual composite material containing internal defects. Gu[4] studies fracture strength of WC–Co_p/Cu bulk metal matrix composites by direct laser sintering, showing that as the relative density increase, the fracture strength decrease. Interfacial debonding between the matrix and inclusions and particle cracking are considered to be the most two important failure mechanisms[5]. Some researches show that the initial void will accelerate the damage of particle, leading to early fracture of material[6]. However, the growth of void is also responsible for the low ductility and low fracture[7].

In this investigation, a homogenization microscopic model is proposed to study the effect of initial void on elasto-plastic and damage behavior of particle-reinforced composite coating.

Effective elasto-plastic constitutive of three-phase composite coating

In the initial state, the microstructure of a three-phase composite coating consisting of a metal matrix, round particles and initial void (see Fig.1), is assumed to be statistically homogeneous and isotropic, with a constant volume fraction of particles and void. When composite coating is subjected to remote uniaxial tensile loading, some particles experience interface debonding between the matrix and particles. Of course, the presence of debonding particle will be subsequent growing. The debonded particle will lose its load-carrying capacity along the debonded direction. Here we assume that the debonded isotropic elastic particle is replaced by an equivalent void.

Considering a representative volume element (RVE) of the composite with total volume V, and let(V_m , V_p , V_v) denote the volumes of the matrix, particles, and voids in the RVE, so that $V = V_m + V_p + V_v$. The volume fractions of the matrix, particles, and voids are, respectively, $c_m = \frac{V_m}{V}$, $c_p = \rho = \frac{V_p}{V}$, $c_v = f = \frac{V_v}{V}$, in which $f + \rho + c_m = 1$.

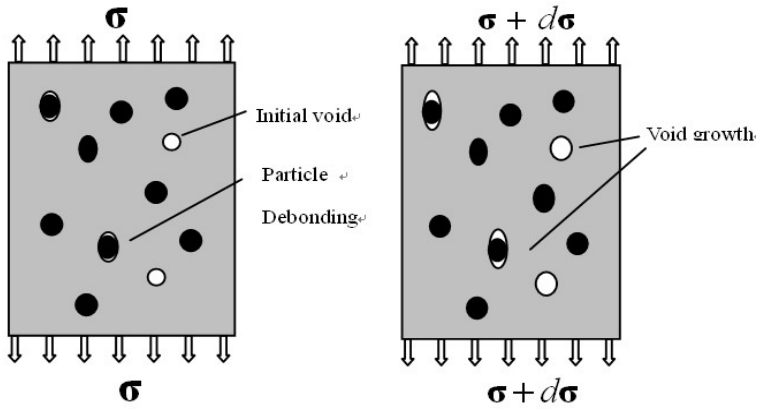

Fig. 1 Deformation of composite coating under remote tensile stress

Elasto-plastic constitutive of matrix. Supposing that the matrix and particle are isotropic materials, and particle is under elastic deformation, but the matrix is under elasto-plastic deformation and meet the Mises yield and isotropic hardening criterion. The constitutive of matrix for classical J_2 elasto-plasticity can be expressed in an incremental form:

$$\dot{\boldsymbol{\sigma}} = \mathbf{C}^m\left(\dot{\boldsymbol{\varepsilon}} - \dot{\boldsymbol{\varepsilon}}^p\right), f = \sigma_{eq} - \sigma_Y \le 0 \tag{1}$$

Where $\mathbf{C}^m$ is elastic stiffness tensor of matrix, σ_{eq} is Mises equivalent stress, σ_Y is yield stress.

So that the continuum elasto-plastic tangent of matrix is :

$$\mathbf{C}_{ep}^{m} = \mathbf{C}^{m} - \frac{4\mu^2}{3\mu + h}\frac{\partial f}{\partial \boldsymbol{\sigma}}\frac{\partial f}{\partial \boldsymbol{\sigma}} \tag{2}$$

Where f is yield function, μ is tangent modulus， h hardening parameter.

Elasto-plastic stiffness of three-phases composite coating. As Benveniste pointed out[8], the stiffness is zero, then the elasto-plastic stiffness tensor of three-phases composite $\overline{\mathbf{C}}_{ep}$ is:

$$\overline{\mathbf{C}}_{ep} = \mathbf{C}_{ep}^{m} + \rho\left(\mathbf{C}^{\mathbf{p}} - \mathbf{C}_{ep}^{m}\right)\mathbf{A}^{\mathbf{p}} - f\mathbf{C}_{\mathbf{ep}}^{\mathbf{m}}\mathbf{A}^{\mathbf{v}} \tag{3}$$

Where $\mathbf{C}^{\mathbf{p}}$ is particle elastic stiffness tensor. When matrix is under elastic deformation, $\mathbf{C}_{ep}^{m}$ will be replaced by $\mathbf{C}^m$. $\mathbf{A}^{\mathbf{p}}, \mathbf{A}^v$ are particle and void strain concentration tensor, respectively.

Based on the fundamental solution of Eshelby[9] of an elastic homogeneous ellipsoidal inclusion in an infinite linear elastic matrix and Mori-Tanaka[8] mean-filed theory, the macro elasto-plastic stiffness tensor can be expressed:

$$\overline{\mathbf{C}}_{ep} = \mathbf{C}_{\mathbf{ep}}^{\mathbf{m}} + \rho\left(\mathbf{C}^{\mathbf{p}} - \mathbf{C}_{\mathbf{ep}}^{\mathbf{m}}\right)\mathbf{T}^{\mathbf{p}}\left[c_m\mathbf{I} + \rho\mathbf{T}^{\mathbf{p}} + f\mathbf{T}^v\right]^{-1} - f\mathbf{C}_{\mathbf{ep}}^{\mathbf{m}}\mathbf{T}^v\left[c_m\mathbf{I} + \rho\mathbf{T}^{\mathbf{p}} + f\mathbf{T}^v\right]^{-1} \tag{4}$$

Where $\mathbf{I}$ is unit tensor， $\mathbf{T}^{\mathbf{p}}$ and $\mathbf{T}^v$ can be expressed as

$$\mathbf{T}^{\mathbf{p}} = \left[\mathbf{I} + \mathbf{E}\left(\mathbf{C}_{\mathbf{ep}}^{\mathbf{m}}\right)^{-1}\left(\mathbf{C}^{\mathbf{p}} - \mathbf{C}_{\mathbf{ep}}^{\mathbf{m}}\right)\right]^{-1}, \quad \mathbf{T}^v = \left[\mathbf{I} - \mathbf{E}\right]^{-1} \tag{5}$$

Where $\mathbf{E}$ is Eshelby tensor. $\mathbf{E}$ depends on the shape of the inclusion and on the tangent operator $\mathbf{C}_{ep}^{m}$ of the matrix.

Evolution of the phase volume fractions. In the absence of particle debonding under remote tensile stress, the volume of particle and void will be changed. The definition of $\rho = \frac{V_m}{V}$ yields

$$\dot{\rho}_g = \frac{V_p}{V} = \frac{-V_p \dot{V}}{V^2} = -\rho \dot{\varepsilon}_{kk} \tag{7}$$

Where $\dot{\varepsilon}_{kk}$ is volumetric deformation rate of RVE. Meanwhile, the void growth can be expressed:

$$\dot{f}_g = (1-f)\dot{\varepsilon}_{kk} \tag{8}$$

However, as the material deforms, new voids nucleate by particle debonding ,thus increasing the void volume ration (porosity) and decreasing the particle volume fraction as particles are turned into voids. For simplicity, the probability of particle interface debonding is controlled by internal tensile stress, and following Weibull distribution[3]:

$$P_v = 1 - \exp\left[-\left(\frac{\sigma^p}{S_0}\right)\right]^m \tag{9}$$

Where m and S_0 are the shape parameter and the scale parameter, respectively. Average debonding stress of the particle is given by

$$\overline{\sigma}^p = S_0 \Gamma\left(1 + \frac{1}{m}\right) \tag{10}$$

Where $\Gamma(\cdot)$ is the Gramma function. if the initial particle volume fraction is denoted by ρ_0, then the cumulative volume fraction of the damaged particle is represented by $\rho_0 P_v$, then we can get the Evolution of the particle and void volume fractions:

$$\dot{f} = (1-f)\dot{\varepsilon}_{kk} + \rho_0 \frac{\partial P_v}{\partial \sigma^p} d\sigma^p \quad , \quad \dot{\rho} = -\rho \dot{\varepsilon}_{kk} - \rho_0 \frac{\partial P_v}{\partial \sigma^p} d\sigma^p \tag{11}$$

Numerical results

The homogenization schemes is implemented into ABQUS software coupled subroutine UMAT. Here Young's modulus and Poisson's ratio of particle are $E_p = 5000\sigma_0$, $v_p = 0.17$, those of matrix are $E_m = 500\sigma_0, v_m = 0.3$. Assuming that particle and void are spherical, and the shape parameter $m = 5$, Average debonding stress $\overline{\sigma}^p_{\max} = 3.0\sigma_0$. The quivalent stress-equivalent plastic strain relation of the matrix is given by:

$$\sigma_e^0 = \sigma_0 \left(1 + \frac{\varepsilon_e^{0p}}{\varepsilon_0}\right)^{0.1}, \varepsilon_0 = \frac{\sigma_0}{E_0} \tag{12}$$

Where σ_0 is yield stress of the matrix. Such material has been studied by Tohko K [10] and L.H.Dai[11] . The initial void fraction are $f_0 = 0$， $f_0 = 5\%$ and $f_0 = 10\%$, the initial particle volume is $\rho_0 = 20\%$.

Fig.2 shows the relationship between modulus and particle volume with three different initial void volume. The first thing we can see that the modulus is increasing as particle volume grows under different intial void. The initial void has a significant influence on modulus, compared with matrix, as the intial void grows 5%, the module increases 10%.

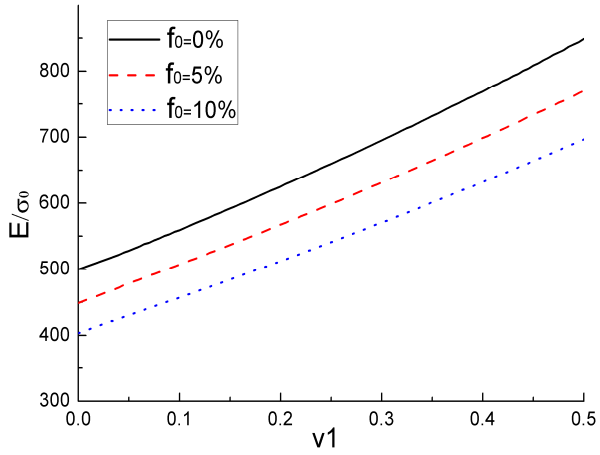

Fig.2 The effect of initial void on modulus

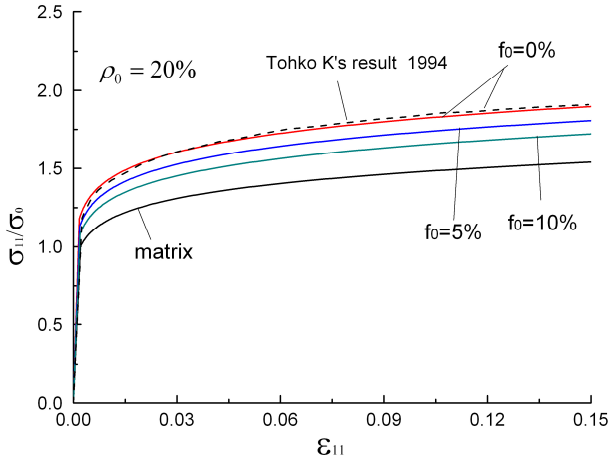

Fig.3 The effect of initial void on elasto-plastic properties without considering the particle damage

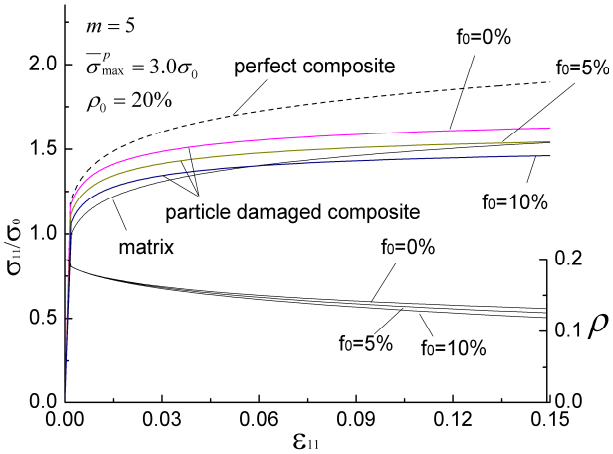

Fig.4 The effect of initial void on elasto-plastic properties considering the particle damage

The proposed theory of elasto-plastic properties is compare with Tohko's[10] result at $f_0 = 0\%$, $\rho_0 = 20\%$ to clarify its feasibility. Fig.3 also shows the effect of initial void on elasto-plastic properties of composite with no consideration of interface debonding. As the initial void volume fraction increase, the yield stress of composite is dramatically enhanced. When taking consideration of interface debonding, the effect of initial void volume on elasto-plastic properties of composite is showed in Fig.4. With continuous deformation of composite materials, debonding particles increased, thus resulting in material soften. At the equivalent plastic strain of 0.15, the volume fraction of particles reduced 7% at $f_0 = 0\%$, and the volume fraction of particles reduced 8.8%, at $f_0 = 10\%$, indicating that the initial volume fraction has increase the mount of interface

debonding. This could be understanding that the stiffness of void is zero, and can not bear any stress in the material under uniaxial tension, which enhanced the particle stress and increase the rate of particle debonding.

Conclusions

Based on Eshelby's equivalence principle and Mori-Tanaka mean-field theory, the macro elasto-plastic stiffness tensor of three-phase composite coating consisting initial void has been extracted. Furthermore, we assume that the interface debonding is controlled by the average stress of particle, and the probability of particle interface debonding is described by Weibull distribution function. The paper deals with the effect of initial void and void growth on elasto-plastic properties of composite material. The results showed that the mechanical properties of materials are greatly influenced by introducing voids. As the content of voids increased, the elastic modulus and yield strength of composites decreased significantly. Continuous deformation of composite materials, the debonding of the particles increases, which causes softening of the material. At the same time, the initial void content increased, broken rate of particle increased accordingly.

Acknowledgments

The authors would like to acknowledge the Project 50975259 and 51105339 supported by Natural Science Foundation of China.

References

[1] D. Liua, S.Q. Zhang, A.Li, H.M.Wanga, Microstructure and tensile properties of laser melting deposited TiC/TA15 titanium matrix composites, Journal of Alloys and Compounds. 485 (2009) 156–162.

[2] W. P. Jiang, P.Mollan, Nanocrystalline TiC powder alloying and glazing of H13 steel using a CO2 laser for improved life of die-casting dies, Surface and Coatings Technology. 135 (2001) 139-149.

[3] H.J. Bohm, A short introduction to basic aspects of continum micromechanics, Mechanics of Microstructured Materials. 55 (2004) 26-56.

[4] D.D. Gu, Y.F. Shen, Influence of reinforcement weight fraction on microstructure and properties of submicron WC-Co/Cu bulk MMCs prepared by direct laser sintering, Journal of Alloys and Compounds. 431(2007) 112–120.

[5] J.K. Kim, X.Sh. Gao , T.S, Srivatsan. Modeling of void growth in ductile solids: effects of stress triaxiality and initial porosity, Engineering Fracture Mechanics. 71 (2004) 379–400.

[6] T.-W. Kim, Heterogeneous void distribution in aluminum metal matrix composites and its effect on deformation-failure processes, Scripta Materialia . 55 (2006) 1115–1118.

[7] T.Pardoen, J.W.Hutchinson, An extended model for void growth and coalescence, Journal of the Mechanics and Physics of Solids. 48 (2000) 2467–2512.

[8] Y. Benveniste, A new approach to the application of Mori–Tanaka's theory in composite materials, Mechanics of Materials. 6 (1987) 147–157.

[9] J.D. Eshelby, The determination of the elastic field of an ellipsoidal inclusion and related problems, Mathematical and Physical Sciences. 241 (1957) 376–396.

[10] K. Tohko, T. W. Chou, Incremental theory of particulate-reinforced composites including damage, JSME International Journal, Series A. 39 (1996) 389-397.

[11] L.H. Dai, G.J. Huang, An incremental micromechanical scheme for nonlinear particulate composites, International Journal of Mechanical Sciences. 43 (2001) 1179-1193.

doi:10.4028/www.scientific.net/AMM.161.286

Analysis on Low Frequency Noise Induced by Spring Floating Slab

Li Li [a], Ye Tian[b] and Chuanzhi Geng[c]

Railway & Urban Mass Transit Research Institute, Tongji University, Shanghai, China, 201804

[a]lilee@tongji.edu.cn(corresponding author), [b]field2000@163.com, [c]gengchzh@163.com

Keywords: Steel spring floating slab, Vibration, Low frequency noise, Viscoelastic damp

Abstract. Floating slab track is a quality-spring vibration isolation system, which is the most effective ways to reduce the ground vibration and noise transmission. However it has other disadvantages, such as there is low frequency noise problem like "gu long gu long" in the carriage when the train runs across steel floating slab track (FST) area. According to this phenomenon, this paper compared the two different bearing floating slab noise data, studied their dynamic characteristics under train loads. From the isolation principle and noise radiation theory, explained the reasons causing the phenomenon and put forward relevant suggestions.

1 Introduction

In order to solve the subway vibration noise to environment influence along the buildings and residents living, during the subway construction process, when train runs across sensitive buildings and dweller building, steel spring floating slab track (FST) structures are used. As the lines with a large number of steel spring FST structure are in operation, there are low frequency noise like "gu long gu long" in the carriage when the train runs over the steel spring floating slab area, which affects passenger's comfort, and also cause the more and more attention of researchers[1]-[3].

2 Noise testing data in carriage when train runs over different track area

Aiming at the problem, noise data from different floating slab areas was measured in the carriage. One group of data (Fig.1-Fig.3) is the train run from common slab track to steel spring FST area. Being the contrast group(Fig.4-Fig.6), test train runs from common slab track area to high damp floating area. The test vehicle is for Shanghai metro line which is a full aluminum metro vehicle. Measured points were located in the center of 1.6 m place above the ground.

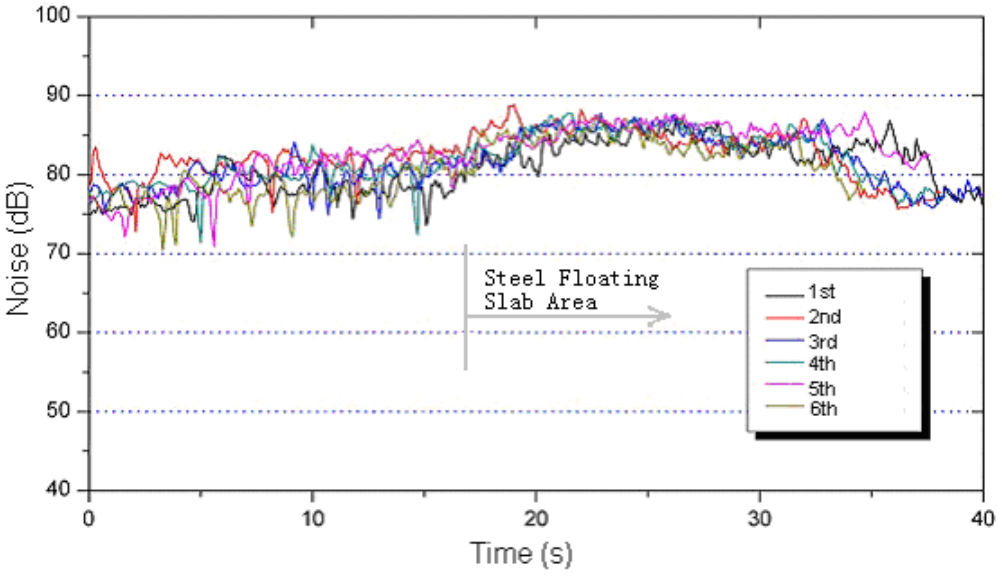

Fig.1 Noise time history curve in the carriage when train running into steel spring FST area from common slab track

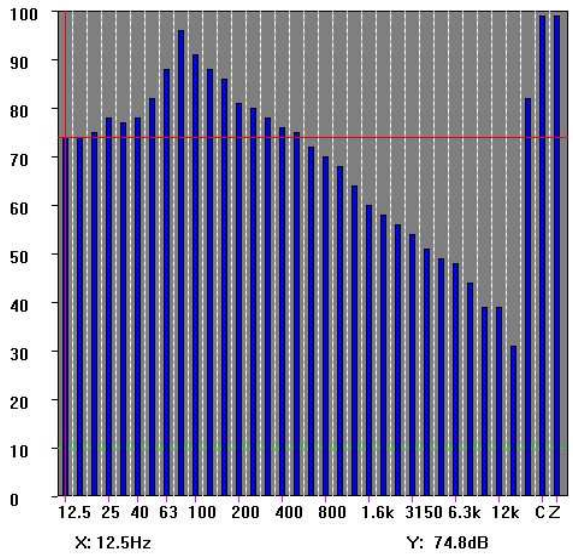

Fig. 2 Noise frequency domain curve (steel spring FST)

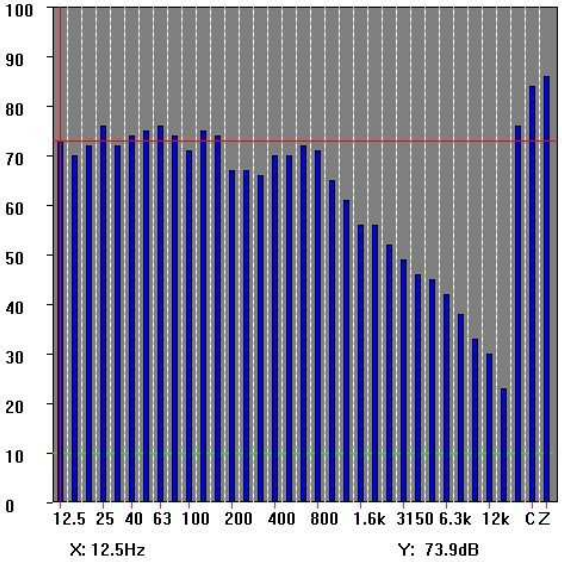

Fig.3 Noise frequency domain curves (common slab track)

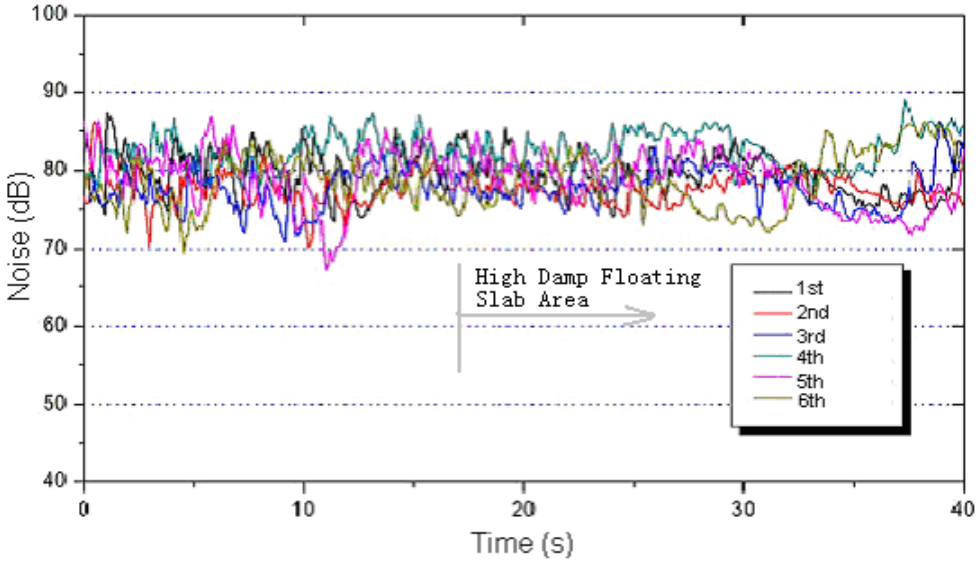

Fig.4 Noise time history curve in the carriage when train running into high damp floating slab area from common slab track

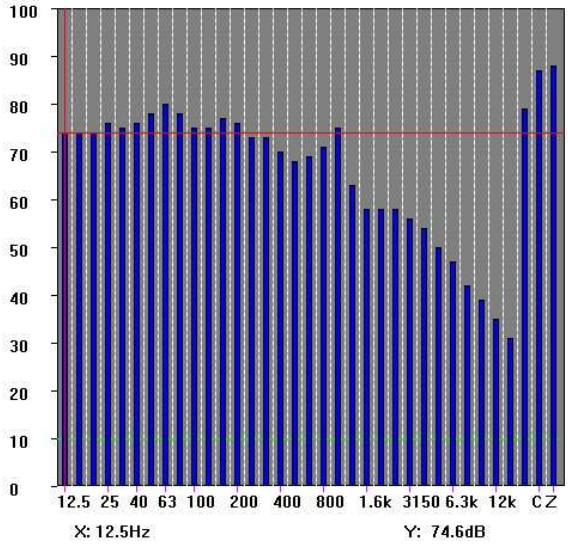

Fig.5 Noise frequency domain curve (high damp floating slab)

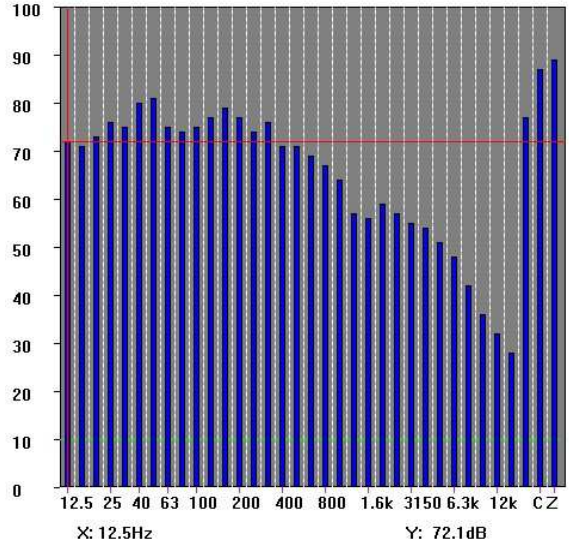

Fig.6 Noise frequency domain curves (common slab track)

The measured results from Fig.1 shows: noise in the carriage rises apparently when the train runs into steel spring floating slab area from common railway track. The different value is approximately 5dB. The frequency distribution can be gotten from the comparison of noise frequency domain curve in Fig.2 and Fig.3. Noise peak in the carriage occurs in the range of 25Hz to 400Hz when the train crosses over steel floating slab. However, there is no such value in common slab track area.

The data from Fig.6 shows: noise in the vehicle rises unapparent when the train moves over high damp floating slab. Noise frequency domain curve in Fig.5 and Fig.6 also indicates there is no obvious change in the area of high damp floating slab and common slab track.

3. Low frequency noise analysis

The low frequency noise refers to the frequency less than 500 Hz. The noise peak in the carriage (25Hz to 400Hz) belongs to the range of low frequencies.

All the noise will cause harm to human body. Although the direct influence of low frequency noise to one's physical is not as obviously as high frequency noise does, the low-frequency noise has the long term effects to human's health. However, the dangers of low frequency noise have not get people's enough attention.

The damage of low frequency noise to the human body is very big. And the most easily overlooked is to hearing damage, especially cardiovascular system and nerve system. Low frequency noise can cause headaches, such as insomnia neural function disorder. It even has big effect on the fetus.

From the tests above it can be known that the low frequency noise (25Hz to 400Hz) is caused by steel spring floating slab. FST is a quality- spring-vibration isolation system. It has good effects to isolate the vibration and vibration-borne sound to the base or ground. Through isolation vibration theory, FST system is equivalent a filter. The vibrations in rail transportation mainly distribute in the range of 20Hz- 80Hz, and the first several orders' natural frequency of the FST is commonly 7Hz-10Hz. The most vibrations below the first several modes are filtered.

However steel spring FST doesn't reduce the vibration and noise in the carriage. Fig. 7 and Fig 9 are vibration of steel spring FST varying in frequency domain. Fig.8 and Fig.10 are vibration of common slab track. From the four figures it can be seen that the value in steel spring FST is bigger about 20 dB than in common slab track. In general there is more low frequencies' vibration in steel spring FST, especially in the range of 100Hz-500Hz.

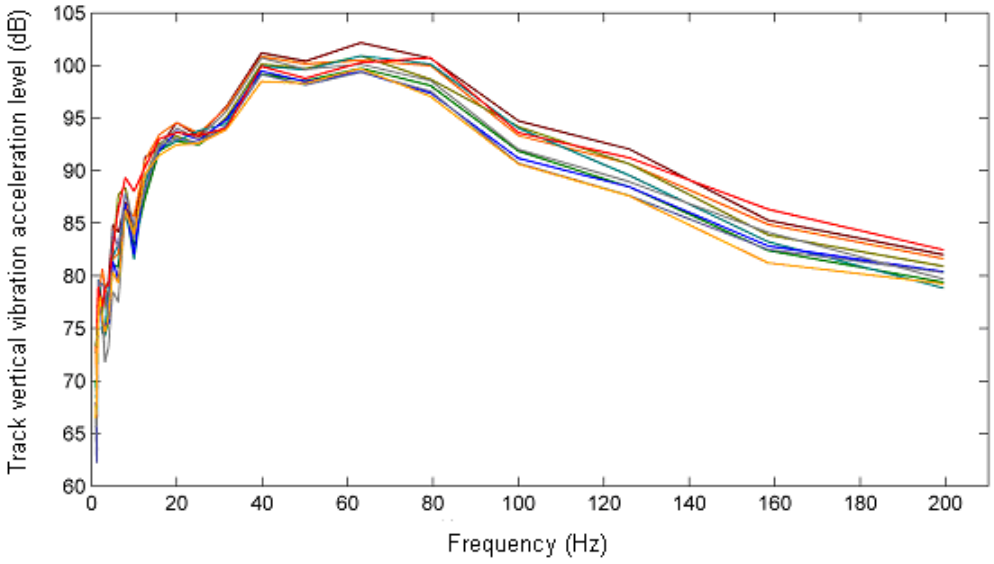

Fig.7 Track vertical vibration acceleration level (steel spring FST)

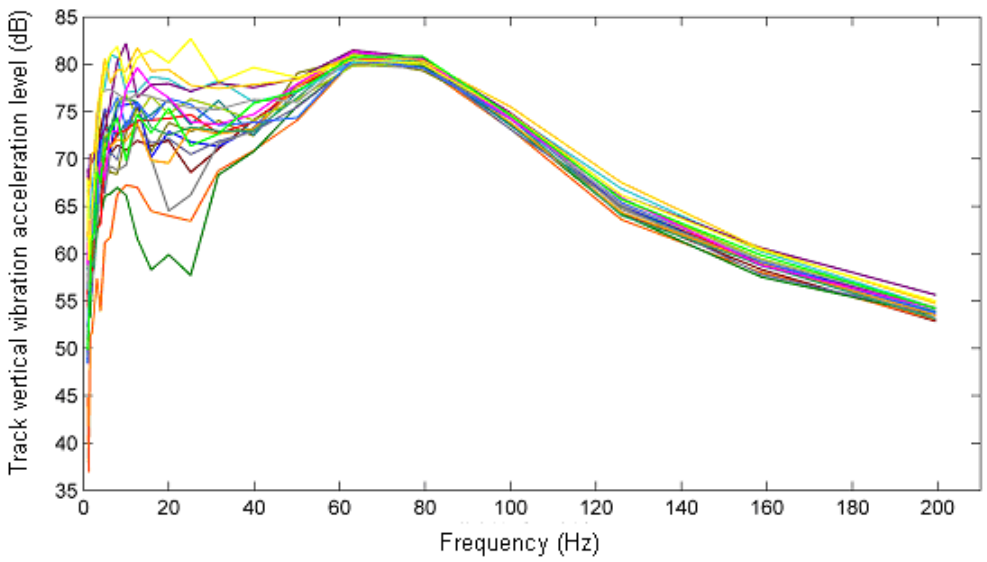

Fig. 8 Track vertical vibration acceleration level (common slab track)

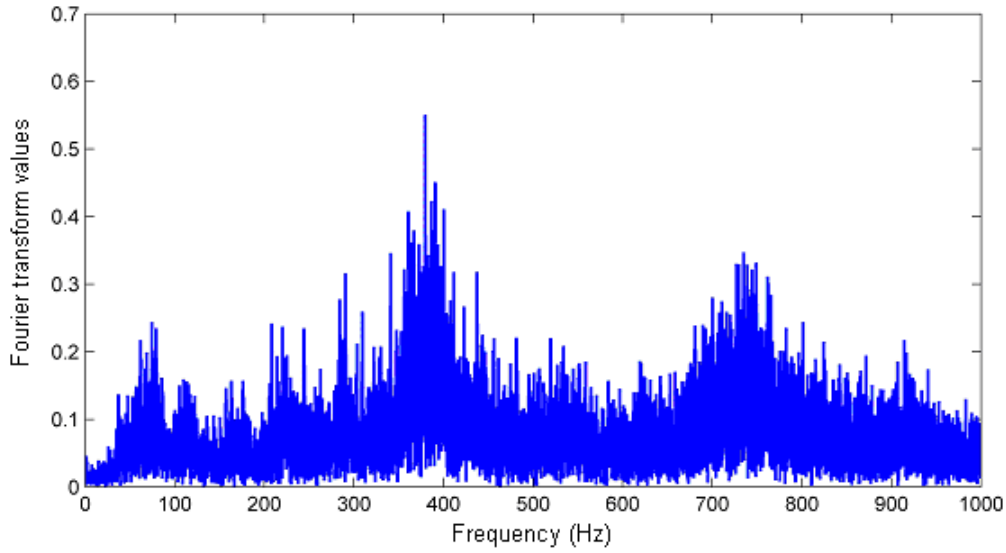

Fig. 9 Track vertical vibration acceleration after Fourier transforms (steel spring FST)

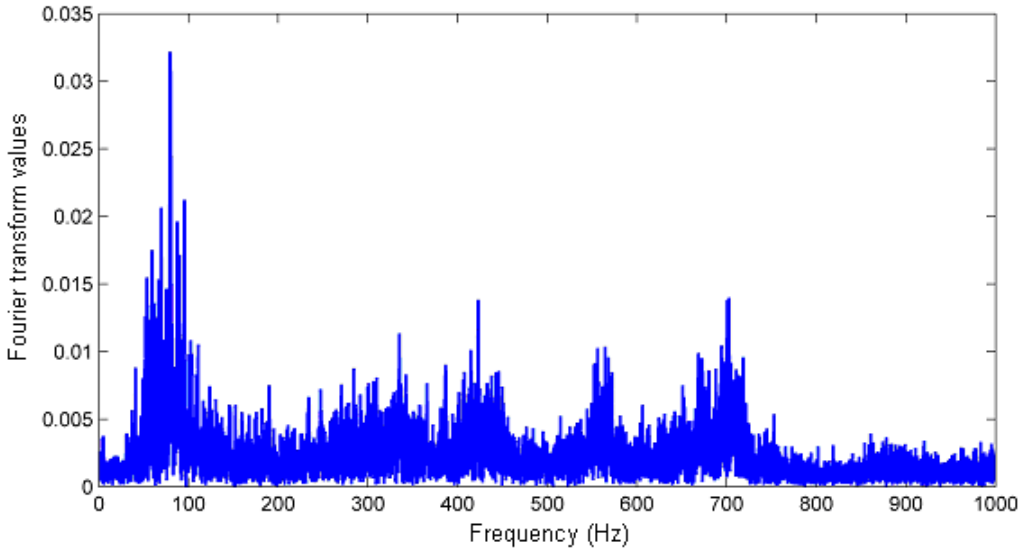

Fig. 10 Track vertical vibration acceleration after Fourier transforms (common slab track)

According to the transmission ways' division, low frequency noises are mainly divided into sound transmission structure, air sound transmission and standing wave [4][5]. In the train- track system, when steel spring FST vibrates, all the components of FST vibrate at the same time, including the steel spring bearing. FST-borne noise is magnified by steel spring bearing. The noise travels into the vehicle by the air from the gap of vehicle structure. In addition the vibration transmits to the vehicle's ground through wheel and bogie, which causes the ground vibrate, and then produces the second noise. The range of low frequency noise (25Hz to 400Hz) covers the above resource noise.

4 Suggestions

As the damping ratio of vibration isolator in steel spring FST is only greater that 0.05, in the process of impact between wheel and rail, vibration energy can not effectively be consumed. On the contrary it aggravates the vibration of floating slab and the vehicle, and results in noise increase. Considering the viscoelastic damping materials with convenient installation, low cost, antivibration noise reduction effect is obvious, it can be developed high damping performance of viscoelastic materials used in floating slab of vibration isolators. The test data in Fig.5 verified this method is feasible.

Acknowledgements

This work was financially supported by the Fundamental Research Funds for the Central Universities (Tongji University), National Science and Technology Support Plan (2009BAG11B02).

References

[1] D. Ding, W. Liu, K. Li, etc, Low frequency vibration tests on a floating slab track in an underground laboratory, J. Zhejiang Univ-Sci A (Appl Phys & Eng) 12(5) (2011) 345-359.

[2] G. Lombaert, G. Degrande, B. Vanhauwere, etc, The control of ground-borne vibration from railway traffic by meas of continuous floating slabs, J. Sound and Vibration, 297 (2006) 946-961.

[3] P. Galvin, A. Romero, J. Dominguez, Vibration induced by HST passage on ballast and non-ballast tracks, Soil Dynamics and Earthquake Eng. 30 (2010) 862-873

[4] L. Cremer, M. Heckl, B. A. T. Petersson, Structure-Borne Sound Structural Vibration and Sound Radiation at Audio Frequencies, third ed., Springer, 2005.

[5] M. Norton, D. Karczub, Fundamentals of Noise and Vibration Analysis for Engineers, second ed., Cambridge Press, 2003

doi:10.4028/www.scientific.net/AMM.161.292

Three Dimensional Surface Patterning atop Poly(methyl methacrylate) (PMMA)

Yong Zhao[1,a], Wei Min Huang[1,b] and Hendra Purnawali[1,c]

[1]School of Mechanical and Aerospace Engineering, Nanyang Technological University, Singapore.

[a]zhao0102@ntu.edu.sg, [b]mwmhuang@ntu.edu.sg (corresponding author), [c]phendra@ntu.edu.sg.

Keywords: Shape memory polymer, 3D surface patterning, shape recovery, swelling.

Abstract. We demonstrate a novel approach to fabricate three dimensional (3-D) surface patterns atop poly(methyl methacrylate) (PMMA). This approach utilizes both shape recovery behavior and swelling phenomenon of the PMMA. The simplicity in the fabrication process affirms the low-cost nature of this approach. Moreover, as obtained 3-D patterned PMMA sample can be used as artificial compound eye.

Introduction

Well defined surface patterns atop a polymer substrate is very much useful in a wide range of applications, such as self-cleaning [1], integrated circuits [2], cell sensors [3], optical elements [4] etc. Comparing with patterns atop flat substrate (two dimensional surface patterns) [5-10], patterning atop a curved substrate (three dimensional, 3-D, surface patterns) [11-15] is much more complicated. Recently, some 3-D surface patterning techniques have been reported, such as polymer replication [11], ultraprecision machining [12], laser lithography [13], soft lithography [14], wrinkling atop curved substrate [15] and so on. However, these methods were either tedious in process [11-13] or poor accuracy in performance [14]. Therefore, a simple and cost-effective fabrication technology is in great demand.

Here, we introduce a new 3-D surface patterning method, which is based on the shape memory effect (SME) and swelling behavior of PMMA. This method is simpler and easier as compared with many existing methods, such as lithography, self-assembly and imprinting; and has the advantage in terms of precise control of the patterned area, which is lacking in wrinkling based patterning method [15]. In this article, this method is applied for patterning atop PMMA, a commonly used optical polymer, i.e. for 3-D patterns, which provides a cost-effective fabrication technique for artificial compound eye in optics applications.

Experimental details

Materials. 1 mm thick PMMA plates and 5 mm diameter PMMA rods were purchased from Ying Kwang Acrylic Trading, Singapore, with grade A and glassy transition temperature (T_g) of about 110°C. Thermal mechanical properties characterization was done on the PMMA plates by dynamic mechanical analysis (DMA) test; and micro protrusive patterns were fabricated atop the PMMA rods. Before experiments, all the PMMA samples were annealed at 140°C for 2 hours. Ethanol (95%) was purchased from Best Chemical Co. (S) Pte Ltd, Singapore and it was used as chemo-stimuli for surface patterning of PMMA.

Thermal mechanical properties of PMMA. Fig. 1 shows the DMA results of PMMA. The DMA test (using DMA7, Perkin Elmer) was conducted at a temperature range from 10°C to 150°C, at a rate of 5°C /min, with a static force of 11 mN, dynamic force of 10 mN and at a frequency of 1 Hz. From the DMA results, onset T_g based on storage modulus curve is about 118°C, which is slightly higher than the value provided by the manufacturer. In this paper, T_g is a very important parameter for designing and conducting surface patterning atop PMMA.

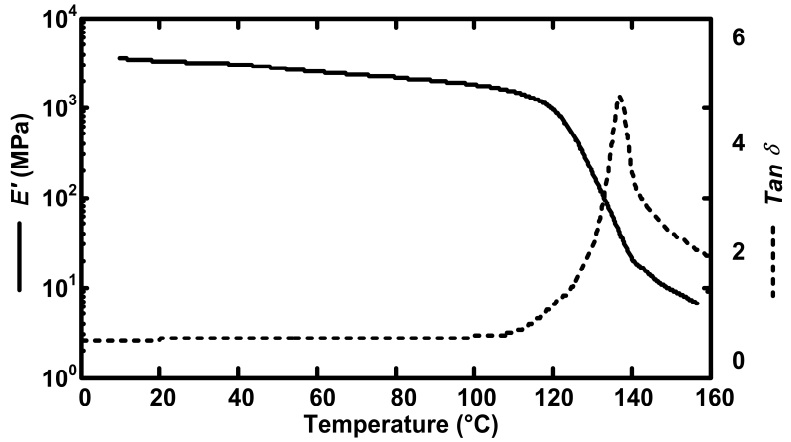

Fig. 1 DMA results of PMMA.

3D surface patterning procedure. Fig. 2 shows 3-D surface patterning procedure atop PMMA. This method is based on two kinds of phenomena. One is pre-strain enhanced swelling (PSES) effect; the other is the SME. Typically, 3-D surface patterns can be fabricated following a four-step procedure:

Step 1: A hemi-spherical (or hemi-cylindrical) PMMA sample is compressed by a maximum load, P_1, using a materials testing machine (e.g. Instron machine). After a loading/unloading process, residual stress field, σ_{r1}, is stored in the deformed sample, as shown in Fig. 2 (a).

Step 2: After compression (step 1), micro-indents array is fabricated atop the pre-compressed PMMA sample by a maximum load, P_2, using a micro indenter (e.g. Micro-Hardness tester, CSM Instrument). After a loading/unloading process, residual stress field, σ_{r2}, is stored around the indents array, as shown in Fig. 2 (b).

Step 3: After indentation (step 2), the PMMA sample is immersed in the ethanol and swelling happens subsequently due to ethanol absorption. Based on the PSES effect, if $\sigma_{r2} > \sigma_{r1}$, the PMMA sample will swell into micro-protrusion array, as shown in Fig. 2 (c).

Step 4: After the micro-protrusion array is formed, the PMMA sample is placed into an oven for ethanol evaporation. Usually, stable protrusion array is obtained after 24 hours heating at 60°C. Then, the PMMA sample is heated to 120°C (higher than T_g) for 1~5 minutes, so that stable 3D surface patterns can be obtained due to the shape recovery process, as shown in Fig. 2 (d).

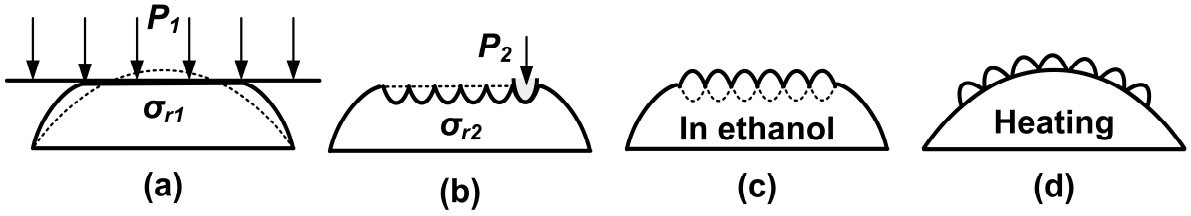

Fig. 2 Illustration of 3D surface patterning procedure.

Results and discussion

3-D patterns fabrication. Fig. 3 shows typical results of micron-protrusions array (4×2 and 5×5) atop PMMA cylindrical substrate following the procedure shown in Fig. 2. In the first step, a 5 mm diameter PMMA rod was compressed by 1.5 mm, at a strain rate of $0.001s^{-1}$ at room temperature. Next, 4×2 indents array was fabricated using a 20 μm radius spherical indenter with a maximum load of 0.5 N, at a loading/unloading rate of 15 mN/s and with a 10s holding period. On the other hand, the 5×5 indents array was fabricated using the same indenter and holding period, but now with a maximum load of 0.15 N and at a loading/unloading rate of 5 mN/s. In the third step, the pre-indented PMMA sample was immersed into room temperature ethanol. Due to the PSES effect,

protrusions were fully formed after 12 hours in ethanol. Finally, the sample was heated to 60°C for 24 hours for ethanol desorption; and then the stable sample was heated to 120°C for 1 mins. Due to the SME, the flattened PMMA sample recovered its original cylindrical shape. A surface scanning instrument (e.g. Talyscan 150 3D, Taylor Hobson) was used to obtain the 3-D surface profiles, as shown in Fig.3. The size of a single protrusion in Fig. 3 (a) is about 200 ± 2 μm in width and 40 ± 0.5 μm in height; and in Fig. 3 (b) is about 100 ± 1 μm in width and 7 ± 1 μm in height.

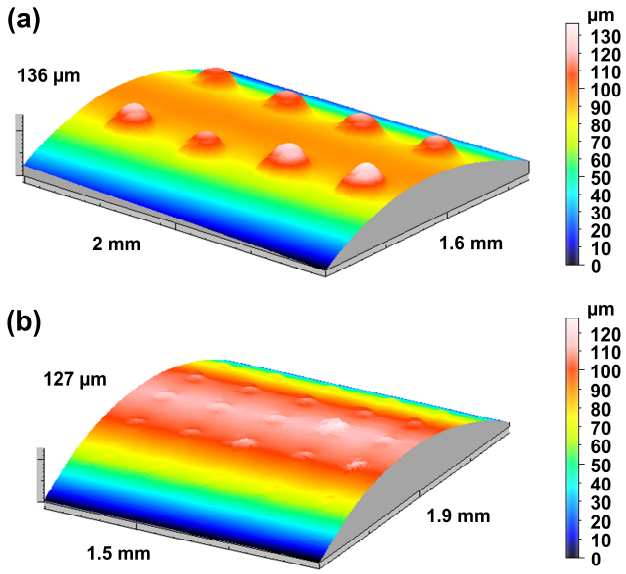

Fig. 3 3-D surface patterns atop PMMA. (a) 4×2 protrusions array; (b) 5×5 protrusions array.

Applications. As obtained 3-D PMMA patterns can be used as artificial compound eye. Compound eye is very efficient for local and global motion analysis over a large field-of-view (FOV) [11]. Moreover, it can provide a more efficient visual ability for large FOV imaging and motion analysis. Here, the optical performance of 3-D PMMA patterns was characterized using an optical microscope system (Axiotech 100 HD, Carl Zeiss) (reported in our previous paper [16]). The 3-D patterned PMMA sample was fixed on the sample stage and illuminated with white light through a mask, which is made of a black paper with a word "NTU" cut out of it. Miniaturized image of the "NTU" word was projected through the 3-D PMMA patterns and captured by a CCD system. Fig. 4 shows the protrusions and projected images of the "NTU" words. The projected image is clear in the center protrusion since the light focus is on the center plane and therefore, further away from the center, the projected image is blurred. Each protrusion has its own focus spot depending on its position, which is just the character of a compound eye.

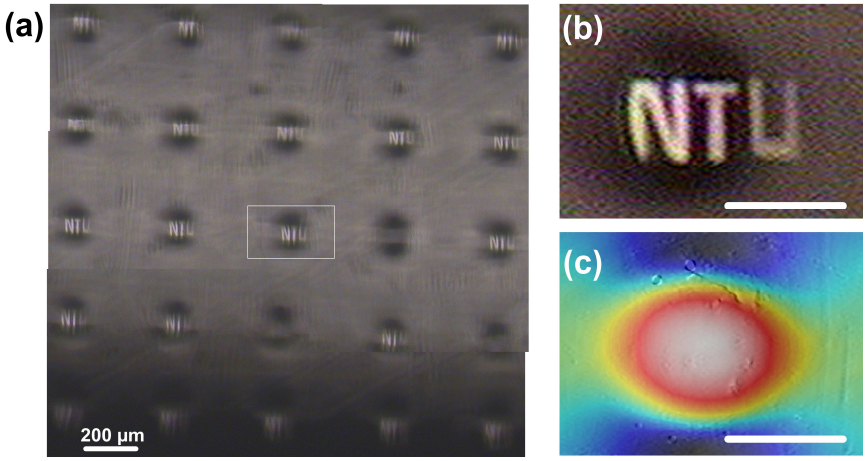

Fig. 4 5×5 protrusions array atop 5 mm diameter PMMA rod. (a) Projected image; (b) zoom-in view of the center plane of (a); (c) surface image of a single protrusion. Scale bar in (b) and (c) is 50μm.

Conclusions

In summary, we demonstrate a novel technology to fabricate 3-D surface patterns atop PMMA. This technology utilizes the combination of the SME and the PSES effect, which is simple and cost-effective. As fabricated 3-D PMMA patterns can be used in optics applications as artificial compound eye.

Acknowledgements

This project is partially supported by A*STAR (SERC Grant NO: 092 137 0016), and DSO (DSOCL09292), Singapore.

References

[1] R. Blossey, Self-cleaning surfaces-virtual realities, Nat. Mater. 2 (2003) 301-306.
[2] D. Y. Khang, H. Jiang, Y. Huang and J. A. Rogers, A stretchable form of single-crystal silicon for high-performance electronics on rubber substrates, Science 311 (2006) 208-212.
[3] E. Ostuni, C. S. Chen, D. E. Ingber and G. M. Whitesides, Selective deposition of proteins and cells in arrays of microwells, Langmuir 17 (2001) 2828-2834.
[4] P. Yang, G. Wirnsberger, H. C. Huang, S. R. Cordero, M. D. McGehee, B. Scott, T. Deng, G. M. Whitesides, B. F. Chmelka, S. K. Buratto and G. D. Stucky, Mirrorless lasing from mesostructured waveguides patterned by soft lithography, Science 287 (2000) 465-467.
[5] Y. Xia and G. M. Whitesides, Soft lithography, Annu. Rev. Mater. Sci. 1998, 28, 153-184.
[6] S. H. Kim, M. J. Misner, T. Xu, M. Kimura and T. P. Russell, Highly oriented and ordered arrays from block copolymers via solvent evaporation, Adv. Mater. 16 (2004) 226.
[7] J. L. Guo, Nanoimprint lithography: Methods and material requirements, Adv. Mater. 19 (2007) 495-513.
[8] N. Bowden, S. Brittain, A. G. Evans, J. W. Hutchinson and G. M. Whitesides, Spontaneous formation of ordered structures in thin films of metals supported on an elastomeric polymer, Nature 393 (1998) 146-149.
[9] Y. Zhao, W. M. Huang and Y. Q. Fu, Formation of micro/nano-scale wrinkling patterns atop shape memory polymers, J. Micromech. Microeng. 21 (2011) 067007.
[10] C. J. Kloxin, T. F. Scott, H. Y. Park and C. N. Bowman, Mechanophotopatterning on a photoresponsive elastomer, Adv. Mater. 23 (2011) 1977-1981.
[11] K. H. Jeong, J. Kim and L. P. Lee, Biologically inspired artificial compound eyes, Science 312 (2006) 557-561.
[12] L. Li and A. Y. Yi, Development of a 3D artificial compound eye, Opt. Express 18 (2010) 18125-18137.
[13] D. Radtke, J. Duparré, U. D. Zeitner and A. Tünermann, Laser lithographic fabrication and characterization of a spherical artificial compound eye, Opt. Express 15 (2007) 3067-3077.
[14] X. F. Gao, X. Yan, X. Yao, L. Xu, K. Zhang, J. H. Zhang, B. Yang and L. Jiang, The dry-style antifogging properties of mosquito compound eyes and artificial analogues prepared by soft lithography, Adv. Mater. 19 (2007) 2213-2217.
[15] L. Sun, Y. Zhao, W. M. Huang and T. H. Tong, Formation of combined surface features of protrusion array and wrinkles atop shape-memory polymer, Surf. Rev. Lett. 16 (2009) 929-933.
[16] Y. Zhao, C. C. Wang, W. M. Huang, H. Purnawali and L. An, Formation of micro protrusive lens arrays atop poly(methyl methacrylate), Opt. Express 19 (2011) 26000-26005.

Keywords Index

Authors Index

Z